SLAC-417
SLAC/SSRL-0027
UC-411, 413
(SSRL-M)

NUCLEAR DYNAMICAL DIFFRACTION USING SYNCHROTRON RADIATION*

Dennis Eugene Brown

Stanford Linear Accelerator Center
Stanford Synchrotron Radiation Laboratory
Stanford University, Stanford, California 94309

May 1993

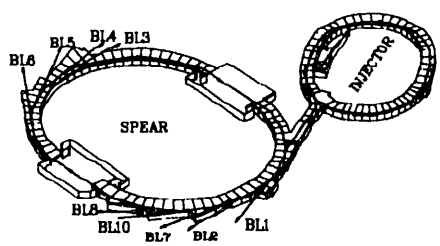

Prepared for the Department of Energy under contract number DE-AC03-76SF00515

Printed in the United States of America. Available from the National Technical Information Service, U.S. Department of Commerce, 5285 Port Royal Road, Springfield, Virginia 22161

* Ph.D. thesis

This thesis is dedicated to Mom and Dad:

Joyce and Isaiah Brown

ABSTRACT

The scattering of synchrotron radiation by nuclei is extensively explored in this thesis. From the multipole electric field expansion resulting from time-dependent nonrelativistic perturbation theory, a dynamical scattering theory is constructed. This theory is shown, in the many particle limit, to be equivalent to the semi-classical approach where a quantum mechanical scattering amplitude is used in the Maxwell inhomogeneous wave equation. The Mössbauer specimen whose low-lying energy levels were probed is a ferromagnetic lattice of ^{57}Fe embedded in a yttrium iron garnet (YIG) crystal matrix. The hyperfine fields in YIG thin films were studied at low and room temperature using time-resolved quantum beat spectroscopy. Nuclear hyperfine structure quantum beats were measured using a fast plastic scintillator coincidence photodetector and associated electronics having a time resolution of 2.5 nsec. The variation of the quantum beat patterns near the Bragg [0 0 2] diffraction peak gave a Lamb-Mössbauer factor of 8.2 ± 0.4. Exploring characteristic dynamical features in the higher order YIG [0 0 10] reflection revealed that one of the YIG crystals had bifurcated into two different layers. The dynamics of nuclear superradiance was explored. This phenomenon includes the radiative speedup exhibited by a collective state of particles, and, in striking concurrence, resonance frequency shifts. A speedup of a factor of 4 in the total decay rate and a beat frequency shift of $1\frac{1}{2}$ natural resonance linewidths were observed. Nuclear resonance scattering was also found to be a useful way of performing angular interferometry experiments, and it was used to observe the phase shift of a rotated quantum state. On the whole, nuclear dynamical diffraction theory has superbly explained many of the fascinating features of resonant magnetic dipole radiation scattered by a lattice of nuclei.

ACKNOWLEDGMENTS

I wish to thank all the members of the nuclear resonance scattering group at the Stanford Synchrotron Radiation Laboratory (SSRL) for their help in making this research possible. I give special thanks to George Brown, my research advisor, for giving me the opportunity to do this thesis. I greatly appreciate his tireless, diplomatic efforts that lead to doing experiments on PEP and on SPEAR (whose arms he had to twist to obtain special timing mode runs on SPEAR are unknown, but hopefully his efforts will have contributed to making timing mode operations a necessary feature on all synchrotrons). I also must thank John Arthur for all the help he provided me throughout my project--he had an unerring, keen insight into understanding the multitude of interesting physical phenomena and puzzles frequently faced by the nuclear scattering group. I also must thank Stan Ruby for the wealth of ideas he provided me--he had a seemingly uncanny ability to come up with fascinating, novel ideas in fundamental physics almost weekly. I also thank Alfred Baron for many thoughtful discussions and for trudging through portions of this thesis paper and correcting some of the formulas in the text.

I give thanks and praise to the members of the staff at SSRL (such as Arthur Bienenstock for allowing timing mode runs on SPEAR, Sean Brennan for his SUPER 4-circle diffractometer program and his database of Cromer and Liberman's electronic scattering factors, Teresa Troxel for initial beamline support, Glen Kerr and Pierre Capeder for electronics support, and Hans Przybylski and Chuck Troxel, Jr. who were machine shop wizards at constructing the precision apparatus needed to do crystal diffraction experiments, and to many others), at SLAC (such as Burt Richter for allowing parasitic synchrotron user runs on PEP during high energy physics runs), and at CHESS (such as Bob Batterman who provided a bright and dilligent grad student, Sarvjit Shastri, to collaborate with during a run on CESR). I also thank Gopal Shenoy and Ercan Alp from Argonne National Labs for their collaborative help during initial nuclear resonance scattering experiments on SPEAR. I thank Dr. D. M. Gualtieri from the Electronic Materials and Devices Lab at Allied-Signal and William Lavender for the preparation and construction of the ^{57}Fe-enriched YIG crystals used in this thesis.

From the Stanford Physics Department, I am greatly indebted to Fanny VanBuren for her esteemed advice and precious help during my initial, unsteady years at Stanford. Her abrupt departure from the physics administration is a truly incalculable loss to the Stanford Physics Department and to future physics grad students.

Support for this research was provided by the U.S. Department of Energy, Office of Basic Energy Science, Division of Materials Sciences.

TABLE OF CONTENTS

Table of Contents

LIST OF TABLES

LIST OF ILLUSTRATIONS

List of Illustrations

List of Illustrations

NUCLEAR DYNAMICAL DIFFRACTION USING SYNCHROTRON RADIATION

1. INTRODUCTION

The field of nuclear resonance fluorescence has developed considerably since Kuhn initiated the first search for this phenomena in 1929.[1] In the late 1950's, a variety of techniques were developed to probe the low-lying energy levels of nuclei. One method used Coulomb-excitation reactions where nuclei were excited by the electromagnetic fields of bombarding particles[2,3] (this later developed into the field of perturbed angular correlations[4]). Another method used nuclear reactions as a gamma ray source for exciting nuclei.[5,6] However, it was Mössbauer's discovery in 1958 of the recoil free resonance absorption of nuclei excited by radioactive sources that enabled the field of nuclear resonance fluorescence to blossom and to become useful in a wide variety of disciplines, ranging from biology to chemistry and physics.[7]

The construction of man-made x-ray sources provided a new way to excite nuclear transitions. Use of betatron bremsstrahlung radiation as an x-ray source was first proposed in 1945,[8] but it was not until 1962 that nuclear fluorescence radiation was observed using a conventional x-ray tubes as a source.[9] The problem of detecting the nuclear signal resulted mainly from the huge photoelectric background that occurred when x-rays were simultaneously scattered from the electrons. For this reason, pulsed x-ray sources and time-gated detectors were proposed.[9] Because electrons scatter x-rays promptly compared to nuclear lifetimes, properly gating out the effects due to electronically scattered x-rays leaves the nuclear signal with almost no background. The pulsed nature of synchrotron storage rings made them highly desirable candidates as x-ray sources for exciting nuclei. The first proposal for using synchrotron x-rays was made in 1974,[10] and the first observation of nuclear fluorescence radiation using synchrotron x-rays was made in 1978.[11]

In this first experiment, an iron foil was used in reflection geometry as a target, and the foil was enriched with ^{57}Fe to enhance the nuclear resonance signal. The experiment was performed on a bending magnet beamline which produced, when using a silicon monochromator having a 2 eV wide bandpass, roughly 10^9 electronically scattered photons for each nuclear scattered photon. Since the gating method was not completely effective, background problems produced serious difficulties limiting the usefulness of this technique. Crystals were introduced to further suppress the electronic background. For certain crystals, the ^{57}Fe ferromagnetic or antiferromagnetic lattice is distinct from the electronic lattice. This allows, for certain crystal orientations, the electronic reflection to be

forbidden while the nuclear reflection is still allowed. The first observations of nuclear scattered radiation from perfect crystals using synchrotron x-rays were made in the early and mid 1980's.[12,13] Since then, many nuclear resonance fluorescence experiments have followed at synchrotron radiation facilities to explore the dynamics of nuclear diffraction from crystals.[14-19]

The question usually arises as to why should one use multi-million dollar synchrotron storage rings to do Mössbauer experiments when much cheaper radioactive sources costing a few hundred dollars can be used. For instance, Bragg diffraction off polycrystalline materials using radioactive sources was observed more than two decades earlier in 1960 and off perfect crystals in 1969.[20,21] As described earlier, what makes synchrotron storage rings useful is the pulsed nature of the photons. This allows one to use gated photodetectors and electronics to reduce the electronic background. Also, unlike a radioactive source, the energy bandwidth of the synchrotron radiation is much larger than the nuclear energy bandwidth. This allows all resonant nuclear hyperfine lines to be excited, and results in nuclear hyperfine quantum beats that reveal information about the internal hyperfine fields and the collective nature of the excitation. And, unlike synchrotron sources, time-resolved resonance fluorescence experiments using radioactive sources require deconvoluting out the time response of the source which can significantly alter the resonance signal from the target. Also, synchrotron radiation can provide radiation over a broad range of energies which, with present day undulators and wigglers, can be up to 50 keV. The design of longer, high powered, undulators and wigglers can extend this energy range up to 250 keV,[22] thus making it feasible to perform experiments with most types of Mössbauer samples. Also, synchrotron rings provide linearly polarized beams of x-rays that can be used for doing polarization sensitive experiments.

However, a radioactive source can produce many more resonant photons than present day synchrotrons. For instance, a readily obtainable ^{57}Co source having a strength of 250 mCi produces about 10^{10} resonant photons/sec. However, these photons radiate into 4π steradians, so a better measure of photon production is spectral brilliance--the number of photons per second per square millimeter of source size per square milliradian of photon beam size per 0.1% frequency bandwidth. A 250 mCi source having an emission area of $1\,\mathrm{mm}^2$ produces about $250\,\mathrm{photons/sec\cdot mm^2\cdot mrad^2}$. For an energy bandwidth of

$$\Delta E/E = 4.67\times10^{9}\,\mathrm{eV}/14413\,\mathrm{eV} \approx 3\times10^{-13},$$

the spectral brilliance is about $10^{12}\,\mathrm{photons/sec\cdot mm^2\cdot mrad^2}$(0.1% bandwidth). Examining Fig. 1-1, the brilliance of radioactive sources is better than x-ray tubes, but is

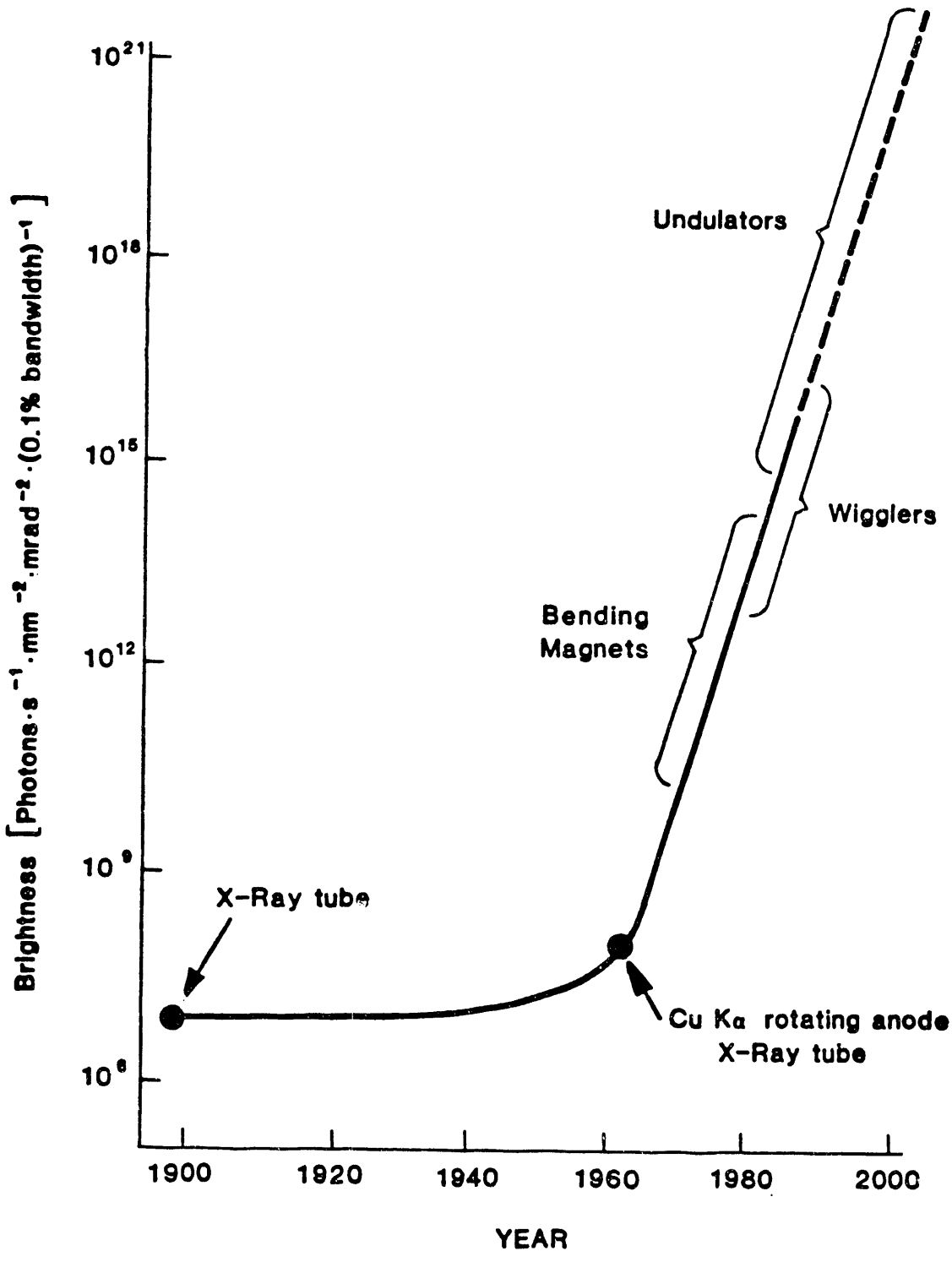

Fig. 1-1. Exponential increase in the spectral brilliance from man-made sources of x-rays. Free electron lasers (FELs) currently in the design phase are estimated to yield a spectral brilliance on the order of 10^{31}. In comparison, the strongest radioactive sources yield a spectral brilliance on the order of 10^{12}. (Reprinted with permission from H. Winick)[23]

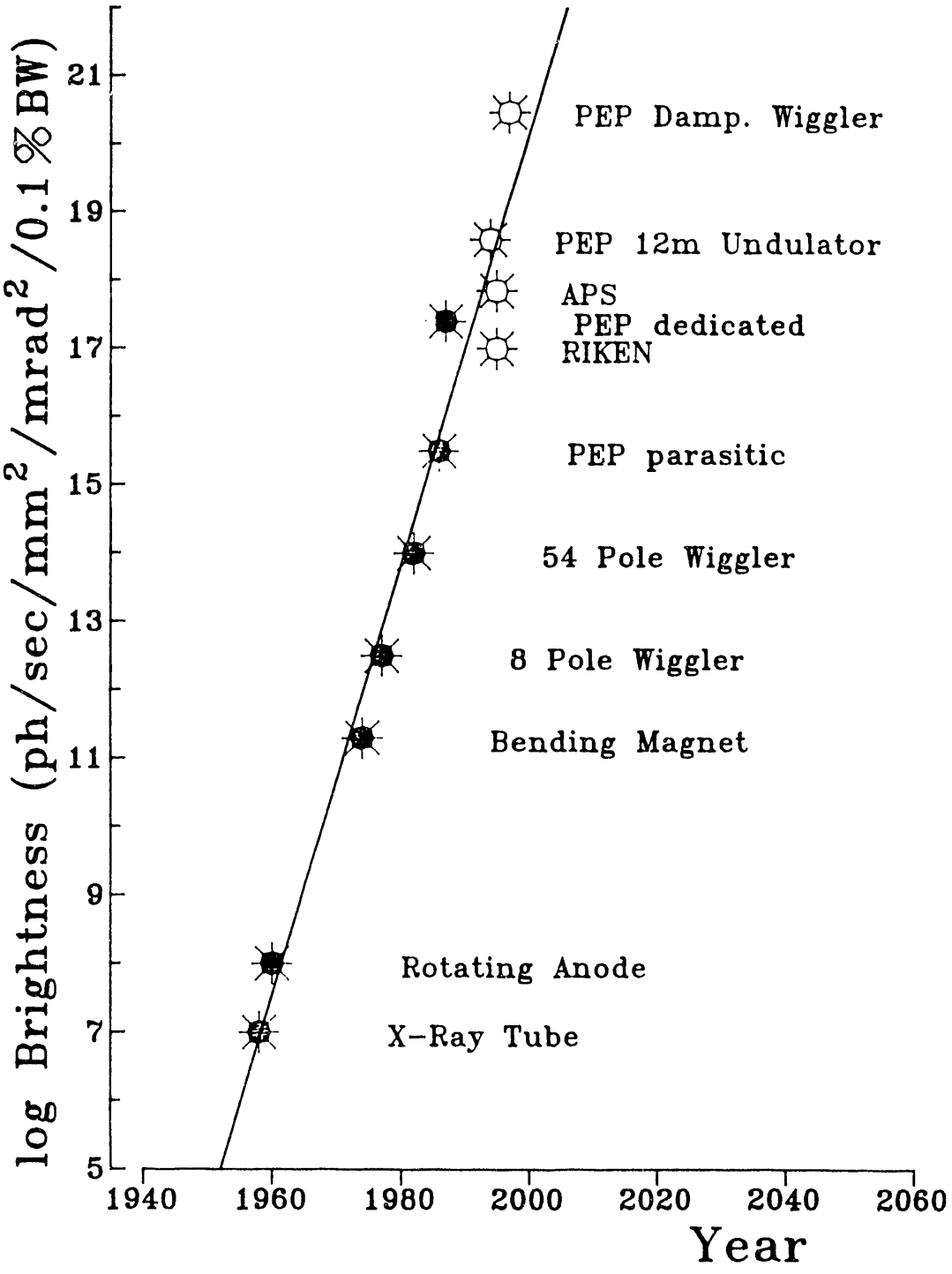

Fig. 1-2. Optimistic 1988 forcast of the spectral brilliance from the PEP synchrotron ring. The bending magnet and the 8 and 54 pole wigglers are insertion devices on the SPEAR ring. PEP parasitic and dedicated were calculated using a 2 m undulator. The open circles are proposed operations which never came about, and PEP was never run in a dedicated mode at 14 GeV. For the experiments completed in this thesis project, PEP was operated in a colliding beam optics mode (parasitic running), and a 2 meter undulator was used. (Reprinted with permission from H. Wiedemann)[24]

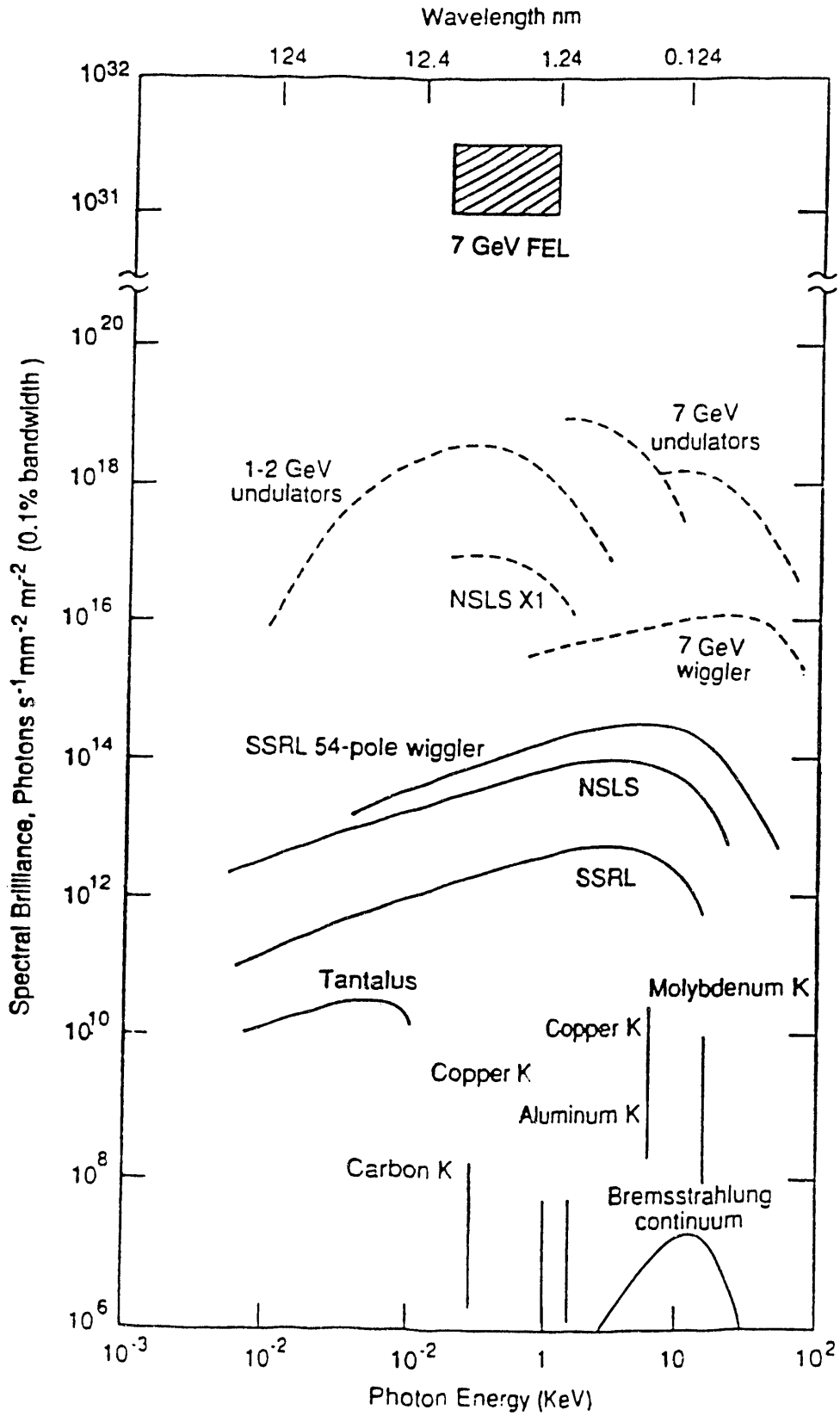

Fig. 1-3. Spectral brilliance curves for various x-ray sources. Note the break of 11 orders of magnitude in the chart to include the FEL results. (Reprinted with permission from K.-J. Kim)[25]

only comparable with synchrotron beamlines having bending magnet sources. However, when wigglers and undulators are used, dramatic increases in the brilliance many orders of magnitude greater than radioactive sources can be achieved, thus making synchrotron sources much more desirable than radioactive sources.

In this thesis, synchrotrons having wiggler and undulator devices were used for the first time to do nuclear diffraction experiments. For bending magnet beamlines, the nuclear counting rate is no more than a few counts/sec. On wiggler and undulator beamlines, the counting rate increased by a factor of 100 (for the 10-2 wiggler at the 3 GeV SPEAR storage ring, counting rates of 80 counts/sec were observed, and for the PBF1 undulator at the 15 GeV PEP storage ring, counting rates as high as 800 counts/sec were obtained, but these rates are highly dependent upon the quality of the monochromator (heating problems occur at high x-ray intensities), the x-ray beam optics, the detector efficiency, and the electron beam current and optics). As seen in Figs. 1-2 and 1-3, the SPEAR 54 pole wiggler has a spectral brilliance of about 10^{14} photons/sec·mm^2·mrad^2(0.1% bandwidth) at 14.4 keV, while the brilliance of the 2 meter PEP undulator is a factor of 10 greater when run in parasitic, or colliding beam, mode (When run in a dedicated, or nonparasitic, low emittance optics mode, the brilliance of the PEP undulator is expected to be 10,000 times greater than the SPEAR wiggler. Unfortunately, before PEP could be run at 14 GeV in this low emittance optics mode, PEP was decommissioned by the Stanford Linear Accelerator Center (SLAC) for fiscal reasons).[24-26]

The development of high energy storage rings specifically dedicated for synchrotron experiments is expected to push counting rates even higher. Already, the 6.5 GeV Accumulator Ring at the KEK high energy facility in Japan that has recently been outfitted with a 3.6 meter undulator, and there are reports of nuclear signal rates as high as 10,000 counts/sec.[27,28] The 7 GeV APS ring under construction at Argonne, the 6 GeV ESRF ring under construction in France, and the 8 GeV Spring-8 ring under construction in Japan will have beamlines equipped with 4 to 5 meter long undulators that are expected to be 1000 times more brilliant (see Fig. 1-4) than the PEP undulator (when, that is, PEP is operated in colliding beam mode--the brilliance would be comparable to PEP were it to be operated in a very low emittance optics mode). A feasibility study under way at KEK is looking into the possibility of converting the electron-positron Tristan Collider Main Ring into a dedicated, exceptionally intense, synchrotron light source called the TSLF (Tristan Super Light Facility).[29] The TSLF, with a 6 meter undulator operating at 10 GeV, is expected to provide an extremely brilliant source of x-rays that is 3 orders of magnitude greater than the third generation synchrotron sources under construction described above and 6 orders of magnitude greater than PEP (The design of TSLF envisages using damping

wigglers to reduce the electron beam emittance. If PEP were outfitted with damping wigglers, its brilliance would be comparable to TSLF--see Figs. 1-2 and 1-4). Also in the conceptual design stage is an effort to insert a 50-60 meter FEL undulator into the SLAC linac.[25] If the technical difficulties of operating FELs near 1 Å are overcome (such as modulating the electron bunch structure to a 1 Å periodicity), the SLAC FEL is expected to have an extraordinary brilliance of 10^{31} photons/sec·mm^2·mrad^2(0.1% bandwidth)--this is 15 orders of magnitude brighter than PEP and makes the nuclear photon flux alone (from nuclear resonance scattering experiments) greater than the photon flux generated by present day synchrotron light sources! The prospects of doing useful physics across many science disciplines using the highly monochromatic (micro eV energy width), very collimated (20 μrad or 4 arcsec angular spread), extremely coherent (30 m coherence length) fluorescence radiation from nuclear systems looks very encouraging.

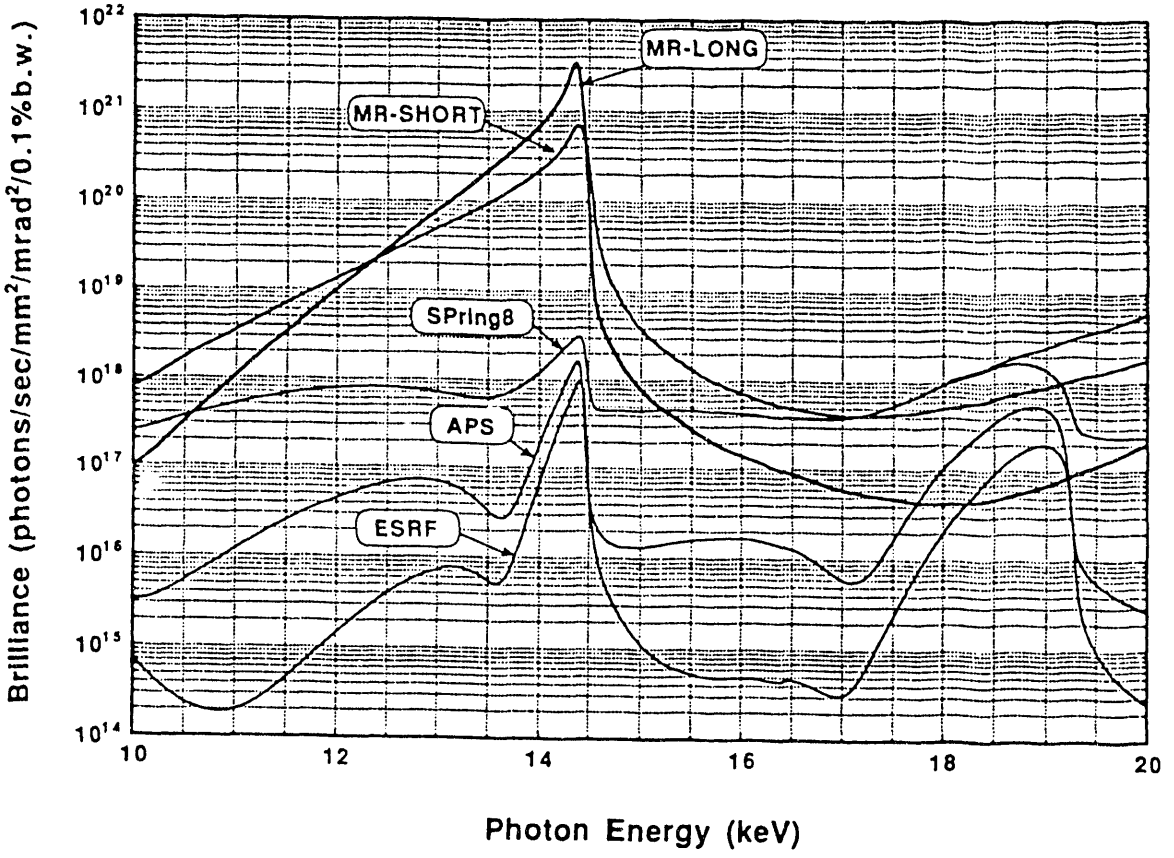

Fig. 1-4. Spectral brilliance curves for various synchrotron storage rings. MR-short and MR-long correspond to a 6 m short undulator and a 70 m long undulator on the TSLF ring. The APS and ESRF calculations were done for a 4.5 m undulator, a 5 m undulator was used for the Spring-8 calculations, and all calculations used an electron beam current of 100 mA. (Reprinted with permission from T. Ishikawa)[29]

This thesis is organized in the following manner. In Chapters 1-4, elementary scattering theory is reviewed, culminating in the construction of the spherical multipole electric fields scattered by resonant particles. In Chapter 5, I have constructed the complete form of the multipole polarization tensor for magnetic dipole scattering in a linear polarization basis. Nuclear level mixing is reviewed, and I give several interesting examples of magnetic dipole scattering. In Chapter 6, I have worked out a novel formulation of dynamical scattering from resonant systems using the principles of linearity and time invariance present in system theory. This theory is used to examine the interaction between two resonant particles, and it reveals that superradiance is due to very elementary multiple scattering effects. I also show that the dynamical scattering equations, in the many particle limit, give the same results as the Maxwell equations for a medium, thus connecting quantum mechanics with classical electrodynamics. Chapter 7 reviews nuclear dynamical diffraction theory, with an emphasize on the superradiant effects of radiative speedup and resonance frequency shifts. Chapter 8 describes the EWALD computer code I wrote to perform the numerically intensive nuclear dynamical diffraction theory calculations. The program is written generally enough to handle any crystal type, to handle reflections from multiple crystals, and can be used for systems containing nuclei other than ^{57}Fe. Chapter 9 describes the general experimental setup along with details about the detector and fast timing electronics.

Chapters 10 and 11 summarize my analysis of the results of the experiments carried out by the Stanford nuclear resonance scattering group composed of myself along with Dr. G. S. Brown (my thesis advisor), Dr. S. Ruby, Dr. J. Arthur, and A. Q. R. Baron. The experiments done on the SPEAR and PEP rings were done in collaboration with Dr. E. Alp and Dr. G. K. Shenoy of Argonne National Labs, and S. Sastri from the Cornell High Energy Synchrotron Source (CHESS) collaborated in experiments done on the CESR ring.

In the Appendices, a copy of a Physical Review Letter article titled "Phase Shift of a Rotated Quantum State Observed in an X-Ray Scattering Experiment" is given. Also given are two time domain calculations using the dynamical scattering equations I formulated. These calculations illustrate that the dynamical scattering equations can be used to examine and understand the physics behind multiple scattering in a way that is not possible using the conventional, index of refraction, approach where the Maxwell equations for a medium are solved in the frequency domain and Fourier transformed into the time domain.

REFERENCES

[1] W. Kuhn, *Phil. Mag.* **8**, 625 (1929).

[2] A. Abragam and R. V. Pound, *Phys. Rev.* **92**, 943 (1953).

[3] K. Alder, A. Bohr, T. Huus, B. Mottelson, and A. Winther, *Revs. Mod. Phys.* **28**, 432 (1956).

[4] R. M. Steffen and H. Frauenfelder, *Perturbed Angular Correlations*, edited by E. Karisson, E.Matthias, K. Siegbahn (North-Holland, Amsterdam, 1964).

[5] C. P. Swann and F. R. Metzger, *Phys. Rev.* **108**, 982 (1957).

[6] P. B. Smith and P. M. Endt, *Phys. Rev.* **110**, 397 (1958).

[7] R. L. Mössbauer, *Z. Physik* **151**, 124 (1958).

[8] L. I. Schiff, *Phys. Rev.* **70**, 761 (1946).

[9] E. J. Seppi and F. Boehm, *Phys. Rev.* **128**, 2334 (1962).

[10] S. L. Ruby, *J. Phys. (Paris) Colloq.* **6**, 209 (1974).

[11] R. L. Cohen, G. L. Miller, and K. W. West, *Phys. Rev. Lett.* **41**, 381 (1978).

[12] A. I. Chechin, N. V. Andronova, M. V. Zelepukhin, A. N. Artem'ev, and E. P. Stepanov, *JETP Lett.* **37**, 633 (1983).

[13] E. Gerdau, R. Rüffer, H. Winkler, W. Tolksdorf, C. P. Klages, and J. P. Hannon, *Phys. Rev. Lett.* **54**, 835 (1985).

[14] E. Gerdau and R. Rüffer, *Hyp. Int.* **27**, 59 (1986).

[15] R. Rüffer, E. Gerdau, and R. Hollatz, *Phys. Rev. Lett.* **58**, 2359 (1987).

[16] U. van Bürck, R. L. Mössbauer, E. Gerdau, R. Rüffer, R. Hollatz, G. V. Smirnov, and J. P. Hannon, *Phys. Rev. Lett.* **59**, 355 (1987).

[17] G. Faigel, D. P. Siddons, J. B. Hastings, P. E. Haustein, J. R. Grover, and L. E. Berman, *Phys. Rev. Lett.* **61**, 2794 (1988).

[18] J. Arthur, G. S. Brown, D. E. Brown, and S. L. Ruby, *Phys. Rev. Lett.* **63**, 1629 (1989).

[19] S. Kikuta, Y. Yoda, Y. Kudo, K. Izumi, T. Ishikawa, C. K. Suzuki, H. Ohno, H. Takei, K. Nakayama, X. W. Zhang, T. Matsushita, S. Kishimoto, and M. Ando, *Jpn. J. App. Phys.* **30**, L 1686 (1991).

[20] P. J. Black and P. B. Moon, *Nature (London)* **188**, 481 (1960).

[21] G. V. Smirnov, V. V. Sklyarevskii, R. A. Voskanyan, and A. N. Artem'ev, *JETP Lett.* **9**, 123 (1969).

[22] J. M. Paterson, *PEP as a Synchrotron Radiation Source: Status and Review,* SSRL ACD-NOTE **68**, (1989) [SLAC-PUB-4899, March 1989].

[23] H. Winick, *Synchrotron Radiation*, Physics of Particle Accelerators (AIP Conference

Proceedings No. **184**), vol. 2, edited by M. Month and M. Dienes (American Institute of Physics, New York, 1989).

[24] H. Wiedemann, *Storage Ring Optimization,* Handbook on Synchrotron Radiation, vol. 3, edited by G. S. Brown and D. E. Moncton (North-Holland, Amsterdam, 1991).

[25] K. Bane, K. Halbach, K.-J. Kim, J. Kirz, P. Morton, H.-D. Nuhn, C. Pellegrini, J. Rosenzweig, J. Seeman, R. Tatchyn, and H. Winick, *The 2 to 4 nm High Power Linear Coherent Light Source*, Workshop on Applications of X-ray FELs (Stanford Synchrotron Radiation Laboratory, Stanford University, 1992).

[26] R. Coisson, private communications and PEP paper (Stanford Synchrotron Radiation Laboratory, Stanford University, 1987).

[27] T. Ishikawa, Y. Yoda, K. Izumi, C. K. Suziki, X. W. Zhang, M. Ando, and S. Kikuta, *Rev. Sci. Instrum.* **63**, 1015 (1992).

[28] X. W. Zhang, T. Mochizuki, H. Sugiyama, S. Yamamoto, H. Kitamura, T. Sioya, M. Ando, Y. Yoda, T. Ishikawa, S. Kikuta, and C. K. Suzuki, *Rev. Sci. Instrum.* **63**, 404 (1992).

[29] H. Sugawara, *The Tristan Super Light Facility*, KEK Progress Report 92-1, (National Laboratory for High Energy Physics, Tsukuba, Japan, 1992).

2. TIME DEPENDENT NONRELATIVISTIC PERTURBATION THEORY

2.1 Perturbation Theory

The essential problem in nuclear dynamical diffraction is to adequately describe the interaction of a charged particle with an electromagnetic field. This chapter will develop the fundamentals of a time dependent perturbation theory that will be used to explore this interaction process.[1-8] The following approach leads to a direct form of a scattering amplitude in terms of a series expansion. Once the scattering amplitude is formulated, many types of scattering processes can be examined.

In determining the quantum mechanical behavior of a charged particle in the presence of a time-varying interaction potential, $V(\mathbf{x},t)$, the time independent part, $H_0(\mathbf{x})$, is separated from the total Hamiltonian,

$$H(\mathbf{x},t) = H_0(\mathbf{x}) + V(\mathbf{x},t). \tag{2-1.1}$$

If the solution of the time independent Schrödinger equation can be found, then the time dependent solution can be written in terms of a perturbative expansion of the known solution. The time independent Schrödinger equation obeys the relation

$$H_0(\mathbf{x})\phi_n(\mathbf{x}) = E_n(\mathbf{x}), \tag{2-1.2}$$

where ϕ_n are the stationary eigenstates of the unperturbed Hamiltonian and satisfies the orthonormal relation

$$\int_V \phi_m^*(\mathbf{x})\phi_n(\mathbf{x})d^3x = \delta_{mn}. \tag{2-1.3}$$

The solutions of the time dependent Schrödinger equation,

$$i\hbar\frac{\partial}{\partial t}\psi(\mathbf{x},t) = \left[H_0(\mathbf{x}) + V(\mathbf{x},t)\right]\psi(\mathbf{x},t), \tag{2-1.4}$$

expressed in terms of an expansion of the stationary states are

$$\psi(\mathbf{x},t) = \sum_n a_n(t)\phi_n(\mathbf{x})e^{-iE_nt/\hbar}. \tag{2-1.5}$$

To determine the coefficients, $a_n(t)$, this solution is inserted back into the Schrödinger equation. The result of this operation is

$$i\hbar\sum_n \dot{a}_n(t)\phi_n(\mathbf{x})e^{-iE_nt/\hbar} = V(\mathbf{x},t)\sum_n a_n(t)\phi_n(\mathbf{x})e^{-iE_nt/\hbar}.$$

Multiplying both sides of the equation above by $\phi_f^*(\mathbf{x})$ and integrating over all space gives

$$\dot{a}_f(t) = -\frac{i}{\hbar}\sum_n a_n(t)V_{fn}(t)e^{i\omega_{fn}t}, \tag{2-1.6}$$

where
$$V_{fn}(t) = \int_V \phi_f^*(\mathbf{x})V(\mathbf{x},t)\phi_n(\mathbf{x})d^3x \tag{2-1.7}$$

and
$$\omega_{fn} = \left(E_f - E_n\right)/\hbar. \tag{2-1.8}$$

So far, this formalism is exact, and solving the coupled differential equations, Eq. 2-1-6, is equivalent to solving the Schrödinger equation. However, in general, an analytical solution to $a_f(t)$ cannot be found, and thus $a_f(t)$ must be expressed in terms of a series expansion. The convergence of this series will be determined by whether the perturbation $V(\mathbf{x},t)$ is small enough. The series expansion of $a_f(t)$ will be defined as

$$a_f(t) \equiv a_f^{(0)}(t) + a_f^{(1)}(t) + a_f^{(2)}(t) + \cdots + a_f^{(N-1)}(t). \tag{2-1.9}$$

Using the information that the system is definitely in a stationary eigenstate, $\phi_i(\mathbf{x})$, at time $t = -\infty$, the zeroth order term in the expansion can be found. At time $t = -\infty$, the solution to Eq. 2-1.5,

$$\psi(\mathbf{x},t=-\infty) = \phi_i(\mathbf{x})e^{-iE_it/\hbar}\Big|_{t=-\infty} = \sum_n a_n(t)\phi_n(\mathbf{x})e^{-iE_nt/\hbar}\Big|_{t=-\infty},$$

is $a_n(-\infty) = \delta_{ni}$. The zeroth order term in the expansion is the solution to the Schrödinger equation when the perturbation is absent:

$$\dot{a}_f^{(0)}(t) = 0 \tag{2-1.10}$$

$$a_f^{(0)}(t) = \delta_{ni}. \tag{2-1.11}$$

The next order term in the expansion is obtained by substituting the zeroth order term into the relation for $\dot{a}_f(t)$, Eq. 2-1.6:

$$\dot{a}_f^{(1)}(t) = (-i/\hbar)V_{fi}(t)e^{i\omega_{fi}t} \tag{2-1.12}$$

$$a_f^{(1)}(t) = (-i/\hbar)\int_{-\infty}^{t} V_{fi}(t')e^{i\omega_{fi}t'}\,dt'. \tag{2-1.13}$$

This substitution process can be done recursively to obtain all the other higher orders. The second order terms are:

$$\dot{a}_f^{(2)}(t) = (-i/\hbar)^2\sum_{n\neq i} V_{fn}(t)e^{i\omega_{fn}t}\int_{-\infty}^{t} V_{ni}(t')e^{i\omega_{ni}t'}\,dt' \tag{2.1-14}$$

$$a_f^{(2)}(t) = (-i/\hbar)^2\sum_{n\neq i}\int_{-\infty}^{t} dt_1 V_{fn}(t_1)e^{i\omega_{fn}t_1}\int_{-\infty}^{t_1} dt_2 V_{ni}(t_2)e^{i\omega_{ni}t_2}\,. \tag{2.1-15}$$

The constraint on the sum, $n \neq i$, forces any intermediate state, $|n\rangle$, to be different from the initial state (there is also the constraint that $n \neq f$). Thus the intermediate state transitions

do not conserve energy: $\omega_{fn} \neq 0$ and $\omega_{ni} \neq 0$. The self energy terms, V_{ii}, will be partially ignored. They are described by single particle scattering loops in Feynman scattering diagrams, and, when they are more carefully evaluated in a covariant perturbation theory, they will only contribute energy shifts to the scattering amplitude. No attempt will be made to calculate such energy shifts--they will simply be lumped with the experimentally measured isomer shifts and appropriately inserted into the scattering amplitude.

The third order amplitude is listed below:

$$\dot{a}_f^{(3)}(t) = (-i/\hbar)^3 \sum_{m\neq i}\sum_{n\neq m} V_{fn}(t) e^{i\omega_{fn}t} \int_{-\infty}^{t} dt_1 V_{nm}(t_1) e^{i\omega_{nm}t_1} \int_{-\infty}^{t_1} dt_2 V_{mi}(t_2) e^{i\omega_{mi}t_2} \tag{2-1.16}$$

$$a_f^{(3)}(t) = (-i/\hbar)^3 \sum_{m\neq i}\sum_{n\neq m} \int_{-\infty}^{t} dt_1 V_{fn}(t_1) e^{i\omega_{fn}t_1} \int_{-\infty}^{t_1} dt_2 V_{nm}(t_2) e^{i\omega_{nm}t_2} \int_{-\infty}^{t_2} dt_3 V_{mi}(t_3) e^{i\omega_{mi}t_3} \; . \tag{2-1.17}$$

2.2 The Scattering S and T Matrices

After the interaction perturbation ceases, the system resides in a definite stationary state, $\phi_f(\mathbf{x},t)$. Then the transition amplitude for a transition from an initial state to a final state can be defined in terms of the elements of a scattering operator S,

$$\begin{aligned} S_{fi} &= \langle \phi_f | S | \phi_i \rangle = \langle \phi_f(\mathbf{x},t) | \psi(\mathbf{x},t) \rangle = \sum\nolimits_n a_n(t) e^{-iE_n t/\hbar} \int_V \phi_f^*(\mathbf{x}) \phi_n(\mathbf{x}) e^{iE_f t/\hbar} \\ &= a_f(t) \end{aligned} \tag{2-2.1}$$

The S-operator is then a unitary operator that describes the evolution of an initial state, $|\phi_i(\mathbf{x},t)\rangle$, to a final state, $|\psi(\mathbf{x},t)\rangle$, during the action of the perturbation:

$$S|\phi_i(\mathbf{x},t)\rangle = |\psi(\mathbf{x},t)\rangle. \tag{2-2.2}$$

The unitarity of S can be seen by noting that

$$\langle \psi | \psi \rangle = 1 = \langle \phi_i | S^\dagger S | \phi_i \rangle. \tag{2-2.3}$$

This is true only if $S^\dagger S = 1$. Summing over all the possible final states gives a total probability for a scattering event to occur of unity,

$$\sum\nolimits_f [S^\dagger S]_{fi} = \sum\nolimits_f \langle \psi | \phi_f \rangle \langle \phi_f | \psi \rangle = \langle \psi | \psi \rangle = 1. \tag{2-2.4}$$

The matrix elements of the scattering operator can be found by evaluating the perturbative expansion terms of $a_f(t)$, Eqs. 2-1.10 to 2-1.17. The transition probability is

$|S_{fi}|^2$, and the transition probability per unit time, or transition rate, is the time rate of change of the transition probability,[5]

$$\Gamma_{fi} = \frac{\partial}{\partial t}|S_{fi}|^2 = S_{fi}^{*}\dot{S}_{fi} + \dot{S}_{fi}^{*}S_{fi}. \tag{2-2.5}$$

The other interesting quantity desired is the T-matrix element, T_{fi}, which should be differentiated from the transition probability in that it describes the amplitude of a scattered wave rather than the probability for a transition from an initial state to a final state. The structure of the T-matrix can be seen by evaluating the transition rate for the simple case of a constant interaction perturbation,

$$V(\mathbf{x},t) = \begin{cases} 0 & t \to -\infty \\ V(\mathbf{x}) & \end{cases}. \tag{2-2.6}$$

The zeroth and first order terms of the S-matrix elements can be found using the perturbative expansions of Eqs. 2-1.10 to 2-1.13:

$$S_{fi} = \delta_{fi} + (-i/\hbar)\int_{-\infty}^{t} V_{fi}e^{i\omega_{fi}t'}\,dt' \tag{2-2.7}$$

$$\dot{S}_{fi} = (-i/\hbar)V_{fi}e^{i\omega_{fi}t}. \tag{2-2.8}$$

The transition rate is then

$$\Gamma_{fi} = (i/\hbar)V_{fi}^{*}e^{-i\omega_{fi}t}\left[\delta_{fi} + (-i/\hbar)\int_{-\infty}^{t} V_{fi}e^{i\omega_{fi}t'}\,dt'\right]$$

$$+(-i/\hbar)V_{fi}e^{i\omega_{fi}t}\left[\delta_{fi} + (i/\hbar)\int_{-\infty}^{t} V_{fi}^{*}e^{-i\omega_{fi}t'}\,dt'\right].$$

The δ-function terms yield

$$(i/\hbar)\left[V_{ii}^{*} - V_{ii}\right] = (i/\hbar)\left[\langle\phi_i|V^{\dagger}|\phi_i\rangle - \langle\phi_i|V|\phi_i\rangle\right] = 0$$

since the interaction perturbation Hamiltonian, $V(\mathbf{x},t)$, is Hermetian: $V^{\dagger} = V$. Then,

$$\Gamma_{fi} = (1/\hbar^2)V_{fi}^{*}V_{fi}\left[\int_{-\infty}^{t} e^{i\omega_{fi}(t'-t)}\,dt' + \int_{-\infty}^{t} e^{i\omega_{fi}(t-t')}\,dt'\right].$$

Making the change of variables $u = t' - t$ for the first integral and $u = t - t'$ for the second integral results in

$$\Gamma_{fi} = (1/\hbar^2)V_{fi}^{*}V_{fi}\left[\int_{-\infty}^{0} e^{i\omega_{fi}u}\,du - \int_{\infty}^{0} e^{i\omega_{fi}u}\,du\right] = (1/\hbar^2)|V_{fi}|^2\int_{-\infty}^{\infty} e^{i\omega_{fi}u}\,du$$

$$= \frac{2\pi}{\hbar}|V_{fi}|^2\,\delta(E_f - E_i), \tag{2-2.9}$$

where the following relations were used:

$$\int_{-\infty}^{\infty} e^{ikx}\,dx = 2\pi\delta(k) \tag{2-2.10}$$

$$\delta(ax) = \frac{1}{|a|}\delta(x). \tag{2-2.11}$$

Equation 2-2.9 is the Fermi Golden Rule to first order. Also the δ-function preserves the conservation of energy condition--this is usually termed in the scattering language as the on-energy-shell condition.

To obtain the Fermi Golden Rule to second order, the S-matrix elements must be evaluated to second order:

$$S_{fi} = \delta_{fi} + (-i/\hbar)\int_{-\infty}^{t} V_{fi}e^{i\omega_{fi}t'}\,dt' + (-i/\hbar)^2\sum_{n\neq i}\int_{-\infty}^{t} dt_1 V_{fn}e^{i\omega_{fn}t_1}\int_{-\infty}^{t_1} dt_2 V_{ni}e^{i\omega_{ni}t_2}. \tag{2-2.12}$$

Inserting a small positive imaginary quantity, $i\varepsilon$ where $\varepsilon > 0$, into the exponent of the last integral allows one to perform the integral to get a meaningful result. After integration, taking the limit as $\varepsilon \to 0$ gives the final result. This procedure, though seemingly ad hoc, is very important in ensuring that the S-matrix obeys the accepted rules of causality for incoming and outgoing particles. The last integral in the third term above then integrates to

$$\int_{-\infty}^{t_1} dt_2 V_{ni}e^{i\omega_{ni}t_2} = \lim_{\varepsilon\to 0}\int_{-\infty}^{t_1} dt_2 V_{ni}e^{i(E_n - E_i - i\varepsilon)t_2/\hbar} = i\hbar V_{ni}\frac{e^{i(E_n-E_i)t_1/\hbar}}{E_i - E_n}.$$

Then,

$$S_{fi} = \delta_{fi} + (-i/\hbar)\left[V_{fi} + \sum_{n\neq i}\frac{V_{fn}V_{ni}}{E_i - E_n}\right]\int_{-\infty}^{t} e^{i\omega_{ni}t'}\,dt' \tag{2-2.13}$$

and

$$\dot{S}_{fi} = (-i/\hbar)\left[V_{fi} + \sum_{n\neq i}\frac{V_{fn}V_{ni}}{E_i - E_n}\right]e^{i\omega_{fi}t}. \tag{2-2.14}$$

S_{fi} and $\dot{S}_{fi}$ have the same form as their first order expressions for the substitution

$$V_{fi} \to V_{fi} + \sum_{n\neq i}\frac{V_{fn}V_{ni}}{E_i - E_n}.$$

Then employing the same techniques as before gives

$$\Gamma_{fi} = \frac{2\pi}{\hbar}\left|V_{fi} + \sum_{n\neq i}\frac{V_{fn}V_{ni}}{E_i - E_n}\right|^2 \delta(E_f - E_i). \tag{2-2.15}$$

This gives the on-energy-shell T-matrix elements to second order,

$$T_{fi} = V_{fi} + \sum_{n \neq i} \frac{V_{fn} V_{ni}}{E_i - E_n}. \tag{2-2.16}$$

The Fermi Golden rule to all orders can now be written in a compact form:

$$\Gamma_{fi} = \frac{2\pi}{\hbar} |T_{fi}|^2 \, \delta(E_f - E_i), \tag{2-2.17}$$

where

$$T_{fi} = V_{fi} + \sum_{n \neq i} \frac{V_{fn} V_{ni}}{E_i - E_n} + \sum_{m \neq i} \sum_{n \neq m} \frac{V_{fn} V_{nm} V_{mi}}{(E_i - E_n)(E_i - E_m)} + \cdots. \tag{2-2.18}$$

2.3 The Scattering Amplitude

In dealing with scattering problems, knowledge of the total cross section of a scattering event is very useful. The total cross section can be evaluated from the transition rate using the following definition:

$$\sigma_{tot} = \frac{\text{all scattered photons/sec}}{\text{flux of incident photons}} \equiv \frac{\sum_f \Gamma_{fi}}{n_i v_i / V_0}, \tag{2-3.1}$$

where n_i and v_i are the number and velocity of the incident particles, and V_0 is the volume of space enclosing the interaction region. Summing over all the possible final states gives the total cross section. Using the Fermi Golden rule, the total cross section can be expressed in the form

$$\sigma_{tot} = \frac{2\pi/\hbar}{n_i v_i / V_0} \sum_f |T_{fi}|^2 \, \delta(E_f - E_i). \tag{2-3.2}$$

Notice that T_{fi} in the expression above is in units of energy. The expression for a scattering amplitude in units of length can be obtained by showing that σ_{tot} satisfies the optical theorem. To do so, first note that the S-matrix elements, for $t \to \infty$, follows the relation

$$S_{fi} = \delta_{fi} - 2\pi i T_{fi} \delta(E_f - E_i). \tag{2-3.3}$$

Using the unitarity properties of the S-matrix yields

$$\begin{aligned} (S^\dagger S)_{fi} = \delta_{fi} &= \sum_n S_{nf}^* S_{ni} \\ &= \sum_n \left[\delta_{fn} \delta_{ni} + 2\pi i \delta_{ni} T_{nf}^* \delta(E_f - E_n) - 2\pi i \delta_{nf} T_{ni} \delta(E_n - E_i) \right] \end{aligned}$$

$$+ (2\pi)^2 T_{nf}^* T_{ni} \delta(E_f - E_n)\delta(E_n - E_i)\Big].$$

Then,

$$\Big[(T_{if}^* - T_{fi}) - 2\pi i \textstyle\sum_n T_{nf}^* T_{ni} \delta(E_n - E_i)\Big]\delta(E_f - E_i) = 0,$$

where the identity $\delta(E_f - E_n)\delta(E_n - E_i) = \delta(E_f - E_i)\delta(E_n - E_i)$ has been used. The above expression is true on the energy shell if

$$(T_{if}^* - T_{fi}) - 2\pi i \textstyle\sum_n T_{nf}^* T_{ni} \delta(E_n - E_i) = 0. \qquad (2\text{-}3.4)$$

This is simply an equivalent expression of the unitary condition expressed in terms of the scattering amplitude. The diagonal elements yield the meaningful result

$$T_{ii} - T_{ii}^* = 2i\,\mathrm{Im}\{T_{ii}\} = -2\pi i \textstyle\sum_n |T_{ni}|^2 \delta(E_n - E_i). \qquad (2\text{-}3.5)$$

The total cross section is then

$$\sigma_{tot} = -\frac{2V_0}{\hbar n_i v_i}\mathrm{Im}\{T_{ii}\}. \qquad (2\text{-}3.6)$$

This is the optical theorem, and it relates the total cross section to the imaginary part of the scattering amplitude. The photons have been elastically scattered since the final state of the system is identical to the initial state.

A normalized scattering amplitude in units of length can then be defined as

$$F_{fi}(\mathbf{k}_f, \mathbf{k}_i) = -A_0 T_{fi}, \qquad (2\text{-}3.7)$$

where

$$A_0 = \frac{1}{\sqrt{n_i}} \frac{V_0 k_f}{2\pi\hbar v_i}. \qquad (2\text{-}3.8)$$

The factor $1/\sqrt{n_i}$ normalizes the square modulus of the scattering amplitude to the number of incoming particles, and $\mathbf{k}_i$ and $\mathbf{k}_f$ are the incoming and outgoing photon wavectors respectively. Then, for one incoming particle undergoing elastic scattering

$$\sigma_{tot} = \frac{4\pi}{k_f}\mathrm{Im}\{F_{ii}(\mathbf{k}_f, \mathbf{k}_i)\}. \qquad (2\text{-}3.9)$$

This is the familiar form of the optical theorem seen in classical electrodynamics. However, when many scatterers are present, the total cross section is proportional to the forward scattering amplitude, $F(\mathbf{k}_f = \mathbf{k}_i)$. This multiparticle scattering behavior will explored later.

Basic assumptions about certain symmetry laws in physics have been made in the construction of σ_{tot}. For instance, a generalized scattering cross section can be constructed from Eq. 2-3.4

$$\sigma_{tot}^{gen} = -\frac{2\pi i}{k_f}\left[F_{fi}(\mathbf{k}_f,\mathbf{k}_i) - F_{if}^{*}(\mathbf{k}_i,\mathbf{k}_f)\right]. \tag{2-3.10}$$

This expression can be put in a form similar to Eq. 2-3.9 by applying the law of reciprocity for systems possessing space-inversion symmetry.[9] The law of reciprocity states that a scattering event in which an incoming particle scatters from $\mathbf{k}_i$ to $\mathbf{k}_f$ is identical to a scattering event in which the particle scatters in the reverse direction from $-\mathbf{k}_f$ to $-\mathbf{k}_i$. Then

$$F_{fi}(\mathbf{k}_f,\mathbf{k}_i) = F_{if}(-\mathbf{k}_i,-\mathbf{k}_f) \tag{2-3.11}$$

satisfies the principle of reciprocity (see Fig 2-3.1). As long as one remains on the energy shell, reciprocity is simply another way of stating that time reversal invariance holds.[10]

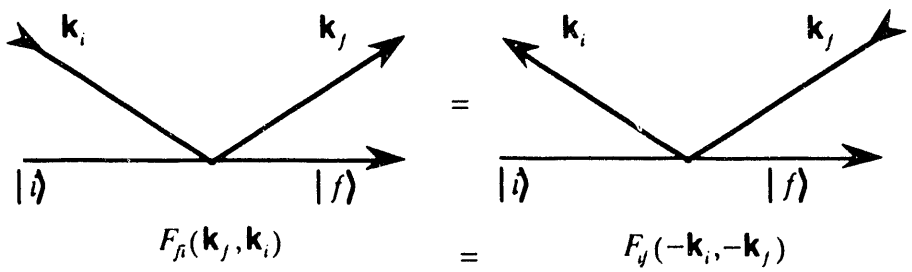

Fig. 2-3.1. Illustration of reciprocity where the scattering amplitudes for a scattering process and its time reversed process are equivalent.

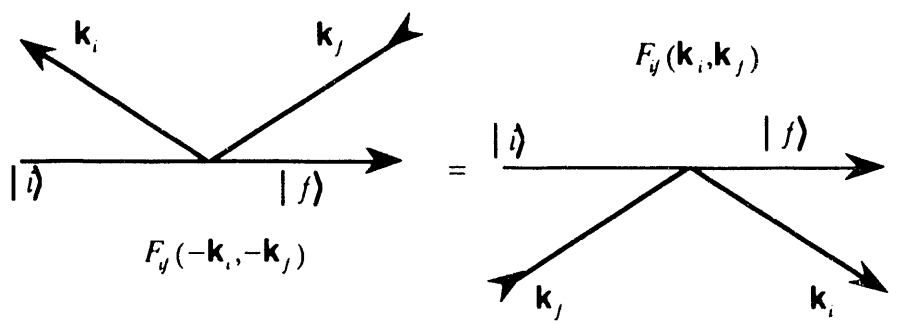

Fig. 2-3.2. Illustration of space inversion symmetry. Photons traveling in the **x** direction sees the same interaction as those traveling in the **−x** directon.

If the scattering system possesses space inversion symmetry (that is, the interaction perturbation satisfies $V(\mathbf{x}) = V(-\mathbf{x})$) then, from Fig 2-3.2, the scattering amplitude obeys the relation

$$F_{if}\left(-\mathbf{k}_i,-\mathbf{k}_f\right) = F_{if}\left(\mathbf{k}_i,\mathbf{k}_f\right). \tag{2-3.12}$$

This makes the scattering amplitude (and the scattering T-matrix) symmetric

$$T_{if} = T_{fi} \quad \text{or} \quad F_{if}\left(\mathbf{k}_i,\mathbf{k}_f\right) = F_{fi}\left(\mathbf{k}_f,\mathbf{k}_i\right). \tag{2-3.13}$$

Under such conditions, the generalized cross section reduces to

$$\sigma_{tot}^{gen} = \frac{4\pi}{k_f}\,\mathrm{Im}\left\{F_{fi}\left(\mathbf{k}_f,\mathbf{k}_i\right)\right\}. \tag{2-3.14}$$

The generalized cross section reduces to the elastic cross section, Eq. 2-3.9, when the initial and final states are identical. This also shows that the elastic cross section is valid only when the scattering system possesses space-inversion symmetry and time reversal invariance holds.

REFERENCES

[1] M. L. Goldberger and K. M. Watson, *Collision Theory* (Wiley, New York, 1964).

[2] F. Halzen and A. D. Martin, *Quarks and Leptons* (Wiley, New York, 1984).

[3] W. Heitler, *The Quantum Theory of Radiation* (Clarendon Press, Oxford, 1954).

[4] M. Lax, *Rev. Mod. Phys.* **23**, 287 (1951).

[5] B. A. Lippmann and J. Schwinger, *Phys. Rev.* **79**, 469 (1950).

[6] J. J. Sakurai, *Advanced Quantum Mechanics* (Addison-Wesley, Reading, Mass., 1967).

[7] H. Frauenfelder, *Subatomic Physics* (Prentice-Hall, Englewood Cliffs, N. J., 1974).

[8] C. Cohen-Tannoudji, B. Diu, and F. Lalöe, *Quantum Mechanics* (Wiley, New York, 1977).

[9] L. I. Schiff, *Quantum Mechanics* (McGraw-Hill, New York, 1968).

[10] A. Messiah, *Quantum Mechanics* (Wiley, New York, 1962), vol. 2.

3. SCATTERING THEORY

3.1 Semiclassical Wave Theory

So far, a quantum mechanical, microscopic description of the scattering amplitude has been derived for a single incoming particle interacting with a scatterer. The goal is to derive a macroscopic description of the scattering amplitude for one or more incoming particles interacting with many scatterers. And, if the scatterers are densely distributed in space such that their interparticle separation is on the order of or less than the wavelength of the incoming particle, multiple scattering events must be taken in to account. Purely quantum mechanical calculations become quite difficult to compute when dealing with the interaction of more than two particles, and are, in many cases, impossible to compute when the number of particles exceeds several hundred. A small solid target with interatomic distances on the order of 1 Å and that is 10 μm thick with a surface area of 1 mm will have on the order of 10^{19} scatterers. Clearly, a purely quantum mechanical approach toward solving the scattering problem is not possible.

One must therefore rely upon some other approach, such as a semiclassical theory, to obtain a macroscopic scattering amplitude. Fortunately, the inhomogeneous classical wave equation inherently describes multiple scattering--it describes the propagation of a wave (a packet of many incoming particles) in a many particle medium. Its superb success in describing wave phenomena in classical physics is why the semiclassical framework is commonly used to make the bridge between classical and quantum physics.

From here on, the emphasis will mainly be on scattering processes in which photons are the incoming particles (with the knowledge that inhomogeneous wave equations can be constructed for other particles, such as electrons). In the classical picture, their interaction with matter is adequately described by the Maxwell equations. Jackson[1] shows how to go from the microscopic Maxwell equations,

$$\nabla \cdot \mathbf{b} = 0 \qquad \nabla \times \mathbf{e} + \frac{1}{c}\frac{\partial \mathbf{b}}{\partial t} = 0$$

$$\nabla \cdot \mathbf{e} = 4\pi\eta \qquad \nabla \times \mathbf{b} - \frac{1}{c}\frac{\partial \mathbf{e}}{\partial t} = \frac{4\pi}{c}\mathbf{j}, \tag{3-1.1}$$

where $\mathbf{e}$ and $\mathbf{b}$ are the microscopic electric and magnetic fields and η and $\mathbf{j}$ are the microscopic charge and current densities, to the macroscopic Maxwell equations,

$$\nabla\cdot\mathbf{B}=0 \qquad \nabla\times\mathbf{E}+\frac{1}{c}\frac{\partial\mathbf{B}}{\partial t}=0$$

$$\nabla\cdot\mathbf{D}=4\pi\rho \qquad \nabla\times\mathbf{H}-\frac{1}{c}\frac{\partial\mathbf{D}}{\partial t}=\frac{4\pi}{c}\mathbf{J}, \tag{3-1.2}$$

where ρ and $\mathbf{J}$ are the macroscopic free charge and current densities. The transition from the classical microscopic equations to a semiclassical macroscopic description is done by taking the expectation values and spatially averaging over all microscopic quantities. Spatially averaging over the microscopic fluctuations due to thermal motion, zero point fluctuations, and orbital motion, gives the smooth, slowly varying macroscopic quantities present in the Maxwell equations for a medium. The macroscopic picture is taken to be on the order of Avagadro's number of atoms per cubic centimeter, 10^{24} atoms/cm^3, where the length scale, 100 Å, is taken as an absolute lower limit to the macroscopic domain. The macroscopic electric displacement, $\mathbf{D}$, and magnetic field, $\mathbf{H}$, come from the spatial average over the microscopic charge and current densities

$$D_\alpha = E_\alpha + 4\pi\left\{P_\alpha - \sum_\beta \frac{\partial Q'_{\alpha\beta}}{\partial x_\beta} + \cdots\right\} \tag{3-1.3}$$

$$H_\alpha = B_\alpha - 4\pi\{M_\alpha + \cdots\} \tag{3-1.4}$$

where $\mathbf{P}(\mathbf{x},t)$, $\mathbf{Q}'(\mathbf{x},t)$, and $\mathbf{M}(\mathbf{x},t)$ are the macroscopic electric polarization, quadrupole density, and magnetization. For a substance that has a linear response (that is, any induced electric or magnetic polarization is proportional to the magnitude of the applied field),

$$\mathbf{D}=\boldsymbol{\varepsilon}\mathbf{E} \tag{3-1.5}$$

$$\mathbf{H}=\boldsymbol{\mu}^{-1}\mathbf{B} \tag{3-1.6}$$

where $\boldsymbol{\varepsilon}$ and $\boldsymbol{\mu}$ are the dielectric and magnetic permeability tensors. Note that the dielectric and permeability tensors are proportional to the electric and magnetic multipole moments.

As a simple example, let both tensors be diagonal, with all diagonal elements equal, as for an isotropic medium. Then

$$D_\alpha = \varepsilon_0 E_\alpha \quad , \quad H_\alpha = \mu_0^{-1} B_\alpha \tag{3-1.7}$$

and thus

$$\varepsilon_0 = 1 + 4\pi\left\{\frac{P_\alpha}{E_\alpha} - \frac{1}{E_\alpha}\sum_\beta \frac{\partial Q'_{\alpha\beta}}{\partial x_\beta} + \cdots\right\} \tag{3-1.8}$$

and $$\mu_0^{-1} = 1 - 4\pi\left\{\frac{M_\alpha}{B_\alpha} + \cdots\right\}. \tag{3-1.9}$$

For multipole moments small in comparison to the electric and magnetic fields that generate them, the quantity $\varepsilon_0\mu_0$, which is the square of the index of refraction, is then

$$n^2 = \varepsilon_0\mu_0 = 1 + 4\pi\left\{\frac{P_\alpha}{E_\alpha} + \frac{M_\alpha}{B_\alpha} - \frac{1}{E_\alpha}\sum_\beta \frac{\partial Q'_{\alpha\beta}}{\partial x_\beta} + \cdots\right\}$$
$$+(4\pi)^2 \times \text{Multipole Mixtures}. \tag{3-1.10}$$

This shows that the index of refraction of a medium is proportional to the electric and magnetic multipole moments generated by that medium, and it also has terms proportional to mixtures, or products, of electric and magnetic multipoles. The quantum mechanical expectation value of this quantity will be taken to produce a semiclassical theory for the scattering amplitude.

3.2 Inhomogeneous Wave Equation

The inhomogeneous wave equation can be constructed from the Maxwell macroscopic equations. However, one must note that the relationship between **D** and **E** can be nonlocal. In other words, **D** at time t and position **x** can depend upon **E** at times and positions other than t and **x**. The relationship between the sources, $\boldsymbol{\varepsilon}(\mathbf{x},t)$, and the fields they generate, $\mathbf{D}(\mathbf{x},t)$, must be causal to ensure that the fields do not instantaneously propagate from one point in space to another. For the electric displacement[1]

$$D_\alpha(\mathbf{x},t) = \sum_\beta \int d^3x' \int dt' \varepsilon_{\alpha\beta}(\mathbf{x}',t') E_\beta(\mathbf{x}-\mathbf{x}', t-t'). \tag{3-2.1}$$

In frequency space,

$$D_\alpha(\mathbf{k},\omega) = \sum_\beta \varepsilon_{\alpha\beta}(\mathbf{k},\omega) E_\beta(\mathbf{k},\omega) \tag{3-2.2}$$

and similarly

$$H_\alpha(\mathbf{k},\omega) = \sum_\beta \mu^{-1}_{\alpha\beta}(\mathbf{k},\omega) B_\beta(\mathbf{k},\omega) \tag{3-2.3}$$

where the Fourier transform is defined as

$$f(\mathbf{k},\omega) = \int d^3x \int dt f(\mathbf{x},t) e^{-i\mathbf{k}\cdot\mathbf{x}+i\omega t}. \tag{3-2.4}$$

The inhomogeneous wave equation in frequency space can now be constructed. The Fourier transform of the **E** and **B** fields in the second relation of Eq. 3-1.2 gives

$$\nabla \times \mathbf{E}(\mathbf{x},\omega) - i\frac{\omega}{c}\mathbf{B}(\mathbf{x},\omega) = 0. \tag{3-2.5}$$

Doing the same for the fourth relation of Eq. 3-1.2, for no free current, gives

$$\int d\omega e^{-i\omega t}\int d^3x' e^{i\mathbf{k}\cdot\mathbf{x}'}\left\{\nabla\times\left[\boldsymbol{\mu}^{-1}(\mathbf{x}',\omega)\mathbf{B}(\mathbf{x}-\mathbf{x}',\omega)\right]+i\frac{\omega}{c}\boldsymbol{\varepsilon}(\mathbf{x}',\omega)\mathbf{E}(\mathbf{x}-\mathbf{x}',\omega)\right\}=0.$$

The dielectric and permeability tensors depend upon the observation point **x** since they may have an overall spatial distribution throughout the interaction volume. If the spatial frequencies of the inverse magnetic permeability are far smaller than those of the magnetic field, spatial derivatives of the inverse permeability tensor can be neglected. If the sources that generate the multipole fields have dimensions that are small compared to the spatial variation of the **E** and **B** fields in the medium, then they can be considered to be sharply localized around the points **x′** with negligible effects outside a small volume around **x′**. Then, for particles such as electrons and nuclei that have diameters much smaller than the spatial variation of light down to X-ray wavelengths, the tensor quantities can be approximated as

$$\boldsymbol{\mu}^{-1}(\mathbf{x}',\omega) = \delta(\mathbf{x}-\mathbf{x}')\boldsymbol{\mu}^{-1}(\mathbf{x},\omega) \tag{3-2.6}$$

$$\boldsymbol{\varepsilon}(\mathbf{x}',\omega) = \delta(\mathbf{x}-\mathbf{x}')\boldsymbol{\varepsilon}(\mathbf{x},\omega). \tag{3-2.7}$$

Then the expression above reduces to

$$\nabla\times\mathbf{B}(\mathbf{x},\omega)+i\frac{\omega}{c}\boldsymbol{\mu}(\mathbf{x},\omega)\boldsymbol{\varepsilon}(\mathbf{x},\omega)\mathbf{E}(\mathbf{x},\omega)=0. \tag{3-2.8}$$

Taking the curl of Eq.3-2.5 and substituting the results into Eq.3-2.8 give the Maxwell wave equation for a medium:

$$\nabla^2\mathbf{E}(\mathbf{x},\omega)+(\omega/c)^2\boldsymbol{\mu}(\mathbf{x},\omega)\boldsymbol{\varepsilon}(\mathbf{x},\omega)\mathbf{E}(\mathbf{x},\omega)=0 \tag{3-2.9}$$

where the observation point has been placed far from the scatterer to make the longitudinal components of the **E** field negligible so that $\nabla\cdot\mathbf{E}\approx 0$.

A quantity $2\boldsymbol{\varepsilon}_0$ will be defined where

$$n^2 = 1+2\boldsymbol{\varepsilon}_0(\mathbf{x},\omega) = \boldsymbol{\mu}(\mathbf{x},\omega)\boldsymbol{\varepsilon}(\mathbf{x},\omega). \tag{3-2.10}$$

The quantity $2\boldsymbol{\varepsilon}_0$ carries all the information about the electric and magnetic multipoles. This leads to an expression of the inhomogeneous wave equation for transverse electric fields within a medium

$$\left(\nabla^2+k_{0v}^2+k_{0v}^2\left[2\boldsymbol{\varepsilon}_0(\mathbf{x},\omega)\right]\right)\mathbf{E}(\mathbf{x},\omega)=0, \tag{3-2.11}$$

where $k_{0v} = \omega/c$ (3-2.12)

and $\nabla \cdot \mathbf{E} = 0.$ (3-2.13)

3.3 Integral Scattering Equation

There is a scalar wave equation for each component of **E**. Let φ be one of those components of the **E** field in a basis that diagonalizes the index of refraction tensor. Also define

$$U(\mathbf{x},\omega) = k_{0v}^2[2\varepsilon_0(\mathbf{x},\omega)]. \tag{3-3.1}$$

The scalar wave equation is then

$$(\nabla^2 + k_{0v}^2)\varphi(\mathbf{x},\omega) = -U(\mathbf{x},\omega)\varphi(\mathbf{x},\omega). \tag{3-3.2}$$

The Green function techniques can be used to solve this inhomogeneous scalar wave equation. Constructing a Green function that satisfies

$$(\nabla^2 + k_{0v}^2)G(\mathbf{x},\mathbf{x}') = -4\pi\delta(\mathbf{x}-\mathbf{x}') \tag{3-3.3}$$

leads to the solution of Eq.3-3.2:

$$\varphi(\mathbf{x},\omega) = \phi_i(\mathbf{x},\omega) + \int G(\mathbf{x},\mathbf{x}')U(\mathbf{x}',\omega)\varphi(\mathbf{x}',\omega)d^3x', \tag{3-3.4}$$

where $\phi_i(\mathbf{x},\omega)$ is the solution to homogeneous wave equation

$$(\nabla^2 + k_{0v}^2)\phi_i(\mathbf{x},\omega) = 0. \tag{3-3.5}$$

Thus $\phi_i(\mathbf{x},t)$ represents the state of the system, or the wavefield in the medium, before the perturbation $U(\mathbf{x},t)$ exists -- $\phi_i(\mathbf{x},t)$ is the initial, or incoming, wavefield.

Equation 3-3.4 is commonly referred to as the integral scattering equation or the Lippmann-Schwinger integral equation.[2-4] The second term describes the scattered part of the incoming wave. To see this more clearly, note that the Green function for outgoing spherical waves is[1]

$$G(\mathbf{x},\mathbf{x}') = \frac{e^{ik_{0v}|\mathbf{x}-\mathbf{x}'|}}{4\pi|\mathbf{x}-\mathbf{x}'|}. \tag{3-3.6}$$

For observation distances far from the scatterer, $|\mathbf{x}| >> |\mathbf{x}'|$, then

$$|\mathbf{x}-\mathbf{x}'| = \sqrt{x^2 + x'^2 - 2\mathbf{x}\cdot\mathbf{x}'} \approx x - \frac{\mathbf{x}\cdot\mathbf{x}'}{x}.$$

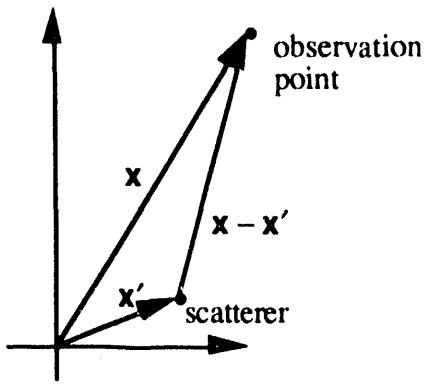

Fig. 3-3.1. Scattering Geometry

Also note that $\mathbf{x}$ is approximately the direction of the fields emanating from the scatterer. Defining a propagation vector

$$\mathbf{k}_f = k_{0v}(\mathbf{x}/x), \tag{3-3.7}$$

gives

$$\varphi(\mathbf{x},\omega) = \phi_i(\mathbf{x},\omega) + \frac{1}{4\pi}\frac{e^{ik_{0v}x}}{x}\int e^{i\mathbf{k}_f\cdot\mathbf{x}'}U(\mathbf{x}',\omega)\varphi(\mathbf{x}',\omega)d^3x'. \tag{3-3.8}$$

Letting the final wavefunction, which exists when the perturbation $U(\mathbf{x},\omega)$ ceases, be a normalized plane wave state

$$\phi_f(\mathbf{x},\omega) = \frac{e^{i\mathbf{k}_f\cdot\mathbf{x}}}{(2\pi)^{3/2}}, \tag{3-3.9}$$

and, assuming that $\varphi(\mathbf{x},\omega)$ will also have a normalized plane wave structure, then

$$\varphi(\mathbf{x},\omega) = \phi_i(\mathbf{x},\omega) + \frac{e^{ik_{0v}x}}{x}f(\mathbf{k}_f,\mathbf{k}_i) \tag{3-3.10}$$

where a scattering amplitude, $f(\mathbf{k}_f,\mathbf{k}_i)$, has been defined as

$$f(\mathbf{k}_f,\mathbf{k}_i) = 2\pi^2\int\phi_f(\mathbf{x}',\omega)U(\mathbf{x}',\omega)\varphi(\mathbf{x}',\omega)d^3x', \tag{3-3.11}$$

and the incoming wavevector is defined as

$$\mathbf{k}_i = k_{0v}(\mathbf{x}'/x). \tag{3-3.12}$$

So far, only a classical approach towards scattering has been followed. To obtain a semiclassical formalism that is general enough to deal with many types of incoming particles and scatterers, the scattering amplitude is related to the expectation value of a perturbation operator

$$f(\mathbf{k}_f,\mathbf{k}_i) = 2\pi^2\langle\phi_f|U|\psi\rangle \tag{3-3.13}$$

where $|\phi_f\rangle$ is the total final quantum state of the system which includes both the incoming particle and the scatterer, and $|\psi\rangle$ is the total quantum state of the system during the perturbation.

The form of the operator $U(\mathbf{x},\omega)$ can easily be obtained from quantum mechanics. For instance, nonrelativistic particles with mass obey the Schrödinger equation which can be put into the form of a scalar inhomogeneous wave equation. In frequency space the Schrödinger equation can be written in the form

$$\left(\nabla^2 + k_{0v}^2\right)\psi(\mathbf{x},\omega) = \left(2m/\hbar^2\right)V(\mathbf{x},\omega)\psi(\mathbf{x},\omega) \tag{3-3.14}$$

where

$$k_{0v}^2 = 2mE/\hbar^2. \tag{3-3.15}$$

The scattering amplitude for particles with mass is then

$$f\left(\mathbf{k}_f,\mathbf{k}_i\right) = -\left(4\pi^2 m/\hbar^2\right)\langle\phi_f|V|\psi\rangle. \tag{3-3.16}$$

3.4 Scattering Amplitude for Photons

To derive the scattering amplitude for massless incoming particles, a relativistic Schrödinger equation must be developed. This can be done by utilizing the Schrödinger time dependent equation

$$i\hbar\frac{\partial}{\partial t}\psi(\mathbf{x},t) = H\psi(\mathbf{x},t). \tag{3-4.1}$$

The relativistic energy-momentum equation allows the construction of a Lorentz invariant Hamiltonian for the photon:

$$H^2 = p^2c^2 \tag{3-4.2}$$

where $\mathbf{p} = -i\hbar\nabla$ and, from the Schrödinger time dependent equation,

$$H = i\hbar\frac{\partial}{\partial t}. \tag{3-4.3}$$

Then Eq. 3-4.2 reduces to

$$\left(\frac{1}{c^2}\frac{\partial^2}{\partial t^2} - \nabla^2\right)\psi(\mathbf{x},t) = 0 \tag{3-4.4}$$

when it operates on a wavefunction $\psi(\mathbf{x},t)$.

Define the space-time 4-momentum operator product as

$$-p^{\mu}p_{\mu} = \frac{1}{c^2}\frac{\partial^2}{\partial t^2} - \nabla^2 = -\partial^{\mu}\partial_{\mu} \tag{3-4.5}$$

where
$$\partial_{\mu} = \left(\frac{1}{c}\frac{\partial}{\partial t}, \nabla\right), \quad \partial^{\mu} = \left(\frac{1}{c}\frac{\partial}{\partial t}, -\nabla\right) \tag{3-4.6}$$

and
$$p^{\mu} = i\partial^{\mu}. \tag{3-4.7}$$

Then, the relativistic operator wave equation for a photon can be written in the form

$$\partial^{\mu}\partial_{\mu}\psi(\mathbf{x},t) = 0. \tag{3-4.8}$$

The first quantization condition instructs one to perform a gauge transformation on the 4-momentum

$$p^{\mu} \rightarrow p^{\mu} + (e/c)A^{\mu} \tag{3-4.9}$$

where A^{μ} is the 4-vector potential, $A^{\mu} = (\Phi, \mathbf{A})$, and Φ and $\mathbf{A}$ are the scalar and vector potentials of the state consisting of both the photon and the scatterer. The gauge transformation then results in

$$p^{\mu}p_{\mu} = (i\partial^{\mu})(i\partial_{\mu}) \rightarrow \left(i\partial^{\mu} + \frac{e}{c}A^{\mu}\right)\left(i\partial_{\mu} + \frac{e}{c}A_{\mu}\right).$$

Then

$$\partial^{\mu}\partial_{\mu}\psi(\mathbf{x},t) = V(\mathbf{x},t)\psi(\mathbf{x},t) \tag{3-4.10}$$

where
$$V(\mathbf{x},t) = i(e/c)\left[\partial_{\mu}A^{\mu} + A^{\mu}\partial_{\mu}\right] + (e/c)^2 A^{\mu}A_{\mu}. \tag{3-4.11}$$

Equation 3-4.10 is the Klein-Gordon wave equation for a massless particle. Written out explicitly, it has the form of an inhomogeneous wave equation

$$\left(\nabla^2 - \frac{1}{c^2}\frac{\partial^2}{\partial t^2} + V(\mathbf{x},t)\right)\psi(\mathbf{x},t) = 0. \tag{3-4.12}$$

This expression can be written in frequency space by using the same methods as in Section 3.2 where, to maintain causality between sources and the fields they emit, the product $V(\mathbf{x},t)\psi(\mathbf{x},t)$ is more accurately expressed as the convolution in space and time of the two quantities. The frequency space representation of the Klein-Gordon wave equation is then

$$\left[\nabla^2 + k_{0v}^2 + V(\mathbf{x},\omega)\right]\psi(\mathbf{x},\omega) = 0. \tag{3-4.13}$$

This equation has the same form as the classical wave equation, Eq. 3-2.11. Both equations must be equivalent in the many particle limit where the quantum and classical pictures converge. Thus, the index of refraction effect is the physical observable found by taking the expectation value and spatially averaging over the interaction volume of the interaction perturbation Hamiltonian

$$k_{0v}^2[2\varepsilon_0(\mathbf{x},\omega)] = const \times \overline{\langle \phi_f | V | \psi \rangle}. \tag{3-4.14}$$

The constant can be determined though the optical theorem. From the Maxwell equations the exponential decay of the intensity of a field traversing a distance d through a medium is related to a macroscopic total cross section

$$I = I_0 e^{-n_f \overline{\sigma_{tot}} d/V_0} \tag{3-4.15}$$

where n_f is the number of scatterers, I_0 is the incoming field intensity, and the macroscopic total cross section is the spatial average of the microscopic cross section derived in Section 2.3. But,

$$I = I_0 \left| e^{i\mathbf{k}_f \cdot \mathbf{x}} \right|^2 = I_0 e^{-k_f d \,\mathrm{Im}\{2\varepsilon_0\}}. \tag{3-4.16}$$

Then, for one scatterer

$$\mathrm{Im}\{2\varepsilon_0\} = \overline{\sigma_{tot}}/k_f V_0 = \frac{4\pi}{k_f^2 V_0} \mathrm{Im}\left\{\overline{F(\mathbf{k}_f, \mathbf{k}_i)}\right\}. \tag{3-4.17}$$

If the imaginary parts of the two quantities are related by the expression above, then by analytical continuation both the real and imaginary parts are related by

$$2\varepsilon_0(\mathbf{x},\omega) = \frac{4\pi}{k_f^2 V_0} \overline{F(\mathbf{k}_f, \mathbf{k}_i)} = -\frac{4\pi}{k_f^2 V_0} A_0 \overline{T_{fi}}. \tag{3-4.18}$$

This is a form of the Lorentz relation seen in classical electrodynamics.[5] The constant in Eq. 3-4.14 has then been determined along with a direct form of the T-matrix elements

$$T_{fi} = \langle \phi_f | V | \psi \rangle. \tag{3-4.19}$$

The T-matrix elements on the energy shell are given in Eq. 2-2.18. A more general expression can now be derived by making use of the series expansion of the perturbed wavefunction, Eq. 2-1.5

$$\langle \phi_f(\mathbf{x},t) | V(\mathbf{x},t) | \psi(\mathbf{x},t) \rangle = \sum\nolimits_n a_n(t) e^{-iE_n t/\hbar} e^{iE_f t/\hbar} \int_{V_0} \phi_f^*(\mathbf{x}) V(\mathbf{x},t) \phi_n(\mathbf{x}) d^3x$$

$$= i\hbar \dot{S}_{fi}(t). \tag{3-4.20}$$

Thus, the T-matrix elements are proportional to the time rate of change of the transition amplitude from the final to the initial state. Also note that

$$\langle \phi_f | V | \psi \rangle = \langle \phi_f | T | \phi_i \rangle \tag{3-4.21}$$

which leads to

$$T|\phi_i\rangle = V|\psi\rangle = VS|\phi_i\rangle \tag{3-4.22}$$

and thus

$$T = VS. \tag{3-4.23}$$

The T-operator is then a scattering operator that describes the combined effect of a perturbation and an S-scattering operator.

3.5 Coherence Properties of the Scattering Amplitude

An examination of the S-matrix elements for a constant perturbation will yield useful information about the coherence properties of the scattering amplitude. From Eqs. 2-1.10 to 2-1.17 in the section on perturbation theory, and using the $i\varepsilon$ convergence factor to do the integrals as was done in Section 2.2, gives an expression for T_{fi} up to third order for the constant perturbation, Eq. 2-2.6:

$$T_{fi} = i\hbar\dot{S}_{fi}(t) = i\hbar\Big[(-i/\hbar)V_{fi}e^{i\omega_{fi}t} + (-i/\hbar)^2\sum_{n\neq i}V_{fn}e^{i\omega_{fn}t}\int_{-\infty}^{t}V_{ni}e^{i\omega_{ni}t'}\,dt'$$

$$+(-i/\hbar)^3\sum_{m\neq i}\sum_{n\neq m}V_{fn}e^{i\omega_{fn}t}\int_{-\infty}^{t}V_{nm}e^{i\omega_{nm}t_1}\,dt_1\int_{-\infty}^{t_1}V_{mi}e^{i\omega_{mi}t_2}\,dt_2+\cdots\Big]$$

$$= e^{i\omega_{fi}t}\left[V_{fi}+\sum_{n\neq i}\frac{V_{fn}V_{ni}}{E_i-E_n}+\sum_{m\neq i}\sum_{n\neq m}\frac{V_{fn}V_{nm}V_{mi}}{(E_i-E_m)(E_i-E_n)}+\cdots\right]. \qquad (3\text{-}5.1)$$

The variable t in the expressions above is simply a parameter that indicates when the perturbation is turned off. Since the lower limit of the integral in the evaluation of T_{fi} was $t=-\infty$, an assumption was made that the perturbation was left on for a time long compared to the period of the oscillator (many oscillations occured during the perturbation)

$$t >> \frac{1}{\omega_{fi}}. \qquad (3\text{-}5.2)$$

The coherence properties of T_{fi} are now readily evident. On the energy shell, or for energy conserving transitions where $E_i = E_f$, the overall phase factor disappears and gives, as expected, the on-energy-shell T-matrix elements expressed in Eq. 2-2.18. Off the energy shell, or for non-energy conserving transitions where $E_i \neq E_f$, the overall phase factor remains attached to T_{fi}. At this point one should note that there are no physical systems that can instantaneously turn off a perturbation--sources have an effective decay time associated with the lifetime of the atomic systems comprising the sources. There is then an uncertainty relation associated with when the perturbation is turned off which will

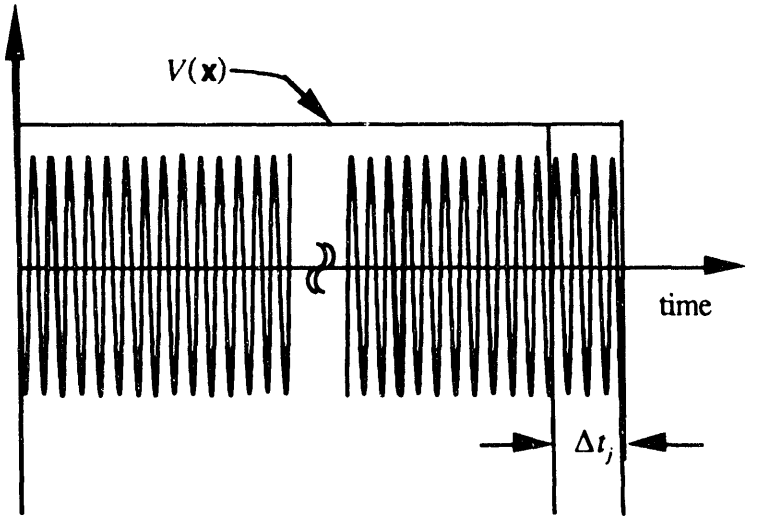

Fig. 3-5.1. Uncertainty, Δt_j, in when constant perturbation ceases.

be called a jitter, Δt_j. The jitter should be on the order of the inverse spontaneous linewidth, or decay rate, of the source

$$\Delta t_j \sim 1/\Gamma. \tag{3-5.3}$$

Typically Γ is on the order of or greater than 10^9/sec (for atomic sources). Photons with frequencies in the visible to X-ray regime have energies $E > 0.1$ eV or frequencies $\nu > 10^{14}$ cycles/sec. Thus, for X-ray photons, the jitter will cover many periods of oscillation. Since the time parameter, t, is uncertain to within Δt_j, the phase is then essentially random. If $\omega_{fi} \neq 0$, then T_{fi} will exhibit a type of temporal incoherence.

The coherence properties can be observed in the definition of the differential scattering cross section

$$\frac{d\sigma}{d\Omega} = \left|F(\mathbf{k}_f, \mathbf{k}_i)\right|^2 = A_0^2 \left|T_{fi}\right|^2. \tag{3-5.4}$$

If there is more than one final and initial state, then the total differential cross section is the sum over all possible states

$$\frac{d\sigma}{d\Omega} = A_0^2 \left|\sum_{fi} T_{fi}\right|^2 = A_0^2 \left|\sum_{fi} B_{fi} e^{i\phi_{fi}}\right|^2 \tag{3-5.5}$$

where B_{fi} is some complex scattering factor for the transition from $i \rightarrow f$ and $\phi_{fi} = \omega_{fi} t$ is a random phase factor. For the example in this section,

$$B_{fi} = V_{fi} + \sum_{n \neq i} \frac{V_{fn} V_{ni}}{E_i - E_n} + \sum_{m \neq i} \sum_{n \neq m} \frac{V_{fn} V_{nm} V_{mi}}{(E_i - E_m)(E_i - E_n)} + \cdots \tag{3-5.6}$$

Since ϕ_{fi} is a random phase, all the interference terms average to zero and

$$\frac{d\sigma}{d\Omega} = A_0^2 \left| \sum_{i,f=i} B_{fi} \right|^2 + A_0^2 \sum_{i,f\neq i} |B_{fi}|^2 . \tag{3-5.7}$$

The total differential cross section is composed of two terms. The first term is a coherent sum of amplitudes that have the same temporal phase factor: $\phi_{fi} = 0$. Since each amplitude always lies on the energy shell, the scattering is elastic. The second term is an incoherent sum of amplitudes with nonzero random temporal phase factors. Since each amplitude always lies off the energy shell, the scattering is inelastic. Imbedded within each of the terms in Eq. 3-5.7 is a coherent sum over all possible intermediate states as represented by the expression for B_{fi} in Eq. 3-5.6. For this reason, calling the scattering process represented by each term in Eq. 3-5.7 as either a coherent or an incoherent process is misleading and ambiguous. For elastic scattering all scattering amplitudes are coherent with each other, whereas for inelastic scattering the scattering amplitudes may or may not be coherent with each other. This discussion is summarized below :

Transition 1: $i \rightarrow f_1$
Transition 2: $i \rightarrow f_2$
Transition 3: $j \rightarrow k$

Amplitudes T_1 and T_2 are incoherent with respect to each other for $f_1 \neq f_2$. If $f_1 \neq f_2 \neq i$ the scattering amplitudes are inelastic $(\omega_{fi} \neq 0)$. If $\omega_{kj} = \omega_{f_1 i}$ then T_1 and T_3 are coherent with respect to each other (and inelastic if $f_1 \neq i$ and $k \neq j$)

Transition 1: $i \rightarrow n_1 \rightarrow f$
Transition 2: $i \rightarrow n_2 \rightarrow f$
Transition 3: $j \rightarrow k \rightarrow m$

Amplitudes T_1 and T_2 are coherent with respect to each other, and if $f \neq i$ the scattering is inelastic. If $\omega_{mj} = \omega_{fi}$ then T_3 is coherent with respect to both T_1 and T_2.

Transition 1: $i \rightarrow n_1 \rightarrow i$
Transition 2: $i \rightarrow n_2 \rightarrow i$
Transition 3: $j \rightarrow k \rightarrow j$

Amplitudes T_1 , T_2 , and T_3 are all coherent with respect to each other and the scattering is elastic.

3.6 Harmonic Perturbation

The interaction of a photon with a scatterer is modeled in perturbation theory by forcing the interaction perturbation to be a harmonic potential. Before second quantizing

the scattering theory, important information can be extracted by examining the semiclassical perturbation of a monochromatic harmonic potential

$$V(\mathbf{x},t)=\begin{cases}0 & t\to-\infty\\ 2V(\mathbf{x})\cos\omega t\end{cases}. \tag{3-6.1}$$

The T-matrix elements, to second order, are then

$$T_{fi}=V_{fi}\left[e^{i(\omega_{fi}+\omega)t}+e^{i(\omega_{fi}-\omega)t}\right]+\sum_{n\neq i}V_{fn}V_{ni}\left[\frac{e^{i\omega_{fi}t}+e^{i(\omega_{fi}+2\omega)t}}{E_i-(E_n+\hbar\omega)}+\frac{e^{i\omega_{fi}t}+e^{i(\omega_{fi}-2\omega)t}}{E_i-(E_n-\hbar\omega)}\right]. \tag{3-6.2}$$

Examining only the T-matrix elements that lie on the energy shell reveals that there can be both elastic and inelastic scattering processes (in the constant perturbation case of the last section only elastic scattering processes existed on the energy shell). These processes are summarized in the diagrams below.

(1). Single photon absorption (inelastic scattering):

$\omega_{fi}-\omega=0 \qquad T_{fi}=V_{fi}$

$\underbrace{E_i+\hbar\omega}_{\text{initial state energy}}=\underbrace{E_f}_{\text{final state energy}} \qquad \Omega_{fi}=\omega_{\mathbf{k}_i}$

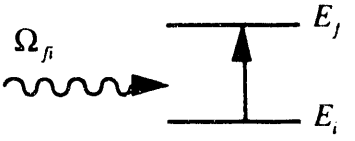

Fig. 3–6.1. Single photon absorption.

(2) Single photon emission (inelastic scattering):

$\omega_{fi}+\omega=0 \qquad T_{fi}=V_{fi}$

$\underbrace{E_i}_{\text{initial state energy}}=\underbrace{E_f+\hbar\omega}_{\text{final state energy}} \qquad \Omega_{fi}=-\omega_{\mathbf{k}_f}$

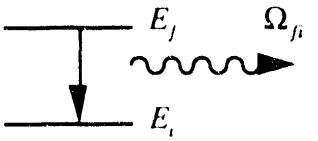

Fig. 3–6.2. Single photon emission.

(3) Two photon absorption (inelastic scattering):

$$\omega_{fi} - 2\omega = 0 \qquad T_{fi} = \sum_{n \neq i} \frac{V_{fn} V_{ni}}{E_i - E_n + \hbar\Omega_{ni}}$$

$$E_i + 2\hbar\omega = E_f \qquad \Omega_{ni} = \omega_{\mathbf{k}_i}$$

$$2\omega = \omega_{\mathbf{k}_i} + \omega'_{\mathbf{k}_i} \qquad \Omega_{fn} = \omega'_{\mathbf{k}_i}$$

For monochromatic incoming beam: $\omega_{\mathbf{k}_i} = \omega'_{\mathbf{k}_i}$

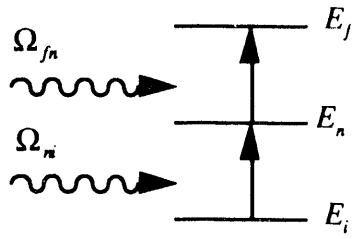

Fig. 3–6.3. Two photon absorption.

(4) Two photon emission (inelastic scattering):

$$\omega_{fi} + 2\omega = 0 \qquad T_{fi} = \sum_{n \neq i} \frac{V_{fn} V_{ni}}{E_i - E_n + \hbar\Omega_{ni}}$$

$$E_i = E_f + 2\hbar\omega \qquad \Omega_{ni} = -\omega_{\mathbf{k}_f}$$

$$2\omega = \omega_{\mathbf{k}_f} + \omega'_{\mathbf{k}_f} \qquad \Omega_{fn} = -\omega'_{\mathbf{k}_f}$$

For monochromatic outgoing beam: $\omega_{\mathbf{k}_f} = \omega'_{\mathbf{k}_f}$

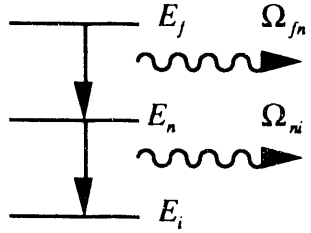

Fig. 3–6.4. Two photon emission.

(5) Absorption reemission (elastic if $\omega_{\mathbf{k}_i} = \omega_{\mathbf{k}_f}$):

$$\omega_{fi} = 0 \qquad T_{fi} = \sum_{n \neq i} \frac{V_{fn} V_{ni}}{E_i - E_n + \hbar\Omega_{ni}}$$

$$E_i = E_f \qquad \Omega_{ni} = \omega_{\mathbf{k}_i}$$

$$\Omega'_{ni} = -\omega_{\mathbf{k}_f}$$

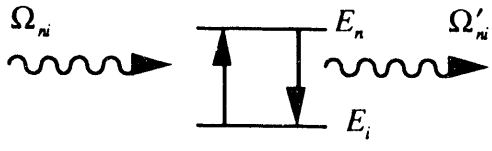

Fig. 3–6.5. Absorption reemission.

(6) Emission reabsorption (elastic if $\omega_{\mathbf{k}_i} = \omega_{\mathbf{k}_f}$):

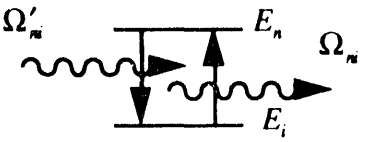

Fig. 3--6.6. Emission reabsorption.

$$\omega_{fi} = 0 \qquad T_{fi} = \sum_{n \neq i} \frac{V_{fn} V_{ni}}{E_i - E_n + \hbar\Omega_{ni}}$$

$$E_i = E_f \qquad \Omega_{ni} = -\omega_{\mathbf{k}_f}$$

$$\Omega'_{ni} = \omega_{\mathbf{k}_i}$$

Notice that even though the harmonic potential describes a single incoming particle, some of the processes (and all of the higher order terms) have more than one photon interacting with the oscillator. Perturbation theory then allows for many photon transitions to occur. Even though the semiclassical perturbation was not second quantized, it must consist of many discrete photons in order for the perturbation expansion to make sense. This is then a reconfirmation of what a classical field is--a distribution of quantum particles.

Note that the emission reabsorption case is simply the time reversed process of the absorption reemission case. There are also time reversed processes for the two photon absorption and emission cases that have been omitted. Performing a coherent sum over all these different processes leads to a total scattering amplitude which is similar to that derived in the constant perturbation case restricted to the energy shell

$$T_{fi} = V_{fi} + \sum_{n \neq i} \frac{V_{fn} V_{ni}}{E_i - (E_n - \hbar\Omega_{ni})} + \sum_{m \neq i} \sum_{n \neq m} \frac{V_{fn} V_{nm} V_{mi}}{[E_i - (E_m - \hbar\Omega_{mi})][E_i - (E_n - \hbar\Omega_{ni})]} + \cdots \quad (3\text{-}6.3)$$

3.7 Resonant Transitions

The expression in Eq. 3-6.3 is valid as long as all possible time ordered events are included. However, there appears to be a major problem for resonant transitions. For instance, for resonant two-photon processes, $\hbar\Omega_{ni} \approx E_n - E_i$, thus the second and all higher order terms in Eq. 3-6.3 go to infinity--the expansion appears to diverge. To keep the perturbation expansion convergent, a sum over many higher order terms must be performed. To do this, note that T_{fi} can be rewritten in a form similar to the Lippman-Schwinger equation

$$T_{fi} = V_{fi} + \sum_{n \neq i} \frac{V_{fn} T_{ni}}{E_i - E_n + \hbar\Omega_{ni}}. \tag{3-7.1}$$

For instance, the third order term can be constructed by inserting the second order term in for T_{ni}. Doing so results in Eq. 3-6.3 when T_{mi} is set equal to V_{mi}. This procedure can be done indefinitely to obtain all the higher order terms.

Another problem that must be properly dealt with is the correct expression for $1/x$. From Dirac one finds that[6]

$$1/x = \mathrm{P}\{1/x\} - i\pi\delta(x) \tag{3-7.2}$$

where P is the principal value and $\delta(x)$ is a Dirac delta function. This relationship can be inferred from noting that one would usually expect that

$$\frac{d}{dx} \ln x = 1/x. \tag{3-7.3}$$

However, upon integrating both sides of the expression near $x = 0$ gives

$$\int_{-\eta}^{+\eta} d(\ln x) = \ln(-1) \quad \text{and} \quad \int_{-\eta}^{+\eta} 1/x\, dx = 0,$$

where the second integral is zero because $1/x$ is a well behaving odd function. The integration then leads to the contradiction: $\ln(-1) = 0$.

Using the relation for the log of a complex number

$$\ln x = \ln|x| + i \arg(x) \tag{3-7.4}$$

allows the correction of Eq. 3-7.3 by setting $1/x$ to its expression in Eq. 3-7.2. This is the justification for Eq 3-7.2 (Note that $\arg(-1) = \pm\pi$. The minus sign was chosen for Eq. 3-7.2 because $1/x \sim 1/(E_i - E_n + \hbar\Omega_{ni} + i\varepsilon)$. The $i\varepsilon$ factor discussed in Section 2.2 has been suppressed in all preceding equations for convenience, but when it is considered in the integration above, one finds the minus sign to be the appropriate sign for Eq. 3-7.2. The $i\varepsilon$ factor, as discussed earlier, ensures that causality is obeyed.). For compactness define, as Heitler does, a ζ-function:[7]

$$\zeta(x) \equiv 1/x = \mathrm{P}\{1/x\} - i\pi\delta(x). \tag{3-7.5}$$

If only two photon processes are of interest, then the second order term in Eq. 3-6.3 must be split from all the other terms. This is accomplished by summing up two photon and all higher two photon scattering processes. Noting that there is no first order term, V_{fi}, for two photon processes gives (converting Eq. 3-7.1 to operator form)

$$T = V\frac{1}{E-H_0}T$$

$$= V\frac{1}{E-H_0}V + V\frac{1}{E-H_0}V\frac{1}{E-H_0}V\frac{1}{E-H_0}V + \cdots \tag{3-7.6}$$

where $H_0|n\rangle = E_n'|n\rangle = (E_n - \hbar\Omega_{ni})|n\rangle$ gives the energy of the intermediate state.

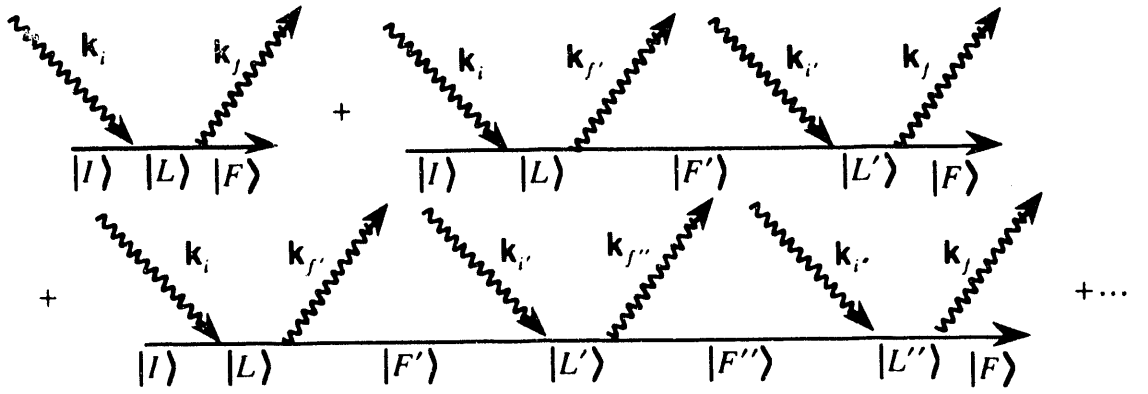

Fig. 3-7.1. Two photon absorption reemission scattering diagrams to all orders. The sum of all the scattering diagrams gives the total two photon scattering T-matrix elements.

This expansion is equivalent to summing two photon processes to all orders as shown in Fig.3-7.1 (for absorption reemission). This is a common procedure in quantum field theory, and there are plenty of tools available for performing the infinite sum (yielding, unfortunately, the same problems with ultraviolet divergences that must be dealt properly with renormalization theory). Using the identity[8]

$$\frac{1}{X+Y} = \frac{1}{X} - \frac{1}{X}Y\frac{1}{X} + \frac{1}{X}Y\frac{1}{X}Y\frac{1}{X} - \cdots \tag{3-7.7}$$

gives

$$T = V\frac{1}{E-H_0+V\dfrac{1}{E-H_0}V} \tag{3-7.8}$$

or, in matrix element form,

$$T_{fi} = \sum_{n\neq i}\frac{\langle f|V|n\rangle\langle n|V|i\rangle}{E_i - E_n + \hbar\Omega_{ni}} - \sum_{f\neq n}\frac{\langle n|V|f\rangle\langle f|V|n\rangle}{E_n - E_f + \hbar\Omega_{fn}}$$

$$= \sum_{n \neq i} \frac{V_{fn} V_{ni}}{E_i - E_n + \hbar\Omega_{ni} - \dfrac{\Gamma_n(E_{nf})}{2}} \tag{3-7.9}$$

When adding up all higher order terms (as shown in Fig. 3-7.1), the two photon T-matrix elements acquires a term, $\Gamma_n(E_{nf})$, in the denominator which prevents it from diverging on resonance ($E_i = E_n - \hbar\Omega_{ni}$). $\Gamma_n(E_{nf})$ is the sum of all transitions from some intermediate state, $|n\rangle$, to all possible final states, $|f\rangle$. It is therefore usually called a complex spontaneous transition rate. Its real and imaginary parts can be examined in more detail by using the ζ-function in Eq. 3-7.5:

$$\Gamma_n(E_{nf}) = 2\sum_{f \neq n} V_{nf} V_{fn} \left[\mathrm{P}\left\{ \frac{1}{E_n - E_f + \hbar\Omega_{fn}} \right\} - i\pi\delta(E_n - E_f + \hbar\Omega_{fn}) \right]. \tag{3-7.10}$$

For absorption reemission, the resulting photon, Ω_{fn}, is an emitted photon, $-\omega_{\mathbf{k}_f}$. Then

$$\Gamma_n(E_{nf}) = \Gamma_n(E_{\mathbf{k}_f}) = \mathrm{P}\left\{ 2\sum_{f \neq n} \frac{|V_{fn}|^2}{E_n - E_f - \hbar\omega_{\mathbf{k}_f}} \right\} - 2\pi i \sum_{f \neq n} |V_{fn}|^2 \delta(E_n - E_f - \hbar\omega_{\mathbf{k}_f}). \tag{3-7.11}$$

The real part of $\Gamma_n(E_{\mathbf{k}_f})$ is a level shift which is due to the self-energy of the scatterer and has a magnitude on the order of the natural linewidth.[5] The imaginary part corresponds to the natural linewidth and is a damping term caused by the effect of the emitted radiation on the oscillator--the oscillator produces its own damping self-force. This expression can be rewritten by substituting the non-physical, infinitely sharp δ-function by a density of states.

Let $d\rho(E)dE$ be the number of states in the interval E to $E + dE$. The density of states, $d\rho(E)$, can be obtained by solving for a particle in a box with sides of length L and imposing periodic boundary conditions. This gives rise to a discrete set of modes within the box:

$$e^{i\mathbf{k}\cdot\mathbf{x}} = e^{i\mathbf{k}\cdot(\mathbf{x}+\mathbf{L})}. \tag{3-7.12}$$

This is satisfied if

$$k_i = (2\pi/L)N_i \qquad i = x, y, z; \quad N = 0, \pm1, \pm2, \ldots \ . \tag{3-7-13}$$

The number of modes in the interval $N_x + dN_x$, $N_y + dN_y$, and $N_z + dN_z$ is then

$$dN = dN_x dN_y dN_z = (L/2\pi)^3 dk_x dk_y dk_z = \left[V_0/(2\pi)^3\right] k^2 dk d\Omega \tag{3-7.14}$$

where V_0 is the volume of the box. The number of states in the wavevector interval $\mathbf{k}$ and $\mathbf{k} + d\mathbf{k}$ is then

$$d\rho(k)dk = \left[V_0/(2\pi)^3\right]k^2 dk d\Omega. \tag{3-7.15}$$

Since $d\rho(E)dE = d\rho(k)dk$, then for $E = \hbar ck$ the density of states is

$$d\rho(E) = \frac{V_0}{(2\pi)^3}(E/\hbar)^2 \frac{d\Omega}{\hbar c^3}. \tag{3-7.16}$$

Notice that $d\rho(E)$ is defined only within a narrow cone of angles $d\Omega$. For a single isolated oscillator, the emitted photon can travel in any direction, thus the spontaneous transition probability is obtained by integrating over all the possible final photon states and all possible final photon directions

$$\Gamma_n\left(E_{\mathbf{k}_f}\right) = \mathrm{P}\left\{2\sum_{f\neq n}\int dE_{\mathbf{k}_f} \frac{\left|V_{fn}\right|^2}{E_n - E_f - E_{\mathbf{k}_f}} d\rho\left(E_{\mathbf{k}_f}\right)\right\}$$

$$-2\pi i\sum_{f\neq n}\int dE_{\mathbf{k}_f}\left|V_{fn}\right|^2 \delta\left(E_n - E_f - E_{\mathbf{k}_f}\right)d\rho\left(E_{\mathbf{k}_f}\right)$$

$$= 2D_n^+\left(E_{\mathbf{k}_f}\right) - i\Gamma_n^+\left(E_{\mathbf{k}_f}\right) \tag{3-7.17}$$

where,

$$D_n^+\left(E_{\mathbf{k}_f}\right) = \mathrm{P}\left\{\sum_{f\neq n}\int dE_{\mathbf{k}_f} d\Omega_{\mathbf{k}_f} \frac{\left|V_{fn}\right|^2}{E_n - E_f - E_{\mathbf{k}_f}} \rho\left(E_{\mathbf{k}_f}\right)\right\} \tag{3-7.18}$$

$$\Gamma_n^+\left(E_{\mathbf{k}_f}\right) = 2\pi\sum_{f\neq n}\int d\Omega_{\mathbf{k}_f}\left|V_{fn}\right|^2 \rho\left(E_{nf}\right) \tag{3-7.19}$$

and

$$\rho(E) = \frac{V_0}{(2\pi)^3\hbar c^3}(E/\hbar)^2. \tag{3-7.20}$$

The energy level shift is $2D_n^+\left(E_{\mathbf{k}_f}\right)$, $\Gamma_n^+\left(E_{\mathbf{k}_f}\right)$ is the natural linewidth, and $\rho\left(E_n - E_f = E_{nf}\right)$ is the density of states. Note that $\Gamma_n^+\left(E_{\mathbf{k}_f}\right)$ is independent of the outgoing photon energy--this is because the δ-function is infinitely sharp at $E_{\mathbf{k}_f} = E_n - E_f$. Broadening out the delta function will yield a natural linewidth that slowly varies with the photon energy.

In the case of emission reabsorption (Fig. 3-6.6), $\Gamma_n(E_{\mathbf{k}_i})$ is now a spontaneous absorption probability

$$\Gamma_n(E_{\mathbf{k}_i}) = 2D_n^-(E_{\mathbf{k}_i}) - i\Gamma_n^-(E_{\mathbf{k}_i}), \tag{3-7.21}$$

where

$$D_n^-(E_{\mathbf{k}_i}) = \mathrm{P}\left\{\sum_{f\neq n}\int dE_{\mathbf{k}_i}d\Omega_{\mathbf{k}_i}\frac{|V_{fn}|^2}{E_n - E_f + E_{\mathbf{k}_i}}\rho(E_{\mathbf{k}_i})\right\} \tag{3-7.22}$$

$$\Gamma_n^-(E_{\mathbf{k}_i}) = 2\pi\sum_{f\neq n}\int d\Omega_{\mathbf{k}_i}|V_{fn}|^2\rho(E_{fn}). \tag{3-7.23}$$

The first order two photon T-matrix element is the sum of all allowable two photon processes (absorption reemission, emission reabsorption, two photon absorption, two photon emission)

$$T_{fi} = \sum_{n\neq f}\left\{\frac{V_{fn}^a V_{ni}^a}{E_i - E_n + \hbar\omega_{\mathbf{k}_i} - D_n^+(E_{\mathbf{k}_f}) + i\Gamma_n^+/2} + \frac{V_{fn}^b V_{ni}^b}{E_i - E_n - \hbar\omega_{\mathbf{k}_f} - D_n^-(E_{\mathbf{k}_i}) + i\Gamma_n^-/2}\right.$$

$$\left. + \left[\frac{V_{fn}^c V_{ni}^c}{E_i - E_n + \hbar\omega_{\mathbf{k}_i} - D_n^-(E_{\mathbf{k}_i'}) + i\Gamma_n^-/2} + \frac{V_{fn}^d V_{ni}^d}{E_i - E_n - \hbar\omega_{\mathbf{k}_f} - D_n^+(E_{\mathbf{k}_f'}) + i\Gamma_n^+/2}\right]_{f\neq i}\right\}. \tag{3-7.24}$$

When $i = f$, elastic scattering occurs and the last two terms become zero. When $i \neq f$, the first two terms describe inelastic spin-flip scattering since usually the exiting photon has a different spin that the incoming photon. However, in such a case, the scattering process is off the energy shell, and one would therefore have to multiply the two terms by a random phase factor as described in Section 3.5. When $i \neq f$, the last two terms describe an inelastic scattering process than can still lie on the energy shell if energy conservation is satisfied, $\hbar(\omega_{\mathbf{k}} + \omega_{\mathbf{k}}') = \pm(E_f - E_i)$ as described in Figs. 3-6.3 and 3-6.4. For instance, the third term conserves energy as long as the oscillator stays in the excited state for the duration of one's observation. However, when both of the last two terms are considered on the energy shell, they describe a scattering process that appears elastic since now two photons enter and leave the system.

Finally, notice that the natural linewidth, $\Gamma_n^{\pm}$, is the sum of all transitions from an intermediate state to all possible final states. Thus $\Gamma_n^{\pm}$ contains contributions from both

elastic and inelastic transitions. Then, $\Gamma_n^{\pm}$ can be described as the sum of the transitions rates for all the elastic and inelastic channels

$$\Gamma_n^{\pm} = \sum_i \Gamma^i_{\text{elastic}} + \sum_i \Gamma^i_{\text{inelastic}} . \tag{3-7.25}$$

The level shift $D_n^{\pm}$ is discussed in Goldberger and Watson.[5] It linearly diverges since the limits of integration in the expression is taken from $E_k = \infty \rightarrow 0$. This is an example of the common problem of ultraviolet divergences found in quantum field theory. Through renormalization of the scatterer's mass when taking care of the scatterer's self-energy, the divergence can be eliminated. In doing so one will find that the level shift is on the order of a natural linewidth, $\Gamma_n^{\pm}$.

REFERENCES

[1] J. D. Jackson, *Classical Electrodynamics* (Wiley, New York, 1975).

[2] H. Frauenfelder, *Subatomic Physics* (Prentice-Hall, Englewood Cliffs, N.J., 1974).

[3] B. A. Lippmann and J. Schwinger, *Phys. Rev.* **79**, 469 (1950).

[4] C. Cohen-Tannoudji, B. Diu, and F. Lalöe, *Quantum Mechanics* (Wiley, New York, 1977).

[5] M. L. Goldberger and K. M. Watson, *Collision Theory* (Wiley, New York, 1964).

[6] P. A. M. Dirac, *The Principles of Quantum Mechanics* (Clarendon Press, Oxford, 1958).

[7] W. Heitler, *The Quantum Theory of Radiation* (Clarendon Press, Oxford, 1954).

[8] J. J. Sakurai, *Advanced Quantum Mechanics* (Addison-Wesley, Reading, Mass., 1967).

4. MULTIPOLE FIELDS

4.1 Interaction Perturbation Hamiltonian

A multipole scattering amplitude can be constructed through evaluating the T-matrix elements described in Section 3.4.[1-8] In that section the T-matrix elements were shown to be proportional to the inhomogeneous term in the Klein-Gordon wave equation, or the interaction perturbation Hamiltonian described by Eq. 3-4.11, which describes the interaction of the electromagnetic field of a photon with a charged scatterer. Noting that the total wavefunction includes both the photon and the scatterer's wavefunction, the following decomposition can be made:

$$|\phi\rangle = |\phi^p; \phi^s\rangle \tag{4-1.1}$$

where $|\phi^p\rangle$ is the photon wavefunction, $|\phi^s\rangle$ is the scatterer's wavefunction, and $|\phi\rangle$ is the total stationary state wavefunction.

To compute T_{fi} the expectation value of the interaction perturbation over the initial and final stationary states must be evaluated. The contribution from only the scatterer's part of the total wavefunction is

$$V_{fi}^s = \int_{V_0} \phi_f^{s*} V \phi_i^s \, d^3x \, . \tag{4-1.2}$$

Then inserting Eq. 3-4.11 yields

$$V_{fi}^s = (ie/c)\int_{V_0} d^3x \left\{ \phi_f^{s*} \left[\partial_\mu \left(A^\mu \phi_i^s \right) \right] + \phi_f^{s*} A^\mu \left(\partial_\mu \phi_i^s \right) \right\} + (e/c)^2 \int_{V_0} d^3x \, \phi_f^{s*} A^\mu A_\mu \phi_i^s \, . \tag{4-1.3}$$

Integrating the first term by parts leads to

$$\int_{V_0} \phi_f^{s*} \left[\partial_\mu \left(A^\mu \phi_i^s \right) \right] d^3x = \phi_f^{s*} A^\mu \phi_i^s \Big|_{V_0} - \int_{V_0} \left(\partial_\mu \phi_f^{s*} \right) A^\mu \phi_i^s \, d^3x \, .$$

The surface term goes to zero as the volume expands to infinity since the potential varies as $1/|\mathbf{x}|$. Then

$$V_{fi}^s = \frac{1}{c} \int_{V_0} d^3x \, j_\mu^{fi} A^\mu + (e/c)^2 \int_{V_0} d^3x \, \phi_f^{s*} A^\mu A_\mu \phi_i^s \tag{4-1.4}$$

where

$$j_\mu^{fi} = ie\left[\phi_f^{s*} \left(\partial_\mu \phi_i^s \right) - \left(\partial_\mu \phi_f^{s*} \right) \phi_i^s \right] \tag{4-1.5}$$

and j_μ^{fi} is the electromagnetic current of the charged spinless scatterer.

The Dirac equation can be used to evaluate j_μ^{fi} for a charged particle with spin:

$$\left(\gamma_\mu p^\mu - m\right)\psi^s = 0 \tag{4-1.6}$$

where γ_μ is a Dirac γ-matrix and m is the mass of the particle. Applying a gauge transformation on the 4-momentum, Eq. 3-4.9, leads to the expression

$$\left[\gamma_\mu p^\mu - m + (e/c)\gamma_\mu A^\mu\right]\psi^s = 0. \tag{4-1.7}$$

Defining the perturbation as[9]

$$\gamma^0 V(\mathbf{x},t) = (e/c)\gamma_\mu A^\mu(\mathbf{x},t) \tag{4-1.8}$$

leads to an interaction perturbation term similar to Eq. 4-1.4:

$$V_{fi}^s = \frac{1}{c}\int_{V_0} d^3x\, j_\mu^{fi} A^\mu + (e/c)^2 \int_{V_0} d^3x\, \psi_f^{s\dagger} A^\mu A_\mu \psi_i^s \tag{4-1.9}$$

where $$j_\mu^{fi} = e\overline{\psi}_f^s \gamma_\mu \psi_i^s \tag{4-1.10}$$

and the quadratic potential term obtained from the Klein-Gordon equation has been simply added on (the Dirac equation is simply a linearized form of the Klein-Gordon equation and therefore does not yield this quadratic term). In this formalism, the wavefunction, ψ^s, of a charged particle is a 4-component spinor where each component satisfies the Klein-Gordon wave equation. The covariant normalization of fermions is usually defined as

$$\int \psi^\dagger \psi\, d^3x = 2E \approx 2m \tag{4-1.11}$$

where, in the nonrelativistic case, $E \approx m$.

When the photon wavefunctions are included, the matrix elements of the interaction perturbation becomes

$$V_{fi} = \left\langle \phi_f^p \middle| \frac{1}{c}\int_{V_0} d^3x\, j_\mu^{fi} A^\mu \middle| \phi_i^p \right\rangle + \frac{e^2}{2mc^2}\left\langle \phi_f^p; \phi_f^s \middle| A^\mu A_\mu \middle| \phi_i^p; \phi_i^s \right\rangle. \tag{4-1.12}$$

The timelike component of A^μ, or the scalar electrostatic potential, will be partially ignored. The scalar electrostatic potential contributes to an energy level shift called the isomer shift, and its effect will be included in the scattering amplitude where appropriate. Therefore, when computing the scattering amplitude, the 4-potential will be assumed to be

$$A^\mu = (0, \mathbf{A}) \tag{4-1.13}$$

where $\mathbf{A}$ is the magnetic vector potential.

4.2 Second Quantization

To conveniently manipulate the photon wavefunctions, the technique of second quantization will be applied. Here, the fields are quantized in a Hilbert space in which the basis states are the eigenstates of the number operator

$$N_{\mathbf{k}\lambda} = a^{\dagger}_{\mathbf{k}\lambda} a_{\mathbf{k}\lambda} \tag{4-2.1}$$

$$N_{\mathbf{k}\lambda}\left|n_{\mathbf{k}\lambda}\right\rangle = n_{\mathbf{k}\lambda}\left|n_{\mathbf{k}\lambda}\right\rangle \tag{4-2.2}$$

$$a_{\mathbf{k}\lambda}\left|n_{\mathbf{k}\lambda}\right\rangle = \sqrt{n_{\mathbf{k}\lambda}}\left|n_{\mathbf{k}\lambda}-1\right\rangle \tag{4-2.3}$$

$$a^{\dagger}_{\mathbf{k}\lambda}\left|n_{\mathbf{k}\lambda}\right\rangle = \sqrt{n_{\mathbf{k}\lambda}+1}\left|n_{\mathbf{k}\lambda}+1\right\rangle \tag{4-2.4}$$

$$n_{\mathbf{k}\lambda} = 0,1,2,\ldots.$$

The operators $a_{\mathbf{k}\lambda}$ and $a^{\dagger}_{\mathbf{k}\lambda}$ are the familiar annihilation and creation operators, $\mathbf{k}$ is a photon propagation vector, λ is a polarization index, $n_{\mathbf{k}\lambda}$ is an occupation number, and $\hat{\boldsymbol{\varepsilon}}_{\mathbf{k}\lambda}$ is the polarization of the photon of frequency $\omega_{\mathbf{k}}$.

In this notation (the notation used in Weissbluth[7]), the vector potential is the sum over all the normal modes and polarizations of the system

$$\mathbf{A}(\mathbf{x},t) = \sum_{\mathbf{k}\lambda}\sqrt{\frac{2\pi\hbar c^2}{V_0\omega_{\mathbf{k}}}}\,\hat{\boldsymbol{\varepsilon}}_{\mathbf{k}\lambda}\left[a_{\mathbf{k}\lambda}e^{i(\mathbf{k}\cdot\mathbf{x}-\omega_{\mathbf{k}}t)} + a^{\dagger}_{\mathbf{k}\lambda}e^{-i(\mathbf{k}\cdot\mathbf{x}-\omega_{\mathbf{k}}t)}\right]. \tag{4-2.5}$$

The basis states for the system will be written, for the sake of clarity, as

$$\left|\phi_i\right\rangle = \left|\phi_i^p;\phi_i^s\right\rangle = \left|\mathrm{I}\right\rangle = \left|n_{\mathbf{k}_i\lambda};i_s\right\rangle \tag{4-2.6}$$

$$\left|\phi_f\right\rangle = \left|\phi_f^p;\phi_f^s\right\rangle = \left|\mathrm{F}\right\rangle = \left|n_{\mathbf{k}_f\lambda};f_s\right\rangle. \tag{4-2.7}$$

The T-matrix elements, Eq. 2-2.18, can now be evaluated with the help of the scattering diagrams shown in Fig. 4-2.1.

Examining just the quadratic A^2 term in the interaction perturbation, Eq. 4-1.12, the T-matrix elements, up to first order, are

$$T_{fi} = \frac{q^2}{2m_qc^2}\left\langle\phi_f^p;\phi_f^s\left|\mathbf{A}\cdot\mathbf{A}^*\right|\phi_i^p;\phi_i^s\right\rangle$$

$$= \frac{q^2}{2m_qc^2}\sum_{\mathbf{k}\lambda}\sum_{\mathbf{k}'\lambda'}\frac{2\pi\hbar c}{V_0\sqrt{kk'}}\hat{\boldsymbol{\varepsilon}}_{\mathbf{k}\lambda}\cdot\hat{\boldsymbol{\varepsilon}}^*_{\mathbf{k}'\lambda'}\left\langle\mathrm{I}\right|\left[a_{\mathbf{k}\lambda}e^{i(\mathbf{k}\cdot\mathbf{x}-\omega_{\mathbf{k}}t)} + a^{\dagger}_{\mathbf{k}\lambda}e^{-i(\mathbf{k}\cdot\mathbf{x}-\omega_{\mathbf{k}}t)}\right]$$

$$\times\left[a_{\mathbf{k}'\lambda'}e^{i(\mathbf{k}'\cdot\mathbf{x}-\omega_{\mathbf{k}'}t)} + a^{\dagger}_{\mathbf{k}'\lambda'}e^{-i(\mathbf{k}'\cdot\mathbf{x}-\omega_{\mathbf{k}'}t)}\right]\left|\mathrm{F}\right\rangle \tag{4-2.8}$$

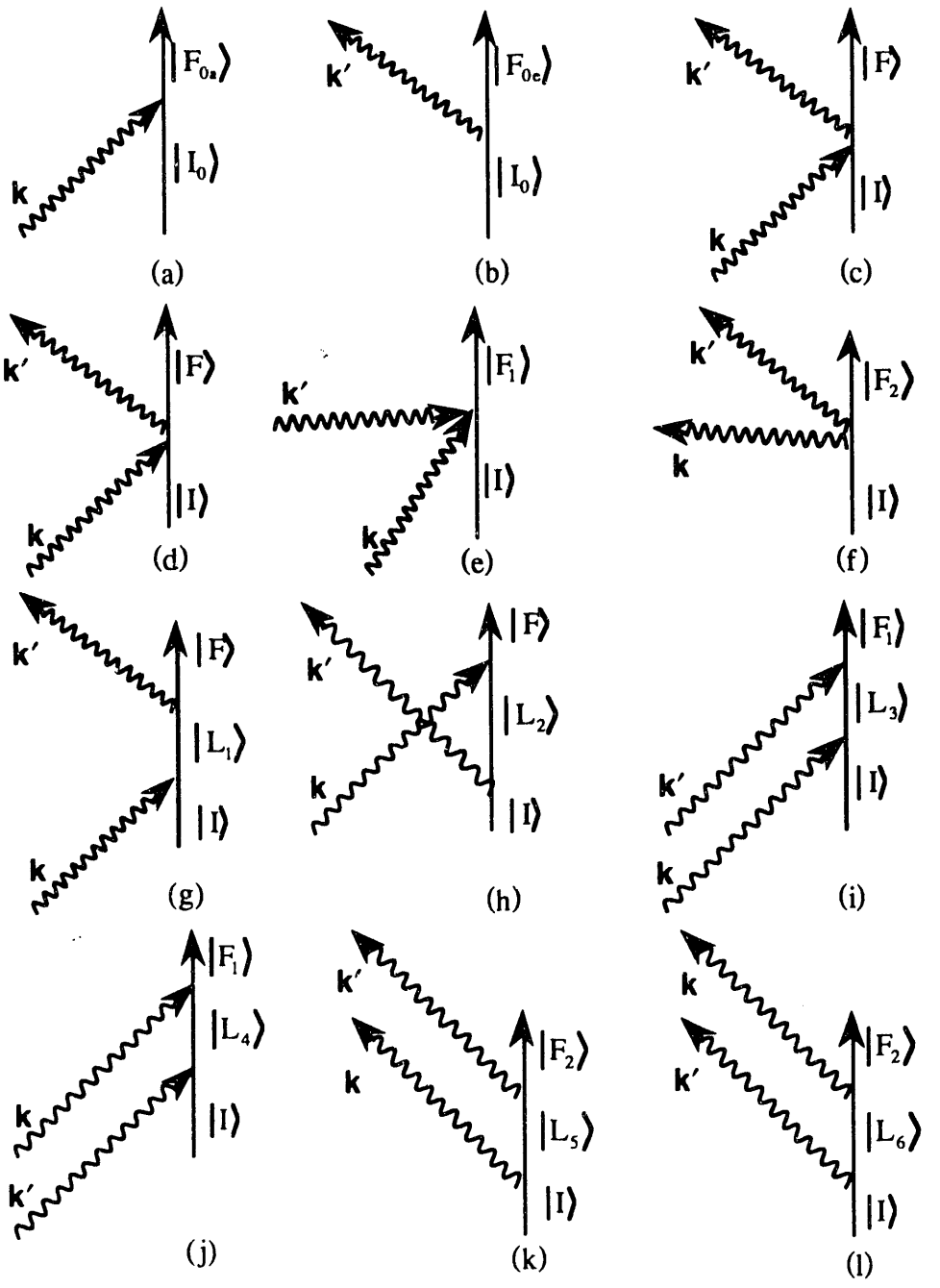

Fig. 4-2.1. Scattering diagrams: (a) and (b) single photon absorption and emission, (c) and (d) prompt two photon scattering [that the diagrams for prompt scattering and its time reversed process are the same can be seen by shrinking the intermediate state lifetime of diagrams (g) and (h) to zero], (e) and (f) prompt two photon absorption and emission [omitted the time reversed process since it corresponds to an equivalent diagram], (g) absorption reemission, (h) emission reabsorption [the time reversed diagram of (g)], (i) and (j) two photon absorption and its time reversed diagram, (k) and (l) two photon emission and its time reversed diagram.

Let the initial state of the system have occupation numbers $n_{\mathbf{k}\lambda}$ and $n_{\mathbf{k}'\lambda'}$:

$$|\mathrm{I}\rangle = |n_{\mathbf{k}\lambda}, n_{\mathbf{k}'\lambda'}; i_s\rangle. \tag{4-2.9}$$

For prompt scattering the final state of the system has occupation numbers $n_{\mathbf{k}'\lambda'}+1$ and $n_{\mathbf{k}\lambda}-1$ where one photon mode has gained a photon (the scattered photon) and another mode has lost a photon (the incoming photon):

$$|\mathrm{F}\rangle = |n_{\mathbf{k}\lambda}-1, n_{\mathbf{k}'\lambda'}+1; f_s\rangle. \tag{4-2.10}$$

The diagrams for this process and its time reversed process are shown in Figs. 4-2.1 (c) and (d).

The bilinear combinations of $a_{\mathbf{k}\lambda}$ and $a_{\mathbf{k}'\lambda'}$ and their Hermetian conjugates in Eq. 4-2.8 gives

$$\langle n_{\mathbf{k}\lambda}-1, n_{\mathbf{k}'\lambda'}+1 | a_{\mathbf{k}\lambda} a_{\mathbf{k}'\lambda'} | n_{\mathbf{k}\lambda}, n_{\mathbf{k}'\lambda'}\rangle = 0$$

$$\langle n_{\mathbf{k}\lambda}-1, n_{\mathbf{k}'\lambda'}+1 | a^\dagger_{\mathbf{k}\lambda} a^\dagger_{\mathbf{k}'\lambda'} | n_{\mathbf{k}\lambda}, n_{\mathbf{k}'\lambda'}\rangle = 0$$

$$\langle n_{\mathbf{k}\lambda}-1, n_{\mathbf{k}'\lambda'}+1 | a_{\mathbf{k}\lambda} a^\dagger_{\mathbf{k}'\lambda'} | n_{\mathbf{k}\lambda}, n_{\mathbf{k}'\lambda'}\rangle = \sqrt{n_{\mathbf{k}\lambda}(n_{\mathbf{k}'\lambda'}+1)}.$$

Acknowledging that prompt scattering and its time reversed process are equivalent and associating $\mathbf{k}$ with the incoming photon $\mathbf{k}_i$, and $\mathbf{k}'$ with the outgoing photon $\mathbf{k}_f$, leads to the scattering amplitude

$$F(\mathbf{k}_f, \mathbf{k}_i) = -r_q \sqrt{k_f/k_i}\sqrt{n_f+1}\,(\hat{\boldsymbol{\varepsilon}}^*_f \cdot \hat{\boldsymbol{\varepsilon}}_i)\langle f_s | e^{-i(\mathbf{k}_f-\mathbf{k}_i)\cdot\mathbf{x}} | i_s\rangle \tag{4-2.11}$$

where

$$r_q = \frac{q^2}{m_q c^2} \tag{4-2.12}$$

and q is the charge of the scatterer with mass m_q. For electrons $r_q = r_e$ -- the electron radius. The minus comes from the optical theorem, Eq. 2-3.6, and it is expected since an oscillator tends to resist driving fields by producing induced fields that partially cancel the incoming fields--the induced fields are 180° out of phase with the driving fields.

The differential scattering cross section is related to the scattering amplitude by the relation shown in Eq. 3-5.4. It has a term proportional to the number of scattered photons n_f. This term is the result of stimulated scattering and is only significant at high intensities. For elastic scattering $k_i = k_f$ and, in the dipole approximation, the differential scattering cross section reduces to the familiar Thomson cross section

$$\frac{d\sigma}{d\Omega} = r_q^2 (\hat{\boldsymbol{\varepsilon}}^*_f \cdot \hat{\boldsymbol{\varepsilon}}_i) |f_0|^2 \tag{4-2.13}$$

where

$$f_0 = \langle i_s | e^{-i(\mathbf{k}_f-\mathbf{k}_i)\cdot\mathbf{x}} | i_s\rangle \tag{4-2.14}$$

and f_0 is a scattering angle dependent form factor.

There is also a T-matrix element term for prompt two-photon absorption and emission arising from the bilinear combinations $a_{\mathbf{k}\lambda}a_{\mathbf{k}'\lambda'}$ and $a^\dagger_{\mathbf{k}\lambda}a^\dagger_{\mathbf{k}'\lambda'}$ of the interaction perturbation [see Figs. 4-2.1 (e) and (f)]. The final state occupation numbers for prompt two photon absorption are $n_{\mathbf{k}\lambda}-1$ and $n_{\mathbf{k}'\lambda'}-1$, and for prompt two photon emission the occupation numbers are $n_{\mathbf{k}\lambda}+1$ and $n_{\mathbf{k}'\lambda'}+1$. Each mode $\mathbf{k}$ and $\mathbf{k}'$ in the final state have either simultaneously lost or gained a photon. The scattering amplitude is then

$$F(\mathbf{k}_i',\mathbf{k}_i)=-r_e\sqrt{k_i'/k_i}\sqrt{n_i'}\,(\hat{\boldsymbol{\varepsilon}}_i'^{*}\cdot\hat{\boldsymbol{\varepsilon}}_i)\langle f_s|e^{i(\mathbf{k}_i'+\mathbf{k}_i)\cdot\mathbf{x}}|i_s\rangle \tag{4-2.15}$$

for prompt two photon absorption, and

$$F(\mathbf{k}_f',\mathbf{k}_f)=-r_e\sqrt{k_f'/k_f}\sqrt{(n_f'+1)(n_f+1)/n_f}\,(\hat{\boldsymbol{\varepsilon}}_f'^{*}\cdot\hat{\boldsymbol{\varepsilon}}_f)\langle f_s|e^{-i(\mathbf{k}_f'+\mathbf{k}_f)\cdot\mathbf{x}}|i_s\rangle \tag{4-2.16}$$

for prompt two photon emission. Since prompt two photon absorption and emission are inelastic processes, they can be safely ignored when considering only elastic processes.

Second order A^2 scattering gives rise to scattering of more than two photons and will therefore not be investigated.

For the current-vector potential coupling term in the interaction perturbation, Eq. 4-1.12, the T-matrix elements, up to second order, are

$$T_{fi}=\langle\phi_f^p;f_\alpha|\frac{1}{c}\int_{V_0}d^3x\,\mathbf{j}_{fi}\cdot\mathbf{A}|\phi_i^p;i_\alpha\rangle$$

$$+\sum_n\frac{\langle\phi_f^p;f_\alpha|\frac{1}{c}\int_{V_0}d^3x\,\mathbf{j}_{fn}\cdot\mathbf{A}|\phi_n^p;n_\alpha\rangle\langle\phi_n^p;n_\alpha|\frac{1}{c}\int_{V_0}d^3x\,\mathbf{j}_{ni}\cdot\mathbf{A}|\phi_i^p;i_\alpha\rangle}{E_I-E_N}. \tag{4-2.17}$$

States with the index α have been added to include quantum processes not described so far (such as phonon scattering). The scattering diagrams (along with their time reversed processes) are shown in Figs. 4-2.1 (g) through (l).

For the absorption reemission and its time reversed emission reabsorption process, the initial, final, and intermediate states shown in Figs. 4-2.1 (g) and (h) are

$$|\mathrm{I}\rangle=|n_{\mathbf{k}\lambda},n_{\mathbf{k}'\lambda'};i_\alpha\rangle$$

$$|\mathrm{L}_1\rangle=|n_{\mathbf{k}\lambda}-1,n_{\mathbf{k}'\lambda'};\ell_{1\alpha}\rangle$$

$$|\mathrm{L}_2\rangle=|n_{\mathbf{k}\lambda},n_{\mathbf{k}'\lambda'}+1;\ell_{2\alpha}\rangle$$

$$|\mathrm{F}\rangle=|n_{\mathbf{k}\lambda}-1,n_{\mathbf{k}'\lambda'}+1;f_\alpha\rangle.$$

Since these scattering events have intermediate states, they are properly described only by the second order T-matrix element term

$$F(\mathbf{k}_f,\mathbf{k}_i) = -A_0 \sum_{\ell} \frac{\langle \mathrm{F}|\frac{1}{c}\int_{V_0} d^3x\, \mathbf{j}_{f\ell}\cdot\mathbf{A}|\mathrm{L}\rangle\langle \mathrm{L}|\frac{1}{c}\int_{V_0} d^3x\, \mathbf{j}_{\ell i}\cdot\mathbf{A}|\mathrm{I}\rangle}{E_{\mathrm{I}} - E_{\mathrm{L}}} \tag{4-2.18}$$

where

$$\mathbf{A} = \sum_{\mathbf{k}\lambda} \sqrt{2\pi\hbar c/V_0 k}\, \hat{\boldsymbol{\varepsilon}}_{\mathbf{k}\lambda}\left[A_{\mathbf{k}\lambda} + A^{\dagger}_{\mathbf{k}\lambda}\right] \tag{4-2.19}$$

and

$$A_{\mathbf{k}\lambda} = a_{\mathbf{k}\lambda} e^{i\mathbf{k}\cdot\mathbf{x}}, \quad A^{\dagger}_{\mathbf{k}\lambda} = a^{\dagger}_{\mathbf{k}\lambda} e^{-i\mathbf{k}\cdot\mathbf{x}}. \tag{4-2.20}$$

One must now find those combinations of the matrix elements of $\mathbf{A}$ that yield nonzero values for each scattering process. For the case where $|\mathrm{L}_1\rangle$ is an intermediate state, $A_{\mathbf{k}\lambda}$ must be used to decrease the number of $\mathbf{k}$ photons by one in the state $|\mathrm{L}_1\rangle$, and $A^{\dagger}_{\mathbf{k}'\lambda'}$ must be used to increase the number of $\mathbf{k}'$ photons by one in the state $|\mathrm{F}\rangle$. Thus, the only nonzero matrix element combination is

$$\begin{aligned}&\langle n_{\mathbf{k}\lambda}-1, n_{\mathbf{k}'\lambda'}+1; f_\alpha | A^{\dagger}_{\mathbf{k}'\lambda'} | n_{\mathbf{k}\lambda}-1, n_{\mathbf{k}'\lambda'}; \ell_{1\alpha}\rangle\langle n_{\mathbf{k}\lambda}-1, n_{\mathbf{k}'\lambda'}; \ell_{1\alpha}|A_{\mathbf{k}\lambda}|n_{\mathbf{k}\lambda}, n_{\mathbf{k}'\lambda'}; i_\alpha\rangle \\ &\quad = \langle f_\alpha | e^{-i\mathbf{k}'\cdot\mathbf{x}} | \ell_{1\alpha}\rangle\langle \ell_{1\alpha}|e^{i\mathbf{k}\cdot\mathbf{x}}|i_\alpha\rangle\sqrt{n_{\mathbf{k}\lambda}\left(n_{\mathbf{k}'\lambda'}+1\right)}.\end{aligned}$$

The initial and intermediate state energies can be read right off the scattering diagram, Fig. 4-2.1 (g).

$$E_{\mathrm{I}} = E_i + \hbar\omega_{\mathbf{k}} \tag{4-2.21}$$

$$E_{\mathrm{L}_1} = E_{\ell_1}. \tag{4-2.22}$$

Then the scattering amplitude is

$$F_{\ell_1}(\mathbf{k}_f,\mathbf{k}_i) = -\sqrt{k_f/k_i}\sqrt{n_f+1}\,\frac{\langle f_\alpha|1/c\int d^3x\,\hat{\boldsymbol{\varepsilon}}_f\cdot\mathbf{j}_{f\ell_1}\,e^{-i\mathbf{k}_f\cdot\mathbf{x}}|\ell_{1\alpha}\rangle\langle\ell_{1\alpha}|1/c\int d^3x\,\hat{\boldsymbol{\varepsilon}}_i\cdot\mathbf{j}_{\ell_1 i}\,e^{i\mathbf{k}_i\cdot\mathbf{x}}|i_\alpha\rangle}{E_i - \left(E_{\ell_1} - \hbar\omega_{\mathbf{k}_i}\right)}. \tag{4-2.23}$$

For the emission reabsorption case, there is a loss of a $\mathbf{k}$ photon in the state $|\mathrm{F}\rangle$ and a gain of a $\mathbf{k}'$ photon in the state $|\mathrm{L}_2\rangle$. From the scattering diagram, Fig. 4-2.1 (h), the initial and intermediate state energies are

$$E_{\mathrm{I}} = E_i + \hbar\omega_{\mathbf{k}} \tag{4-2.24}$$

$$E_{\mathrm{L}_2} = E_{\ell_2} + \hbar\omega_{\mathbf{k}'} + \hbar\omega_{\mathbf{k}}. \tag{4-2.25}$$

The scattering amplitude for this process is then

$$F_{\ell_2}(\mathbf{k}_f,\mathbf{k}_i)=-\sqrt{k_f/k_i}\sqrt{n_f+1}\,\frac{\langle f_\alpha|1/c\int d^3x\,\hat{\boldsymbol{\varepsilon}}_i\cdot\mathbf{j}_{f\ell_2}\,e^{i\mathbf{k}_i\cdot\mathbf{x}}|\ell_{2\alpha}\rangle\langle\ell_{2\alpha}|1/c\int d^3x\,\hat{\boldsymbol{\varepsilon}}_f\cdot\mathbf{j}_{\ell_2 i}\,e^{-i\mathbf{k}_f\cdot\mathbf{x}}|i_\alpha\rangle}{E_i-\left(E_{\ell_2}+\hbar\omega_{\mathbf{k}_f}\right)}. \tag{4-2.26}$$

For the other scattering events in Fig. 4-2.1:

$$|\mathrm{I}_0\rangle=|n_{\mathbf{k}\lambda};i_\alpha\rangle$$

$$|\mathrm{F}_{0a}\rangle=|n_{\mathbf{k}\lambda}-1;f_\alpha\rangle$$

$$|\mathrm{F}_{0e}\rangle=|n_{\mathbf{k}'\lambda'}+1;f_\alpha\rangle$$

$$|\mathrm{L}_3\rangle=|n_{\mathbf{k}\lambda}-1,n_{\mathbf{k}'\lambda'};\ell_{3\alpha}\rangle\ ;\quad E_{\mathrm{L}_3}=E_{\ell_3}+\hbar\omega_{\mathbf{k}'}\ ;\quad E_{\mathrm{I}}=E_i+\hbar\omega_{\mathbf{k}}+\hbar\omega_{\mathbf{k}'}$$

$$|\mathrm{L}_4\rangle=|n_{\mathbf{k}\lambda},n_{\mathbf{k}'\lambda'}-1;\ell_{4\alpha}\rangle\ ;\quad E_{\mathrm{L}_4}=E_{\ell_4}+\hbar\omega_{\mathbf{k}}\ ;\quad E_{\mathrm{I}}=E_i+\hbar\omega_{\mathbf{k}}+\hbar\omega_{\mathbf{k}'}$$

$$|\mathrm{L}_5\rangle=|n_{\mathbf{k}\lambda}+1,n_{\mathbf{k}'\lambda'};\ell_{5\alpha}\rangle\ ;\quad E_{\mathrm{L}_5}=E_{\ell_5}+\hbar\omega_{\mathbf{k}}\ ;\quad E_{\mathrm{I}}=E_i$$

$$|\mathrm{L}_6\rangle=|n_{\mathbf{k}\lambda},n_{\mathbf{k}'\lambda'}+1;\ell_{6\alpha}\rangle\ ;\quad E_{\mathrm{L}_6}=E_{\ell_6}+\hbar\omega_{\mathbf{k}'}\ ;\quad E_{\mathrm{I}}=E_i$$

$$|\mathrm{F}_1\rangle=|n_{\mathbf{k}\lambda}-1,n_{\mathbf{k}'\lambda'}-1;f_\alpha\rangle$$

$$|\mathrm{F}_2\rangle=|n_{\mathbf{k}\lambda}+1,n_{\mathbf{k}'\lambda'}+1;f_\alpha\rangle$$

and their scattering amplitudes are found to be

$$F_{0a}(\mathbf{k}_i)=-\sqrt{V_0k_i/2\pi\hbar c}\,\langle f_\alpha|1/c\int d^3x\,\hat{\boldsymbol{\varepsilon}}_i\cdot\mathbf{j}_{fi}\,e^{i\mathbf{k}_i\cdot\mathbf{x}}|i_\alpha\rangle \tag{4-2.27}$$

$$F_{0e}(\mathbf{k}_f)=-\sqrt{V_0k_f/2\pi\hbar c}\sqrt{(n_f+1)/n_f}\,\langle f_\alpha|1/c\int d^3x\,\hat{\boldsymbol{\varepsilon}}_f\cdot\mathbf{j}_{fi}\,e^{-i\mathbf{k}_f\cdot\mathbf{x}}|i_\alpha\rangle \tag{4-2.28}$$

$$F_{\ell_3}(\mathbf{k}_i',\mathbf{k}_i)=-\sqrt{k_i'/k_i}\sqrt{n_i'}$$

$$\times\frac{\langle f_\alpha|1/c\int d^3x\,\hat{\boldsymbol{\varepsilon}}_i'\cdot\mathbf{j}_{f\ell_3}\,e^{i\mathbf{k}_i'\cdot\mathbf{x}}|\ell_{3\alpha}\rangle\langle\ell_{3\alpha}|1/c\int d^3x\,\hat{\boldsymbol{\varepsilon}}_i\cdot\mathbf{j}_{\ell_3 i}\,e^{i\mathbf{k}_i\cdot\mathbf{x}}|i_\alpha\rangle}{E_i-\left(E_{\ell_3}-\hbar\omega_{\mathbf{k}_i}\right)} \tag{4-2.29}$$

$$F_{\ell_4}(\mathbf{k}_i,\mathbf{k}_i')=-\sqrt{k_i'/k_i}\sqrt{n_i'}$$

$$\times\frac{\langle f_\alpha|1/c\int d^3x\,\hat{\boldsymbol{\varepsilon}}_i\cdot\mathbf{j}_{f\ell_4}\,e^{i\mathbf{k}_i\cdot\mathbf{x}}|\ell_{4\alpha}\rangle\langle\ell_{4\alpha}|1/c\int d^3x\,\hat{\boldsymbol{\varepsilon}}_i'\cdot\mathbf{j}_{\ell_4 i}\,e^{i\mathbf{k}_i'\cdot\mathbf{x}}|i_\alpha\rangle}{E_i-\left(E_{\ell_4}-\hbar\omega_{\mathbf{k}_i'}\right)} \tag{4-2.30}$$

$$F_{\ell_5}(\mathbf{k}'_f,\mathbf{k}_f) = -\sqrt{k'_f/k_f}\sqrt{(n_f+1)(n'_f+1)/n_f}$$

$$\times \frac{\langle f_\alpha|1/c\int d^3x\,\hat{\boldsymbol{\varepsilon}}'_f\cdot\mathbf{j}_{f\ell_5}e^{-i\mathbf{k}'_f\cdot\mathbf{x}}|\ell_{5\alpha}\rangle\langle\ell_{5\alpha}|1/c\int d^3x\,\hat{\boldsymbol{\varepsilon}}_f\cdot\mathbf{j}_{\ell_5 i}e^{-i\mathbf{k}_f\cdot\mathbf{x}}|i_\alpha\rangle}{E_i-(E_{\ell_5}+\hbar\omega_{\mathbf{k}_f})} \qquad (4\text{-}2.31)$$

$$F_{\ell_6}(\mathbf{k}_f,\mathbf{k}'_f) = -\sqrt{k'_f/k_f}\sqrt{(n_f+1)(n'_f+1)/n_f}$$

$$\times \frac{\langle f_\alpha|1/c\int d^3x\,\hat{\boldsymbol{\varepsilon}}_f\cdot\mathbf{j}_{f\ell_6}e^{-i\mathbf{k}_f\cdot\mathbf{x}}|\ell_{6\alpha}\rangle\langle\ell_{6\alpha}|1/c\int d^3x\,\hat{\boldsymbol{\varepsilon}}'_f\cdot\mathbf{j}_{\ell_6 i}e^{-i\mathbf{k}'_f\cdot\mathbf{x}}|i_\alpha\rangle}{E_i-(E_{\ell_6}+\hbar\omega_{\mathbf{k}'_f})} \qquad (4\text{-}2.32)$$

When considering only elastic scattering, the inelastic scattering amplitudes expressed by Eqs. 4-2.27 to 4.2-32 can be ignored.

For resonant transitions, all of the higher order terms of all the on-energy-shell scattering amplitudes must be taken into account as was done in Section 3.7. Following precisely the same procedures used in that section produces a natural linewidth that prevents the scattering amplitudes from becoming infinite on resonance.

4.3 Multipole Scattering Amplitude

The next step needed to be taken in investigating the scattering amplitude is the examination of its multipole structure. Following Frauenfelder's approach,[2] this can be accomplished by applying a spherical wave expansion on the plane wave

$$e^{i\mathbf{k}\cdot\mathbf{x}} = 4\pi\sum_{\ell=0}^{\infty} i^\ell j_\ell(kr)\sum_{m=-\ell}^{\ell} Y^*_{\ell m}(\theta_{\mathbf{k}},\phi_{\mathbf{k}})Y_{\ell m}(\theta_{\mathbf{r}},\phi_{\mathbf{r}}) \qquad (4\text{-}3.1)$$

where

$$j_\ell(kr) = (\pi/2kr)^{1/2}J_{\ell+\frac{1}{2}}(kr) \qquad (4\text{-}3.2)$$

and $j_\ell(kr)$ is a spherical Bessel function, the coordinate $(\theta_{\mathbf{k}},\phi_{\mathbf{k}})$ is the direction of the wavevector $\mathbf{k}$, and the coordinate $(r,\theta_{\mathbf{r}},\phi_{\mathbf{r}})$ is the location of the observation point in a coordinate system attached to the scatterer. The sum over ℓ, as will be shown later, gives the various multipole components of the plane wave (for instance, the dipole field corresponds to the $\ell = 0$, 1, and 2 terms, the quadrupole field corresponds to the $\ell = 1$, 2,

and 3 terms, etc.) A matrix element U_{ni} defined as (temporarily dropping the f_α and n_α quantum numbers)

$$U_{ni} = 1/c \int d^3x\, \hat{\boldsymbol{\varepsilon}} \cdot \mathbf{j}_{ni}\, e^{i\mathbf{k}\cdot\mathbf{x}} \tag{4-3.3}$$

can then be expressed as

$$U_{ni} = \hat{\boldsymbol{\varepsilon}} \cdot \sum_{\ell=0}^{\infty} \sum_{m=-\ell}^{\ell} \sum_{q=-1}^{1} Y^*_{\ell m}(\theta_k, \phi_k)(-1)^q \hat{\mathbf{e}}_{-q} \left[1/c \int d\mathbf{r}\; j_q^{ni}(\mathbf{r}) Y_{\ell m}(\theta_r, \phi_r) g_\ell(kr) \right] \tag{4-3.4}$$

where the current $\mathbf{j}_{ni}$ of the scatterer has been expressed in a spherical basis

$$\mathbf{j}_{ni} = \sum_{q=-1}^{1} (-1)^q j_q^{ni} \hat{\mathbf{e}}_{-q} \tag{4-3.5}$$

where

$$\hat{\mathbf{e}}_{\pm 1} = \mp 1/\sqrt{2} \left(\hat{\mathbf{e}}_x \pm i \hat{\mathbf{e}}_y \right) \tag{4-3.6}$$

$$\hat{\mathbf{e}}_0 = \hat{\mathbf{e}}_z \tag{4-3.7}$$

$$(-1)^q \hat{\mathbf{e}}_{-q} = \hat{\mathbf{e}}_q^* \tag{4-3.8}$$

and

$$g_\ell(kr) = 4\pi i^\ell j_\ell(kr) \tag{4-3.9}$$

The notation used in this section will closely follow the notation used by Weissbluth and Edmonds.[7, 10]

Note that the tensor product of two tensor operators of rank l and l' can be expressed as

$$V_Q^{(K)} = \left[\mathbf{T}^{(l)} \mathbf{U}^{(l')} \right]_Q^{(K)} = \sum_{qq'} T_q^{(l)} U_{q'}^{(l')} \langle lql'q' | ll'KQ \rangle. \tag{4-3.10}$$

The spherical harmonic $Y_{\ell m}(\theta_r, \phi_r)$ is a component of an irreducible tensor operator of rank ℓ. Then, since $\mathbf{j}_{ni}$ is a vector and therefore an irreducible tensor operator of rank 1,

$$\left[\mathbf{Y}^{(\ell)} \mathbf{j}^{(1)} \right]_M^{(L)} = \sum_{mq} Y_m^{(\ell)} j_q^{(1)} \langle \ell m 1 q | \ell 1 L M \rangle \tag{4-3.11}$$

where the ni index on $\mathbf{j}_{ni}$ is momentarily suppressed. Using the orthogonality relation for Clebsch-Gordan coefficients,

$$\sum_{jm} \langle j_1 m_1' j_2 m_2' | j_1 j_2 j m \rangle \langle j_1 m_1 j_2 m_2 | j_1 j_2 j m \rangle = \delta_{m_1' m_1} \delta_{m_2' m_2}, \tag{4-3.12}$$

gives

$$\sum_{LM}\left[\mathbf{Y}^{(\ell)}\mathbf{j}^{(1)}\right]_M^{(L)}\langle \ell m 1q|\ell 1LM\rangle = \sum_{m'q'} Y_{m'}^{(\ell)} j_{q'}^{(1)} \sum_{LM}\langle \ell m' 1q'|\ell 1LM\rangle\langle \ell m 1q|\ell 1LM\rangle$$

$$= Y_m^{(\ell)} j_q^{(1)}. \tag{4-3.13}$$

Using this relation U_{ni} becomes

$$U_{ni} = \hat{\boldsymbol{\varepsilon}}\cdot\sum_{\ell=0}^{\infty}\sum_{m=-\ell}^{\ell}\sum_{q=-1}^{1}\sum_{LM} Y_{\ell m}^{*}(\Omega_{\mathbf{k}})\hat{\mathbf{e}}_q^{*}\langle \ell m 1q|\ell 1LM\rangle\langle j_n, m_n|1/c\int d\mathbf{r}\left[\mathbf{Y}^{(\ell)}\mathbf{j}^{(1)}\right]_M^{(L)} g_\ell(kr)|j_i, m_i\rangle \tag{4-3.14}$$

where the matrix elements of the current are defined in terms of the scatterer's spin and angular momentum components

$$\mathbf{j}_{ni} = \langle \phi_n^s|\mathbf{j}|\phi_i^s\rangle = \langle j_n, m_n|\mathbf{j}|j_i, m_i\rangle. \tag{4-3.15}$$

Note that the tensor product in Eq. 4-3.13 can be written in terms of a dot product of a vector spherical harmonic with the current. A vector spherical harmonic of rank J follows the relation

$$\mathbf{Y}_{JLSM} = \sum_{mq} Y_{Lm}\hat{\mathbf{e}}_q\langle LmSq|LSJM\rangle. \tag{4-3.16}$$

The vector spherical harmonic is proportional to the amplitude of the incoming particle. The total angular momentum of the particle is the sum of the orbital and spin angular momentum

$$\mathbf{J} = \mathbf{L} + \mathbf{S}, \tag{4-3.17}$$

and the vector spherical harmonic is the simultaneous eigenfunction of J^2, L^2, S^2, J_z, L_z, and S_z. The numbers M, m, and q are the projection quantum numbers of the total orbital, orbital, and spin angular momentum vectors respectively. For a photon vector field, $S = 1$, and the photon vector spherical harmonic, with the S subscript suppressed, is

$$\mathbf{Y}_{JLM} = \sum_{mq} Y_{Lm}\hat{\mathbf{e}}_q\langle Lm1q|L1JM\rangle. \tag{4-3.18}$$

The tensor product in Eq. 4-3.14 can be written in the more convenient form of a dot product between a vector spherical harmonic and the current

$$\mathbf{Y}_{LM}\cdot\mathbf{j} = \sum_{mq} Y_{\ell m}\langle \ell m 1q|\ell 1LM\rangle\sum_{q'} j_{q'}\hat{\mathbf{e}}_q\cdot\hat{\mathbf{e}}_{q'}^{*}. \tag{4-3.19}$$

But, unit vectors in the spherical basis follow the orthogonality rule

$$\hat{\mathbf{e}}_q\cdot\hat{\mathbf{e}}_p^{*} = \delta_{pq}, \tag{4-3.20}$$

so

$$\mathbf{Y}_{L\mathcal{M}} \cdot \mathbf{j} = \sum_{mq} Y_{\ell m} j_q \langle \ell m 1 q | \ell 1 L M \rangle = \left[\mathbf{Y}^{(\ell)} \mathbf{j}^{(1)} \right]_M^{(L)} \tag{4-3.21}$$

by comparison with Eq. 4-3.11.

Applying the Wigner-Eckart theorem,

$$\langle \alpha j m | T_q^{(k)} | \alpha' j' m' \rangle = \frac{1}{\sqrt{2j+1}} \langle j' m' k q | j' k j m \rangle \langle \alpha j \| \mathbf{T}^{(k)} \| \alpha' j' \rangle \tag{4-3.22}$$

and using the relation in Eqs. 4-3.18 and 4-3.21, the matrix elements can be written in terms of its reduced matrix elements

$$U_{ni} = \sum_{\ell=0}^{\infty} \sum_{LM} \left[\hat{\boldsymbol{\varepsilon}} \cdot \mathbf{Y}^*_{L\mathcal{M}}(\Omega_k) \right] \frac{\langle j_i m_i L M | j_i L j_n m_n \rangle}{\sqrt{2j_n + 1}} \chi(L, \ell) \tag{4-3.23}$$

where $$\chi(L,\ell) = \left| \langle j_n \| 1/c \int d\mathbf{r}\, \mathbf{A}_{L\mathcal{M}}(r, \Omega_r) \cdot \mathbf{j}(\mathbf{r}) \| j_i \rangle \right| e^{i\eta(L,\ell)} \tag{4-3.24}$$

and $$\mathbf{A}_{L\mathcal{M}}(r, \Omega_r) = \mathbf{Y}_{L\mathcal{M}}(\Omega_r) g_\ell(kr). \tag{4-3.25}$$

The quantity $\chi(L,\ell)$ with phase $\eta(L,\ell)$ is a reduced matrix element that no longer depends upon m_n or m_f. Note that the z-axis of the coordinate system in which the angles $(\theta_k, \phi_k) = \Omega_k$ are measured is now the quantum axis of the scatterer (such as an electron or nucleon).

Since

$$\mathbf{Y}_{L\mathcal{M}}(\Omega_k) = \sum_{mq} Y_{\ell m} \hat{\mathbf{e}}_q \langle \ell m 1 q | \ell 1 L M \rangle, \tag{4-3.26}$$

the Clebsch-Gordan coefficient gives a constraint on the possible values of ℓ due to the selection rules for the coupling of two angular momentum

$$|\ell - 1| \le L \le \ell + 1. \tag{4-3.27}$$

Then, the only possible values of ℓ for a given L are

$$\ell = L, L \pm 1 \tag{4-3.28}$$

The selection rules also constrain the possible values of M

$$M = m + q. \tag{4-3.29}$$

The expression for U_{ni} in Eq. 4-3.23 contains information about transverse electric and magnetic and longitudinal multipole fields. To see this, first examine the $\ell = L$ component of $\mathbf{Y}_{L\mathcal{M}}$:

$$\mathbf{Y}_{LLM} = \sum_q Y_{L,M-q}\hat{\mathbf{e}}_q \langle L, M-q, 1, q | L\,1\,LM\rangle$$

$$= (-1)^{1-L-M}\sqrt{2L+1}\left\{\begin{pmatrix} L & 1 & L \\ M-1 & 1 & -M \end{pmatrix} Y_{\ell,M-1}\hat{\mathbf{e}}_{+1} + \begin{pmatrix} L & 1 & L \\ M & 0 & -M \end{pmatrix} Y_{\ell M}\hat{\mathbf{e}}_0 \right.$$

$$\left. + \begin{pmatrix} L & 1 & L \\ M+1 & -1 & -M \end{pmatrix} Y_{\ell,M+1}\hat{\mathbf{e}}_{-1} \right\}$$

$$= \sqrt{2L+1}\left\{(-1)\sqrt{\frac{(L+M)(L-M+1)}{(L+1)(2L+1)2L}} Y_{\ell,M-1}\hat{\mathbf{e}}_{+1} + \frac{M}{\sqrt{(2L+1)(L+1)L}} Y_{\ell M}\hat{\mathbf{e}}_0 \right.$$

$$\left. + (-1)^{-2(L+M)}\sqrt{\frac{(L-M)(L+M+1)}{(L+1)(2L+1)2L}} Y_{\ell,M+1}\hat{\mathbf{e}}_{-1} \right\} \qquad (4\text{-}3.30)$$

where the following identity between the Clebsch-Gordan coefficients and the Wigner 3-j symbol was used:

$$\langle j_1 m_1\, j_2 m_2 | j_1\, j_2\, j\, m\rangle = (-1)^{j_2 - j_1 - m}\sqrt{2j+1}\begin{pmatrix} j_1 & j_2 & j \\ m_1 & m_2 & -m \end{pmatrix}. \qquad (4\text{-}3.31)$$

Tables , such as in Weissbluth or Edmonds,[7, 10, 11] give formulas for special types of 3-j symbols. The exponent $2(L+M)$ is an even integer because if L is either integral or half integral then so is M since $M = L, L-1, \ldots, -L$. Utilizing the properties of the lowering and raising operators of angular momentum

$$L_{\pm} Y_{\ell m} = \mp\frac{1}{\sqrt{2}}\sqrt{\ell(\ell+1) - m(m\pm 1)}\; Y_{\ell,m\pm 1} \qquad (4\text{-}3.32)$$

$$L_0 Y_{\ell m} = m Y_{\ell m} \qquad (4\text{-}3.33)$$

yields

$$\mathbf{Y}_{LLM} = \frac{-(1/\sqrt{2})\sqrt{L(L+1) - M(M-1)}}{\sqrt{L(L+1)}} Y_{\ell,M-1}\hat{\mathbf{e}}_{+1} + \frac{M}{\sqrt{L(L+1)}} Y_{\ell M}\hat{\mathbf{e}}_0$$

$$+ \frac{(1/\sqrt{2})\sqrt{L(L+1) - M(M+1)}}{\sqrt{L(L+1)}} Y_{\ell,M+1}\hat{\mathbf{e}}_{-1}$$

$$= \frac{-L_- Y_{\ell,M-1}\hat{\mathbf{e}}_{+1} + L_0 Y_{\ell M}\hat{\mathbf{e}}_0 + L_+ Y_{\ell,M+1}\hat{\mathbf{e}}_{-1}}{\sqrt{L(L+1)}} = \frac{1}{\sqrt{L(L+1)}}\left(\sum_q (-1)^q L_q \hat{\mathbf{e}}_{-q}\right) Y_{LM}$$

$$= \frac{\mathbf{L} Y_{LM}}{\sqrt{L(L+1)}}. \tag{4-3.34}$$

The angular momentum operator can be written as

$$\mathbf{L} = \mathbf{r} \times \mathbf{p} = -i(\mathbf{r} \times \nabla) \tag{4-3.35}$$

where $\mathbf{r}$ a radial vector. Then

$$\hat{\mathbf{r}} \cdot \mathbf{Y}_{LLM} = \left(-i/\sqrt{L(L+1)}\right)\hat{\mathbf{r}} \cdot (\mathbf{r} \times \nabla) = \left(-i/\sqrt{L(L+1)}\right)\nabla \cdot (\hat{\mathbf{r}} \times \mathbf{r})$$

$$= 0. \tag{4-3.36}$$

Thus, $\mathbf{Y}_{LLM}$ is a transverse vector spherical harmonic, and, since it is related to the angular momentum operator, it is associated with the magnetic multipole electric field. Akhiezer and Berestetskii[8] define this field as $\mathbf{Y}^{(0)}_{LM}$ and Rose[5] as a magnetic multipole field $\mathbf{Y}^{(m)}_{LM}$. Thus, depending upon notation

$$\mathbf{Y}_{LLM} = \mathbf{Y}^{(0)}_{LM} = \mathbf{Y}^{(m)}_{LM}. \tag{4-3.37}$$

To obtain the electric multipole electric field, the cross product between the magnetic multipole field and $\hat{\mathbf{r}}$ is taken as defined below

$$i\mathbf{Y}^{(e)}_{LM} = \hat{\mathbf{r}} \times \mathbf{Y}^{(m)}_{LM}. \tag{4-3.38}$$

Also similarly

$$i\mathbf{Y}^{(m)}_{LM} = \hat{\mathbf{r}} \times \mathbf{Y}^{(e)}_{LM}. \tag{4-3.39}$$

From Akhiezer and Berestetskii, the electric multipole field is related to the vector spherical harmonics as follows

$$\mathbf{Y}^{(1)}_{jm} = \mathbf{Y}^{(e)}_{jm} = \sqrt{\frac{j}{2j+1}}\,\mathbf{Y}_{j,j+1,m} + \sqrt{\frac{j+1}{2j+1}}\,\mathbf{Y}_{j,j-1,m}. \tag{4-3.40}$$

From the differential properties of the gradient of a scalar[8, 12]

$$r\nabla Y_{jm} = j\sqrt{\frac{j+1}{2j+1}}\,\mathbf{Y}_{j,j+1,m} + (j+1)\sqrt{\frac{j}{2j+1}}\,\mathbf{Y}_{j,j-1,m}, \tag{4-3.41}$$

one can see that the electric multipole electric field is related to the linear momentum operator

$$\mathbf{Y}^{(e)}_{jm} = \frac{ir}{\hbar\sqrt{j(j+1)}}\mathbf{p}Y_{jm} \tag{4-3.42}$$

where $\mathbf{p} = -i\hbar\nabla$.

The other vector field has only longitudinal components along $\hat{\mathbf{r}}$:

$$\mathbf{Y}_{jm}^{(-1)} = \mathbf{Y}_{jm}^{(l)} = \hat{\mathbf{r}} Y_{jm} = \sqrt{\frac{j}{2j+1}}\,\mathbf{Y}_{j,j-1,m} - \sqrt{\frac{j+1}{2j+1}}\,\mathbf{Y}_{j,j+1,m}. \tag{4-3.43}$$

These three vector fields form an orthogonal basis about which any field can be expanded.

Going back to the expression for U_{ni}, there is a summation term

$$\sum_{\ell=L-1}^{L+1} \mathbf{Y}_{LM}(\Omega_k)\mathbf{Y}_{LM}(\Omega_r)g_\ell(kr) = \mathbf{Y}_{LLM}(\Omega_k)\mathbf{Y}_{LLM}(\Omega_r)g_L(kr)$$
$$+ \mathbf{Y}_{L,L-1,M}(\Omega_k)\mathbf{Y}_{L,L-1,M}(\Omega_r)g_{L-1}(kr) + \mathbf{Y}_{L,L+1,M}(\Omega_k)\mathbf{Y}_{L,L+1,M}(\Omega_r)g_{L+1}(kr).$$

The first term can be expressed in terms of the magnetic multipole field $\mathbf{Y}_{LM}^{(m)}$. The next two terms give the electric and longitudinal fields. First note that the vector spherical harmonics of angular momenta $j \pm 1$ can be expressed in terms of the multipole fields

$$\mathbf{Y}_{j,j+1,m} = \left(1/\sqrt{2j+1}\right)\left(\sqrt{j}\,\mathbf{Y}_{jm}^{(1)} - \sqrt{j+1}\,\mathbf{Y}_{jm}^{(-1)}\right) \tag{4-3.44}$$

$$\mathbf{Y}_{j,j-1,m} = \left(1/\sqrt{2j+1}\right)\left(\sqrt{j+1}\,\mathbf{Y}_{jm}^{(1)} + \sqrt{j}\,\mathbf{Y}_{jm}^{(-1)}\right). \tag{4-3.45}$$

Then

$$\sum_{\ell=L-1}^{L+1} \mathbf{Y}_{LM}(\Omega_k)\mathbf{Y}_{LM}(\Omega_r)g_\ell(kr) = \sum_{\lambda=-1}^{1} \mathbf{Y}_{LM}^{(\lambda)}(\Omega_k)\mathbf{A}_{LM}^{(\lambda)}(r,\Omega_r) \tag{4-3.46}$$

where

$$\mathbf{A}_{LM}^{(0)}(r,\Omega_r) = \mathbf{Y}_{LLM}(\Omega_r)g_L(kr) \tag{4-3.47}$$

$$\mathbf{A}_{LM}^{(\pm)}(r,\Omega_r) = \frac{1}{2L+1}\left\{\left[Lg_{L\pm1}(kr) + (L+1)g_{L\mp1}(kr)\right]\mathbf{Y}_{LM}^{(\pm)}(\Omega_r)\right.$$
$$\left. + \sqrt{L(L+1)}\left[g_{L-1}(kr) - g_{L+1}(kr)\right]\mathbf{Y}_{LM}^{(\mp)}(\Omega_r)\right\}. \tag{4-3.48}$$

The matrix elements, U_{ni}, can now be expressed as a sum of the transverse and longitudinal multipole fields

$$U_{ni} = \sum_{\lambda=-1}^{1}\sum_{LM}\left[\hat{\boldsymbol{\varepsilon}}\cdot\mathbf{Y}_{LM}^{(\lambda)*}(\Omega_k)\right]\frac{\langle j_i m_i\, LM | j_i\, L\, j_n m_n\rangle}{\sqrt{2j_n+1}}\chi(L,\lambda) \tag{4-3.49}$$

where $$\chi(L,\lambda) = \left|\left\langle j_n \middle\| 1/c\int d\mathbf{r}\;\mathbf{A}_{LM}^{(\lambda)}(r,\Omega_r)\cdot\mathbf{j}(\mathbf{r}) \middle\| j_i\right\rangle\right| e^{i\eta(L,\lambda)}. \tag{4-3.50}$$

Another expression for the expansion of a vector field plane wave has thus been derived

$$\hat{\boldsymbol{\varepsilon}} e^{i\mathbf{k}\cdot\mathbf{x}} = \sum_{LM}\sum_{\lambda=-1}^{1}\left[\hat{\boldsymbol{\varepsilon}}\cdot\mathbf{Y}_{LM}^{(\lambda)*}(\Omega_{\mathbf{k}})\right]\mathbf{A}_{LM}^{(\lambda)}(r,\Omega_{\mathbf{r}})$$

$$= \sum_{LM}\left\{\left[\hat{\boldsymbol{\varepsilon}}\cdot\mathbf{Y}_{LM}^{(\mathrm{e})*}(\Omega_{\mathbf{k}})\right]\mathbf{A}_{LM}^{(\mathrm{e})}(r,\Omega_{\mathbf{r}}) + \left[\hat{\boldsymbol{\varepsilon}}\cdot\mathbf{Y}_{LM}^{(\mathrm{m})*}(\Omega_{\mathbf{k}})\right]\mathbf{A}_{LM}^{(\mathrm{m})}(r,\Omega_{\mathbf{r}}) + \left[\hat{\boldsymbol{\varepsilon}}\cdot\mathbf{Y}_{LM}^{(l)*}(\Omega_{\mathbf{k}})\right]\mathbf{A}_{LM}^{(l)}(r,\Omega_{\mathbf{r}})\right\}. \tag{4-3.51}$$

This shows the decomposition of a vector field into its transverse electric and magnetic (e and m or $\lambda = 1$ and 0) and longitudinal (l or $\lambda = -1$) multipole components. This is basically what Rose has done but in a different manner.[5] Another expression for the vector potential is then

$$\mathbf{A}(\mathbf{x},t) = \sum_{\mathbf{k}\lambda}\sqrt{\frac{2\pi\hbar c^2}{V_0\omega_{\mathbf{k}}}}\left\{\sum_{LM}\sum_{\ell=L-1}^{L+1}\left(a_{\mathbf{k}\lambda}\left[\hat{\boldsymbol{\varepsilon}}_{\mathbf{k}\lambda}\cdot\mathbf{Y}_{\ell M}^{*}(\Omega_{\mathbf{k}})\right]\mathbf{A}_{\ell M}(r,\Omega_{\mathbf{r}})e^{-i\omega_{\mathbf{k}}t}\right.\right.$$
$$\left.\left. + a_{\mathbf{k}\lambda}^{\dagger}\left[\hat{\boldsymbol{\varepsilon}}_{\mathbf{k}\lambda}^{*}\cdot\mathbf{Y}_{\ell M}(\Omega_{\mathbf{k}})\right]\mathbf{A}_{\ell M}^{*}(r,\Omega_{\mathbf{r}})e^{i\omega_{\mathbf{k}}t}\right)\right\} \tag{4-3.52}$$

$$= \sum_{\mathbf{k}\lambda}\sqrt{\frac{2\pi\hbar c^2}{V_0\omega_{\mathbf{k}}}}\left\{\sum_{LM}\sum_{p=-1}^{1}\left(a_{\mathbf{k}\lambda}\left[\hat{\boldsymbol{\varepsilon}}_{\mathbf{k}\lambda}\cdot\mathbf{Y}_{LM}^{(p)*}(\Omega_{\mathbf{k}})\right]\mathbf{A}_{LM}^{(p)}(r,\Omega_{\mathbf{r}})e^{-i\omega_{\mathbf{k}}t}\right.\right.$$
$$\left.\left. + a_{\mathbf{k}\lambda}^{\dagger}\left[\hat{\boldsymbol{\varepsilon}}_{\mathbf{k}\lambda}^{*}\cdot\mathbf{Y}_{LM}^{(p)}(\Omega_{\mathbf{k}})\right]\mathbf{A}_{LM}^{(p)*}(r,\Omega_{\mathbf{r}})e^{i\omega_{\mathbf{k}}t}\right)\right\} \tag{4-3.53}$$

where the vector spherical harmonics are constructed in the quantum coordinate system of the scatterer.

The scattering amplitude can now be expressed in terms of multipole fields. For the case of spontaneous absorption reemission $(n_f = 0)$, the scattering amplitude on the energy shell is

$$F_n(\mathbf{k}_f,\mathbf{k}_i) = \frac{U_{fn}U_{ni}}{E_i - E_n + \hbar\omega_{\mathbf{k}_i} + i\Gamma_n/2} \tag{4-3.54}$$

where

$$U_{fn} = \langle j_f, m_f; f_\alpha | 1/c\int d^3x\,\hat{\boldsymbol{\varepsilon}}_f^{*}\cdot\mathbf{j}e^{-i\mathbf{k}_f\cdot\mathbf{x}} | j_n, m_n; n_\alpha\rangle \tag{4-3.55}$$

$$U_{ni} = \langle j_n, m_n; n_\alpha | 1/c\int d^3x\,\hat{\boldsymbol{\varepsilon}}_i\cdot\mathbf{j}e^{i\mathbf{k}_i\cdot\mathbf{x}} | j_i, m_i; i_\alpha\rangle. \tag{4-3.56}$$

The polarization of the scattered photon has been complex conjugated to handle complex polarizations.

The natural linewidth, Γ_n, described in Section 3.7, can be readily evaluated in terms of the reduced matrix elements $\chi(L,\ell)$. In terms of the matrix elements U_{fn},

$$\Gamma_n = 2\pi \sum_{f\neq n} \int d\Omega_{\mathbf{k}_f} \frac{|U_{fn}|^2}{A_0} \rho(E_{in}) \tag{4-3.57}$$

where A_0 is given by Eq. 2-3.8, and the density of states, $\rho(E_{in})$, is given by Eq. 3-7.25. $U_{fn} = U_{ni}^*$ with the interchange of indices $i \rightarrow f$, and U_{ni} is given by Eq. 4-3.23 or 4-3.49. The sum over all final states is the sum over all final angular momentum, spin, photon modes, and polarization states: $\sum_{f\neq n} = \sum_{j_f m_f} \sum_{\mathbf{k}_f \lambda}$. For only one photon mode, $\mathbf{k}_f$, the sum over photon modes can be ignored. With the help of the orthogonality of spherical harmonics,

$$\int d\Omega Y_{\ell m}^*(\Omega) Y_{\ell' m'}(\Omega) = \delta_{\ell\ell'}\delta_{mm'}, \tag{4-3.58}$$

the angular integral in Γ_n is then

$$\sum_\lambda \int d\Omega_{\mathbf{k}_f} \left|\hat{\boldsymbol{\varepsilon}}_\lambda \cdot \mathbf{Y}_{L\mathcal{M}}^*(\Omega_{\mathbf{k}_f})\right|^2 = \sum_\lambda \int d\Omega_{\mathbf{k}_f} \left[\sum_{mq} Y_{\ell m}^* \langle \ell m 1 q | \ell 1 L M\rangle \hat{\boldsymbol{\varepsilon}}_\lambda \cdot \hat{\mathbf{e}}_q^*\right]$$

$$\times \left[\sum_{m'q'} Y_{\ell' m'} \langle \ell' m' 1 q' | \ell' 1 L' M'\rangle \hat{\boldsymbol{\varepsilon}}_\lambda^* \cdot \hat{\mathbf{e}}_{q'}\right]$$

$$= \sum_{\lambda m m'} \int d\Omega_{\mathbf{k}_f} Y_{\ell m}^*(\Omega_{\mathbf{k}_f}) Y_{\ell' m'}(\Omega_{\mathbf{k}_f}) \langle \ell m 1\lambda | \ell 1 L M\rangle \langle \ell' m' 1\lambda | \ell' 1 L' M'\rangle$$

$$= \delta_{\ell\ell'}\delta_{LL'}\delta_{MM'}. \tag{4-3.59}$$

The natural linewidth then reduces to

$$\Gamma_n = (k_f/2\pi) \sum_{j_f m_f} \sum_{\mathcal{L}M} \sum_{\ell' L' M'} \frac{\langle j_i m_i L M | j_i L j_n m_n\rangle \langle j_f m_f L' M' | j_f L' j_n m_n\rangle}{(2j_n+1)}$$

$$\times \chi(L,\ell)\chi^*(L',\ell')\delta_{\ell\ell'}\delta_{LL'}\delta_{MM'}$$

$$= (k_f/2\pi) \sum_{j_f} \sum_{\mathcal{L}} \sum_{m_f M} \frac{\langle j_i m_i L M | j_i L j_n m_n\rangle \langle j_f m_f L M | j_f L j_n m_n\rangle}{(2j_n+1)} |\chi(L,\ell)|^2$$

$$= (k_f/2\pi)\sum_{L\ell}\sum_{j_f}|\chi(L,\ell)|^2/(2j_n+1)$$

$$\equiv \sum_{L\ell}\Gamma(L,\ell) \tag{4-3.60}$$

The multipole linewidth, $\Gamma(L,\ell)$, is a function of the multipole index L and an index ℓ which determines whether the process is transverse magnetic, transverse electric, or longitudinal scattering (see Table 4-3.1). Then, the reduced matrix element expressed in terms of the multipole linewidth is

$$\sum_{j_f}|\chi(L,\ell)|^2 = (2\pi/k_f)(2j_n+1)\Gamma(L,\ell). \tag{4-3.61}$$

For a two level system the sum over j_f can be ignored.

Multipole index	Electric: $\lambda = 1$	Magnetic: $\lambda = 0$
$L=1$ $\begin{cases}\ell=0,2\\ \ell=1\end{cases}$	dipole	dipole
$L=2$ $\begin{cases}\ell=1,3\\ \ell=2\end{cases}$	quadrupole	quadrupole
$L=3$ $\begin{cases}\ell=2,4\\ \ell=3\end{cases}$	sextupole	sextupole

Table 4-3.1. Multipole fields designated by multipole index L.

The spontaneous absorption reemission on-energy-shell scattering amplitude can now be expressed in terms of the multipole spontaneous radiative linewidth[1-3]

$$F_n(\mathbf{k}_f,\mathbf{k}_i,\mathbf{x}_0) = -(2\pi/k_f)e^{-i(\mathbf{k}_f-\mathbf{k}_i)\cdot\mathbf{x}_0}\sum_{\ell LM}\sum_{\ell' L'M'}\left[\hat{\boldsymbol{\varepsilon}}_f^*\cdot\mathbf{Y}_{LM}(\Omega_{\mathbf{k}_f})\right]\left[\mathbf{Y}^*_{L'\ell'M'}(\Omega_{\mathbf{k}_i})\cdot\hat{\boldsymbol{\varepsilon}}_i\right]$$

$$\times\frac{\sqrt{\Gamma(L,\ell)\Gamma(L',\ell')}\,e^{i[\eta(L,\ell)-\eta(L',\ell')]}}{E_i-E_n+\hbar\omega_{\mathbf{k}_i}+i\Gamma_n/2}\langle j_f m_f LM|j_f Lj_n m_n\rangle\langle j_i m_i L'M'|j_i L' j_n m_n\rangle \tag{4-3.62}$$

or

$$F_n(\mathbf{k}_f,\mathbf{k}_i,\mathbf{x}_0) = -(2\pi/k_f)e^{-i(\mathbf{k}_f-\mathbf{k}_i)\cdot\mathbf{x}_0}\sum_{\lambda LM}\sum_{\lambda' L'M'}\left[\hat{\boldsymbol{\varepsilon}}_f^{*}\cdot\mathbf{Y}_{LM}^{(\lambda)}(\Omega_{\mathbf{k}_f})\right]\left[\mathbf{Y}_{L'M'}^{(\lambda')*}(\Omega_{\mathbf{k}_i})\cdot\hat{\boldsymbol{\varepsilon}}_i\right]$$

$$\times\frac{\sqrt{\Gamma(L,\lambda)\Gamma(L',\lambda')}\,e^{i[\eta(L,\lambda)-\eta(L',\lambda')]}}{E_i-E_n+\hbar\omega_{\mathbf{k}_i}+i\Gamma_n/2}\langle j_f m_f LM|j_f L j_n m_n\rangle\langle j_i m_i L'M'|j_i L' j_n m_n\rangle \quad (4\text{-}3.63)$$

For convenience of notation in later sections, $F_n(\mathbf{k}_f,\mathbf{k}_i)\equiv F_n(\mathbf{k}_f,\mathbf{k}_i,\mathbf{x}_0=0)$. If the scattering process preserves time reversal invariance, the phase difference, $\eta(L,\lambda)-\eta(L',\lambda')$, between two multipoles is zero or π.[13, 14] The spatial phase factor, $\phi_{\mathbf{x}}=-(\mathbf{k}_f-\mathbf{k}_i)\cdot\mathbf{x}_0$, comes from shifting the scatterer from the origin by the displacement $\mathbf{x}_0$ as shown in Fig.4-3.1.

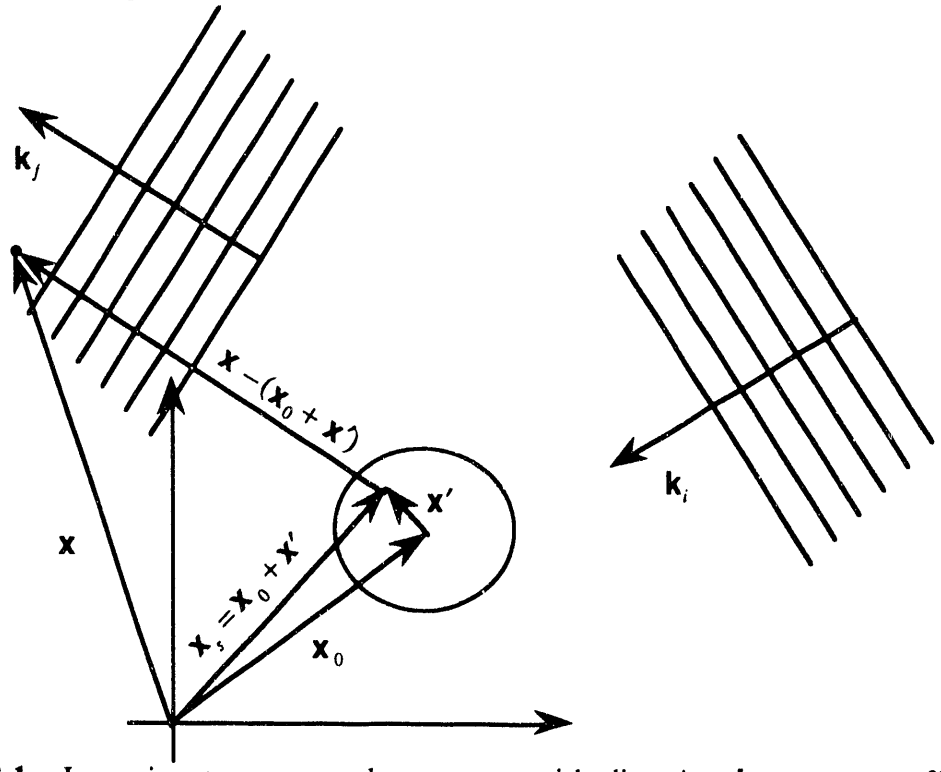

Fig. 4-3.1. Incoming transverse plane waves with direction $\mathbf{k}_i$ scatterers off particle located at $\mathbf{x}_0$ to produce outgoing transverse plane waves traveling in direction $\mathbf{k}_f$.

In general, the scattering is usually expressed as

$$F_n^{f_\alpha i_\alpha} = \langle f_\alpha|F_n|i_\alpha\rangle \quad (4\text{-}3.64)$$

where the matrix elements of F_n must be summed over other quantum states not discussed so far (such as phonon states) to arrive at a final value for the scattering amplitude. For instance, in phonon scattering,[3, 6, 15, 16] the plane wave can be approximated as having an

additional oscillatory spatial function, **u**, that describes displacements about an equilibrium position **x** of a scatterer

$$e^{i\mathbf{k}\cdot\mathbf{x}} \rightarrow e^{i\mathbf{k}\cdot(\mathbf{x}+\mathbf{u})}. \tag{4-3.65}$$

In such a case, the scattering amplitude changes to

$$F_n^{f_\alpha i_\alpha} = F_n' \sum_{n_\alpha} \langle f_\alpha | e^{-i\mathbf{k}_f\cdot\mathbf{u}} | n_\alpha \rangle \langle n_\alpha | e^{i\mathbf{k}_i\cdot\mathbf{u}} | i_\alpha \rangle \tag{4-3.66}$$

The vibrational factor usually lead to a diminution in the scattering amplitude, and, for nuclear scattering, is called a Lamb-Mössbauer factor, or, for electronic scattering, a Debye-Waller factor. The resonant denominator of F_n also changes to include frequency terms that give rise to frequency sidebands.

4.4 Spherical Multipole Electric Fields

In the computations done so far, the incoming and exiting waves have been described as plane waves. Such a description is inadequate for a single scatterer since it usually scatters waves spherically that fall off as $1/R$ where R is the distance from the scatterer to an observation point. To include this effect, the incoming and outgoing vector fields of the photon are described as spherical Green functions

$$\mathbf{A}_{out}(\mathbf{x},\mathbf{x}') = \hat{\boldsymbol{\varepsilon}}_f^* \frac{e^{ik|\mathbf{x}-\mathbf{x}'|}}{|\mathbf{x}-\mathbf{x}'|} \tag{4-4.1}$$

$$\mathbf{A}_{in}(\mathbf{x}_0,\mathbf{x}') = \hat{\boldsymbol{\varepsilon}}_i \frac{e^{ik|\mathbf{x}_0+\mathbf{x}'|}}{|\mathbf{x}_0+\mathbf{x}'|} \tag{4-4.2}$$

where the incoming spherical wave originates at point $\mathbf{x}_0$ in Fig.4-3.1, the scattered spherical is observed at point **x**, and $\mathbf{x}'$ are the internal coordinates of the scatterer. Inserting these vector potentials into the expressions for U_{fn} and U_{ni} in Eqs. 4-3.55 and 4-3.56 will give the spherical multipole electric field amplitudes scattered from a particle.

The spherical wave expansion of the spherical Green function is[17]

$$\frac{e^{ik|\mathbf{x}-\mathbf{x}'|}}{|\mathbf{x}-\mathbf{x}'|} = 4\pi ik \sum_{\ell=0}^{\infty} j_\ell(kr_<) h_\ell^{(1)}(kr_>) \sum_{m=-\ell}^{\ell} Y_{\ell m}(\theta_k,\phi_k) Y_{\ell m}^*(\theta_r,\phi_r) \tag{4-4.3}$$

where $h_\ell^{(1)}(kr)$ is a spherical Hankel function

$$h_\ell^{(1)}(kr) = \sqrt{\frac{\pi}{2x}}\left[J_{\ell+1/2}(x) + iN_{\ell+1/2}(x)\right]. \tag{4-4.4}$$

Inserting the spherical wave expansions into the expressions for U_{fn} and U_{ni} and carrying out computations similar to those performed in Section 4.3 leads to the spherical multipole electric fields in a form very similar to Eq. 4-3.62

$$\mathbf{E}_n(\mathbf{k}_f,\mathbf{k}_i) = \hat{\boldsymbol{\varepsilon}}_f F_n'(\mathbf{k}_f,\mathbf{k}_i) = \hat{\boldsymbol{\varepsilon}}_f F_n(\mathbf{k}_f,\mathbf{k}_i)\Big|_{\mathbf{Y}_{LM}(\Omega_k)\to\mathbf{Z}_{LM}(r_k,\Omega_k)} \tag{4-4.5}$$

where $F_n'(\mathbf{k}_f,\mathbf{k}_i)$ is similar to $F_n(\mathbf{k}_f,\mathbf{k}_i)$ in Eq. 4-3.62 but with the substitution $\mathbf{Y}_{LM}(\Omega_k) \to \mathbf{Z}_{LM}(r_k,\Omega_k)$ (the spatial phase is now contained in the spherical Hankel functions). The spherical Hankel harmonics follow the relation

$$\mathbf{Z}_{LM}(r_k,\Omega_k) = kf_\ell(kr_k)\mathbf{Y}_{Lm}(\theta_k,\phi_k) \tag{4-4.6}$$

$$f_\ell(kr_k) = i(-i)^{-\ell}h_\ell(kr_k) \tag{4-4.7}$$

$$r_{k_f} \approx |\mathbf{x}-\mathbf{x}_0| \quad \text{for} \quad |\mathbf{x}-\mathbf{x}_0| >> |\mathbf{x}'| \tag{4-4.8}$$

$$r_{k_i} \approx |\mathbf{x}_0| \quad \text{for} \quad |\mathbf{x}_0| >> |\mathbf{x}'| \tag{4-4.9}$$

One can also construct magnetic, electric, and longitudinal multipole electric fields in a manner similar to that in the last section:[12]

$$\mathbf{Z}_{jm}^{(m)} = \mathbf{Z}_{jjm} = kf_j(kr)\mathbf{Y}_{jjm} \tag{4-4.10}$$

$$i\mathbf{Z}_{jm}^{(e)} = -\frac{i}{k}\nabla\times\mathbf{Z}_{jm}^{(m)} = i(-i)^{-j}\left\{\sqrt{\frac{j+1}{2j+1}}h_{j-1}(kr)\mathbf{Y}_{j,j-1,m} - \sqrt{\frac{j}{2j+1}}h_{j+1}(kr)\mathbf{Y}_{j,j+1,m}\right\} \tag{4-4.11}$$

$$\mathbf{Z}_{jm}^{(l)} = -\frac{i}{k}\nabla Z_{jm} \qquad = i(-i)^{-j}\left\{\sqrt{\frac{j}{2j+1}}h_{j-1}(kr)\mathbf{Y}_{j,j-1,m} - \sqrt{\frac{j+1}{2j+1}}h_{j+1}(kr)\mathbf{Y}_{j,j+1,m}\right\} \tag{4-4.12}$$

The magnetic multipole field is still a transverse field, but, since the electric and longitudinal multipoles now have spherical Hankel functions multiplying the vector spherical harmonics, they are no longer purely transverse or longitudinal fields--they both now have mixtures of transverse and longitudinal field components. The spherical multipole electric field expressed in terms of these multipoles can still be cast in a form very similar to that in Eq. 4-3.63

$$\mathbf{E}_n(\mathbf{k}_f,\mathbf{k}_i) = \hat{\boldsymbol{\varepsilon}}_f F_n'(\mathbf{k}_f,\mathbf{k}_i) = \hat{\boldsymbol{\varepsilon}}_f F_n(\mathbf{k}_f,\mathbf{k}_i)\Big|_{\mathbf{Y}_{LM}^{(\lambda)}(\Omega_k)\to\mathbf{Z}_{LM}^{(\lambda)}(r_k,\Omega_k)}. \tag{4-4.13}$$

Typically the approximation is made that the incoming fields are plane waves and the scattered fields are spherical waves. Also, if the observation point is far from the scatterer compared to a wavelength, a far field approximation can be made for the scattered spherical field. The spherical Hankel functions, to all multipoles, approaches

$$f_\ell(kr) \underset{kr>>1}{\rightarrow} \frac{e^{ikr}}{kr} \tag{4-4.14}$$

and

$$\mathbf{Z}_{LM}^{(\lambda)} \underset{kr>>1}{\rightarrow} \frac{e^{ikr}}{r}\mathbf{Y}_{LM}^{(\lambda)}. \tag{4-4.15}$$

In the far field limit, the electric and magnetic multipoles now become purely transverse fields, and the longitudinal multipoles are purely longitudinal fields. The total electric field at the point $\mathbf{x}$ is then

$$\mathbf{E}(\mathbf{x}) = \hat{\boldsymbol{\varepsilon}}_i E_0 e^{i\mathbf{k}_i\cdot\mathbf{x}} + \hat{\boldsymbol{\varepsilon}}_f E_0 \frac{e^{ikr_{\mathbf{k}_f}}}{r_{\mathbf{k}_f}} e^{i\mathbf{k}_i\cdot\mathbf{x}_0} F_n\left(\mathbf{k}_f,\mathbf{k}_i\right) \tag{4-4.16}$$

where the first term is the incoming plane wave field of amplitude E_0, the second term is the spherically scattered multipole electric field with F_n given by Eq. 4-3.62 or 4-3.63, and $r_{\mathbf{k}_f}$ is given by Eq. 4-4.8. Notice that the expression for each transverse electric field component is now equivalent to the solution of the integral scattering equation discussed in Section 3.3 (see Eq. 3-3.10) when $|\mathbf{x}| >> |\mathbf{x}_0|$. Now that the scattered fields from a single particle have been found, one can then go on to solve for the net field scattered from several particles (this is done in Chapters 6 and 7). When there are many particles and frequent multiple scatterings, the computations become too time consuming, and one must rely upon the Maxwell inhomogeneous wave equation for transverse electric fields. Fortunately, a wide range of problems involving many particle media can be handled well by the Maxwell inhomogeneous wave equation (as shown in Chapters 6 and 7).

REFERENCES

[1] M. Blume and O. C. Kistner, *Phys. Rev.* **171**, 417 (1968).

[2] H. Frauenfelder, D. E. Nagle, R. D. Taylor, D. R. F. Cochran, and W. M. Visscher, *Phys. Rev.* **126**, 1065 (1962).

[3] J. P. Hannon and G. T. Trammell, *Phys. Rev.* **186**, 306 (1969).

[4] R. M. Housley, R. W. Grant, and U. Gonser, *Phys. Rev.* **178**, 514 (1969).

[5] M. E. Rose, *Elementary Theory of Angular Momentum* (Wiley, New York, 1957).

[6] G. T. Trammell, *Phys. Rev.* **126**, 1045 (1962).

[7] M. Weissbluth, *Atoms and Molecules* (Academic Press, New York, 1978).

[8] A. I. Akhiezer, *Quantum Electrodynamics* (Interscience Publishers, New York, 1965).

[9] F. Halzen and A. D. Martin, *Quarks and Leptons* (Wiley, New York, 1984).

[10] A. R. Edmonds, *Angular Momentum in Quantum Mechanics* (Princeton University Press, Princeton, New Jersey, 1960).

[11] D. M. Brink and G. R. Satchler, *Angular Momentum* (Clarendon Press, Oxford, 1968).

[12] J. Mathews, *Tensor Spherical Harmonics* (California Institute of Technology, 1981).

[13] S. P. Lloyd, *Phys. Rev.* **81**, 161 (1950).

[14] J. P. Hannon and G. T. Trammell, *Phys. Rev. Lett.* **21**, 726 (1968).

[15] A. M. Afanas'ev and Y. Kagan, *Sov. Phys. JETP* **21**, 215 (1965).

[16] A. Y. Dzyublik, *Phys. stat. sol. (b)* **123**, 53 (1984).

[17] J. D. Jackson, *Classical Electrodynamics* (Wiley, New York, 1975).

5. DIPOLE POLARIZATION PROPERTIES AND STATIC FIELD INTERACTIONS

5.1 Polarization Properties of Electric and Magnetic Dipole Scattering

For the case of Thomson scattering, the scattering amplitude, Eq. 4-2.11, can be written in tensor form where a polarization matrix contains all the polarization information about the scattering process

$$\mathbf{F}_T(\mathbf{k}_f,\mathbf{k}_i) = -r_q f_0 P_T \tag{5-1.1}$$

where

$$P_T = \hat{\boldsymbol{\varepsilon}}^i \cdot \hat{\boldsymbol{\varepsilon}}^{f*} = \begin{pmatrix} \hat{\boldsymbol{\varepsilon}}_x^i \cdot \hat{\boldsymbol{\varepsilon}}_x^{f*} & \hat{\boldsymbol{\varepsilon}}_x^i \cdot \hat{\boldsymbol{\varepsilon}}_y^{f*} \\ \hat{\boldsymbol{\varepsilon}}_y^i \cdot \hat{\boldsymbol{\varepsilon}}_x^{f*} & \hat{\boldsymbol{\varepsilon}}_y^i \cdot \hat{\boldsymbol{\varepsilon}}_y^{f*} \end{pmatrix}. \tag{5-1.2}$$

Since there are two directions corresponding to the incoming and outgoing photons, there are two separate polarization bases for each direction, and the orientation of each basis with respect to one another is arbitrary. Usually a convenient orientation is chosen that diagonalizes the polarization matrix and simplifies calculations. Constraining one polarization component, say the x-component of both the incoming and outgoing fields, to be perpendicular to the scattering plane--$\hat{\boldsymbol{\varepsilon}}_x = \hat{\boldsymbol{\sigma}}$ = sigma polarized--forces the other component to lie in the scattering plane--$\hat{\boldsymbol{\varepsilon}}_y = \hat{\boldsymbol{\pi}}$ = pi polarized--(see Fig. 5-1.1). Under such conditions the polarization matrix diagonalizes to

$$P_T = \begin{pmatrix} \hat{\boldsymbol{\sigma}}_i \cdot \hat{\boldsymbol{\sigma}}_f & \hat{\boldsymbol{\sigma}}_i \cdot \hat{\boldsymbol{\pi}}_f \\ \hat{\boldsymbol{\pi}}_i \cdot \hat{\boldsymbol{\sigma}}_f & \hat{\boldsymbol{\pi}}_i \cdot \hat{\boldsymbol{\pi}}_f \end{pmatrix} = \begin{pmatrix} 1 & 0 \\ 0 & \cos 2\theta_B \end{pmatrix} \tag{5-1.3}$$

where $2\theta_B$ is the scattering angle between $\mathbf{k}_i$ and $\mathbf{k}_f$. The polarization matrix reveals that Thomson radiation has an angular distribution commonly associated with electric dipole scattering--horizontally polarized fields are reflected by the same amount regardless of scattering angle while vertically polarized fields suffer a decrease in amplitude proportional to the cosine of the scattering angle between the incoming and outgoing wave directions.

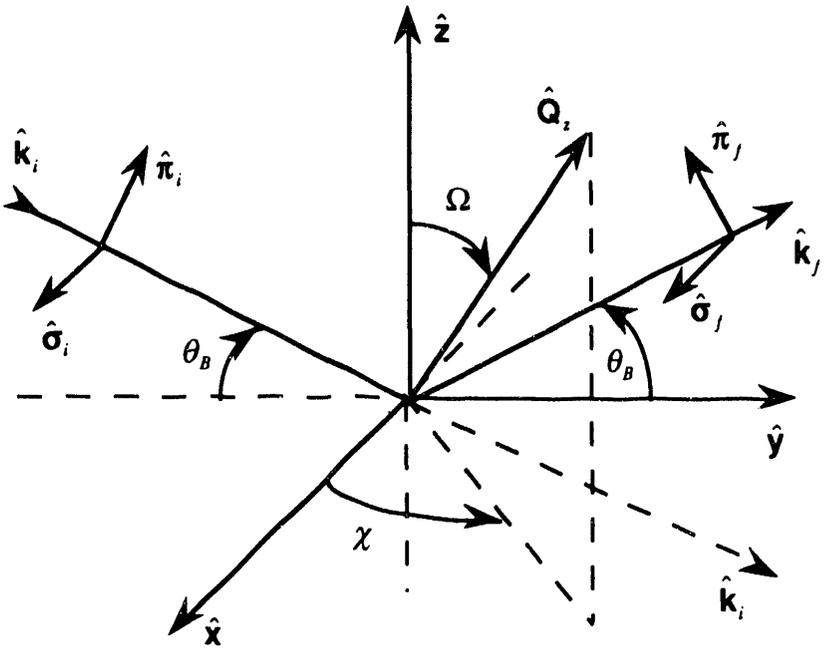

Fig. 5-1.1. Scattering geometry for a particle at the origin. Sigma (pi) polarizations are perpendicular (parallel) to the yz scattering plane. $\hat{\mathbf{Q}}_z$ is the quantization axis direction with polar and azimuthal angles Ω and χ. $2\theta_B$ is the scattering angle.

For dipole scattering (and no polarization mixing), the tensor form of the scattering amplitude is (from Eq. 4-3.63)

$$\mathbf{F}(\mathbf{k}_f,\mathbf{k}_i,\mathbf{x}_0)=-(2\pi/k_f)e^{-i(\mathbf{k}_f-\mathbf{k}_i)\cdot\mathbf{x}_0}\sum_{\lambda LM}P_{LM}^{(\lambda)}\frac{\Gamma(L,\lambda)}{E_i-E_n+\hbar\omega_{\mathbf{k}_i}+i\Gamma_n/2}\langle j_f m_f LM|j_f L j_n m_n\rangle^2 \tag{5-1.4}$$

where the polarization matrix is of the form

$$P_{LM}^{(\lambda)}=\hat{\boldsymbol{\varepsilon}}^i\cdot\mathbf{Y}_{LM}^{(\lambda)*}(\Omega_{\mathbf{k}_i})\mathbf{Y}_{LM}^{(\lambda)}(\Omega_{\mathbf{k}_f})\cdot\hat{\boldsymbol{\varepsilon}}^{f*}$$

$$=\begin{pmatrix}\left[\hat{\boldsymbol{\varepsilon}}_x^i\cdot\mathbf{Y}_{LM}^{(\lambda)*}(\Omega_{\mathbf{k}_i})\right]\left[\mathbf{Y}_{LM}^{(\lambda)}(\Omega_{\mathbf{k}_f})\cdot\hat{\boldsymbol{\varepsilon}}_x^{f*}\right] & \left[\hat{\boldsymbol{\varepsilon}}_x^i\cdot\mathbf{Y}_{LM}^{(\lambda)*}(\Omega_{\mathbf{k}_i})\right]\left[\mathbf{Y}_{LM}^{(\lambda)}(\Omega_{\mathbf{k}_f})\cdot\hat{\boldsymbol{\varepsilon}}_y^{f*}\right]\\ \left[\hat{\boldsymbol{\varepsilon}}_y^i\cdot\mathbf{Y}_{LM}^{(\lambda)*}(\Omega_{\mathbf{k}_i})\right]\left[\mathbf{Y}_{LM}^{(\lambda)}(\Omega_{\mathbf{k}_f})\cdot\hat{\boldsymbol{\varepsilon}}_x^{f*}\right] & \left[\hat{\boldsymbol{\varepsilon}}_y^i\cdot\mathbf{Y}_{LM}^{(\lambda)*}(\Omega_{\mathbf{k}_i})\right]\left[\mathbf{Y}_{LM}^{(\lambda)}(\Omega_{\mathbf{k}_f})\cdot\hat{\boldsymbol{\varepsilon}}_y^{f*}\right]\end{pmatrix}, \tag{5-1.5}$$

and $\lambda=1\equiv$ e for electric dipole scattering, $\lambda=0\equiv$ m for magnetic dipole scattering, and $L=1$ for dipole scattering. The vector spherical harmonics for dipole (and also quadrupole) scattering are given in Table 5-1.1. The scattering geometry presented in Fig. 5-1.1 will be used to examine the structure of the dipole polarization matrix.

			$\mathbf{Y}^{e}_{jm}$		$\mathbf{Y}^{m}_{jm}$	
j	m	factor	$\hat{\theta}$	$\hat{\phi}$	$\hat{\theta}$	$\hat{\phi}$
1	1	$\sqrt{\frac{3}{16\pi}}e^{i\phi}$	$-\cos\theta$	$-i$	1	$i\cos\theta$
1	0	$\sqrt{\frac{3}{8\pi}}\sin\theta$	-1	0	0	i
1	-1	$\sqrt{\frac{3}{16\pi}}e^{-i\phi}$	$\cos\theta$	$-i$	1	$-i\cos\theta$
2	2	$\sqrt{\frac{5}{16\pi}}\sin\theta e^{2i\phi}$	$\cos\theta$	i	-1	$-i\cos\theta$
2	1	$\sqrt{\frac{5}{16\pi}}e^{i\phi}$	$1-2\cos^2\theta$	$-i\cos\theta$	$\cos\theta$	$i(2\cos^2\theta-1)$
2	0	$\sqrt{\frac{15}{8\pi}}\sin\theta$	$-\cos\theta$	0	0	$i\cos\theta$
2	-1	$\sqrt{\frac{5}{16\pi}}e^{-i\phi}$	$2\cos^2\theta-1$	$-i\cos\theta$	$\cos\theta$	$i(1-2\cos^2\theta)$
2	-2	$\sqrt{\frac{5}{16\pi}}\sin\theta e^{-2i\phi}$	$\cos\theta$	$-i$	1	$-i\cos\theta$

Table 5-1.1. Electric and magnetic dipole, $j=1$, and quadrupole, $j=2$, vector spherical harmonics.[1]

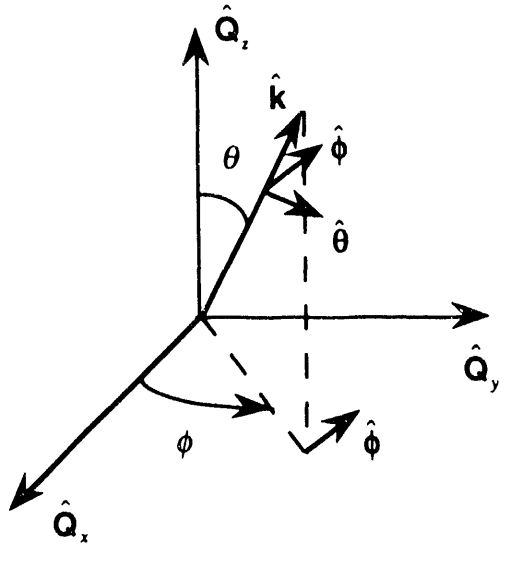

Fig. 5-1.2. Wavector in quantization system defines the spherical coordinates and unit vectors of a vector spherical harmonic.

The dipole direction, or quantization axis $\hat{\mathbf{Q}}_z$, points in some arbitrary direction specified by the polar and azimuthal angles Ω and χ:

$$\hat{\mathbf{Q}}_z = \cos\chi\sin\Omega\,\hat{\mathbf{x}} + \sin\chi\sin\Omega\,\hat{\mathbf{y}} + \cos\Omega\,\hat{\mathbf{z}}. \tag{5-1.6}$$

Recall that the spherical coordinate system for the vector spherical harmonics is defined by the quantum axis of the scatterer. The polar angle, $\theta_{(i,f)}$, is the angle between the incoming or outgoing photon and the quantization axis--see Fig. 5-1.2.

$$\cos\theta_{(i,f)} = \hat{\mathbf{Q}}_z \cdot \hat{\mathbf{k}}_{(i,f)} = \cos\theta_B \sin\chi\sin\Omega \mp \sin\theta_B\cos\Omega \tag{5-1.7}$$

where

$$\hat{\mathbf{k}}_{(i,f)} = \cos\theta_B\,\hat{\mathbf{y}} \mp \sin\theta_B\,\hat{\mathbf{z}}, \tag{5-1.8}$$

and the top sign in the $\mp$ corresponds to $\hat{\mathbf{k}}_i$ and the bottom sign corresponds to $\hat{\mathbf{k}}_f$. Since the $\left(\hat{\mathbf{Q}}_x, \hat{\mathbf{Q}}_y\right)$ basis can be arbitrarily oriented in a plane perpendicular to the quantization axis, only the azimuthal phase difference, $\Delta\phi = \phi_f - \phi_i$, is meaningful. This phase difference can be found through the angle addition rule

$$\cos 2\theta_B = \cos\theta_f\cos\theta_i + \sin\theta_f\sin\theta_i\cos\left(\phi_f - \phi_i\right). \tag{5-1.9}$$

To perform the dot products in the polarization matrix, Eq. 5-1.5, the spherical unit vectors must be transformed into Cartesian unit vectors. This transformation can be accomplished by noting that the azimuthal unit vector, $\hat{\boldsymbol{\phi}}$, is perpendicular to both $\hat{\mathbf{k}}$ and $\hat{\mathbf{Q}}_z$

$$\hat{\boldsymbol{\phi}} = \hat{\mathbf{Q}}_z \times \hat{\mathbf{k}} \Big/ \left|\hat{\mathbf{Q}}_z \times \hat{\mathbf{k}}\right|, \tag{5-1.10}$$

and the polar unit vector, $\hat{\boldsymbol{\theta}}$,is perpendicular to both $\hat{\boldsymbol{\phi}}$ and $\hat{\mathbf{k}}$

$$\hat{\boldsymbol{\theta}} = \hat{\boldsymbol{\phi}} \times \hat{\mathbf{k}} \Big/ \left|\hat{\boldsymbol{\phi}} \times \hat{\mathbf{k}}\right|. \tag{5-1.11}$$

After some algebra, the spherical unit vectors can be written down as

$$\hat{\boldsymbol{\phi}}_{(i,f)} = \frac{-\left(\cos\theta_B\cos\Omega \pm \sin\theta_B\sin\chi\sin\Omega\right)\hat{\mathbf{x}} + \cos\chi\sin\Omega\left(\cos\theta_B\,\hat{\mathbf{z}} \pm \sin\theta_B\,\hat{\mathbf{y}}\right)}{\sqrt{N_{(i,f)}}} \tag{5-1.12}$$

$$\hat{\boldsymbol{\theta}}_{(i,f)} = \frac{-\cos\chi\sin\Omega\,\hat{\mathbf{x}} - \left(\sin\theta_B\sin\chi\sin\Omega \pm \cos\theta_B\cos\Omega\right)\left(\sin\theta_B\,\hat{\mathbf{y}}\cos\theta_B\,\hat{\mathbf{z}} \pm \cos\theta_B\,\hat{\mathbf{z}}\right)}{\sqrt{N_{(i,f)}}}$$

where (5-1.13)

$$N_{(i,f)} = \left(\cos\theta_B\cos\Omega \pm \sin\theta_B\sin\chi\sin\Omega\right)^2 + \left(\cos\chi\sin\Omega\right)^2. \tag{5-1.14}$$

The polarization vector directions can be read directly from Fig. 5-1.1

$$\hat{\boldsymbol{\varepsilon}}_x^{(i,f)} \equiv \hat{\boldsymbol{\sigma}}_{(i,f)} = \hat{\mathbf{x}} \tag{5-1.15}$$

$$\hat{\boldsymbol{\varepsilon}}_y^{(i,f)} \equiv \hat{\boldsymbol{\pi}}_{(i,f)} = \pm \sin\theta_B\, \hat{\mathbf{y}} + \cos\theta_B\, \hat{\mathbf{z}}. \tag{5-1.16}$$

Then, all of the dot products in the dipole polarization matrix can be put in the form (see Fig. 5-1.3)

$$\hat{\boldsymbol{\sigma}}_{(i,f)} \cdot \hat{\boldsymbol{\phi}}_{(i,f)} = \hat{\boldsymbol{\pi}}_{(i,f)} \cdot \hat{\boldsymbol{\theta}}_{(i,f)} = \cos\beta_{(i,f)} = -\left(\cos\theta_B \cos\Omega \pm \sin\theta_B \sin\chi \sin\Omega\right)\Big/\sqrt{N_{(i,f)}} \tag{5-1.17}$$

$$\hat{\boldsymbol{\sigma}}_{(i,f)} \cdot \hat{\boldsymbol{\theta}}_{(i,f)} = -\left(\hat{\boldsymbol{\pi}}_{(i,f)} \cdot \hat{\boldsymbol{\phi}}_{(i,f)}\right) = \sin\beta_{(i,f)} = -\cos\chi \sin\Omega\Big/\sqrt{N_{(i,f)}}\,. \tag{5-1.18}$$

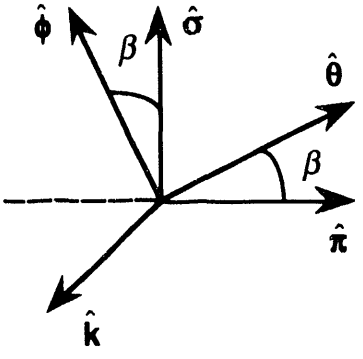

Fig. 5-1.3. Orientation of polarization vectors with respect to spherical unit vectors lying in the $(\hat{\sigma}, \hat{\pi})$ plane and the wavector direction.

There is now enough information to construct the dipole polarization matrix. For magnetic dipole scattering, the $M = 0$ term is

$$P_{10}^{(m)} = \frac{3}{8\pi}\begin{pmatrix} \sin\theta_i \sin\theta_f \cos\beta_i \cos\beta_f & -\sin\theta_i \sin\theta_f \cos\beta_i \sin\beta_f \\ -\sin\theta_i \sin\theta_f \sin\beta_i \cos\beta_f & \sin\theta_i \sin\theta_f \sin\beta_i \sin\beta_f \end{pmatrix}, \tag{5-1.19}$$

the $M = 1$ term is

$$P_{11}^{(m)} = \frac{3}{16\pi} e^{i(\phi_f - \phi_i)}$$

$$\times \begin{pmatrix} (\sin\beta_i - i\cos\theta_i \cos\beta_i)(\sin\beta_f + i\cos\theta_f \cos\beta_f) & (\sin\beta_i - i\cos\theta_i \cos\beta_i)(\cos\beta_f - i\cos\theta_f \sin\beta_f) \\ (\cos\beta_i - i\cos\theta_i \sin\beta_i)(\sin\beta_f + i\cos\theta_f \cos\beta_f) & (\cos\beta_i - i\cos\theta_i \sin\beta_i)(\cos\beta_f + i\cos\theta_f \sin\beta_f) \end{pmatrix} \tag{5-1.20}$$

and the $M = -1$ term is obtained by taking the complex conjugate of the $M = 1$ term because a linear polarization basis was chosen

$$P_{1,-1}^{(m)} = \left(P_{11}^{(m)}\right)^*. \tag{5-1.21}$$

For electric dipole scattering, the polarization matrices are equivalent except for the substitution $\beta \to \beta - \pi/2$ since the electric dipole vector fields are orthogonal to the magnetic dipole vector fields. For simple orientations of the quantization axis with respect to the photon directions, three examples illustrating the structure of polarization matrices are given below.

CASE 1: Quantization axis is perpendicular to the scattering plane: $\hat{\mathbf{Q}}_z = \hat{\mathbf{x}}$.

$$\Omega = \pi/2, \quad \chi = 0, \quad \theta_i = \theta_f = \pi/2, \quad \phi_f - \phi_i = 2\theta_B$$

$$\hat{\boldsymbol{\sigma}}_{(i,f)} = -\hat{\boldsymbol{\theta}}_{(i,f)}, \quad \hat{\boldsymbol{\pi}}_{(i,f)} = \hat{\boldsymbol{\phi}}_{(i,f)}, \quad \beta_{(i,f)} = -\pi/2$$

Then,

$$P_{10}^{(m)} = \frac{3}{8\pi}\begin{pmatrix} 0 & 0 \\ 0 & 1 \end{pmatrix}, \qquad P_{1,\pm1}^{(m)} = \frac{3}{16\pi}e^{\pm i2\theta_B}\begin{pmatrix} 1 & 0 \\ 0 & 0 \end{pmatrix} \tag{5-1.22}$$

$$P_{10}^{(e)} = \frac{3}{8\pi}\begin{pmatrix} 1 & 0 \\ 0 & 0 \end{pmatrix}, \qquad P_{1,\pm1}^{(e)} = \frac{3}{16\pi}e^{\pm i2\theta_B}\begin{pmatrix} 0 & 0 \\ 0 & 1 \end{pmatrix} \tag{5-1.23}$$

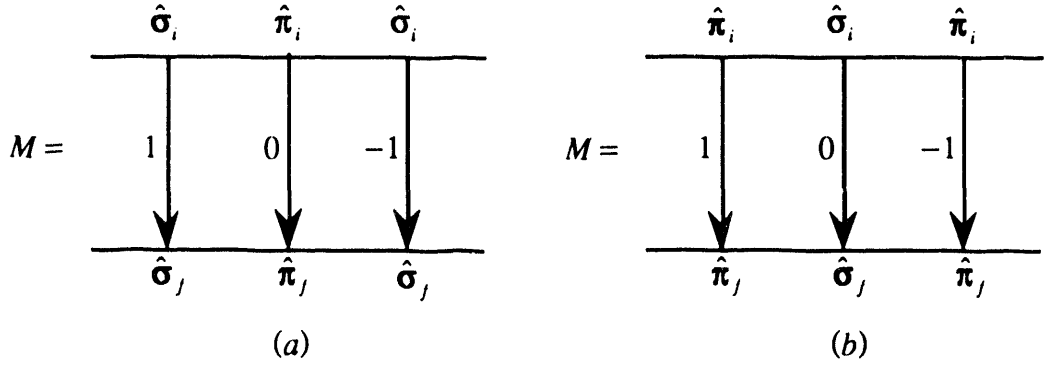

(a) (b)

Fig. 5-1.4. For a dipole transition $M = m_n - m_f$, incoming linearly polarized fields scatter into outgoing linearly polarized fields: (a) magnetic dipole transitions, (b) electric dipole transitions.

The polarization matrices show that the $M = m_n - m_f$ transitions emit only linearly polarized light. For $M = 0$, the scattered magnetic dipole radiation is vertically, or pi, polarized while for $M = \pm 1$ the scattered radiation is horizontally, or sigma, polarized. For scattered electric dipole radiation the situation is opposite to that of magnetic dipole radiation as shown in Fig. 5-1.4.

CASE 2: Quantization axis is parallel to the scattering plane but vertically oriented: $\hat{\mathbf{Q}}_z = \hat{\mathbf{z}}$.

$$\Omega = \chi = 0, \quad \theta_{(i,f)} = \theta_B \pm \pi/2, \quad \phi_f - \phi_i = \pi$$

$$\hat{\boldsymbol{\sigma}}_{(i,f)} = -\hat{\boldsymbol{\phi}}_{(i,f)}, \quad \hat{\boldsymbol{\pi}}_{(i,f)} = -\hat{\boldsymbol{\theta}}_{(i,f)}, \quad \beta_{(i,f)} = \pi$$

Then

$$P_{10}^{(m)} = \frac{3}{8\pi}\begin{pmatrix} -\cos^2\theta_B & 0 \\ 0 & 0 \end{pmatrix}, \qquad P_{1,\pm1}^{(m)} = -\frac{3}{16\pi}\begin{pmatrix} -\sin^2\theta_B & \pm i\sin\theta_B \\ \pm i\sin\theta_B & 1 \end{pmatrix} \tag{5-1.24}$$

$$P_{10}^{(e)} = \frac{3}{8\pi}\begin{pmatrix} 0 & 0 \\ 0 & -\cos^2\theta_B \end{pmatrix}, \qquad P_{1,\pm1}^{(e)} = -\frac{3}{16\pi}\begin{pmatrix} 1 & \mp i\sin\theta_B \\ \mp i\sin\theta_B & -\sin^2\theta_B \end{pmatrix} \tag{5-1.25}$$

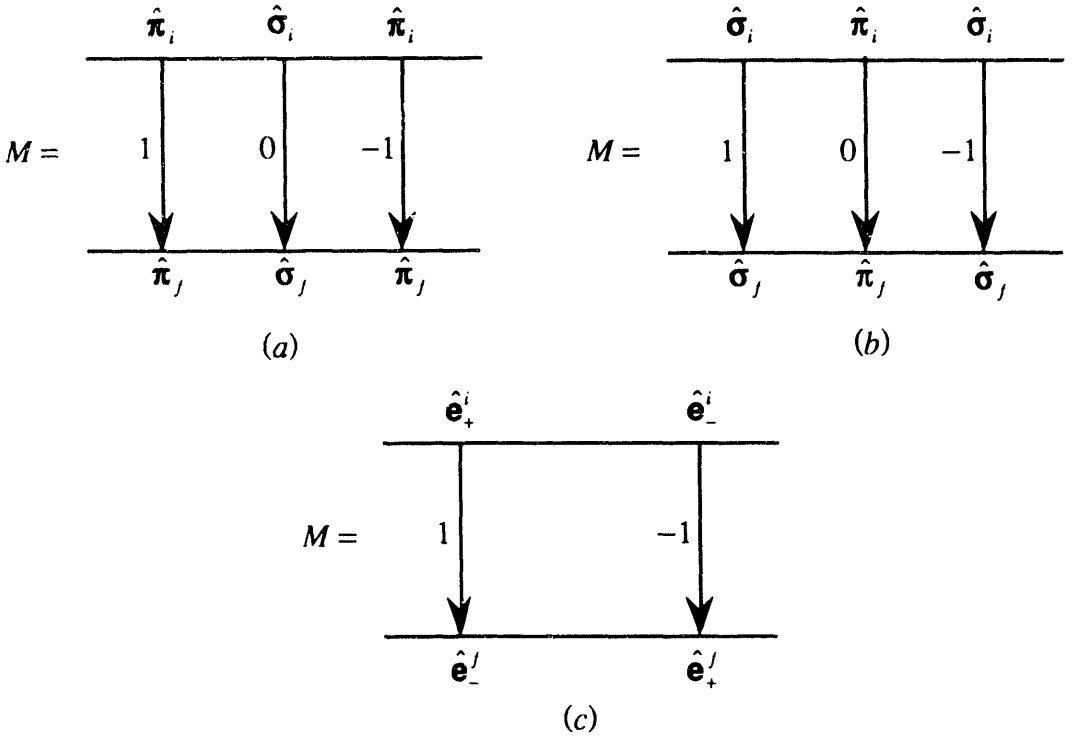

Fig. 5-1.5. For forward scattering $(2\theta_B = 0)$ incoming fields scatter into outgoing linearly polarized fields: (a) magnetic dipole transitions, (b) electric dipole transitions. For backscattering $(2\theta_B = 180°)$ polarization reversal occurs for circularly polarized fields: (c) magnetic and electric dipole transitions.

For $M = 0$, the scattered magnetic (electric) dipole radiation is horizontally (vertically) polarized. For $M = \pm 1$, the scattered dipole radiation is generally elliptically polarized--this is an example of polarization mixing where an incoming polarized field can be scattered into an outgoing field of a different polarization. However, for forward scattering, $(2\theta_B = 0)$, the scattered field is linearly polarized (no polarization mixing occurs), and for backscattering, $(2\theta_B = 180°)$, the scattered field is circularly polarized.

For backscattering the polarization matrix for both magnetic (upper sign) and electric (lower sign) dipole radiation is (for $M = 1$)

$$P_{11}^{(m,e)} = -\frac{3}{16\pi}\begin{pmatrix} \mp 1 & \pm i \\ \pm i & \pm 1 \end{pmatrix}. \tag{5-1.26}$$

If the incoming field is left circularly polarized

$$\hat{\boldsymbol{\varepsilon}}_i = \hat{\mathbf{e}}_+^i = -\frac{1}{\sqrt{2}}(\hat{\boldsymbol{\sigma}}_i + i\hat{\boldsymbol{\pi}}_i), \tag{5-1.27}$$

then the scattered field has polarization

$$P_{11}^{(m,e)} \cdot \hat{\mathbf{e}}_+^i = \frac{3}{16\pi}\frac{1}{\sqrt{2}}\begin{pmatrix} \mp 1 & \pm i \\ \pm i & \pm 1 \end{pmatrix}\begin{pmatrix} 1 \\ i \end{pmatrix} = \mp\frac{3}{8\pi}\frac{1}{\sqrt{2}}\begin{pmatrix} 1 \\ -i \end{pmatrix} = \mp\left(\frac{3}{8\pi}\right)\hat{\mathbf{e}}_-^f.$$

This shows that left circularly polarized fields scatter into right circularly polarized fields for $M = 1$. However, right circularly polarized fields do not scatter since

$$P_{11}^{(m,e)} \cdot \hat{\mathbf{e}}_-^i = -\frac{3}{16\pi}\frac{1}{\sqrt{2}}\begin{pmatrix} \mp 1 & \pm i \\ \pm i & \pm 1 \end{pmatrix}\begin{pmatrix} 1 \\ -i \end{pmatrix} = 0.$$

This is an extreme case of polarization mixing--it corresponds to complete polarization reversal.

For $M = -1$, the converse happens--incoming right circularly polarized fields scatter into left circularly polarized fields whereas incoming left circularly polarized radiation does not scatter at all. This is all shown schematically in Fig. 5-1.5 (c).

CASE 3: Quantization axis is parallel to the scattering plane but horizontally oriented: $\hat{\mathbf{Q}}_z = \hat{\mathbf{y}}$.

$$\Omega = \chi = \pi/2, \qquad \theta_{(i,f)} = \theta_B, \qquad \phi_f - \phi_i = \pi$$

$$\hat{\boldsymbol{\sigma}}_i = -\hat{\boldsymbol{\phi}}_i, \qquad \hat{\boldsymbol{\sigma}}_f = \hat{\boldsymbol{\phi}}_f, \qquad \hat{\boldsymbol{\pi}}_i = -\hat{\boldsymbol{\theta}}_i, \qquad \hat{\boldsymbol{\pi}}_f = \hat{\boldsymbol{\theta}}_f, \qquad \beta_i = \pi, \qquad \beta_f = 0$$

Then

$$P_{10}^{(m)} = \frac{3}{8\pi}\begin{pmatrix} -\sin^2\theta_B & 0 \\ 0 & 0 \end{pmatrix}, \qquad P_{1,\pm 1}^{(m)} = -\frac{3}{16\pi}\begin{pmatrix} -\cos^2\theta_B & \pm i\cos\theta_B \\ \mp i\cos\theta_B & -1 \end{pmatrix} \tag{5-1.28}$$

$$P_{10}^{(e)} = \frac{3}{8\pi}\begin{pmatrix} 0 & 0 \\ 0 & -\sin^2\theta_B \end{pmatrix}, \qquad P_{1,\pm 1}^{(e)} = -\frac{3}{16\pi}\begin{pmatrix} -1 & \pm i\cos\theta_B \\ \mp i\cos\theta_B & -\cos^2\theta_B \end{pmatrix} \tag{5-1.29}$$

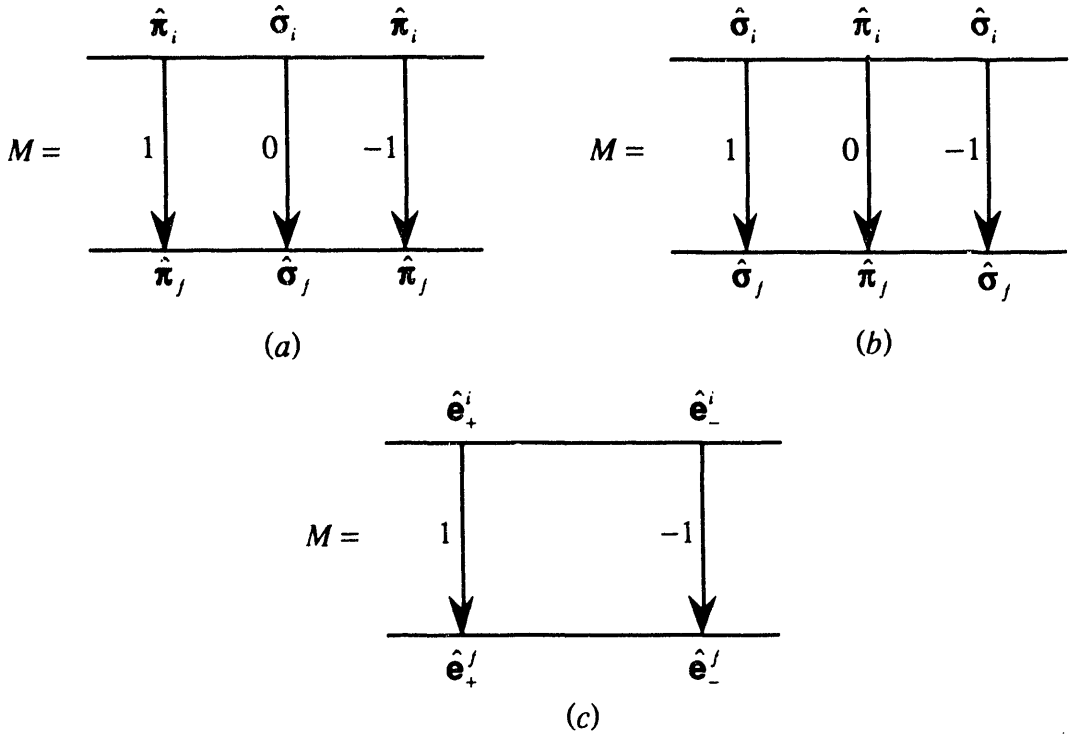

Fig. 5-1.6. For backscattering $(2\theta_B = 180°)$ incoming fields scatter into outgoing linearly polarized fields: (a) magnetic dipole transitions, (b) electric dipole transitions. For forward scattering $(2\theta_B = 0)$ incoming fields scatter into outgoing circularly polarized fields: (c) magnetic and electric dipole transitions.

For $M = 0$, the scattered magnetic (electric) dipole radiation is horizontally (vertically) polarized. For $M = \pm 1$, the scattered dipole radiation is generally elliptically polarized. However, for forward scattering the scattered field is circularly polarized, and for backscattering the scattered field is linearly polarized (this the reverse of Case 2).

For forward scattering the polarization matrix for both magnetic and electric dipole radiation is the same:

$$P^{(m)}_{1,\pm 1} = P^{(e)}_{1,\pm 1} = -\frac{3}{16\pi}\begin{pmatrix} -1 & \pm i \\ \mp i & -1 \end{pmatrix}, \tag{5-1.30}$$

and for $M = 0$ the polarization matrices are zero. For $M = 1$, incoming left circularly polarized fields scatter into outgoing left circularly polarized fields since

$$P^{(m,e)}_{11} \cdot \hat{\mathbf{e}}^i_+ = \frac{3}{16\pi}\frac{1}{\sqrt{2}}\begin{pmatrix} -1 & i \\ -i & -1 \end{pmatrix}\begin{pmatrix} 1 \\ i \end{pmatrix} = -\frac{3}{8\pi}\frac{1}{\sqrt{2}}\begin{pmatrix} 1 \\ i \end{pmatrix} = \left(\frac{3}{8\pi}\right)\hat{\mathbf{e}}^f_+,$$

while incoming right circularly polarized fields do not scatter. Similarly, for $M = -1$, the converse occurs (see Fig. 5-1.6). No polarization reversal occurs as happened in Case 2.

There can be no polarization reversal for sigma or pi polarized fields because scattering can only change the amplitude or phase of the incoming field. There is no way a phase change can transform a sigma polarized field to a pi polarized field. However, by introducing an additional quantization axis, and arranging a set of scatterers in a convenient lattice structure, this limitation can be overcome. This is discussed in Section 5.2 and 5.3.

The scattering amplitude, Eq. 5-1.4, can be greatly simplified for those cases in which all the angular momentum spin states are degenerate, or when operating far from any dipole resonance. The scattering amplitude can then be spin averaged by summing over all intermediate, final, and initial state projection quantum numbers, or spins, m_f, m_i, m_n, and averaging over all initial state spins

$$\mathbf{F}_{ave}^{(\lambda)}(\mathbf{k}_f,\mathbf{k}_i)=\sum_{m_f m_n m_i}\mathbf{F}^{(\lambda)}(\mathbf{k}_f,\mathbf{k}_i)\Big/(2j_i+1) \tag{5-1.31}$$

where $2j_i+1$ is the number of initial state spins, m_i.

For elastic scattering $j_f = j_i$ and $m_f = m_i$, and thus the sum over m_i in the triple sum above can be omitted. Since all of the angular momentum spin states are degenerate, or nearly degenerate, the energy, E_n, of the state with spin m_n is the energy of the unsplit angular momentum state with angular momentum quantum number j_n

$$E_n = E_{j_n}. \tag{5-1.32}$$

The resonance denominator of the scattering amplitude is then the same for all spins m_n and can therefore be pulled out of the sum (assuming also that the total decay rates, Γ_n, from each state with spin m_n are all the same). Since the quantization axis is now unimportant--it can point in an arbitrary direction--let it point in the same direction as in Case 3:

$$\hat{\mathbf{Q}}_z = \hat{\mathbf{y}}. \tag{5-1.33}$$

Then the polarization matrices of Case 3, Eqs. 5-1.28 and 5-1.29, can be used to perform the spin average.

Concentrating on just magnetic dipole scattering, the main part of the spin average calculation involves the term

$$\sum_{m_f m_n M} P_{1M}^{(m)}\left\langle j_f m_f 1\, M \middle| j_f 1\, j_n m_n\right\rangle^2 = \frac{3}{16\pi}\begin{pmatrix} s_{11} & s_{12} \\ s_{21} & s_{22}\end{pmatrix}, \tag{5-1.34}$$

where (since $m_n = m_f + M$ the sum over m_n can be suppressed)

$$s_{11} = s_{22}\cos^2\theta_B - \sum_{m_f} 2\sin^2\theta_B\left\langle j_f, m_f, 1, 0 \middle| j_f, 1, j_n, m_f\right\rangle^2 \tag{5-1.35}$$

$$s_{12} = \sum_{m_f} i\cos\theta_B\left(\left\langle j_f, m_f, 1, -1 \middle| j_f, 1, j_n, m_f - 1\right\rangle^2 - \left\langle j_f, m_f, 1, 1 \middle| j_f, 1, j_n, m_f + 1\right\rangle^2\right) \quad (5\text{-}1.36)$$

$$s_{21} = s_{12}^* \quad (5\text{-}1.37)$$

$$s_{22} = \sum_{m_f}\left(\left\langle j_f, m_f, 1, 1 \middle| j_f, 1, j_n, m_f + 1\right\rangle^2 + \left\langle j_f, m_f, 1, 1 \middle| j_f, 1, j_n, m_f + 1\right\rangle^2\right) \quad (5\text{-}1.38)$$

Since, for dipole transitions, $j_n = j_f + 1$, the Clebsch-Gordan coefficients reduce to simple relations[2]

$$\left\langle j_f, m_f, 1, 0 \middle| j_f, 1, j_f + 1, m_f\right\rangle^2 = \frac{(j_f - m_f + 1)(j_f + m_f + 1)}{(2j_f + 1)(j_f + 1)} \quad (5\text{-}1.39)$$

$$\left\langle j_f, m_f, 1, \pm 1 \middle| j_f, 1, j_f + 1, m_f \pm 1\right\rangle^2 = \frac{(j_f \pm m_f + 1)(j_f \pm m_f + 2)}{2(2j_f + 1)(j_f + 1)}. \quad (5\text{-}1.40)$$

Then the off-diagonal elements sum to zero since

$$s_{12} = -\frac{i\cos\theta_B(2j_f + 3)}{(2j_f + 1)(j_f + 1)} \sum_{m_f = -j_f}^{j_f} m_f = 0. \quad (5\text{-}1.41)$$

This result already shows that polarization mixing is not possible for the spin averaged scattering amplitude since the polarization matrix is diagonal.

For the diagonal element s_{22}:

$$s_{22} = \frac{1}{2(2j_f + 1)(j_f + 1)}\left[(2j_f^2 + 6j_f + 4)(2j_f + 1) + 2\sum_{m_f} m_f^2\right]$$

$$= \frac{1}{2(2j_f + 1)(j_f + 1)}\left[2(j_f + 2)(j_f + 1)(2j_f + 1) + 4\frac{j_f(j_f + 1)(2j_f + 1)}{6}\right]$$

$$= \frac{2}{3}(2j_f + 3) = \frac{2}{3}(2j_n + 1). \quad (5\text{-}1.42)$$

Noting that

$$\sum_{m_f}\left\langle j_f, m_f, 1, 0 \middle| j_f, 1, j_f + 1, m_f\right\rangle^2 = \frac{1}{(2j_f + 1)(j_f + 1)}\left[(j_f^2 + 2j_f + 1)(2j_f + 1) - \sum_{m_f} m_f^2\right]$$

$$= \frac{1}{3}(2j_n + 1) \tag{5-1.43}$$

gives

$$s_{11} = \cos^2\theta_B\left[\frac{2}{3}(2j_n+1)\right] - 2\sin^2\theta_B\left[\frac{1}{3}(2j_n+1)\right]$$

$$= \frac{2}{3}(2j_n+1)\cos 2\theta_B \tag{5-1.44}$$

The spin average scattering amplitude is then

$$\mathbf{F}_{ave}^{(m)}(\mathbf{k}_f, \mathbf{k}_i) = -\frac{1}{4k_f}\frac{(2j_n+1)}{(2j_i+1)}\frac{\Gamma_{rad}}{\hbar}P_{ave}^{(m)}\frac{1}{\omega_{\mathbf{k}_i} - \omega_0 + i\Gamma/2\hbar} \tag{5-1.45}$$

where $$P_{ave}^{(m)} = \begin{pmatrix} \cos 2\theta_B & 0 \\ 0 & 1 \end{pmatrix}, \tag{5-1.46}$$

and $\Gamma_{rad} = \Gamma(1,m)$, and Γ is the total decay rate from the angular momentum state with angular momentum number j_n. For electric dipole scattering, the average scattering amplitude is of the same form as Eq. 5-1.45 except that the polarization matrix is now

$$P_{ave}^{(e)} = \begin{pmatrix} 1 & 0 \\ 0 & \cos 2\theta_B \end{pmatrix}. \tag{5-1.47}$$

Note that the polarization matrix for spin averaged electric dipole scattering is equivalent to that for Thomson scattering--this is one reason why Thomson scattering is sometimes called electric dipole scattering at high photon energies. The scattering amplitude for dipole radiation can then be written (in nontensor form) in a manner similar to that for Thomson radiation

$$F_{ave}^{(\lambda)}(\mathbf{k}_f, \mathbf{k}_i) = -\frac{1}{4k_f}\frac{(2j_n+1)}{(2j_i+1)}\frac{\Gamma_{rad}}{\hbar}\left(\hat{\mathbf{u}}_f^{(\lambda)*}\cdot\hat{\mathbf{u}}_i^{(\lambda)}\right)\frac{1}{\omega_{\mathbf{k}_i} - \omega_0 + i\Gamma/2\hbar} \tag{5-1.48}$$

where for electric dipole scattering

$$\hat{\mathbf{u}}^{(e)} = \hat{\boldsymbol{\varepsilon}}, \tag{5-1.49}$$

and for magnetic dipole scattering

$$\hat{\mathbf{u}}^{(m)} = \hat{\mathbf{h}} = \hat{\mathbf{k}} \times \hat{\boldsymbol{\varepsilon}}. \tag{5-1.50}$$

If the polarization of an electric field is $\hat{\boldsymbol{\varepsilon}}$, then the polarization of the corresponding magnetic field is $\hat{\mathbf{h}}$. Then, the scattering amplitude reveals that magnetic dipole electric fields have the same polarization characteristics as electric dipole magnetic fields.

The total cross section for electric or magnetic dipole scattering is, from the optical theorem,

$$\sigma_{tot} = \frac{4\pi}{k_f}\mathrm{Im}\left\{F_{ave}\left(\mathbf{k}_f,\mathbf{k}_i\right)\right\} = \sigma_0 \frac{(\Gamma/2\hbar)^2}{\left(\omega_{\mathbf{k}_i} - \omega_0\right)^2 + (\Gamma/2\hbar)^2} \tag{5-1.51}$$

where σ_0 is the total cross section on resonance

$$\sigma_0 = \frac{2\pi}{k_f^2}\left(\frac{2j_n+1}{2j_i+1}\right)\left(\frac{\Gamma_{rad}}{\Gamma}\right)\left(\hat{\mathbf{u}}_f^* \cdot \hat{\mathbf{u}}_i\right). \tag{5-1.52}$$

This is the familiar form for the spin averaged total cross section for dipole scattering.[3]

For nuclear scattering, the ratio of the radiative decay rate to the total decay rate is a measure of how dominant the internal conversion rate is

$$\frac{\Gamma_{rad}}{\Gamma} = \frac{1}{1+\alpha_{ic}}, \tag{5-1.53}$$

where α_{ic} is the internal conversion coefficient. In nuclear scattering, since the photon energy is so high, the probability that the nuclear excited state will emit an electron, rather than a photon, to decay back to the ground state (that is, will result in internal conversion) can be quite high. For instance, for ^{57}Fe, a common Mössbauer isotope, $\alpha_{ic} = 8.23$, thereby limiting to 11% the chance that an isolated atom will scatter a photon instead of emitting an electron.[4] However, when there is a collection of atoms, this limitation can be overcome and there can be more than an 11% chance of photon emission through a collective phased excitation effect. This is discussed in the dynamical scattering theory of Chapters 6 and 7.

For nuclei having simple two-level systems, the total decay rate and the internal conversion coefficient can be easily measured, and the total cross section, Eq. 5-1.51, can be readily computed. However, electronic systems usually have many level systems with many radiative decay schemes and cascades of Auger emissions from many different angular momentum states. Performing a spin average over all the possible transitions is a formidable task for multielectron systems (recall Eq. 5-1.48 was only for a two level system with initial and intermediate states specified by j_i and j_n). Therefore, the total cross section is usually decomposed into a sum of all the possible types of scattering processes, and the dominant processes are selected

$$\sigma_{tot} = \sigma_{photoelectric}^{elas+inelas} + \sigma_{Compton}^{elas+inelas} + \sigma_{Thomson} + \sigma_{pair\ production} + \cdots. \tag{5-1.54}$$

The photoelectric cross section describes a scattering event in which an incoming photon causes an electron to be ejected into the continuum, and the atom subsequently decays to a final state through radiative or Auger emissions. If the final state is identical to the initial state, the scattering is "elastic" even though the incoming and outgoing particles are different particles--energy conservation still holds. The Compton cross section describes elastic or inelastic absorption reemission for a multilevel system (these are bound state transitions)--the elastic, or Rayleigh, part is expressed in Eq. 5-1.51 for a two level system. Pair production, where an incoming photon scatters into an outgoing photon but changes the electron into its antiparticle in the process, becomes important at energies greater than one MeV. In the dipole approximation, the Thomson cross section is zero since the scattering amplitude is real. Cases for nonzero Thomson cross sections are discussed later in this chapter.

As will be shown in the next chapter, the elastic cross sections are greatly enhanced over the inelastic cross sections in scattering channel directions, such as in the forward direction. When operating far from any bound state resonances, mainly photoelectric scattering occurs, and Compton scattering can be neglected. Cromer and Liberman have made self-consistent Hartree Fock calculations of the relativistic photoelectric cross section of individual atoms for scattering into the forward direction.[5] The imaginary part of the scattering amplitude is proportional to the total cross section, and the real part of the scattering amplitude can be obtained by using the Kramer-Kronig relations (which is equivalent to performing a Hilbert transform). Cromer and Liberman have made these calculations along with a computation of the nonrelativistic Thomson scattering amplitude and tabulated them in the form of parameters f_0, f', and f''.[5] Their parameters are related to the scattering amplitude as follows:

$$F_T(\mathbf{k}_f,\mathbf{k}_i)+F_{photoel}(\mathbf{k}_f,\mathbf{k}_i)=-r_e(\hat{\boldsymbol{\varepsilon}}_f^*\cdot\hat{\boldsymbol{\varepsilon}}_i)(e^{-2W}f_0+f'-if'') \qquad (5\text{-}1.55)$$

where e^{-2W} is a Debye Waller factor that takes into account the vibrations of the atoms about their equilibrium positions. The major contribution to f_0 comes from Thomson scattering described by Eq. 5-1.1 with small relativistic corrections from the photoelectric cross section. The Debye Waller factor is essentially the form factor, Eq. 4-2.14, modified to take into account vibrating scatterers

$$e^{-2W}=\langle i_s|e^{-i(\mathbf{k}_f-\mathbf{k}_i)\cdot\mathbf{u}}|i_s\rangle, \qquad (5\text{-}1.56)$$

where $\mathbf{u}$ is a displacement vector describing the vibrations of the atoms about their equilibrium positions. The factor W turns out to be proportional to the mean square displacement of the atom from equilibrium in the direction of the momentum transfer [6]

$$\mathbf{H} = (\mathbf{k}_f - \mathbf{k}_i) \tag{5-1.57}$$

$$W = 8\pi^2 \langle u_H^2 \rangle (\sin\theta_B/\lambda). \tag{5-1.58}$$

The form factor is essentially the Fourier transform of the charge density

$$f_0(\mathbf{H}) = \int d^3x \rho_s(\mathbf{x}) e^{-i\mathbf{H}\cdot\mathbf{x}}, \tag{5-1.59}$$

where $\mathbf{H}$ is given by Eq. 5-1.57, and $\rho_s(\mathbf{x}) = \phi_s^*(\mathbf{x})\phi_s(\mathbf{x})$. Since the charge density is a real function of the spatial coordinates, the form factor is in general Hermitian

$$f_0(\mathbf{H}) = f_0^*(-\mathbf{H}). \tag{5-1.60}$$

If the charge density has space inversion symmetry (the assumed case for all Cromer and Liberman calculations), the form factor is real and symmetric

$$\rho_s(\mathbf{x}) = \rho_s(-\mathbf{x}) \Rightarrow f_0(\mathbf{H}) = f_0^*(\mathbf{H}) = f_0(-\mathbf{H}). \tag{5-1.61}$$

However, when atoms are brought together into a solid, the electronic charge distributions of an atom may be distorted by the electronic and magnetic potentials of nearby atoms, thereby, possibly breaking space inversion symmetry.[7]

5.2 Hyperfine Interactions for Magnetostatic and Electrostatic Fields

If the incoming electric field is a small perturbation, too small to significantly shift energy levels or cause level splitting of those states that existed before the perturbation, the eigenenergies during the perturbation can be approximated as being the eigenenergies before the perturbation. The major effect of the perturbation will then be to cause transitions between the various energy levels as described by the transition probability, or S-matrix elements. In this approximation, the resonant frequencies, $\omega_{ni} = (E_n - E_i)/\hbar$, in the multipole scattering amplitude are simply the eigenvalues of the constant perturbation, H_0, in Eq. 2-1.1. For magnetostatic and electrostatic interactions, the constant perturbation can be written in the form

$$H_0 = H_0' + H_{mag} + H_{el} \tag{5-2.1}$$

where

$$H_0' = p^2/2m + H_{int}, \tag{5-2.2}$$

and H_{int} includes other possible interactions not discussed so far.

Under the assumption that a nucleus is a pointlike magnetic dipole, H_{mag} can be constructed by examining how the nuclear dipole interacts with the magnetic dipole field of the electron

$$H_{mag} = -\boldsymbol{\mu} \cdot \mathbf{B}_{dipole} - \boldsymbol{\mu} \cdot \mathbf{B}_F . \tag{5-2.3}$$

The first term represents the dipole interaction between an electron's orbital and spin momentum with the magnetic moment of the nucleus[8]

$$\mathbf{B}_{dipole} = -2\beta \left[\frac{\mathbf{L} - \mathbf{S}}{r^3} + \frac{3\mathbf{r}(\mathbf{S} \cdot \mathbf{r})}{r^5} \right] \tag{5-2.4}$$

where $\mathbf{L}$ and $\mathbf{S}$ are the orbital and spin angular momenta of an electron, and β is the electron Bohr magneton

$$\beta = e\hbar / 2m_e c . \tag{5-2.5}$$

Only the orbital electrons that do not lie in an s-state, $l \neq 0$, contribute to the dipolar magnetic field.

The second term in Eq. 5-2.3 represents the Fermi contact interaction between an s orbital electron and the nucleus[8]

$$\mathbf{B}_F = -\frac{16\pi}{3} \beta \delta(\mathbf{r}) \mathbf{S} . \tag{5-2.6}$$

The computation of the total magnetic field at the nucleus can be quite involved for multielectron atoms embedded in a medium because one must take into account the exchange interactions among all the internal electrons and between the internal and external conduction electrons.[9, 10] For example, examination of Eq. 5-2.6 will show that the net Fermi contact field is zero for a filled s shell because the two electrons in that shell have opposite spin. The exchange interaction between electrons from outer unfilled shells and the filled s shells polarizes the s shell electrons to produce a nonzero net Fermi contact field at the nucleus.[10] The polarization of s electrons is a small effect, but since the Fermi contact field for an unpaired $1s$ electron can be hundreds of megagauss, the polarization effect can easily produce sizable fields on the order of hundreds of kilogauss. The field strength of the dipole fields is an order to two orders of magnitude smaller that the net Fermi contact field, and there is also a contribution from the polarization of the conduction s electrons that can also produce Fermi contact fields on the order of a hundred kilogauss.[9]

For the purpose of constructing the magnetostatic interaction Hamiltonian, the detailed structure of the dipole and Fermi contact fields will be not be investigated, and the magnetostatic interaction Hamiltonian will simply be expressed as

$$H_{mag} = -\boldsymbol{\mu} \cdot \mathbf{B}_{int} \tag{5-2.7}$$

where $\mathbf{B}_{int}$ is the total magnetic field at the nucleus.

The electrostatic interaction Hamiltonian is

$$H_{el} = -\sum_{pc} \frac{e^2}{|r_p - r_c|} \tag{5-2.8}$$

where r_p is the position of a proton within the nucleus, and r_c is the position of an electron outside the nucleus (including those from surrounding atoms). Expanding $1/|r_p - r_c|$ in terms of spherical harmonics enables H_{el} to be rewritten as[11, 12]

$$H_{el} = \sum_{l=0}^{\infty} \mathbf{T}^{(l)} \cdot \mathbf{V}^{(l)} \tag{5-2.9}$$

where $\mathbf{T}^{(l)}$ and $\mathbf{V}^{(l)}$ are nuclear and electronic multipole electrostatic operators

$$\mathbf{T}_q^{(l)} = \sqrt{\frac{4\pi}{2l+1}} \sum_p e r_p^l Y_{lq}(\theta_p, \phi_p) \tag{5-2.10}$$

$$\mathbf{V}_q^{(l)} = -\sqrt{\frac{4\pi}{2l+1}} \sum_c e \frac{1}{r_c^{l+1}} Y_{lq}(\theta_c, \phi_c) \tag{5-2.11}$$

Since the nuclear states have a well defined parity, the odd nuclear multipole operators (those with odd l) give vanishing matrix elements. The even nuclear operators yield nonvanishing matrix elements, and the major contribution come from the lowest order multipoles--the Coulomb and electric quadrupoles ($l = 0$ and 2).

The Coulomb interaction is

$$H_{coul} = -Ze_p \sum_c \frac{e_c}{r_c} \tag{5-2.12}$$

where Z is the number of protons within the nucleus. To this a correction term must be added that is due to the finite size of the nucleus--the isomer shift[8]

$$H_{isomer} = \frac{2}{3} \pi e^2 Z |\phi(0)|^2 \langle R^2 \rangle \tag{5-2.13}$$

where $\langle R^2 \rangle$ is the mean square charge radius of the nucleus and $e^2|\phi(0)|^2$ is the electronic charge density at the nucleus.

The introduction of the electric quadrupole interaction produces additional complexities. The electric quadrupole Hamiltonian has matrix elements that are proportional the electric field gradient at the nucleus. However, the electric field gradient tensor has a principal axis that may not be aligned with the quantum axis of the nucleus. Then, there are two possible quantum axes. This arrangement gives rise to nuclear level

mixing (a competition between quantum axes towards defining the state of the system) in which there no longer exists any well defined, or "good", quantum numbers describing the nuclear or electronic states. Matthias, Schneider, and Steffen have extensively worked out this problem.[13]

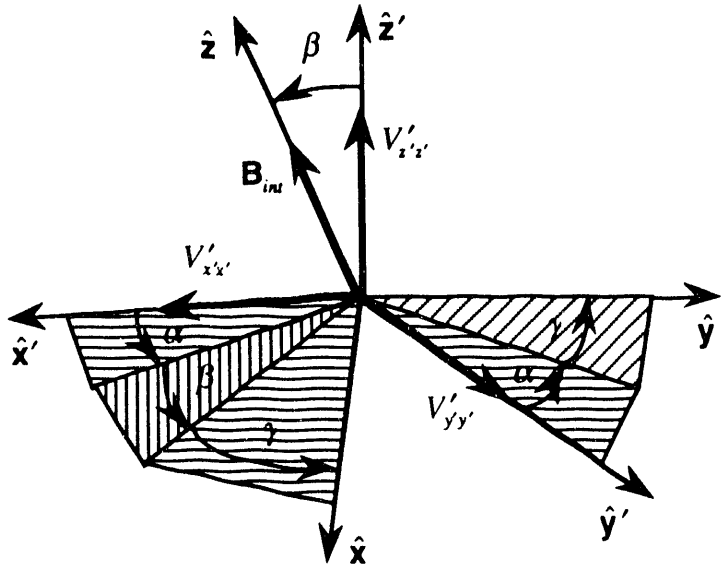

Fig. 5-2.1. Orientation of electric field gradient axes (primed system) to the quantization axes (unprimed system).[13]

Fig. 5-2.1 shows the orientation of the electric field gradient system, system S' with principal axes $(\hat{\mathbf{x}}',\hat{\mathbf{y}}',\hat{\mathbf{z}}')$, with respect to the nuclear quantum axis system, system S, in which the magnetic field direction specifies the quantum $\hat{\mathbf{z}}$ axis. The Euler angles, (α,β,γ), specify how to rotate system S' so that it coincides with system S. For an electric field gradient that has axial symmetry with respect to the $\hat{\mathbf{z}}'$ axis, the angle α can be set to zero. For nonaxial symmetry, an asymmetry parameter η is introduced

$$\eta = \frac{V'_{x'x'} - V'_{y'y'}}{V'_{z'z'}} \tag{5-2.14}$$

where
$$V'_{uv} = \frac{\partial^2 V'}{\partial u \partial v} \qquad u,v = x,y,z. \tag{5-2.15}$$

Using the rotation matrix, $D^{(2)}_{mm'}(\alpha,\beta,\gamma)$, to rotate the electric field gradient principal axis system upon the quantum axis system gives the matrix elements of the quadrupole electrostatic Hamiltonian. (The nuclear dipole magnetostatic matrix elements are also included below. Also, nuclear total angular momentum quantum numbers are conventionally represented as I.)

$$H_{mm} = -\hbar\omega_B m + \hbar\omega_E \frac{1}{2}\left(3\cos^2\beta - 1 + \eta\sin^2\beta\cos 2\alpha\right)\left[3m^2 - I(I+1)\right] \quad (5\text{-}2.16)$$

$$H_{m,m\pm1} = \hbar\omega_E \frac{3}{2}\sin\beta\left\{\cos\beta \mp \frac{\eta}{6}\left[(1\pm\cos\beta)e^{i2\alpha} - (1\mp\cos\beta)e^{-i2\alpha}\right]\right\}$$
$$\times e^{\pm i\gamma}(2m\pm1)\sqrt{(I\mp m)(I\pm m+1)} \quad (5\text{-}2.17)$$

$$H_{m,m\pm2} = \hbar\omega_E \frac{3}{4}\left\{\sin^2\beta + \frac{\eta}{6}\left[(1\pm\cos\beta)^2 e^{i2\alpha} + (1\mp\cos\beta)^2 e^{-i2\alpha}\right]\right\}$$
$$\times e^{\pm i2\gamma}\sqrt{(I\pm m+2)(I\pm m+1)(I\mp m)(I\mp m-1)} \quad (5\text{-}2.18)$$

where $\hbar\omega_B = \mu B_{int}/I$ (5-2.19)

$$\hbar\omega_E = \frac{e^2qQ}{4I(2I-1)}. \quad (5\text{-}2.20)$$

The magnetic moment of the nucleus has been defined as

$$\mu = \langle I, m_I = I|\mu_0^{(1)}|I, m_I = I\rangle = \begin{pmatrix} I & 1 & I \\ -I & 0 & I \end{pmatrix}\langle I\|\boldsymbol{\mu}^{(1)}\|I\rangle = \frac{I}{\sqrt{(2I+1)(I+1)I}}\langle I\|\boldsymbol{\mu}^{(1)}\|I\rangle, \quad (5\text{-}2.21)$$

the nuclear electric quadrupole moment has been defined as

$$eQ/2 = \langle I, m_I = I|T_0^{(2)}|I, m_I = I\rangle = \begin{pmatrix} I & 2 & I \\ -I & 0 & I \end{pmatrix}\langle I\|\mathbf{T}^{(2)}\|I\rangle$$

$$= \frac{I(2I-1)}{\sqrt{(2I+3)(I+1)(2I+1)2I(2I-1)}}\langle I\|\mathbf{T}^{(2)}\|I\rangle, \quad (5\text{-}2.22)$$

and the electronic electric quadrupole has been defined as (averaging over space)

$$eq/2 = \langle V_0'^{(2)}\rangle \quad (5\text{-}2.23)$$

where $V_0'^{(2)} = V'_{z'z'}/2$ (5-2.24)

$$V_{\pm1}'^{(2)} = \mp\frac{1}{2}\sqrt{\frac{2}{3}}\left(V'_{z'x'} \pm iV'_{y'z'}\right) = 0 \quad (5\text{-}2.25)$$

$$V_{\pm2}'^{(2)} = \frac{1}{4}\sqrt{\frac{2}{3}}\left(V'_{x'x'} - V'_{y'y'} \pm 2iV'_{x'y'}\right) = \frac{1}{4}\sqrt{\frac{2}{3}}\eta V'_{z'z'}, \quad (5\text{-}2.26)$$

and a coordinate system has been chosen so that $V'_{uv} = 0$ when $u \neq v$. The angular factors come from the rotation relation

$$V_q^{(2)} = \sum_{l=-2}^{2} V_l'^{(2)} D_{lq}^{(2)}(\alpha,\beta,\gamma). \tag{5-2.27}$$

When the electric quadrupole interaction is small compared to the magnetic dipole interaction, a first order approximation can be made by dropping all of the off diagonal matrix elements of the total Hamiltonian. In such a first order approximation, the eigenvalues are given by H_{mm}, and the eigenfunctions can be written in column form as

$$\phi_{mn}^{(0)T} = (0,0,0,\cdots,1,\cdots,0) \tag{5-2.28}$$

where the unity factor is in the n^{th} place for $1 \le n \le 2I+1$, and $2I+1$ is the number of eigenvalues. Each quantum number m is then a "good" quantum number in that they all define a unique state of the system--the n^{th} state is specified by only one number: m.

When no approximations are made to the total Hamiltonian, the eigenfunctions become a linear combination of the first order states of the system

$$\phi_{mn} = \sum_{q=-m'}^{m'} c_{nq} \phi_{qn}^{(0)} \tag{5-2.29}$$

where c_{nq} is a complex number and m' ranges from the minimum to the maximum possible value of m. Each quantum number m is now a "poor" quantum number since they no longer well define the states of the system--the n^{th} state is now specified by a sum over all possible m quantum numbers.

The polarization matrix of Eq. 5-1.5 must now be modified to include these changes

$$\left(P_{Ln}^{(\lambda)}\right)_{xy} = \left[\hat{\boldsymbol{\varepsilon}}_x^{f*} \cdot \sum_{q=-m'}^{m'} \mathbf{Y}_{LM}^{(\lambda)}\left(\Omega_{\mathbf{k}_f}\right)\left(\phi_{mn} \cdot \phi_{qn}^{(0)}\right)\right]\left[\sum_{q'=-m'}^{m'}\left(\phi_{mn}^{*} \cdot \phi_{q'n}^{(0)}\right)\mathbf{Y}_{LM'}^{(\lambda)*}\left(\Omega_{\mathbf{k}_i}\right) \cdot \hat{\boldsymbol{\varepsilon}}_y^{i}\right] \tag{5-2.30}$$

where $\phi_{mn} \cdot \phi_{qn}^{(0)} = c_{nq}$ of Eq. 5-2.29, $M = q - m_f$, and $M' = q' - m_f$ (the scattering amplitude in Eq. 5-1.4 must now be summed over L and n rather than L and M as before). Examples of magnetic dipole scattering for ^{57}Fe are given in the following sections.

5.3 Linear Polarization Reversal of Fields Scattered from a Ferromagnetic Lattice

The hyperfine energy level diagram for ^{57}Fe is shown in Fig. 5-3.1 (all energy shifts are greatly exaggerated). The isomer shifts for the excited and ground states are designated by ΔE_{Is}^{e} and ΔE_{Is}^{g}. The excited and ground state magnetic splittings are $\hbar\omega_B^e = 2\mu_e B_{int}/3$ and $\hbar\omega_B^g = 2\mu_g B_{int}$. The ground and excited state quadrupole shifts are $\Delta E_Q^g = 0$ and

$$\Delta E_Q^e = \frac{1}{4} e^2 qQ \left(\frac{3\cos^2\beta - 1}{2} \right). \tag{5-3.1}$$

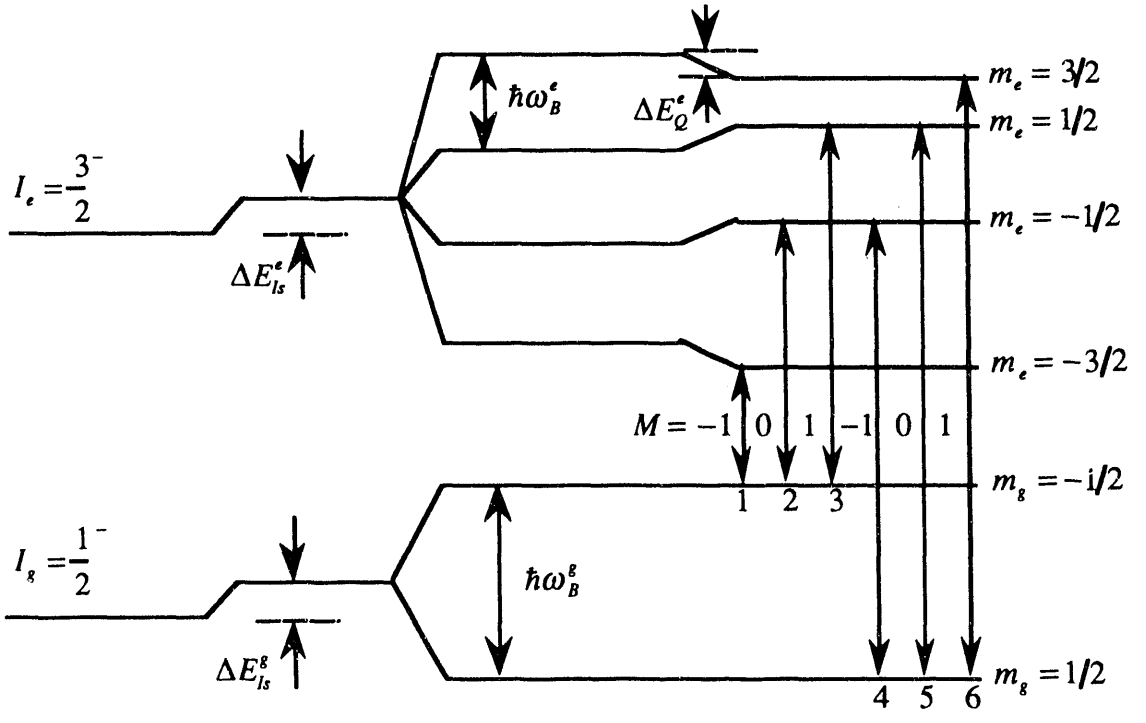

Fig. 5-3.1. Hyperfine energy levels of ^{57}Fe of d-sites in a YIG crystal. Quadrupole shift for ground states is zero, and $\mu_e < 0$ and $B_{int} < 0$.

where the electric field gradient tensor is assumed to be axially symmetric so that $\eta = 0$.

The electric quadrupole shift is small compared to the magnetic dipole shift for ^{57}Fe, so in most cases first order perturbation theory is adequate. The excited states are then labeled by good quantum numbers, and the unitary eigenvector matrix (whose columns are the eigenfunctions) that diagonalizes the Hamiltonian is diagonal

$$\Phi^{(0)} = \left(\phi^{(0)}_{\frac{3}{2},1}, \phi^{(0)}_{\frac{1}{2},2}, \phi^{(0)}_{-\frac{1}{2},3}, \phi^{(0)}_{-\frac{3}{2},4}\right) = \begin{pmatrix} 1 & & & \\ & 1 & & 0 \\ & & 1 & \\ 0 & & & 1 \end{pmatrix}. \tag{5-3.2}$$

When the full theory is employed, the unitary eigenvector matrix that diagonalizes the Hamiltonian is no longer diagonal

$$\Phi = \left(\phi_{\frac{3}{2},1}, \phi_{\frac{1}{2},2}, \phi_{-\frac{1}{2},3}, \phi_{-\frac{3}{2},4}\right) = \begin{pmatrix} c_{1,\frac{3}{2}} & c_{2,\frac{3}{2}} & c_{3,\frac{3}{2}} & c_{4,\frac{3}{2}} \\ c_{1,\frac{1}{2}} & c_{2,\frac{1}{2}} & c_{3,\frac{1}{2}} & c_{4,\frac{1}{2}} \\ c_{1,-\frac{1}{2}} & c_{2,-\frac{1}{2}} & c_{3,-\frac{1}{2}} & c_{4,-\frac{1}{2}} \\ c_{1,-\frac{3}{2}} & c_{2,-\frac{3}{2}} & c_{3,-\frac{3}{2}} & c_{4,-\frac{3}{2}} \end{pmatrix}. \tag{5-3.3}$$

Since the ground states have no electric quadrupole interaction, their eigenvector matrix is always diagonal. The Φ-matrix elements for the excited states are found by diagonalizing the full Hamiltonian matrix to get the eigenvectors. The magnitude of the diagonal elements are close to unity, and the off diagonal terms are small (magnitudes on the order of 0.1 or less). The energy level diagram is negligibly changed (the energy levels change by about 1% of a natural linewidth). The change in the nuclear states, though, is large enough to produce noticeable effects.

One interesting effect is the case of complete polarization reversal of the linear polarization basis of an incoming electric field. In Section 5.1, where nuclear level mixing was neglected, incoming right circularly polarized fields could be scattered into left circularly polarized fields and visa-versa for a convenient orientation of the quantization axis. Nuclear level mixing now enables vertically polarized fields to scatter into horizontally polarized fields and visa-versa.

For example, for the [0 0 2] reflection of a YIG crystal, two ^{57}Fe sublattices within the unit cell, called $d1$ and $d2$ sites, contribute to a nonzero diffracted beam. The iron in these sites have identical hyperfine environments except that the electric field gradients lying in the [0 0 2] plane are oriented 90° with respect to each site. Also, the two sublattices are situated such that the reflected wave from each site is 180° out of phase. Each site produces a six line emission pattern which will be labeled $(\ell_1, \ell_2, \ell_3, \ell_4, \ell_5, \ell_6)$ for the $d1$ sites and $(\ell'_1, \ell'_2, \ell'_3, \ell'_4, \ell'_5, \ell'_6)$ for the $d2$ sites (see Fig. 5-3.1). In first order perturbation theory, if the internal magnetic field was oriented by an external magnetic field so that it bisected the angle between the electric field gradients, see Fig. 5-3.2, the

quadrupole shifts of the iron atoms in the two sites would be identical for each pair of lines (ℓ_i, ℓ_i') since $\beta = \pm 45°$ and $(3\cos^2\beta - 1)/2 = 1/4$. Then, to first order, no net reflected intensity is possible because the reflected field amplitudes from each site would cancel as a result of the 180° phase difference and because each pair of lines lie at the same energy.

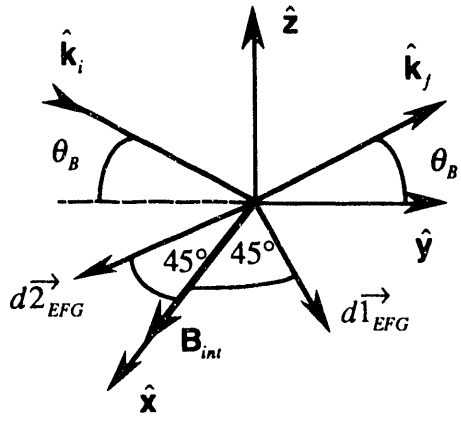

Fig. 5-3.2. Orientation of YIG electric field gradient directions for $d1$ and $d2$ sites lying in the xy plane. Internal magnetic field direction bisects angle between them.

However, when nuclear level mixing is accounted for, there is no complete cancellation. For instance, the polarization matrix of line ℓ_1 is (using Eq. 5-2.30 for the case where $n = 1$, keeping only terms that satisfy the dipole selection rules $M = 0, \pm 1$, and knowing that ^{57}Fe radiates only magnetic dipole fields)

$$\left(P_{11}^{(m)}\right)_{xy} = \left[\hat{\boldsymbol{\varepsilon}}_x^{f*} \cdot \left(\mathbf{Y}_{1,1}^{(m)} c_{1,\frac{1}{2}} + \mathbf{Y}_{1,0}^{(m)} c_{1,\frac{1}{2}} + \mathbf{Y}_{1,-1}^{(m)} c_{1,-\frac{1}{2}}\right)\right]\left[\left(\mathbf{Y}_{1,1}^{(m)*} c_{1,\frac{1}{2}}^{*} + \mathbf{Y}_{1,0}^{(m)*} c_{1,\frac{1}{2}}^{*} + \mathbf{Y}_{1,-1}^{(m)*} c_{1,-\frac{1}{2}}^{*}\right) \cdot \hat{\boldsymbol{\varepsilon}}_y^{i}\right]. \tag{5-3.4}$$

The scattering geometry is exactly that of Case 1 in Section 5.1. Then, using Eqs. 5-1.19 to 5-1.21 and the results of Case 1 gives the polarization matrix elements:

$$\left(P_{11}^{(m)}\right)_{xx} = \frac{3}{16\pi}\left(-e^{i2\theta_B} c_{1,\frac{1}{2}} - e^{-i2\theta_B} c_{1,-\frac{1}{2}}\right)\left(-e^{i2\theta_B} c_{1,\frac{1}{2}}^{*} - e^{-i2\theta_B} c_{1,-\frac{1}{2}}^{*}\right) \tag{5-3.5}$$

$$\left(P_{11}^{(m)}\right)_{xy} = \frac{3}{16\pi}\left(i\sqrt{2}\, c_{1,\frac{1}{2}}\right)\left(-e^{i2\theta_B} c_{1,\frac{1}{2}}^{*} - e^{-i2\theta_B} c_{1,-\frac{1}{2}}^{*}\right) \tag{5-3.6}$$

$$\left(P_{11}^{(m)}\right)_{yx} = \frac{3}{16\pi}\left(-e^{i2\theta_B} c_{1,\frac{1}{2}} - e^{-i2\theta_B} c_{1,-\frac{1}{2}}\right)\left(-i\sqrt{2}\, c_{1,\frac{1}{2}}^{*}\right) \tag{5-3.7}$$

$$\left(P_{11}^{(m)}\right)_{yy} = \frac{3}{8\pi}\left|c_{1,\frac{1}{2}}\right|^2. \tag{5-3.8}$$

Note that the Euler azimuthal angle for ℓ_1 is $\gamma_1 = -\pi/2$ and for ℓ_1' is $\gamma_1' = \pi/2$. Applying a unitary transformation upon the Hamiltonian, Eqs. 5-2.16 to 5-2.18, gives in matrix form [12]

$$H(\alpha,\beta,0) = A(\gamma)H(\alpha,\beta,\gamma)A^{-1}(\gamma) \tag{5-3.9}$$

where $$A_{kl}(\gamma) = \delta_{kl}e^{il\gamma} \qquad (k,l = I, I-1,\ldots,-I). \tag{5-3.10}$$

The eigenvectors can then be written in the form

$$\Phi(\alpha,\beta,\gamma) = \Phi(\alpha,\beta,0)A(\gamma). \tag{5-3.11}$$

Since $\alpha = 0$, $\Phi(\alpha = 0,\beta,0)$ is a real matrix. So, when $\gamma \to -\gamma$, the eigenvectors transform into their complex conjugates. Therefore, the eigenfunction associated with ℓ_1 is the complex conjugate of the one associated with ℓ_1'

$$c_{nq}' = c_{nq}^{*}. \tag{5-3.12}$$

Attaching a minus sign to the amplitude of line ℓ_1' to take care of the phase difference of the reflected fields from each sublattice, and summing the polarization matrices for lines ℓ_1 and ℓ_1' gives

$$P_{11}^{(m)}\Big|_{\ell_1} + P_{11}^{(m)}\Big|_{\ell_1'} = \begin{pmatrix} 0 & C \\ C & 0 \end{pmatrix} \tag{5-3.13}$$

where $$C = 2\sqrt{2}\,\frac{3}{16\pi}\left(e^{i2\theta_B}\,\mathrm{Im}\left\{c_{1,\frac{1}{2}}c_{1,\frac{1}{2}}^{*}\right\} + e^{-i2\theta_B}\,\mathrm{Im}\left\{c_{1,\frac{1}{2}}c_{1,-\frac{1}{2}}^{*}\right\}\right). \tag{5-3.14}$$

Because the polarization matrix has only off diagonal matrix elements, complete linear polarization reversal occurs. For example,

$$\begin{pmatrix} 0 & C \\ C & 0 \end{pmatrix}\cdot\hat{\boldsymbol{\sigma}}_i = \begin{pmatrix} 0 & C \\ C & 0 \end{pmatrix}\cdot\begin{pmatrix} 1 \\ 0 \end{pmatrix} = C\begin{pmatrix} 0 \\ 1 \end{pmatrix} = C\hat{\boldsymbol{\pi}}_f.$$

This shows that incoming horizontally polarized fields scatter into vertically polarized fields with an amplitude proportional to C. However, since the off diagonal elements of the eigenvector matrix are small, $|C|$ is small, and thus the scattered intensity is very low. The nuclear resonance scattering group at Hamburg[14, 15] has observed the effect of nonzero cancellation, but to date no polarization analysis has been done to observe the effect of polarization reversal.

5.4 Linear Polarization Reversal of Fields Scattered from an Antiferromagnetic Lattice

The added complexity of nuclear level mixing is not needed to produce linear polarization reversal for scattering from an antiferromagnetic lattice. However, similar to the case for a ferromagnetic lattice, one still relies upon the phase difference between the reflected fields from different iron sites within the lattice.

For this example, take the case of $^{57}FeBO_3$. It has a rhombohedral unit cell structure containing two iron atoms located at two different b-sites. For certain reflections, such as $[n\ n\ n]$ reflections where n is an odd integer, the reflected fields from the two sites are 180° out of phase. However, because of the antiferromagnetic structure of the crystal lattice (further explained in Chapter 8), the electric fields scattered from the nuclei do not cancel out.

Let the internal magnetic field at each nuclei at the two b-sites be parallel to both the scattering plane and the $[n\ n\ n]$ planes (this corresponds to Case 3 in Section 5.1). The polarization matrices for the iron site in which the internal magnetic field lies in the $\hat{\mathbf{y}}$ direction (see Fig. 5-1.1) is given by Eq. 5-1.28, and the polarization matrices for the other site in which the internal magnetic field lies in the $-\hat{\mathbf{y}}$ direction is given by the complex conjugate of Eq. 5-1.28:

$$P_{10}^{(m)} = \frac{3}{8\pi}\begin{pmatrix} -\sin^2\theta_B & 0 \\ 0 & 0 \end{pmatrix}, \qquad P_{1,\pm1}^{(m)} = -\frac{3}{16\pi}\begin{pmatrix} -\cos^2\theta_B & \mp i\cos\theta_B \\ \pm i\cos\theta_B & -1 \end{pmatrix}. \tag{5-4.1}$$

For incident horizontally polarized fields, the polarization of lines ℓ_i for the case $\hat{\mathbf{B}}_{int} = +\hat{\mathbf{y}}$ is:

$$\ell_2 \text{ and } \ell_5 \Rightarrow \frac{3}{8\pi}\begin{pmatrix} -\sin^2\theta_B & 0 \\ 0 & 0 \end{pmatrix}\begin{pmatrix} 1 \\ 0 \end{pmatrix} = -\frac{3}{8\pi}\sin^2\theta_B\begin{pmatrix} 1 \\ 0 \end{pmatrix},$$

$$\ell_1 \text{ and } \ell_4 \Rightarrow -\frac{3}{16\pi}\begin{pmatrix} -\cos^2\theta_B & +i\cos\theta_B \\ -i\cos\theta_B & -1 \end{pmatrix}\begin{pmatrix} 1 \\ 0 \end{pmatrix} = \frac{3}{16\pi}\begin{pmatrix} \cos^2\theta_B \\ i\cos\theta_B \end{pmatrix},$$

and

$$\ell_3 \text{ and } \ell_6 \Rightarrow \frac{3}{16\pi}\begin{pmatrix} \cos^2\theta_B \\ -i\cos\theta_B \end{pmatrix}.$$

The polarization of lines ℓ_i' for the case $\hat{\mathbf{B}}_{inc} = -\hat{\mathbf{y}}$ is the complex conjugate of the expressions above. Pictorially, the polarizations the lines for the two b-sites are shown in Fig. 5-4.1 where, for the lines ℓ_i', a minus sign was included to take into account that the fields reflected the iron sites giving rise to these lines are 180° out of phase with those fields reflected from the other iron sites giving rise to the lines ℓ_i.

Since pairs of resonance lines lie at the same energy, the superposition of each pair of lines ℓ_i and ℓ_i' gives the net amplitude. As shown in Fig. 5-4.1, the net resultant field is completely vertically polarized. Incident horizontally polarized fields are scattered into outgoing vertically polarized fields, and visa-versa. Unlike the case for a ferromagnet, linear polarization reversal of fields scattered from an antiferromagnet is a strong effect and has been clearly observed in an experiment using $^{57}Fe_2O_3$.[16]

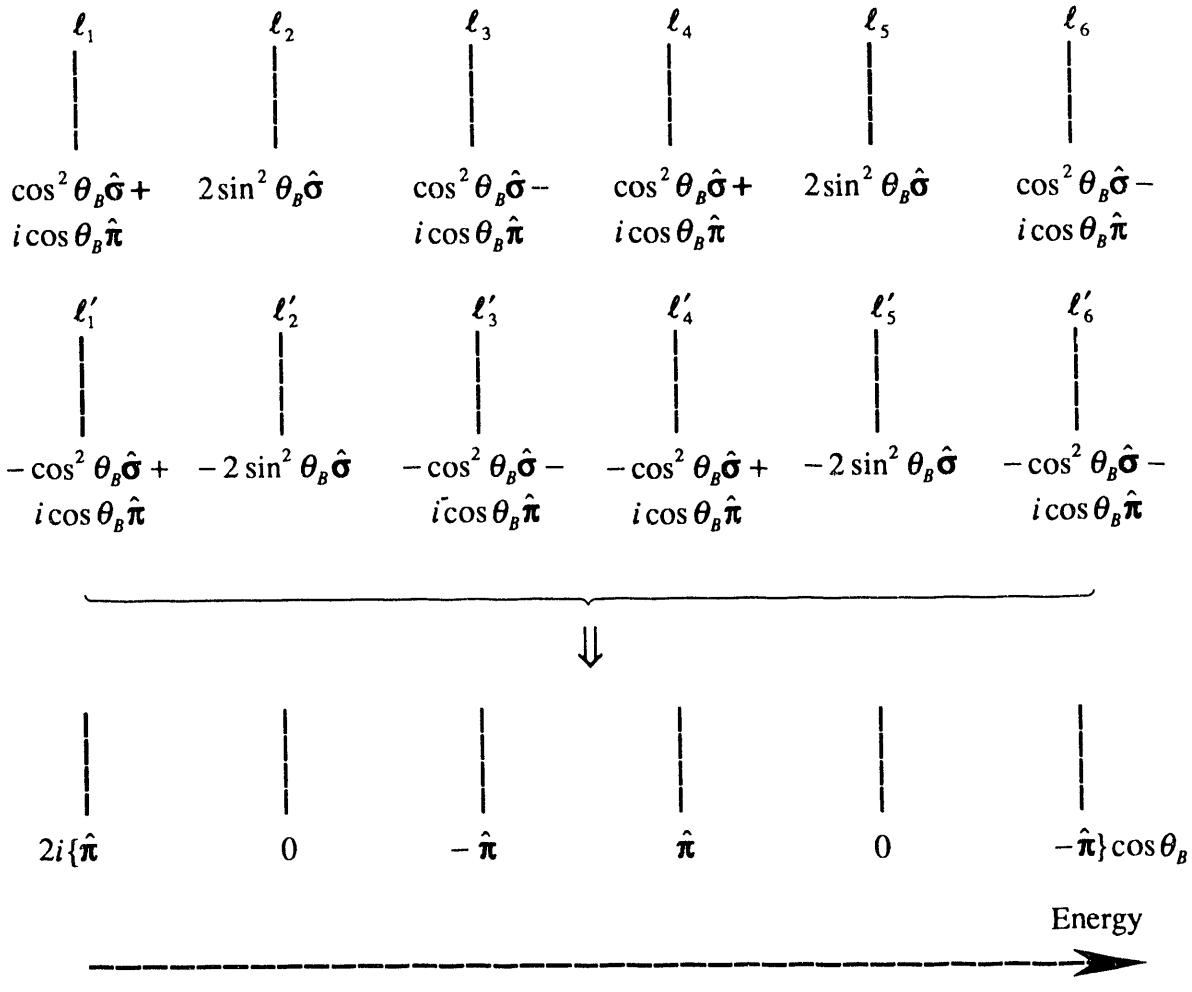

Fig. 5-4.1 Demonstration of linear polarization reversal. An incident $\hat{\sigma}$ polarized field is scattered by iron nuclei in an antiferromagnetic lattice. The sum of the scattered fields is a resultant field that is $\hat{\pi}$ polarized.

5.5 Angular Interferometry

As shown in Section 5.1, the direction of the quantization axis strongly influences the nature of the scattered fields. Major differences in the spectra of scattered fields can also be seen when the internal magnetic field is oriented to lie in an antiparallel direction. This phenomena allows one to do angular interferometry where quantum beat interference patterns depend not upon the spatial distances photons travel such as in a Michelson-Morley interferometer, but upon the angles through which photons are rotated. The example below describes this type of interferometry using the scattering theory developed in this chapter. An alternate description of this phenomena utilizing the rotational symmetry properties of free space is given in Appendix A.[17]

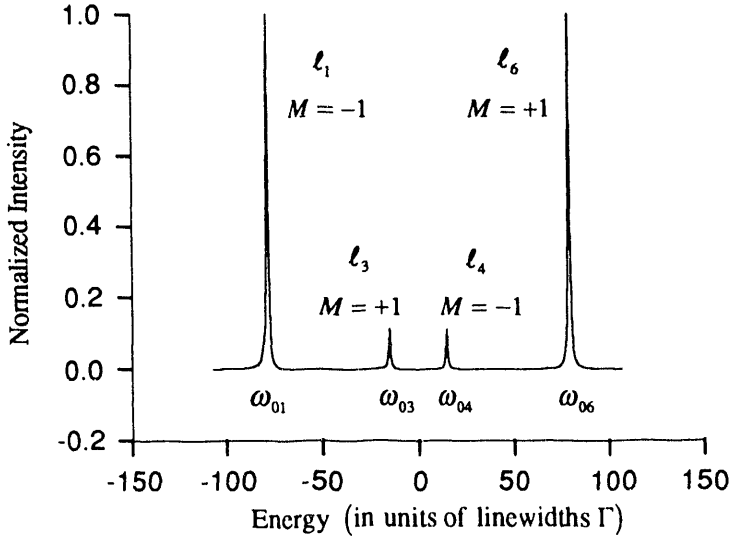

Fig. 5-5.1. Four line magnetic dipole energy spectrum when incoming field is horizontally polarized.

As an example, consider just one site in YIG, such as the d 1-site discussed in the last section. When the internal magnetic field is oriented perpendicular to the scattering plane (see Fig. 5-1.1 where $\hat{\mathbf{B}}_{int}$ is now the quantization axis $\hat{\mathbf{Q}}_z$),

$$\hat{\mathbf{B}}_{int} = \hat{\mathbf{x}}, \tag{5-5.1}$$

and, for incoming horizontally polarized fields, the intensity of the scattered fields exhibits the 4-line spectrum shown in Fig. 5-5.1. The orientation corresponds to Case 1 in Section 5.1, and thus lines ℓ_2 and ℓ_5 are forbidden by polarization selection rules.

In the kinematical limit, the total electric field amplitude scattered from the crystal is simply the sum of the amplitudes from each particle within the crystal. Since the scattered field from each particle is proportional to the scattering amplitude, the field amplitude of the four allowed lines for a single particle are as follows (from Eqs. 5-1.4, 5-1.22, and 5-1.23):

$$\ell_1(\omega) = a_1 e^{-i2\theta_B} / (\omega - \omega_{01} + i\Gamma/2\hbar) \tag{5-5.2}$$

$$\ell_3(\omega) = a_3 e^{i2\theta_B} / (\omega - \omega_{03} + i\Gamma/2\hbar) \tag{5-5.3}$$

$$\ell_4(\omega) = a_3 e^{-i2\theta_B} / (\omega - \omega_{04} + i\Gamma/2\hbar) \tag{5-5.4}$$

$$\ell_6(\omega) = a_1 e^{i2\theta_B} / (\omega - \omega_{06} + i\Gamma/2\hbar) \tag{5-5.5}$$

where $a_1 = c_0 \cdot 1$, $a_3 = c_0 \cdot 1/3$, and c_0 is a quantity proportional to the incoming field amplitude. The factors multiplying c_0 are the squares of the Clebsch-Gordan coefficients for those lines (see Eqs. 5-1.39 and 5-1.40).

When the internal magnetic field is oriented into an antiparallel direction,

$$\hat{\mathbf{B}}_{\text{int}} = -\hat{\mathbf{x}}, \tag{5-5.6}$$

the phase of the amplitudes will change, but their magnitudes stay the same. For such an orientation, from Fig. 5-5.2, the conditions in Case 1 in Section 5.1 change to

$$\theta_i = \theta_f = \pi/2, \qquad \phi_f - \phi_i = -2\theta_B,$$

$$\hat{\boldsymbol{\sigma}}_{(i,f)} = \hat{\boldsymbol{\theta}}_{(i,f)}, \qquad \hat{\boldsymbol{\pi}}_{(i,f)} = -\hat{\boldsymbol{\phi}}_{(i,f)}, \qquad \beta_{(i,f)} = \pi/2.$$

Because the azimuthal phase difference is now minus the scattering angle, the polarization matrices in Eqs. 5-1.22 and 5-1.23 change to their complex conjugates. As a result, the amplitudes of the lines for this new orientation are

$$\ell_1'(\omega) = a_1 e^{i2\theta_B} / (\omega - \omega_{01} + i\Gamma/2\hbar) \tag{5-5.7}$$

$$\ell_3'(\omega) = a_3 e^{-i2\theta_B} / (\omega - \omega_{03} + i\Gamma/2\hbar) \tag{5-5.8}$$

$$\ell_4'(\omega) = a_3 e^{i2\theta_B} / (\omega - \omega_{04} + i\Gamma/2\hbar) \tag{5-5.9}$$

$$\ell_6'(\omega) = a_1 e^{-i2\theta_B} / (\omega - \omega_{06} + i\Gamma/2\hbar). \tag{5-5.10}$$

Far off resonance where $\omega - \omega_{0i} >> \Gamma/2\hbar$, the amplitudes for the two inverted orientations of the internal magnetic field are the phase conjugates of each other: $\ell_i' = \ell_i^*$. This is so because the amplitudes a_i are real. This calculation has neglected nuclear level mixing, however, if it were included the amplitudes would still be the complex conjugates of each other even though the amplitudes a_i are now complex (this is because the Euler γ angle undergoes the transformation $\gamma \rightarrow -\gamma$ upon an inversion of the quantum axis, and

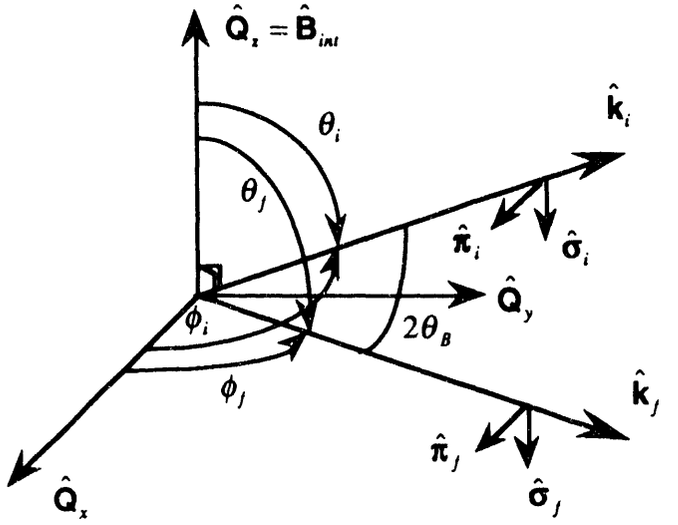

Fig. 5-5.2. Scattering geometry for inverted quantization axis. Wavectors $\mathbf{k}_i$ and $\mathbf{k}_f$ lie in the Q_xQ_y-plane.

by Eqs. 5-3.10 and 5-3.11 the amplitudes a_i change to their complex conjugates). Because of the resonant denominator, resonant systems cannot experience true phase conjugate scattering.

In frequency space this phase effect is not easily observed for spectra having resonance lines separated by many natural linewidths--one would have to carefully examine the interference between widely spaced lines that have little overlap. However, in the time domain the effect stands out more because the phase of the beat patterns due to the interference of two oscillators with different frequencies can be more easily measured.

This can be seen by examining the beating between the two dominant resonance lines ℓ_1 and ℓ_6. The Fourier transform of their frequency amplitudes gives the familiar damped sinusoidal expressions

$$\ell_1(t) = -ia_1 e^{-i\Gamma t/2\hbar} e^{-i(\omega_{01}t + 2\theta_B)} \tag{5-5.11}$$

$$\ell_6(t) = -ia_1 e^{-i\Gamma t/2\hbar} e^{-i(\omega_{06}t - 2\theta_B)}. \tag{5-5.12}$$

For just these two lines, the kinematic intensity from crystal is then proportional to

$$\begin{aligned} I(t) &\sim \left[\ell_1(t) + \ell_6(t)\right]\left[\ell_1^*(t) + \ell_6^*(t)\right] \\ &= 2a_1^2 e^{-\Gamma t/\hbar}\left\{1 + \cos\left[(\omega_{06} - \omega_{01})t - 4\theta_B\right]\right\}. \end{aligned} \tag{5-5.13}$$

When the internal magnetic field is inverted, the phase of the intensity pattern changes sign so that

$$I'(t) \sim 2a_1^2 e^{-\Gamma t/\hbar}\left\{1 + \cos\left[(\omega_{03} - \omega_{01})t + 4\theta_B\right]\right\}. \tag{5-5.14}$$

Thus, adjusting the Bragg angle tunes the phase difference, $\Delta\varphi = 8\theta_B$, between the beat patterns of the two intensity distributions. For Bragg angles near 22.5° this is a very noticeable effect. For instance, if $2\theta_B = \pi/4$ then the intensity distributions are 180° out of phase and, therefore, the the peaks of one intensity pattern will lie in the valleys of the other. This is one of the kinematical effects investigated experimentally in this thesis, and the results are given in Chapter 10.

REFERENCES

[1] J. Mathews, *Tensor Spherical Harmonics* (California Institute of Technology,1981).

[2] A. R. Edmonds, *Angular Momentum in Quantum Mechanics* (Princeton University Press, Princeton, New Jersey, 1960).

[3] H. Frauenfelder, *The Mössbauer Effect* (W. A. Benjamin, New York, 1962).

[4] C. M. Lederer and V. S. Shirley, *Table of Isotopes* (Wiley, New York, 1978).

[5] D. T. Cromer and D. Liberman, *J. Chem. Phys.* **53**, 1891 (1970).

[6] R. W. James, *The Optical Principles of the Diffraction of X-Rays* (Ox Bow Press, Woodbridge, Connecticut, 1982).

[7] B. E. Warren, *X-Ray Diffraction* (Dover, New York, 1990).

[8] M. Weissbluth, *Atoms and Molecules* (Academic Press, New York, 1978).

[9] V. I. Goldanskii and R. H. Herber, *Chemical Applications of Mössbauer Spectroscopy* (Academic Press, New York, 1968).

[10] A. J. Freeman and R. B. Frankel, *Hyperfine Interactions* (Academic Press, New York, 1967).

[11] R. V. Pound, *Phys. Rev.* **79**, 685 (1950).

[12] E. Matthias, W. Schneider, and R. M. Steffen, *Phys. Rev.* **125**, 261 (1962).

[13] E. Matthias, W. Schneider, and R. M. Steffen, *Arkiv Fur Fysik* **24**, 97 (1963).

[14] H. D. Rüter, R. Rüffer, R. Hollatz, W. Sturhahn, and E. Gerdau, *Hyp.Int.* **58**, 2477 (1990).

[15] R. Hollatz, W. Sturhahn, H. D. Rüter, and E. Gerdau, *International Conference on the Applications of the Mössbauer Effect* (Budapest, Hungary, 1989), vol. 2, 14.11

[16] D. P. Siddons, J. B. Hastings, G. Faigel, L. E. Berman, P. E. Haustein, and J. R. Grover, *Phys. Rev. Lett.* **62**, 1384 (1989).

[17] D. E. Brown, J. Arthur, A. Q. R. Baron, G. S. Brown, and S. Shastri, *Phys. Rev. Lett.* **69**, 699 (1992).

6. DYNAMICAL SCATTERING BY RESONANT SYSTEMS

6.1 Kinematical Scattering Theory

In kinematical scattering a photon scattered from one particle does not interact with other particles-multiple scattering is nonexistent. The field amplitude at a point $\mathbf{x}$ is then just the sum of the individually scattered fields emanating from each scatterer within the medium. From the spherical multipole electric field equation, Eq. 4-4.16, this sum (over N identical particles) is

$$I(\mathbf{x}) = I_0 \left| F(\mathbf{k}_f, \mathbf{k}_i) \right|^2 \left| \sum_{n=1}^{N} e^{-i(\mathbf{k}_f - \mathbf{k}_i)\cdot \mathbf{x}_n} \right|^2$$

$$= I_0 \left| F(\mathbf{k}_f, \mathbf{k}_i) \right|^2 \left(N + \sum_{n=1}^{N} \sum_{m=1}^{N} e^{-i(\mathbf{k}_f - \mathbf{k}_i)\cdot(\mathbf{x}_n - \mathbf{x}_m)} \right) \qquad (6.1\text{-}1)$$

where $\mathbf{x}$ is far from any scatterer, I_0 is a constant proportional to the incoming beam intensity, and the incoming field term has been excluded so that only the properties of the scattered fields are examined. The scattering amplitude is given by Eq. 4-3.63 or 4-3.64 with $\mathbf{x}_0 = 0$.

For scattering into the forward direction, $\mathbf{k}_f = \mathbf{k}_i$, all spatial phases, $\phi_{\mathbf{x}} = -(\mathbf{k}_f - \mathbf{k}_i)\cdot \mathbf{x}$, are zero. This is a scattering channel direction--a scattering direction in which the scattered fields from all the particles in a medium have the same spatial phase. In the forward direction, the intensity is proportional to the square of the number of scatterers. To find the scattered intensity in other directions, the second term in Eq. 6-1.1 must be evaluated. As $N \to \infty$ this term, for an isotropic medium, can be approximated as a sum over a random distribution of spatial phases which averages to zero--in such a case, the nonforward scattered field intensity is formed from an incoherent sum of the scattered fields from each scatterer. Then, the nonforward scattered intensity is proportional to the number of scatterers, and the net intensity for elastic scattering is

$$I^{elas}(\mathbf{x}) = I_0 N \left| F(\mathbf{k}_f \neq \mathbf{k}_i) \right|^2 + I_0 N^2 \left| F(\mathbf{k}_f = \mathbf{k}_i) \right|^2. \qquad (6\text{-}1.2)$$

For off-energy-shell inelastic scattering where $k_f \neq k_i$, a random temporal phase, ϕ_n^{fi}, must be added to the field as discussed in Section 3.5. Because of this factor,

irrespective of the scattering direction, the scattered intensity is formed from an incoherent sum over all the scattered fields from each scatterer

$$I^{inel}(\mathbf{x}) = I_0\left|F_{inel}\left(\mathbf{k}_f,\mathbf{k}_i\right)\right|^2\left|\sum_{n=1}^{N} e^{i\left(\mathbf{k}_f-\mathbf{k}_i\right)\cdot\mathbf{x}_n} e^{i\phi_n^{fi}}\right|^2 = I_0 N\left|F_{inel}\left(\mathbf{k}_f,\mathbf{k}_i\right)\right|^2 \qquad (6\text{-}1.3)$$

where $F_{inel}\left(\mathbf{k}_f,\mathbf{k}_i\right)$ is an inelastic scattering amplitude.

For an anisotropic medium, such as a crystal, there can be many scattering channel directions (such as those resulting from Bragg diffraction in a crystal) in addition to the forward direction. Normally, a structure factor for a unit cell is constructed to calculate the total field scattered from a crystal.

The structure factor is the sum of the scattering amplitudes from all of the particles in the unit cell. For electronic scattering (operating far from any any bound state resonances or absorption edges) or for nuclear scattering the structure factor of a unit cell with scatterers of type α located at $\mathbf{r}_{n_\alpha}$ is

$$F_H = -r_e\left(\hat{\boldsymbol{\varepsilon}}_f^*\cdot\hat{\boldsymbol{\varepsilon}}_i\right)\sum_{\alpha n_\alpha}\left(e^{-2W_\alpha} f_{0\alpha} + f_\alpha' - if_\alpha''\right)e^{-i\mathbf{H}\cdot\mathbf{r}_{n_\alpha}} \qquad \text{(electronic scattering)} \quad (6\text{-}1.4)$$

$$F_H = \sum_{\alpha n_\alpha} F_\alpha\left(\mathbf{k}_f,\mathbf{k}_i\right)e^{-i\mathbf{H}\cdot\mathbf{r}_{n_\alpha}} \qquad \text{(nuclear scattering)} \quad (6\text{-}1.5)$$

where $\mathbf{H} = \mathbf{k}_f - \mathbf{k}_i,$ (6-1.6)

and the scattering amplitudes are given by Eq. 5-1.55 (electronic scattering) and Eqs 4-3.62 or 4-3.63 (nuclear scattering). If the origin is placed at the corner, $\mathbf{x}_0$, of one of the unit cells in the crystal, then any other unit cell can be found through an integral number of lattice displacements

$$\mathbf{x}' = \mathbf{x}_0 + n_1\mathbf{a}_1 + n_2\mathbf{a}_2 + n_3\mathbf{a}_3. \qquad (6\text{-}1.7)$$

After calculating the structure factor for one unit cell, then, for one scattering channel, the total scattering amplitude from the whole crystal is constructed by summing the scattering amplitude from each cell multiplied by a phase factor, $e^{-i\mathbf{H}\cdot(n_i\mathbf{a}_i)}$ ($n_i = 0,1,2,\ldots,N_i - 1$ and $i = 1,2,3$), each cell acquires. The resulting scattered intensity is given by[1, 2]

$$I(\mathbf{x}) = I_0\left|F_{tot}(\mathbf{x})\right|^2 = I_0\left|F_H\right|^2\prod_{i=1}^{3}\frac{\sin^2\left(N_i\mathbf{H}\cdot\mathbf{a}_i/2\right)}{\sin^2\left(\mathbf{H}\cdot\mathbf{a}_i/2\right)}. \qquad (6\text{-}1.8)$$

The reflectivity is maximized at the Bragg peaks according to the Laue equation

$$\mathbf{H}\cdot\mathbf{a}_i = 2\pi H_i \qquad (6\text{-}1.9)$$

where H_i are integers and $\mathbf{H}$ is a reciprocal lattice vector

$$\mathbf{H} = h\mathbf{b}_1 + k\mathbf{b}_2 + \ell\mathbf{b}_3. \qquad (6\text{-}1.10)$$

When the Bragg condition is satisfied, the scattered fields travel mainly in scattering channel directions, $\hat{\mathbf{H}}$, and have narrow angular spreads. At the Bragg peaks, the intensity is again proportional to the square of the number of scatterers

$$I(\mathbf{x}) = I_0 N^2 |F_H|^2 \tag{6-1.11}$$

where $N = N_1 N_2 N_3$ is the total number of unit cells within the crystal. The angular width of an outgoing beam is inversely proportional to the number of scatters. Since most materials studied are macroscopic in size (as discussed in Section 3.1)--their dimensions are much greater than 100 Å and $N >> 10^6$--the angular widths are essentially delta functions at the scattering angle $2\theta_B$. Examination of Eq. 6-1.8 shows that the average intensity off the Bragg peaks is half the scattered intensity from a single unit cell--this extremely small factor can be safely ignored.

In the kinematic domain, crystalline and isotropic media give reflectivities proportional to the square of the number of scatterers when examining fields traveling in scattering channel directions. However, when examining fields not traveling in scattering channel directions, isotropic media give intensities proportional to the number of scatterers, while crystalline material give intensities that are essentially zero. Inelastic scattering in crystalline media is identical to that in isotropic media because of the effect of the random temporal phase factors of the scattering amplitude.

6.2 Dynamical Scattering Theory

Dynamical scattering includes the multiple scattering effects that are ignored in kinematical scattering theory. For linear time-invariant causal systems, multiple scattering can be handled by linear system theory. In such a theory, if the impulse response of a system is known (that is, the response of a system to a delta function in time), then the response of the system to any arbitrary analytic function is known (this is proved by imposing linearity, or using superposition arguments).[3] The frequency response of a scatterer to an incoming plane wave is described by the spherical multipole electric field in Eq. 4-4.16

$$H_\alpha(\omega, \mathbf{x}_{n_\alpha}, \mathbf{x}) = \frac{e^{ikr_{n_\alpha}}}{r_{n_\alpha}} F_\alpha(\mathbf{k}_f, \mathbf{k}_i) \tag{6-2.1}$$

where $\mathbf{x}_{n_\alpha}$ is the position of scatterer of type α, and $r_{n_\alpha} = |\mathbf{x} - \mathbf{x}_{n_\alpha}|$ is the distance from the scatterer to an observation point.

In multiple scattering, the spherical wave generated by a scatterer can interact with all other scatterers which in turn produce spherical waves that can interact with the original scatterer and all other scatterers. This multiple scattering behavior can be investigated by examining each step in the scattering process. For instance, for an incoming wave (the zeroth order scattered wave)

$$\mathbf{a}_0(\omega,\mathbf{x}) = \mathbf{E}_0(\omega,\mathbf{x}), \tag{6-2.2}$$

the response of the system (first order, or single scattering), is

$$\mathbf{a}_1(\omega,\mathbf{x}) = \sum_{\alpha=1}^{N_t}\sum_{n_\alpha=1}^{N_\alpha}\mathbf{a}_0\left(\omega,\mathbf{x}_{n_\alpha}\right)H\left(\omega,\mathbf{x}_{n_\alpha},\mathbf{x}\right) \tag{6-2.3}$$

where N_α is the number of scatterers of type α, and N_t is the number of different types of scatterers. Note that Eq. 6-2.3 represents a symmetric state of excited scatterers since interchanging the indices of identical scatters, $\mathbf{x}_{i_\alpha} \leftrightarrow \mathbf{x}_{j_\alpha}$, does not change the final sum. Double scattering (second order scattering) occurs when the single scattered wave interacts with all the particles

$$\mathbf{a}_2(\omega,\mathbf{x}) = \sum_{\alpha=1}^{N_t}\sum_{n_\alpha=1}^{N_\alpha}\mathbf{a}_1\left(\omega,\mathbf{x}_{n_\alpha}\right)H\left(\omega,\mathbf{x}_{n_\alpha},\mathbf{x}\right). \tag{6-2.4}$$

By iteration, one can determine the amplitudes for triple and all higher order scattered fields

$$\mathbf{a}_m(\omega,\mathbf{x}) = \sum_{\alpha=1}^{N_t}\sum_{n_\alpha=1}^{N_\alpha}\mathbf{a}_{m-1}\left(\omega,\mathbf{x}_{n_\alpha}\right)H\left(\omega,\mathbf{x}_{n_\alpha},\mathbf{x}\right) \qquad (m \geq 1). \tag{6-2.5}$$

For some problems, working in the time picture rather than in frequency space may be more convenient or illustrative. In the time picture multiple scattering involves the convolution of the frequency response with the incoming wave

$$\mathbf{a}_m(t,\mathbf{x}) = \sum_{\alpha=1}^{N_t}\sum_{n_\alpha=1}^{N_\alpha}\int_0^t \mathbf{a}_{m-1}\left(t',\mathbf{x}_{n_\alpha}\right)H\left(t-t',\mathbf{x}_{n_\alpha},\mathbf{x}\right)dt' \qquad (m \geq 1) \tag{6-2.6}$$

where the limits of the convolution integral were constrained by assuming the functions are causal:

$$\mathbf{a}_m(t',\mathbf{x}) = 0 \qquad \text{for} \quad t' < 0 \tag{6-2.7}$$

$$H\left(t-t',\mathbf{x}_{n_\alpha},\mathbf{x}\right) = 0 \quad \text{for} \quad t-t' < 0 \quad \text{or} \quad t' > t. \tag{6-2.8}$$

Working in the time domain, the multiple scattering formalism can be shown to be equivalent to a Feynman path integral approach where a sum is made over all the possible scattering paths of a collection of scatterers.[4]

The total scattered wavefield emanating from the medium is the sum of all the multiply scattered fields

$$\mathbf{E}_s(\omega,\mathbf{x}) = \sum_{m=0}^{\infty} \mathbf{a}_m(\omega,\mathbf{x}). \tag{6-2.9}$$

Note that Eq. 6-2.9 is still a quantum mechanical expression (the multipole scattering amplitude was obtained by finding matrix elements of quantum mechanical operators). No connection with classical electrodynamics has been made yet. The connection comes when the number of scatterers becomes so large ($N >> 10^6$) that computing Eq. 6-2.9 becomes too time consuming. In certain cases, however, such as for an isotropic medium, one can show that summing up an infinite number of scattering diagrams leads to the Maxwell equations for a medium (this is done in Section 6.5).

6.3 Two Coupled Oscillators

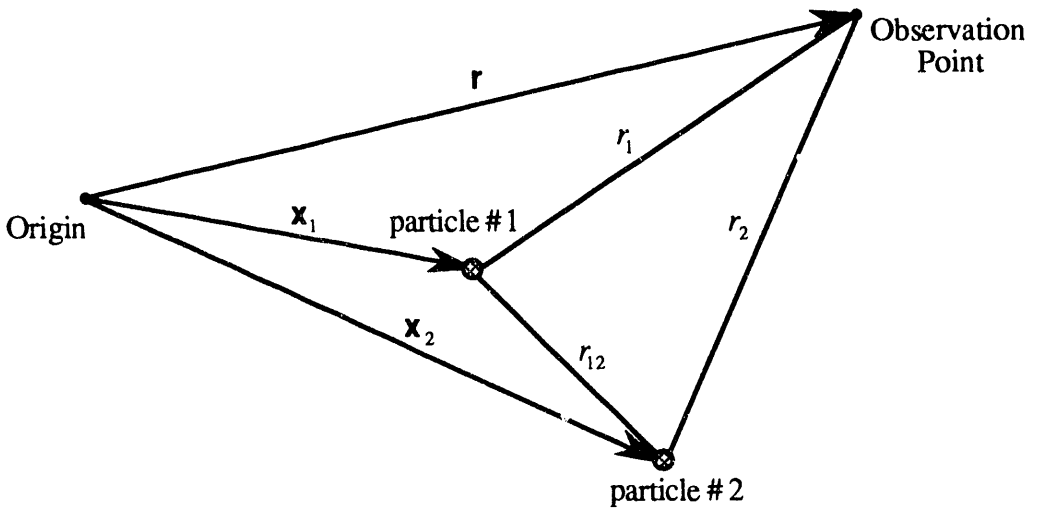

Fig. 6-3.1. Scattering geometry for two coupled oscillators.

For a simple example of multiple scattering scattering, consider the case of two identical particles situated a distance $r_{12} = |\mathbf{x}_1 - \mathbf{x}_2|$ apart as shown in Fig. 6-3.1. Assume, for further simplicity, that at some time $t = 0$ both particles are in the excited state and

decay with a probability amplitude $F_0(t)$. This allows the zeroth order scattering term, $a_0(t)$, to be ignored along with all the spatial phase factors associated with it.

Then, for the frequency response given by Eq. 6-2.1, all of the higher order scattering terms can be computed through the use of the multiple scattering equation, Eq. 6-2.5. (Below, $r_1 = |\mathbf{r} - \mathbf{x}_1|$, $r_2 = |\mathbf{r} - \mathbf{x}_2|$, and the polarization matrix describing scattering from particle #1 to $\mathbf{r}$ has been assumed to be equal to the polarization matrix describing scattering from particle #2 to $\mathbf{r}$)

$$a_1(\omega,\mathbf{r}) = F_0(\omega)\frac{e^{ikr_1}}{r_1} + F_0(\omega)\frac{e^{ikr_2}}{r_2}$$

$$a_2(\omega,\mathbf{r}) = \left(F_0(\omega)\frac{e^{ikr_{12}}}{r_{12}}\right)\frac{e^{ikr_1}}{r_1}F(\mathbf{k}_f,\mathbf{k}_i) + \left(F_0(\omega)\frac{e^{ikr_{12}}}{r_{12}}\right)\frac{e^{ikr_2}}{r_2}F(\mathbf{k}_f,\mathbf{k}_i)$$

$$= F_0(\omega)\left[\frac{e^{ikr_{12}}}{r_{12}}F(\mathbf{k}_f,\mathbf{k}_i)\right]\left(\frac{e^{ikr_1}}{r_1} + \frac{e^{ikr_2}}{r_2}\right)$$

$$a_3(\omega,\mathbf{r}) = F_0(\omega)\left[\frac{e^{ikr_{12}}}{r_{12}}F(\mathbf{k}_f,\mathbf{k}_i)\right]^2\left(\frac{e^{ikr_1}}{r_1} + \frac{e^{ikr_2}}{r_2}\right)$$

$$a_m(\omega,\mathbf{r}) = F_0(\omega)\left[\frac{e^{ikr_{12}}}{r_{12}}F(\mathbf{k}_f,\mathbf{k}_i)\right]^{m-1}\left(\frac{e^{ikr_1}}{r_1} + \frac{e^{ikr_2}}{r_2}\right). \tag{6-3.1}$$

The total scattered electric field is then

$$E_s(\omega,\mathbf{r}) = F_0(\omega)\left(\frac{e^{ikr_1}}{r_1} + \frac{e^{ikr_2}}{r_2}\right)\sum_{m=0}^{\infty}\left[\frac{e^{ikr_{12}}}{r_{12}}F(\mathbf{k}_f,\mathbf{k}_i)\right]^m$$

$$= \frac{F_0(\omega)\left(\dfrac{e^{ikr_1}}{r_1} + \dfrac{e^{ikr_2}}{r_2}\right)}{1 - \dfrac{e^{ikr_{12}}}{r_{12}}F(\mathbf{k}_f,\mathbf{k}_i)}. \tag{6-3.2}$$

Evaluating this expression for dipole scattering using the spin averaged scattering amplitude, Eq. 5-1.48, gives interesting results. Eq. 6-3.2 is then valid for sigma polarized electric dipole fields or pi polarized magnetic dipole fields. Assuming $F_0(\omega)$ has the same resonance characteristics as the scattering amplitude

$$F_0(\omega) = F_0/(\omega - \omega_0 + i\Gamma/2\hbar), \tag{6-3.3}$$

and for $r >> |\mathbf{x}_1|, |\mathbf{x}_2|$ Eq. 6-3.2 reduces to

$$E_s(\omega,r) = \frac{2F_0(e^{ikr}/r)e^{i\mathbf{k}\cdot(\mathbf{x}_1+\mathbf{x}_2)/2}\cos[\mathbf{k}\cdot(\mathbf{x}_1-\mathbf{x}_2)/2]}{\omega-(\omega_0-\omega_s)+i(\Gamma+\Gamma_s)/2\hbar} \tag{6-3.4}$$

where $\mathbf{k} = k(\mathbf{r}/r)$, and ω_s and Γ_s are a coupled oscillator frequency shift and decay rate speedup factor

$$\omega_s = \frac{1}{4}\left(\frac{2j_n+1}{2j_i+1}\right)\left(\frac{\Gamma_{rad}}{\hbar}\right)\frac{\cos(kr_{12})}{kr_{12}} \tag{6-3.5}$$

$$\Gamma_s = \frac{1}{2}\left(\frac{2j_n+1}{2j_i+1}\right)\Gamma_{rad}\frac{\sin(kr_{12})}{kr_{12}}. \tag{6-3.6}$$

This result shows that a pair of coupled oscillators will radiate fields with a natural frequency and natural linewidth that is different from an isolated oscillator. This is not surprising since, as shown in Section 3.7, a single oscillator interacting with its own electromagnetic field results in a frequency shift and a natural linewidth. In this problem there are two oscillators interacting with the electromagnetic fields generated by both oscillators.

For two ^{57}Fe nuclei, the coupled frequency shift and speedup rate are $(j_n = 3/2, j_i = 1/2)$

$$\omega_s = \frac{1}{2}\left(\frac{\Gamma_{rad}}{\hbar}\right)\frac{\cos(kr_{12})}{kr_{12}} \tag{6-3.7}$$

$$\Gamma_s = \Gamma_{rad}\frac{\sin(kr_{12})}{kr_{12}}. \tag{6-3.8}$$

As $kr_{12} \to 0$, the speedup rate goes to

$$\Gamma_s \to \Gamma_{rad}. \tag{6-3.9}$$

Since $\Gamma = \Gamma_{ic} + \Gamma_{rad}$, where Γ_{ic} is the decay rate due to internal conversion, then, when the separation between the oscillators is small compared to a wavelength, the radiative decay rate doubles. This confirms Dicke's supperadiant result that a symmetric state of two coupled oscillators has a radiative decay rate that is double that of a single oscillator.[5] However, as $kr_{12} \to 0$ the frequency shift becomes infinite. This is understandable because the electric field amplitude varies as $1/kr_{12}$. The particles are then bathed in a very high intensity electric field which will induce extremely large energy level shifts.

The frequency shift and speedup rate are also affected by the spatial separation of the particles--by increasing or decreasing the separation produces negative or positive frequency shifts and results in an increase or decrease of the the natural frequency. There is also an effect due to the angular momentum states of the particle. For very high angular momentum states and as $kr_{12} \rightarrow 0$, the speedup rate approaches $\Gamma_s \rightarrow 3\Gamma_{rad}/2$.

If the two particles are excited by an plane wave, the problem becomes slightly more complicated because the spatial phase of the plane wave must be taken into account. Performing computations similar to before, except now with an incoming plane wave

$$a_0(\omega,\mathbf{r}) = E_0 e^{i\mathbf{k}_i\cdot\mathbf{r}} \tag{6-3.10}$$

yields

$$E_s(\omega,\mathbf{r}) = E_0 e^{i\mathbf{k}_i\cdot\mathbf{r}} - E_0 \frac{1}{4}\left(\frac{2j_n+1}{2j_i+1}\right)\left(\frac{\Gamma_{rad}}{\hbar}\right)\frac{e^{ikr}}{kr} e^{-i\mathbf{H}\cdot(\mathbf{x}_1+\mathbf{x}_2)/2}$$

$$\times\left\{\cos[\mathbf{H}\cdot\mathbf{x}_{12}/2]\left(\frac{1}{R^+(\omega)}+\frac{1}{R^-(\omega)}\right)+\cos[(\mathbf{k}_f+\mathbf{k}_i)\cdot\mathbf{x}_{12}/2]\left(\frac{1}{R^+(\omega)}-\frac{1}{R^-(\omega)}\right)\right\} \tag{6-3.11}$$

where

$$R^+(\omega) = \omega - (\omega_0 - \omega_s) + i(\Gamma+\Gamma_s)/2\hbar \tag{6-3.12}$$

$$R^-(\omega) = \omega - (\omega_0 + \omega_s) + i(\Gamma-\Gamma_s)/2\hbar, \tag{6-3.13}$$

and $\mathbf{k}_f = k(\mathbf{r}/r)$, $\mathbf{H} = \mathbf{k}_f - \mathbf{k}_i$, $\mathbf{x}_{12} = \mathbf{x}_1 - \mathbf{x}_2$, and ω_s and $\Gamma_s$are given by Eqs. 6-3.5 and 6-3.6 . For this arrangement there are two normal modes that can exist. There is one mode in which there are negative frequency shifts and decay rate speedups, and another with just the reverse--positive frequency shifts and decay rate slowdowns.

6.4 Scattering Channel Fields

Multiple scattering computations can be simplified if scattering is examined only along the highly directional scattering channels where most of the radiation exits a medium (such as in the forward or Bragg directions for an isotropic medium or a crystal). For example, consider the case of a one dimensional line of scatterers, as shown in Fig. 6-4.1, where there is an incident plane wave traveling parallel to the line of scatters. The forward direction is a scattering channel direction since the spatial phase of a scattered wave from a

particle located at z_η, $\phi_s = \mathbf{H}\cdot\mathbf{z}_\eta$, is always zero. The single scattered field observed at a distance far from any scatterer, $r >> z_\eta$, is then

$$a_1(\omega,r) = \sum_\eta \left(E_0 e^{i\mathbf{k}_i\cdot\mathbf{z}_\eta}\right)\left[\frac{e^{ikr_\eta}}{r_\eta}F(\mathbf{k}_f=\mathbf{k}_i)\right] \approx \sum_\eta \left(E_0 e^{i\mathbf{k}_i\cdot\mathbf{z}_\eta}\right)\left[\frac{e^{ikr}e^{-i\mathbf{k}_f\cdot\mathbf{z}_\eta}}{r}F(\mathbf{k}_f=\mathbf{k}_i)\right]$$

$$= \sum_\eta \left[E_0\frac{e^{ikr}}{r}F(\mathbf{k}_f=\mathbf{k}_i)\right] = N_\eta E_0\frac{e^{ikr}}{r}F(\mathbf{k}_f=\mathbf{k}_i) \qquad (6\text{-}4.1)$$

where $r_\eta = r - z_\eta$, and N_η is the number of scatterers. All the single scattered fields have the same overall spatial phase factor, and therefore the net scattered field is a coherent sum of all of the single scattered fields.

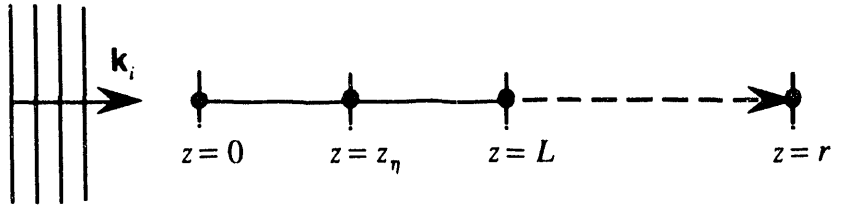

Fig. 6-4.1. Plane wave field incident upon a line of scatterers of length L.

For the double scattered fields,

$$a_2(\omega,r) = \sum_\eta\sum_{\eta'}\left[\frac{e^{ikr_{\eta\eta'}}}{r_{\eta\eta'}}e^{i\mathbf{k}_i\cdot\mathbf{z}_{\eta'}}F(\mathbf{k}_f=\mathbf{k}_i)\right]\left[\frac{e^{ikr_\eta}}{r_\eta}F(\mathbf{k}_f=\mathbf{k}_i)\right] \qquad (6\text{-}4.2)$$

where $r_{\eta\eta'} = |z_\eta - z_{\eta'}|$. Since double scattering has been constrained to occur only in the forward direction (backscattering is ignored), $z_\eta > z_{\eta'}$ and thus $r_{\eta\eta'} = z_\eta - z_{\eta'}$. Then all of the doubled scattered fields also have the same overall spatial phase factor

$$a_2(\omega,r) = E_0\frac{e^{ikr}}{r}\sum_{\eta\eta'}\frac{\left[F(\mathbf{k}_f=\mathbf{k}_i)\right]^2}{z_\eta - z_{\eta'}}. \qquad (6\text{-}4.3)$$

By iteration, the total forward scattered electric field at the observation point is

$$E_s(\omega,r) = E_0 e^{ikr} + E_0\frac{e^{ikr}}{r}F(\mathbf{k}_f=\mathbf{k}_i)\sum_\eta\left\{1+\sum_{\eta'}\frac{F(\mathbf{k}_f=\mathbf{k}_i)}{z_\eta - z_{\eta'}} + \sum_{\eta'\eta''}\frac{\left[F(\mathbf{k}_f=\mathbf{k}_i)\right]^2}{(z_{\eta'}-z_{\eta''})(z_\eta - z_{\eta'})} + \cdots\right\}. \qquad (6\text{-}4.4)$$

This infinite series expression is equivalent to the sum of an infinite number of scattering diagrams where the vector potential of each photon, except the incoming photon,

is defined as a spherical wave (see Fig. 6-4.2). All photons travel in the same direction, and each photon can either exit the medium or scatter with a downstream particle. As seen before for a single particle, the sum over an infinite number of scattering diagrams can lead to frequency shifts and to changes in the natural radiative decay rate.

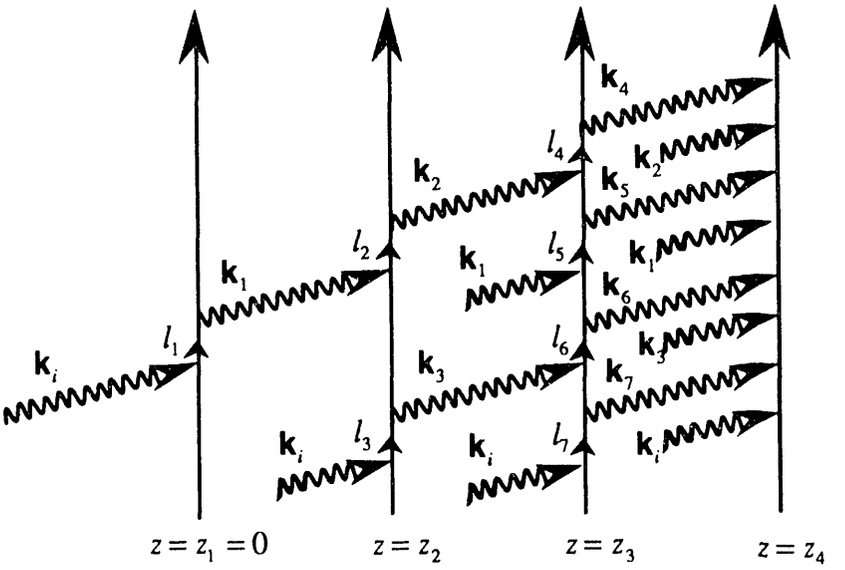

Fig. 6-4.2. Scattering diagram for multiple scattering along a scattering channel direction. All wavectors have the same magnitude and are in the same direction. The first four particles are shown with time represented by the vertical axis and intermediate states by l_j. (For convenience, the photon arrival time at each scatterer is not correctly drawn. Actually, photon $\mathbf{k}_i$ strikes all scatterers at the same time, photon $\mathbf{k}_1$ strikes all scatterers located at $z \geq z_2$ at the same time, etc.)

When there are many scatterers with an interparticle separation comparable to or less than the wavelength of the incoming field, the discrete line of particles can be approximated as a continuous linear distribution of particles. Eq. 6-4.4 can then be rewritten as

$$E_s(\omega,r) = E_0 e^{ikr} + E_0 \frac{e^{ikr}}{r} nF_\omega L \int_0^1 ds \left\{ 1 + nF_\omega \int_0^{1-\delta} \frac{1}{1-s'} + \left[nF_\omega\right]^2 \int_0^{1-\delta} \frac{ds'}{1-s'} \int_0^{1-\delta'} \frac{ds''}{1-s''} + \cdots \right\} \tag{6-4.5}$$

where $s = z/L$, $s' = z'/z$, $s'' = z''/z'$, etc., n is the number of particles per unit length, and $F_\omega = F\left(\mathbf{k}_f = \mathbf{k}_i\right)$. The small parameters in the upper limits, $\delta = d/z, \delta' = d/z', \delta'' = d/z''$, etc., are included to prevent the integrals from diverging. The quantity d is the average interparticle separation. The integral series can be evaluated to first order by making the approximation $\delta \approx d/L$. For such a case

$$E_s(\omega,r) = E_0 e^{ikr} + \frac{E_0 \dfrac{e^{ikr}}{r} nF(\mathbf{k}_f = \mathbf{k}_i)L}{1 + nF(\mathbf{k}_f = \mathbf{k}_i)\ln\delta}. \qquad (6\text{-}4.6)$$

Inserting the dipole scattering amplitude, Eq. 5-1.48, into the expression above gives

$$E_s(\omega,r) = E_0 e^{ikr} - E_0 \frac{e^{ikr}}{r}\frac{nL}{4\mathbf{k}_f}\left(\frac{2j_n+1}{2j_i+1}\right)\left(\frac{\Gamma_{rad}}{\hbar}\right)\frac{1}{\omega - (\omega_0 + \omega_s) + i\Gamma/2\hbar} \qquad (6\text{-}4.7)$$

where $$\omega_s = \frac{n}{4\mathbf{k}_f}\left(\frac{2j_n+1}{2j_i+1}\right)\left(\frac{\Gamma_{rad}}{\hbar}\right)\ln\delta. \qquad (6\text{-}4.8)$$

This shows that, for forward scattering from a line of particles, there is no change in the natural linewidth, but there is a shift from the natural frequency of an isolated particle. The frequency shift diverges logarithmically with decreasing interparticle separation rather than linearly as was the case for the two particle system, but the reason for the divergence is the same--the electric field strength of spherical waves is very intense at small distances from the scatterer.

So far only scattering purely in the forward direction has been mentioned. Another way a wave can scatter and end up in the forward direction is to scatter in the backward direction and then scatter again into the forward direction. In doing so, the scattered wave can pick up a nonzero phase factor. For instance, for double scattering where the wave backscatters and then scatters into the forward direction, the field amplitude is that of Eq. 6-4.3 multiplied by the spatial phase factor: $-e^{i2k(z_n - z_{n'})}$. For n^{th} order scattering there are $n! - 1$ ways a field can scatter away and then back into the scattering channel direction--all of the amplitudes and associated phase factors for each order must then be evaluated. For an ordered line of scatterers (such as a linear lattice), all types of multiple scattering must be computed to determine the total scattered field--an extremely tedious task since all orders of scattering must be computed, and each order has $n!$ terms. However, if the line of scatterers is randomly ordered (such as an isotropic distribution of a large number of scatterers), the phase factors of fields scattered back into the scattering channel direction will be essentially random. In such a situation, these fields can be neglected because their contribution to the total scattered intensity will be down by a factor of $1/N$ compared to the intensity of the scattering channel fields (fields scattered purely in the scattering channel direction).

A plane or volume of a large number of ordered scatterers (such as a planar lattice or a crystal lattice) has more degrees of freedom than a line of scatterers. Because of the

extra degrees of freedom, the intensity of scattering channel fields is a factor of N times greater than of multiply scattered fields scattered in directions other that the scattering channel direction--the nonscattering channel fields fields pick up additional phase factors that are essentially random for a many particle medium. Therefore, mainly the scattering channel fields will be investigated, and all other types of scattered fields will be neglected.

6.5 Plane Parallel Slab of Scatterers

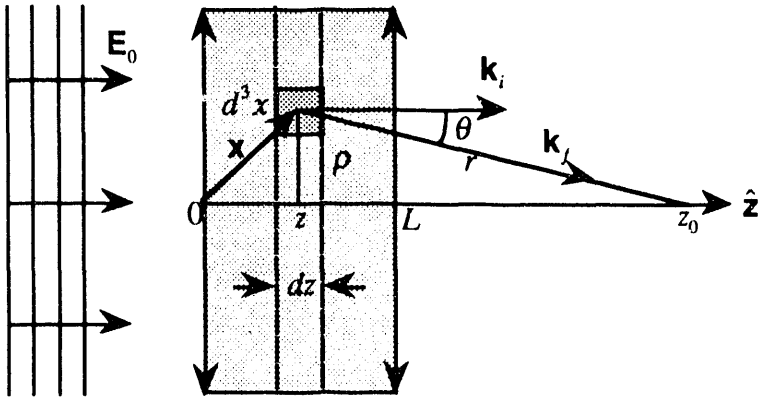

Fig. 6-5.1. Plane wave field incident upon a plane parallel slab of thickness L.[6]

The sum over the infinite number of scattering diagrams in Fig. 6-4.2 should, in the continuous limit, lead to a description of a scattered electric field that converges to the expression obtained by solving the Maxwell equations for a medium. This will be shown to be true for a plane parallel slab where boundary conditions are neglected.

In the continuous limit, the multiple scattering equations, Eq. 6-2.5, can be written in the form (for identical particles and for scattering channel fields)

$$a_1(\omega,z,z_0)dz = a_0(\omega,z,z_0)H(\omega,z,z_0)dz \tag{6-5.1}$$

$$a_m(\omega,z,z_0)dz = \left[\int_0^z dz' a_{m-1}(\omega,z',z)\right]H(\omega,z,z_0)dz \tag{6-5.2}$$

where z_0 is the observation point. This gives the m^{th} order field amplitude for a slice within the slab at position z of thickness dz by summing up all of the lower order field amplitudes of all preceding slices and multiplying by the frequency response at point z. The net scattering channel field at the position z in the medium is then

$$E_{scf}(\omega,z,z_0)=a_0(\omega,z,z_0)+\sum_{m=1}^{\infty}\int_0^z dz'\,a_m(\omega,z',z_0)\,. \tag{6-5.3}$$

For forward scattering within a line of scatterers, the frequency response observed at point z for a segment of thickness dz' located at point z' is

$$H(\omega,z',z)dz'=F(\mathbf{k}_f=\mathbf{k}_i)\frac{(n_l\,dz')}{z-z'} \tag{6-5.4}$$

where n_l is the number of particles per unit length. The frequency response for a slice of thickness dz' within a plane parallel slab is simpler. Consider a slab of thickness L and infinite in the dimensions transverse to the beam propagation direction as shown in Fig. 6-5.1. Jackson has shown that the sum of single scattered fields from a slice of thickness dz within the slab yields a net field with an amplitude that is independent of the distance from the slice[6]

$$dE_{slice}=\frac{2\pi i}{k}F(\mathbf{k}_f=\mathbf{k}_i)E_0e^{ikz_0}(n\,dz) \tag{6-5.5}$$

where n is the number of scatterers per unit volume, and the incident field was a plane wave. The frequency response for a slice is then

$$H(\omega,z',z)dz'=\frac{2\pi i}{k}nF(\mathbf{k}_f=\mathbf{k}_i)dz'. \tag{6-5.6}$$

For forward scattering, the plane wave incident field can be written as

$$a_0(\omega,z,z_0)=a_0(\omega,z_0)=E_0(\omega)e^{ikz_0} \tag{6-5.7}$$

where the amplitude $E_0(\omega)$ is independent of z and z_0. The spatial phase factor e^{ikz} is ignored because, recalling from the previous section, for forward scattering the spatial phase of a scattered wave is zero. However, an overall phase factor e^{ikz_0} must be attached to the net scattering channel field to include the phase the field picks up in traveling from the slab to the observation point z_0. For such an incident plane wave field, using the multiple scattering equations for a medium, Eq. 6-5.2, the scattering channel field within the medium is

$$\begin{aligned}E_{scf}(\omega,z,z)&=a_0(\omega,z)\left\{1+[i\varepsilon_0(\omega)k]\int_0^z\sum_{m=0}^{\infty}\frac{[i\varepsilon_0(\omega)kz]^m}{m!}dz\right\}\\&=a_0(\omega,z)e^{i\varepsilon_0(\omega)kz}\end{aligned} \tag{6-5.8}$$

where

$$\varepsilon_0(\omega)=\frac{2\pi}{k^2}nF(\mathbf{k}_f=\mathbf{k}_i). \tag{6-5.9}$$

This is precisely the solution to the Maxwell equations when neglecting boundary conditions (and it also agrees with the semiclassical results of Section 3.4). For instance, for a plane parallel slab of thickness L, the solution to the inhomogeneous wave equation for transverse electric fields, Eqs. 3-2.9 and 3-2.10, is

$$E_{Max}(\omega, L, z_0) = E_0(\omega) e^{in(\omega)kL} e^{ik(z_0 - L)} = E_{scf}(\omega, L, z_0) \qquad (6\text{-}5.10)$$

where the quantity $n(\omega) = 1 + \varepsilon_0(\omega)$ is the index of refraction of the medium, and the last phase factor, $e^{ik(z_0 - L)}$, takes care of propagation through free space to the point z_0. Since, in the many particle limit, the multiple scattering equations for scattering channel fields give the same answer as the inhomogeneous wave equation, for more complicated problems, such as including boundary conditions or examining dynamical diffraction in crystals, the inhomogeneous wave equation will be used for constructing the scattering channel fields. No attempt will be made to examine the multiple scattered fields not traveling in scattering channel directions--full dynamical scattering theory will not be investigated any further than the discussion in this chapter.

The frequency shifts and speedup rates are no longer clearly observable in Eq. 6-5.8. In some cases, calculating the scattered fields in the time domain allows these effects to be seen more clearly. One can then either take the Fourier transform of Eq. 6-5.8, or, equivalently, express the multiple scattering equations for scattering channel fields in the time domain

$$a_1(t, z, z_0)\,dz = \int_0^t a_0(t', z, z_0) H(t - t', z, z_0)\,dt'\,dz \qquad (6\text{-}5.11)$$

$$a_m(t, z, z_0)\,dz = \int_0^t \left[\int_0^z dz'\, a_{m-1}(t', z', z) \right] H(t - t', z, z_0)\,dt'\,dz \qquad (6\text{-}5.12)$$

and

$$E_{scf}(t, z, z_0) = a_0(t, z, z_0) + \sum_{m=1}^{\infty} \int_0^z dz'\, a_m(t, z', z_0)\,. \qquad (6\text{-}5.13)$$

As an example, multiple scattering of dipole fields will be examined where the incident plane wave field is a synchrotron pulse

$$a_0(\omega, z, z_0) = E_0 e^{ikz_0} \quad \text{or in time,} \quad a_0(t, z, z_0) = E_0 e^{ikz_0} \delta(t) \qquad . \quad (6\text{-}5.14)$$

For dipole fields

$$\varepsilon_0(\omega) kL = -(\Gamma_s/4\hbar)/(\omega - \omega_0 + i\Gamma/2\hbar) \qquad (6\text{-}5.15)$$

where

$$\Gamma_s/\hbar = n\sigma_0(\Gamma/\hbar)L, \qquad (6\text{-}5.16)$$

L is the thickness of the slab, and σ_0 is the resonant cross section given by Eq. 5-1.52 (with the polarization factor set to unity). Inserting this factor into Eq. 6-5.8 and taking the Fourier transform will give the scattering channel field in the time domain. A contour

integral must be performed to complete the Fourier transform, and Lynch, Holland, and Hamermesh have carefully described how to do this.[7]

The other approach involves evaluating the time response of the system. Taking the Fourier transform of the forward scattering amplitude (Eq. 5-1.48 with the polarization factor set to unity) by performing a simple contour integral where there is only one pole in the lower half complex z-plane gives

$$H(t,z',z) = -(\Gamma_s/4\hbar L)e^{-i\omega_0 t-\Gamma t/2\hbar}\theta(t) \tag{6-5.17}$$

where

$$\theta(t) = \begin{cases} 1 & t \geq 0 \\ 0 & t < 0 \end{cases}. \tag{6-5.18}$$

The multiple scattered field amplitudes are then

$$\sum_{m=1}^{\infty} a_m(t,z',z_0) = -E_0 e^{ikz_0}\frac{\Gamma_s}{4\hbar L}e^{-i\omega_0 t-\Gamma t/2\hbar}\left[1-\left(\frac{\Gamma_s zt}{4\hbar L}\right)+\frac{1}{(2!)^2}\left(\frac{\Gamma_s zt}{4\hbar L}\right)^2-\frac{1}{(3!)^2}\left(\frac{\Gamma_s zt}{4\hbar L}\right)^3+\cdots\right]$$

$$= -E_0 e^{ikz_0}(\Gamma_s/4\hbar L)e^{-i\omega_0 t-\Gamma t/2\hbar}J_0\left(\sqrt{\Gamma_s zt/\hbar L}\right)\theta(t) \tag{6-5.19}$$

where the following Bessel function identity was used

$$J_0\left(2\sqrt{y}\right) = 1 - y + \frac{y^2}{(2!)^2} - \frac{y^3}{(3!)^2} + \cdots. \tag{6-5.20}$$

Then, using the integral relationship for a Bessel function of order zero

$$\int uJ_0(u) = uJ_1(u) \tag{6-5.21}$$

yields the scattering channel field

$$E_{scf}(t,L,z_0) = E_0 e^{ikz_0}\left\{\delta(t) - e^{-i\omega_0 t-\Gamma t/2\hbar}\frac{1}{2t}\int_0^{\sqrt{\Gamma_s t/\hbar}} uJ_0(u)\right\}\theta(t)$$

$$= E_0 e^{ikz_0}\left\{\delta(t) - e^{-i\omega_0 t-\Gamma t/2\hbar}\left(\frac{\Gamma_s}{2\hbar}\right)\frac{J_1\left(\sqrt{\Gamma_s t/\hbar}\right)}{\sqrt{\Gamma_s t/\hbar}}\right\}\theta(t). \tag{6-5.22}$$

This is the same result Lynch, Holland, and Hamermesh would get if they were to substitute their ^{57}Co source with a broadband frequency source (such as a synchrotron pulse).[7,8] There happens to be no frequency shifts for forward scattering through a plane parallel slab, but the natural decay rate is modified by a Bessel function (see Fig. 6-5.2). As $\Gamma_s \to 0$ the collection of particles within the slab behave independently instead of cooperatively, and the collective state decays with the natural lifetime of an isolated particle (kinematical scattering occurs). As Γ_s increases the lifetime of the collective state

decreases. Thus, Γ_s indicates the extent a system has undergone homogeneous line broadening. The homogeneous broadened linewidth can be approximated as (after examining Eq. 6-5.8 more carefully)

$$\Gamma_{hom} = \begin{cases} \Gamma & ,\text{for } \Gamma_s << \Gamma \\ \Gamma\sqrt{\dfrac{1}{\ln 2}\left(\dfrac{\Gamma_s}{\Gamma}\right) - 1} & ,\text{for } \Gamma_s >> \Gamma \end{cases}. \tag{6-5.23}$$

Note that Γ_s in Eq. 6-5.16 depends upon a thickness parameter $T = n\sigma_0 L$. T must also be multiplied by an enrichment factor for samples that contain nonresonant particles and by a Lamb-Mössbauer factor to take into account vibrating scatterers.[9] The graphs below were calculated for a 100% enriched slab of ^{57}Fe nuclei with a Lamb-Mössbauer factor of unity and for no photoelectric absorption. If the photoelectric frequency response is constant over the frequency range of the dipole resonance, then Eq. 6-5.22 need only be multiplied by the factor $e^{i\mu_e(\omega_0)L/2}$ where $\mu_e(\omega_0)$ is the photoelectric absorption coefficient at the resonant frequency. The time spectra in Fig. 6-5.2 ignores the prompt delta-function pulse.

Two more examples of multiple scattering worked out in the time domain are given in Appendix B. In Appendix B.1, Lynch, Holland, and Hamermesh's solution is rederived for the problem where a ^{57}Co source excites a plane parallel slab of resonant scatterers. In Appendix B.2, the time domain multiple scattering equations are used for a case in which they turn out to be more convenient to use than the Fourier transform method. In this problem the dynamical phase between two widely separated resonance lines excited by a synchrotron pulse is examined.

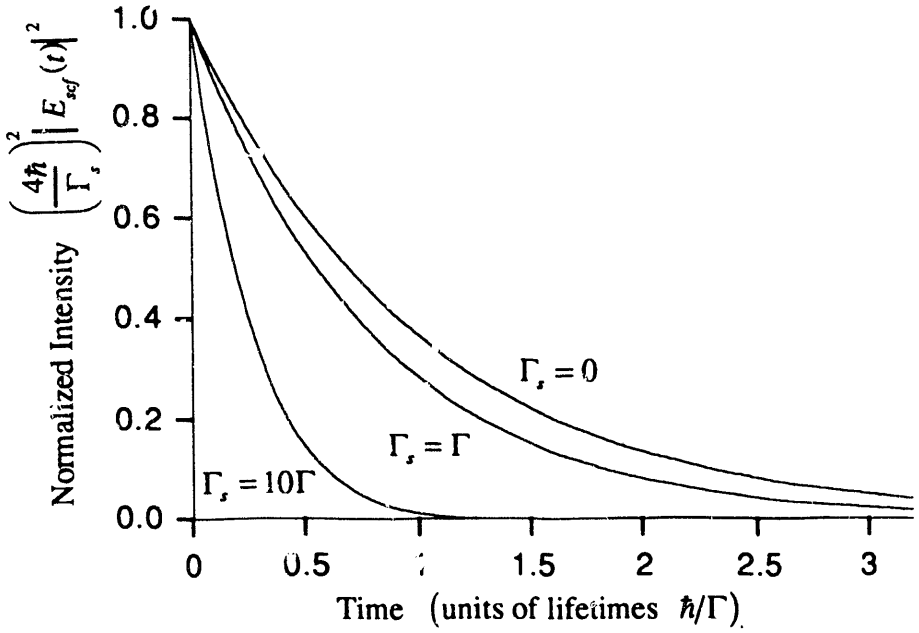

(a)

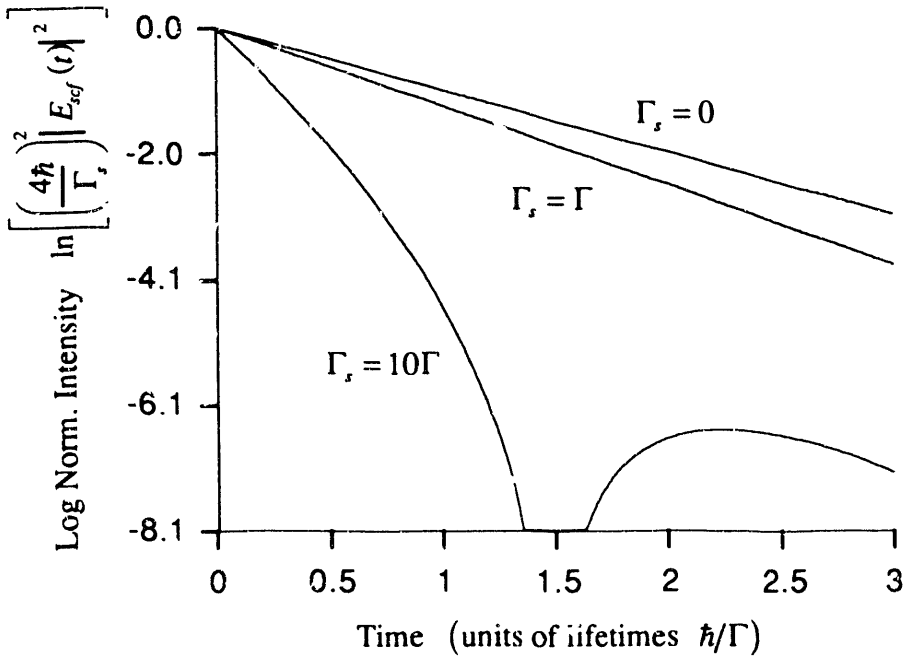

(b)

Fig 6-5.2. Time spectra of ^{57}Fe for various speedup rates: (a) linear scale, (b) log scale. The presence of dynamical beats becomes evident in the log plot for large speedups.

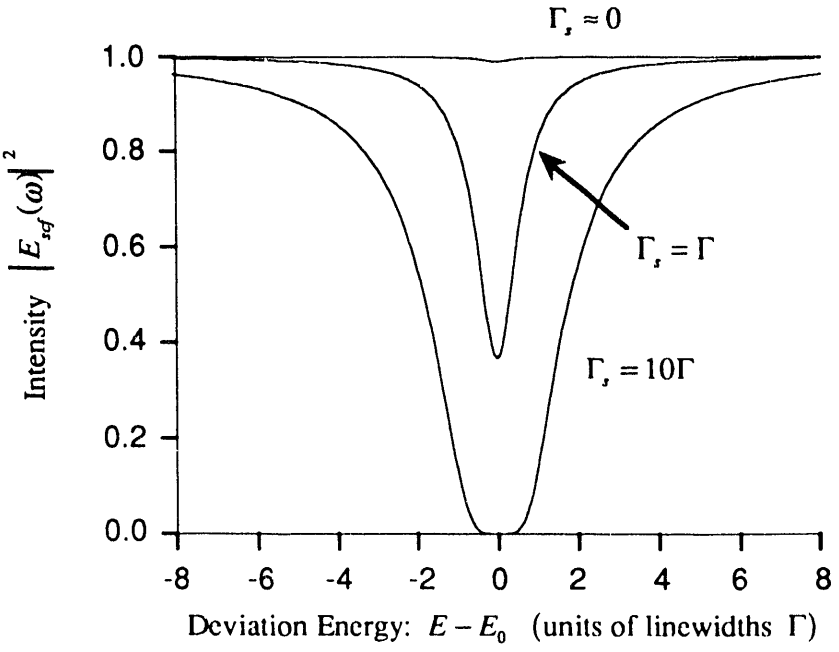

(a)

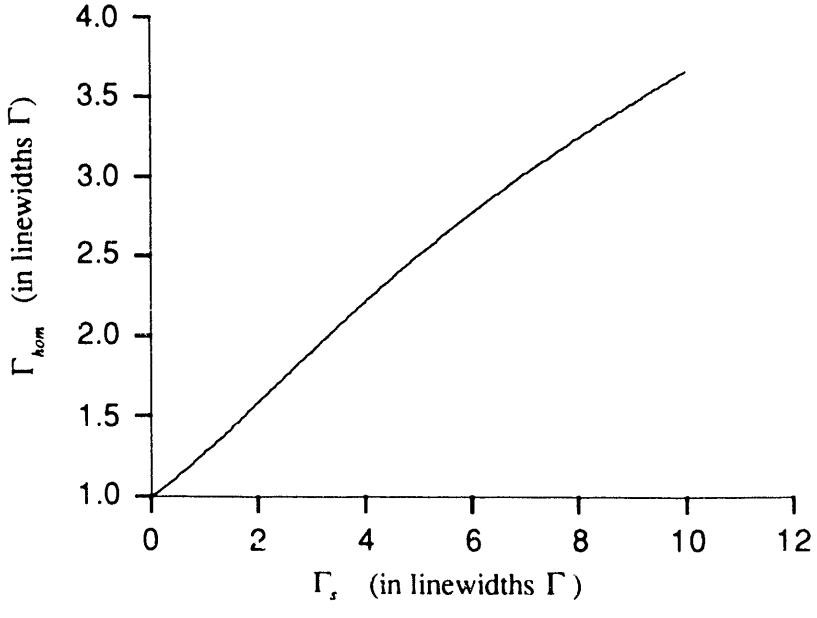

(b)

Fig 6-5.3. The decrease in the lifetime of the collective state, as shown in Fig 6-5.2 (a), corresponds, by the uncertainty principle, to a broadening of the linewidth in frequency space: (a) homogeneous line broadening due to multiple scattering, (b) homogeneous linewidth as a function of the speedup rate.

REFERENCES

[1] W. H. Zachariasen, *Theory of X-Ray Diffraction in Crystals* (Dover Publications, New York, 1945).

[2] R. W. James, *The Optical Principles of the Diffraction of X-Rays* (Ox Bow Press, Woodbridge, Connecticut, 1982).

[3] A. Papoulis, *The Fourier Integral and its Applications* (McGraw-Hill, New York, 1962).

[4] S. Ruby (private communications, 1991).

[5] R. H. Dicke, *Phys. Rev.* **93**, 99 (1954).

[6] J. D. Jackson, *Classical Electrodynamics* (Wiley, New York, 1975).

[7] F. J. Lynch, R. E. Holland, and M. Hamermesh, *Phys. Rev.* **120**, 513 (1960).

[8] Y. Kagan, A. M. Afanas'ev, and V. G. Kohn, *J. Phys. C* **12**, 615 (1979).

[9] S. Margulies and J. R. Ehrman, *Nucl. Instr. and Meth.* **12**, 131 (1961).

7. DYNAMICAL DIFFRACTION BY CRYSTALS

The underlying theory of the principles of dynamical diffraction in crystals was developed in the early 1900's independently by Darwin and Ewald. The two theories are quite different explanations of the same phenomenon. The Darwin-Prin's theory carefully examines the reflected and transmitted field amplitudes from each plane of atoms within a crystal in order to build up a total diffracted and transmitted amplitude (one ends up solving a set of coupled difference equations). On the other hand, the Ewald-Laue theory solves the Maxwell equations for a medium having a periodic index of refraction (one ends up solving a set of coupled dispersion equations). A well written discussion of both treatments can be found in James (as well as almost anything one desires to know about X-ray diffraction).[1] A good discussion of the Darwin-Prins treatment can be found in Warren[2] and the Ewald-Laue approach is well discussed in Zachariason[3] and in a paper by Batterman and Cole.[4] In the field of nuclear dynamical diffraction, the Darwin-Prins method has been extended by Hannon and Trammel,[5-8] and the Ewald-Laue approach has been utilized by Kagan and Afanas'ev.[9-11] The discussion in this chapter will concentrate on the Ewald-Laue method of dynamical diffraction theory.

7.1 Dispersion Relations for a Medium having a Tensor Index of Refraction

Solving the inhomogeneous wave equation for transverse electric fields in a mediu[illegible]q. 3-2.11, gives insight into the nature of fields propagating through materials along scattering channels. Recall that the index effect, $2\boldsymbol{\varepsilon}_0$, is a tensor quantity proportional to the multipole scattering amplitude developed in Chapter 4. Thus, the inhomogeneous wave equation is also a tensor wave equation.

For an anisotropic medium, the spatially averaged index effect can be modeled as a continuous periodic function of the spatial coordinates (see Eqs. 3-4.18, 6-1.4, and 6-1.5):

$$2\boldsymbol{\varepsilon}_0(\mathbf{x},\omega) = \frac{4\pi}{k_{0v}^2 V_0}\sum_H \mathbf{F}_H e^{i\mathbf{H}\cdot\mathbf{x}} \tag{7-1.1}$$

where a sum over all the possible scattering channels denoted by the index H is performed, and the magnitude of the scattered wavevector within the medium is assumed to be approximately equal to the vacuum wavenumber: $k_f \approx k_{ov}$. The expression above shows that the index effect can be written as a Fourier series of the spatial frequency components of the scattering amplitude (the multipole scattering amplitude is given by Eq 4-3.63 or 4-3.64 with $\mathbf{x}_0 = 0$). Similarly, the electric field can be expressed as a sum of Fourier components. When this is done, the inhomogeneous wave equation transforms to

$$\left[\nabla\cdot\nabla\cdot + k_{0v}^2 + k_{0v}^2\left(\frac{4\pi}{k_{ov}^2 V_0}\right)\sum_{H'}\mathbf{F}_{H'}e^{i\mathbf{H}'\cdot\mathbf{x}}\right]\sum_H \mathbf{E}_H e^{i\mathbf{k}_H\cdot\mathbf{x}} = 0,$$

and thus

$$\sum_H\left(1-\frac{\mathbf{k}_H\cdot\mathbf{k}_H}{k_{0v}^2}\right)\mathbf{E}_H e^{i\mathbf{k}_H\cdot\mathbf{x}} + \frac{4\pi}{k_{ov}^2 V_0}\sum_S\sum_{H'}\mathbf{F}_{H'}\mathbf{E}_S e^{i(\mathbf{k}_S+\mathbf{H}')\cdot\mathbf{x}} = 0. \qquad (7\text{-}1.2)$$

The above equation can be satisfied if, term by term, the arguments of the exponentials are the same. They will be if one remains on the energy shell:

$$\mathbf{k}_S + \mathbf{H}' = \mathbf{k}_H. \qquad (7\text{-}1.3)$$

This can also be seen through examining the Ewald sphere (or energy shell) construction in reciprocal lattice space, Fig. 7-1.1. The reciprocal lattice points, H and S, lie on the Ewald sphere, $\mathbf{k}_0$ is the forward scattered beam within the medium (reciprocal lattice vector is $H = 0$), and $\mathbf{k}_H$ and $\mathbf{k}_S$ are outgoing scattering directions. To satisfy Bragg's law, the incoming and outgoing wavevectors must lie on the Ewald sphere. The relation in Eq. 7-1.3 shows that there are fields within the medium traveling in S-channels that are scattered by the spatial distribution of the index of refraction having spatial frequency components denoted by H', and these scattered fields end up traveling in the outgoing H-channel.

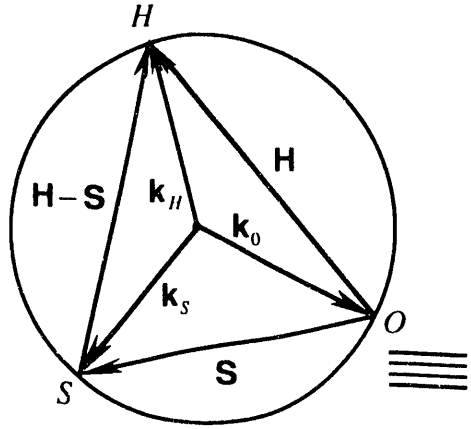

Fig. 7-1.1. Ewald sphere construction for scattering. $\mathbf{k}_0$ is the forward scattered wavevector for fields scattering off crystal planes having reciprocal lattice vectors **H** and **S** to produce fields with wavevectors $\mathbf{k}_H$ and $\mathbf{k}_S$.

From the Ewald sphere construction, one can see that $\mathbf{S}+\mathbf{H}'=\mathbf{H}$. Then, Eq. 7-1.2 reduces to

$$\left(1-\frac{\mathbf{k}_H\cdot\mathbf{k}_H}{k_{0v}^2}\right)E_\alpha^H+\sum_S\sum_\beta g_{\alpha\beta}^{HS}E_\beta^S=0 \tag{7-1.4}$$

where, using terminology similar to Kagan's,[9] the scattering tensor is defined as

$$g_{\alpha\beta}^{HS}=\frac{4\pi}{k_{0v}^2V_0}F_{\alpha\beta}^{(H-S)}, \tag{7-1.5}$$

and α and β are polarization indices of the electric field. Equation 7-1.4 is the dispersion equation for a medium having a tensor index of refraction.

7.2 The Scattering Tensor

The scattering tensor contains important polarization information about scattering processes. For the case of photoelectric scattering far from any bound state resonance or absorption edge, the scattering tensor is

$$\mathbf{g}^{HS}=\begin{pmatrix}g_{xx}^{HS} & g_{xy}^{HS}\\ g_{yx}^{HS} & g_{yy}^{HS}\end{pmatrix}=\left(\frac{4\pi}{k_{0v}^2V_0}\right)f^{H-S}P^{HS} \tag{7-2.1}$$

where the polarization independent part of the structure factor is, from Eq. 6-1.4 for n identical particles,

$$f^{H-S}=-r_e\sum_n\left(D_W(\mathbf{H}-\mathbf{S})f_0+f'-if''\right)e^{-i(\mathbf{H}-\mathbf{S})\cdot\mathbf{r}_n}, \tag{7-2.2}$$

and the polarization matrix is defined as

$$P^{HS}=\begin{pmatrix}P_{xx}^{HS} & P_{xy}^{HS}\\ P_{yx}^{HS} & P_{yy}^{HS}\end{pmatrix}=\begin{pmatrix}\hat{\boldsymbol{\varepsilon}}_x^S\cdot\hat{\boldsymbol{\varepsilon}}_x^H & \hat{\boldsymbol{\varepsilon}}_x^S\cdot\hat{\boldsymbol{\varepsilon}}_y^H\\ \hat{\boldsymbol{\varepsilon}}_y^S\cdot\hat{\boldsymbol{\varepsilon}}_x^H & \hat{\boldsymbol{\varepsilon}}_y^S\cdot\hat{\boldsymbol{\varepsilon}}_y^H\end{pmatrix} \tag{7-2.3}$$

where $\hat{\boldsymbol{\varepsilon}}_x^H$ and $\hat{\boldsymbol{\varepsilon}}_y^H$ are the two transverse polarizations of the scattered electric field with wavevector $\mathbf{k}_H$, and the other two polarizations correspond to the wavevector $\mathbf{k}_S$. The Debye-Waller factor, $D_W(\mathbf{H})$, is a function of the scattering vector and is given by Eq. 5-1.56.

The structure of the scattering tensor can be understood by examining some simple cases. For instance, for scattering from a transmission channel ($S=0$) to a reflection channel (H),

$$\mathbf{g}^{H0} = \left(\frac{4\pi}{k_{0v}^2 V_0}\right) f^H \begin{pmatrix} \hat{\boldsymbol{\varepsilon}}_x^0 \cdot \hat{\boldsymbol{\varepsilon}}_x^H & \hat{\boldsymbol{\varepsilon}}_x^0 \cdot \hat{\boldsymbol{\varepsilon}}_y^H \\ \hat{\boldsymbol{\varepsilon}}_y^0 \cdot \hat{\boldsymbol{\varepsilon}}_x^H & \hat{\boldsymbol{\varepsilon}}_y^0 \cdot \hat{\boldsymbol{\varepsilon}}_y^H \end{pmatrix}. \tag{7-2.4}$$

For the reverse process, scattering from a reflection channel ($S = H$) to a transmission channel ($H = 0$),

$$\mathbf{g}^{0H} = \left(\frac{4\pi}{k_{0v}^2 V_0}\right) f^H \begin{pmatrix} \hat{\boldsymbol{\varepsilon}}_x^H \cdot \hat{\boldsymbol{\varepsilon}}_x^0 & \hat{\boldsymbol{\varepsilon}}_x^H \cdot \hat{\boldsymbol{\varepsilon}}_y^0 \\ \hat{\boldsymbol{\varepsilon}}_y^H \cdot \hat{\boldsymbol{\varepsilon}}_x^0 & \hat{\boldsymbol{\varepsilon}}_y^H \cdot \hat{\boldsymbol{\varepsilon}}_y^0 \end{pmatrix}. \tag{7-2.5}$$

For scattering from a transmission channel ($S = 0$) to a transmission channel ($H = 0$) [normal transmission through a material], or, for scattering from a reflection channel ($S = H$) to a reflection channel (H) [normal transmission in the diffraction direction],

$$\mathbf{g}^{00} = \mathbf{g}^{HH} = \left(\frac{4\pi}{k_{0v}^2 V_0}\right) f^0 \begin{pmatrix} 1 & 0 \\ 0 & 1 \end{pmatrix}. \tag{7-2.6}$$

Since the polarization basis of an electric field is orthonormal, the polarization matrices for transmission are diagonal. The polarization matrices for diffraction are diagonal only if a convenient polarization basis is chosen such as the sigma-pi basis used in Section 5.1 and shown in Fig. 5-1.1--in such a basis polarization mixing is no longer possible.

When the sigma-pi polarization basis discussed in Section 5.1 is used, the two electric field components completely decouple in the dispersion relation, and the dispersion relation reduces to two independent relations for each electric field component

$$\left(1 - \frac{\mathbf{k}_H \cdot \mathbf{k}_H}{k_{0v}^2}\right) E_\alpha^H + \sum_S g_{\alpha\alpha}^{HS} E_\alpha^S = 0. \tag{7-2.7}$$

For the electronic scattering described above or for spin averaged dipole scattering, the polarization matrices, P^{0H} and P^{H0}, are equivalent, and they are given by Eq. 5-1.47 for electric dipole scattering or Eq. 5-1.46 for magnetic dipole scattering. For spin averaged dipole scattering from q identical particles

$$f^{H-S} = -\frac{L_M(\mathbf{k}_i) L_M(\mathbf{k}_f) C}{4k_{0v}} \left(\frac{2j_n + 1}{2j_i + 1}\right) \frac{\Gamma_{rad}}{\hbar} \frac{1}{\omega_{\mathbf{k}_i} - \omega_0 + i\Gamma/2\hbar} \sum_q e^{-i(\mathbf{H}-\mathbf{S})\cdot\mathbf{r}_q}. \tag{7-2.8}$$

The quantities $L_M(\mathbf{k}_i)$ and $L_M(\mathbf{k}_f)$ are the Lamb-Mössbauer factors that take into account the vibrations of the scatterers. From Eq. 4-3.66

$$L_M(\mathbf{k}_i) = \langle f_\alpha | e^{i\mathbf{k}_i \cdot \mathbf{u}} | i_\alpha \rangle, \quad L_M(\mathbf{k}_f) = \langle f_\alpha | e^{-i\mathbf{k}_f \cdot \mathbf{u}} | i_\alpha \rangle \tag{7-2.9}$$

where $|i_\alpha\rangle$ and $|f_\alpha\rangle$ are initial and final phonon states. The quantity C is the enrichment factor describing the concentration of resonant scatterers at the lattice sites.

In general, when multipole scattering is included, polarization mixing occurs in both the transmission and reflection channels. For nuclear scattering the scattering tensor in Eq. 7-2.1 has an angular independent structure factor defined as (from Eq. 5-1.4 for q identical particles and averaged over the initial state spins)

$$f^{H-S} = -(2\pi/k_{0v})\frac{L_M(\mathbf{k}_i)L_M(\mathbf{k}_f)C\Gamma(L,\lambda)}{E_i - E_n + \hbar\omega_{\mathbf{k}_i} + i\Gamma_n/2}\frac{\langle j_f m_f LM | j_f L j_n m_n\rangle^2}{(2j_i+1)}\sum_q e^{-i(\mathbf{H}-\mathbf{S})\cdot\mathbf{r}_q}, \quad (7\text{-}2.10)$$

and the polarization matrix is given by Eq. 5-1.5 with the substitution $\hat{\boldsymbol{\varepsilon}}^f_\alpha \rightarrow \hat{\boldsymbol{\varepsilon}}^H_\alpha$ and $\hat{\boldsymbol{\varepsilon}}^i_\alpha \rightarrow \hat{\boldsymbol{\varepsilon}}^S_\alpha$, where $\alpha = x,y$.

7.3 Linearized Dispersion Equations

The dispersion equations, Eq. 7-1.4, are a set of homogeneous nonlinear coupled field equations. The nonlinearity comes from the quadratic term k_H^2 and the polarization directions of the fields inside the medium represented in the polarization matrices. However, for X-ray photons, the dispersions equations can be linearized because most materials are essentially transparent to such photons. Since incoming X-ray photons are only slightly affected by the presence of a medium, the polarization directions of the fields inside a medium can be approximated as the polarization directions of the fields in vacuum. This is a common approximation used in dynamical diffraction theory.

If the index of refraction in the H channel is $\sqrt{1+2\varepsilon_H}$ where ε_H is a small complex number, then the quadratic term in the dispersion equation is $k_H^2 = (1+2\varepsilon_H)k_{0v}^2$ where k_{0v} is the vacuum wavenumber. The dispersion equation, Eq. 7-1.4, then reduces to the simpler form

$$2\varepsilon_H E^H_\alpha = \sum_{S\beta} g^{HS}_{\alpha\beta} E^S_\beta. \quad (7\text{-}3.1)$$

Making the further approximation that

$$k_H \approx (1+\varepsilon_H)k_{0v} \quad (7\text{-}3.2)$$

completes the linearization of the dispersion equations. This is shown for a two-beam (or two-channel) example in the following section.

7.4 Two-Beam Analytical Solution

In certain situations reasonably simple analytical expressions can be constructed for the scattered fields within a medium. This occurs for electronic scattering with a wise choice of the sigma and pi polarization vectors that diagonalize the scattering tensor. The multipole scattering tensor can also be diagonalized for certain orientations between the quantization axis of the scatterer and the scattering plane. For the two beam case where there are only two scattering channels, $S = 0$ and $S = H$, along which travel a forward scattered and a diffracted electric field, the decoupled dispersion relations can be written in the form

$$\begin{pmatrix} (g_{xx}^{00} - 2\varepsilon_0) & g_{xx}^{01} & 0 & 0 \\ g_{xx}^{10} & (g_{xx}^{11} - 2\varepsilon_1) & 0 & 0 \\ 0 & 0 & (g_{yy}^{00} - 2\varepsilon_0) & g_{yy}^{01} \\ 0 & 0 & g_{yy}^{10} & (g_{yy}^{11} - 2\varepsilon_1) \end{pmatrix} \begin{pmatrix} T_x \\ R_x \\ T_y \\ R_y \end{pmatrix} = \mathbf{G} \cdot \mathbf{v} = 0. \quad (7\text{-}4.1)$$

where

$$\mathbf{T} = \mathbf{E}^{S=0} \quad \text{(transmitted field)} \quad (7\text{-}4.2)$$

$$\mathbf{R} = \mathbf{E}^{S=H} \quad \text{(diffracted, or reflected, field)}. \quad (7\text{-}4.3)$$

$H \equiv 1$, and x,y denote the two transverse polarizations of the electric field (in the sigma and pi polarization basis shown in Fig. 5-1.1, $x = \sigma$, and $y = \pi$).

To solve the dispersion equation, a relationship between ε_0 and ε_1 must be found. This can be done by noting that refraction occurs for a wave entering a medium from free space

$$\mathbf{k}_0 = \mathbf{k}_{0v} + k_{0v}\delta\hat{\mathbf{n}} \quad (7\text{-}4.4)$$

where $\mathbf{k}_{0v}$ is the vacuum wavevector in the forward direction (all vacuum quantities will have the index v), $\hat{\mathbf{n}}$ is an interior normal to the crystal surface, and δ is a quantity describing how much refraction has taken place.

Using Eqs. 7-3.2 and 7-4.4, to first order in δ and ε_0 (to linearize the dispersion equations), one finds that

$$\delta = \varepsilon_0 / \gamma_0 \quad (7\text{-}4.5)$$

where

$$\gamma_0 = \hat{\mathbf{k}}_{0v} \cdot \hat{\mathbf{n}}. \quad (7\text{-}4.6)$$

Applying Bragg's law,

$$\mathbf{k}_1 = \mathbf{k}_0 + \mathbf{H}, \quad (7\text{-}4.7)$$

yields, to first order in $\varepsilon_1, \varepsilon_0$,and δ,

$$k_{0v}^2(1+2\varepsilon_1) = k_{0v}^2(1+2\varepsilon_0) + H^2 + 2\left(\mathbf{k}_{0v} + k_{0v}\delta\hat{\mathbf{n}}\right)$$

which reduces to

$$\varepsilon_1 = \varepsilon_0 + \frac{\mathbf{H}\cdot(\mathbf{H}+2\mathbf{k}_{0v})}{2k_{0v}^2} + \delta\left(\hat{\mathbf{k}}_1 - \hat{\mathbf{k}}_0\right)\cdot\hat{\mathbf{n}}$$

$$\approx \alpha_B/2 + \varepsilon_0/b \tag{7-4.8}$$

where α_B is a deviation from Bragg parameter

$$\alpha_B = \mathbf{H}\cdot(\mathbf{H}+2\mathbf{k}_{0v})/k_{0v}^2. \tag{7-4.9}$$

The parameter b is an asymmetry factor

$$b = \gamma_0/\gamma_1 \tag{7-4.10}$$

where

$$\gamma_1 = \hat{\mathbf{k}}_1\cdot\hat{\mathbf{n}}. \tag{7-4.11}$$

The α_B parameter describes how close a reciprocal lattice point must be to the Ewald sphere in order to still satisfy the Bragg condition. The parameter can be evaluated by examining how Bragg's law varies near the Ewald sphere

$$H = |\mathbf{k}_1 - \mathbf{k}_0| = \sqrt{k_1^2 + k_0^2 - 2k_1k_0\cos 2\theta_B}$$

$$\approx 2k_{0v}\sin\theta_B\left(1 + \frac{\varepsilon_1+\varepsilon_0}{2}\right) \tag{7-4.12}$$

where $2\theta_B$ is the scattering angle between $\mathbf{k}_1$ and $\mathbf{k}_0$, and θ_B is the Bragg angle. Also note that

$$\mathbf{H}\cdot\mathbf{k}_{0v} = -Hk_{0v}\sin\theta_0 \tag{7-4.13}$$

where $\theta_0 + \pi/2$ is the angle between $\mathbf{H}$ and $\mathbf{k}_{0v}$ (see Fig. 7-4.1). When the Bragg condition is satisfied, θ_0 is nearly equal to θ_B. Defining a deviation angle

$$\Delta\theta = \theta_0 - \theta_B \tag{7-4.14}$$

that is a measure of the angular deviation from Bragg gives

$$\alpha_B = -2\Delta\theta\sin 2\theta_B - 4(\Delta E/E)\sin^2\theta_B \tag{7-4.15}$$

where E is the incoming photon energy, and ΔE is the deviation of the Bragg energy from the incoming photon energy

$$\Delta E = E - E_B = \hbar c\left[k_{0v} - (k_1+k_0)/2\right]. \tag{7-4.16}$$

The Bragg energy has been defined to be proportional to the average wavenumber inside the medium. To remain close to the Bragg condition, either an angular or energy constraint must be satisfied: $\Delta\theta$ or ΔE must be close to zero. For instance, when examining the angular spectrum of a scattered field, the Bragg energy is set equal to the incoming photon

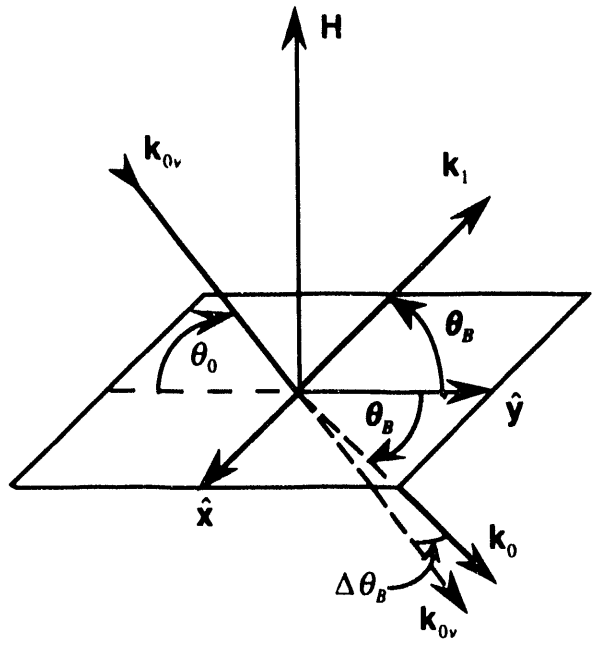

Fig. 7-4.1. Diffraction from crystal planes. The xy-plane is the crystal surface, and **H** is a reciprocal lattice vector perpendicular to the crystal planes. Present geometry shows a symmetric Bragg reflection ($b=-1$). Incoming beam from vacuum, $\mathbf{k}_{0v}$, strikes the surface, and refraction produces outgoing beam, $\mathbf{k}_0$, shifted by $\Delta\theta_B$ from the incident angle θ_0.

energy, $E_B = E$ or $\Delta E = 0$, and the Bragg angle is obtained through Bragg's law and $\alpha_B = -2\Delta\theta\sin 2\theta_B$. When examining the energy spectrum of a scattered field, the Bragg angle is set equal to the incoming photon angle, $\theta_B = \theta_0$ or $\Delta\theta = 0$, and the Bragg energy is obtained from Bragg's law and $\alpha_B = -4(\Delta E/E)\sin^2\theta_B$. Bragg's law, Eq. 7-4.7, can be rewritten as the following expression:

$$E_B \sin\theta_B = \hbar cH/2 \tag{7-4.17}$$

where

$$H = 2\pi/d_{hkl}, \tag{7-4.18}$$

and d_{hkl} is the lattice spacing of the $[hkl]$ reflection.

The solution to Eq. 7-4.1 then reduces to solving a familiar eigenvalue-eigenvector problem. The characteristic equation is

$$\det(\mathbf{G}_{lin} - 2\varepsilon_0\mathbf{I}) = 0 \tag{7-4.19}$$

where

$$\mathbf{G}_{lin} = \begin{pmatrix} g_{xx}^{00} & g_{xx}^{01} & 0 & \\ g_{xx}^{10} & (bg_{xx}^{11} - b\alpha_B) & & \\ & & g_{yy}^{00} & g_{yy}^{01} \\ 0 & & g_{yy}^{10} & (bg_{yy}^{11} - b\alpha_B) \end{pmatrix}. \tag{7-4.20}$$

The solution to the characteristic equation yields the four eigenvalues

$$\varepsilon_{0\beta}^{(1,2)} = \frac{1}{4}\left(g_{\beta\beta}^{00} + bg_{\beta\beta}^{11} - b\alpha_B\right) \pm \frac{1}{4}\sqrt{\left(g_{\beta\beta}^{00} - bg_{\beta\beta}^{11} + b\alpha_B\right)^2 + 4bg_{\beta\beta}^{01}g_{\beta\beta}^{10}} \tag{7-4.21}$$

where $\beta = x, y$.

To complete the solution to the inhomogeneous wave equation, boundary conditions must be supplied. In order to obtain analytical expressions to the reflected and transmitted fields, interfacial reflections at the entrant and exit crystal surfaces will be neglected. These reflections occur when a field crosses from one medium to another (such as from vacuum to the crystal medium). The Bragg and Laue solutions are given below using this approximation.

BRAGG CASE: At the top and bottom surfaces of the crystal (see Fig. 7-4.2), the boundary conditions are

$$\hat{\mathbf{n}}\cdot\mathbf{r} = 0: \qquad \mathbf{E}_{0_v} = \mathbf{T} = \sum_{l=1}^{2}\sum_{\alpha} T_\alpha^l \hat{\boldsymbol{\varepsilon}}_\alpha^0 \tag{7-4.22}$$

$$\hat{\mathbf{n}}\cdot\mathbf{r} = d: \qquad 0 = \mathbf{R} = e^{i(\mathbf{k}_{0_v}+\mathbf{H})\cdot\mathbf{r}} \sum_{l=1}^{2}\sum_{\alpha} R_\alpha^l e^{i\kappa_\alpha^l d}\hat{\boldsymbol{\varepsilon}}_\alpha^H \tag{7-4.23}$$

where

$$\mathbf{k}_0 = \mathbf{k}_{0_v} + \kappa_\alpha^l \hat{\mathbf{n}} \tag{7-4.24}$$

$$\mathbf{k}_H \equiv \mathbf{k}_1 = \mathbf{k}_0 + \mathbf{H} \tag{7-4.25}$$

$$\kappa_\alpha^l = k_{0_v}\varepsilon_{0\alpha}^l/\gamma_0 \tag{7-4.26}$$

$\alpha = x, y$, $l = 1,2$ is the eigenvector index, and $\mathbf{E}_{0_v}$ is the incoming electric field from the vacuum. For Bragg diffraction and for no interfacial reflections, all of the incoming field scatters into the transmission channel, and, at the exit surface there is no incoming field scattering into the reflection channel.

For each eigenvalue in Eq. 7-4.21, there is a unique eigenvector

$$\mathbf{v}_\alpha^l = \begin{pmatrix} T_\alpha^l \\ R_\alpha^l \end{pmatrix}. \tag{7-4.27}$$

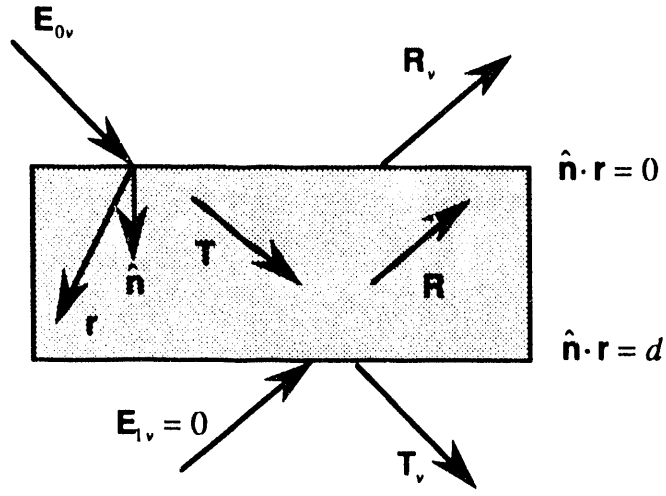

Fig. 7-4.2. Bragg diffraction geometry.

The reflection amplitudes can then be expressed in terms of the transmission amplitudes

$$R_\alpha^l = D_\alpha^l T_\alpha^l \tag{7-4.28}$$

where

$$D_\alpha^l = \left(v_\alpha^l\right)_2 / \left(v_\alpha^l\right)_1, \tag{7-4.29}$$

and $\left(v_\alpha^l\right)_i$ is the i^{th} component of $\mathbf{v}_\alpha^l$. Expressing the reflection amplitudes in terms of the transmission amplitudes enables one to solve a decoupled boundary value equation for the four transmission and four reflected wavefields inside the crystal

$$\mathbf{u}_{in} = \mathbf{B}_c \cdot \mathbf{w} \tag{7-4.30}$$

or, written out explicitly,

$$\begin{pmatrix} E_{0vx} \\ 0 \\ E_{0vy} \\ 0 \end{pmatrix} = \begin{pmatrix} 1 & 1 & 0 & \\ D_x^1 e^{i\kappa_x^1 d} & D_x^2 e^{i\kappa_x^2 d} & & \\ & & 1 & 1 \\ 0 & & D_y^1 e^{i\kappa_y^1 d} & D_y^2 e^{i\kappa_y^2 d} \end{pmatrix} \begin{pmatrix} T_x^1 \\ T_x^2 \\ T_y^1 \\ T_y^2 \end{pmatrix}. \tag{7-4.31}$$

After some algebra, the solution to the boundary condition equation can be written in the form

$$\mathbf{T}\left(\hat{\mathbf{n}}\cdot\mathbf{r} = z\right) = e^{i\mathbf{k}_{0v}\cdot\mathbf{r}} \sum_{l=1}^{2} \sum_{\alpha} T_\alpha^l e^{i\kappa_\alpha^l z} \hat{\boldsymbol{\varepsilon}}_\alpha^0$$

$$= e^{i\mathbf{k}_{0v}\cdot\mathbf{r}} \sum_{\alpha} E_{0v\alpha} \hat{\boldsymbol{\varepsilon}}_\alpha^0 \frac{e^{i\left(\kappa_\alpha^1 z + \kappa_\alpha^2 d\right)}\left(g_{\alpha\alpha}^{00} - 2\varepsilon_{0\alpha}^2\right) - e^{i\left(\kappa_\alpha^2 z + \kappa_\alpha^1 d\right)}\left(g_{\alpha\alpha}^{00} - 2\varepsilon_{0\alpha}^1\right)}{e^{i\kappa_\alpha^2 d}\left(g_{\alpha\alpha}^{00} - 2\varepsilon_{0\alpha}^2\right) - e^{i\kappa_\alpha^1 d}\left(g_{\alpha\alpha}^{00} - 2\varepsilon_{0\alpha}^1\right)}, \tag{7-4.32}$$

and, at the exit surface $z = d$,

$$\mathbf{T}\left(\hat{\mathbf{n}}\cdot\mathbf{r} = d\right) = e^{i\mathbf{k}_{0v}\cdot\mathbf{r}}\sum_{\alpha} E_{0v\alpha}\hat{\boldsymbol{\varepsilon}}_{\alpha}^{0}\frac{e^{i\left(\kappa_{\alpha}^{2}+\kappa_{\alpha}^{1}\right)d}\left(2\varepsilon_{0\alpha}^{1}-2\varepsilon_{0\alpha}^{2}\right)}{e^{i\kappa_{\alpha}^{2}d}\left(g_{\alpha\alpha}^{00}-2\varepsilon_{0\alpha}^{2}\right)-e^{i\kappa_{\alpha}^{1}d}\left(g_{\alpha\alpha}^{00}-2\varepsilon_{0\alpha}^{1}\right)}. \tag{7-4.33}$$

The reflection channel field is

$$\mathbf{R}\left(\hat{\mathbf{n}}\cdot\mathbf{r} = z\right) = e^{i(\mathbf{k}_{0v}+\mathbf{H})\cdot\mathbf{r}}\sum_{l=1}^{2}\sum_{\alpha} D_{\alpha}^{l}T_{\alpha}^{l}e^{i\kappa_{\alpha}^{l}z}\hat{\boldsymbol{\varepsilon}}_{\alpha}^{H}$$

$$= e^{i(\mathbf{k}_{0v}+\mathbf{H})\cdot\mathbf{r}}\sum_{\alpha} E_{0v\alpha}\hat{\boldsymbol{\varepsilon}}_{\alpha}^{H}\frac{bg_{\alpha\alpha}^{10}\left(e^{i\left(\kappa_{\alpha}^{2}d+\kappa_{\alpha}^{1}z\right)}-e^{i\left(\kappa_{\alpha}^{1}d+\kappa_{\alpha}^{2}z\right)}\right)}{e^{i\kappa_{\alpha}^{2}d}\left(g_{\alpha\alpha}^{00}-2\varepsilon_{0\alpha}^{2}\right)-e^{i\kappa_{\alpha}^{1}d}\left(g_{\alpha\alpha}^{00}-2\varepsilon_{0\alpha}^{1}\right)}, \tag{7-4.34}$$

and, at the entrant surface $z = 0$,

$$\mathbf{R}\left(\hat{\mathbf{n}}\cdot\mathbf{r} = 0\right) = e^{i(\mathbf{k}_{0v}+\mathbf{H})\cdot\mathbf{r}}\sum_{\alpha} E_{0v\alpha}\hat{\boldsymbol{\varepsilon}}_{\alpha}^{H}\frac{bg_{\alpha\alpha}^{10}\left(e^{i\kappa_{\alpha}^{2}d}-e^{i\kappa_{\alpha}^{1}d}\right)}{e^{i\kappa_{\alpha}^{2}d}\left(g_{\alpha\alpha}^{00}-2\varepsilon_{0\alpha}^{2}\right)-e^{i\kappa_{\alpha}^{1}d}\left(g_{\alpha\alpha}^{00}-2\varepsilon_{0\alpha}^{1}\right)}. \tag{7-4.35}$$

LAUE CASE: The boundary conditions for this case are (see Fig. 7-4.3)

$$\hat{\mathbf{n}}\cdot\mathbf{r} = 0: \qquad \mathbf{E}_{0v} = \mathbf{T} = \sum_{l=1}^{2}\sum_{\alpha} T_{\alpha}^{l}\hat{\boldsymbol{\varepsilon}}_{\alpha}^{0} \tag{7-4.36}$$

$$\hat{\mathbf{n}}\cdot\mathbf{r} = 0: \qquad 0 = \mathbf{R} = \sum_{l=1}^{2}\sum_{\alpha} R_{\alpha}^{l}\hat{\boldsymbol{\varepsilon}}_{\alpha}^{H}. \tag{7-4.37}$$

For Laue diffraction and for no interfacial reflections, all of the incoming field scatters into the transmission channel, and, at the entrant surface, there is no incoming field scattering into the reflection channel.

The boundary condition matrix for Laue diffraction is

$$\mathbf{B}_{c} = \begin{pmatrix} 1 & 1 & & \\ D_{x}^{1} & D_{x}^{2} & \mathbf{0} & \\ & & 1 & 1 \\ \mathbf{0} & & D_{y}^{1} & D_{y}^{2} \end{pmatrix}. \tag{7-4.38}$$

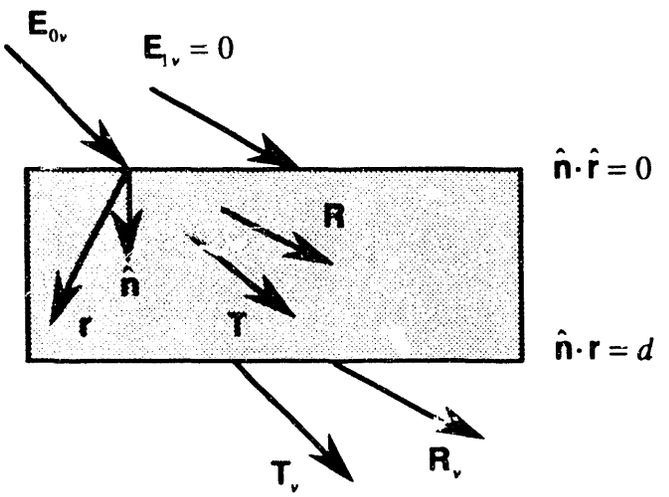

Fig. 7-4.3. Laue diffraction geometry.

Solving the boundary condition equation for the scattering channel field yields

$$\mathbf{T}(\hat{\mathbf{n}}\cdot\mathbf{r}=z)=e^{i\mathbf{k}_{0v}\cdot\mathbf{r}}\sum_{\alpha}E_{0v\alpha}\hat{\boldsymbol{\varepsilon}}_{\alpha}^{0}\frac{e^{i\kappa_{\alpha}^{1}z}\left(g_{\alpha\alpha}^{00}-2\varepsilon_{0\alpha}^{2}\right)-e^{i\kappa_{\alpha}^{2}z}\left(g_{\alpha\alpha}^{00}-2\varepsilon_{0\alpha}^{1}\right)}{\left(2\varepsilon_{0\alpha}^{1}-2\varepsilon_{0\alpha}^{2}\right)} \tag{7-4.40}$$

$$\mathbf{R}(\hat{\mathbf{n}}\cdot\mathbf{r}=z)=e^{i(\mathbf{k}_{0v}+\mathbf{H})\cdot\mathbf{r}}\sum_{\alpha}E_{0v\alpha}\hat{\boldsymbol{\varepsilon}}_{\alpha}^{H}\frac{bg_{\alpha\alpha}^{10}\left(e^{i\kappa_{\alpha}^{2}z}-e^{i\kappa_{\alpha}^{1}z}\right)}{\left(2\varepsilon_{0\alpha}^{1}-2\varepsilon_{0\alpha}^{2}\right)}. \tag{7-4.41}$$

7.5 Dynamical Characteristics of Angular Spectra

In kinematical diffraction theory the angular distribution of the scattered fields consists of delta function peaks situated at Bragg angles. In dynamical diffraction theory the angular width of the Bragg peaks are broadened due to multiple scattering. The angular distribution at a Bragg peak can be characterized by an η_{α}' parameter (or a y_{α} parameter described by Zachariasen)[3, 4]

$$\eta_{\alpha}'=\frac{\left[(1-b)/2\right]\mathrm{Re}\left\{g_{\alpha\alpha}^{00}\right\}+(b/2)\alpha_{B}}{\sqrt{|b|}\left|\mathrm{Re}\left\{g_{\alpha\alpha}^{10}\right\}\right|}. \tag{7-5.1}$$

The above formula assumes that the scatterers in the crystal have space-inversion symmetry and that the origin is chosen at an inversion center (that is, the crystal is centrosymmetric and $g_{\alpha\alpha}^{10}=g_{\alpha\alpha}^{01}$). Also, forward scattering in the transmission channel is assumed to be

identical to forward scattering in the reflection channel: $g^{00}_{\alpha\alpha} = g^{11}_{\alpha\alpha}$. For thick crystals most of the scattered intensity lies in the range $|\eta'_\alpha| < 1$ (see Figs. 7-5.1 and 7-5.2). Thus, an angular width, or Darwin width, of the diffracted beam can be defined as

$$\Delta\theta^\alpha_D = \frac{2\left|\mathrm{Re}\left\{g^{10}_{\alpha\alpha}\right\}\right|}{\sqrt{|b|}\sin 2\theta_B} = \frac{\Delta\theta^\alpha_{Ds}}{\sqrt{|b|}} \tag{7-5.2}$$

where $\Delta\theta^\alpha_{Ds}$ is the symmetric Darwin width for a thick crystal (this definition is useful mainly for Bragg diffraction as can be seen by examining Figs. 7-5.1 and 7-5.2). From Eq. 7-5.1 note that, for Bragg diffraction, the Darwin curve is not centered at the Bragg angle. There is an index of refraction shift from the Bragg angle where the center of the Darwin curve (the point $\eta'_\alpha = 0$) now lies at

$$\theta^\alpha_c = \theta_B + \frac{[(1-b)/2]\mathrm{Re}\left\{g^{00}_{\alpha\alpha}\right\}}{b\sin 2\theta_B}. \tag{7-5.3}$$

The electric field inside the crystal consists of traveling waves propagating perpendicular to the scattering vector, **H**, and standing waves with wavevectors parallel to the scattering vector. Whether a standing wave field has its nodes or antinodes at the scattering planes depends upon the scattering angle and, thus, upon the η'_α parameter. When a standing wave has its antinodes lying at the scattering planes (that is, on the atoms) enhanced absorption occurs, and when it has its nodes lying at the scattering planes absorption processes are suppressed.

From the solution of the dispersion equation there turns out to be, for each scattering channel and for each polarization, two eigenwaves that are a function of the energy of the incident field and the deviation from Bragg, α_B (the two eigenwaves corresponds to the $l = 1$ and 2 solutions having eigenvalues given by Eq. 7-4.21). For Laue diffraction the two eigenwaves are damped exponentially with distance into the crystal. One wave has its nodes lying at the scattering planes (the alpha wave) and the other has its antinodes lying at the scattering planes (the beta wave).[4] Since the beta waves suffer enhanced absorption, these fields die out more quickly leaving only the alpha waves to contribute to the total field amplitude that exits a thick crystal. Since the alpha waves experience suppressed absorption, these fields can travel much further through crystals than would be expected when only photoelectric or resonant absorption is considered. This phenomena is the Borrmann effect--anomalous transmission through crystals.

For Bragg diffraction one eigenwave is damped exponentially while the other grows exponentially with distance inside the crystal. For photoelectric scattering they both have their nodes lying at the scattering planes when $\eta'_\alpha = -1$ and their antinodes lying at the

scattering planes when $\eta'_\alpha = +1$.[1, 3, 4] Thus, as η'_α varies from -1 to $+1$, the electric field experiences suppressed absorption to enhanced absorption--this is the reason for the asymmetrical shape of the Darwin curve in Fig. 7-5.1. For resonant scattering the phase of the eigenwaves changes by π as the resonance curve is traversed from frequencies above the resonant frequency to those below the resonant frequency. Thus, the η'_α points where suppressed and enhanced absorption occur are at opposite sides of the Darwin curve when operating on opposite sides of the resonant curve--this is shown in Fig 7-5.3. As the absorption in the forward channel, $\mathrm{Im}\{g^{00}_{\alpha\alpha}\}$, becomes more predominant than the effective absorption resulting from scattering from the transmission to the reflection channel, $\mathrm{Im}\{g^{10}_{\alpha\alpha}\}$, the peak intensity shifts from $\eta'_\alpha = -1$ to $\eta'_\alpha = 0$, and the Darwin curve becomes more symmetrical. Since in general $\mathrm{Im}\{g^{00}_{\alpha\alpha}\} > \mathrm{Im}\{g^{10}_{\alpha\alpha}\}$, there is always a shift in the peak intensity towards $\eta'_\alpha = 0$.

The Borrmann effect is of particular interest in resonant scattering because absorption processes are always present and are usually predominant. For instance, for an isolated ^{57}Fe atom, internal conversion prevents the efficiency of photon production for a scattering event from being greater that 11%. However, by scattering off a lattice of ^{57}Fe atoms, the efficiency can be made much greater than 11% through the Borrmann effect.[12]

The figures below are rocking curves for pi polarized 14.4 keV radiation diffracting from a body centered cubic crystal of $\alpha-{}^{56}\mathrm{Fe}{}^{57}\mathrm{Fe}$ having a lattice spacing of 5 Å. There is one ^{56}Fe and ^{57}Fe atom per unit cell, and the ^{57}Fe atom lies at the center. No such iron crystal has yet been fabricated, but such a structure lets one examine resonant scattering by partially turning off the nonresonant photoelectric scattering. For instance, resonant nuclear diffraction is allowed for any combination of Miller indices that satisfies Bragg's law, but when the sum of the Miller indices is odd ($h+k+l = 2n+1$, $n = 0,1,2,\ldots$) photoelelectric diffraction is forbidden. For simplicity the resonant ^{57}Fe nuclei are assumed to have no internal hyperfine fields--they are therefore single line emitters (An iron crystal is inherently magnetic, but by adding impurities, such as was done for stainless steel or for YIG,[13] the internal fields can be suppressed. α - Fe naturally has a bcc crystal structure with a lattice spacing of 2.8665 Å. The lattice spacing of 5 Å is used as an attempt at approximating the larger unit cell constructed when impurities are added to produce a single line emitter.). Also, all Debye-Waller factors, Lamb-Mössbauer factors, and resonant enrichment factors have been set to unity.

Figures 7-5.1 and 7-5.2 are photoelectric rocking curves for the allowed [0 0 2] reflection and for various thicknesses. Resonant nuclear scattering, though also allowed, is ignored in the calculations. In Fig. 7-5.1 the oscillations, or Pendellösung fringes, for the $10\mu m$ thick crystal are caused by the interference of the two eigenwaves traveling in the

reflection channel. For $d = 1cm$ one of the eigenwaves has completely died off exponentially with distance which eliminates the possibility for interference between the eigenwaves to occur at the exit surface.

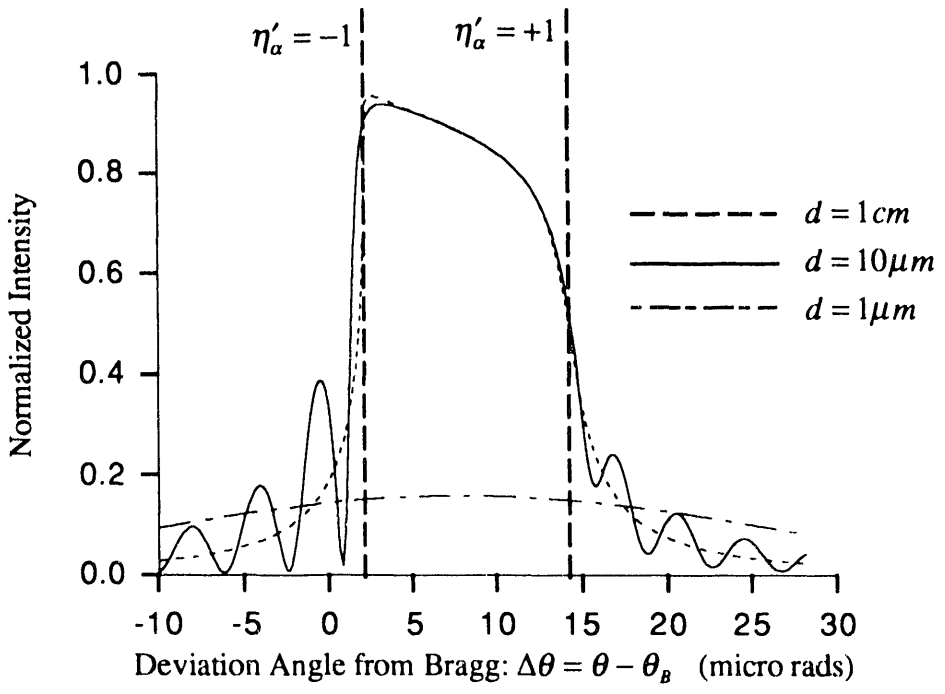

Fig. 7-5.1. Bragg diffraction rocking curves for [0 0 2] reflection for various thicknesses. Only photoelectric scattering is being considered --resonant nuclear scattering is being ignored.

For Bragg diffraction the primary extinction length, or crystal penetration depth through which most of the transmission channel fields are reflected out of the crystal, can be approximated from Bragg's law, Eq. 7-4.17, as

$$d_{ext} = \frac{2\pi}{\Delta H} = \frac{2\pi}{H}\frac{\tan\theta_B}{\Delta\theta_w} \tag{7-5.4}$$

where $\Delta\theta_w$ is the angular width of the Darwin curve (full width at half maximum). This expression describes how much of a crystal is involved in diffraction by how far a reciprocal lattice point can be from the Ewald sphere before Bragg's law is seriously violated. For the crystal considered in this example, the Bragg angle for the [0 0 2] reflection is 9.9° for 14.4 keV photons, and $2\pi/H = 5\text{Å}/2$. For $d = 1\text{cm}$ the Darwin width is $12\mu\text{rad}$, and thus $d_{ext} \approx 3.6\mu\text{m}$ and the crystal is several thousand extinction lengths thick. When $d = 10\mu\text{m}$ a far less number of planes contribute toward diffraction,

thus the angular width is slightly broader than for the 1cm thick crystal. The extinction length is now approximately 3.3μm, and the fields penetrate a far greater fraction of the crystal thickness. When $d = 1\mu$m, the Darwin width is 41μrad and the fields penetrate the entire thickness of the crystal: $d_{ext} \approx 1\mu$m.

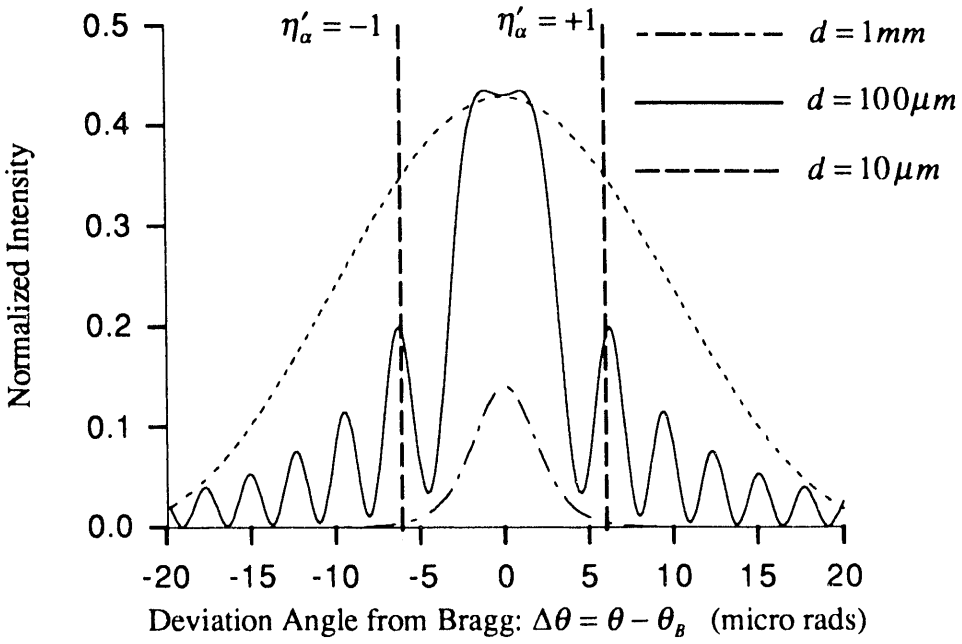

Fig. 7-5.2. Laue diffraction rocking curves for [0 0 2] reflection for various thicknesses. Only photoelectric scattering is being considered--resonant nuclear scattering is being ignored.

The photoelectric absorption length for this crystal is roughly $0.5\mu m$. Thus, the Borrmann effect is readily seen in the Laue diffraction rocking curves in Fig. 7-5.2. When the crystal is $10\mu m$, or 20 absorption lengths thick, the transmitted intensity peaks at 40% whereas a value 9 orders of magnitude less would be expected if only photoelectric absorption was considered.

For pure resonant scattering when $\omega - \omega_0 = 0$, the Darwin width goes to zero since the scattering tensor becomes pure imaginary. The Borrmann effect persists at the center of the profile because the nodes of the fields inside the crystal lie at the scattering planes. Increasing the crystal thickness so that more planes contribute to reflecting the field out of the crystal pushes the peak reflectivity closer to unity. This effect is commonly referred to as the suppression of the inelastic channel.[9] Because the effective transmission absorption length is roughly 600 Å when the incoming field is on resonance, the transmitted field is quite negligible for the 10μm thick crystal used in Figs. 7-5.3 and 7-5.4.

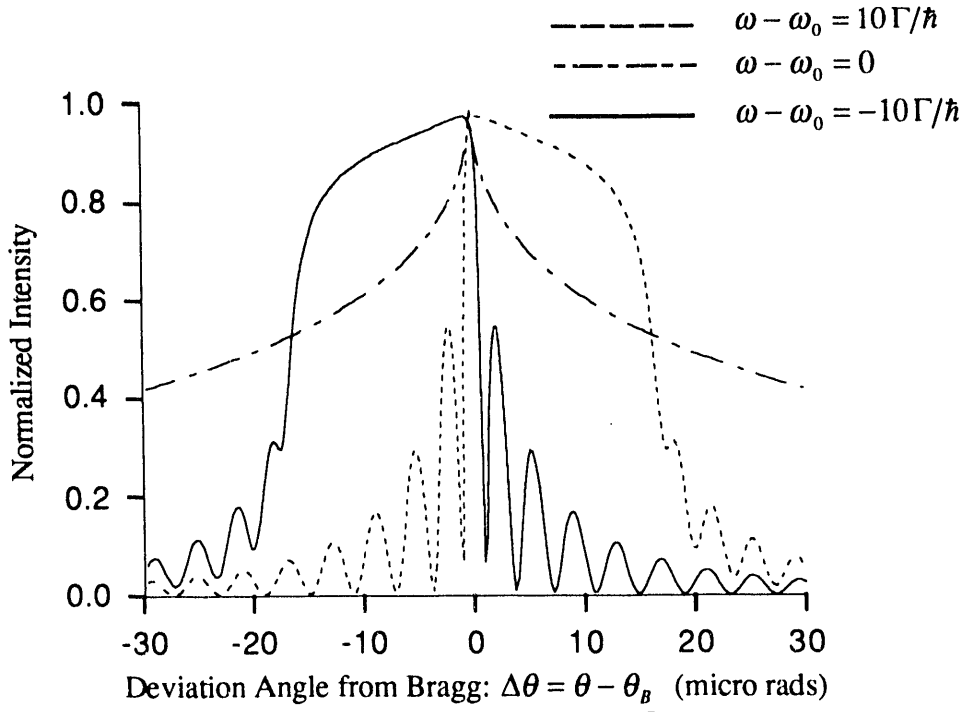

Fig. 7-5.3. Bragg diffraction rocking curves for [0 0 1] reflection for various positions on the resonance curve. Only resonant nuclear scattering is being considered--photoelectric scattering is being ignored. Crystal thickness is 10μm.

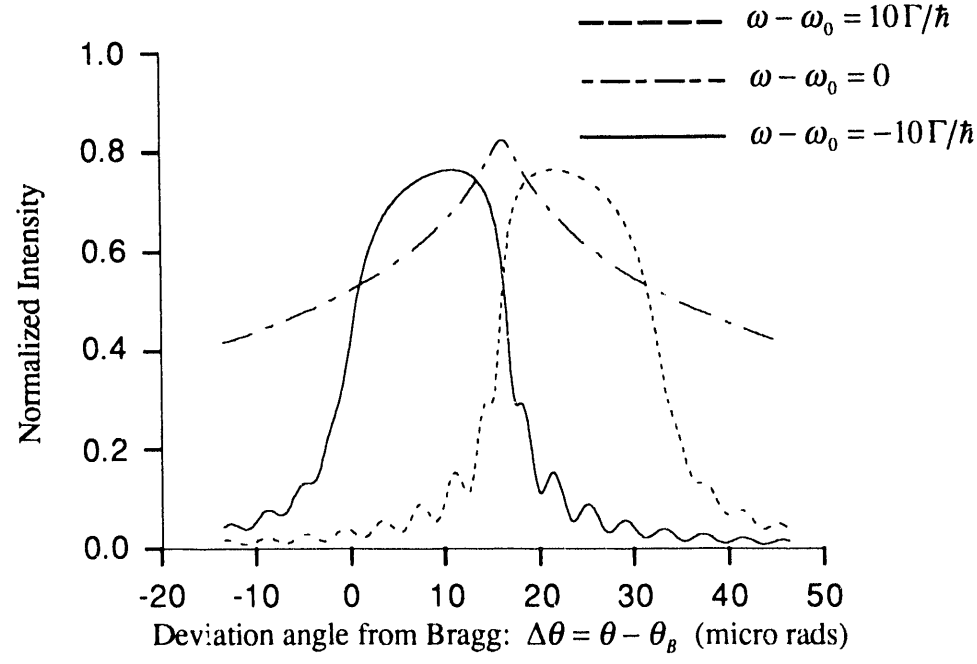

Fig. 7-5.4. Bragg diffraction rocking curves for [0 0 1] reflection for various positions on the resonance curve. Both resonant nuclear and photoelectric scattering is considered. Crystal thickness is 10μm. The point $\Delta\theta \approx 16\mu$rad occurs at $\eta'_\alpha = \pm 1,0$ for the central curve (this is where the central curve peaks), at $\eta'_\alpha = -1$ for the curve on the right, and at $\eta'_\alpha = +1$ for the curve on the left.

7.6 Dynamical Characteristics of Energy Spectra

The expressions for the transmission and reflection channel fields are too complicated in their present form to see the dynamical effects of frequency shifts and speedup rates resulting from multiple scattering. Also, since there are now two eigenwaves traveling in a particular channel, ascribing a single frequency shift or speedup rate to an exiting field is no longer generally possible. However, in certain limiting cases in which only one predominant eigenwave manages to exit the crystal, one can easily examine the dynamical effects of multiple scattering. These limiting cases are described below.

CASE 1: Far Off Bragg.

When the direction of the incoming field is set to be far from any Bragg angle,

$$\alpha_B >> \left|g_{\alpha\alpha}^{00}\right| \text{ and } \left|g_{\alpha\alpha}^{10}\right|, \tag{7-6.1}$$

the eigenvalues reduce to

$$\varepsilon_{0\beta}^{(1,2)} = \frac{1}{4}\left[g_{\beta\beta}^{00}(1+b) - b\alpha_B\right] \pm \frac{1}{4}\left[\left|b\alpha_B\right| - g_{\beta\beta}^{00}(1-b)\frac{\left|b\alpha_B\right|}{b\alpha_B}\right] \tag{7-6.2}$$

for Bragg ($b < 0$) and Laue ($b > 0$) diffraction. For both Bragg and Laue diffraction, the reflection channel field is negligible, $\mathbf{R}(\omega) \approx 0$, since it falls off as $g_{\beta\beta}^{10}/\alpha_B$ while the transmission channel field reduces to

$$\mathbf{T}(\omega) = e^{i\mathbf{k}_{0\nu}\cdot\mathbf{r}} \sum_{\alpha} E_{0\nu\alpha}(\omega)\hat{\boldsymbol{\varepsilon}}_{\alpha}^{0} e^{i\left[g_{\alpha\alpha}^{00}(\omega)/2\right]k_{0\nu}L} \tag{7-6.3}$$

where $$L = d/\gamma_0 . \tag{7-6.4}$$

For combined resonant dipole and nonresonant scattering, the scattering tensor element for forward scattering is (from Eqs. 5-1.48 and 7-1.5)

$$g_{\alpha\alpha}^{00}(\omega)/2 = \frac{2\pi}{k_{0\nu}^2} nF\left(\mathbf{k}_f = \mathbf{k}_i\right) + \mu^{00}(\omega)/2k_{0\nu} . \tag{7-6.5}$$

The Lamb-Mössbauer and resonant enrichment factors have been included in the scattering amplitude, and $\mu^{00}(\omega)/k_{0\nu} = \left[g_{\alpha\alpha}^{00}(\omega)\right]_{nonres}$ is given by Eqs 7-2.1 and 7-2.2 for photoelectric scattering

$$\mu^{00}(\omega) = -\left(\frac{4\pi}{k_{0\nu}}\right) nr_e\left[D_W(0)f_0 + f'(\omega) - if''(\omega)\right] \tag{7-6.6}$$

(the imaginary part of $\mu^{00}(\omega)$ is the absorption coefficient). For the simple two-beam solution in Section 7.4, the expressions on the right side of Eq. 7-6.5 are independent of polarization since they describe forward scattering. Equation 7-6.3 is precisely the same

solution as that obtained for the transmitted field from an isotropic medium in Section 6.5. The dynamical effects explored in that section then also apply equally well for this off-Bragg case.

CASE 2: Thin Crystal Approximation.

For the thin crystal approximation

$$k_{0v}\varepsilon'_{0\beta}d/\gamma_0 << 1. \tag{7-6.7}$$

In this approximation, the transmission channel fields for both Bragg and Laue diffraction are almost unity. Using the approximation $e^x \approx 1+x$ for $|x| << 1$ gives

$$\mathbf{T}_{Bragg}(\omega) = e^{i\mathbf{k}_{0v}\cdot\mathbf{r}}\sum_\alpha E_{0v\alpha}(\omega)\hat{\boldsymbol{\varepsilon}}^0_\alpha \frac{1+ik_{0v}L\left[g^{00}_{\alpha\alpha}(1+b)-b\alpha_B\right]/2}{1+ik_{0v}L\left(bg^{00}_{\alpha\alpha}-b\alpha_B\right)/2} \tag{7-6.8}$$

$$\mathbf{T}_{Laue}(\omega) = e^{i\mathbf{k}_{0v}\cdot\mathbf{r}}\sum_\alpha E_{0v\alpha}(\omega)\hat{\boldsymbol{\varepsilon}}^0_\alpha\left[1+ik_{0v}L\left(g^{00}_{\alpha\alpha}/2\right)\right]. \tag{7-6.9}$$

The solution for Laue transmission is equivalent to Case 1 (being far off Bragg) for a thin crystal, or equivalent to transmission through a thin isotropic slab. For combined resonant dipole and nonresonant scattering

$$\mathbf{T}_{Laue}(\omega) = e^{i\mathbf{k}_{0v}\cdot\mathbf{r}}\sum_\alpha E_{0v\alpha}(\omega)\hat{\boldsymbol{\varepsilon}}^0_\alpha\left[1-\frac{i\Gamma^{00}_s/4\hbar}{\omega-\omega_0+i\Gamma/2\hbar}+i\mu^{00}(\omega)L/2\right] \tag{7-6.10}$$

where, similar to the expression in Eq. 6-5.16 in section 6.5,

$$\Gamma^{00}_s = L_M(\mathbf{k}_i)L_M(\mathbf{k}_f=\mathbf{k}_i)Cn\sigma_0\Gamma L \tag{7-6.11}$$

and $L = d/\gamma_0$. Thus, for a thin crystal, Laue transmission channel fields exhibit no frequency shifts or decay rate speedups.

For Bragg scattering the transmission channel field is

$$\mathbf{T}_{Bragg}(\omega) = e^{i\mathbf{k}_{0v}\cdot\mathbf{r}}\sum_\alpha E_{0v\alpha}(\omega)\hat{\boldsymbol{\varepsilon}}^0_\alpha\left[\xi+\frac{ia\left[\xi b-(1+b)\right]}{\omega-\omega_0+i\Gamma/2\hbar-iab}\right] \tag{7-6.12}$$

where

$$a = \frac{\Gamma^{00}_s/4\hbar}{1+ib\mu^{00}(\omega)L/2-ib\alpha_B k_{0v}L/2} \tag{7-6.13}$$

and

$$\xi = \frac{1+i(1+b)\mu^{00}(\omega)L/2-ib\alpha_B k_{0v}L/2}{1+ib\mu^{00}(\omega)L/2-ib\alpha_B k_{0v}L/2}. \tag{7-6.14}$$

Since $\xi \approx 1$ in the thin crystal approximation, the transmitted field can be simplified to

$$\mathbf{T}_{Bragg}(\omega) = e^{i\mathbf{k}_{0v}\cdot\mathbf{r}} \sum_{\alpha} E_{0v\alpha}(\omega)\hat{\boldsymbol{\varepsilon}}_{\alpha}^{0}\left[1 - \frac{(\omega_s - i\Gamma_s/2\hbar)/b}{\omega - (\omega_0 + \omega_s) + i(\Gamma + \Gamma_s)/2\hbar}\right] \tag{7-6.15}$$

where
$$\omega_s = \mathrm{Re}\left\{\frac{ib(\Gamma_s^{00}/4\hbar)}{1 + ib\mu^{00}(\omega)L/2 - ib\alpha_B k_{0v}L/2}\right\}$$

$$= \frac{b(\Gamma_s^{00}/4\hbar)\left(\mathrm{Re}\{b\mu^{00}(\omega)\}L/2 - b\alpha_B k_{0v}L/2\right)}{\left(1 - \mathrm{Im}\{b\mu^{00}(\omega)\}L/2\right)^2 + \left(\mathrm{Re}\{b\mu^{00}(\omega)\}L/2 - b\alpha_B k_{0v}L/2\right)^2} \tag{7-6.16}$$

and
$$\Gamma_s = -\mathrm{Im}\left\{\frac{ib(\Gamma_s^{00}/2)}{1 + ib\mu^{00}(\omega)L/2 - ib\alpha_B k_{0v}L/2}\right\}$$

$$= \frac{-b(\Gamma_s^{00}/2)\left(1 - \mathrm{Im}\{b\mu^{00}(\omega)\}L/2\right)}{\left(1 - \mathrm{Im}\{b\mu^{00}(\omega)\}L/2\right)^2 + \left(\mathrm{Re}\{b\mu^{00}(\omega)\}L/2 - b\alpha_B k_{0v}L/2\right)^2}. \tag{7-6.17}$$

The second term in the brackets of Eq. 7-6.15 exhibits, in contrast to the transmitted field through an isotropic thin slab, a frequency shift, ω_s, and a speedup rate, Γ_s. However, since ω_s is proportional to the square of the crystal thickness, it is an exceedingly small quantity. The speedup rate is roughly proportional to the on-resonance thickness rate, $\Gamma_s \approx -b(\Gamma_s^{00}/2)$, for thin crystals.

Applying the thin crystal approximation to the reflection channel field for Bragg and Laue diffraction gives

$$\mathbf{R}_{Bragg}(\omega) = e^{i(\mathbf{k}_{0v}+\mathbf{H})\cdot\mathbf{r}} \sum_{\alpha} E_{0v\alpha}(\omega)\hat{\boldsymbol{\varepsilon}}_{\alpha}^{II} \frac{-ik_{0v}Lbg_{\alpha\alpha}^{10}/2}{1 + ik_{0v}L(bg_{\alpha\alpha}^{00} - b\alpha_B)/2} \tag{7-6.18}$$

$$\mathbf{R}_{Laue}(\omega) = e^{i(\mathbf{k}_{0v}+\mathbf{H})\cdot\mathbf{r}} \sum_{\alpha} E_{0v\alpha}(\omega)\hat{\boldsymbol{\varepsilon}}_{\alpha}^{II}\left(-ik_{0v}Lbg_{\alpha\alpha}^{10}/2\right). \tag{7-6.19}$$

For combined resonant dipole and nonresonant scattering the Laue diffracted field reduces to

$$\mathbf{R}_{Laue}(\omega) = e^{i(\mathbf{k}_{0v}+\mathbf{H})\cdot\mathbf{r}} \sum_{\alpha} E_{0v\alpha}(\omega)\hat{\boldsymbol{\varepsilon}}_{\alpha}^{II}\left[\frac{ib\Gamma_{s\alpha}^{10}/4\hbar}{\omega - \omega_0 + i\Gamma/2\hbar} - ib\mu_{\alpha}^{10}(\omega)L/2\right] \tag{7-6.20}$$

where, for resonant dipole scattering,

$$\Gamma_{s\alpha}^{10} = L_M(\mathbf{k}_i)L_M(\mathbf{k}_f)C\sigma_0\Gamma L(\mathbf{u}_\alpha^{H*}\cdot\mathbf{u}_\alpha^0)\frac{1}{V_0}\sum_n e^{-i\mathbf{H}\cdot\mathbf{r}_n} \tag{7-6.21}$$

and, for nonresonant photoelectric scattering,

$$\mu_\alpha^{10}(\omega) = -\left(\frac{4\pi}{k_{0v}V_0}\right)r_e(\hat{\boldsymbol{\varepsilon}}_\alpha^{H*}\cdot\hat{\boldsymbol{\varepsilon}}_\alpha^0)\sum_n\left[D_W(\mathbf{H})f_0 + f'(\omega) - if''(\omega)\right]e^{-i\mathbf{H}\cdot\mathbf{r}_n}. \tag{7-6.22}$$

Again, as was the case for the Laue transmission field, there are no frequency shifts or speedup rates for Laue diffraction from a thin crystal.

The Bragg diffracted field reduces to

$$\mathbf{R}_{Bragg}(\omega) = e^{i(\mathbf{k}_{0v}+\mathbf{H})\cdot\mathbf{r}}\sum_\alpha E_{0v\alpha}(\omega)\hat{\boldsymbol{\varepsilon}}_\alpha^H\left[\xi_\alpha' + \frac{ib(\xi_\alpha' a + a_\alpha')}{\omega-\omega_0+i\Gamma/2\hbar - iab}\right] \tag{7-6.23}$$

where
$$a_\alpha' = \frac{\Gamma_{s\alpha}^{10}/4\hbar}{1+ib\mu^{00}(\omega)L/2 - ib\alpha_B k_{0v}L/2} \tag{7-6.24}$$

and
$$\xi_\alpha' = \frac{-\mu_\alpha^{10}(\omega)L/2}{1+ib\mu^{00}(\omega)L/2 - ib\alpha_B k_{0v}L/2} \tag{7-6.25}$$

and a is given by Eq. 7-6.13. This expression can also be simplified under some assumptions about the structure of the crystal lattice. If the lattice of resonant scatterers is different than the lattice of nonresonant scatterers, certain reflections may be found where, due to the geometrical structure factor, diffraction from resonant particles is allowed whereas diffraction from nonresonant particles is not allowed. This holds for certain iron crystals such as YIG, $FeBO_3$, and α - Fe_2O_3 enriched with ^{57}Fe. Under such conditions, $\xi_\alpha' = 0$, and the diffracted field simplified to

$$\mathbf{R}_{Bragg}(\omega) = e^{i(\mathbf{k}_{0v}+\mathbf{H})\cdot\mathbf{r}}\sum_\alpha E_{0v\alpha}(\omega)\hat{\boldsymbol{\varepsilon}}_\alpha^H\frac{(\omega_s - i\Gamma_s/2\hbar)(\Gamma_{s\alpha}^{10}/\Gamma_s^{00})}{\omega-(\omega_0+\omega_s)+i(\Gamma+\Gamma_s)/2\hbar} \tag{7-6.26}$$

where Γ_s and ω_s are given by Eqs. 7-6.16 and 7-6.17. The frequency shift and speedup rate are the same as that for Bragg transmission through a thin crystal. Also note that these quantities are dependent upon forward scattering factors and not upon diffraction scattering factors, and they are polarization independent.

A crystal will also appear "thin" when the eigenvalues are near zero: $\varepsilon_{0\alpha}^l \approx 0$. The eigenvalues can be exactly zero for Bragg diffraction when $\alpha_B = 0$, $g_{\alpha\alpha}^{00} = g_{\alpha\alpha}^{11}$, and $g_{\alpha\alpha}^{00}g_{\alpha\alpha}^{11} = g_{\alpha\alpha}^{01}g_{\alpha\alpha}^{10}$. Under such conditions, an infinitely thick crystal will appear "thin" in the thin crystal approximation. And as $d \to \infty$, the transmission channel field becomes

negligibly small and the reflection channel field goes to unity. These are the conditions for the suppression of the inelastic channel.[9] They result in an interesting demonstration of the Borrmann effect for resonant scattering where resonant absorption is completely suppressed in an infinitely thick crystal. Here an infinite number of planes contribute toward reflecting all of the incident field back out of the crystal--the reflectivity becomes unity. This Borrmann effect can be seen in Fig. 5-7.3 (at $\Delta\theta = 0$) for a crystal 3 primary extinction lengths thick (unity reflectivity is nearly achieved). However, note that the condition $g_{\alpha\alpha}^{00} g_{\alpha\alpha}^{11} = g_{\alpha\alpha}^{01} g_{\alpha\alpha}^{10}$ cannot be met for nonresonant scattering since the Debye-Waller factor for forward scattering (which is unity) is never equal to that for diffraction. Thus, unity reflectivity through the Borrmann effect can never be achieved for nonresonant scattering.

CASE 3: Thick Crystal Approximation.

In the thick crystal approximation

$$k_{0\nu}\varepsilon_{0\beta}^{l} d/\gamma_0 >> 1. \tag{7-6.27}$$

For Laue diffraction the two eigenwaves of each polarization in each scattering channel exponentially die off with distance into the crystal. Since both eigenwaves persist at the exit surface, ascribing a single frequency shift or speedup rate to the net exiting field is not possible. In addition, the analytical form of each eigenwave in Eqs. 7-4.40 and 7-4.41 cannot be further simplified other than that they approach zero as $d \to \infty$.

For Bragg diffraction one of the two eigenwaves exponentially dies off with distance while the other increases exponentially with distance. For the thick crystal approximation, the transmission channel field is negligibly small while the reflection channel field approaches

$$\mathbf{R}_{Bragg}(\omega) = e^{i(\mathbf{k}_{0\nu}+\mathbf{H})\cdot\mathbf{r}} \sum_{\alpha} E_{0\nu\alpha}(\omega)\hat{\boldsymbol{\varepsilon}}_{\alpha}^{II} \frac{b g_{\alpha\alpha}^{10}}{g_{\alpha\alpha}^{00} - 2\varepsilon_{0\alpha}^{(1,2)}} \tag{7-6.28}$$

where the eigenvalue that yields exponentially growing waves is chosen in the denominator. For combined resonant dipole and nonresonant scattering, the reflected field reduces to

$$\mathbf{R}_{Bragg}(\omega) = e^{i(\mathbf{k}_{0\nu}+\mathbf{H})\cdot\mathbf{r}} \sum_{\alpha} E_{0\nu\alpha}(\omega)\hat{\boldsymbol{\varepsilon}}_{\alpha}^{II}\left(b/\Omega_{s\alpha}\right)$$

$$\times\left[\omega - (\omega_0+\omega_s) + i(\Gamma+\Gamma_s)/2\hbar \pm \sqrt{\left[\omega - (\omega_0+\omega_s) + i(\Gamma+\Gamma_s)/2\hbar\right]^2 + \Omega_{s\alpha}^2/b}\right]$$

where (7-6.29)

$$\omega_s = \mathrm{Re}\left\{\frac{(1-b)(\Gamma_s^{00}/4\hbar)}{(1-b)\mu^{00}(\omega)L/2 + b\alpha_B k_{0v}L/2}\right\}$$

$$= \frac{(1-b)(\Gamma_s^{00}/4\hbar)\left[(1-b)\mathrm{Re}\{\mu^{00}(\omega)\}L/2 + b\alpha_B k_{0v}L/2\right]}{\left[(1-b)\mathrm{Re}\{\mu^{00}(\omega)\}L/2 + b\alpha_B k_{0v}L/2\right]^2 + \left[(1-b)\mathrm{Im}\{\mu^{00}(\omega)\}L/2\right]^2} \quad (7\text{-}6.30)$$

$$\Gamma_s = -\mathrm{Im}\left\{\frac{(1-b)(\Gamma_s^{00}/2)}{(1-b)\mu^{00}(\omega)L/2 + b\alpha_B k_{0v}L/2}\right\}$$

$$= \frac{(1-b)(\Gamma_s^{00}/2)\left[(1-b)\mathrm{Im}\{\mu^{00}(\omega)\}L/2\right]}{\left[(1-b)\mathrm{Re}\{\mu^{00}(\omega)\}L/2 + b\alpha_B k_{0v}L/2\right]^2 + \left[(1-b)\mathrm{Im}\{\mu^{00}(\omega)\}L/2\right]^2} \quad (7\text{-}6.31)$$

$$\Omega_{s\alpha} = (\omega_s - i\Gamma_s/2\hbar)(\Gamma_{s\alpha}^{10}/\Gamma_s^{00})[2b/(1-b)]. \quad (7\text{-}6.32)$$

Γ_s^{00} and $\Gamma_{s\alpha}^{10}$ are given by Eqs. 7-6.11 and 7-6.21, and, as before, a reflection was chosen for a crystal structure that forbids nonresonant diffraction but allows resonant dipole diffraction. Though the crystal is infinitely thick, a length factor, L, was inserted for comparisons to previous calculations. All quantities computed for this case are actually independent of L.

The extrema in Eq. 7-6.30 occur at

$$\Delta\theta_M = \frac{1-b}{2b\sin 2\theta_B}\left(\mathrm{Re}\{g_{\alpha\alpha}^{00}(\omega)\} \pm \mathrm{Im}\{g_{\alpha\alpha}^{00}(\omega)\}\right)_{nonres} \quad (7\text{-}6.33)$$

where $[g_{\alpha\alpha}^{00}(\omega)]_{nonres} = \mu^{00}(\omega)/k_{0v}$ is a nonresonant scattering tensor element. The maximum frequency shift is then

$$\omega_s(\Delta\theta_M) = \frac{1}{k_{0v}L}\frac{(\Gamma_s^{00}/4\hbar)}{\mathrm{Im}\{g_{\alpha\alpha}^{00}(\omega)\}_{nonres}}. \quad (7\text{-}6.34)$$

The maximum speedup parameter occurs at the nonresonant Bragg peak:

$$2|\Omega_{s\alpha}(\Delta\theta_P)| = \frac{1}{k_{0v}L}\frac{(\Gamma_s^{00}/\hbar)}{\mathrm{Im}\{g_{\alpha\alpha}^{00}(\omega)\}_{nonres}}(\Gamma_{s\alpha}^{10}/\Gamma_s^{00})[2b/(1-b)] \quad (7\text{-}6.35)$$

where the nonresonant Bragg peak is situated at

$$\Delta\theta_P = \frac{(1-b)\mathrm{Re}\{g_{\alpha\alpha}^{00}\}_{nonres}}{2b\sin 2\theta_B} \quad (7\text{-}6.36)$$

due to the index of refraction shift. The angular width of the speedup parameter, $2|\Omega_{s\alpha}|$, is (full width at half maximum)

$$\Delta\theta_{\Omega} = \frac{\sqrt{3}(1-b)\mathrm{Im}\{g_{\alpha\alpha}^{00}\}_{NONRES}}{b\sin 2\theta_B}. \qquad (7\text{-}6.37)$$

Because of the non-Lorentzian form of the reflected field, the quantities ω_s and Γ_s no longer fully represent a frequency shift and speedup rate, but, for certain ranges of α_B, they do roughly describe the magnitude of these dynamical effects. The non-Lorentzian characteristics of the energy spectrum embodied by Eq. 7-6.29 can be seen in Figs. 7.6-1 and 7.6-2 for various angles near the Bragg angle. The α–$^{56}Fe^{57}Fe$ crystal examined earlier in Section 7-5 was used again in these calculations. Far from Bragg the energy spectrum asymptotically approaches the Lorentzian lineshape a single nucleus exhibits. On resonance and near the Bragg peak (which occurs at $\Delta\theta_P = 16\mu$rads) the collection of nuclei generate a field intensity with a cusp-like distribution and long tails centered at the natural frequency (this is where the Borrmann effect is predominant).

Plots of $\hbar\omega_s(\Delta\theta)$, the centroid of the energy spectrum, and the energy at the peak intensity versus the angle from Bragg are shown in Fig. 7-6.3. The centroid and $\omega_s(\Delta\theta)$ generally follow each other with discrepancies largest at the Bragg peak, and they converge to the energy of peak intensity at large deviations from Bragg (that is, deviations larger that two photoelectric Darwin widths--the photoelectric Darwin width for the α–$^{56}Fe^{57}Fe$ infinitely thick crystal is roughly 12μrad for the [0 0 2] nearest order allowed photoelectric reflection). The energy shifts represented by $\hbar\omega_s(\Delta\theta)$ and the centroid maximize very close to the Bragg peak positioned at $\Delta\theta_P$--at about three-fourths of a microrad from the peak for $\hbar\omega_s(\Delta\theta)$ and about 1μrad from the peak for the centroid.

The angular position of the on-resonance Bragg peak is totally determined by photoelectric forward scattering since the real part of the resonant forward scattering amplitude goes to zero (note that the first term in Eq. 7-6.33 is the index of refraction shift, $\Delta\theta_P$, for on resonance scattering). Therefore, the extrema of $\omega_s(\Delta\theta)$ are slightly shifted from $\Delta\theta_P$ since nonresonant photoelectric absorption is generally much smaller than nonresonant scattering: $(1-b)\mathrm{Im}\{\mu^{00}(\omega)/k_{0v}\}/2b\sin 2\theta_B \approx 3/4\,\mu$rad (note that $b=-1$,

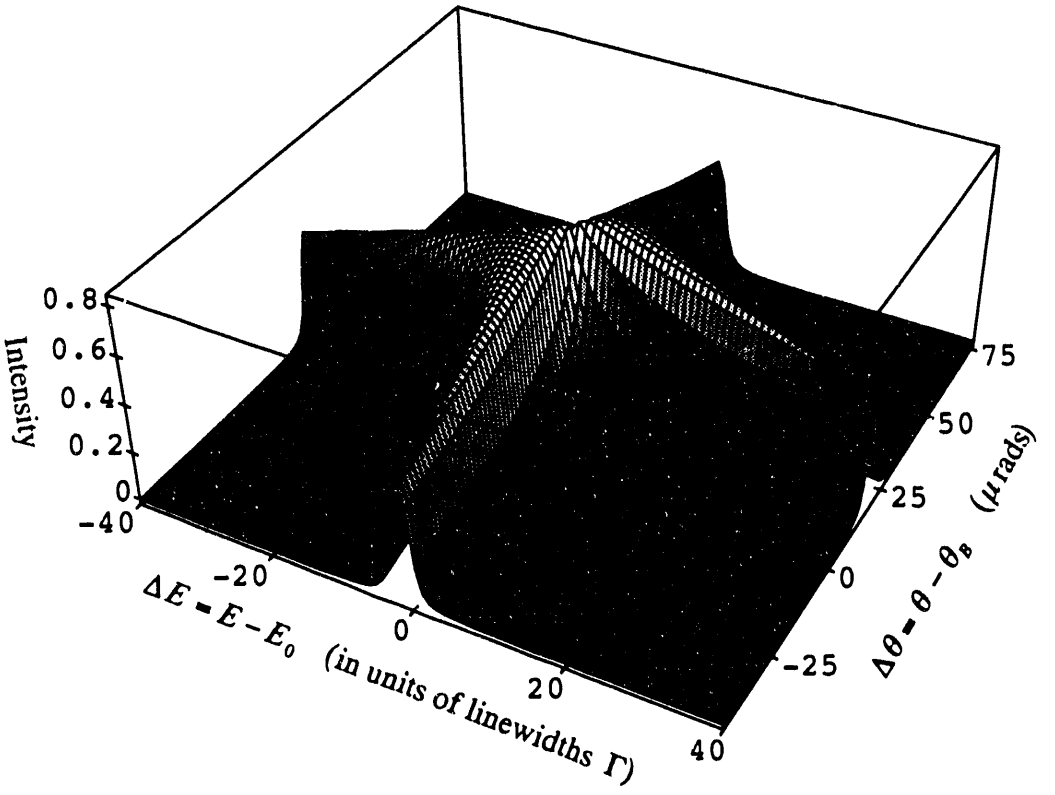

Fig. 7-6.1. Diffracted field intensity versus deviation angle from Bragg and deviation from the resonant energy.

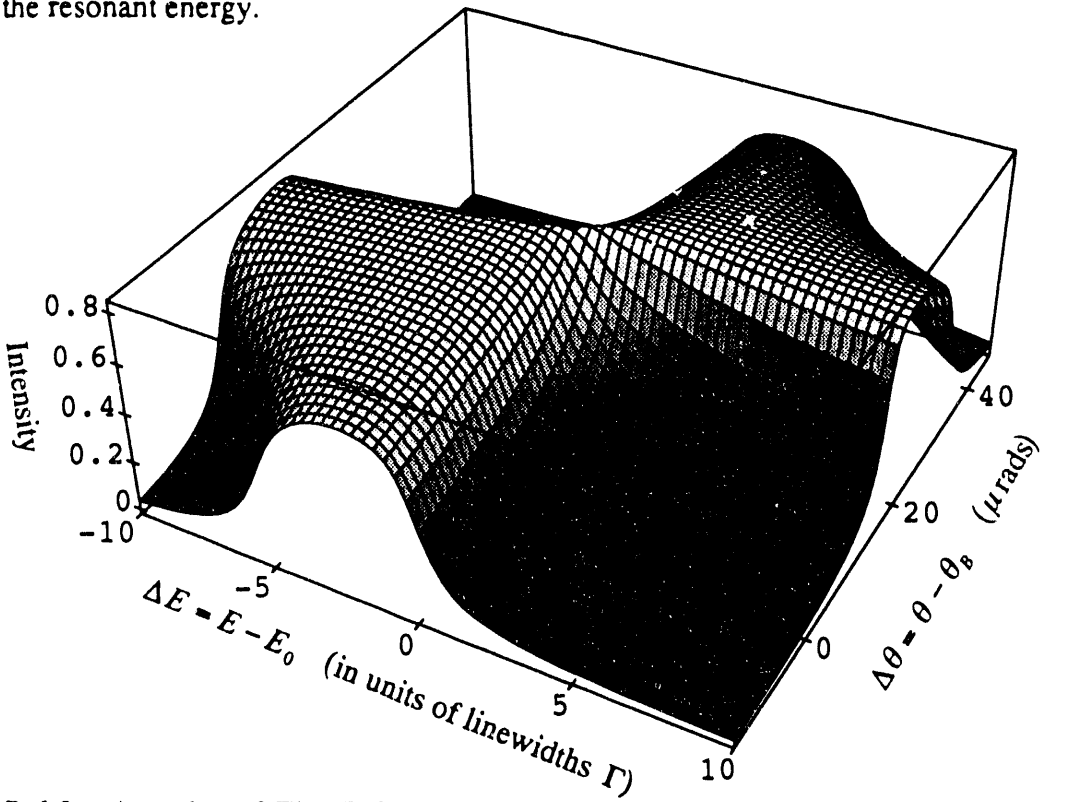

Fig. 7-6.2. A replot of Fig. 7-6.1 over smaller energy and angle ranges. The non-Lorentzian energy distribution is now clearly observable along with homogeneous line broadening and resonant energy shifts for these energy and angle ranges.

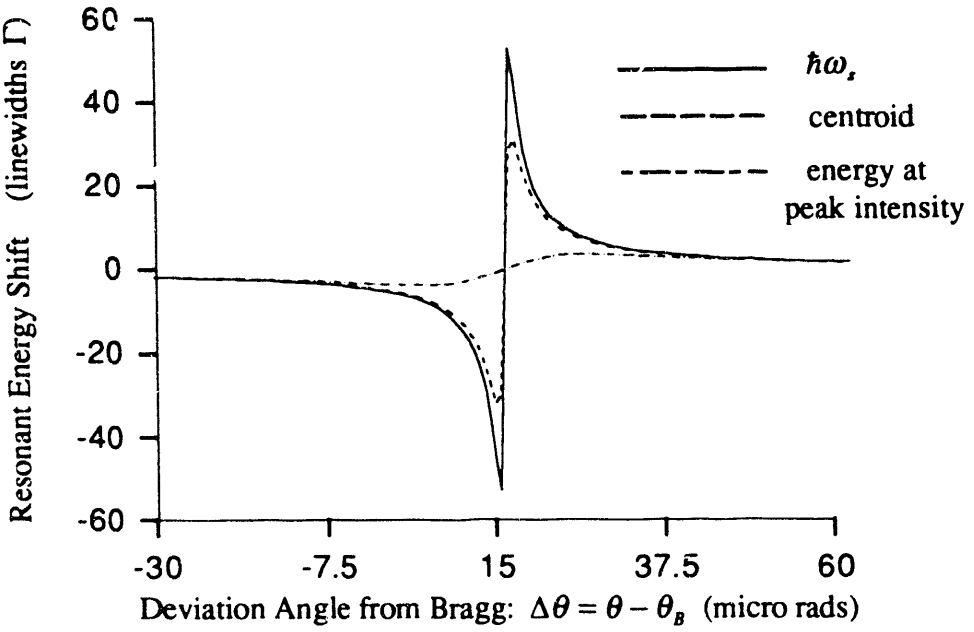

Fig. 7-6.3. Plots of $\omega_s(\Delta\theta)$, the centroid, and the energy at which the diffracted intensity peaks.

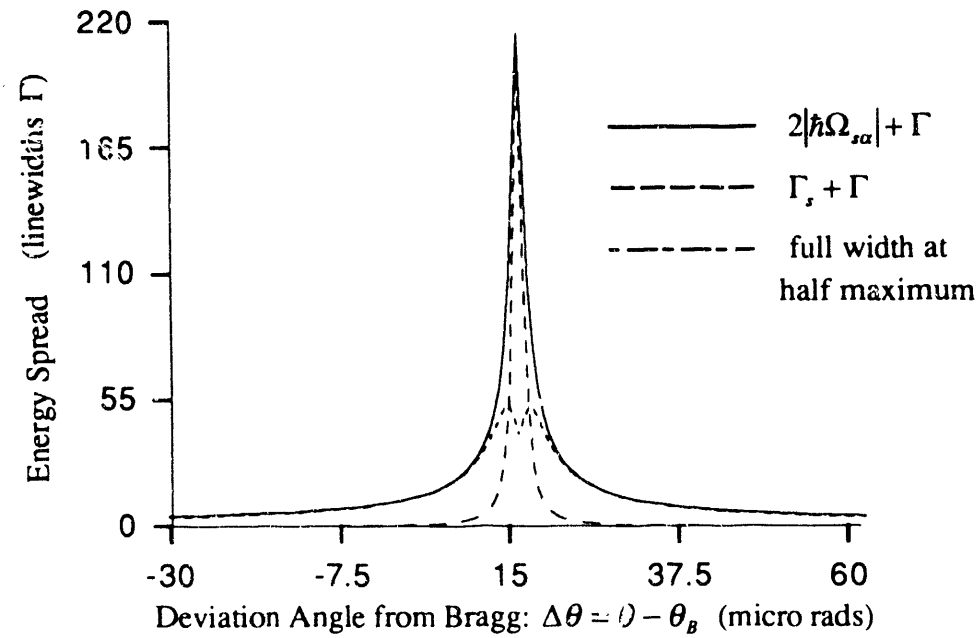

Fig. 7-6.4. Plots of speedup factors $2|\Omega_{s\alpha}|$ and Γ_s, and the full width at half maximum versus deviation angle.

$\theta_B \approx 4.9°$, and $\mu^{00}(\omega)/k_{0\nu} \approx (-2.8 + i0.13)\times 10^{-6}$ for the [0 0 1] symmetric reflection of bcc α–^{56}Fe^{57}Fe having a lattice spacing of 5Å). The energy shift seen by examining the energy at which the field intensity is maximized has extrema that are roughly 15 times less than that for $\omega_s(\Delta\theta)$ and peaks (at about 11μrads) much further from the angular position of the on-resonant Bragg peak.

From Fig. 7-6.4 one can also see that $2|\Omega_{s\alpha}| + \Gamma$ approaches the full width at half maximum as the deviation angle progresses beyond half a photoelectric Darwin width. Thus, far off Bragg, the quantities ω_s and $2|\Omega_{s\alpha}|$ become good approximations for a frequency shift and speedup rate.

The dynamical quantities ω_s, Γ_s, and $2|\Omega_{s\alpha}|$ can be understood in another light by examining the diffracted intensity in the time domain. Fortunately, due to the efforts of Kohn,[10] an analytical expression for the Fourier transform of the diffracted field, Eq. 7-6.29, has been evaluated through contour integral methods for the case where the frequency spectrum of the incoming field is constant: $E_{0\nu\alpha}(\omega) = E_{0\nu\alpha}$ (as is the case for a synchrotron beam). The integral of interest is

$$I = \frac{1}{2\pi}\int_{-\infty}^{\infty} e^{-i\omega t}\left[(\omega - z_0) \pm \sqrt{(\omega - z_1)(\omega - z_2)}\right] d\omega \qquad (7\text{-}6.38)$$

where

$$z_0 = (\omega_0 + \omega_s) - i(\Gamma + \Gamma_s)/2\hbar \qquad (7\text{-}6.39)$$

$$z_{(1,2)} = (\omega_0 + \omega_s) - i(\Gamma + \Gamma_s)/2\hbar \pm \Omega'_{s\alpha} \qquad (7\text{-}6.40)$$

and

$$\Omega'_{s\alpha} = \mathrm{P}\left\{\sqrt{\Omega_{s\alpha}^2/b}\right\}. \qquad (7\text{-}6.41)$$

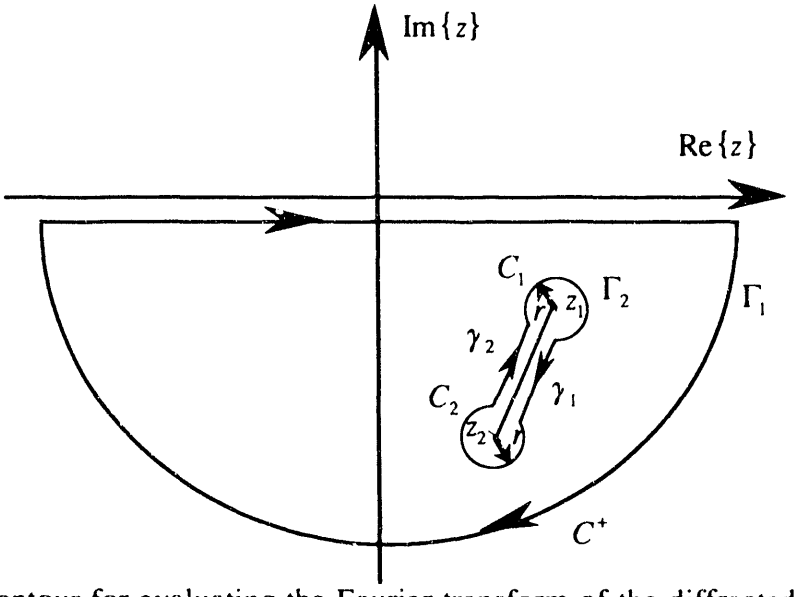

Fig. 7-6.5. Contour for evaluating the Fourier transform of the diffracted field from an infinitely thick crystal.

Since $\Omega_{s\alpha}$ is complex, the principal value of the square root in Eq. 7-6.41 must be evaluated.

Since ω_s is much smaller that the natural frequency and $\Omega_{s\alpha} \leq (\omega_s - i\Gamma_s/2\hbar)$ when examining only the real and imaginary parts separately, an appropriate contour to integrate over is shown in Fig. 7-6.5 which has a branch-cut between the two branch points z_1 and z_2. For this contour where ω is set to be complex valued

$$\left(\oint_{\Gamma_1} - \oint_{\Gamma_2}\right) e^{-izt}\left[(z-z_0) \pm \sqrt{(z-z_1)(z-z_2)}\right] dz = 0 \qquad (7\text{-}6.42)$$

since there are no poles in the region between the closed contours Γ_1 and Γ_2. The integral over arc C^+ of contour Γ_1 is zero by the Jordan Lemma (this can be seen by rewriting the argument of the integral in the form of a quotient of one over a polynomial of degree 1). The integral over the contour Γ_2 of the first term in the integral above also vanishes since it has no poles within the contour. Then

$$I = \pm\frac{1}{2\pi}\oint_{\Gamma_2} e^{-izt}\sqrt{(z-z_1)(z-z_2)}\,dz$$

$$= \pm\frac{1}{2\pi}\left(\int_{C_1} + \int_{C_2} + \int_{\gamma_1} + \int_{\gamma_2}\right) e^{-izt}\sqrt{(z-z_1)(z-z_2)}\,dz \qquad (7\text{-}6.43)$$

where C_1 and C_2 are two circles each of radius r, and γ_1 and γ_2 are two line segments on opposite sides of the branch-cut between the branch points z_1 and z_2. For the integral over circle C_1 let $z = z_1 + re^{i\theta}$. Then, since

$$\left|\int_{C_1} e^{-izt}\sqrt{(z-z_1)(z-z_2)}\,dz\right| < \left|2\pi r e^{-i(z_1 + r\sin\theta)t}\sqrt{re^{i\theta}\left(\Omega'_{s\alpha} + re^{i\theta}\right)}\right| \underset{r\to 0}{\to} 0,$$

the integral over C_1 vanishes as $r \to 0$ for $t > 0$. The same happens to the integral over the other circle C_2.

For the line segments let

$$z = \left[\frac{z_1 + z_2}{2}\right] + \left[\frac{z_1 - z_2}{2}\right] w. \qquad (7\text{-}6.44)$$

The principal value of the square root in the integral can then be expressed as

$$\sqrt{(z-z_1)(z-z_2)} = \Omega'_{s\alpha}\sqrt{1-w^2}\,e^{\frac{i}{2}[\arg(-1+w)+\arg(1+w)]}. \qquad (7\text{-}6.45)$$

Then, along γ_1 from z_1 to z_2 the square root transforms to

$$\sqrt{(z-z_1)(z-z_2)} = i\Omega'_{s\alpha}\sqrt{1-w^2} \qquad (7\text{-}6.46)$$

when w is set to $w = \lim_{\varepsilon\to 0} a + i\varepsilon$ where $|a| \leq 1$. Similarly, $w = \lim_{\varepsilon\to 0} a - i\varepsilon$ along γ_2 from z_2 to z_1 and thus

$$\sqrt{(z-z_1)(z-z_2)} = -i\Omega'_{s\alpha}\sqrt{1-w^2}. \tag{7-6.47}$$

Then

$$I = \mp e^{-i(\omega_0+\omega_s)t} e^{-(\Gamma+\Gamma_s)t/2\hbar} \frac{i\Omega_{s\alpha}/b}{2\pi}\left(\int_{-1}^{1} - \int_{1}^{-1}\right)\sqrt{1-w^2}\, e^{-i\Omega'_{s\alpha}wt}\, dw$$

$$= \mp e^{-i(\omega_0+\omega_s)t} e^{-(\Gamma+\Gamma_s)t/2\hbar} \frac{i\Omega_{s\alpha}/b}{\pi}\int_{-1}^{1}\sqrt{1-w^2}\cos(\Omega'_{s\alpha}wt)dw. \tag{7-6.48}$$

With help from the integral tables in Abramowitz and Stegun,[14] the integral evaluates to

$$\int_{-1}^{1}\sqrt{1-w^2}\cos(\Omega'_{s\alpha}wt)dw = \pi\frac{J_1(\Omega'_{s\alpha}t)}{\Omega'_{s\alpha}t}. \tag{7-6.49}$$

The reflection channel field in the time domain is then

$$\mathbf{R}_{Bragg}(t) = e^{i(\mathbf{k}_{0v}+\mathbf{H})\cdot\mathbf{r}}\sum_{\alpha} E_{0v\alpha}\hat{\boldsymbol{\varepsilon}}''_{\alpha} e^{-i(\omega_0+\omega_s)t} e^{-(\Gamma+\Gamma_s)t/2\hbar} i\Omega_{s\alpha}\frac{J_1(\Omega_{s\alpha}t)}{\Omega_{s\alpha}t}\theta(t). \tag{7-6.50}$$

The principal value of the square root expressed by $\Omega'_{s\alpha}$ has been dropped since $J_1(\Omega'_{s\alpha}t)/\Omega'_{s\alpha}t = J_1(\Omega_{s\alpha}t)/\Omega_{s\alpha}t$ (this can be seen by expanding the Bessel function in terms of a series expansion in $\Omega'_{s\alpha}t$). Also, the $\pm$ sign has been dropped because, as a result of the boundary conditions, the overall phase of the reflected field is indeterminable (though the phase can be determined when the reflection channel field interferes with another wave such as with the incoming field at the crystal surface). Examination of the reflected field reveals that it is frequency shifted by ω_s, and the natural decay rate is modified by a speedup factor Γ_s resulting only from forward scattering and by a speedup factor $\Omega_{s\alpha}$ resulting from diffraction.

The reason for the non-Lorentzian frequency response of the reflected field has now been isolated to the dynamical beat and speedup factor $J_1(\Omega_{s\alpha}t)/\Omega_{s\alpha}t$ in the time response. As a result, a decay rate attributed to the entire time response is no longer possible. However, the time behavior of the reflected field simplifies in the limits of the Bessel function for large and small arguments.[10] For instance, in the short time domain when $|\Omega_{s\alpha}t| << 1$

$$\mathbf{R}_{Bragg}(t) \approx e^{i(\mathbf{k}_{0v}+\mathbf{H})\cdot\mathbf{r}}\sum_{\alpha} E_{0v\alpha}\hat{\boldsymbol{\varepsilon}}''_{\alpha} e^{-i(\omega_0+\omega_s)t} e^{-(\Gamma+\Gamma_s)t/2\hbar} i\frac{\Omega_{s\alpha}}{2}\theta(t), \tag{7-6.51}$$

and the reflected field suffers a frequency shift, ω_s, and a speedup, Γ_s, of the decay rate. In the long time domain when $|\Omega_{s\alpha}t| >> 1$

$$\mathbf{R}_{Bragg}(t) \approx e^{i(\mathbf{k}_{0v}+\mathbf{H})\cdot\mathbf{r}} \sum_{\alpha} E_{0v\alpha}\hat{\boldsymbol{\varepsilon}}_{\alpha}^{H} e^{-i(\omega_0+\omega_s)t} e^{-(\Gamma+\Gamma_s)t/2\hbar} i\sqrt{\frac{2}{\pi}} \frac{\cos(\Omega_{s\alpha}t - 3\pi/4)}{t\sqrt{\Omega_{s\alpha}t}}\theta(t). \quad (7\text{-}6.52)$$

Since

$$\cos(\Omega_{s\alpha}t - 3\pi/4) = \left(e^{i(\mathrm{Re}\{\Omega_{s\alpha}t\}-3\pi/4)} e^{-\mathrm{Im}\{\Omega_{s\alpha}t\}} + e^{-i(\mathrm{Re}\{\Omega_{s\alpha}t\}-3\pi/4)} e^{+\mathrm{Im}\{\Omega_{s\alpha}t\}}\right)/2$$

this long time limit exhibits both positive and negative frequency shifts and speedup and slowdown rates. However, since $\left|\mathrm{Im}\{\Omega_{s\alpha}\}\right| \le \Gamma_s/2\hbar$ there are never runaway solutions in which the reflected field grows exponentially with time. In fact, for the case in which $\left|\mathrm{Im}\{\Omega_{s\alpha}\}\right| = \Gamma_s/2\hbar$ the reflected field reduces to

$$\mathbf{R}_{Bragg}(t) \approx e^{i(\mathbf{k}_{0v}+\mathbf{H})\cdot\mathbf{r}} \sum_{\alpha} E_{0v\alpha}\hat{\boldsymbol{\varepsilon}}_{\alpha}^{H} i \frac{e^{i\pi/4}}{\sqrt{2\pi}} \frac{e^{-i\omega_0 t} e^{-\Gamma t/2\hbar}}{t\sqrt{\Omega_{s\alpha}t}}\theta(t). \quad (7\text{-}6.53)$$

For this situation the reflected field intensity undergoes no frequency shift and decays faster than the natural decay rate by the factor $1/t^3$.

For the intermediate case in which $|\Omega_{s\alpha}t|$ is neither very large or small, an approximation of the decay behavior can be made using the result of the solution for the scattering channel field from an isotropic slab as a guide

$$\left|\mathbf{R}_{Bragg}(t)\right|^2 = C^2(\delta\theta) e^{-\left(\frac{\Gamma}{\hbar} + \frac{|\Omega_{s\alpha}|}{2\zeta(\delta\theta)\sqrt{\ln 2}}\right)t} \theta(t) \quad (7\text{-}6.54)$$

where

$$\zeta(\delta\theta) = 1 + \frac{3}{2}\frac{|\delta\theta|}{|\delta\theta| + 25\mu rads}. \quad (7\text{-}6.55)$$

Here, $\delta\theta$ is a measure of the angular deviation from the on-resonance Bragg peak (determined by the photoelectric index of refraction shift):

$$\delta\theta = \Delta\theta - \Delta\theta_P \quad (7\text{-}6.56)$$

where $\Delta\theta_P$ is given by Eq. 7-6.36. For this estimate $\zeta(\delta\theta)$ is a function that varies from unity to 2.5 as the deviation angle varies from the center of the Bragg profile to far from Bragg. The coefficient $C(\delta\theta)$ rapidly varies from approximately 0.75 right on the Bragg peak to a plateau of 1.1 a few microrads from the Bragg peak.

Plots of normalized reflected intensity versus time are shown in Figs 7-6.6 to 7-6.8 for angular deviations from the Bragg peak of 0, 50, and 200 μrad respectively.

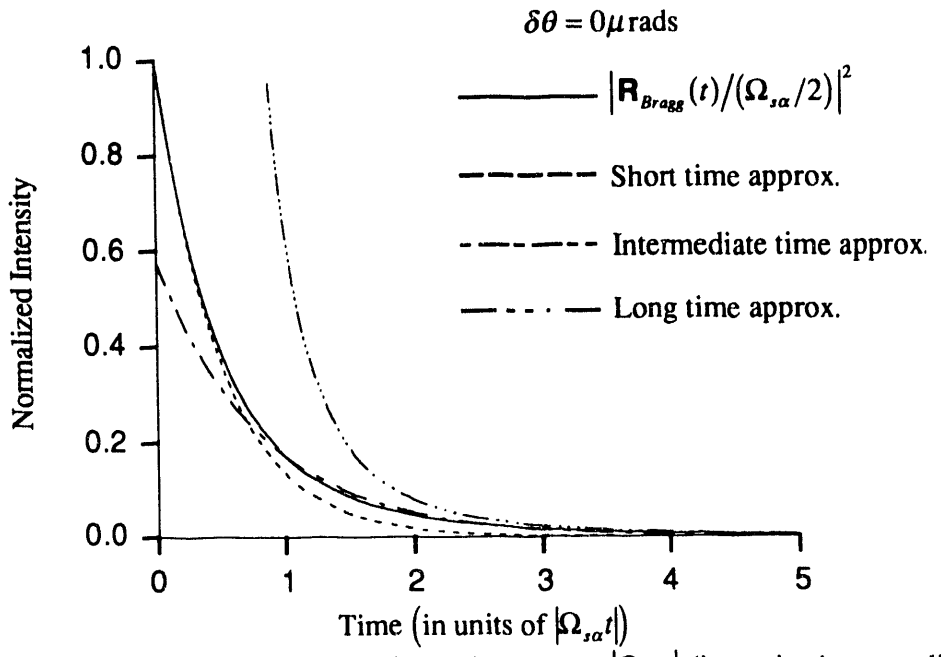

Fig. 7-6.6. Plots of normalized Bragg intensity versus $|\Omega_{s\alpha}t|$ (intensity is normalized by dividing by $|\Omega_{s\alpha}/2|^2$). The angular deviation from Bragg is 16μrad--this is right on the Bragg peak. The speedup factors are $1/2|\Omega_{s\alpha}| \approx \hbar/\Gamma_s \approx 0.66$ nsec.

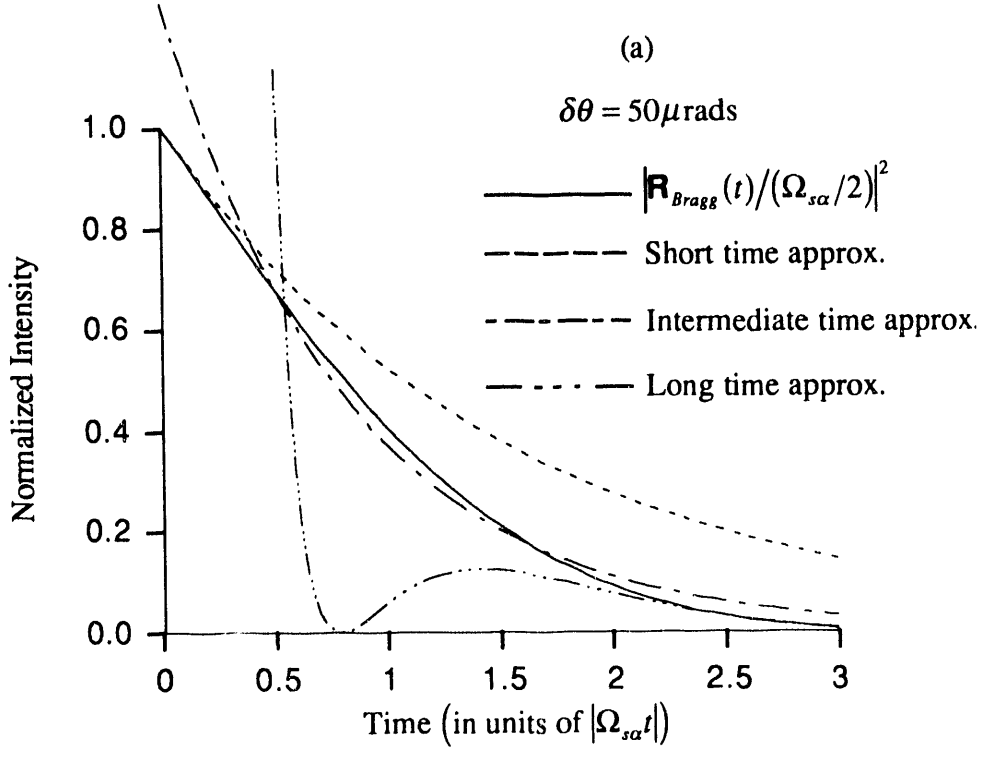

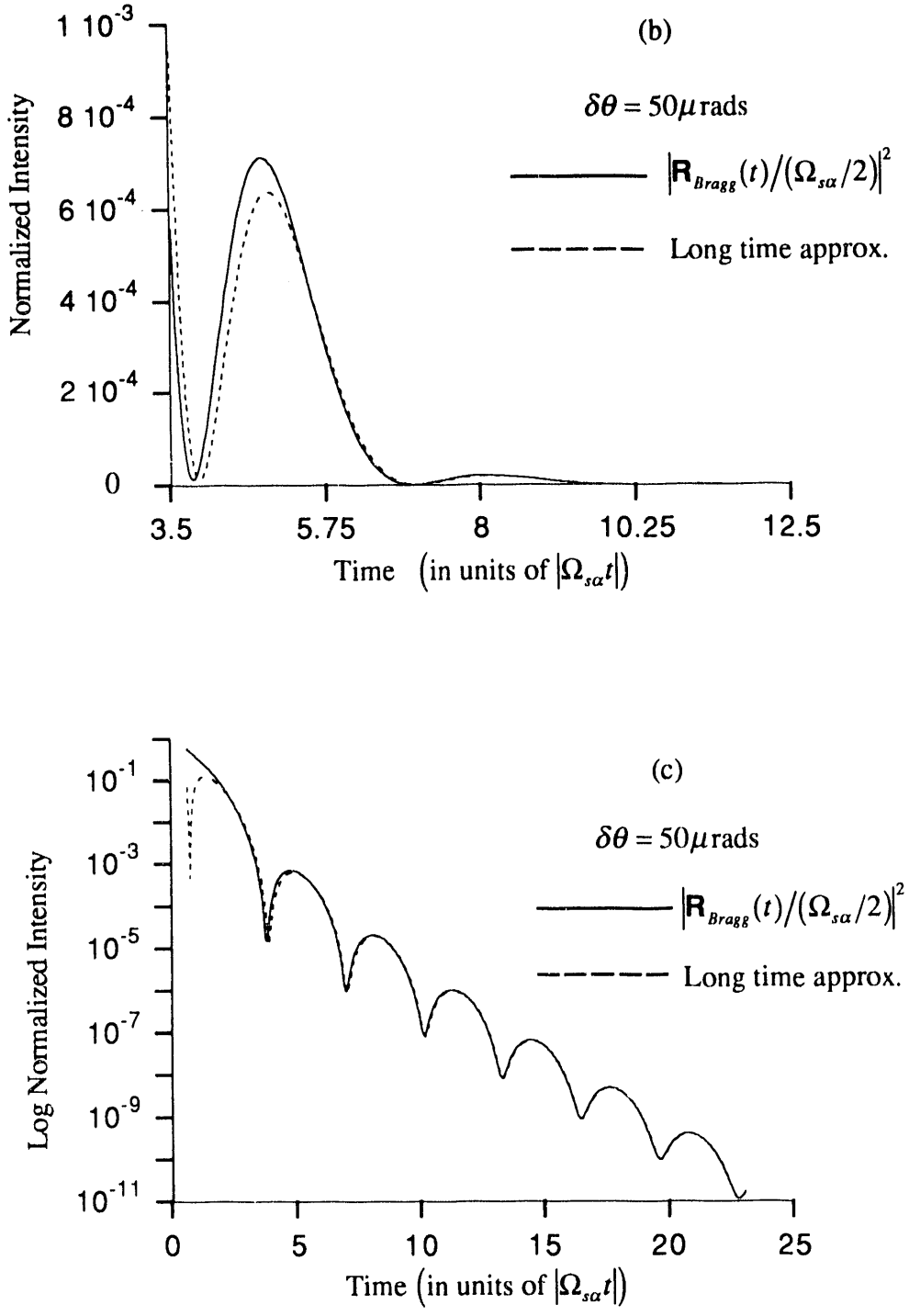

Fig. 7-6.7. The angular deviation from Bragg is 66μrad--this is 50μrad from the Bragg peak. The speedup factors are $1/2|\Omega_{s\alpha}| \approx 43$ nsec and $\hbar/\Gamma_s \approx 2.8\,\mu$sec. The dynamical beats are now apparent at long times as can be seen in Figs. 7-6.7 (b) and (c).

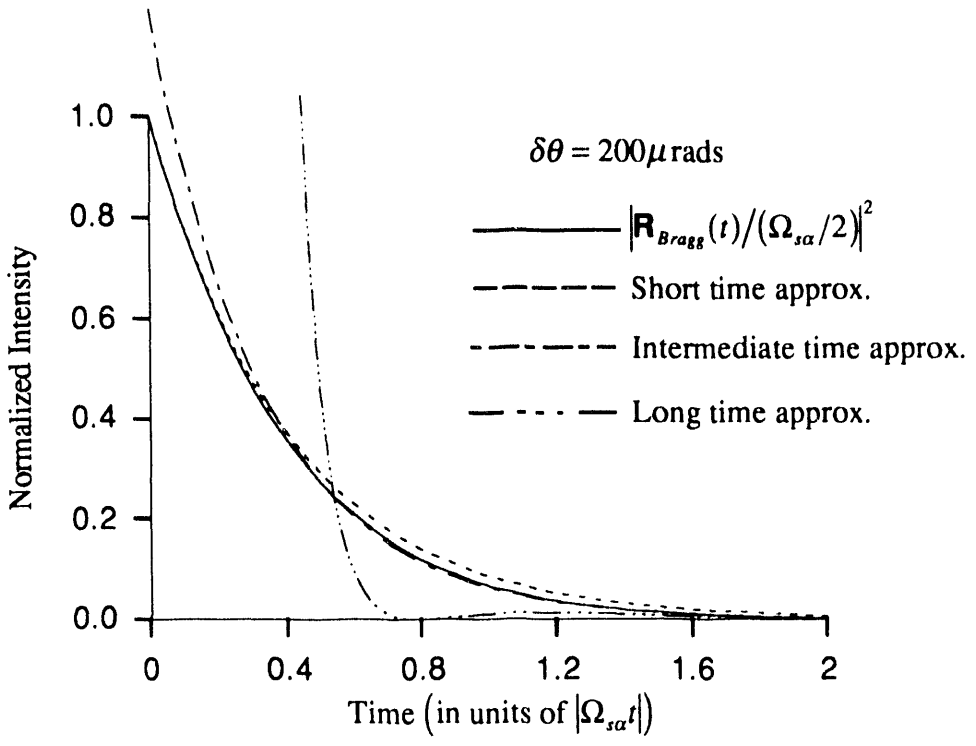

Fig. 7-6.8. The angular deviation from Bragg is 216μrad--this is 200μrad from the Bragg peak. The speedup factors are $1/2|\Omega_{s\alpha}| \approx 173$ nsec and $\hbar/\Gamma_s \approx 45$ μsec. Far from Bragg the field intensity decays with nearly the natural lifetime.

7.7 Dynamical Characteristics of Crystals with Hyperfine Split Spectra

To date, all crystals examined for nuclear resonant scattering have hyperfine split spectra rather than single line spectra. If the resonant lines for a particular crystal are very close together, the effects caused by interference between the various lines must be carefully examined in addition to any frequency shifts and speedup rates of each individual line. This significantly complicates the problem of analyzing the dynamical characteristics of the reflected field (in addition, no analytical form of the Bragg diffracted intensity in the time domain has been found).

If the resonant lines are far apart then the interference effects among the lines can be neglected, and the results of Sections 7.5 and 7.6 can be used for each individual line. For each individual line caused by a transition from an intermediate state $|n\rangle$ to a final state $|f\rangle$, the dynamical quantities ω_s, Γ_s, and $\Omega_{s\alpha}$ are given by Eqs. 7-6.30, 7-6.31, and 7-6.32 with substitution of $\Gamma_s^{00}/k_{0v}L$ and $\Gamma_{s\alpha}^{10}/k_{0v}L$ by

$$\Gamma^{00}_{s(fn)}/k_{0v}L = \frac{(4\pi)^2}{k_{0v}^3} nL_M(\mathbf{k}_i)L_M(\mathbf{k}_f = \mathbf{k}_i)C\Gamma_{rad}\frac{\langle j_f m_f LM | j_f L j_n m_n\rangle^2}{(2j_i+1)}P^{00}_{LM} \qquad (7\text{-}7.1)$$

and

$$\Gamma^{10}_{sa(fn)}/k_{0v}L = \frac{(4\pi)^2}{k_{0v}^3} L_M(\mathbf{k}_i)L_M(\mathbf{k}_f)C\Gamma_{rad}\frac{\langle j_f m_f LM | j_f L j_n m_n\rangle^2}{(2j_i+1)}P^{10}_{LM}\frac{1}{V_0}\sum_q e^{-i\mathbf{H}\cdot\mathbf{r}_q}. \qquad (7\text{-}7.2)$$

where P^{HS}_{LM} is a polarization matrix described in Section 7-2.

Plots of $\omega_s(\Delta\theta)$ and $2|\Omega_{sa}(\Delta\theta)|$ are shown below for three different crystals: α-Fe_2O_3, $FeBO_3$, and YIG (only for the d1-site). All these crystals have been used for nuclear resonant scattering experiments, and they all exhibit hyperfine split six line spectra. They can all be grown with enriched ^{57}Fe atoms, and they all have the property, because of either antiferromagnetic ordering or a ferromagnetic sublattice structure, where photoelectric diffraction for certain lattice planes is forbidden whereas resonant nuclear diffraction is allowed. The plots where constructed for the case in which the polarization matrix P^{HS}_{LM} diagonalizes: there is an applied magnetic field oriented perpendicular to the scattering plane. For lines $(\ell_1,\ell_2,\ell_3,\ell_4,\ell_5,\ell_6)$, $\mathrm{Re}(P^{10}_{1,\pm1})_{\sigma\sigma} = (3/16\pi)\cos 2\theta_B(1,0,1,1,0,1)$ for incoming horizontally polarized fields, and $(P^{10}_{10})_{\pi\pi} = (3/16\pi)(0,2,0,0,2,0)$ for

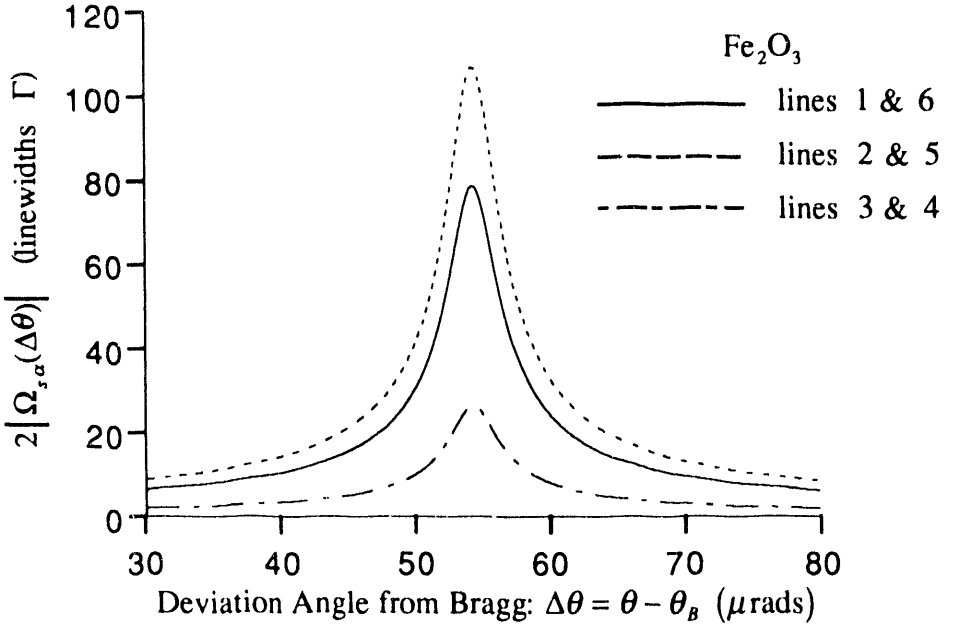

(a)

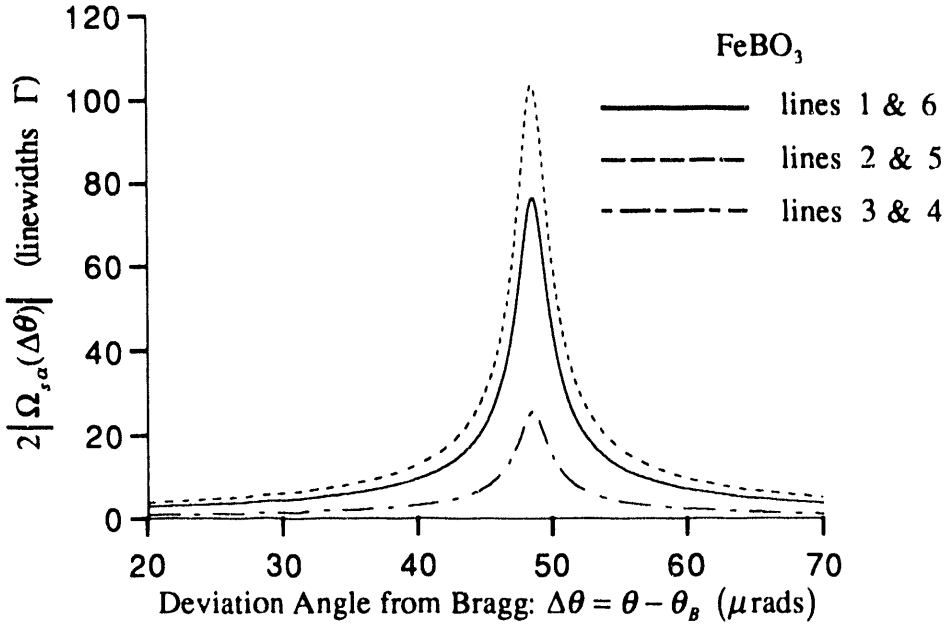

(b)

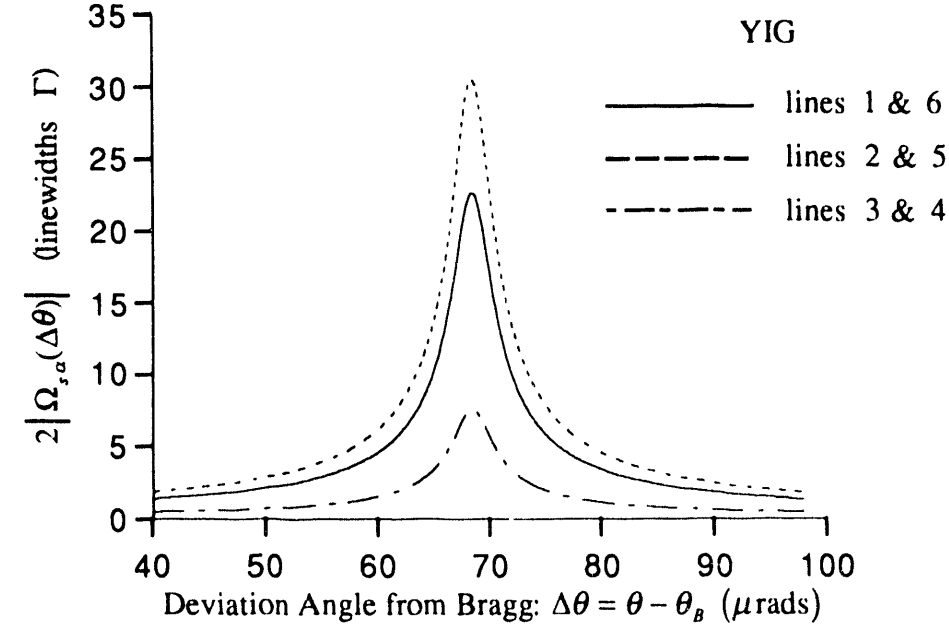

(c)

Fig. 7-7.1. Homogeneous line broadening parameter, or decay rate speedup factor, for the various hyperfine split lines of:(a) α - Fe_2O_3, (b) $FeBO_3$, and (c) YIG.

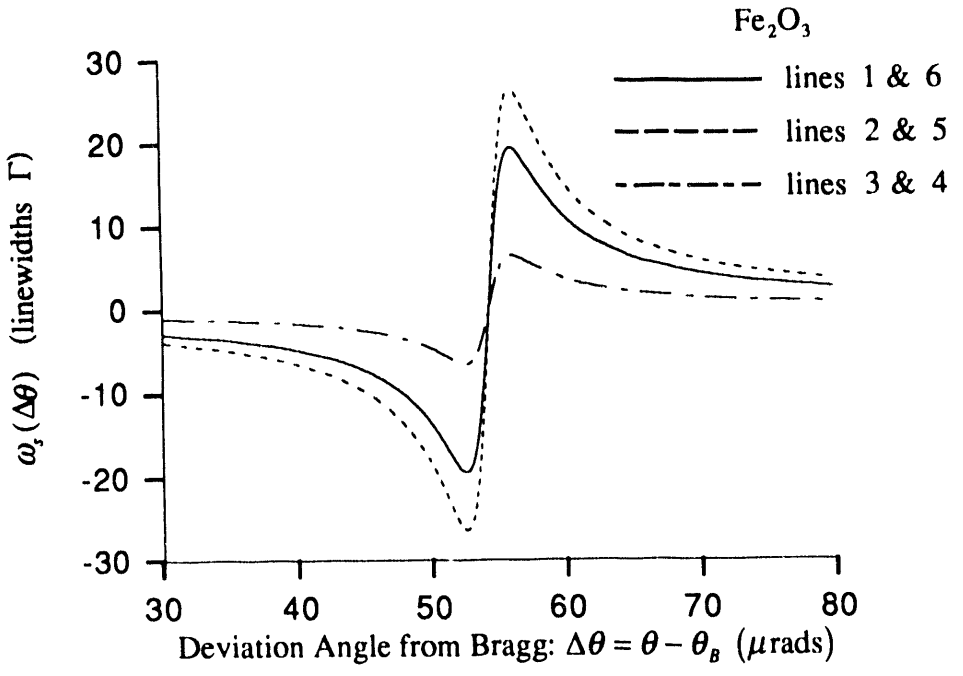
Fe_2O_3
lines 1 & 6
lines 2 & 5
lines 3 & 4
30
20
10
0
-10
-20
-30
30
40
50
60
70
80
$\omega_s(\Delta\theta)$ (linewidths Γ)
Deviation Angle from Bragg: $\Delta\theta = \theta - \theta_B$ (μrads)

(a)

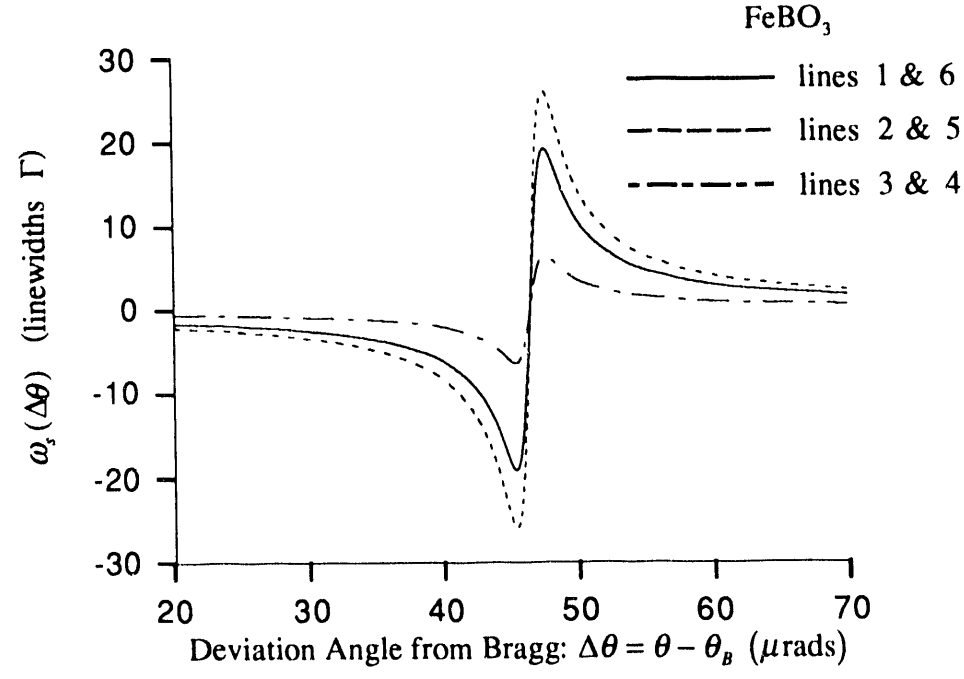
$FeBO_3$
lines 1 & 6
lines 2 & 5
lines 3 & 4
30
20
10
0
-10
-20
-30
20
30
40
50
60
70
$\omega_s(\Delta\theta)$ (linewidths Γ)
Deviation Angle from Bragg: $\Delta\theta = \theta - \theta_B$ (μrads)

(b)

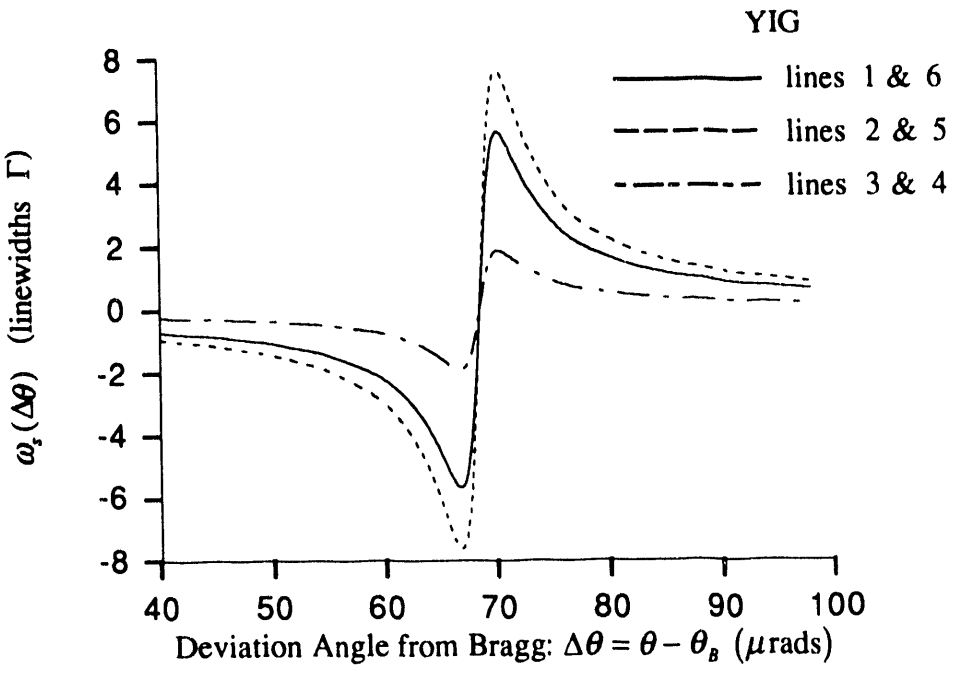

(c)

Fig. 7-7.2. Resonant frequency shift for the various hyperfine split lines of: (a) α - Fe_2O_3, (b) $FeBO_3$, and (c) YIG.

lines $(\ell_1,\ell_2,\ell_3,\ell_4,\ell_5,\ell_6)$ are (1,2/3,1/3,1/3,2/3,1). The Lamb-Mössbauer and resonant enrichment factors have been set to unity: $L_M(\mathbf{k}_i)L_M(\mathbf{k}_f)=1$ and $C=1$. The resonant energy is 14.4125 keV, the resonant linewidth is 4.67×10^{-9} eV, and $j_i = 1/2$. The [1 1 1] reflection from α - Fe_2O_3 and $FeBO_3$ have Bragg angles of 5.4° and 5.1° respectively. The Bragg angle of the [0 0 2] reflection from YIG is 4.0°.

Since the photoelectric absorption due to the spectator oxygen atoms is small compared to the iron atoms for α - Fe_2O_3 and $FeBO_3$, the extrema in the frequency shift and speedup parameter characterized by Eqs. 7-6.34 and 7-6.35 are nearly identical as can be seen in Figs. 7-7.1 (a) and (b) (the extrema are naturally independent of unit cell volume and crystal thickness, but, if the photoelectric absorption of the spectator atoms is completely neglected, they also become independent of the number of resonant nuclei per unit cell). However, YIG has many more spectator atoms (32 other iron atoms, 24 yittrium atoms, and 96 oxygen atoms). The photoelectric absorption from these spectator atoms significantly limits the maximum frequency shift and speedup.

The angular range over which there is a moderate speedup is described by Eq. 7-6.37. By decreasing the Bragg angle (such as by increasing the lattice spacing) or by increasing the photoelectric absorption (such as by increasing the number of resonant nuclei

per unit cell), the angular range for moderate speedup can be greatly extended. However, increasing the photoelectric absorption by increasing the number of spectator atoms instead of the number of resonant nuclei will decrease the maximum speedup.

7.8 Numerical Solutions of the Linearized Dispersion Relations

The analytical two beam solution of the linearized dispersion equation was possible because the polarization matrices were diagonal for a particular eigenpolarization basis. The dispersion equation decoupled into two relations for each eigenpolarization, and this resulted in simple analytical solutions for the transmitted and diffracted fields. The eigenpolarizations for nonresonant photoelectric scattering are the sigma and pi polarizations since mainly Thomson scattering occurs. For resonant magnetic dipole scattering with an applied magnetic field perpendicular to the scattering plane, the eigenpolarizations are also the sigma and pi polarizations. When the applied magnetic field is parallel to the scattering plane and horizontally oriented (Case 3 in Section 5.1) the eigenpolarizations are the right and left circular polarizations (however, a polarization matrix must be reconstructed in this basis since the polarization matrices in the linear basis represented by Eqs. 5-1.19 and 5-1.20 no longer apply).

In general eigenpolarizations for resonant scattering are not easy to find for an arbitrary orientation of the quantum axis. Therefore the polarization matrices are usually constructed in a simple polarization basis (such as the sigma and pi basis), and then one proceeds to solve the dispersion equations (which may no longer be uncoupled) through numerical techniques. This involves solving the characteristic eigenvalue equation expressed in Eq. 7-4.19 where

$$\mathbf{G}_{lin} = \begin{pmatrix} g_{xx}^{00} & g_{xx}^{01} & g_{xy}^{00} & g_{xy}^{01} \\ g_{xx}^{10} & \left(bg_{xx}^{11} - b\alpha_B\right) & g_{xy}^{10} & g_{xy}^{11} \\ g_{yx}^{00} & g_{yx}^{01} & g_{yy}^{00} & g_{yy}^{01} \\ g_{yx}^{10} & g_{yx}^{11} & g_{yy}^{10} & \left(bg_{yy}^{11} - b\alpha_B\right) \end{pmatrix}. \tag{7-8.1}$$

The G_{lin}-matrix is a $2n \times 2n$ matrix where n is the number of scattering channels (or beams as it is termed in the literature). For the two-beam case G_{lin} is a 4×4 matrix, but when there are many umveg, or simultaneous, reflections G_{lin} can rapidly become very large to

the point where a fast computer is a necessary tool for solving the characteristic equation. Resonant umveg reflections are not explored in this paper, thus the largest G_{lin}-matrix investigated is the linearized 4×4 matrix shown above. With the help of readily available computer programs (such as EISPACK or the NAG eigenvector-eigenvalue routines) numerically solving the dispersion equation for both the eigenvalues and eigenvectors is a straightforward procedure. However, insight into the dynamics of the scattering process is lost. This insight can be partly recovered by examining simple analytical solutions such as those presented in Sections 7-3 to 7-7.

When the incoming photon beam is near the surface grazing angle of the crystal, the boundary conditions described in Section 7-4 are no longer adequate--the specular reflection off the crystal surface is no longer negligible. One must now properly insure that the normal components of the **D** and **B** fields and the tangential components of the **E** and **H** fields of the Maxwell equations are continuous across the top and bottom surfaces of the crystal. When this is done for the two-beam case, instead of having 4 eigenvalues to solve for, there are now 8 to find. Four come from solving the characteristic equation in Eq. 7-4.19, and four more come from solving two separate dispersion equations describing fields propagating through the crystal that have been internally reflected from the top and bottom surface of the crystal. The continuity boundary conditions yields 16 equations (eight involving the transmission channel eigenwaves and eight involving the reflection channel eigenwaves). They can be reduced to 8 equations by eliminating the exiting fields and the specularly reflected field.[15] Resonant grazing angle scattering from crystals is also not explored in this thesis.

7.9 Nonlinear Dispersion Equation

The linearized dispersion equation is valid in the limit of finite and nonzero asymmetry factors. As $b \to 0$ or as $b \to \pm\infty$ (that is, when the forward scattered or diffracted field propagates nearly parallel to the crystal surface), the nonlinear dispersion equation presented in Eq. 7-1.4 may be required. This involves finding the solution to a quadratic characteristic equation.[15]

Projecting the wavectors within the crystal onto unit vectors normal and parallel to the crystal surface ($\hat{\mathbf{n}}$ and $\hat{\mathbf{u}}$ respectively) produces a nonlinear characteristic dispersion relation in terms of the projection of the transmission channel wavector onto the surface normal:

$$k_{0\hat{n}} = \mathbf{k}_0 \cdot \hat{\mathbf{n}}. \tag{7-9.1}$$

Noting that $\mathbf{k}_1 = \mathbf{k}_0 + \mathbf{H}_1$ (Bragg's law) gives

$$\mathbf{k}_1 \cdot \mathbf{k}_1 / k_{0v}^2 = k_{0\hat{n}}^2 + k_{0\hat{n}}\left(2H_{1\hat{n}}/k_{0v}\right) + \left(H_{1\hat{n}}/k_{0v}\right)^2 + k_{1\hat{u}}^2. \tag{7-9.2}$$

The quadratic characteristic relation is then

$$\left(k_{0\hat{n}}^2\mathbf{B}_2 + k_{0\hat{n}}\mathbf{B}_1 + \mathbf{B}_0 - \mathbf{G}\right)\boldsymbol{\upsilon} = 0 \tag{7-9.3}$$

where

$$\mathbf{B}_2 = \begin{pmatrix} 1 & & \\ & 1 & 0 \\ & 0 & 1 \end{pmatrix}, \quad \mathbf{B}_1 = \begin{pmatrix} 0 & & \\ & 0 & 0 \\ & 0 & 2H_{1\hat{n}}/k_{0v} \end{pmatrix},$$

$$\mathbf{B}_0 = \begin{pmatrix} -1 & & \\ & -1 & 0 \\ & 0 & \left(H_{1\hat{n}}/k_{0v}\right)^2 + k_{1\hat{u}}^2 - 1 \end{pmatrix},$$

$$\mathbf{G} = \begin{pmatrix} g_{xx}^{00} & g_{xx}^{01} & g_{xy}^{00} & g_{xy}^{01} \\ g_{xx}^{10} & g_{xx}^{11} & g_{xy}^{10} & g_{xy}^{11} \\ g_{yx}^{00} & g_{yx}^{01} & g_{yy}^{00} & g_{yy}^{01} \\ g_{yx}^{10} & g_{yx}^{11} & g_{yy}^{10} & g_{yy}^{11} \end{pmatrix}, \text{ and } \boldsymbol{\upsilon} = \begin{pmatrix} T_x \\ T_y \\ R_x \\ R_y \end{pmatrix}. \tag{7-9.4}$$

By defining an eigenvector $\boldsymbol{\omega}$ such that

$$\boldsymbol{\upsilon} = k_{0\hat{n}}\boldsymbol{\omega} \tag{7-9.5}$$

allows the quadratic characteristic equation to be modified to

$$k_{0\hat{n}}\mathbf{B}_1\mathbf{B}_2^{-1}\boldsymbol{\upsilon} + \left(\mathbf{B}_0 - \mathbf{G}\right)\mathbf{B}_2^{-1}k_{0\hat{n}}\boldsymbol{\omega} = -k_{0\hat{n}}^2\boldsymbol{\upsilon}. \tag{7-9.6}$$

This relation becomes linear in $k_{0\hat{n}}$ when both sides of the equation are divided by that parameter. The new linear characteristic equation to be solved for is then

$$\left(\mathbf{Q} - k_{0\hat{n}}\mathbf{I}\right)\mathbf{b} = 0 \tag{7-9.7}$$

where

$$\mathbf{Q} = \begin{pmatrix} -\mathbf{B}_1\mathbf{B}_2^{-1} & -\left(\mathbf{B}_0 - \mathbf{G}\right)\mathbf{B}_2^{-1} \\ \mathbf{I} & \mathbf{0} \end{pmatrix} \tag{7-9.8}$$

$$\mathbf{b} = \begin{pmatrix} \upsilon \\ \omega \end{pmatrix} \tag{7-9.9}$$

and I is the identity matrix.

Since the B and G-matrices are of order 4, the Q-matrix is of order 8. Then the linear characteristic equation will give 8 eigenvalues, $k_{0\hat{n}}^{\ell}$, and eigenvectors, $\mathbf{b}^{\ell}$. The first four elements of the eigenvector $\mathbf{b}^{\ell}$ yields υ^{ℓ} which is the desired eigenvector for the nonlinear dispersion equation. The boundary conditions are found by the same method explained in Section 7.8: ensuring that the normal components of $\mathbf{D}$ and $\mathbf{B}$ and the tangential components of $\mathbf{E}$ and $\mathbf{H}$ are continuous across the crystal interfaces. Instead of there being 16 eigenwaves inside the crystal that exists for the linearized dispersion relation with simple boundary conditions, there are now 32 eigenwaves traveling inside the crystal--16 for each polarization and 8 for each scattering channel direction.

When examining highly asymmetric reflections (which are also not explored in this thesis) one may need to solve the nonlinear dispersion equation rather that the linearized dispersion equation.

7.10 Umweganregung, or Simultaneous, Reflections

In the previous sections only 2-beam diffraction was investigated. However, n-beam diffraction from a crystal can occur when more than one set of crystal planes reflect the incident beam into the same outgoing direction. These umweganregung (umveg for short) reflections occur simultaneously with the primary reflection. The Ewald sphere for a 3-beam diffraction case is shown in Fig. 7-1.1. In the figure, $\mathbf{k}_0$ is shown to scatter into the $\mathbf{k}_H$ direction due to planes having a primary scattering vector $\mathbf{H}$. Simultaneously, $\mathbf{k}_0$ is scattered into the $\mathbf{k}_S$ direction due to planes having a scattering vector $\mathbf{S}$, and then $\mathbf{k}_S$ is scattered into the $\mathbf{k}_H$ direction due to planes having a scattering vector $\mathbf{H}-\mathbf{S}$.

Bragg's law for satisfying both the primary $\mathbf{H}$ reflection and the secondary $\mathbf{S}$ reflection can be obtained by studying the scattering geometry shown in Fig. 7-10.1. The scattering plane $(\hat{\mathbf{x}}, \hat{\mathbf{y}})$ consists of $\mathbf{k}_0$, $\mathbf{H}$, and $\mathbf{k}_H$, and $\mathbf{H}$ points in the $\hat{\mathbf{z}}$-direction. $\mathbf{S}$ is a secondary reciprocal lattice vector that makes and angle θ_S with respect to $\mathbf{H}$:

$$\hat{\mathbf{S}} = \sin\theta_S \cos\phi\,\hat{\mathbf{x}} + \sin\theta_S \sin\phi\,\hat{\mathbf{y}} + \cos\theta_S\,\hat{\mathbf{z}}. \tag{7-10.1}$$

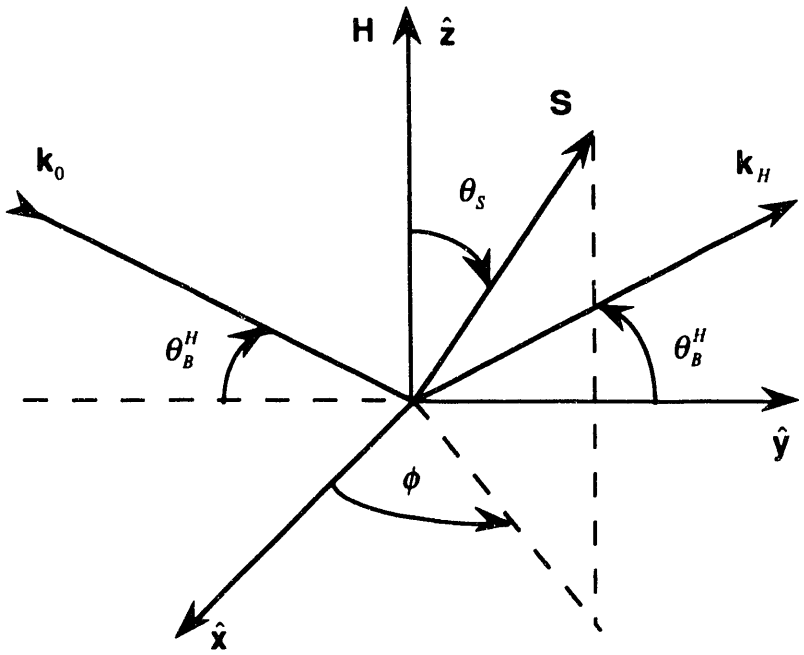

Fig. 7-10.1 Scattering geometry for 3-beam diffraction.

The Bragg angle between **H** and $\mathbf{k}_H$ is $90°-\theta_B^H$, and the Bragg angle between **S** and $\mathbf{k}_H$ is $90°-\theta_B^S$. Then, from Fig. 7-10.1,

$$\sin\theta_B^S = \hat{\mathbf{k}}_H \cdot \hat{\mathbf{S}} = \sin\theta_B^H \cos\theta_S + \cos\theta_B^H \sin\theta_S \sin\phi . \tag{7-10.2}$$

Bragg's law for each of the separate reflections is (recall Eq. 7-4.17)

$$\sin\theta_B^H = \hbar cH/2E_B \quad \text{and} \quad \sin\theta_B^S = \hbar cS/2E_B . \tag{7-10.3}$$

The azimuthal angle for which both of these reflections occur simultaneously is then

$$\sin\phi = \frac{\hbar c}{2E_B \sin\theta_S}\left(\frac{L - H\cos\theta_S}{\sqrt{1-(\hbar cH/2E_B)^2}}\right), \tag{7-10.4}$$

and the energy at which this occurs is

$$E_B = \frac{\hbar c}{2}\sqrt{\left(\frac{L - H\cos\theta_S}{\sin\theta_S \sin\phi}\right)^2 + H^2} . \tag{7-10.5}$$

Umveg reflections can show up as undesirable glitches in crystallography experiments. Or, they can be useful as precise energy calibration markers. As a result, knowledge of the intensity of umveg reflections is valuable information. As a first order approximation, the intensity of an umveg reflection is proportional to the product of the structure factors of the umveg's two sets of reflections:

$$I_{umveg} \approx F_S F_{H-S} \tag{7-10.6}$$

where F is the structure factor of a unit cell (see Eqs. 6-1.4 and 6-1.5).[16] More about these umveg reflections are discussed in Section 9.5 where they are used as energy calibration markers and where ϕ-energy graphs are constructed to chart out the regions that should be avoided.

REFERENCES

[1] R. W. James, *The Optical Principles of the Diffraction of X-Rays* (Ox Bow Press, Woodbridge, Connecticut, 1982).

[2] B. E. Warren, *X-Ray Diffraction* (Dover, New York, 1990).

[3] W. H. Zachariasen, *Theory of X-Ray Diffraction in Crystals* (Dover, New York, 1945).

[4] B. W. Batterman and H. Cole, *Rev. Mod. Phys.* **36**, 681 (1964).

[5] J. P. Hannon and G. T. Trammell, *Phys. Rev.* **169**, 169 (1968).

[6] J. P. Hannon and G. T. Trammell, *Phys. Rev.* **186**, 306 (1969).

[7] J. P. Hannon, N. J. Carron, and G. T. Trammell, *Phys. Rev. B* **9**, 2791 (1974).

[8] J. P. Hannon, N. J. Carron, and G. T. Trammell, *Phys. Rev. B* **9**, 2810 (1974).

[9] A. M. Afanas'ev and Y. Kagan, *Sov. Phys. JETP* **21**, 215 (1965).

[10] Y. Kagan, A. M. Afanas'ev, and I. P. Perstnev, *Sov. Phys. JETP* **27**, 819 (1968).

[11] Y. Kagan, A. M. Afanas'ev, and V. G. Kohn, *J. Phys. C* **12**, 615 (1979).

[12] H. J. Maurus, U. van Bürck, G. V. Smirnov, and R. L. Mössbauer, *J. Phys. C* **17**, 1991 (1984).

[13] I. S. Lyubutin, E. F. Makarov, and V. A. Povitskii, *Sov. Phys. JETP* **26**, 44 (1967).

[14] M. Abramowitz and I. A. Stegun, *Handbook of Mathematical Functions* (National Bureau of Standards, Washington D.C., 1972).

[15] R. Colella, *Acta Cryst.* **A30**, 413 (1974).

[16] Q. Shen, *Acta Cryst.* **A42**, 525 (1986).

8. NUMERICAL ANALYSIS PROCEDURES

8.1 Crystal Structure of Fe_2O_3, $FeBO_3$,and YIG

The principle crystals used in the field of nuclear resonance scattering have been hematite $(\alpha-Fe_2O_3)$,[1-4] rhombohedral iron borate $(FeBO_3)$,[5-7] yittrium iron garnet (YIG),[8, 9] and orthorhombic iron borate (Fe_3BO_6)[10, 11] (and, to a lesser extent, potassium ferrocyanide $(K_4Fe(CN)_6 \cdot 3H_2O)$,[12] sodium nitroprusside $(Na_2Fe(CN)_5NO \cdot 2H_2O)$,[13] ^{157}Te crystals,[14] and mosaic ^{119}Sn crystals[15] -- these crystals have very large mosaic spreads, and perfect crystals of these compounds are difficult to fabricate). All these crystals (except for the mosaic ^{119}Sn crystals) have the feature that, for certain crystallographic reflections, nonresonant photoelectric diffraction is forbidden whereas resonant nuclear diffraction is allowed.[16] This feature allows the nonresonant background to be significantly reduced in order to observe the nuclear signal.

$\alpha-Fe_2O_3$ and $FeBO_3$ both have a rhombohedral calcite crystal structure (space group $R\bar{3}c - D_{3d}^6$)[17-19] and exhibit a canted antiferromagnet system[20-23] (see Fig. 8.1-1). They each have two molecules per unit cell which lead to the formation of magnetic sublattices below the Néel temperature (948°K for $\alpha-Fe_2O_3$ and 348°K for $FeBO_3$).[20, 23] The magnetic moments lie within the (1 1 1) plane with two adjacent planes being antiferromagnetically coupled (however, below the Morin temperature of 253°K the $\alpha-Fe_2O_3$ magnetic moments align themselves perpendicular to the (1 1 1) planes[24]). Because the antiferromagnetic moments are canted, there is a small ferromagnetic moment lying within the (1 1 1) plane. The ferromagnetic moments will align themselves parallel to an external magnetic field, therefore, an applied external magnetic field can be used to orient the antiferromagnetic moments (an alignment field of about 1 kGauss[25, 26] is needed for $\alpha-Fe_2O_3$ and only several Gauss (~ 5Gauss)[22, 27] is needed for $FeBO_3$).

Because of the antiferromagnet sublattice structure, resonant nuclear reflections are allowed from certain lattice planes whereas photoelectric reflections are forbidden. For instance, from planes A and B for the crystals in Fig. 8.1-1, the electric fields are reflected 180° out of phase. However, since the magnetic moments lie in nearly antiparallel directions for the two planes, the polarization of the reflected fields for each hyperfine line for the two planes is different (for perfect antiferromagnets, the polarizations are

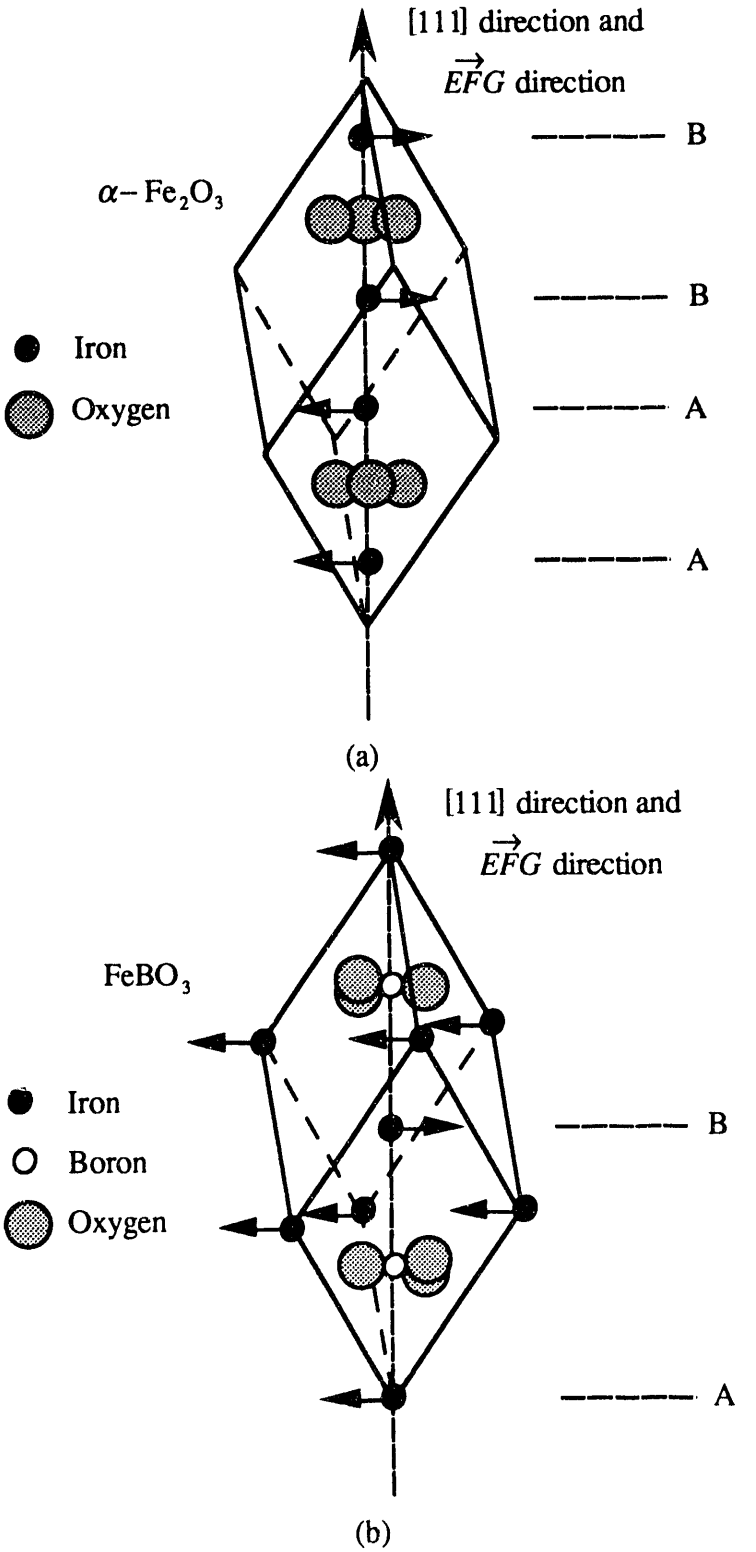

Fig. 8.1-1. Antiferromagnetic structure of (a) $\alpha-Fe_2O_3$ and (b) $FeBO_3$. The electric field gradients lie perpendicular to the (1 1 1) planes. Planes A and B have magnetic moments in antiparallel directions.

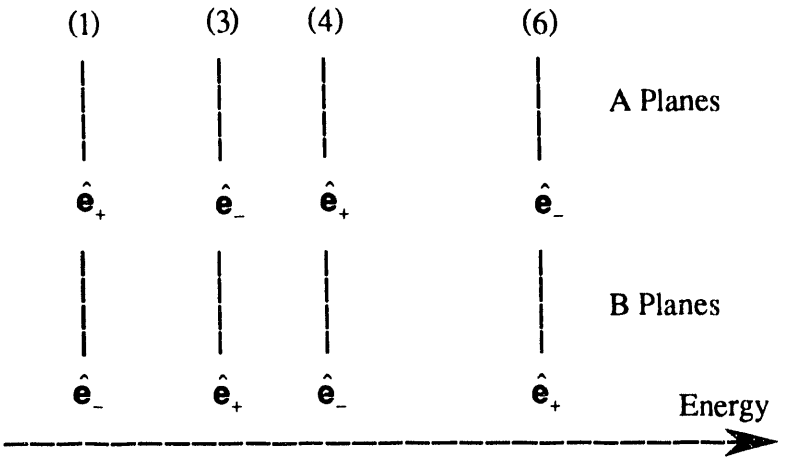

Fig. 8.1-2. Hyperfine energy spectrum illustrating the case where the applied magnetic field is perpendicular to the scattering plane (only hyperfine lines 1,3,4, and 6 are then possible). For small canting and Bragg angles, the polarization of each hyperfine line of the reflected field can be approximated as right and left circularly polarized: $\hat{\mathbf{e}}_-$ and $\hat{\mathbf{e}}_+$. Since the internal hyperfine fields are identical for the iron atoms in the A and B planes (except for the direction of the internal magnetic fields), the hyperfine lines from the two planes overlap with a 180° phase difference due to the position of atoms within the unit cell. However, due to polarization differences, there is no cancellation of the fields reflected from the two planes.

orthogonal--see Fig. 8.1-2). Complete cancellation of the reflected fields is then no longer possible.

YIG $(Y_3Fe_5O_{12})$ is the crystal examined in this thesis. Even though it has a cubic crystal structure, its unit cell is much more complex than the rhombohedral structure of the other crystals. YIG belongs to the space group Ia3d - O_h^{10}, and it has 96 O^{3-} ions located at the $h-$sites, 24 Y^{2+} located at the $c-$sites, and 40 Fe^{3+} ions located at the a and $d-$sites.[28] During the 1960's and 1970's when magnetic bubbles appeared to be a promising way to store megabytes of information, the technology was developed to grow high quality YIG crystal films on GGG (gadolinium gallium garnet) substrates by liquid-phase epitaxy methods. Because these YIG films can be grown nearly free of dislocations and other crystal defects and with very uniform lattice spacings, YIG is an attractive choice for nuclear resonant diffraction experiments.

YIG is a ferrimagnet below the Curie temperature of 559°K for ceramic materials and 549.2°K for YIG films grown from $PbO - V_2O_5$ fluxes.[29] The easy direction of magnetization is the [111] direction, though alignment fields of 100 Gauss are sufficient to orient the magnetic moments to the [001] direction. The $d-$site iron atoms are surrounded by a distorted oxygen tetrahedron stretched along a fourfold inversion axis oriented in the [001] direction, and the $a-$site iron atoms are surrounded by a distorted octahedron

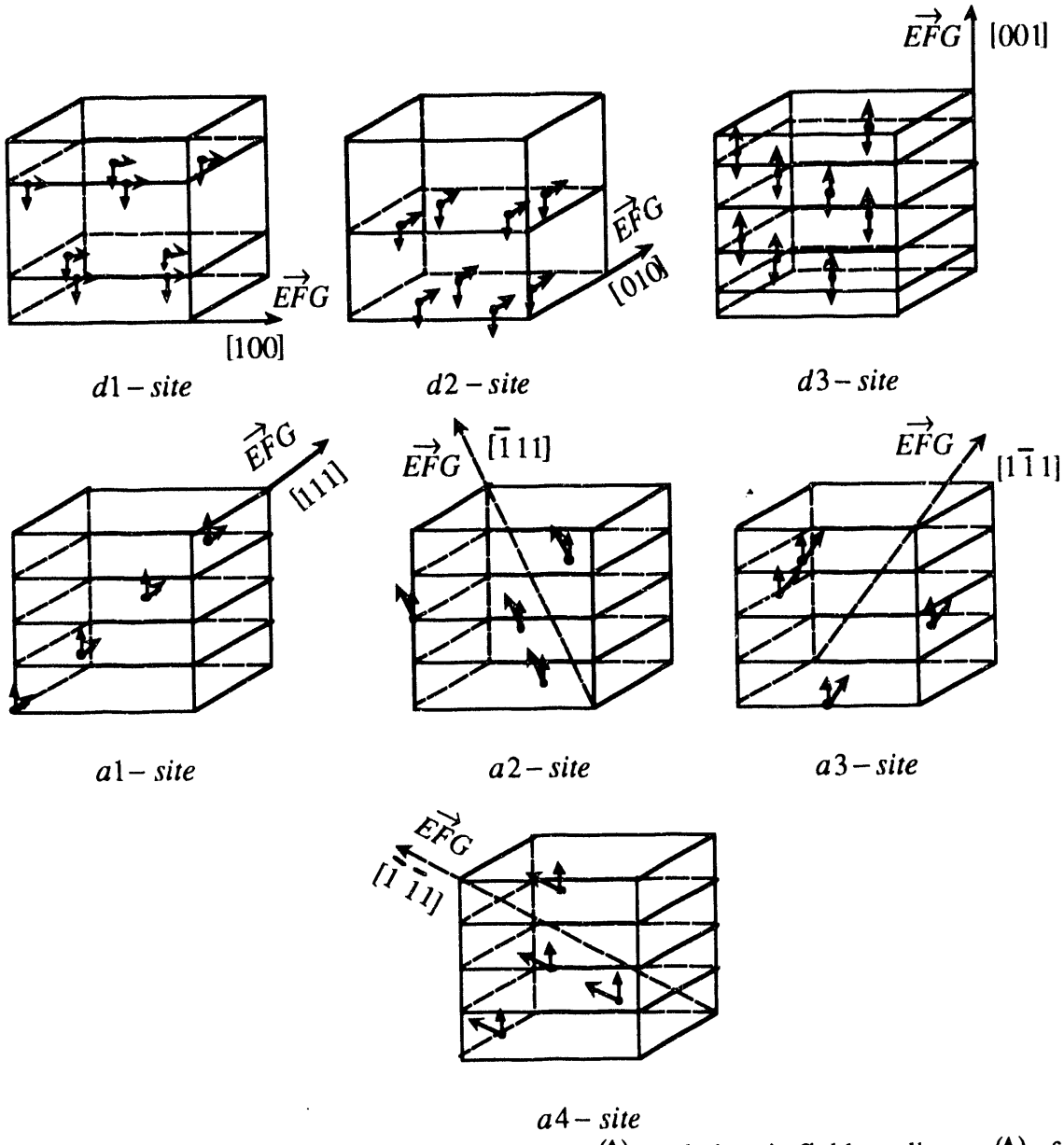

Fig. 8-1.3. Orientation of magnetic moments, (↑), and electric field gradients, (↑), for the seven magnetic sublattices of YIG. To orient the magnetic moments, there is an applied magnetic field in the [001] direction.

stretched along a threefold symmetry axis oriented in the [111] direction. The electric field gradients formed within these distorted oxygen polyhedra lie along the symmetry axis. The seven ferromagnetic sublattices within the YIG unit cell are shown in Fig. 8-1.3 with the orientation of the magnetic moments and electric field gradients.[30, 31]

For the experiments done in this thesis, crystal planes were chosen where all the a – site reflections were forbidden and all the d – site reflections were allowed except for the $d3$ – site. Therefore, ferromagnetic ordering was utilized to examine nuclear resonant

scattering instead of antiferromagnetic ordering as was used for the $\alpha-Fe_2O_3$ and $FeBO_3$ crystals. Nonzero reflected fields now occur because of different electric quadrupole shifts between the $d-$sites rather than because of polarization differences that occur for antiferromagnetic crystals (See Fig. 8-1.4).

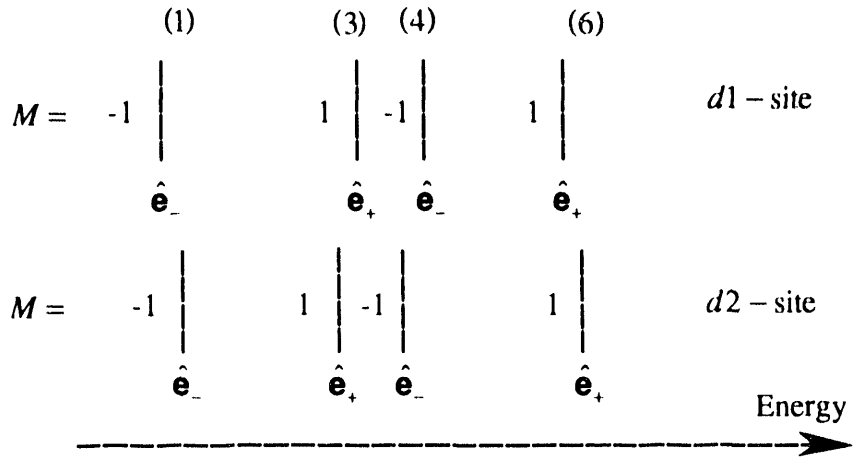

Fig. 8-1.4. Hyperfine energy spectrum illustrating the case where the applied magnetic field is parallel to the scattering plane.[32] For small Bragg angles the polarization of each hyperfine line can be approximated as right and left circularly polarized: $\hat{\mathbf{e}}_-$ and $\hat{\mathbf{e}}_+$. The magnetic moments of the two sites are parallel, but the electric field gradients are in perpendicular directions. This introduces small differences in the electric quadrupole field which show up as different quadrupole shifts in the hyperfine lines for each $d-$site.

8.2 Crystallography

To orient a general crystal for diffraction, an orientation matrix must be found that can perform the transformation of a vector in reciprocal space to an orthogonal lab coordinate system. Let there be a vector $\mathbf{v}$ in reciprocal space with basis axes $\left(\hat{\mathbf{a}}^*,\hat{\mathbf{b}}^*,\hat{\mathbf{c}}^*\right)$:

$$\mathbf{v} = \mathbf{h}^{\mathrm{T}}\hat{\mathbf{r}}^* = h\hat{\mathbf{a}}^* + k\hat{\mathbf{b}}^* + \ell\hat{\mathbf{c}}^* \qquad (8\text{-}2.1)$$

where $\hat{\mathbf{r}}^* = \hat{\mathbf{a}}^* + \hat{\mathbf{b}}^* + \hat{\mathbf{c}}^*$ is a unit radial vector in reciprocal space and $\mathbf{h}^{\mathrm{T}} = (h,k,\ell)$ is a row vector containing the Miller indices, or reciprocal space coordinates, of the reciprocal vector $\mathbf{v}$. Let the laboratory system have a fixed orthogonal basis $\left(\hat{\mathbf{x}}_L,\hat{\mathbf{y}}_L,\hat{\mathbf{z}}_L\right)$ (see Fig. 8-2.1). The problem is then to find the components of $\mathbf{v}$ in the lab space.

A solution can be found if there are three known reflections from the crystal. Then there are three reciprocal vectors $\mathbf{v}_1$, $\mathbf{v}_2$, and $\mathbf{v}_3$ which are known to point in some direction in lab space--their components in lab space are then known. This is summarized

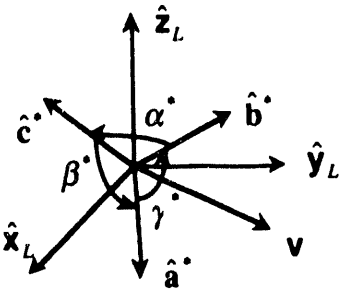

Fig. 8-2.1. Vector **v** in reciprocal and lab space.

by the following relation:[33]

$$\left.\begin{aligned} v_{1L} &= v_1 \\ v_{2L} &= v_2 \\ v_{3L} &= v_3 \end{aligned}\right\} \Rightarrow \begin{pmatrix} h_{1L} & k_{1L} & \ell_{1L} \\ h_{2L} & k_{2L} & \ell_{2L} \\ h_{3L} & k_{3L} & \ell_{3L} \end{pmatrix} \begin{pmatrix} \hat{x}_L \\ \hat{y}_L \\ \hat{z}_L \end{pmatrix} = \begin{pmatrix} h_1 & k_1 & \ell_1 \\ h_2 & k_2 & \ell_2 \\ h_3 & k_3 & \ell_3 \end{pmatrix} \begin{pmatrix} \hat{a}^* \\ \hat{b}^* \\ \hat{c}^* \end{pmatrix}$$

or
$$\mathbf{H}_L^{\mathrm{T}} \hat{\mathbf{r}}_L = \mathbf{H}^{\mathrm{T}} \hat{\mathbf{r}}^* \tag{8.2-2}$$

(the superscript T denotes the transpose of the matrix, and vectors are always column vectors). The coordinate axes then transform as

$$\hat{\mathbf{r}}_L = \mathbf{U}' \hat{\mathbf{r}}^* \tag{8-2.3}$$

where
$$\mathbf{U}' = \left(\mathbf{H}_L^{\mathrm{T}}\right)^{-1} \mathbf{H}^{\mathrm{T}}. \tag{8-2.4}$$

From Eqs. 8-2.2 and 8-2.3, one also gets a relationship detailing how the coordinates transform:

$$\mathbf{h}_L^{\mathrm{T}} \mathbf{U}' = \mathbf{h}^{\mathrm{T}} \tag{8-2.5}$$

which leads to

$$\mathbf{h}_L = \left(\mathbf{U}'^{-1}\right)^{\mathrm{T}} \mathbf{h} \tag{8-2.6}$$

or
$$\mathbf{h}_L = \mathbf{U}\mathbf{h} \tag{8-2.7}$$

where
$$\mathbf{U} = \mathbf{H}_L \mathbf{H}^{-1}. \tag{8-2.8}$$

As expected, the coordinates transform in an inverse way to the axes since $\mathbf{U}^{\mathrm{T}} = \mathbf{U}'^{-1}$. Thus, from a knowledge of the elements of $\mathbf{H}_L$ and $\mathbf{H}^{-1}$ for three reciprocal vectors, the components of any reciprocal vector can be obtained in terms of lab coordinates by using Eq. 8-2.7.

The determination of the orientation matrix can be simplified if a primary reflection, $\mathbf{h}_p$, is known and a secondary reflection, $\mathbf{h}_s$, lies in the scattering plane such that $\mathbf{h}_s \cdot \mathbf{k}_f > 0$ where $\mathbf{k}_f$ is the scattered wavevector of the primary reflection (see Fig. 8-2.2). The third reciprocal vector can be found by taking the cross product between the primary

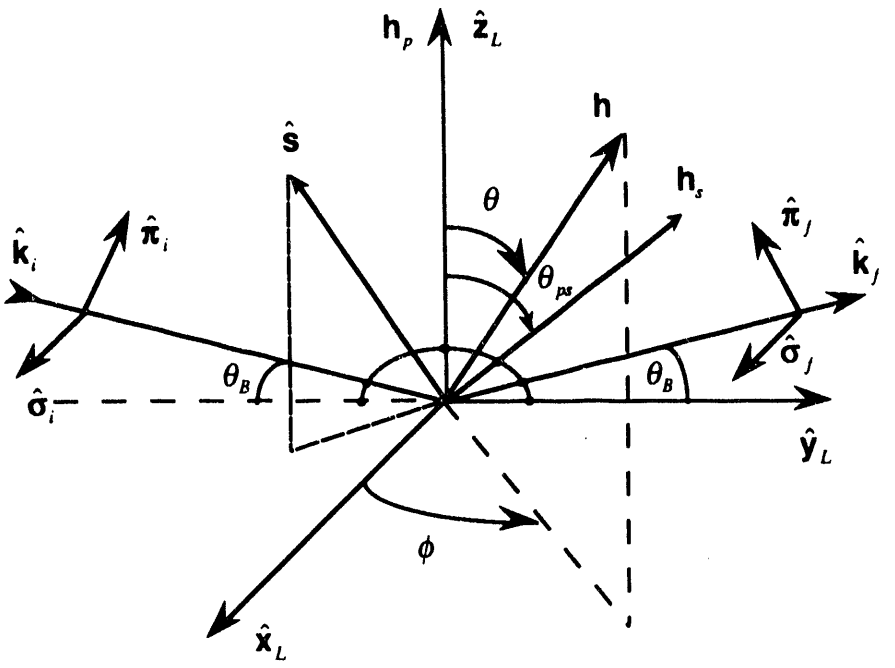

Fig. 8-2.2. Orientation geometry for diffraction. $\mathbf{k}_i, \mathbf{k}_f, \mathbf{h}_p, \mathbf{h}_s, \hat{\mathbf{y}}_L$, and $\hat{\mathbf{z}}_L$ all lie in the scattering plane. $\mathbf{k}_f$ diffracts from planes perpendicular to $\mathbf{h}_p$, $\mathbf{h}_p$ is parallel to $\hat{\mathbf{z}}_L$, $\hat{\mathbf{x}}_L$ is perpendicular to the scattering plane, and $\hat{\mathbf{s}}$ is the outward surface normal of the crystal. $(\hat{\mathbf{x}}_L, \hat{\mathbf{y}}_L, \hat{\mathbf{z}}_L)$ lab system is fixed in space and never rotates--same for $\mathbf{k}_i$ since it comes from a fixed source. $\mathbf{h}_p, \mathbf{h}_s, \mathbf{k}_f$, and $\hat{\mathbf{s}}$ all rotate with crystal as it is oriented in space. $\mathbf{h}$ is the desired reflection and is always eventually oriented to lie in the $\hat{\mathbf{z}}_L$-direction.

and secondary reciprocal vectors. Cross products can be done only in spaces with an orthonormal basis, therefore, for crystals with noncubic structure, such as rhombohedral crystals, one must project the reciprocal basis onto an orthonormal basis, then take the cross product, and then project the results back into reciprocal space. The matrix that transforms a reciprocal vector to an orthogonal space with basis $(\hat{\mathbf{x}}_0, \hat{\mathbf{y}}_0, \hat{\mathbf{z}}_0)$ is[34, 35]

$$\mathbf{B} = \begin{pmatrix} a^* & b^* \cos\gamma^* & c^* \cos\beta^* \\ 0 & b^* \sin\gamma^* & -c^* \sin\beta^* \cos\alpha \\ 0 & 0 & 1/c \end{pmatrix} \tag{8-2.9}$$

$$\mathbf{B}^{-1} = \begin{pmatrix} a\sin\beta\sin\gamma^* & -a\sin\beta\cos\gamma^* & a\cos\beta \\ 0 & b\sin\alpha & b\cos\alpha \\ 0 & 0 & c \end{pmatrix} \tag{8-2.10}$$

where $(\hat{\mathbf{a}}, \hat{\mathbf{b}}, \hat{\mathbf{c}})$ are the direct crystal axes with interaxis angles α, β, γ where $\cos\alpha = \hat{\mathbf{b}} \cdot \hat{\mathbf{c}}$, $\cos\beta = \hat{\mathbf{c}} \cdot \hat{\mathbf{a}}$, $\cos\gamma = \hat{\mathbf{a}} \cdot \hat{\mathbf{b}}$, and $(\hat{\mathbf{a}}^*, \hat{\mathbf{b}}^*, \hat{\mathbf{c}}^*)$ are the reciprocal lattice axes with interaxis

reciprocal angles α^*, β^*, γ^* defined in a similar manner. In the orthogonal space $\hat{\mathbf{x}}_0$, $\hat{\mathbf{y}}_0$, $\hat{\mathbf{a}}^*$, and $\hat{\mathbf{b}}^*$ all lie in a plane perpendicular to $\hat{\mathbf{z}}_0$, and $\hat{\mathbf{a}}^*$ is parallel to $\hat{\mathbf{x}}_0$.

A third reflection is then

$$\mathbf{h}_3 = \mathbf{h}_p \times \mathbf{h}_s = \mathbf{B}^{-1}\left[(\mathbf{B}\mathbf{h}_p)\times(\mathbf{B}\mathbf{h}_s)\right]. \tag{8-2.11}$$

From Fig. 8-2.2, the lab coordinates of the reciprocal vectors can easily be seen. The primary reflection is in the $\hat{\mathbf{z}}_L$-direction, the third reflection is in the $\hat{\mathbf{x}}_L$-direction, and the secondary reflection is

$$\mathbf{h}_{sL} = |\mathbf{h}_s|\left(\sin\theta_{ps}\hat{\mathbf{y}}_L + \cos\theta_{ps}\hat{\mathbf{z}}_L\right) \tag{8-2.12}$$

where

$$\cos\theta_{ps} = \mathbf{h}_p \cdot \mathbf{h}_s / |\mathbf{h}_p||\mathbf{h}_s|. \tag{8-2.13}$$

To take the dot product of two vectors in a nonorthogonal basis, the two vectors must again be transformed to an orthogonal space in which the dot product can be properly taken:

$$\mathbf{h}_p \cdot \mathbf{h}_s = (\mathbf{B}\mathbf{h}_p)^{\mathrm{T}} \cdot (\mathbf{B}\mathbf{h}_s). \tag{8-2.14}$$

Note that the dot product relationship gives the metric for reciprocal space:

$$\mathbf{B}^{\mathrm{T}}\mathbf{B} = \begin{pmatrix} \mathbf{a}^*\cdot\mathbf{a}^* & \mathbf{a}^*\cdot\mathbf{b}^* & \mathbf{a}^*\cdot\mathbf{c}^* \\ \mathbf{a}^*\cdot\mathbf{b}^* & \mathbf{b}^*\cdot\mathbf{b}^* & \mathbf{b}^*\cdot\mathbf{c}^* \\ \mathbf{a}^*\cdot\mathbf{c}^* & \mathbf{b}^*\cdot\mathbf{c}^* & \mathbf{c}^*\cdot\mathbf{c}^* \end{pmatrix} = \mathbf{G}^{-1}. \tag{8-2.15}$$

The dot product can then be written in the familiar way for the dot product of two vectors within a space defined by a metric $\mathbf{G}$:

$$\mathbf{h}_p \cdot \mathbf{h}_s = h_{p\mu} G^{\mu\nu} h_{s\nu} \tag{8-2.16}$$

where $h_{p\mu}$ and $h_{s\nu}$ are the covariant components of the vectors $\mathbf{h}_p$ and $\mathbf{h}_s$ (that is, they are the components of those vectors in reciprocal space), and $G^{\mu\nu}$ are the contravariant elements of the metric for the direct crystal axes space (that is, they are the elements of the reciprocal space metric $\mathbf{G}^{-1}$). The cross product given in Eq. 8-2.11 can also be written in terms of the metric as[36]

$$(\mathbf{h}_p \times \mathbf{h}_s)_\ell = G_{\ell i}\varepsilon^{ijk} h_{pj} h_{sk} \tag{8-2.17}$$

where ε^{ijk} is the contravariant antisymmetric tensor for a space with metric $\mathbf{G}^{-1}$:

$$\varepsilon^{ijk} = \begin{cases} \sqrt{\det|\mathbf{G}^{-1}|} & \text{if } i,j,k \text{ is a cyclic permutation of } 1,2,3 \\ -\sqrt{\det|\mathbf{G}^{-1}|} & \text{if } i,j,k \text{ is a cyclic permutation of } 2,1,3 \\ 0 & \text{otherwise} \end{cases} \qquad (8\text{-}2.18)$$

and G_{ti} are the covariant elements of the metric for the direct crystal axes space (that is, they are the elements of the metric **G**).

The orientation matrix **U** can now be constructed since $\mathbf{H}_L$ and **H** are completely determined:

$$\mathbf{H}_L = \begin{pmatrix} 0 & 0 & |\mathbf{h}_3| \\ 0 & |\mathbf{h}_s|\sin\theta_{ps} & 0 \\ |\mathbf{h}_p| & |\mathbf{h}_s|\cos\theta_{ps} & 0 \end{pmatrix} \qquad (8.2\text{-}19)$$

$$\mathbf{H} = \begin{pmatrix} h_p & h_s & h_3 \\ k_p & k_s & k_3 \\ \ell_p & \ell_s & \ell_3 \end{pmatrix} \qquad (8\text{-}2.20)$$

and $$\mathbf{U} = \mathbf{H}_L\mathbf{H}^{-1}. \qquad (8\text{-}2.21)$$

The Fortran code, **Orient_cryst**, embodying all of this section's discussion on orienting a general crystal follows. The subroutine uses the same framework as Busing and Levy's Algol program designed for 3 and 4-circle diffractometers.[35] In addition to what has been discussed, the subroutine can perform rotations about the desired reflection, **h**, and rotations about the incoming photon direction, $\mathbf{k}_i$, that preserve the Bragg condition.

The subroutine must be linked with another subroutine package called EIS_LIN_PACK. This package contains the popular LINPACK code for solving simultaneous equations and the EISPACK code for solving eigenvalue problems.[37, 38] They were obtained from the National Energy Software Center at Argonne National Laboratory. The subroutine **Lineq** in LINPACK was used to find the inverse matrix $\mathbf{H}^{-1}$ for constructing the orientation matrix.

In the Fortran code below, and in the EWALD code that follows later, to preserve space, several lines of code are piled up onto a single line. A semicolon (never used in actual Fortran code) separates each line of code.

```
      Subroutine Orient_cryst(Ee,a,alpha,hp,hs,h,S,Uo,sigmai,pii,sigmaf,pif,b)
c This Subroutine sets up the Crystal Orientation for Diffraction.  Uo is  the Net Orientation Matrix -- to
c Transform any Reciprocal Lattice Vector to the Orthogonal Lab Coordinate System, Operate Uo on it:
c                              V_lab = Uo(dot)V_recip.
c VARIABLES:
c  a(i) = Crystal Lattice Spacings a,b,c (cm) ; alpha(i) = Crystal Lattice angles alpha,beta,gamma (deg)
c  Vo = Unit Cell Volume (cm**3) ; Ee = Incoming Photon Energy (Ev) ; hp,hs = Primary and Secondary
c  Reciprocal Lattice Vectors ; S = Outward Surface Direction ; h = Desired Reciprocal Lattice Scattering
c  Vector ; Ki,Kf = Incoming and Diffracted wavevectors (1/Angstrom) ; sigma,pi = sigma and pi
c  polarization vectors ; Bragg = Bragg Angle (radians) ; b = Asymmetry Factor
c  PhiKi,phiH = azimuthal rotation angles about Ki and h directions (deg)
c  psi = azimuthal rotation angle about h after azimuthal rotation about Ki has been done.
c  NOTE:
c(1)  The Lab coordinate system is determined by Ki and its polarization vectors.
c(2)  PhiKi = rotation of a plane perpendicular to Ki direction.  For example, phiKi = 90 deg ==> h rotates
c          from Lab_z to a vector lying in [Lab_x,Lab_y] plane.  PhiH = azimuthal rotation of plane
c          perpendicular to h direction.  PhiKi,PhiH rotations both preserve Bragg's Condition.
c  LINK:      Link with EIS_LIN_PACK
c D.E.Brown 1990            (SSRL/STANFORD)
      Real*8   **Everything possible** (all Matrices are 3x3 arrays)
      Common /stup/ hbarc,sinBragg,Vo,phiKi,phiH,psi,Ki,Kf,kis
      Common /Lab/ x_Lab,y_Lab,z_Lab  ;  Common /conv/ rad,pi
c Construct a matrix Bo that transforms from non-orthogonal axes to an orthogonal axes system.
c Boi is the inverse of Bo.
      Call Generate_Bo(a,alpha,Vo,Bo,Boi)
c Determining angle between hs and hp which gives orientation of hs in Lab coordinate system
      Call General_Dot(hp,hp,Bo,hpp)  ;  Call General_Dot(hs,hs,Bo,hss)
      Call General_Dot(hp,hs,Bo,hps)  ;  Call General_Dot(S,S,Bo,ss)
      hpp = Dsqrt(hpp)  ;  hss = Dsqrt(hss)  ;  ss = Dsqrt(ss)
      cosps = hps/(hpp*hss)     ! angle between hs and hp  ;  sinps = Dsqrt(1.0d0 - cosps**2)
c To construct a third vector, take cross product of hs and hp
      Call General_Cross(hs,hp,Bo,Boi,h3)  ;  Call General_Dot(h3,h3,Bo,h33)  ;  h33 = Dsqrt(h33)
c One can now construct the Orientation Matrix U that transforms any vector in reciprocal coordinate space to
c the Lab coordinate space.  Note that: hp is in Lab_z direction, hs = cosps(Lab_z) + sinps(Lab_y), and h3 is in
c Lab_x direction.
      Call Lab_Vectors(hpp,hss,h33,sinps,cosps,hplab,hslab,h3lab)
      Call Orientation(hp,hs,h3,hplab,hslab,h3lab,U)
c Computation of the Bragg angle of the Desired Reflection.  Note that hmag = 1.0/d(hkl) ,
c where d(hkl) = interplaner spacing for indices h,k,l (units = angstroms)
      Call General_Dot(h,h,Bo,hmag)          ;  hmag = Dsqrt(hmag)
      sinBragg = pi*hbarc*hmag*1.0d8/Ee  ;  cosBragg = Dsqrt(1.0 - sinBragg**2)
c The h reflection is desired.  Then rotate h so that is is pointing in the Lab_z direction--h will point in the
c direction hp used to be directed.  To Do this, transform h to Lab system, h --> Uh = hLab.  From its polar and
c azimuthal angles, one can now rotate h to point in the Lab_z direction--and one can rotate all of the other
c vectorsattached to the crystal system with rotatation matrix Rz.
      Call Mv(U,h,hLab)  ;  Call Polar(hLab,x_Lab,y_Lab,z_Lab,theta,phi)  ;  Call Generate_Rz(theta,phi,Rz)
c Now, the crystal can be rotated about h and Ki and still preserve the Bragg condition.  The Rkh matrix
c performs this rotation.  First the crystal is rotated azimuthally about h, and then azimuthally about Ki.  The
c Rpsi matrix performs an addition azimuthal rotation about h after the rotation Rkh has been done (necessary
c only when a rotation about Ki has been done).  Uo is the Net Orientation Matrix.  First it transforms reciprocal
c lattic vector to Lab system.  Then it rotates it by Rz in aligning h to point in the +z_Lab direction.  Then it
c makes Rkh Bragg preserving rotation.
      Call Generate_Rkh(phiH*rad,phiKi*rad,cosBragg,sinBragg,Rkh)  ;  Call MM(Rz,U,dum2)
      If(phiKi .Eq. 0.0) Then  ;  Call MM(Rkh,dum2,Uo)     ! Uo is the Net Orientation Matrix
      Else  ;  Call Generate_Rpsi(psi*rad,Rz,Rkh,hLab,Rpsi)  ;  Call MM(Rkh,dum2,dum3)  ;  Call MM(Rpsi,dum3,Uo)
      Endif
c The Diffracted wavevector can now be determined from Bragg's law h = Kf - Ki, as well as the asymmetry
c factor b = ki(dot)n/Kf(dot)n where n = inward surface normal.
      Call Mv(Uo,h,hLab)  ;  Call Mv(Uo,S,SLab)  ;  Ko = Ee*1.0d-8/hbarc
      Do 1 I=1,3
        Ki(i) = Ko*(cosBragg*y_Lab(i) - sinBragg*z_Lab(i))  ;  Kf(i) = 2.0*pi*hLab(i) + Ki(i)
1     pii(i) = sinBragg*y_Lab(i) + cosBragg*z_Lab(i)        ;  sigmai(i) = x_Lab(i)
      Call Cross(Kf,z_Lab,sigmaf,norm)          !diffracted sigma polarization
      Call Cross(sigmaf,Kf,pif,norm)            !diffracted pi polarization
```

```
   Call Dot(Ki,SLab,kis) ; Call Dot(Kf,SLab,kfs) ; b = kis/kfs ; kis = kis/(ss*Ko)
   Do 5 I=1,3
5    Ki(i) = Ki(i)/Ko ; Kf(i) = Kf(i)/Ko
   Return
   End
*****************************************************************************************************
   Subroutine Generate_Rz(theta,phi,Rz)
c This subroutine rotates crystal so that the desired reciprocal lattice scattering vector is in the Lab_z direction.
c Rz = the rotation matrix that does this. First, crystal is rotated azimuthally by phi so that desired vector lies in
c (+x_Lab,+z_Lab) plane. Then, crystal is rotated polarly by theta so that the vector lies points in the +z_Lab
c direction.
   cost = Dcos(theta)    ; sint = Dsin(theta) ; cosp = Dcos(phi)     ; sinp = Dsin(phi)
   Rz(1,1) = cost*cosp   ; Rz(2,1) = -sinp    ; Rz(3,1) = sint*cosp
   Rz(1,2) = cost*sinp   ; Rz(2,2) = cosp     ; Rz(3,2) = sint*sinp
   Rz(1,3) = -sint       ; Rz(2,3) = 0.0d0    ; Rz(3,3) = cost
   Return
*****************************************************************************************************
   Subroutine Generate_Rkh(pH,pK,cosb,sinb,Rkh)
c This subroutine constructs Rotation Matrix Rkh that performs Bragg-preserving rotations first by pH about
c the reciprocal scattering vector and then by pK about the incident photon direction. All rotations obey right
c hand rule.
   cosh = Dcos(pH)       ; sinh = Dsin(pH) ; cosk = Dcos(pK)     ; sink = Dsin(pK)
   Rkh(1,1) = cosk*cosh + sinb*sink*sinh ; Rkh(2,1) = -sinb*sink*cosh + (sinb**2*cosk + cosb**2)*sinh
   Rkh(3,1) = -cosb*sink*cosh + cosb*sinb*(cosk - 1.0d0)*sinh
   Rkh(1,2) = -cosk*sinh + sinb*sink*cosh ; Rkh(2,2) = sinb*sink*sinh + (sinb**2*cosk + cosb**2)*cosh
   Rkh(3,2) = cosb*sink*sinh + cosb*sinb*(cosk - 1.0d0)*cosh
   Rkh(1,3) = cosb*sink ; Rkh(2,3) = cosb*sinb*(cosk - 1.0d0) ; Rkh(3,3) = cosb**2*cosk + sinb**2
   Return
*****************************************************************************************************
   Subroutine Generate_Rpsi(psi,Rz,Rkh,h,Rpsi)
c This subroutine does a crystal plane normal rotation--that is, a rotation about the scattering vector h. The
c Zs-direction is in the h-direction, Xs = h(cross)z_lab, Ys = h(cross)Xs.
   Call Mv(Rz,h,dum) ! Rotate h to Lab_z direction ; Call Mv(Rkh,dum,h) ! Rotate h around itself and Ki
   hx = h(1) ; hy = h(2) ; hz = h(3) ; d1 = Dsqrt(hx**2 + hy**2) ; d2 = Dsqrt(hx**2 + hy**2 + hz**2)
c Transform to [Xs,Ys,Zs] system
   R(1,1) = hy/d1  ; R(2,1) = hz*hx/(d1*d2)          ; R(3,1) = hx/d2
   R(1,2) = -hx/d1 ; R(2,2) = hz*hy/(d1*d2)          ; R(3,2) = hy/d2
   R(1,3) = 0.0d0  ; R(2,3) = -(hx**2 + hy**2)/(d1*d2) ; R(3,3) = hz/d2
c Perform azimuthal psi rotation in [Xs,Ys] plane (right-handed sense)
   Rpsi(1,1) = Dcos(psi) ; Rpsi(2,1) = Dsin(psi) ; Rpsi(3,1) = 0.0d0
   Rpsi(1,2) = -Dsin(psi) ; Rpsi(2,2) = Dcos(psi) ; Rpsi(3,2) = 0.0d0
   Rpsi(1,3) = 0.0d0      ; Rpsi(2,3) = 0.0d0     ; Rpsi(3,3) = 1.0d0
c Inverse Transform back to Lab [Note that R(inverse) = R(transpose) since R is an orthogonal matrix]
   RT(1,1) = hy/d1          ; RT(2,1) = -hx/d1          ; RT(3,1) = 0.0d0
   RT(1,2) = hz*hx/(d1*d2)  ; RT(2,2) = hz*hy/(d1*d2)   ; RT(3,2) = -(hx**2 + hy**2)/(d1*d2)
   RT(1,3) = hx/d2          ; RT(2,3) = hy/d2           ; RT(3,3) = hz/d2
   Call MM(Rpsi,R,dum1)     ; Call MM(RT,dum1,Rpsi)
   Return
*****************************************************************************************************
   Subroutine Generate_Bo(a,alpha,Vo,Bo,Boi)
c This subroutine generates the matrix Bo that transforms crystal reciprocal lattice vectors from their crystal
c bases system to an orthogonal coordinate system. In this way dot and cross products of reciprocal lattice
c vectors can be performed.
c VARIABLES:
c b(i) = Reciprocal Lattice Spacings a*,b*,c* (1/cm) ; cosb(i) = Cosine of Reciprocal Lattice Angles
c alpha*,beta*,gamma* ; Boi(i,j) = Inverse of Bo(i,j) ; Vo = Volume of Unit Cell (cm**3)
   Common /conv/ rad
   Do 1 I=1,3
     a(i) = a(i)*1.0d8        ! Conversion from cm to Angstroms ; cosa(i) = Dcos(alpha(i)*rad)
1    sina(i) = Dsin(alpha(i)*rad)
   V = Dsqrt(1.0d0 - cosa(1)**2 - cosa(2)**2 - cosa(3)**2 + 2.0*cosa(1)*cosa(2)*cosa(3))
   Vo = V*a(1)*a(2)*a(3)*(1.0d-8)**3
   Do 5 I=1,3
     j = i + 1 ; If(j .Gt. 3) j = 1 ; k = j + 1 ; If(k .Gt. 3) k = 1
```

```
      cosb(i) = (cosa(j)*cosa(k) - cosa(i))/(sina(j)*sina(k))  ;  sinb(i) = Dsqrt(1.0d0 - cosb(i)**2)
5     b(i)  = sina(i)/(a(i)*V)
    Bo(1,1) = b(1)                    ; Bo(2,1) = 0.0d0                    ; Bo(3,1) = 0.0d0
    Bo(1,2) = b(2)*cosb(3)            ; Bo(2,2) = b(2)*sinb(3)             ; Bo(3,2) = 0.0d0
    Bo(1,3) = b(3)*cosb(2)            ; Bo(2,3) = -b(3)*sinb(2)*cosa(1)    ; Bo(3,3) = 1.0d0/a(3)
    Boi(1,1) = 1.0d0/b(1)             ; Boi(2,1) = 0.0d0                   ; Boi(3,1) = 0.0d0
    Boi(1,2) = -a(1)*sina(2)*cosb(3)  ; Boi(2,2) = a(2)*sina(1)            ; Boi(3,2) = 0.0d0
    Boi(1,3) = a(1)*cosa(2)           ; Boi(2,3) = a(2)*cosa(1)            ; Boi(3,3) = a(3)
    Return
*****************************************************************************************************

    Subroutine Orientation(h1,h2,h3,h1L,h2L,h3L,U)
c This subroutine constructs the Orientation Matrix U that allows one to transform from the crystal reciprocal
c coordinate space to Lab orthogonal coordinate space: (Lab vector) V_lab = U (dot) V_recip.
    nd = 3 ! # of rows  ;  nr = 3  ! # of columns  ;  n = 3  ! order of matrix
    Do 1 I=1,3
      H(i,1) = h1(i)    ;  H(i,2) = h2(i)    ;  H(i,3) = h3(i)
      HL(i,1) = h1L(i)  ;  HL(i,2) = h2L(i)  ;  HL(i,3) = h3L(i)
      Do 1 J=1,3
1       b(i,j) = 0.0d0
    b(1,1) = 1.0d0   ;  b(2,2) = 1.0d0   ;  b(3,3) = 1.0d0
    Call Lineq(H,b,Hinv,nd,n,nr,aa,ierr)  ;  Call MM(HL,Hinv,U)
    Return
*****************************************************************************************************

    Subroutine Lab_Vectors(hpp,hss,h33,sinps,cosps,h1,h2,h3)
c This subroutine uses the reciprocal lattice vectors in reciprocal space to construct Lab vectors in Lab space.
c Note that this subroutine has taken a special case -- 2 reciprocal lattice vectors lie in the scattering plane and
c one points in the Lab_z direction.  However, if one were to know beforehand the directions of all 3
c vectors h1,h2,h3 in lab space (pointing in general directions), their lab components could be inserted in this
c subroutine, and no other modifications need be done in this program (except some calculations are no longer
c necessary, such as calculating sinps,cosps,etc. ).
c hpp = magnitude of hp, hss = magnitude of hs, h33 = mag. of h3
    Common /Lab/ x_Lab,y_Lab,z_Lab
    h1(1) = 0.0d0  ;  h1(2) = 0.0d0        ;  h1(3) = hpp
    h2(1) = 0.0d0  ;  h2(2) = hss*sinps    ;  h2(3) = hss*cosps
    h3(1) = h33    ;  h3(2) = 0.0d0        ;  h3(3) = 0.0d0
    x_Lab(1) = 1.0d0  ;  x_Lab(2) = 0.0d0  ;  x_Lab(3) = 0.0d0
    y_Lab(1) = 0.0d0  ;  y_Lab(2) = 1.0d0  ;  y_Lab(3) = 0.0d0
    z_Lab(1) = 0.0d0  ;  z_Lab(2) = 0.0d0  ;  z_Lab(3) = 1.0d0
    Return
*****************************************************************************************************

    Subroutine General_Cross(u,v,B,Bi,uv)
c This subroutine takes the general cross product of vectors u,v defined in a non-orthogonal coordinate system.
c Bi = inverse of B
    Call Mv(B,u,Bu)       ;  Call Mv(B,v,Bv)  ;  Call Cross(Bu,Bv,BuBv,norm)  ;  Call Cross(u,v,uv,uvmag)
    Call Mv(Bi,BuBv,uv)  ;  Call Dot(uv,uv,norm)
    Do 1 I=1,3                          ! Giving uv a magnitude equal
1     uv(i) = uvmag*uv(i)/Dsqrt(norm)   ! to magn. of cross product of indices of u,v
    Return
*****************************************************************************************************

    Subroutine General_Dot(u,v,B,uv)
c This subroutine takes the general dot product of vectors u,v defined in a non-orthogonal coordinate system.
    Call Mv(B,u,Bu)  ;  Call Mv(B,v,Bv)  ;  Call Dot(Bu,Bv,uv)
    Return
*****************************************************************************************************

    Subroutine Polar(v,x,y,z,theta,phi)
c  This Subroutine determines the azimuthal and polar angles of a vector "v" in a coordinate system with basis
c vectors x,y,z theta = polar angle, phi = azimuthal angle      -180 < phi < 180,  0 < theta < 180
*****************************************************************************************************

    Subroutine MM(A,B,C)
c This subroutine performs matrix multiplication C = A*B
*****************************************************************************************************

    Subroutine Mv(A,x,Ax)
c This subroutine multiplies column vector x by 3x3 matrix A to obtain column vector Ax :   Ax = A*x
*****************************************************************************************************
```

```
      Subroutine Cross(u,v,w,norm)
c This Subroutine computes the Cross Product of two vectors "u" and "v" in orthogonal space. Returns a unit
c vector "w" and its length "norm"
*****************************************************************************************************
      Subroutine Dot(u,v,w)
c This Subroutine computes the Dot product of two vectors "u" and "v" in orthogonal space:   w = u*v
*****************************************************************************************************
```

8.3 Ewald Program

The EWALD code that follows computes the reflection and transmission amplitudes from a crystal using the Ewald-Laue dynamical diffraction theory.[39-41] The main program **Ewald** controls the calculation by calling the appropriate subroutines. An initialization subroutine is called (Initialize) to set up the dynamical diffraction calculation, and instructions are returned (via iflg) to compute either an energy or angle spectrum over a desired range. Program Ewald then makes calls to subroutine Dispersion at each appropriate energy or angle value. Dispersion returns the reflection and transmission coefficients R and T directly, and it returns the reflected and transmitted electric field amplitudes indirectly through the common block /ts/. When energy spectra are calculated, time spectra can also be determined by taking the Fourier transform of the electric field amplitudes. Since fast Fourier transform routines are quite ubiquitous, the routine that did calculations for EWALD is not shown here--the actual routine used was an adapted version of Brigham's well known Fortran code.[42]

Subroutine **Initialize** reads in the relevant information contained in the files nuclear.dat and atompos.dat, and it initializes physical constants to be used in further calculations. The important physical constants pertinent to ^{57}Fe used in EWALD are the total lifetime, 140.95 nsecs,[43] the internal conversion coefficient, 8.23,[43] and the magnetic moments of the ground and excited states: 0.09024 nm and -0.1549 nm. The ground state magnetic moment was measured by Locher and Geschwind though electron-nuclear double resonance techniques[44] while the excited state magnetic moment was found by Preston, Hanna, and Heberle through Mössbauer measurements.[45]

Calls are made to **Orient_cryst** to get the orientation matrix, U, and, for each site, to **YIG_basis** to construct the quantum coordinate system (Hx,Hy,Hz) where Hz is in the direction of the internal magnetic field. Thus, for multi-site crystals, no universal quantum axis is constructed--their internal magnetic field defines what type of scattering occurs. Using the orientation matrix, the quantum coordinate system, and the information from the data files, an eigenvector representing the nuclear scattering tensor elements for

each polarization combination, quantum level, and site is constructed along with associated eigenvalues. Eigenvector is essentially $\mathbf{g}^{HS}/2$ in Eq. 7-2.1 for magnetic dipole scattering without the resonance denominator.

ElectStrFact is also called to compute the photoelectric structure factor (the contents of the subroutine are not shown here since the calculations are straightforward). Since the photoelectric structure factor is essentially constant over the energy range of the hyperfine nuclear resonance, $\approx 10^{-6}$ eV, they only need to be calculated once. In computing the photoelectric structure factor presented in Eq. 7-2.2, the value for f_0 came from a mean atomic scattering factor (calculated from self-consistent or variational wavefunctions) tabulated in International Tables for X-Ray Crystallography[46] and in Warren.[47] The value for f' came from a database (set up by Sean Brennan at SSRL) of Cromer and Liberman's relativistic Hartree-Fock calculations,[48] and the value for f'' came from a compilation of x-ray cross section measurements contained in McMaster.[49] Compton scattering was also included by adding the incoherent cross section values contained in McMaster to f''. Since the anomalous scattering factors, f' and f'', are insensitive to the scattering angle when operating far from any absorption edge or bound state resonance, the angular dependence of these terms was neglected.

Subroutine **Polarmat** constructs photoelectric and nuclear magnetic dipole polarization matrices for the incident and scattered electric fields. The photoelectric polarization matrix is equivalent to the Thomson polarization matrix given by Eq. 5-1.3. Construction of the magnetic dipole polarization matrix is more involved. Once the spherical unit vectors are calculated through the appropriate cross products outlined in Section 5.1, the vector spherical harmonics can be constructed. Translating from program symbols to those used in Section 5.1:

$$\text{Y10i} = \sqrt{8\pi/3}\mathbf{Y}_{10}^{(0)}\left(\Omega_{\mathbf{k}_i}\right) = i\sin\theta_{\mathbf{k}_i}\hat{\boldsymbol{\phi}}_{\mathbf{k}_i} \tag{8-3.1}$$

$$\text{Y11i} = \sqrt{16\pi/3}\mathbf{Y}_{11}^{(0)}\left(\Omega_{\mathbf{k}_i}\right) = e^{i\phi_{\mathbf{k}_i}}\left(\hat{\boldsymbol{\theta}}_{\mathbf{k}_i} + i\cos\theta_{\mathbf{k}_i}\hat{\boldsymbol{\phi}}_{\mathbf{k}_i}\right). \tag{8-3.2}$$

If nuclear level mixing did not occur, then the final polarization matrices could be constructed in the form given by Eq. 5-1.5. However, to include nuclear level mixing the matrices must be constructed as described in Section 5.2 and given by Eq. 5-2.30. Therefore, Polarmat only finds all of the possible dot products between polarizations and vector spherical harmonics in preparation for making the final polarization matrix given by Eq. 5-2.30.

The coefficients $c_{\kappa q}$ in Eq. 5-2.29 are calculated by the subroutine **Splitting** through diagonalizing the unperturbed Hamiltonian given in Section 5-2. Once the

coefficients are evaluated, the subroutine **Polarmix** puts together the magnetic dipole polarization matrix using the dot product calculations performed in Polarmat. Polarmix returns an array, E, to the calling subroutine, Initialize. This multidimensional array, as explained earlier, is proportional to the scattering tensor given by Eq. 7-2.1, and it carefully tracks which nuclear sites and energy levels were involved in the scattering process for each scattering tensor element and for various incident and scattered photon directions (EWALD only does a two-beam calculation in which there is a forward and only one reflection scattering channel). These terms vary insignificantly over the hyperfine resonance energy range and can therefore also be calculated just once (as was the case for photoelectric scattering).

Once Initialize is finished with its calculations, the subroutine **Dispersion** will be ready to solve the linearized dispersion relation given by Eq. 7-4.19 where, in the most general case, $\mathbf{G}_{lin}$ is given by 7-8.1. When called by Dispersion, subroutine **StrFact** constructs the $\mathbf{G}_{lin}$ matrix as a function of energy and angle. Then, by making a call to **Cgg** of the EIS_LIN_PACK code, Dispersion finds both the eigenvalues and eigenvectors of $\mathbf{G}_{lin}$. Next, a thick crystal approximation is applied if the crystal is thick enough to cause floating point overflow problems. Then, subroutine **TandR_coeff** is called to solve the boundary value relation, Eq. 7-4.30, where, in general, $\mathbf{B}_c$ is not decoupled. These last two steps are explained in more detail in the next section. **Clineq** of EIS_LIN_PACK is used to solve the simultaneous equations represented by the boundary value equation.

Once the boundary value equation is solved, the reflected and transmitted amplitudes are constructed. Dispersion then proceeds to calculate the reflected and transmitted electric field intensities by summing the square moduli of the sigma and pi electric field amplitudes. The amplitude and intensity calculations are finally sent to the main calling program, Ewald, for further analysis such as computing energy averaged angular spectra, angle averaged energy spectra, time spectra, or fitting to experimental data (none of these detailed calculations are shown here).

For the EWALD code below, program Ewald and subroutines Dispersion and TandR_coeff are combined in one Fortran code called EWALD.FOR. Subroutines Initialize, Strfact, Polarmat, Polarmix, YIG_basis, FeBO3_basis, and Cdot are combined in another Fortran code called NUCLEAR.FOR.

```
   Program Ewald
c This Program Uses the Ewald-Laue Dynamical Diffraction Theory to Compute the Reflection and
c Transmission Coefficients from a Crystal.
c In this Program : x = sigma polarization component ; y = pi polarization component
c VARIABLES:  (See INITIALIZE Subroutine for more comments on variables)
c devE = (incoming photon energy) - (Bragg energy) (eV) ; devB = (incoming angle) - (Bragg angle) (radians)
c fconv = conversion factor from Energy to Frequency (/[eV-sec])
c Rx,Ry = Bragg reflected amplitudes ; Rxm,Rym = Laue transmitted amplitudes
c Txm,Tym = Transmission amplitudes ; R,T = reflected and transmitted field intensities
c LINK TO:  NUCLEAR,  EIS_LIN_PACK
c D.E.Brown 1990          (SSRL/STANFORD)
    Complex Txm(600),Tym(600),Rx(600),Ry(600),Rxm(600),Rym(600),uin(4,1)
    Real Freq(600),T(600),R(600) ; Complex zo,xpol,ypol ; Real*8 b
    Common uin ; Common /ts/ zo,Txm,Tym,Rx,Ry,Rxm,Rym
c Initializing Parameters
    Call Initialize(xpol,ypol,Erange,Trange,devE0,devB0,zo,sinBragg,b,fconv,Npts,iflg)
    uin(1,1) = xpol ; uin(3,1) = ypol ; uin(2,1) = 0.0 ; uin(4,1) = 0.0
    If(iflg .Eq. 1) Then  ; delE0 = Erange/(npts-1) ; devE = devE0 - Erange/2.0 - delE0 ; devB = devB0
    Else ;                  delth = Trange/(npts-1) ; devB = devB0 - Trange/2.0 - delth  ; devE = devE0
    Endif
    Do 1 KK=1,npts
      If(iflg .Eq. 1) Then ; devE = devE + delE0 ; Freq(kk) = devE*fconv
      Else                 ; devB = devB + delth
      Endif
1     Call Dispersion(devB,devE,R(kk),T(kk),b,kk)
        ===> Call a Fast Fourier Transform Routine to take the Fourier Transform of Rx,Ry having abscissa
             points contained in the array Freq  ===>  This gives the Reflected Time Spectrum
   End
*****************************************************************************************************
    Subroutine Dispersion(devB,devE,R,T,b,i)
c This subroutine solves the Dispersion equation for Dynamical Diffraction
    Parameter (n1 = 600)
    Complex w(4),g(4,4),e(4),Txm(n1),Tym(n1),Rx(n1),Ry(n1),Rxm(n1),Rym(n1),Tx(n1),Ty(n1)
    Real gr(4,4),gi(4,4),vr(4,4),vi(4,4),wr(4),wi(4),fv1(4),fv2(4),fv3(4),thick(4) ; Complex zo ; Real*8 b
    Common /ts/ zo,Txm,Tym,Rx,Ry,Rxm,Rym ; Common /disp/ e,g,thick
c Initializing Parameters
    n = 4  !order of g matrix ; nm = 4  !rows of g matrix ; matz = 1  !compute eigenvalues and eigenvectors
        ===> Set Tx(i),Ty(i),Rx(i),Ry(i),Rxm(i),Rym(i),Txm(i),Tym(i) to zero
    Call StrFact(devB,devE,b,g)  ! Scattering Amplitude Computation
c Computation of Eigenvalues (returned in w) and Eigenvectors (returned in g) of g-matrix.
    Call Cgg(nm,n,g,matz,w,fv1,fv2,fv3,gr,gi,vr,vi,wr,wi,ierr)
   Do L=1,n
c Thick crystal approx. is used to take care of floating point overflow problem.  Note that the conditional can be
c true only in the Bragg case
     If(Real(zo*w(l)) .Gt. 72.0) Then ; thick(l) = 0.0          ; e(l) = 1.0
     Else                             ; e(l) = Cexp(zo*w(l))  ; thick(l) = 1.0
     Endif
    Enddo
c Computation of Transmission and Reflection Coefficients
    Call TandR_coeff(Tx(i),Ty(i),Txm(i),Tym(i),Rx(i),Ry(i),Rxm(i),Rym(i),b)
    T = Txm(i)*Conjg(Txm(i)) + Tym(i)*Conjg(Tym(i))
    If(b .Lt. 0.0) Then ; R = Rx(i)*Conjg(Rx(i)) + Ry(i)*Conjg(Ry(i))                ! Bragg Case
    Else ;                R = Rxm(i)*Conjg(Rxm(i)) + Rym(i)*Conjg(Rym(i))          ! Laue Case
    Endif
    Return
*****************************************************************************************************
    Subroutine TandR_coeff(Tx,Ty,Txm,Tym,Rx,Ry,Rxm,Rym,b)
    Complex e(4),Bc(4,4),uin(4,1),x(4,1),aa(4,4),v(4,4),D10xx(4),D00yx(4),D10yx(4),D00xx(4),
   1        ex(4),Tx,Ty,Rx,Ry,Txm,Tym,Rxm,Rym,atx,aty,arx,ary,norm
    Real thick(4) ; Real*8 b
    Common uin ; Common /disp/ e,v,thick
    n = 4     !order of Bc-matrix ; nm = 4     !rows of Bc-matrix ; nr = 1   !columns of x and uin arrays
    If(b .Lt. 0.0) Then
      Do 1 J=1,4            ! BRAGG CASE
```

```
1       ex(j) = e(j)
     Else
       Do 5 J=1,4              ! LAUE CASE
5       ex(j) = 1.0
     Endif
     Do 15 J=1,4
       Do K=1,4
         If(Cabs(v(k,j)) .Gt. 1.0e-20) Then ; norm = v(k,j) ; GoTo 10
       Endif
       Enddo
10   D00xx(j) = v(1,j)/norm      ; D10xx(j) = v(2,j)/norm    ; D00yx(j) = v(3,j)/norm      ; D10yx(j) = v(4,j)/norm
15   Bc(1,j) = D00xx(j)*thick(j) ; Bc(2,j) = ex(j)*D10xx(j) ; Bc(3,j) = D00yx(j)*thick(j) ; Bc(4,j) = ex(j)*D10yx(j)
c Boundary Condition Constraints--Evaluation of Simultaneous Equations: Bc*x = uin
     Call Clineq(Bc,uin,x,nm,n,nr,aa,ierr)  ! Bc*x = uin computation
c Computation of Tx,Ty,Ry,Rx by adding up all eigen amplitudes
     Do 20 K=1,4
       atx = x(k,nr)*D00xx(k) ; arx = x(k,nr)*D10xx(k)*thick(k)
       aty = x(k,nr)*D00yx(k) ; ary = x(k,nr)*D10yx(k)*thick(k)
       If(b .Lt. 0.0) Then ;   Rx = Rx + arx          ; Ry = Ry + ary                  ! BRAGG CASE
       Else                ; Rxm = Rxm + arx*e(k) ; Rym = Rym + ary*e(k)           ! LAUE CASE
       Endif
20   Txm = Txm + atx*e(k) ; Tym = Tym + aty*e(k)
     Return
*****************************************************************************************************
      Subroutine Initialize(xpol,ypol,Erange,Trange,devE0,devB0,zo,snBrgg,b,fconv,npts,iflg)
c This Subroutine Receives and Computes the Initialization Factors needed to Calculate Nuclear and
c Photoelectric Structure Factors and their associated Polarization Matrices
c VARIABLES:  (See ORIENT_CRYST Subroutine for more comments on variables)
c U = Net Orientation Matrix ; Erange = Spread of Energy to be Examined (eV) ; Trange = Spread of Angles to
c be Examined (radians) ; devE0,devB0 = Central Deviation Energy (eV) and Angle (radians) ; Npts = # of points
c of Angle or Energy scan ; Nptsi = # of integration points; iflg  = 0 --> angular scan, 1 --> Energy scan
c con = Relative Concentration of resonant nuclei ; DW = Debye Waller Factor for Photoelectric Scattering
c LM = Lamb-Mossbauer Factor for Nuclear Scattering ; efg = Electric Field Gradient direction ; to = Thickness
c of Crystal (cm) ; Z = # of Nuclei per site per unit cell ; QQ = Quadrupole Shift (mm/sec) ; isomer = Isomer
c Shift (mm/sec)  Hint = Internal Magnetic Field (gauss) ; spindp = Spin Dipolar Anisotropic Field (gauss)
c canting = canting angle (deg) ; zo = -ii*k*to/sinBragg , k = wavenumber ; xpol,ypol = Horizontal (Sigma) and
c Vertical (Pi) Polarization factor ; Hz = magnetic field direction in Lab coordinate system
c    Pjk(x,y) = Polarization matrix for Photoelectric scattering
c Yijk(n,x,y) = Polarization matrix element where:  x,y = polarizations
c               i =  mg - me  = difference in quantum level between ground state and excited state
c                 = 0,1,or -1 for dipole transitions
c             j,k = 0 or 1  where 0 = transmission channel,  1 = reflection channel
c               n = 1 for incoming photon,  2 for diffracted or scattered photon
c Eigenvector(x,y,l,iw,isite,igmn) = Scattered Photon Amplitude
c Eigenvalue(l,iw,isite) = Scattered Photon Energy
c               isite = Particular Cluster of atoms within unit cell that have same internal field parameters
c                   l = index for ground  state quantum level  ; iw = index for excited state quantum level
c              igmn = 1 -> g00, 2 -> g10, 3 -> g01, 4 -> g11          gmn is proportional to the scattering tensor
c               x,y = polarizations elements of gmn(x,y)          (see comments in STRFACT)
c NOTE:
c (1) Incoming Beam (for Zero Bragg angle) is in the positive Lab_y direction
c       K-incident = (cosBragg)y_Lab - (sinBragg)z_Lab  ; K-diffracted = (cosBragg)y_Lab + (sinBragg)z_Lab
c (2) The Quantum axis in this program is the Internal Magnetic field direction.
c (3) Initially, Hz is the External Magnetic Field Direction in the LAB coordinate system when hp & hs
c       directions are known.  Later, Hz is changed to point in the Internal Magnetic field direction.
c NEED:
c    (1)  Data File Called nuclear.dat (see read statements for variables needed)
c    (2)  Data File Called atompos.dat -- this contains hyperfine information and unit cell positions of the nuclei
c LINK:  Link with EWALD, ORIENT_CRYST, ELECTSTRFACT, SPLITTING
      Complex Y000(2,2,2),Y010(2,2,2),Y001(2,2,2),Y011(2,2,2),Y100(2,2,2),Y110(2,2,2),Y101(2,2,2),
     1        Y111(2,2,2),F0(15),P00(2,2),P01(2,2),P10(2,2),P11(2,2),FH(15),Eigenvectorlg(4,4),
     2        Eigenvectorle(4,4),F_H(15),Eigenvaluelg(4),Eigenvaluele(4),Eigenvector(2,2,2,4,15,4)
      Real*8 a(3),alpha(3),hp(3),hs(3),h(3),S(3),U(3,3),pii(3),pif(3),sigmai(3),sigmaf(3),Ki(3),Kf(3),
     1       Hz(3),HzLab(3),Hx(3),Hy(3),efg(3),efgLab(3)
```

```
      Real Eigenvalue(2,4,15),fv0(4),fv1(4),fv2(4),fv3(4),d1(4,4),d2(4,4),d3(4,4),d4(4,4),d5(4),d6(4)
      Real*8 pi,rad,c,hbar,hbarc,sinBragg,Vo,phiKi,phiH,norm,beta,gamma,Ee,gamma0,psi,canting,b,rx,ry,rw
     Complex ii,Go,xpol,ypol,zo  ; Real Ie,Ig,Lambda,isomer,LM       ; Character Crystal*10
     Common /stup/ hbarc,sinBragg,Vo,phiKi,phiH,psi,Ki,Kf,gamma0 ; Common /init/ sin2Brgg,sinBrgg2_E0
     Common /strf/ P00,P01,P10,P11,Go,Eigenvector,Eigenvalue      ; Common /Bfield/ Hz,HzLab,Hx,Hy
     Common /conv/ rad,pi,ii       ; Common /site/ isites
          ===> Read in from nuclear.dat file: Crystal;  a;  alpha; Ee, to;  iflg, Npts;  Erange, devB0;
                        Trange, devE0;  hp;  hs;  S;  Hz;  h;  phiH, phiK, psi;  con, LM;  DW;
                        xpolr, xpoli;  ypolr, ypoli
     ii = (0.0,1.0) ; pi = Dacos(-1.0d0) ; rad = pi/180.0d0 ; c = 2.99792d10  !Speed of Light (cm/sec)
     hbar = 6.58217d-16  !Planck Constant (eV-sec)          ; Re = 2.817938e-13 !Classical Electron Radius (cm)
     unu = 3.15245e-12  !Nuclear Magneton (eV/Gauss) ; uex = -0.1549   !Magnetic Moment of Excited State (nm)
     ugr = 0.09024   !Magnetic Moment of Ground State (nm) ; Ttot = 140.95e-9   !Total Lifetime (sec)
     Alp = 8.23   !Internal Conversion Coefficient                  ; Ig = 1.0/2.0  !Ground State Nuclear Energy Level
     Ie = 3.0/2.0  !First Excited State Nucl. Level        ; CG13 = Sqrt(1.0/3.0)  !Clebsch Gordan Coeff. for Lines 3,4
     CG23 = Sqrt(4.0/3.0) !Clebsch Gordan Coeff. for Lines 2,5 (Sqrt(2) Polarization Factor added)
     CG11 = 1.0  !Clebsch Gordan Coeff. for Lines 1,6           ; Trad  = Ttot*(1.0 + Alp)   !Radiative Lifetime (sec)
     hbarc = hbar*c  ; Go    = ii*hbar/(2.0*Ttot)                 ; fconv = 1.0/(2.0*pi*hbar)  ; Polfac = 3.0/(16.0*pi)
c Normalizing polarizations to unity
     xpol = Cmplx(xpolr,xpoli) ; ypol = Cmplx(ypolr,ypoli)
     norm = Csqrt(xpol*Conjg(xpol) + ypol*Conjg(ypol)) ; xpol = xpol/norm  ; ypol = ypol/norm
c Set-up Crystal Orientation for Diffraction.
      Call Orient_cryst(Ee,a,alpha,hp,hs,h,S,U,sigmai,pii,sigmaf,pif,b)
          Hzlab(1) = Hz(1)  ; Hzlab(2) = Hz(2)  ; Hzlab(3) = Hz(3)
     Coeff  = -4.0*pi**2*LM*con*Polfac/((2.0*Ig + 1.0)*(Trad/hbar)*(Ee/hbarc)**3*Vo)
     eCoeff = -2.0*pi*Re*hbarc**2/(Ee**2*Vo)
     sin2Brgg = 2.0*sinBragg*Dsqrt(1.0 - sinBragg**2) ; sinBrgg2_E0 = sinBragg**2/Ee
     zo = -ii*Ee*to/(hbarc*gamma0)  ; Lambda = 2.0*pi*hbarc/Ee  ; snBrgg = sinBragg
          ===> Read in from atompos.dat file:  isites
     Do 10 isite=1,isites
          ===> Read in from atompos.dat file:  efg;  QQ, Hint;  isomer, spindp;  canting
       e2qQ = 2.0*QQ*Ee/(c*10.0)  ; isomer = isomer*Ee/(c*10.0)
c Construct basis of quantum coordinate system where the magnetic field direction is the z-axis
          ===> Call YIG_basis(Hzlab,Kf,Ki,Hint,Hx,Hy,Hz)  when Crystal is YIG
c                              !Incoming Beam Hits Plane from Above; Scattered beam travels in:
      Call Polarmat(pii,sigmai,pii,sigmai,Ki,Ki,Y000,Y100,P00)          !transmission channel.
      Call Polarmat(pii,sigmai,pif,sigmaf,Ki,Kf,Y010,Y110,P10)            !reflection channel.
c                              !Incoming Beam Hits Plane from Below; Scattered beam travels in:
      Call Polarmat(pif,sigmaf,pii,sigmai,Kf,Ki,Y001,Y101,P01)          !transmission channel.
      Call Polarmat(pif,sigmaf,pif,sigmaf,Kf,Kf,Y011,Y111,P11)            !reflection channel.
c Determining Polar Angle Beta and Azimuthal Phi Angle Between Electric Field Gradient and Quantum z-axis
      Call Mv(U,efg,efgLab)          !Transforming efg to Lab coord. system  ; Call Dot(efgLab,efgLab,norm)
     Do 1 I=1,3
1      efgLab(i) = efgLab(i)/Dsqrt(norm)
      Call Polar(efgLab,Hx,Hy,Hz,beta,gamma)  ; Hint = Hint + spindp*(3.0*Dcos(beta)**2 - 1.0)
c Computation of Eigenvectors and Eigenvalues
      ng = 2.0*Ig + 1.01  ; ne = 2.0*Ie + 1.01
       Call Splitting(alph,beta,gamma,eta,Ig,e2qQ,Hint,ugr,unu,EigenvalueIg,EigenvectorIg,ng,
     +              fv0,fv1,fv2,fv3,d1,d2,d3,d4,d5,d6,4)
       Call Splitting(alph,beta,gamma,eta,Ie,e2qQ,Hint,uex,unu,EigenvalueIe,EigenvectorIe,ne,
     +              fv0,fv1,fv2,fv3,d1,d2,d3,d4,d5,d6,4)
c Nuclear Geometrical Structure Factor Calculation for H and -H
          ===> Read in from atompos.dat file:  Z
      Do 5 I=1,Z
          ===> Read in from atompos.dat file:  rx, ry, rw       !Coordinate positions of atoms in unit cell
5       FH(isite) = FH(isite) + Cdexp(ii*2.0*pi*(h(1)*rx + h(2)*ry + h(3)*rw))
      F_H(isite) = Conjg(FH(isite))  ; F0(isite)  = Z
c Computation of Nuclear Scattering Amplitude of Photon
      Do 10 iw=1,ne
        Call Polarmix(Eigenvector,EigenvectorIe,CG11,CG23,CG13,Y000,Y100,Coeff*F0(isite),isite,iw,1)
        Call Polarmix(Eigenvector,EigenvectorIe,CG11,CG23,CG13,Y010,Y110,Coeff*FH(isite),isite,iw,2)
        Call Polarmix(Eigenvector,EigenvectorIe,CG11,CG23,CG13,Y001,Y101,Coeff*F_H(isite),isite,iw,3)
        Call Polarmix(Eigenvector,EigenvectorIe,CG11,CG23,CG13,Y011,Y111,Coeff*F0(isite),isite,iw,4)
       If(Real(Eigenvectorig(1,1)) .Gt. 0.0) Then
```

```
c +1/2 corresponds to first eigenvalue of Ground State
          Eigenvalue(1,iw,isite) = Eigenvaluele(iw) - Eigenvalueig(1) + isomer
          Eigenvalue(2,iw,isite) = Eigenvaluele(iw) - Eigenvalueig(2) + isomer
       Else
c +1/2 corresponds to second eigenvalue of Ground State
          Eigenvalue(1,iw,isite) = Eigenvaluele(iw) - Eigenvalueig(2) + isomer
          Eigenvalue(2,iw,isite) = Eigenvaluele(iw) - Eigenvalueig(1) + isomer
       Endif
 10 Continue
c Electronic Structure Factor Calculation
    Call ElectStrFact(Crystal,h(1),h(2),h(3),sinBragg,Lambda,DW,FH(isite),F_H(isite),F0(isite))
    Do 15 N=1,2
     Do 15 M=1,2                    !Photoelectric Scattering Amplitude
      P00(m,n) = eCoeff*F0(isite)*P00(m,n)   ; P10(m,n) = eCoeff*FH(isite)*P10(m,n)
 15   P01(m,n) = eCoeff*F_H(isite)*P01(m,n) ; P11(m,n) = eCoeff*F0(isite)*P11(m,n)
    Return
*****************************************************************************************************************
    Subroutine StrFact(devB,devE,b,g)
c This Subroutine Computes the Scattering Elements of the Dispersion Equation for Dynamical Diffraction
c For the 2x2 matrices: element (1,1) = xx, (1,2) = xy  ; (2,1) = yx, (2,2) = yy
c In this Program : x = sigma polarization component  ; y = pi polarization component
c VARIABLES:   (see INITIALIZE comments)
c  alpha = deviation from bragg parameter  ; b = asymmetry parameter
     Complex g(4,4),g00(2,2),g11(2,2),g01(2,2),g10(2,2),gg00(2,2),gg11(2,2),gg01(2,2),gg10(2,2),P00(2,2),
    1          P01(2,2),P10(2,2),P11(2,2),Eigenvector(2,2,2,4,15,4),Res,ResJ,Go
    Real*8 b  ; Real Eigenvalue(2,4,15)
    Common /init/ sin2Brgg,sinBrgg2_E0  ; Common /strf/ P00,P01,P10,P11,Go,Eigenvector,Eigenvalue
    Common /site/ isites
    Res = devE + Go   !Resonance Denominator Term
c Incoming Beam Hits Plane from Above; Scattered beam travels in:
c    g00 ==> transmission channel  ; g10 ==> reflection  channel
c Incoming Beam Hits Plane from Below; Scattered beam travels in:
c    g01 ==> transmission channel  ; g11 ==> reflection  channel
    Do 1 N=1,2
     Do 1 M=1,2
 1      gg00(m,n) = P00(m,n)  ; gg10(m,n) = P10(m,n)  ; gg01(m,n) = P01(m,n)  ; gg11(m,n) = P11(m,n)
    Do 5 I=1,isites
     Do 5 iw=1,4
      Do 5 J=1,2
       ResJ = Res - Eigenvalue(j,iw,i)
       Do 5 N=1,2
        Do 5 M=1,2
           gg00(m,n) = gg00(m,n) + Eigenvector(m,n,j,iw,i,1)/ResJ
           gg10(m,n) = gg10(m,n) + Eigenvector(m,n,j,iw,i,2)/ResJ
           gg01(m,n) = gg01(m,n) + Eigenvector(m,n,j,iw,i,3)/ResJ
 5         gg11(m,n) = gg11(m,n) + Eigenvector(m,n,j,iw,i,4)/ResJ
    alpha = -2.0*sin2Brgg*devB  ; e1   = b*alpha/2.0
c Construction of g-matrix pertaining to dynamical diffraction formula
    g(1,1) = gg00(1,1)     ; g(1,2) = gg01(1,1)          ; g(1,3) = gg00(1,2)     ; g(1,4) = gg01(1,2)
    g(2,1) = b*gg10(1,1)  ; g(2,2) = b*gg11(1,1) - e1  ; g(2,3) = b*gg10(1,2)  ; g(2,4) = b*gg11(1,2)
    g(3,1) = gg00(2,1)     ; g(3,2) = gg01(2,1)          ; g(3,3) = gg00(2,2)     ; g(3,4) = gg01(2,2)
    g(4,1) = b*gg10(2,1)  ; g(4,2) = b*gg11(2,1)       ; g(4,3) = b*gg10(2,2)  ; g(4,4) = b*gg11(2,2) - e1
    Return
*****************************************************************************************************************
    Subroutine Polarmat(pii,sigmai,pif,sigmaf,Ki,Kf,Y0,Y1,P)
c  Polarmat Computes Polarization Mixing Matrices
c  VARIABLES:   (See INITIALIZE subroutine for more comments on variables)
c Ki(f) = incoming(diffracted) photon direction (k-unit vector)
c coski(kf) = angle between incoming(diffracted) photon direction and quantum axis
c phiki(kf) = azimuthal phi angle of incoming(diffracted) photon direction in quantum spherical coord. system
c thetai(f) = theta unit vector of incoming(diffracted) photon k-vector in quantum spherical coordinate system
c phii(f)   = phi unit vector of incoming(diffracted) photon k-vector in quantum spherical coordinate system
c sigmai(f) = sigma polarization unit vector of incoming(diffracted) photon  ; pii(f) = pi polarization unit vector of
c incoming(diffracted) photon  ; Hx,Hy,Hz  = Quantum Basis unit vectors in Lab coord. system
```

```
c Y10i(f)  = Vector Spherical Harmonic for J=1,L=1,M=0 ; Y11i(f)  = Vector Spherical Harmonic for J=1,L=1,M=1
c P  = Polarization matrix for Photoelectric scattering
     Complex Y0(2,2,2),Y1(2,2,2),Y10i(3),Y10f(3),Y11i(3),Y11f(3),P(2,2),ii
     Real*8 Hz(3),Hx(3),Hy(3),Ki(3),Kf(3),sigmai(3),sigmaf(3),pii(3),pif(3),phii(3),phif(3),thetai(3),thetaf(3),
    1       HzLab(3),rad,pi,norm,Pss,Psp,Pps,Ppp,phiki,phikf,theta,sinki,sinkf,coski,coskf
     Common /Bfield/ Hz,HzLab,Hx,Hy ; Common /site/ isites ; Common /conv/ rad,pi,ii
c Nuclear Angular Factors
     Call Dot(Hz,Ki,coski)                  ; Call Dot(Hz,Kf,coskf)       ; sinki = Dsqrt(1.0d0 - coski**2)
     sinkf = Dsqrt(1.0d0 - coskf**2)        ; Call Polar(Ki,Hx,Hy,Hz,theta,phiki)
     Call Polar(Kf,Hx,Hy,Hz,theta,phikf) ; Call Cross(Hz,Ki,phii,norm)
     If(norm .Gt. 1.0d-30) Then  ; Call Cross(phii,Ki,thetai,norm)
     Else
       Do 1 I=1,3                                !If Ki // H  then phi and theta unit vectors
 1       phii(i) = sigmai(i) ; thetai(i) = pii(i)    !are set to sigma and pi polarizations
     Endif
     Call Cross(Hz,Kf,phif,norm)
     If(norm .Gt. 1.0d-30) Then  ; Call Cross(phif,Kf,thetaf,norm)
     Else
       Do 5 I=1,3
 5       phif(i) = sigmaf(i) ; thetaf(i) = pif(i)    ! If Kf // H then do the same as stated above
     Endif
     Do 10 I=1,3
       Y10i(i) = ii*sinki*phii(i) ; Y10f(i) = ii*sinkf*phif(i) ; Y11i(i) = (thetai(i) + ii*coski*phii(i))*Cdexp(ii*phiki)
 10  Y11f(i) = (thetaf(i) + ii*coskf*phif(i))*Cdexp(ii*phikf)
c Construction of Polarization Matrices
c M = 0
     Call Cdot(Y10i,sigmai,Y0(1,1,1),1) ; Call Cdot(Y10i,pii,Y0(1,2,1),1) ; Call Cdot(Y10f,sigmaf,Y0(2,1,1),0)
     Call Cdot(Y10f,pif,Y0(2,1,2),0)    ; Y0(1,1,2) = Y0(1,1,1) ; Y0(1,2,2) = Y0(1,2,1) ; Y0(2,2,1) = Y0(2,1,1)
     Y0(2,2,2) = Y0(2,1,2)
c M = 1
     Call Cdot(Y11i,sigmai,Y1(1,1,1),1) ; Call Cdot(Y11i,pii,Y1(1,2,1),1) ; Call Cdot(Y11f,sigmaf,Y1(2,1,1),0)
     Call Cdot(Y11f,pif,Y1(2,1,2),0)    ; Y1(1,1,2) = Y1(1,1,1) ; Y1(1,2,2) = Y1(1,2,1) ; Y1(2,2,1) = Y1(2,1,1)
     Y1(2,2,2) = Y1(2,1,2)
c Electronic Angular Factors
     Call Dot(sigmai,sigmaf,Pss) ; Call Dot(sigmai,pif,Psp) ; Call Dot(pii,sigmaf,Pps) ; Call Dot(pii,pif,Ppp)
     P(1,1) = Pss                ; P(1,2) = Psp             ; P(2,1) = Pps             ; P(2,2) = Ppp
     Return
*****************************************************************************************************************
     Subroutine Polarmix(E,Ele,CG1,CG0,CG_1,Y0,Y1,F,isite,iw,igmn)
c  Polarmix Computes Scattering Tensor Elements of Dispersion Equation
c  VARIABLES: (See Comments in Subroutine INITIALIZE)
c  NOTE:   (1) Spherical Harmonic Y1 = Y(M=+1) = Complex Conjugate Y(M=-1)
      Complex E(2,2,2,4,15,4),Ele(4,4),Y0(2,2,2),Y1(2,2,2),F,Ei1,Ef1,Ei2,Ef2
     Do 1 N=1,2                                  ! M = ±2 Not allowed for magnetic dipole scattering
       Do 1 M=1,2
c +1/2 ground state amplitudes
         Ei1 = CG1*Conjg(Ele(1,iw))*Y1(1,m,n) + CG0*Conjg(Ele(2,iw))*Y0( i,m,n) +
     +         CG_1*Conjg(Ele(3,iw))*Conjg(Y1(1,m,n))
         Ef1 = CG1*Ele(1,iw)*Y1(2,m,n) + CG0*Ele(2,iw)*Y0(2,m,n) + CG_1*Ele(3,iw)*Conjg(Y1(2,m,n))
c -1/2 ground state amplitudes
         Ei2 = CG_1*Conjg(Ele(2,iw))*Y1(1,m,n) + CG0*Conjg(Ele(3,iw))*Y0(1,m,n) +
     +         CG1*Conjg(Ele(4,iw))*Conjg(Y1(1,m,n))
         Ef2 = CG_1*Ele(2,iw)*Y1(2,m,n) + CG0*Ele(3,iw)*Y0(2,m,n) + CG1*Ele(4,iw)*Conjg(Y1(2,m,n))
         E(m,n,1,iw,isite,igmn) = F*(Ei1*Ef1)   ! +1/2
 1       E(m,n,2,iw,isite,igmn) = F*(Ei2*Ef2)   ! -1/2
     Return
*****************************************************************************************************************
     Subroutine YIG_basis(Hzlab,Kf,Ki,Hint,Hx,Hy,Hz)
c This subroutine Constructs the Quantum Coordinate System for YIG or similiar systems
c  The Hx-direction is perpendicular to both Hz and the diffracted wavevector.
     Real*8 Hzlab(3),Hx(3),Hy(3),Hz(3),Kf(3),Ki(3),norm
     If(Hint .Lt. 0.0) Then
       Do 1 I=1,3
 1       Hz(i) = -Hzlab(i)
```

```
      Hint = -Hint
    Else
      Do 5 I=1,3
5       Hz(i) = Hzlab(i)
    Endif
c Hx is perpendicular to Hz and Kf; however if Hz is parallel to Kf, Hx is perpendicular to Hz and Ki.
    Call Cross(Hz,Kf,Hx,norm) ; If(norm .Lt. 1.0e-3) Call Cross(Hz,Ki,Hx,norm) ; Call Cross(Hz,Hx,Hy,norm)
    Return
*****************************************************************************************************
    Subroutine FeBO3_basis(U,canting,Hzlab,Kf,Ki,Hint,Hx,Hy,Hz)
c This subroutine Constructs the Quantum Coordinate System for FeBO3 or similiar systems
*****************************************************************************************************
    Subroutine Cdot(u,v,w,i)
c This Subroutine computes the Dot product of a Complex vector "u" and a real vector "v". It returns the dot
c product "w".
c  i = 0  ==> w = u*ComplexConjugate(v) = u*v  for v real
c  i = 1  ==> w = v*ComplexConjugate(u)
*****************************************************************************************************
    Subroutine Splitting(alpha,beta,gamma,eta,I,e2qQ,Ho,u,un,Val,Ham,nH,M,fv1,fv2,fv3,hr,hi,vr,vi,wr,wi,L)
c  This Subroutine determines the Energy Eigenvalues and Eigenvectors for a Nuclear State that has both Static
c Electric Quadrupole and Magnetic Dipole Interaction
c VARIABLES:
c  Ham Contains the Eigenvectors -- original Hamiltonian matrix is destroyed by Subroutine CGG
c  Val Contains the Eigenvalues  ; nH = Order of Hamiltonian Ham(i,j)  ; I = Nuclear Energy Level
c  un = Nuclear Magneton (Ev/Gauss)  ; beta  = angle between Electric Field Gradient and Magnetic Field
c  gamma = azimuthal angle between Electric Field Gradient and Magnetic Field (radians)
c  alpha = Third Euler Angle needed when the Electric Quadrupole Interaction is non-axially symmetric (radians)
c  eta = (Vxx - Vyy)/Vzz --> the asymmetry parameter which describes the deviation of the Electric Field
c  Gradient from axial symmetry.  ; e2qQ  = Electric Quadrupole Splitting Factor e**2*q*Q  (eV)
c  Ho = External Magnetic Field Strength (Gauss)  ; u = Magnetic Moment (nuclear magnetons)
c  LINKING:  Need to link with Subroutine EIS_LIN_PACK
    Complex Val(L),Ham(L,L),ii,exp2a,expg,exp2g,Hmm1,Hmm_1,Hmm2,Hmm_2
     Real M(L),fv1(L),fv2(L),fv3(L),hr(L,L),hi(L,L),vr(L,L),vi(L,L),wr(L),wi(L),I
    ii = (0.0,1.0)  ; nlevels = 2.0*I + 1.0                ; wE = 0.0  ; wH = Ho*u*un/I
    If(I .Ne. 0.5) wE = e2qQ/(4.0*I*(2.0*I - 1.0))      ; y = wH    ; z = wE
    Cos2a = Cos(2.0*alpha)      ; Cosb = Cos(beta)          ; Sinb = Sin(beta)
    Exp2a = Cexp(ii*2.0*alpha)  ; Expg = Cexp(ii*gamma)  ; Exp2g = Cexp(ii*2.0*gamma)
    Hmm = 0.5*z*(3.0*cosb**2 - 1.0 + eta*sinb**2*cos2a)
    Hmm1 = 1.5*z*sinb*(cosb - (eta/6.0)*((1.0 + cosb)*exp2a - (1.0 - cosb)*Conjg(exp2a)))*expg
    Hmm_1 = 1.5*z*sinb*(cosb + (eta/6.0)*((1.0 - cosb)*exp2a - (1.0 + cosb)*Conjg(exp2a)))*Conjg(expg)
    Hmm2 = 0.75*z*(sinb**2 + (eta/6.0)*((1.0 + cosb)**2*exp2a + (1.0 - cosb)**2*Conjg(exp2a)))*exp2g
    Hmm_2 = 0.75*z*(sinb**2 + (eta/6.0)*((1.0 - cosb)**2*exp2a +
   +            (1.0 + cosb)**2*Conjg(exp2a)))*Conjg(exp2g)
    Do 10 J=1,nlevels
     M(j) = I - (j-1)
     Do 10 K=1,nlevels
10     Ham(k,j) = 0.0
    N = 1
    Do 15 K=N,nlevels
15   Ham(k,k) = -y*M(k) + Hmm*(3.0*M(k)**2 - I*(I + 1.0))
    N = N + 1
    Do 20 K=N,nlevels
      Ham(k-1,k) = Hmm_1*(2.0*M(k-1) - 1.0)*Sqrt((I + M(k-1))*(I - M(k-1) + 1.0))
20   Ham(k,k-1) = Hmm1*(2.0*M(k) + 1.0)*Sqrt((I - M(k))*(I + M(k) + 1.0))
    N = N + 1
    Do 25 K=N,nlevels
      Ham(k-2,k) = Hmm_2*Sqrt((I - M(k-2) + 2.0)*(I - M(k-2) + 1.0)*(I + M(k-2))*(I + M(k-2) - 1.0))
25   Ham(k,k-2) = Hmm2*Sqrt((I + M(k) + 2.0)*(I + M(k) + 1.0)*(I - M(k))*(I - M(k) - 1.0))
    matz = 1   ! Eigenvalue and Eigenvector Calculation
    Call Cgg(L,nH,Ham,matz,Val,fv1,fv2,fv3,hr,hi,vr,vi,wr,wi,ierr)
    Return
*****************************************************************************************************
DATAFILE   NUCLEAR.DAT
```

```
YIG                    ! Crystal Type
12.3797e-8,12.3797e-8,12.3797e-8  !Lattice spacings a,b,c (cm)
90.0,90.0,90.0                    !Lattice angles alpha,beta,gamma (deg)
14412.5,5.0e-4         ! Incoming photon energy(eV),Crystal thickness(cm)
1,400                  ! (iflg=1=Energy scan,iflg=0=Angle scan) ; # points
10.0e-7,65.0e-6        ! Energy range (Ev),deviation from Bragg (rad)
20.0e-6,-0.0e-7        ! Angle range (rad),deviation from incoming Energy (eV)
TWO RECIPROCAL LATTICE VECTORS, 1st is in LAB_z direction, 2nd is in the SCATTERING PLANE where
hs(dot)Kf > 0, Kf(dot)LAB y > 0.  LAB_x is perpendicular to SCATTERING PLANE.
 0. 0. 2.              ! Hp  Kp  Lp  Reciprocal Lattice vector in LAB_z direction
 1. 0. 0.              ! Hs  Ks  Ls  Reciprocal Lattice vector in scattering plane
 0. 0. 2.              ! Outward Surface Direction (in Reciprocal coordinates)
 0. 1. 0.              ! External Magnetic Field Direction (in LAB coordinates)
RECIPROCAL LATTICE VECTOR of desired reflection
 0. 0. 2.              ! H   K   L  Desired Reciprocal Lattice Vector
AZIMUTHAL ROTATIONS that preserve Bragg Condition. Two Rotations are made. The 1st is about H =
Reciprocal Lattice Vector, the 2nd is about Ki, and the 3rd is about H again
0.0,0.0,0.0            ! Azimuthal rotation about H,Ki,H=(H,K,L) (deg)
0.87,0.8               ! Nuclear: Relative Concentration; Lamb-Mossbauer factor
0.987                  ! Electronic: Debeye Waller factor
1.0,0.0                ! Horizontal Polarization of incoming Photon (real,imag)
0.0,0.0                ! Vertical Polarization of incoming Photon (real,imag)
        ! See INITIALIZE subroutine for a more detailed description of these parameters
*****************************************************************************************************

DATAFILE  ATOMPOS.DAT
        This Data file contains the positions of the Fe57 atoms corresponding to various sites in YIG and the
         EFG directions of the iron atoms in the sites, and also associated hyperfine field parameters
             (Winkler, Phys.B,Condensed Matter,49,331,83)
$
7                      ! Number of Sites within Unit Cell
 D1-SITE Fe57 ATOMS   [100] SYMMETRY AXIS
 1. 0. 0.    ! Electric Field Gradient Direction [h k l]
 -0.89d0,-3.68d5    !Quadrupole Shift (mm/sec),Magnetic Field (gauss)
 0.0d0,0.0d0    !Isomer Shift (mm/sec),Spin Dipolar Anisotropy (gauss)
0.0d0    !Canting Angle (deg) ; 8    ! # of atoms in this site
Coordinate of Fe57 atoms within unit cell:
 0.375   0.0   0.25 ; 0.875   0.5   0.75 ; 0.625   0.5   0.25 ; 0.125   0.0   0.75
 0.625   0.0   0.75 ; 0.125   0.5   0.25 ; 0.375   0.5   0.75 ; 0.875   0.0   0.25
 D2-SITE Fe57 ATOMS   [010] SYMMETRY AXIS
 0. 1. 0. ; -0.89d0,-3.68d5 ; 0.0d0,0.0d0 ; 0.0d0 ; 8
 0.25   0.375   0.0 ; 0.75   0.125   0.0 ; 0.75   0.875   0.5 ; 0.25   0.625   0.5
 0.75   0.625   0.0 ; 0.25   0.875   0.0 ; 0.25   0.125   0.5 ; 0.75   0.375   0.5
 D3-SITE Fe57 ATOMS   [001] SYMMETRY AXIS
 0. 0. 1. ; -0.89d0,-3.68d5 ; 0.0d0,0.0d0 ; 0.0d0 ; 8
 0.0   0.25   0.375 ; 0.5   0.25   0.625 ; 0.0   0.75   0.125 ; 0.5   0.75   0.875
 0.0   0.75   0.625 ; 0.5   0.75   0.375 ; 0.0   0.25   0.875 ; 0.5   0.25   0.125
 A1-SITE Fe57 ATOMS   [111] SYMMETRY AXIS
 1. 1. 1. ; -0.41d0,4.40d5 ; 0.226d0,-0.035d5 ; 0.0d0 ; 4
 0.00   0.00   0.00 ; 0.25   0.25   0.25 ; 0.50   0.50   0.50 ; 0.75   0.75   0.75
 A2-SITE Fe57 ATOMS   [-111] SYMMETRY AXIS
-1. 1. 1. ; -0.41d0,4.40d5 ; 0.226d0,-0.035d5 ; 0.0d0 ; 4
 0.50   0.50   0.00 ; 0.75   0.25   0.75 ; 0.00   0.00   0.50 ; 0.25   0.75   0.25
 A3-SITE Fe57 ATOMS   [1-11] SYMMETRY AXIS
 1.-1. 1. ; -0.41d0,4.40d5 ; 0.226d0,-0.035d5 ; 0.0d0 ; 4
 0.00   0.50   0.50 ; 0.75   0.75   0.25 ; 0.50   0.00   0.00 ; 0.25   0.25   0.75
 A4-SITE Fe57 ATOMS   [-1-11] SYMMETRY AXIS
-1.-1. 1. ; -0.41d0,4.40d5 ; 0.226d0,-0.035d5 ; 0.0d0 ; 4
 0.50   0.00   0.50 ; 0.25   0.75   0.75 ; 0.00   0.50   0.00 ; 0.75   0.25   0.25
*****************************************************************************************************
```

8.4 Boundary Conditions and the Thick Crystal Approximation

Since in general the linearized dispersion relations are not decoupled, the dispersion relation given by Eq. 7-4.1 must be modified to

$$\left(\mathbf{G}_{lin} - 2\varepsilon_0 \mathbf{I}\right) \cdot \mathbf{v} = 0 \tag{8-4.1}$$

where $\mathbf{G}_{lin}$ is given by Eq. 7-8.1. Finding the four eigenvectors

$$\mathbf{v}^{\ell} = \begin{pmatrix} T_x^{\ell} \\ R_x^{\ell} \\ T_y^{\ell} \\ R_y^{\ell} \end{pmatrix} \qquad (\ell = 1,\ldots,4) \tag{8-4.2}$$

allows the boundary condition equation, Eq. 7-4.30, to be solved by setting

$$T_x^{\ell} = D_1^{\ell} T_x^{\ell}, \quad R_x^{\ell} = D_2^{\ell} T_x^{\ell}, \quad T_y^{\ell} = D_3^{\ell} T_x^{\ell}, \quad R_y^{\ell} = D_4^{\ell} T_x^{\ell} \tag{8-4.3}$$

where

$$D_n^{\ell} = \left(v^{\ell}\right)_n / \left(v^{\ell}\right)_1 \tag{8-4.4}$$

and $\left(v^{\ell}\right)_n$ is the n^{th} component of $\mathbf{v}^{\ell}$. If $\left(v^{\ell}\right)_1$ is zero, then all of the eigenamplitudes can be expressed in terms of one of the nonzero eigenamplitudes in a similar fashion (that is, in terms of an amlitude other than T_x^{ℓ}). The boundary condition equation can then be explicitly written out as (for $\left(v^{\ell}\right)_1 \neq 0$)

$$\begin{pmatrix} 1 & 1 & 1 & 1 \\ D_2^1 e^{i\kappa^1 d} & D_2^2 e^{i\kappa^2 d} & D_2^3 e^{i\kappa^3 d} & D_2^4 e^{i\kappa^4 d} \\ D_3^1 & D_3^2 & D_3^3 & D_3^4 \\ D_4^1 e^{i\kappa^1 d} & D_4^2 e^{i\kappa^2 d} & D_4^3 e^{i\kappa^3 d} & D_4^4 e^{i\kappa^4 d} \end{pmatrix} \begin{pmatrix} T_x^1 \\ T_x^2 \\ T_x^3 \\ T_x^4 \end{pmatrix} = \begin{pmatrix} E_{0vx} \\ 0 \\ E_{0vy} \\ 0 \end{pmatrix} \tag{8-4.5}$$

where $\kappa^{\ell} = k_{0v}\varepsilon_0^{\ell}/\gamma_0$. This equation is solved by the subroutine TandR_coeff in the EWALD Fortran code.

When the exponential factor $e^{i\kappa^{\ell} d}$ in Eq. 8-4.5 becomes very large (for instance, too large for a computer to handle), numerical solutions can be found by applying a thick crystal approximation. Note that at the exit surface, the transmission channel field is

$$\mathbf{T}\left(\hat{\mathbf{n}} \cdot \mathbf{r} = d\right) = e^{i\mathbf{k}_{0v} \cdot \mathbf{r}} \sum_{l=1}^{4} \sum_{\alpha} T_{\alpha}^{l} e^{i\kappa^{l} d} \hat{\boldsymbol{\varepsilon}}_{\alpha}^{0}. \tag{8-4.6}$$

Then, if $e^{i\kappa^\ell d} \to \infty$, in order for the transmitted field to stay finite, T_α^ℓ must go to zero. This is the heart of the thick crystal approximation:

$$\left\{\begin{matrix} e^{i\kappa^\ell d} \to \infty \ , \quad T_\alpha^\ell \to 0 \\ T_\alpha^\ell e^{i\kappa^\ell d} \to \text{a finite quantity} \end{matrix}\right\}. \tag{8-4.7}$$

This approximation can then be used to modify the boundary condition equations. For instance, let κ^1 be the complex eigenwavenumber that gives rise to exponentially large numbers. Then the boundary value equation to be solved is

$$\begin{pmatrix} 0 & 1 & 1 & 1 \\ D_2^1 & D_2^2 e^{i\kappa^2 d} & D_2^3 e^{i\kappa^3 d} & D_2^4 e^{i\kappa^4 d} \\ 0 & D_3^2 & D_3^3 & D_3^4 \\ D_4^1 & D_4^2 e^{i\kappa^2 d} & D_4^3 e^{i\kappa^3 d} & D_4^4 e^{i\kappa^4 d} \end{pmatrix} \begin{pmatrix} T_x^1 e^{i\kappa^1 d} \\ T_x^2 \\ T_x^3 \\ T_x^4 \end{pmatrix} = \begin{pmatrix} E_{0vx} \\ 0 \\ E_{0vy} \\ 0 \end{pmatrix}. \tag{8-4.8}$$

In the subroutine Dispersion and TandR_coeff, the arrays thick and e keep track of which elements in the boundary condition matrix must be modified.

REFERENCES

[1] G. V. Smirnov, V. V. Sklyarevskii, R. A. Voskanyan, and A. N. Artem'ev, *JETP Lett.* **9**, 123 (1969).

[2] A. I. Chechin, N. V. Andronova, M. V. Zelepukhin, A. N. Artem'ev, and E. P. Stepanov, *JETP Lett.* **37**, 633 (1983).

[3] G. Faigel, D. P. Siddons, J. B. Hastings, P. E. Haustein, and J. R. Grover, *Phys. Rev. Lett.* **58**, 2699 (1987).

[4] S. Kikuta, Y. Yoda, Y. Kudo, K. Izumi, T. Ishikawa, C. K. Suzuki, H. Ohno, H. Takei, K. Nakayama, X. W. Zhang, T. Matsushita, S. Kishimoto, and M. Ando, *Jpn. J. App. Phys.* **30**, L 1686 (1991).

[5] P. P. Kovalenko, V. G. Labushkin, V. V. Rudenko, V. A. Sarkisyan, and V. N. Seleznev, *JETP Lett.* **26**, 85 (1977).

[6] G. V. Smirnov, V. V. Mostovoi, Y. V. Shvyd'ko, V. N. Seleznev, and V. V. Rudenko, *Sov. Phys. JETP* **51**, 603 (1980).

[7] U. van Bürck, G. V. Smirnov, R. L. Mössbauer, H. J. Maurus, and N. A.

Semioschkina, *J. Phys. C: Solid St. Phys.* **13**, 4511 (1980). ; U. van Bürck, R. L. Mössbauer, E. Gerdau, R. Rüffer, R. Hollatz, G. V. Smirnov, and J. P. Hannon, *Phys. Rev. Lett.* **59**, 355 (1987).

[8] E. Gerdau, R. Rüffer, H. Winkler, W. Tolksdorf, C. P. Klages, and J. P. Hannon, *Phys. Rev. Lett.* **54**, 835 (1985).

[9] J. Arthur, G. S. Brown, D. E. Brown, and S. L. Ruby, *Phys. Rev. Lett.* **63**, 1629 (1989).

[10] P. P. Kovalenko, V.G. Labushkin, A.K. Ovsepyan, E. R. Sarkisov, E.V. Smirnov, A. R. Prokopov, and V. N. Seleznev, *Sov. Phys. Solid State* **26**, 1849 (1984).

[11] A. I. Chumakov, G. V. Smirnov, M. V. Zelepukhin, U. van Bürck, E. Gerdau, R. Rüffer, and H. D. Rüter, *Hyp. Int.* **71**, 1341 (1992).

[12] P. J. Black and I. P. Duerdoth, *Proc. Phys. Soc.* **84**, 169 (1964).

[13] R. M. Mirzababaev, G. V. Smirnov, V. V. Sklyarevskii, A. N. Artemev, A. N. Izrailenko, and A. V. Babkov, *Phys. Lett.* **37A**, 441 (1971).

[14] V. S. Zasimov, R. N. Kuz'min, and A. Yu. Aleksandrov, *Sov. Phys. Solid State* **17**, 2044 (1976).

[15] V. K. Voitovetskii, I. L. Korsunskii, A. I. Novikov, and Y. F. Pazhin, *Sov. Phys. JETP* **27**, 729 (1968). ; V. K. Voitovetskii, I. L. Korsunskii, Y. F. Pazhin, and R. S. Silakov, *JETP Lett.* **12**, 212 (1970).

[16] V. A. Belyakov, *Sov. Phys. -Usp.* **18**, 267 (1975).

[17] R. W. G. Wyckoff, *Crystal Structures*, vol. 2 (Robert E. Krieger, Malabar, Florida, 1982)

[18] I. Bernal, C. W. Struck, and J. G. White, *Acta Cryst.* **16**, 849 (1963).

[19] R. Diehl, *Solid St. Commun.* **17**, 743 (1975).

[20] C. G. Shull, W. A. Strauser, and E. O. Wollan, *Phys. Rev.* **83**, 333 (1951).

[21] I. Dzyaloshinsky, *Phys. Chem. Solids* **4**, 241-255 (1958).

[22] M. P. Petrov, G. A. Smolensky, A. P. Paugurt, and S. A. Kizhaev, *Nuclear Magnetic Resonance and Magnetic Properties of* $FeBO_3$*-Type Crystals*, edited by J. C. D. Graham, J. J. Rhynes, Proceedings of the Seventeenth Conference on Magnetism and Magnetic Materials (AIP, New York, 1971), p. 379.

[23] M. Eibschutz and M. E. Lines, *Phys. Rev. B* **7**, 4907 (1973).

[24] M. Brunel and F. D. Bergevin, *Acta Cryst.* **A37**, 324 (1981).

[25] R. Nathans, S. J. Pickart, H. A. Alperin, and P. J. Brown, *Phys. Rev.* **136**, A 1641 (1964).

[26] G. V. Smirnov, V. V. Sklyarevskii, A. N. Artem'ev, and R. A. Voscanyan, *Phys. Lett.* **32A**, 532 (1970).

[27] G. V. Smirnov, Y. V. Shyvd'ko, and E. Realo, *JETP Lett.* **39**, 41 (1984).

[28] R. W. G. Wyckoff, *Crystal Structures*, vol. 3 (Robert E. Krieger, Malabar, Florida, 1982).

[29] D. M. Gualtieri, W. Lavender, and S. L. Ruby, *J. Appl. Phys.* **63**, 3795 (1988).

[30] H. Winkler, R. Eisberg, E. Alp, R. Rüffer, E. Gerdau, S. Lauer, A. X. Trautwein, M. Grodzicki, and A. Vera, *Z. Phys. B* **49**, 331 (1983).

[31] E. Gerdau and R. Ruffer, *Hyp. Int.* **27**, 59 (1986).

[32] J. Arthur, D. E. Brown, S. L. Ruby, G. S. Brown, and G. K. Shenoy, *J. Appl. Phys.* **67**, 5704 (1990).

[33] W. C. Hamilton, *International Tables for X-Ray Crystallography* , edited by J. A. Ibers and W. C. Hamilton (Kynoch Press, Birmingham, England, 1974), vol. 4, p. 275.

[34] J. S. Rollett, *Computing Methods in Crystallography* (Pergamon Press, Oxford, 1965).

[35] W. R. Busing and H. A. Levy, *Angle Calculations for 3- and 4-Circle X-Ray and Neutron Diffractometers,* ORNL Report 4056 (Oak Ridge National Laboratory, Oak Ridge, Tennessee, 1967).

[36] A. I. Borisenko and I. E. Tarapov, *Vector and Tensor Analysis with Applications* (Dover, New York, 1968).

[37] B. S. Garbow, EISPACK (Applied Mathematics Division of Argonne National Laboratory, Netlib%ANL-MCS.ARPA, 1983).

[38] C. Moler and J. Dongarra, LINPACK (Applied Mathematics Division of Argonne National Laboratory, Netlib%ANL-MCS.ARPA, 1978).

[39] W. H. Zachariasen, *Theory of X-Ray Diffraction in Crystals* (Dover, New York, 1945).

[40] B. W. Batterman and H. Cole, *Rev. Mod. Phys.* **36**, 681 (1964).

[41] A. M. Afanas'ev and Y. Kagan, *Sov. Phys. JETP* **21**, 215 (1965).

[42] E. O. Brigham, *The Fast Fourier Transform* (Prentice Hall, Englewood Cliffs, 1974).

[43] C. M. Lederer and V. S. Shirley, *Table of Isotopes* (Wiley, New York, 1978).

[44] P. R. Locher and S. Geschwind, *Phys. Rev.* **139**, A991 (1965).

[45] R. S. Preston, S. S. Hanna, and J. Heberle, *Phys. Rev.* **128**, 2207 (1962).

[46] C. H. MacGillavry and G. D. Rieck, *International Tables for X-Ray Crystallography* (Kynoch Press, Birmingham, England, 1968), vol. 3.

[47] B. E. Warren, *X-Ray Diffraction* (Dover, New York, 1990).

[48] D. T. Cromer and D. Liberman, *J. Chem. Phys.* **53**, 1891 (1970).

[49] W. H. McMaster, N. K. D. Grande, J. H. Mallett, J. H. Hubbell, and National Bureau of Standards, *Compilation of X-Ray Cross Sections*, UCRL Report 50174, Sec. III, Rev. 1 (Lawrence Radiation Laboratory, University of California, Livermore, Ca., 1969).

9. EXPERIMENTAL PROCEDURES

9.1 YIG Epitaxial Films on GGG

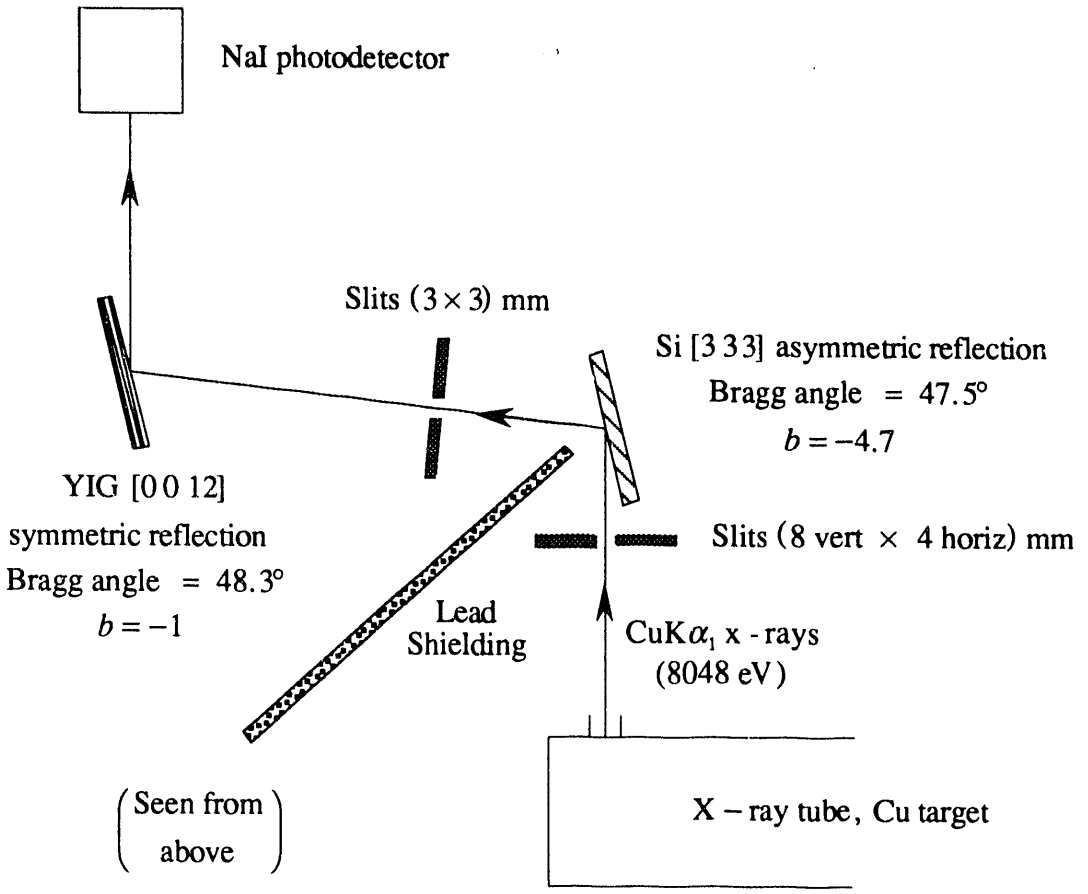

Fig. 9-1.1 Experimental arrangement for high resolution measurements of the YIG Darwin width.

The yttrium iron garnet (YIG) crystals were grown by Gualtieri at Allied-Signal's Electronic Materials and Devices Lab. Each sample was grown using a liquid phase epitaxy method where a (0 0 1) oriented gadolinium gallium garnet (GGG) substrate was inserted into a heated platinum crucible (≈ 890°C) containing yttrium and enriched iron oxides dissolved in a lead oxide-vanadium oxide flux (the isotopic composition of the iron, as measured by Oak Ridge National Lab, was 0.79% ^{54}Fe, 18.24% ^{56}Fe, 80.97% ^{57}Fe, and 0.0% ^{58}Fe). Using techniques very similar to those applied towards growing magnetic bubble memory layers, Gaualtieri was able to epitaxially grow nearly perfect (0 0 1)

oriented YIG crystal films of various thicknesses (2.7 to 9.5 μm) onto six 5 mm thick GGG circular substrates having a diameter of 3 cm. The formula unit for the YIG films, obtained from lattice constant data and Faraday rotation measurements, is

$$(Y_{2.96}Pb_{0.04})Fe_3(Fe_{1.94}Y_{0.06})O_{12}.$$

The lead was incorporated into a few dodecahedral lattice sites normally occupied by yttrium atoms. This was done to alleviate crystal strains by matching the YIG to the GGG lattice spacing. The YIG films are basically free of dislocations and other surface defects (they cover much less than 1% of the surface area), and the films have a thickness variation of only about 0.15 μm (the edges are slightly thicker than the center).[1]

A major area of concern was the degree of crystal perfection of the films--whether the films were composed of a mosaic of small crystal domains or were composed of just a few large crystal domains. Rocking curve measurements were performed to ascertain how perfect the crystal films were using the setup shown in Fig. 9-1.1. An x-ray generator provided a CuKα_1 x-ray source beam (8048 eV) for the measurements. An asymmetric Si [3 3 3] crystal was used as a nondispersive monochromator (the surface normal pointed in the [2 2 0] direction). By reflecting from the (3 3 3) planes in asymmetric geometry, the monochromator produced a highly collimated beam having an angular divergence of about 4.3 μrads. This collimated beam was used to measure any small features in the rocking curves of the YIG films that may be due to crystal imperfections.

Fig. 9-1.2 show the [0 0 12] rocking curves for the six YIG crystals labeled 57-1 to 57-6. The rocking curves are only for YIG films on the side of the GGG substrate that was facing downwards in the crucible melt. The YIG [0 0 12] reflection was chosen so that the incident beam would penetrate deep into the film allowing the entire thickness of the film to be probed (Rocking curve measurements were initially done when the crystals were first received from Gualtieri. However, in these measurements the YIG crystals were rocked against each other for the [0 0 4] reflection. Thus, the angular resolution was 25 to 50 μrads depending upon which YIG crystal was used as the monochromator rather than the 4.3 μrads resolution of the asymmetric Si [3 3 3] crystal, and the YIG [0 0 4] reflection enabled an examination of only the first 2 μm of the YIG film due to primary extinction effects). The GGG substrate reflection, which is less prominent for thick films, is the peak at the lowest angle (which has been set at a deviation angle of 0 μrads) since GGG has a larger lattice spacing than YIG. The figures show that the attempt at matching the YIG to the GGG lattice spacing by substituting a few yttrium atoms with lead has produced unexpected problems. The difference in lattice spacing between bulk GGG

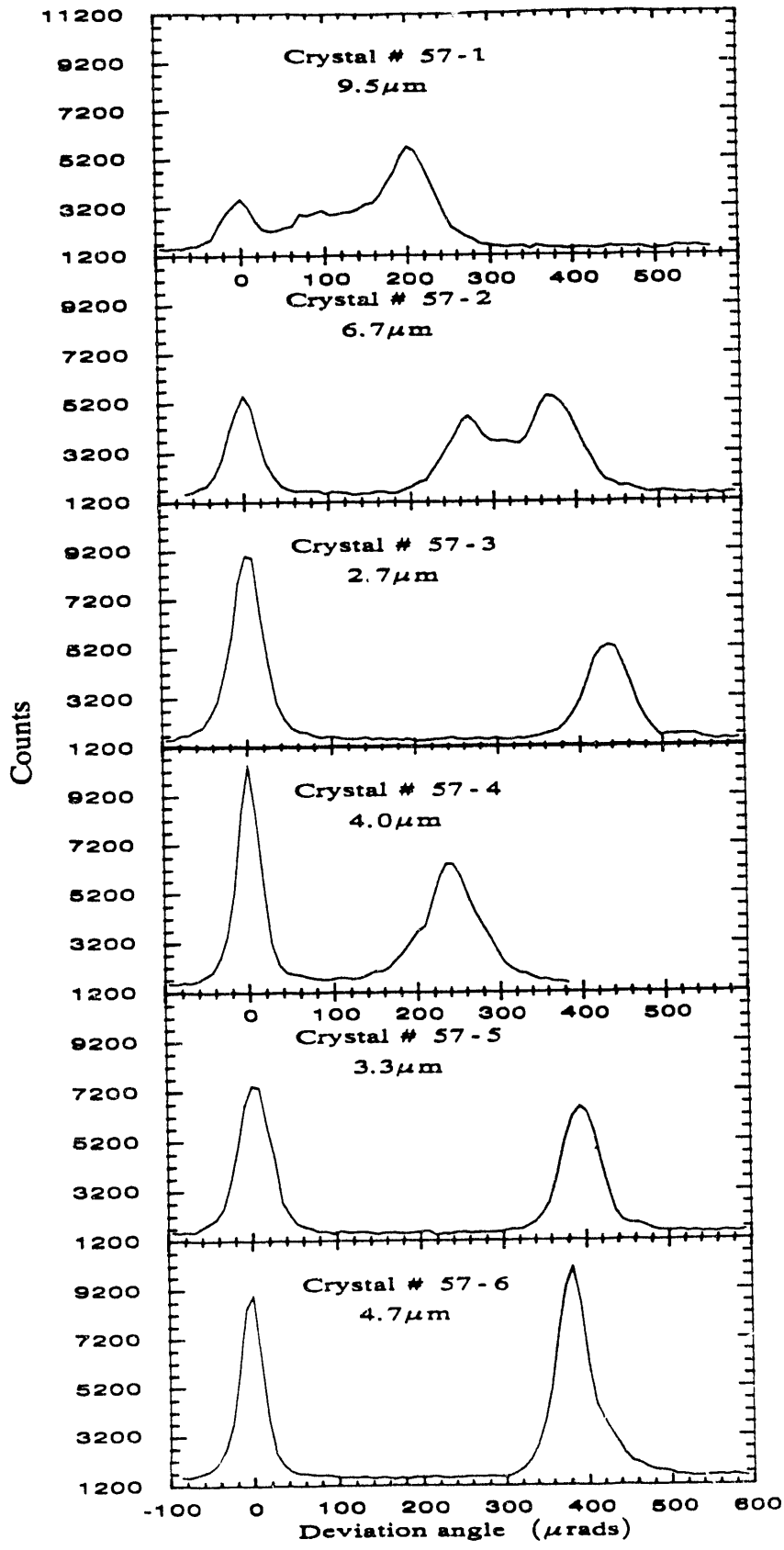

Fig. 9-1.2 Rocking curves for six YIG films 2.7 μm to 9.5 μm thick.

$(12.3840\,\text{Å})$ and bulk YIG $(12.3780\,\text{Å})$ is 6×10^{-3} Å. For the crystals 57-6, 57-5, and 57-3 where the lead had the smallest effect, the lattice mismatch was successfully reduced by 30% without significantly distorting the rocking curves. For the other crystals where the lattice mismatch was reduced by 50-60%, the YIG films separated into two or more regions, or sublayers. Substituting too many yttrium atoms with lead to further increase the YIG lattice spacing appears to lead to the formation of composite YIG films having crystal layers with different lattice spacings. The remarkable feature about this effect, which is noticeable for crystal 57-2, is the tendency for the YIG crystal to form nearly perfect crystals for each sublayer rather than a single layer composed of a homogeneous distribution of mosaic crystals or lattice spacings which would form a single broadened rocking curve.

The difference between the perfect crystal rocking curve and the measured rocking curve gives the degree of crystal perfection of the crystal sample. The silicon crystal used as the monochromator in the rocking curve measurements is of the same stock as those used as SSRL beamline monochromators. They generally have Darwin widths (full width at half maximum) that are not more than 10% greater than the ideal perfect crystal Darwin width--the silicon monochromators are essentially perfect crystals. The YIG crystal films, on the other hand, are not as perfect. The Ewald computer code discussed in Chapter 8 was used to evaluate the rocking curve for a perfect YIG crystal rocked against a fixed asymmetric Si [333] perfect crystal (the asymmetry parameter is $b=-4.7$). For perfect YIG crystals having thicknesses of 4.7, 3.3, and 2.7 μm, the Darwin widths were 24, 34, and 39 μrads respectively. The measured Darwin widths were 43, 55, and 60 μrads. Thus, the Darwin widths for the YIG films were roughly $1\frac{1}{2}$ to 2 times greater than the ideal widths. The YIG crystal perfection, though not up to par with the silicon crystals, is still quite good. One cause for the rocking curve broadening may be due to the incorporation of lead into the crystal in the attempt to create strain free films. The lead increases the lattice constant of the unit cell, and, with lead atoms interspersed throughout the YIG film, this would lead to a nonuniform lattice constant throughout the film which would contribute towards broadening the rocking curve.

9.2 General Experimental Setup

Time resolved nuclear resonance experiments were done at three different beamlines: a 15 period 1.05 m wiggler beamline 10-2 at the 3-3.5 GeV SPEAR storage ring, a 26 period 2 m undulator beamline PBF 1 at the 5-15 GeV PEP storage ring, and a

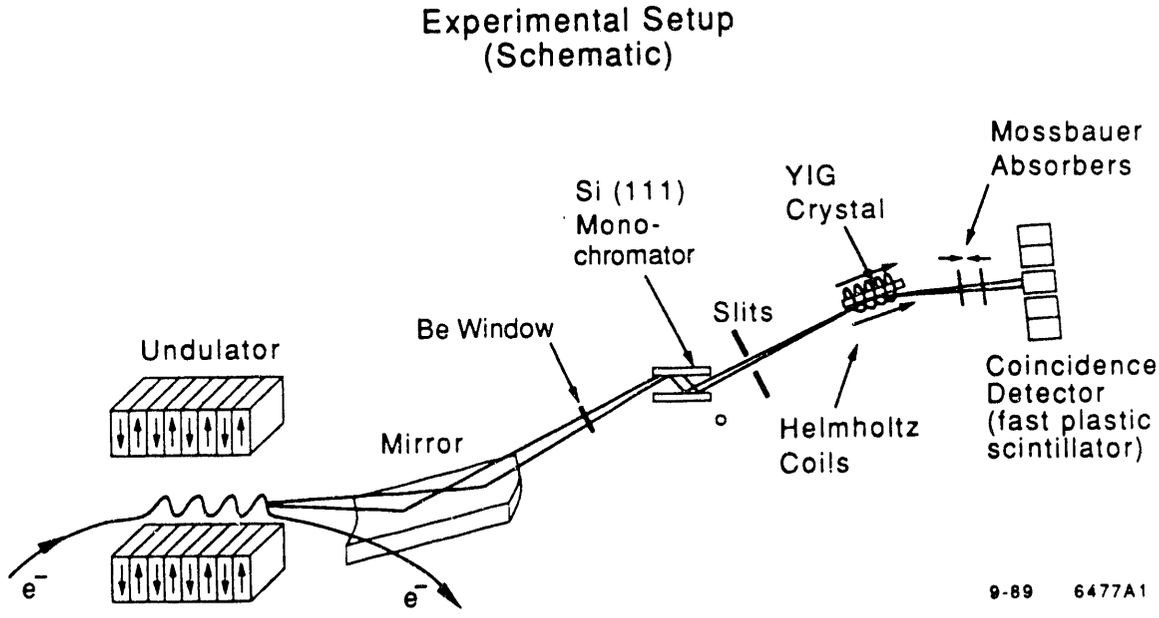

Fig. 9-2.1. General experimental setup. Mirror focusing was done in the horizontal (perpendicular to this page), not vertical, direction.

48 period wiggler beamline F2 at the 5.5 GeV CESR storage ring. The experimental setup at each of these beamlines was similar to that shown in Fig. 9-2.1.

The wiggler or undulator consisted of a periodic dipole arrangement of permanent magnets (Nd-Fe-B magnets for the beamline at SPEAR and Sm-Co magnets for the beamlines at PEP and CESR). The arrangement of magnetic dipoles forces any electron that travels down the axis to oscillate (or wiggle) about the nominal orbit and emit radiation with a range of frequencies that is tunable by varying the magnetic field strength or the dipole period length. The deflection parameter, K, is a measure of this tunability,

$$K = eB_0\lambda_u/2\pi m_e c, \tag{9-2.1}$$

where B_0 is the magnetic field strength at the nominal electron orbit, and λ_u is the dipole period length. For $K > 5$ the magnet dipole array is considered to operate as a wiggler, and the characteristic energy spectrum of the wiggler radiation is broadband up to the critical energy

$$\varepsilon_c = 0.665E^2[GeV]B_0[T] \qquad (9\text{-}2.2)$$

where E is the electron beam energy. For $K \lesssim 2$ the array is considered to operate as an undulator, and the energy spectrum is composed of harmonics that are narrowband for the odd harmonics. By changing K one of the narrowband harmonics can be tuned to a desired operating energy and, to a degree, achieve energy monochromatization.

Tuning was done for the permanent magnetic arrays by changing the magnet gap spacing which changes the magnetic field strength at the nominal electron orbit. For instance, the desired operating energy at PEP was 14.4 keV. Placing the first harmonic at an energy slightly greater than 14.4 keV ensured operation on the safe low energy side of the harmonic peak that varied more slowly with energy than the edge-like high energy side. A magnetic gap spacing of 5.5 cm resulted in a magnetic field of 1.4 kG, a K value of 1.0, and placed the first harmonic at 14.8 keV.

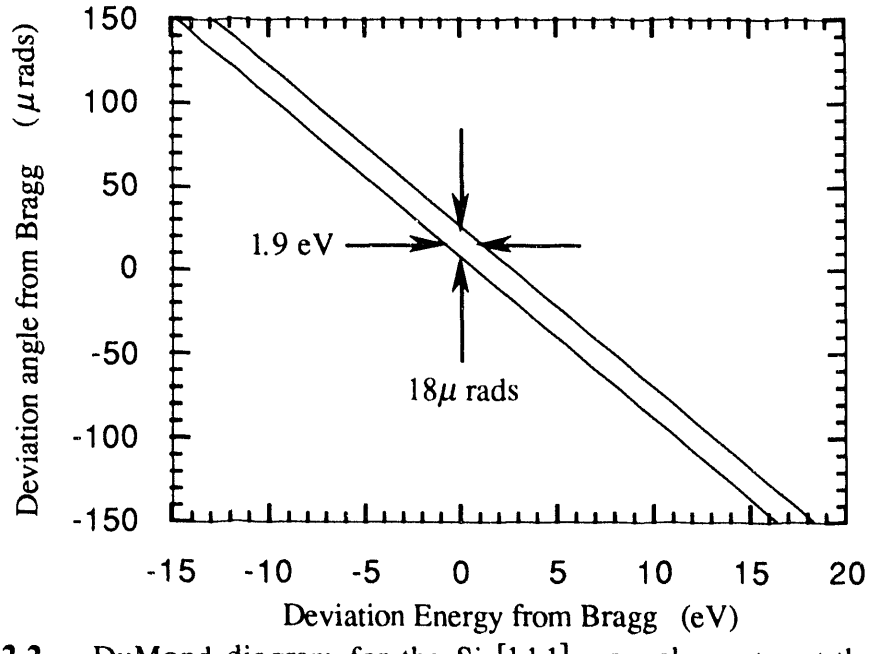

Fig. 9-2.2. DuMond diagram for the Si [1 1 1] monochromator at the SPEAR 10-2 beamline. The angular divergence of the photons arriving at the monochromator spans the 300 μrad range in the figure (the energy ranges over thousands of eVs), but the monochromator allows only those photons having angles and energies lying within the narrow strip having a width of 18 μrads and 1.9 eV.

A double crystal Si [1 1 1] monochromator was used to provide a source beam having a 2 eV wide bandwidth for a given scattering angle (two crystals were used to produce an output beam parallel to the incident beam). The DuMond diagram for such a

crystal arrangement is shown in Fig. 9-2.2. Since the energy spectrum of the radiation impinging upon the monochromator covers thousands of eVs, the monochromator substantially reduces the photoelectric background. However, a Si monochromator has the shortcoming of having a narrow vertical angular acceptance of 18 μrads at a given energy.

Electrons traversing a synchrotron bending magnet or a wiggler emit radiation in a narrow cone having a half angle of $1/\gamma$ where $\gamma = E/m_e c^2$. Depending upon the lattice design of the synchrotron, the electrons also have a vertical angular divergence at the wiggler of $2\sigma_\beta$. The net vertical angular divergence of the photons at the beamline is then the quadrature of the synchrotron radiation and electron half widths

$$2\sigma_T = 2\sqrt{\sigma_\beta^2 + \sigma_s^2} \tag{9-2.3}$$

For a bending magnet or a wiggler

$$\sigma_s = 2/\gamma\sqrt{2\pi} \tag{9-2.4}$$

is the effective rms half width of the synchrotron radiation. For the beamlines used at SPEAR and CESR, the net photon angular divergence was about 300 and 150 μrads respectively (for electron vertical half widths of roughly 50 and 30 μrads respectively for the high energy physics colliding beam mode of running). Clearly the Si monochromator, having an angular acceptance of 18 μrads, blocks out, in angular space, a sizable portion of the beam and, thereby, reduces the beam intensity by a factor of 15 to $7\frac{1}{2}$. The undulator beamline at PEP produces somewhat better results because an undulator collimates the harmonics. The first harmonic lies in a cone with a half angle of

$$\sigma_s = \frac{1}{\gamma}\sqrt{\frac{1+K^2/2}{2N}} \tag{9-2.5}$$

where N is the number of periods. For PEP the electron beam energy was 13.5 GeV, thus $\sigma_s \approx 5$ μrads ($N = 26$ and $K = 1$). The net photon angular divergence of about 100 μrads is then dominated by the electron angular divergence (the vertical half width is roughly 40 μrads for colliding beam operation). The monochromator then reduces the beam intensity by a factor of 5. If PEP were operated in a dedicated low-emittance lattice mode, the electron beam vertical half width could be reduced to as low as 5 μrads. The net photon divergence would then be only about 15 μrads, and all of the beam would pass through the monochromator. Unfortunately, PEP was mothballed before such remarkably brilliant beams could be used for experiments, and it is expected to be replaced by an asymmetric B factory for studying the possibility of CP violation in the B meson system.

At the PEP and SPEAR beamlines, a bent cylinder, fused quartz, platinum coated mirror was a standard instrument positioned upstream of the monochromator. The

cylindrical mirror provided focusing in the horizontal direction to increase the photon flux. The mirror could also be used to focus the photon beam in the vertical direction, however, because this would increase the angular divergence of the beam and result in less photons passing through the narrow vertical angular acceptance width of the Si monochromator, vertical focusing was avoided.

Unfortunately, the monochromator also allowed higher order harmonics from the [3 3 3], [5 5 5], [7 7 7], etc., reflections to pass through. The mirror again proved useful in eliminating these higher order harmonics through grazing angle scattering. By setting the grazing angle of the mirror to be near the critical angle of the [3 3 3] harmonic (29 keV), the intensity of all the harmonics was significantly diminished. The mirror then acts as a low pass filter. At the CESR beamline, there was no standard mirror upstream of the monochromator, so a portable, flat, gold coated mirror was placed downstream of the monochromator (inside the experimental hutch station). Without the mirror the photoelectric background from the harmonics overwhelmed the photodetector, thus making the mirror a critical component to do experiments.

Another typical piece of equipment was a 4 circle diffractometer. The crystals were attached to the ϕ circle of the diffractometer which in turn was attached to a χ circle which in turn was attached to a θ circle. The ϕ-axis could be rotated by rotating the χ circle, and the χ-axis could in turn be rotated by rotating a θ circle. The detector was attached to the 2θ circle which rotates independently of the other circles. These combinations of possible rotations allowed the crystals to be oriented for precision diffraction experiments.[2]

For low temperature experiments a cryogenic refrigerator assembly was attached to the ϕ circle. The assembly consisted of a two stage displex expander (Air Products DE202 expander) that cools by decompressing helium gas. On the tip of this displex unit sat the YIG crystal, and the unit was covered by a vacuum shroud having a cylindrical beryllium window. A water-cooled rotary compressor (Air Products HC-2 compressor) supplied high pressure helium gas to the displex expander. Before the refrigerator was turned on, a roughing pump was used to get the expander down to a low vacuum ($\approx 10^{-6}$ torr). A temperature controller along with a thermistor for feedback and a small heater coil inside the shroud was used to fix the temperature to a desired operating point.

Also attached to the ϕ circle was a magnet assembly that provided a uniform magnetic field of about 100 Gauss across the crystal. At the PEP and SPEAR beamlines a pair of Helmholtz coils provided the uniform magnetic field (the coils were actually attached to an unused ϕ circle on the opposite side of the χ circle). At the CESR beamline a set of Sm-Co permanent bar magnets provided the uniform magnetic field. In all cases, the magnetic field was parallel to the (0 0 1) planes (that is, parallel to the crystal surface).

9.3 Detector and Fast Timing Electronics

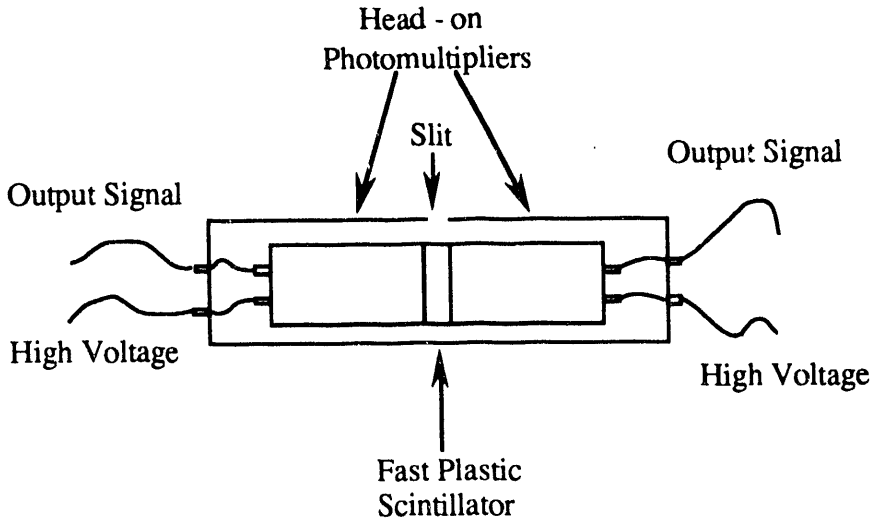

Fig. 9-3.1. General schematic of the coincidence photodetector.

Fast plastic coincidence photodetectors were used to measure the scattered x-rays. Each photodetector consisted of two head-on photomultipliers coupled to a fast plastic scintillator material (Bicron 420) via an index of refraction matching layer of silicon grease (GE Viscasil 600M silicone fluid) as shown in Fig. 9-3.1. The fast plastic is a polyvinyltoluene based organic scintillator that fluoresces with a lifetime of 1.5 nsec. An early photodetector used RCA 8575 photomultipliers borrowed from the Stanford Linear Accelerator Center's (SLAC) high energy physics group (these tubes were leftover photomultipliers used for the SLAC Mark II detector). They were old tubes, and they had significant afterpulses (possibly due to a small amount of residual gases leaking into the tubes) 460 and 540 nsecs after a prompt pulse. Even in coincidence geometry, for every 10 prompt pulses there was 1 afterpulse. However, the tubes could still be used by carefully subtracting out the afterpulse background or by ensuring that the delayed resonant signal was examined in a time window well short of the afterpulses. These photomultipliers were later abandoned in favor of mu-metal shielded Hamamatsu R329 photomultipliers having 12 dynode stages and a rise time of 2.6 nsecs. These tubes had an insignificant afterpulse rate. As measured against a NaI detector, they also had an efficiency for detecting 14.4 keV radiation of about 40%.

The fast electronics signal processing circuitry for a general experiment is shown in Fig. 9-3.3. The electronic modules were capable of processing nanosecond pulse width signals. After the amplified photomultiplier pulses pass through discriminators properly biased to reject low level background, a 2-way logic module examines the signals to see if

they are coincident (it has a double-pulse resolution of 3.3 nsecs). If the pulses are coincident, another logic module checks to see whether the coincident pulses are prompt pulses.

The timing pulse is appropriately delayed or advance in time (using cables lengths or electronic circuitry not shown in the figure) so that it corresponds to the prompt pulse that initiated the nuclear resonant response. The timing pulse is sent to a gate generator which responds by sending out a fixed 10 nsec wide delayed pulse. This 10 nsec wide pulse is the prompt window, and it is sent to veto the 1-way coincidence logic module. Thus, if a coincidence occurs within the prompt time window, it is vetoed and no further action occurs. This was done to prevent the TAC from being triggered by every prompt pulse which would overwork the TAC and lower its performance. Performing this check improved the time resolution of the resonance signal from 5 nsec to 2.5 nsec.

The prompt window is then further delayed by 250 nsec to act as the stop input to the TAC. Thus, the delayed nuclear resonance signal starts the TAC anytime from 10 nsec to 250 nsec after the prompt pulse, and the TAC is always stopped 250 nsec after the prompt pulse (see Fig. 9-3.2). The TAC sends out a signal between 0 to 10 volts that is proportional to the time difference between the stop and start signals. The MCA receives this output signal for data analysis and storage.

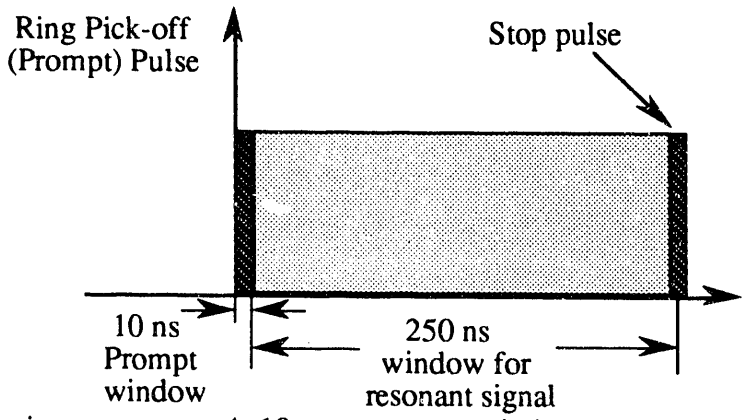

Fig. 9-3.2. Timing structure. A 10 nsec prompt window electronically gates out the prompt pulses. A 250 nsec window is constructed for measuring delayed resonant counts, and the same 10 nsec prompt window delayed by 250 nsec is used as the stop pulse to the TAC.

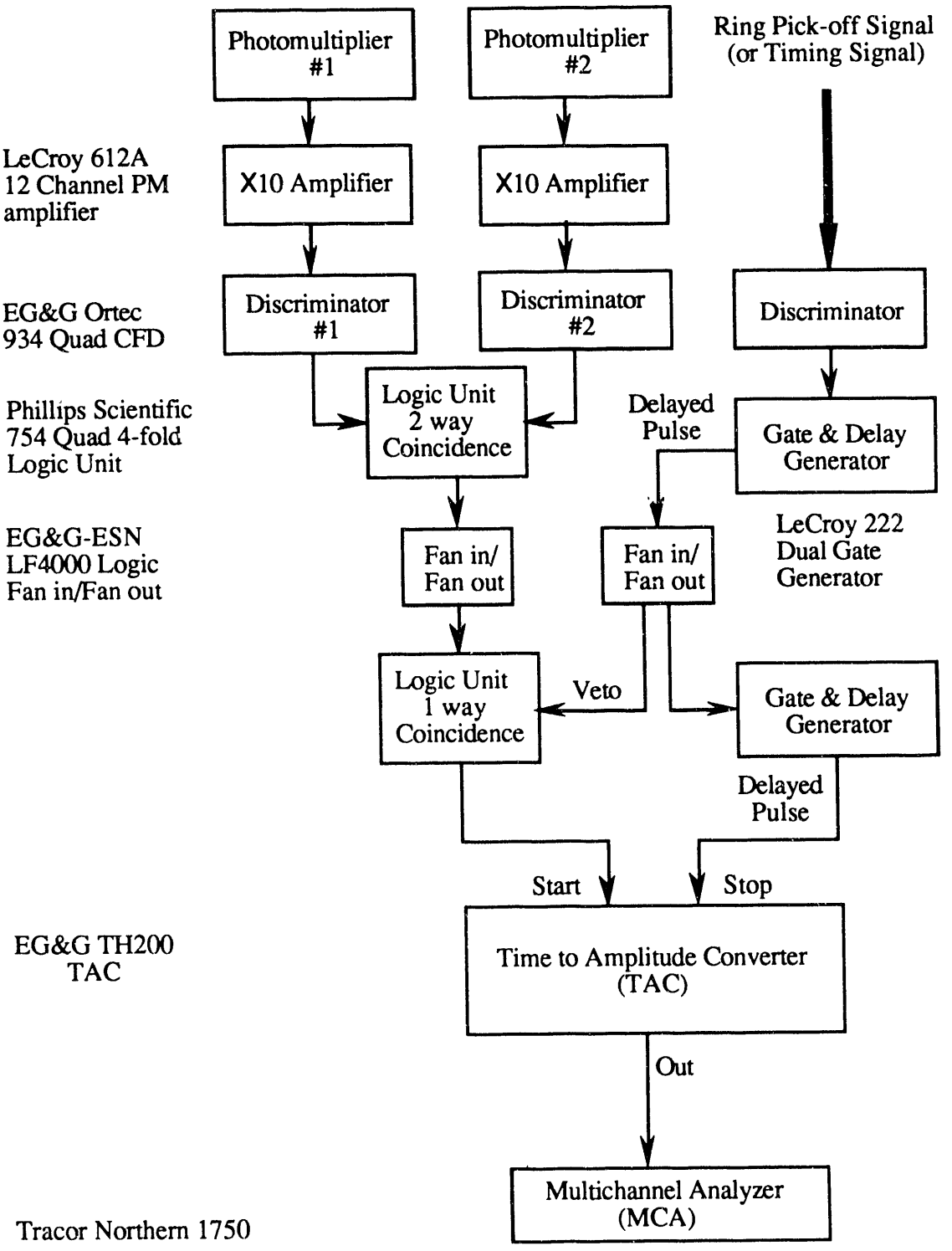

Fig. 9-3.3. General schematic of the fast electronics circuitry.

9.4 Mössbauer Experimental Setup

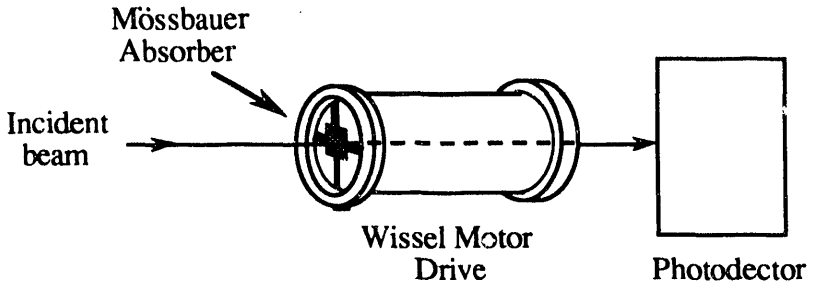

Fig. 9-4.1. General schematic of the Mössbauer experimental setup.

The general setup for doing Mössbauer experiments is shown in Fig. 9-4.1. The hollow core Wissel motor drive was well adapted for doing experiments on synchrotron beamlines. A conventional motor drive is usually designed for moving radioactive sources against a stationary absorber, and it does not need a hollow core. For synchrotron experiments hollow core drives were quite convenient because absorbers must be vibrated against a fixed source. The drive works by vibrating a hollow cylinder using electromagnetic driver coils. Attached to the end of the hollow cylinder is a sturdy diaphragm onto which an absorber can be mounted.

A synchrotron experiment was performed to measure the energy spectra of the hyperfine YIG resonance. To do this a single line sodium ferrocyanide, $Na_4Fe(CN)_6$, absorber was used as an analyzer. In Fig. 9-4.1 the incident beam is the YIG diffracted beam. The electronics set up to measure both the time spectra and the energy spectra is shown in Fig. 9-4.2. The TAC and MCA for measuring the time spectra are taken from Fig. 9-3.3. To measure the energy spectra, a gate having a time window of 250 nsec (positioned 10 nsec after the timing signal) activated the MCA for measuring resonant photons. For each valid start signal, the velocity of the motor drive was measured.

To calibrate the YIG energy spectra, Mössbauer spectroscopy was performed on an enriched ^{57}Fe thin foil using a ^{57}Co radioactive source. Obtaining the well known positions of the Fe hyperfine lines gives the calibration of the velocity drive and enables one to determine the energies of the YIG resonances. The energy spectra of the ferrocyanide absorber was also analyzed to get information on how the absorber disturbs the YIG resonant time signal. The electronics for doing these measurements is shown in Fig. 9-4.3. The transmitted beam through the absorbers was measured by a NaI inorganic scintillator detector, and the resulting signal was sent to a pulse height analyzer. The analyzer output signal was amplified (×20) and sent to the input of the MCA. The pulse

height analyzer was selected to provide an energy window for only 14.4 keV photons. If a photon had the right energy to lie within the window, the analyzer sent a gate signal to the MCA to enable it for receiving the valid input signal (along the way the pulse is shaped to be about 1.5 μsec long and 5 V high by a gate generator so that the MCA could easily handle it).

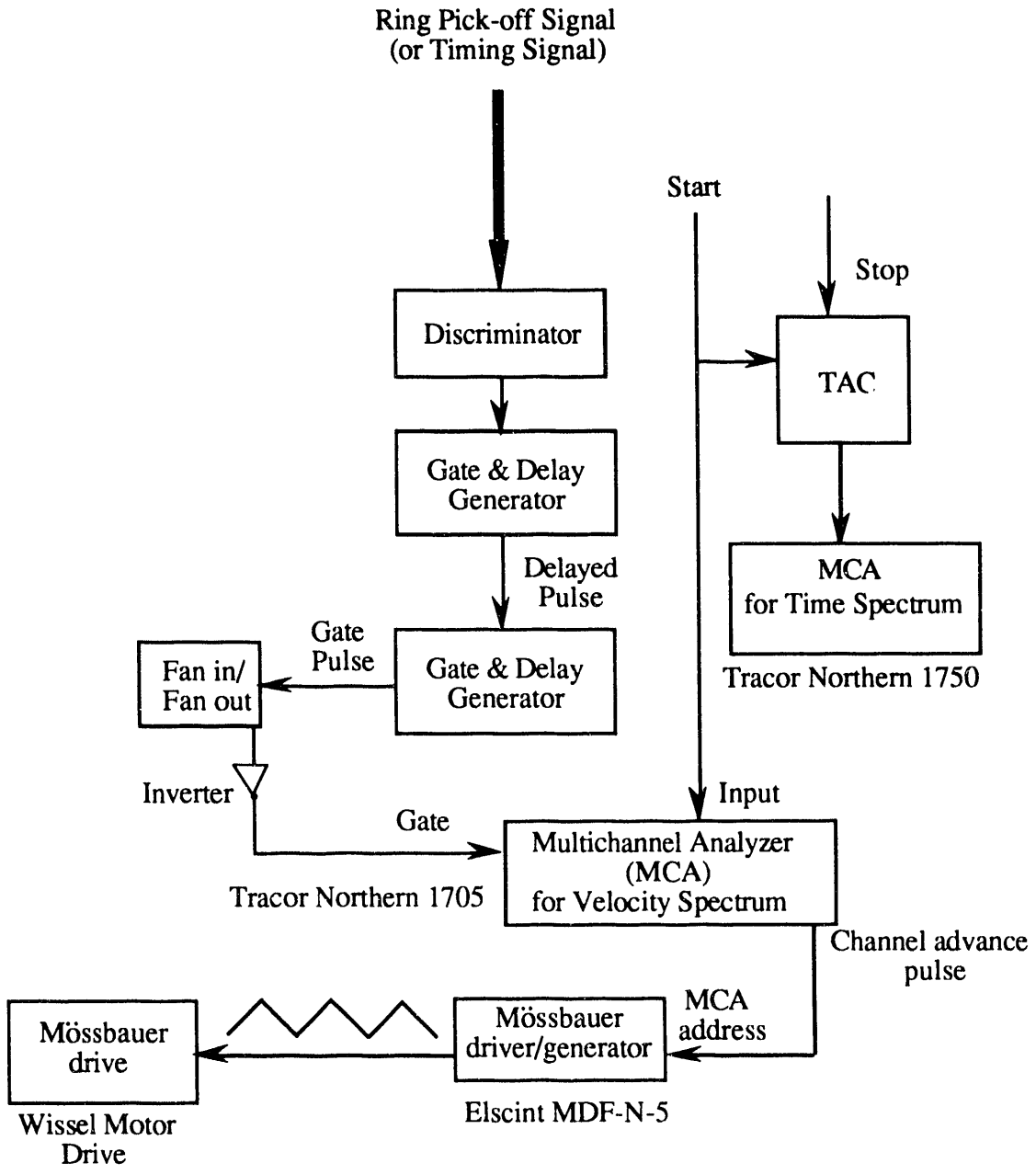

Fig. 9-4.2. General schematic of the electronics for simultaneous measurements of both Mössbauer velocity spectra and quantum beat time spectra. The start and stop signal come from the schematic in Fig. 9-3.2.

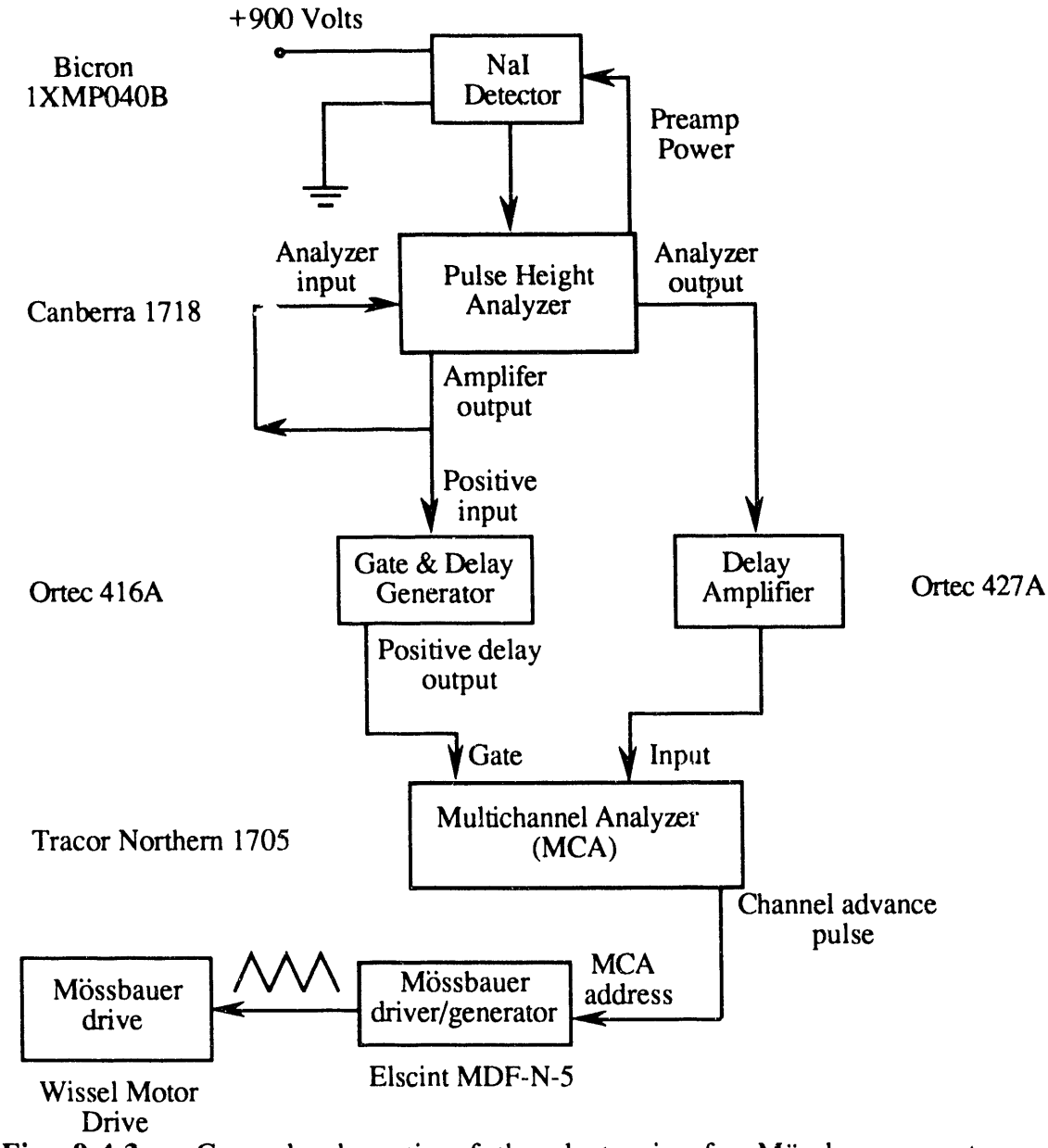

Fig. 9-4.3. General schematic of the electronics for Mössbauer spectroscopy measurements using a radioactive source.

An early Mössbauer experiment is shown in Fig. 9-4.4. This was a push-pull experiment where two black, single line, ammonium lithium ferroflouride absorbers enriched to 91.2% ^{57}Fe were used as notched filters having approximately a 2.5 mm/sec wide absorption line (They were made by Gopal Shenoy and Ersin Alp at Argonne National Labs--they were close collaborators on this experiment). The absorbers were Doppler shifted to filter out the inner two lines (lines 3 and 4) of YIG. To accomplish this, a function generator sent square wavetrains to the Mössbauer drivers. The peak-to-peak amplitude of the square waves was adjusted so that, at any instant of time, one absorber

was Doppler shifted to filter out one of the inner two lines while the other was shifted to filter out the other. The square waves arriving at the drives were in phase, so in order to make the drives operate in an antiphase, or push-pull, mode, the absorbers were fixed onto the opposite ends of the drives (one absorber was fixed to the end where the driver coil was [labeled DC in Fig. 9-4.4] and the other was fixed to the end opposite the driver coil). In this early experiment, Elscint solid core motor drives were used. Therefore, to do transmission experiments they were equipped with long paddles attached to the driver shaft. At the tips of the paddles were attached the Mössbauer absorbers. This arrangement was awkward to do synchrotron experiments, and the instrumentation was susceptible to

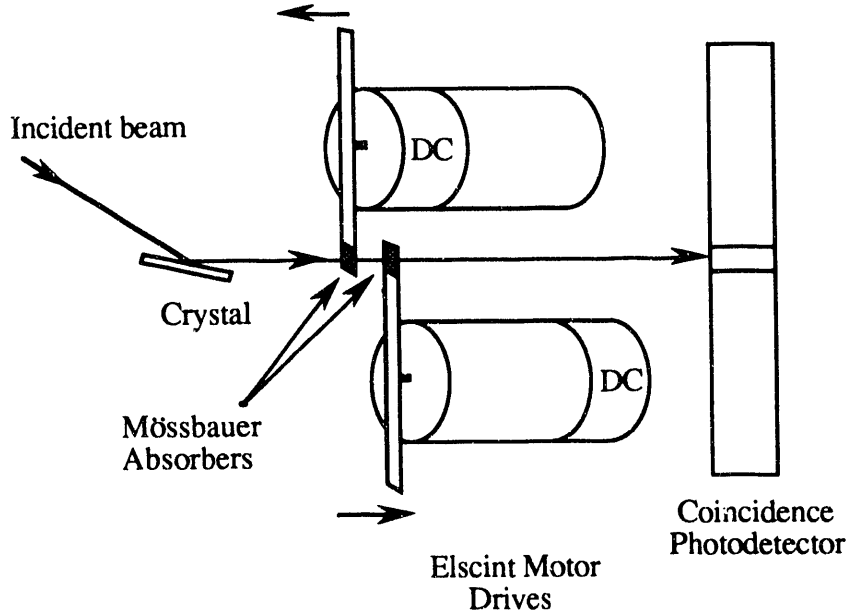

Fig. 9-4.4 Push-pull Mössbauer experiment designed to filter out the inner two hyperfine lines of YIG

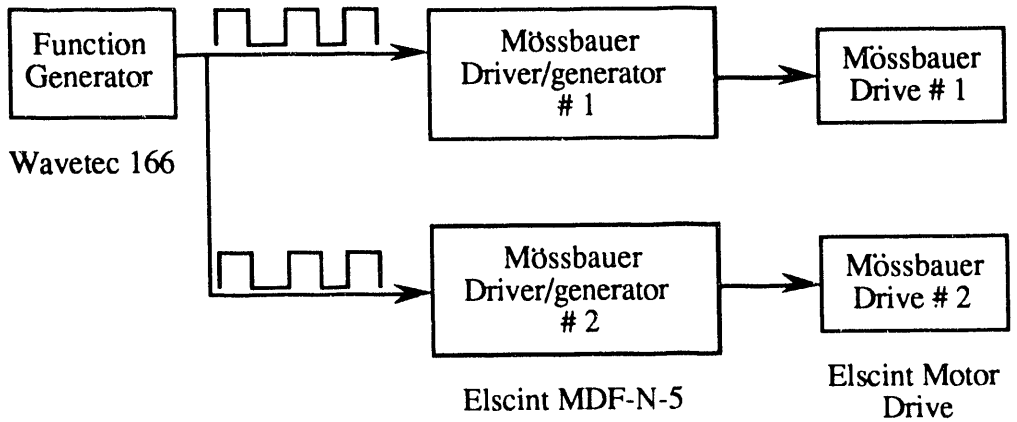

Fig. 9-4.5 Associated electronics for the push-pull Mössbauer experiment.

extraneous vibrations arising from the slippage of the paddles at the joint where they were attached to the driver shaft, the flexure of the paddles themselves, and the movement of the mount holding the absorbers to the paddles. These drives were later abandoned in favor of the hollow core Wissel motor drives.

9.5 Energy Calibration Techniques

The energy width of each of the hyperfine lines of ^{57}Fe is 4.67×10^{-9} eV with the outer two lines separated by about 6×10^{-7} eV (excluding dynamical effects such as linewidth broadening and energy shifts). The 2 eV wide energy bandpass at a given angle from the Si [1 1 1] monochromator easily covers the full range of the hyperfine spectrum. The huge photoelectric scattering (or prompt) background of around 10^{12} counts/sec resulting from the wide bandpass is reduced by 7 orders of magnitude by using a forbidden electronic but allowed nuclear reflection from the YIG crystal. The photomultipliers are not shielded from the resultant prompt pulses (the prompts are gated out electronically from triggering the TAC). Prompt rates greater than 10^6 counts/sec tend to blind the photomultipliers preventing them from seeing the delayed resonant signals--the fluorescent tails of the plastic scintillator combined with the recovery period of the photomultipliers start to become a major problem. For prompts rates of 10^5 counts/sec and nuclear signal rates of 10 to 100 counts/sec, the nuclear resonance is found by performing a monochromator energy scan. This scan is simply a measurement of the coincident delayed resonant counts (the starts in Fig. 9-3.3) versus the monochromator energy setting--the prompts time window in Fig. 9-3.2 is still used to electronically gate out the prompt signal.

To reduce the range in energy that must be searched to locate the resonance, an energy calibration is done using the krypton absorption edge. Since the krypton edge is rather broad (see Fig. 9-5.1), the monochromator can be initially calibrated to only within ± 10 eV. For experiments having a counting rate of 10 to 100 counts/sec, searching over 20 eV for the resonant signal can take a few hours. For low count rate experiments of one count/sec or less and for background rates of the same order of magnitude, a 20 eV search can take an excessive amount of time. However, once the resonance has been found, the krypton edge energy is known precisely. The krypton edge energy of 14326 eV is demarcated in Fig. 9-5.1 where the uncertainty comes from the 2 eV resolution of the monochromator. Gold also has an edge near the iron resonance. The position of its 14353

eV edge is shown in Fig. 9-5.2 and was also calibrated using the ^{57}Fe resonance. Gold also has some near edge oscillatory structure which can be useful for calibration purposes.

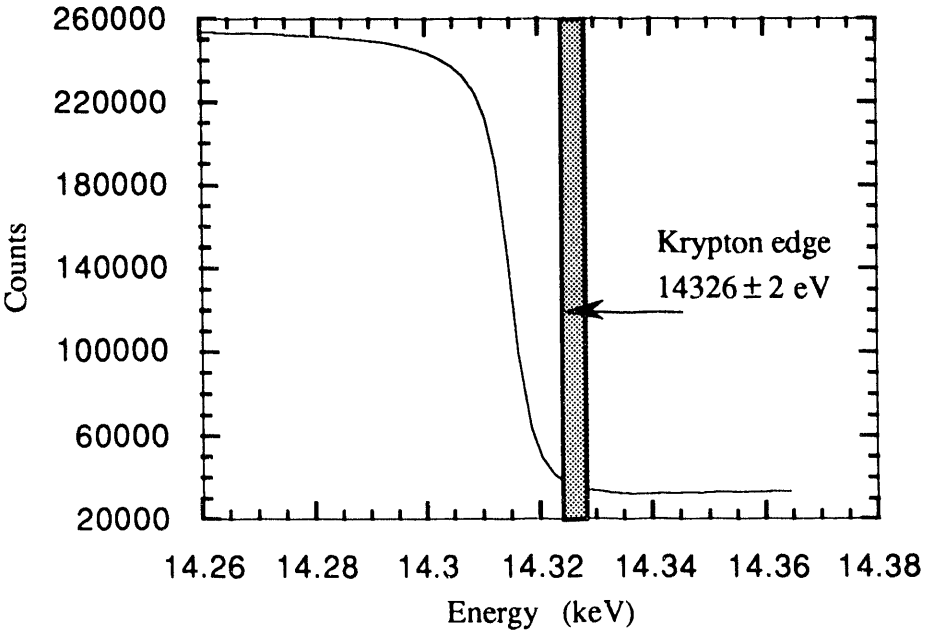

Fig. 9-5.1 Krypton edge energy scan.

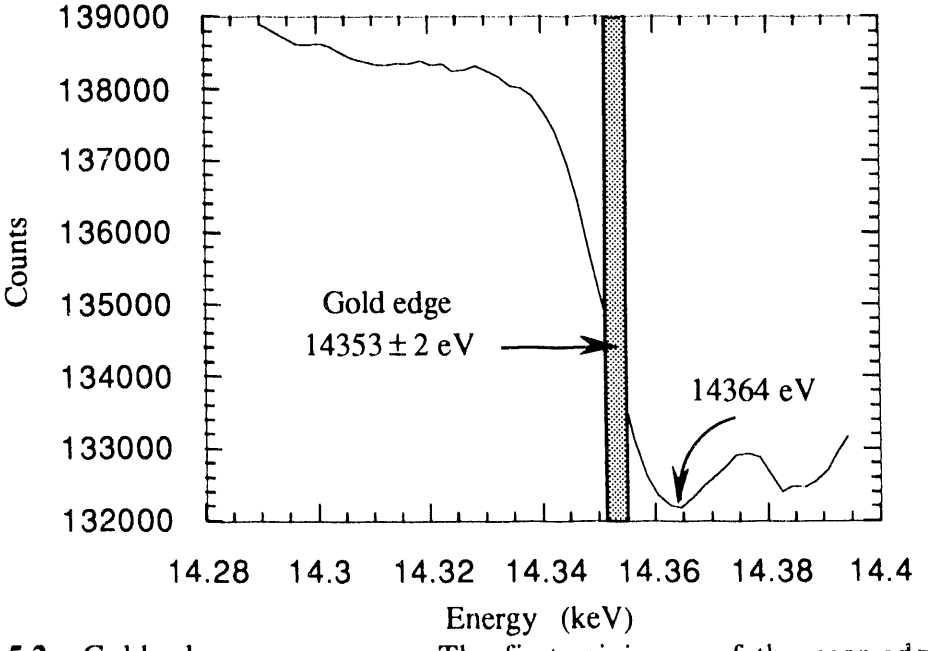

Fig. 9-5.2 Gold edge energy scan. The first minimum of the near edge structure occurs at roughly 14364 eV.

Another method of obtaining an energy calibration is to use noticeable features (or glitches) in the energy spectrum of the monochromator. The silicon monochromator has a strong primary reflection off a particular set of similar crystal planes. From two or more sets of crystal planes, it also has simultaneous weaker reflections that travel in the same direction as the primary reflection. Interference between these simultaneous, or umweganregung, reflections and the primary reflection results in noticeable glitches in the energy spectrum of the monochromator. Since the lattice spacing of Si is known very well (to within 2×10^{-4} Å), these glitches can be used as accurate energy markers. The intensity of the umveg reflections, however, is small compared to the primary reflection, so the glitches show up as small dips in the primary energy spectrum. Finding prominent, narrow glitches at high energies near 14.4 keV is also a problem. Fig. 9-5.3 shows a good candidate near 5931 eV along with its azimuthal ϕ plot. The nearly vertical reflection at 5931 eV in Fig. 9-5.3 (a) corresponds to the deep central 2 eV wide glitch in Fig. (b). This glitch actually consists of two umveg reflections lying on top of each other: the $[2\ 2\ -4]$ and $[3\ 3\ -3]$ reflections. The $[2\ 2\ -4]$ umveg reflection dominates though since it has a larger structure factor. Another good candidate closer to the resonance energy is shown in Fig. 9-5.4. The nearly vertical reflection at 11358 eV in Fig. 9-5.4 (a) corresponds to the small central dip in Fig. (b). The width of this glitch is about 8 eV--four times wider than the 5931 eV glitch. This 11358 eV glitch consists of four umveg reflections: the $[-1\ -1\ -3]$, $[4\ 4\ -8]$, $[5\ 5\ -7]$, and $[6\ 6\ -4]$ reflections. The $[-1\ -1\ -3]$ umveg reflection dominates because of its larger structure factor. A major source of broadening of the glitches comes from the nature of the monochromator. Since the monochromator consists of two parallel Si crystals, there are always two sets of umveg reflections, and this serves to broaden the glitches for Si crystals that are misoriented azimuthally in ϕ.

One of the first tries at finding the nuclear resonance signal was attempted at the SPEAR beamline 10-2. The 11358 eV glitch was used as the energy calibration even though this glitch had a broad energy width. The 5931 eV glitch was too far from the resonance to be reliable for energy calibration. A krypton edge energy scan was done to check the calibration results. The nuclear resonance was precisely right where it was expected to be (Unfortunately, by accident the glitch was labeled an 11364 eV glitch, so the first search was off by precisely the 6 eV error. This mistake was uncovered only after analyzing the beamline experiment results).

The YIG crystal produces much more noticeable umveg reflections since only forbidden reflections are used--they show up as prominent peaks rather than small dips (see Fig. 9-5.6). These umveg reflections are a major problem when searching for the nuclear

resonance because they contribute to the prompt background (the forbidden reflection is only nearly forbidden), and the strong umveg reflections easily reach the saturation limit of 5.12×10^6 counts/sec (the frequency of the electron pulses in the SPEAR storage ring). At high energies, they densely pack $\phi - E$ space as shown in Fig. 9-5.5 (Only the largest umveg reflections are shown where $F_S F_{H-S} \geq 10{,}000$ (F_S is the structure factor described in Section 7.10). Had all nonzero reflections been drawn, the figure would be nearly black). Searching for the resonance then involves finding a good, deep valley in $\phi - E$ space.

The YIG crystals can also be used for energy calibration by making ϕ-cuts and E-cuts in $\phi - E$ space and accurately mapping out the contours of all the prominent umveg reflections. An attempt was made to do this, but, because of the dense thicket of umveg reflections, more confusion resulted than progress. Of all the ways of making energy calibrations, using the krypton edge (after it was calibrated once and for all using the nuclear resonance line) was the simplest and fastest way of finding the ^{57}Fe resonance energy.

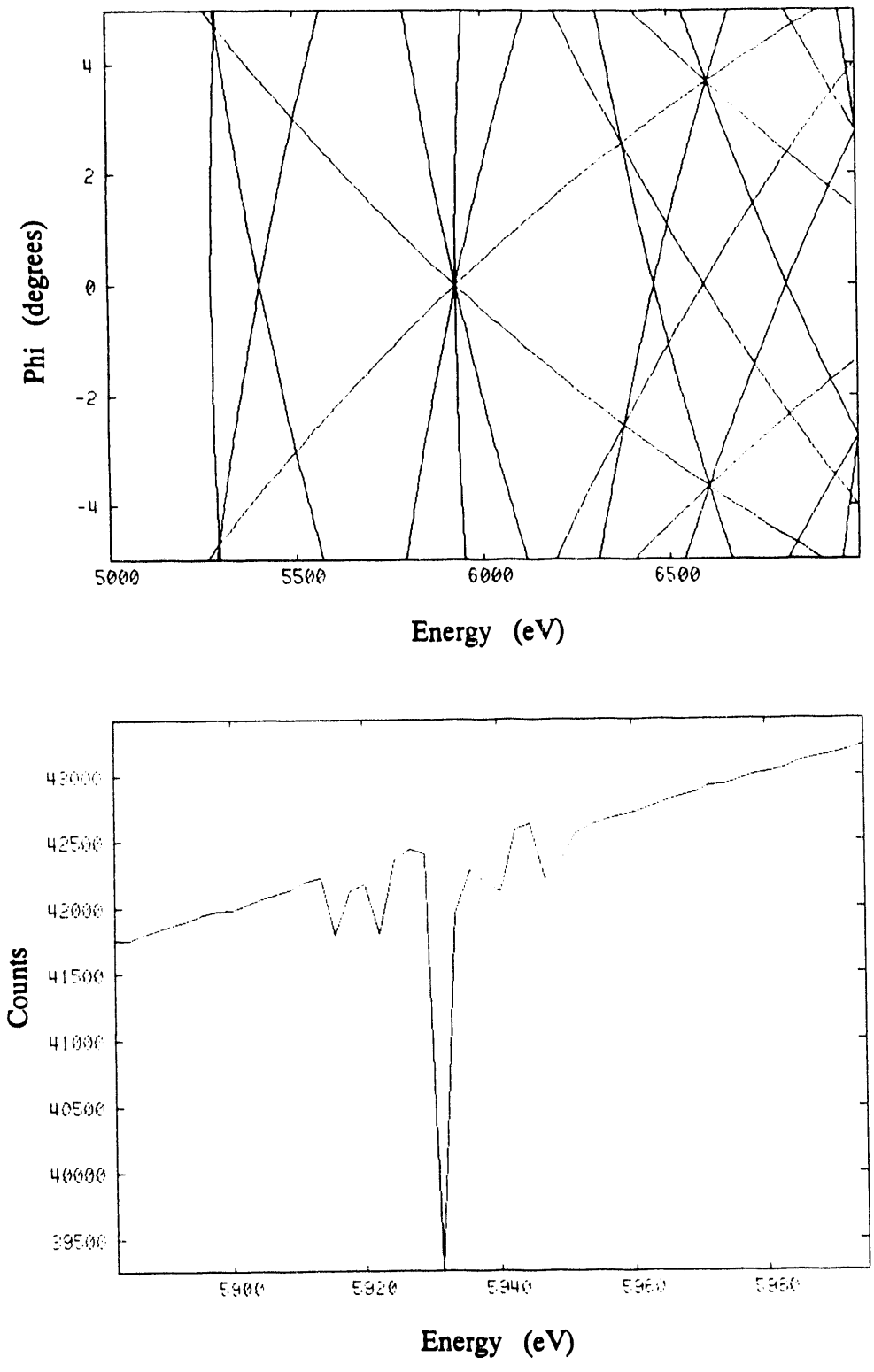

Fig. 9-5.3 (a) ϕ-plot if Si [1 1 1]. (b) Phi scan of the 5931 eV glitch of Si [1 1 1]. The prominent dip at 5931 eV is mainly due to the [2 2 −4] umveg reflection. Since the monochromator was not precisely oriented to the $\phi = 0$ position, there was extra structure in the wings due to other nearby umveg reflections.

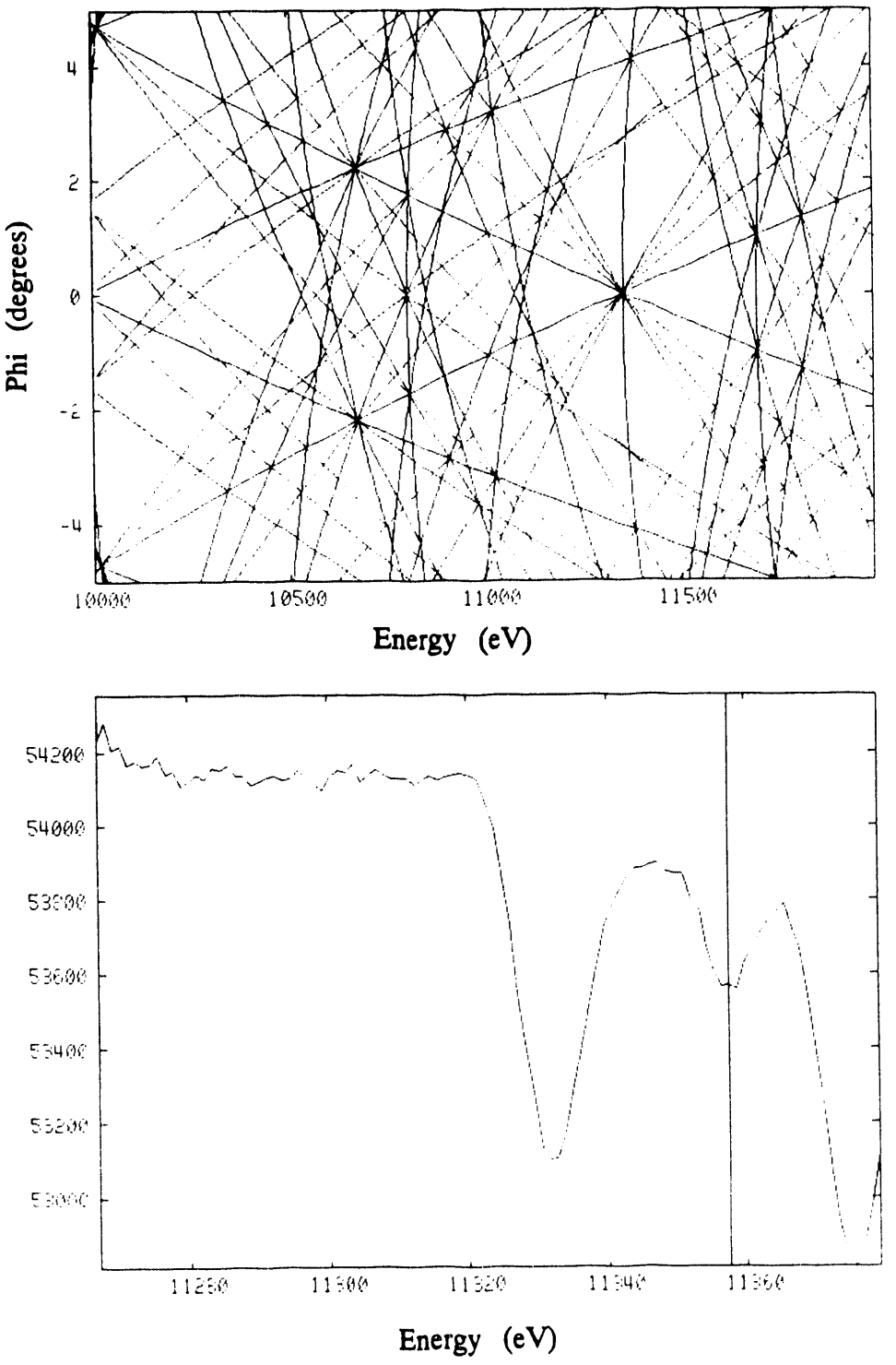

Fig. 9-5.4 (a) Phi plot of Si [1 1 1]. These plots become more densly populated with umveg reflections as the energy increases. However, occasionally there are reasonable clearings having a vertical umveg reflection surrounded by only a few nearby reflections. Vertical umveg reflections are desirable because their energy widths are narrow and give good energy markers. (b) Phi scan of the 11358 eV glitch of Si [1 1 1]. The small central dip at 11358 eV is mainly due to the [−1 −1 −3] umveg reflection--this is the nearly vertical reflection in Fig. (a).

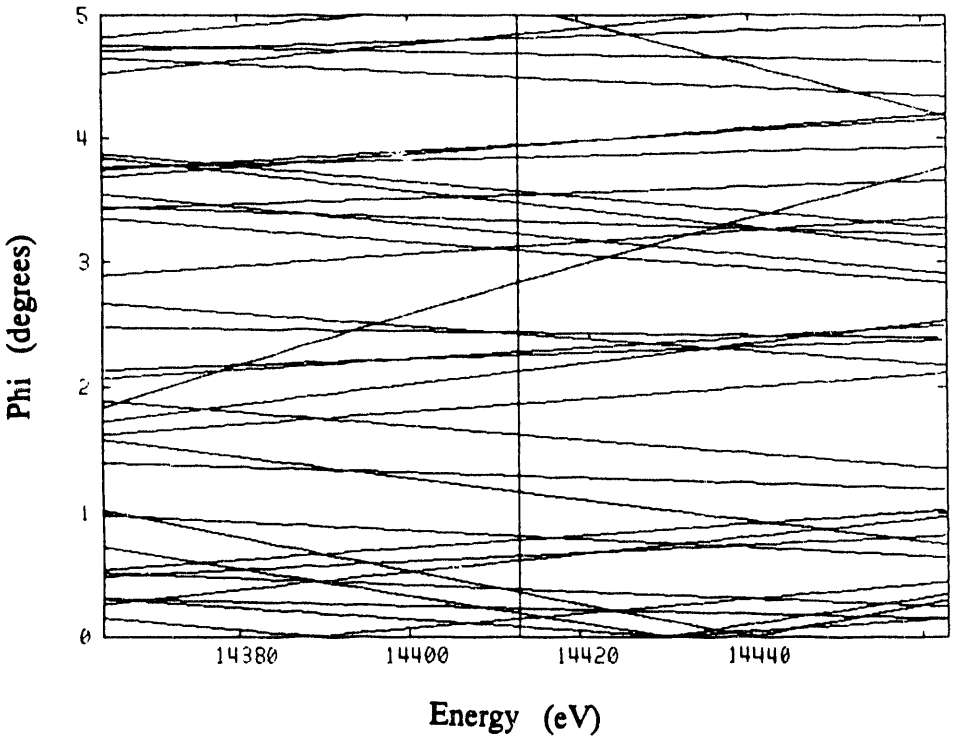

Fig. 9-5.5 ϕ-plot for YIG [0 0 2] reflection. There are no longer any convenient vertical umveg reflections to serve as energy markers (the vertical line in the figure is a marker for the 14412.5 eV nuclear resonance energy). Only the most intense umveg reflections are shown (if all nonzero reflections were shown, they would cover the figure so densly that it would be nearly black). Trying to navigate across such a terrain to find the nuclear resonance becomes a difficult task because most of the reflections are nearly horizontal.

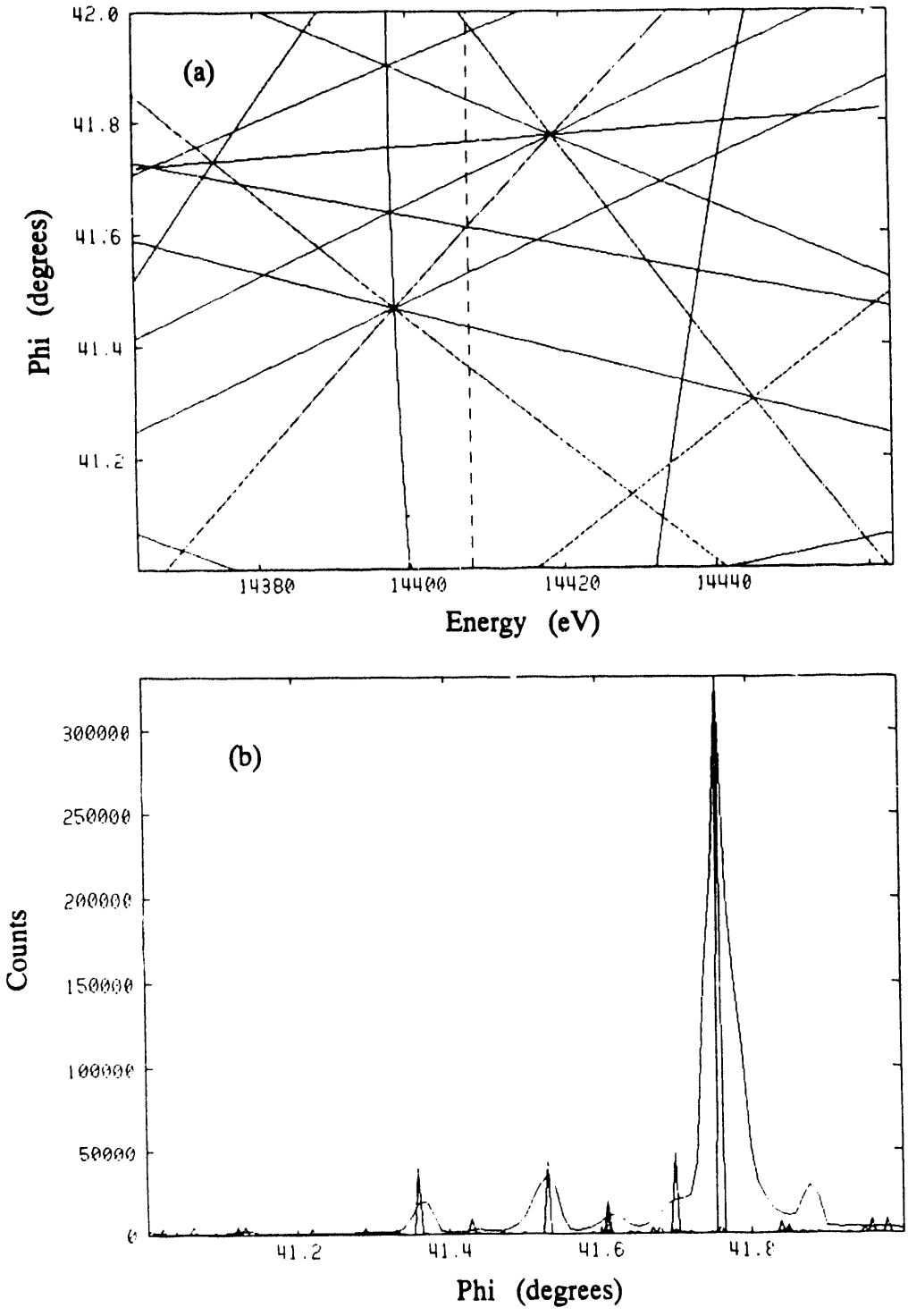

Fig. 9-5.6 (a) ϕ-plot for the YIG [0 0 2] reflection. (b) Phi scan of the [0 0 2] reflection. For forbidden primary reflections the umveg reflections show up as peaks (sometimes called antiglitches) rather than as dips (or glitches) typical in energy scans of allowed primary reflections. The markers where the umveg reflections lie are shown as sharp triangles. The position of these markers indicate that the energy of the incident beam is 14411 ± 1 eV (the dotted line). However, phi angles near 45° are not good operating points because the diffracted nuclear signal goes to zero there (the quadrupole splitting between the different iron sites in YIG goes to zero).

REFERENCES

[1] D. M. Gualtieri, W. Lavender, and S. L. Ruby, *J. Appl. Phys.* **63**, 3795 (1988).

[2] W. R. Busing and H. A. Levy, *Angle Calculations for 3- and 4-Circle X-Ray and Neutron Diffractometers*, ORNL Report 4056 (Oak Ridge National Laboratory, Oak Ridge, Tenn., 1967).

10. KINEMATICAL EFFECTS

10.1 Nuclear Hyperfine Structure Quantum Beats

The kinematical effects described in this chapter can be understood without a thorough knowledge of dynamical diffraction theory. They can be adequately described by single particle interactions rather than by the many particle, collective interactions occuring in the dynamical effects. One such striking kinematical effect is the quantum beat patterns that show up in the nuclear resonant, time-resolved measurements. These quantum beats arise from the interference between a coherent superposition of quantum states. For the case of ^{57}Fe, the coherent states are the set of hyperfine states excited when the nucleus is bombarded with an intense, broadband x-ray pulse. These excited states then fall back to the ground state and emit photons that coherently interfere with each other to produce the quantum beats. The coherence results from the scattering process remaining upon the energy shell--the nuclear state before and after the photon-nucleus interaction is identical.

Quantum beats were first observed in the early 1960's independently by Alexandrov and Dodd in the Zeeman beats arising from a superposition of electronic quantum states.[1-3] Here an external magnetic field was applied to split excited states and produce Zeeman components which could interfere with each other. Hyperfine structure beats arising from excited states naturally split by an internal magnetic field were observed in the early 1970's by Haroche.[4, 5] Also in this same time period, fine structure beats were seen by Haroche and Fabre,[6, 7] and in the late 1970's Hese used an electric field to split excited states to produce Stark quantum beats.[8] The first observation of nuclear hyperfine structure beats resulting from the excitation of nuclear quantum states was made by Gerdau in the late 1980's.[9] One should note that all of the electronic quantum beats described above were measured using gas samples while all measured nuclear quantum beats were done using solid samples. Thus the dynamical collective effects, such as resonance frequency shifts and decay rate speedups, present in nuclear systems have not been observed in electronic systems.

Nuclear hyperfine structure quantum beats are dramatic features in all of the time-resolved measurements of ^{57}Fe enriched YIG. Recall from Section 8.1 that YIG has a complicated antiferrimagnetic sublattice structure capable of producing 7 sets of 6-line hyperfine spectra (42 lines altogether). By using $[0\,0\,(4n-2)]$ YIG reflections $(n = 1,2,3,\ldots)$, electronic reflections are forbidden along with nuclear reflections from all

the a-sites and the $d3$-site. The hyperfine spectra then simplifies to 2 sets of 6-line spectra from the $d1$ and $d2$-sites.

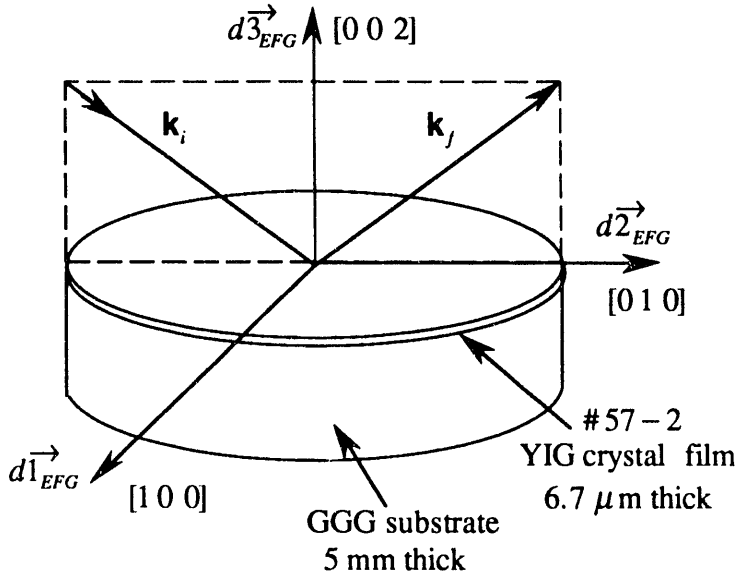

Fig. 10-1.1. Scattering geometry for nuclear resonance diffraction. The electric field gradients in the YIG crystal lie in the cubic $\langle 1\ 0\ 0 \rangle$ symmetry directions. When the applied magnetic field is perpendicular to the scattering plane formed by $\mathbf{k}_i$ and $\mathbf{k}_f$, it lies in the [1 0 0] direction parallel to the electric field gradient of the nuclear $d1$-site. When the applied magnetic field is parallel to the scattering plane, it lies in the [0 1 0] direction parallel to the electric field gradient of the nuclear $d2$-site. The incident beam is horizontally polarized perpendicular to the scattering plane.

For incident horizontally polarized x-rays and for an applied magnetic field perpendicular to the scattering plane (parallel to the polarization direction), each 6-line spectrum reduces to a 4-line spectrum (Case 1 in Section 5-1). Under such conditions, the $M = \pm 1$ transitions are allowed (see Fig. 5-3.1) and the $M = 0$ transitions are not allowed--they would be if the incident x-rays were vertically polarized. The scattering geometry is shown in Fig. 10-1.1, and a simplified hyperfine diagram along with the polarization of each line is shown in Fig. 10-1.2. Since the emitted x-rays from each line all have the same polarization, there will be quantum beats resulting from the interference of x-rays from all the resonance lines. The possible combinations of pairing the 8 lines in Fig. 10-1.2 gives 8 choose 2, or $\binom{8}{2} = 28$, possible beat frequencies. The corresponding beat periods are given in Table 10-1.1.

An experimentally measured time-resolved spectrum for such a scattering geometry is shown in Fig. 10-1.3 (using the YIG [0 0 2] reflection). Since lines 1 and 6 have the largest Clebsch-Gordan coefficients, the amplitude of their beats dominate the overall quantum beat pattern--the beating between lines 1 and 6 gives rise to the fast 7 nsec

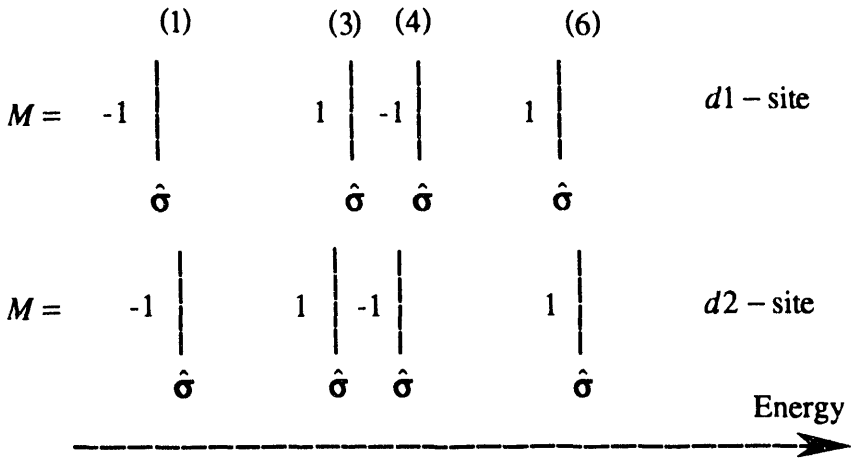

Fig. 10-1.2. Hyperfine energy spectrum illustrating the case where the applied magnetic field is perpendicular to the scattering plane. Each hyperfine line is horizontally, or sigma, polarized: $\hat{\sigma}$.

	ℓ_1	ℓ_3	ℓ_4	ℓ_6	ℓ'_1	ℓ'_3	ℓ'_4	ℓ'_6
ℓ_1								
ℓ_3	18.6							
ℓ_4	13.4	47.6						
ℓ_6	**7.22**	11.8	15.6					
ℓ'_1	**135**	16.4	12.2	**6.85**				
ℓ'_3	16.4	135	73.3	12.9	14.6			
ℓ'_4	12.1	34.4	124	17.9	11.1	46.0		
ℓ'_6	**7.66**	13.0	17.9	**124**	**7.25**	14.4	20.9	

Table 10-1.1. Hyperfine structure quantum beat periods (in nsecs) for the case of an applied magnetic field perpendicular to the scattering plane. Lines ℓ_n are from the nuclear $d1$-site, and the primed lines ℓ'_n are from the $d2$-site. The internal magnetic field strength is -3.69×10^5 Gauss and the electric quadrupole splitting is -0.89 mm/sec. The dominant quantum beats are in bold face. The average fast magnetic quantum beat seen in Fig. 10-1.3 is 7.2 nsec and the average slow electric quadrupole quantum beat is 130 nsec.

magnetic beat period seen in Fig. 10-1.3. There is also a quadrupole beat period of 130 nsec due to the electric quadrupole splitting between lines ℓ_1 and ℓ'_1 of the $d1$ and $d2$-sites (and also between lines ℓ_6 and ℓ'_6 of the two sites). This gives rise to the overall slow modulation of the beat pattern in Fig. 10-1.3. All of the other quantum beats show up as small perturbations upon the overall quantum beat pattern. The fit to the data in Fig. 10-1.3 utilizes the full dynamical diffraction theory for resonant scattering, but it relies heavily upon the energy separation of the hyperfine lines that gives rise to the quantum beat periods given in Table 10-1.1. The dynamical resonance frequency shifts discussed in Sections

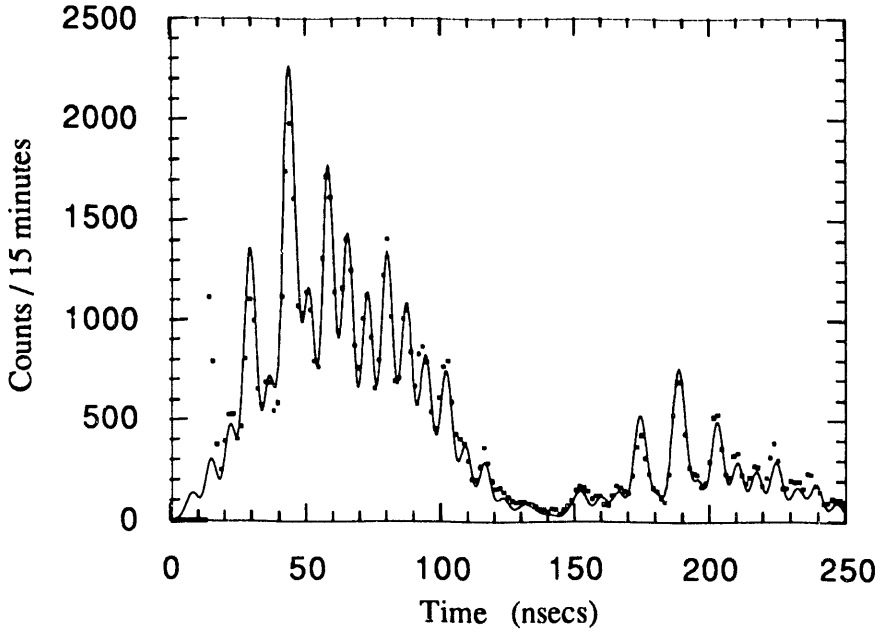

Fig. 10-1.3. Hyperfine structure quantum beat pattern for the case where the applied magnetic field is perpendicular to the scattering plane. Full dynamical diffraction theory has been applied to obtain the fit using the quantum beat periods given in Table 10-1.1. The operating angle was set at -25 μrads below the Bragg peak. Operating off the Bragg peak lessens the decay rate speedup and allows the slow electric quadrupole quantum beat to be seen.

7.6 and 7.7 slightly change these quantum beat periods--these small changes can lead to drastic changes in the quantum beat patterns and are further examined in Chapter 11.

When the applied magnetic field is parallel to the scattering plane and parallel to the crystal surface, all 12 lines from the d-sites are allowed (Case 3 in Section 5-1). For small Bragg angles, the $M = 0$ lines can be neglected, and the 12 lines reduce to 8 (the magnetic field is then nearly parallel to the incident and scattered photon directions). The simplified hyperfine diagram for such a case was discussed earlier and is shown in Fig. 8-1.4. The $M = +1$ lines emit left circularly polarized photons (polarization $\hat{\mathbf{e}}_+$) while the $M = -1$ lines emit right circularly polarized photons (polarization $\hat{\mathbf{e}}_-$). Since photons of orthogonal polarizations do not interfere with each other, the total number of beat frequencies is twice 4 choose 2 combinations of pairs of lines, or 12 possible beat frequencies. The beat periods for such a case are given in Table 10-1.2.

The experimentally measured time-resolved spectrum for such a scattering geometry is shown in Fig. 10-1.4. There are far fewer different beat periods than in the previous case where the magnetic field was perpendicular to the scattering plane. However, there is

	ℓ_1	ℓ_4	ℓ'_4	ℓ'_1	ℓ_6	ℓ_3	ℓ'_3	ℓ'_6
ℓ_1								
ℓ_4	11.1							
ℓ'_4	12.2	124						
ℓ'_1	135	12.1	13.4					
ℓ_6								
ℓ_3					14.4			
ℓ'_3					13.0	135		
ℓ'_6					124	12.9	11.8	

Table 10-1.2. Hyperfine structure quantum beat periods (in nsecs) for the case of an applied magnetic field parallel to the scattering plane. Lines ℓ_n are from the nuclear $d1$-site, and the primed lines ℓ'_n are from the $d2$-site. The internal magnetic field strength is -3.69×10^5 Gauss and the electric quadrupole splitting is -0.89 mm/sec. The upper left-hand and lower right-hand sections of the table represent quantum beats for right and left hand circularly polarized x-rays respectively. The average fast magnetic quantum beat in Fig. 10-1.4 is 12.2 and 13.0 nsec for right and left circularly polarized x-rays respectively. The slow electric quadrupole quantum beat is 135 and 124 nsec for right and left circularly polarized x-rays respectively.

the additional complication of two superimposed quantum beat patterns of two different polarizations (right and left circular polarizations) having slightly different beat periods (about 12 nsec for the right and 13 nsec for the left circular polarization). Due to the slightly different beat periods for the two overlapping beat patterns, they go into and out of phase as time goes on. In Fig. 10-4.1, the point in which the overlapping beat patterns get out of phase is around 60 to 70 nsec and gives rise to the anomalous feature present there where the overall beat pattern is nearly washed out. This null point is one of the most difficult features of the beat pattern to fit because it is very sensitive to a wide host of kinematical and dynamical effects.

In the sections to follow, the quantum beat patterns will be examined to investigate interesting physical properites such as the polarization of the incident beam, the Lamb-Mössbauer factor, and the internal hypefine crystalline fields at room and low temperatures. In the final section angular interferometry is used to explore the phase shift of a rotated quantum state. Quantum beats are seen to be a very useful effect that can be used to understand and explore many fascinating physical phenomena in resonant scattering physics.

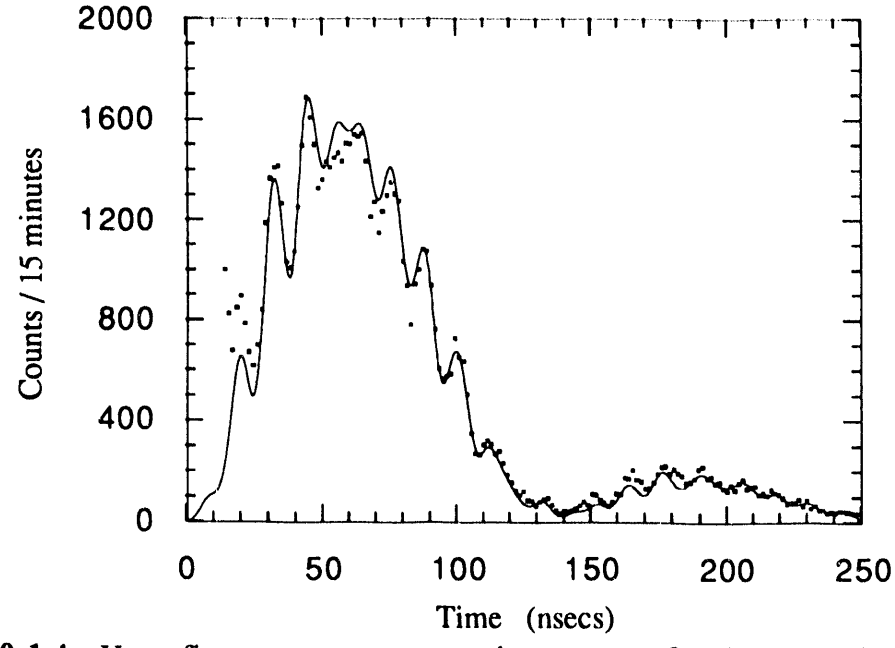

Fig. 10-1.4. Hyperfine structure quantum beat pattern for the case where the applied magnetic field is parallel to the scattering plane. Full dynamical diffraction theory has been applied to obtain the fit using the quantum beat periods given in Table 10-1.2. The operating angle was set at -20 μrads below the Bragg peak.

10.2 Analysis of Internal Hyperfine Fields

Time and frequency lie in dual spaces that are the reciprocal of each other. The decision to examine a scattering process in either temporal or frequency space will not change the underlying physics of that process. A Mössbauer velocity measurement should yield the same information as a time-resolved measurement. However, the collected information may be more difficult or easier to interpret depending upon what type of measurement is made. For instance, the phase information in a scattering process is more easily seen in a time-resolved measurement while the hyperfine resonance energies are more easily seen in a Mössbauer velocity measurement.

In this section, the internal magnetic dipole and electric quadrupole fields are investigated through time-resolved spectroscopy. The main utility this method has over Mössbauer velocity spectroscopy is the length of time needed to take sufficient data for low count rate experiments. For counting rates of around 100 counts/sec, the time spectra can be collected in about 1 minute to get enough statistics to determine the hyperfine field

parameters adequately, while a Mössbauer velocity spectra would need several hours of collection time to get the same information. One reason for this is because the velocity measurement is an absorption measurement collecting information about missing resonant photons, and it therefore has a larger background problem. Also, the velocity analyzer must be a reasonably thin-line absorber in order to scan the hyperfine spectra of the sample without significantly distorting, or modifying, the sample's spectra--this further increases data collection times.

To acquire an intuitive grasp of how the time spectra vary with changing hyperfine field parameters, multiple graphs are given in Figs. 10-2.1, 10-2.2, and 10-2.3. Each plot is normalized to unity and covers the first 250 nsec after the prompt excitation. The YIG [0 0 2] spectra were calculated at an angle -40 μrad below the Bragg peak in order to clearly show the electric quadrupole quantum beat. The higher order YIG [0 0 10] spectra were calculated at an angle right at the Bragg peak. The difference in operating angles gives rise to the difference in intensities between the [0 0 2] and [0 0 10] reflections--operating far off the Bragg peak significantly reduces the reflected intensity. The spectra were calculated for an internal magnetic field, $\mathbf{B}_{int}$, perpendicular and parallel to the scattering plane. When the internal magnetic field strength was varied in steps of 2 kGauss from 364 to 374 kGauss, the electric quadrupole splitting, $e^2qQ/2$, remained fixed at 0.89 mm/sec. When the electric quadrupole splitting was varied in steps of 0.02 mm/sec (or 1 neV) from 0.84 to 0.94 mm/sec (or 40 to 45 neV), the internal magnetic field strength remained fixed at 369 kGauss. The incident x-rays were fixed to be 100% horizontally polarized, and the full dynamical diffraction theory was used to perform the calculations. (The curve in bold-face in the figures is pointed to by the graphic arrow ⇓.)

Increasing the internal magnetic field strength increases the magnetic energy level splitting thus forcing the hyperfine lines to be spaced further apart in energy. Increasing the energy spacing between the hyperfine lines decreases the beat period and causes the beat pattern to be compressed in time. This accordion effect is clearly shown in Fig. 10-2.1 where increasing the internal magnetic field strength compresses the beat pattern and decreasing the field strength expands the pattern. The accordion effect is most dramatic during the second peak of the electric quadrupole beat occurring after 130 nsec. When operating far off the Bragg peak, changes in the internal magnetic field strength of 2 kGauss can be unambiguously seen in the time spectra (this is even more revealing in the fast beat spectra where the internal magnetic field is perpendicular to the scattering plane).

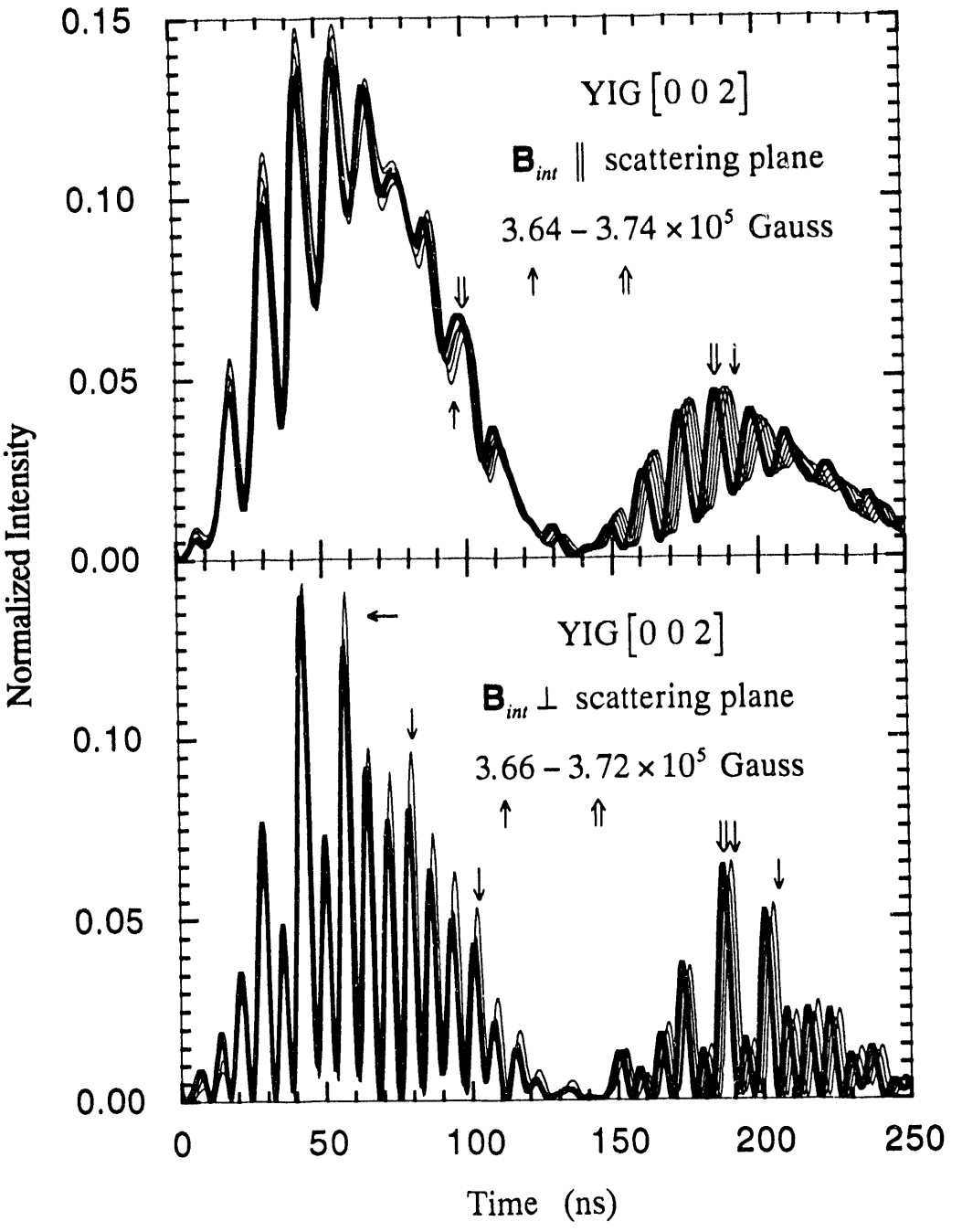

Fig. 10-2.1. YIG [0 0 2] time spectra for various internal magnetic field strengths.

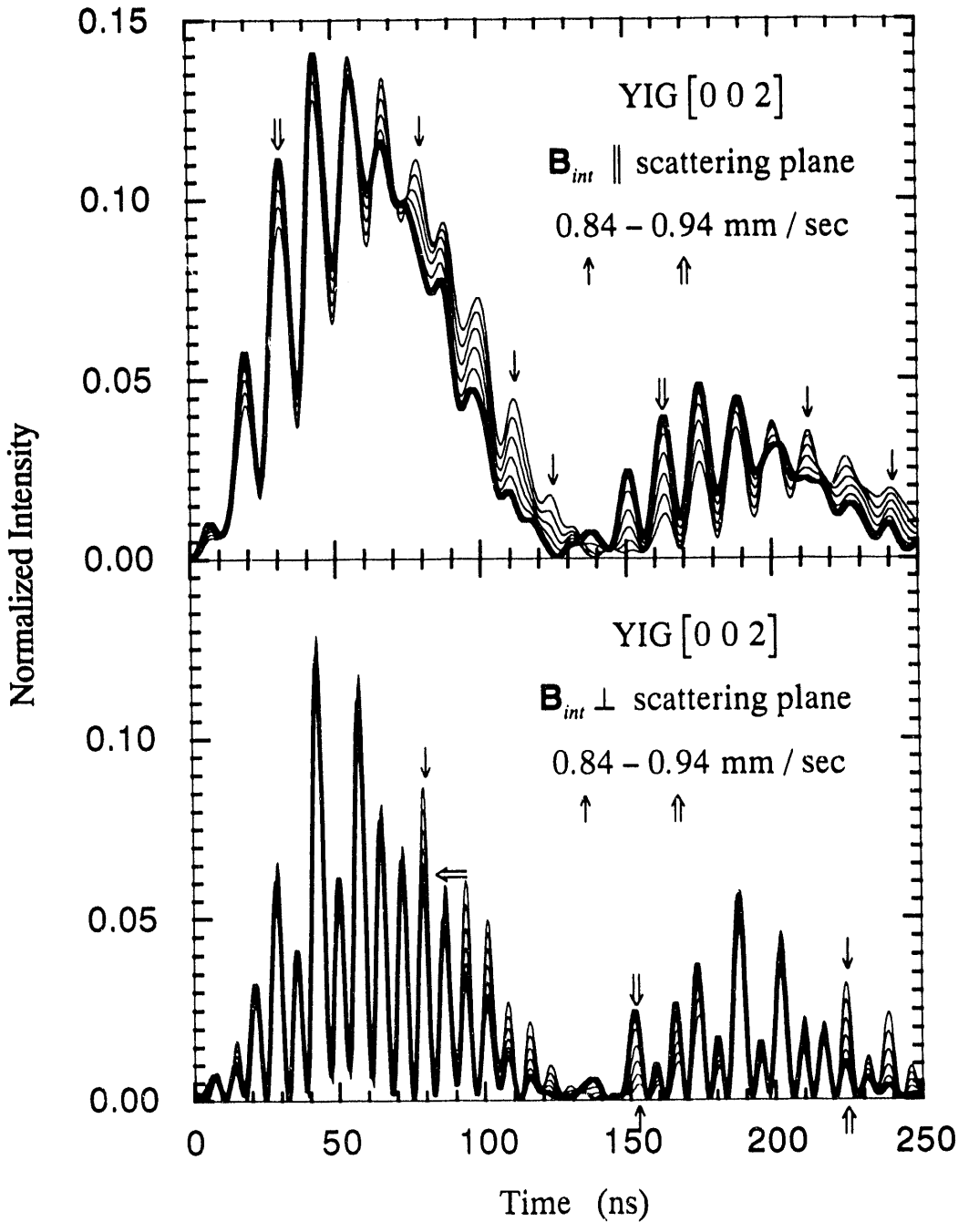

Fig. 10-2.2. YIG [0 0 2] time spectra for various electric quadrupole energy level shifts.

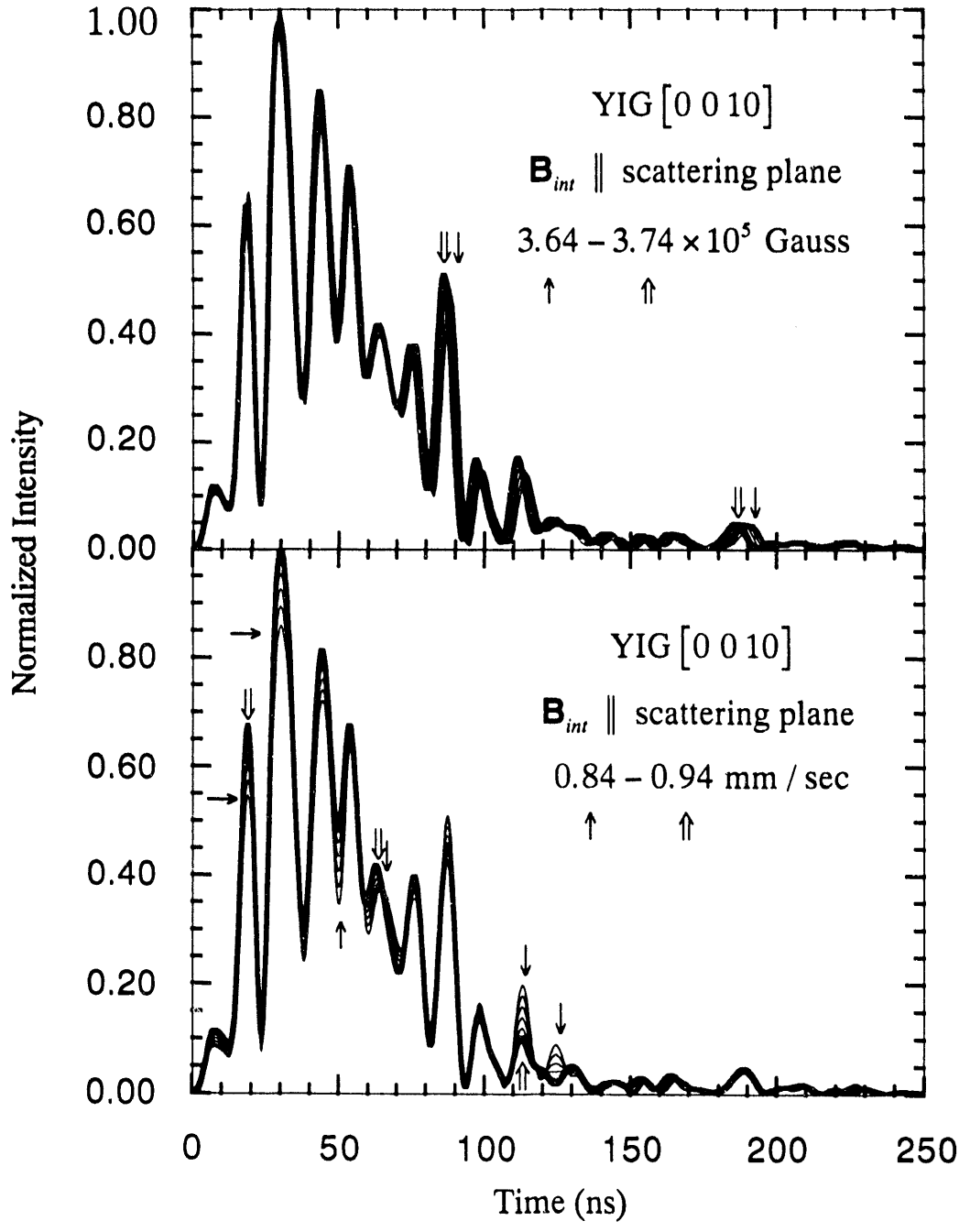

Fig. 10-2.3. YIG [0 0 10] time spectra for various magnetic field strengths and electric quadrupole energy level shifts.

Changes in the internal magnetic field strength dramatically affects the fast magnetic beat pattern. Changes in the electric quadrupole splitting factor, $e^2qQ/2$, dramatically affects the slow electric quadrupole beat pattern. Increasing the quadrupole splitting increases the energy spacing between lines ℓ_1 and ℓ_1' of the $d1$ and $d2$ iron sites (and also between lines ℓ_6 and ℓ_6' of the two d-sites). This leads to a decrease in the quadrupole beat period, and this shows up in Fig. 10-2.2 as a compression of the modulation envelope over the fast magnetic beats. Again, when operating far off the Bragg peak, small changes in $e^2qQ/2$ lead to striking changes in the overall beat pattern. Changes in the beat pattern due to changes in $e^2qQ/2$ of 1 neV are quite evident.

Many other factors can play a role in modifying the quantum beat patterns: variation of the magnitude of the internal hyperfine fields throughout the crystal film, nonuniformity of the applied magnetic field, depolarization of the magnetic dipoles, nonuniformity of the electric field gradient directions at each nuclear site, nonuniformity of the lattice spacing within the crystal film, the mosaic crystal spread, and the polarization of the incident field to name a few. One could probably fit any set of experimental data by varying an unlimited number of parameters. So, only a few factors that were known to have a significant effect were considered.

The polarization of the incident beam had to be considered in certain cases. Since the experiments were done on wiggler or undulator beam lines, elliptically polarized beams were not a problem (Furthermore, there was no strong evidence for elliptically polarized beams in the data. The result may have been different if a bending magnetic beam line was used since elliptically and even circularly polarized x-rays exist when operating above or below the plane of the electron orbit.). A partially unpolarized mix of horizontally polarized x-rays with a small amount of uncorrelated vertically polarized x-rays was considered in the hyperfine field analysis. A few examples of such a mixture containing 70 to 100% horizontally polarized x-rays is shown in Fig. 10-2.4. When the internal magnetic field is parallel to the scattering plane, an admixture containing up to 30% vertically polarized x-rays barely changed the beat pattern--only the sensitive null region near 70 nsec is affected. The beat pattern is significantly affected when the magnetic field is perpendicular to the scattering plane. This is not an unexpected result. When $\mathbf{B}_{int}$ is parallel to the scattering plane, both horizontally and vertically polarized x-rays can excite lines 1,3,4, and 6 which in turn radiate circularly polarized x-rays--horizontally and vertically polarized x-rays do about the same thing. When $\mathbf{B}_{int}$ is perpendicular to the scattering plane, horizontally polarized x-rays can excite lines 1,3,4, and 6, but vertically polarized x-rays can excite only lines 2 and 5. The beat period between lines 2 and 5

The other major factors considered were the mosaic spread of the crystal film and the angular distribution of the incident beam. Both of these factors were treated in a simple

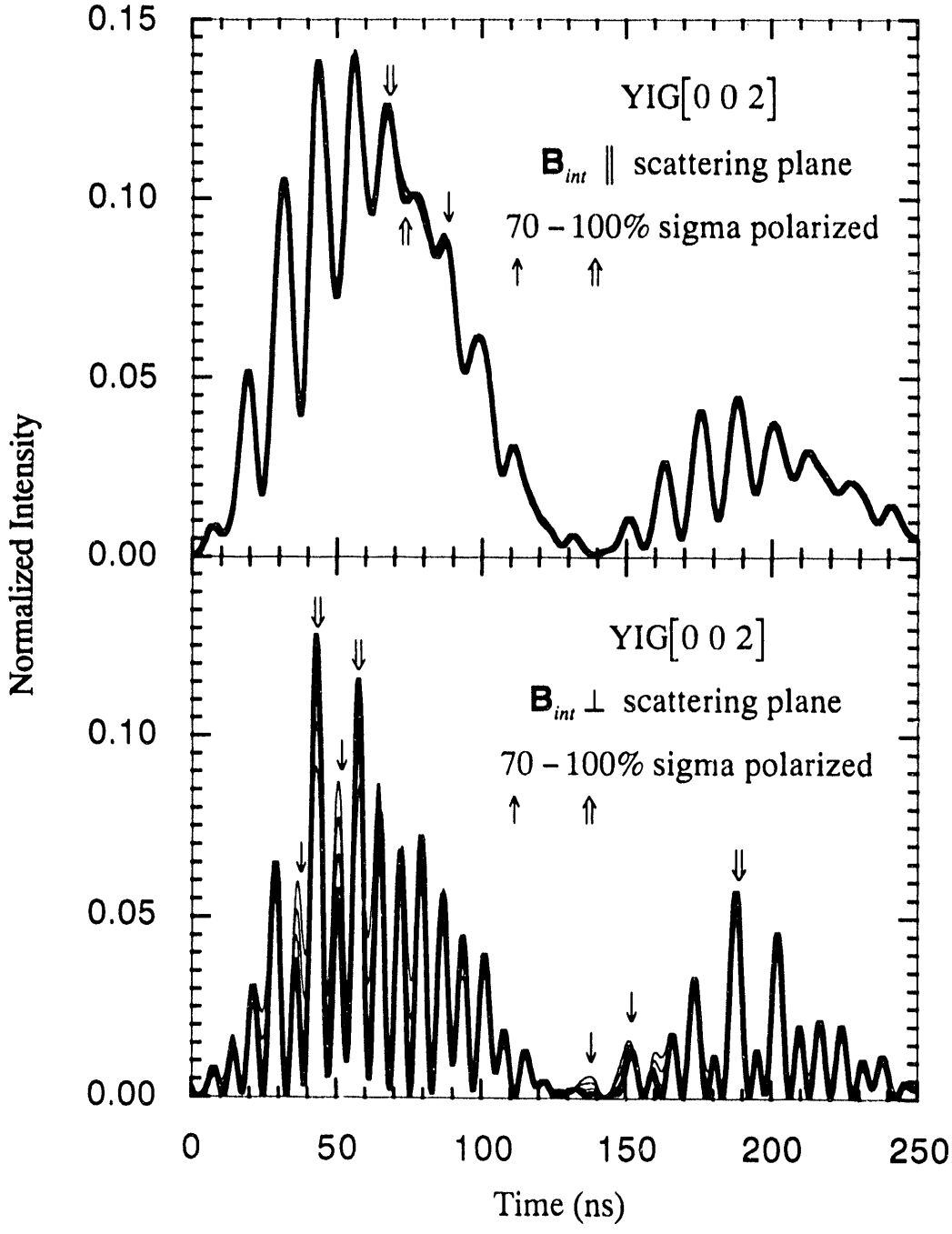

Fig. 10-2.4. Time spectra for various amounts of horizontally and vertically polarized x-rays.

The other major factors considered were the mosaic spread of the crystal film and the angular distribution of the incident beam. Both of these factors were treated in a simple fashion by performing a Gaussian angular average centered over the incident angle. Multiple time spectra were calculated at various incident angles, and the final fit was a Gaussian weighted average of each spectrum. This method takes into account both the angular divergence of the incident beam and the mosaic crystal spread of the YIG thin film.

The time resolution of the detector apparatus was handled by convolving a Gaussian pulse with the beat patterns. This is simply a Gaussian weighted time average, and its main effect is to partially wash out the oscillations in the beat pattern.

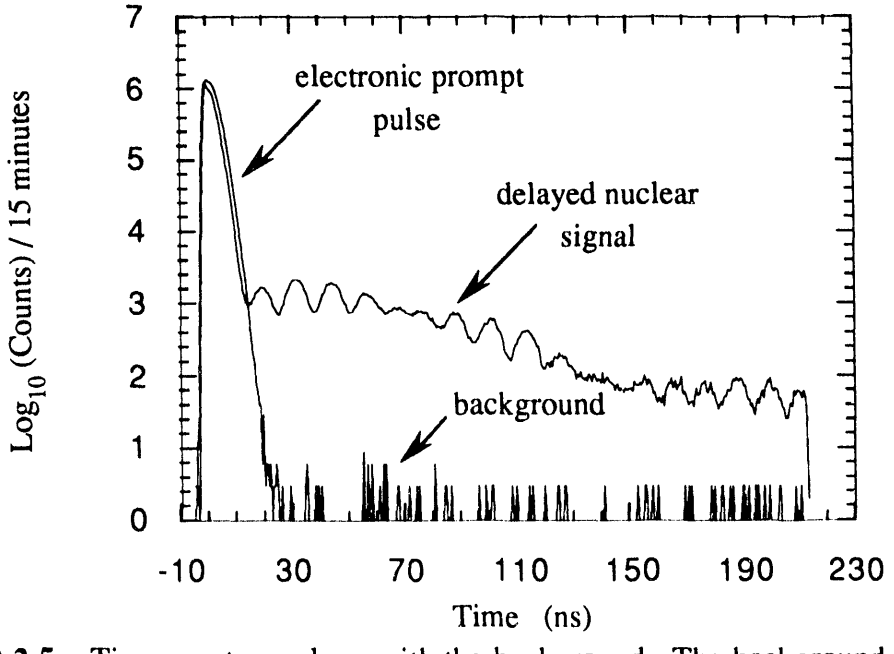

Fig. 10-2.5. Time spectrum along with the background. The background measurement was taken 5 eV above the 14412.5 eV nuclear resonance energy. The YIG [0 0 2] time spectrum was taken about 10 μrad above the Bragg peak with $\mathbf{B}_{int}$ parallel to the scattering plane. This is the second time spectrum ever to be taken at the PBF1 beamline at PEP (the very first was a rough demonstration measurement and was not used in the hyperfine field analysis).

No background subtraction was done to the data. The data was analyzed at a time long enough after the prompt excitation that the fluorescent signal from the photodetector's plastic scintillator was negligible--this was ensured by analyzing the data 25 nsec from the prompt pulse. Fig. 10-2.5 shows a typical beat pattern together with the prompt pulse. The width of the prompt pulse is quite wide (FWHM $\approx$ 4.3 nsec), but this was later found

out to be due to the TAC being overworked trying to process data at a prompt rate of 12,000 counts/sec. When the prompt rate fell to around 5,000 counts/sec, the prompt pulse width fell to a more respectable 2.5 nsec. The background run was done by tuning the monochromator energy 5 eV above the nuclear resonance energy. The background rate beyond 25 nsec was about 0.23 counts/sec. Compared to the delayed nuclear signal rate of roughly 190 counts/sec, the background car be safely ignored.

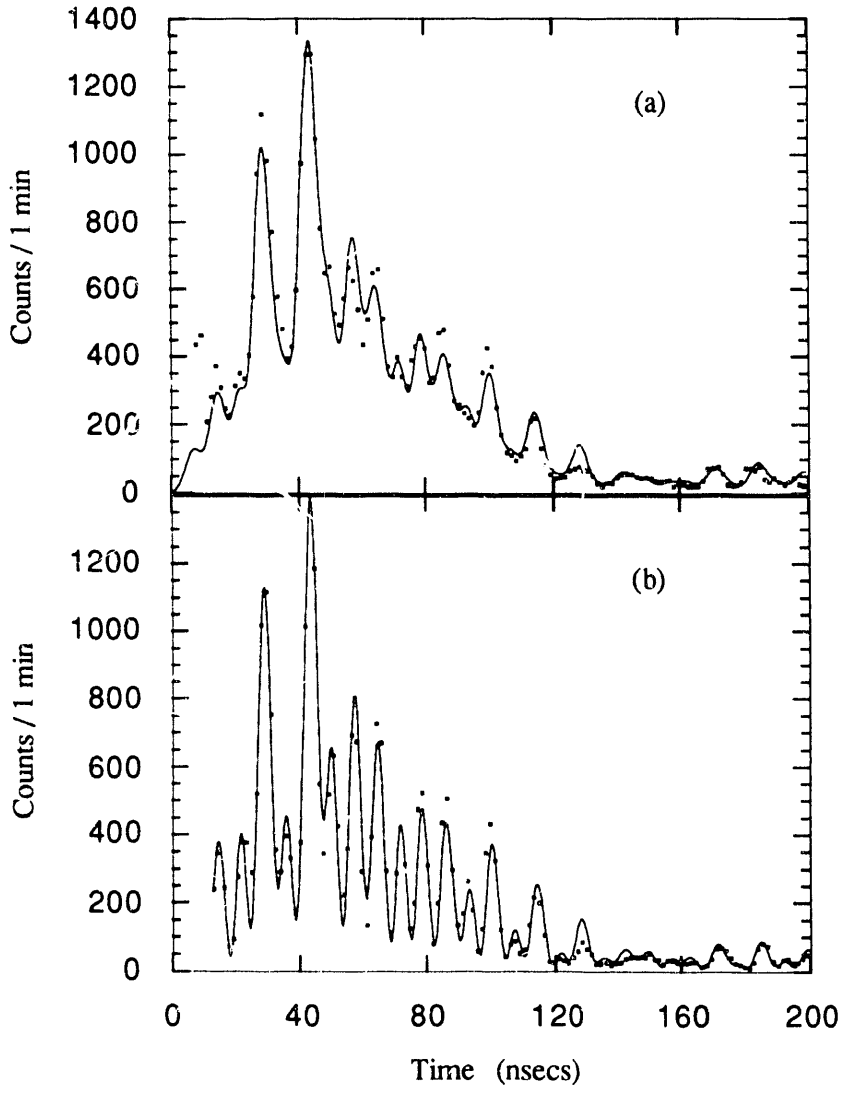

Fig. 10-2.6. Dramatic improvement in the time resolution of the measurements. Fig. (a) is a measurement without the veto signal in Fig. 9-3.3 to the coincidence logic unit; Fig. (b) is a measurement with the veto signal. By not overworking the TAC the time resolution was improved by a factor of two from 5 nsec to 2.5 nsec.

The data shown in Fig. 10-2.5 was taken without the veto signal to the coincidence logic unit shown in Fig. 9-3.3. This resulted in the TAC being overworked at high

counting rates and contributed towards broadening the time resolution of the measurements. By using the veto signal which allowed the TAC to be triggered only at times 10 nsec after the prompt pulse, the TAC could be used at high prompt rates without worsening the inherent time resolution of the photomultipliers. In such an arrangement, data as far back as 10 nsec after the prompt pulse can be measured with very low background rates, and the time resolution improves to around 2.5 nsec. This is shown in Fig. 10-2-6. The improvement in time resolution by a factor of two, however, did not change the values of the hyperfine field parameters used to fit the data. The improvement enabled small subtle effects to be seen in the time distribution. For instance, for data having a 7 nsec beat pattern blurred with a 5 nsec time resolution (see Fig. 10-2.6), the polarization content of the incident beam could not be determined when the crystal was positioned at the Bragg peak. However, he incident polarization content could be measured when the time resolution was reduced to 2.5 nsec.

For the hyperfine field parameters given in Tables 10-2.1 and 10-2.2 (B_{int} is the internal magnetic field strength and $e^2qQ/2$ is the electric quadrupole splitting factor), χ^2 fits were performed. Using a Fortran subroutine, VA02A, acquired from the Argonne National Labs computer center, a grid-gradient search algorithm for minimizing χ^2 was employed by varying 5 to 7 parameters: B_{int}, $e^2qQ/2$, the incident polarization distribution, the Gaussian angular and time resolution, the deviation angle from Bragg, and the starting time.

An analysis of 25 time spectra (from the Run #1 set in Table 10-2.1) where the deviation angle from the Bragg peak was less than $\pm 20\mu$rad and where 6 parameters were varied (the incident polarization was fixed to be 100% horizontally polarized) resulted in a Gaussian angular width (FWHM) of 21 ± 3 μrad--about 17% greater that the perfect Si crystal Darwin width. The fitting routine had a difficult time determining the angular resolution for time spectra taken at deviation angles greater that 20 μrad beyond the Bragg peak giving angular widths of up to 50 μrad, thus these spectra were omitted. The net angular resolution appears to be largely limited by the Darwin width of the Si monochromator (which is 18 μrad for perfect crystals) rather than by the mosaic spread of the YIG crystal.

For fits to all of the data in the tables below, the Gaussian angular resolution was fixed at 20 μrad, and only 6 parameters were varied (Except for the case where $\mathbf{B}_{int}$ was parallel to the scattering plane. The incident polarization was simply fixed to be 100% horizontally polarized since, as shown in Fig 10-2.4, such time spectra are insensitive to the polarization distribution). There was little coupling between the parameters--the

variation of one parameter to minimize χ^2 had little effect upon the value of the other parameters that minimized χ^2.

For data taken without the coincidence logic veto signal blocking out the prompt signal from the TAC, the time resolution was 4.1±0.8 nsec (This was compiled from the Run #1 data in Table 10-2.1 and from some of the Run #2 data in the same table. The Run #2 data was taken during a beamline run were the improvement in time resolution was tested and implemented). When the coincidence logic veto signal was used, the time resolution improved to 2.4±0.1 nsec (This was compiled from the data in Tables 10-2.1 and 10-2.2).

The polarization of the incident radiation differed at the PEP and CESR synchrotron ring beamlines. The polarization of the incident beam at the PBF1 undulator beamline at PEP was found to consist of 93±3% horizontally polarized radiation (the data in Table 10-2.1 taken during the two different runs gave the same result). At the F2 wiggler beamline at CESR the incident beam consisted of 84±2% horizontally polarized radiation. This decrease in polarization of the source beam may be due to the use of a wiggler rather than an undulator, and because the electron beam energy was lower at CESR than at PEP (5.5 GeV versus 14 GeV).

The hyperfine field parameters for the crystals labeled 57-2 and 57-6 are given in the Tables 10-2.1 and 10-2.2. An extensive investigation of the combined hyperfine interactions in YIG was made by Winkler through Mössbauer transmission spectroscopy measurements.[10] He found that for YIG single crystals 60 μm thick:

$$B_{int} = -399.9 \pm 1.5 \text{ kGauss} \quad \text{and} \quad e^2qQ/2 = -0.89 \pm 0.01 \text{ mm/sec}.$$

The YIG thin crystal films exhibit somewhat different hyperfine properties. For crystal #57-2, B_{int} is roughly 6% to 8% less than B_{int} for a pure single crystal, and, for crystal #57-6, B_{int} is smaller by 4%. The reduction in B_{int} is primarily due to the films being impregnated with a small amount of lead occupying the yttrium lattice sites. This has changed the local electrostatic and magnetostatic environment around the iron atoms and has resulted in a decrease in the internal magnetic field at the iron nuclei.

There is an interesting problem with crystal #57-2. For two different beamline runs different hyperfine fields were measured. B_{int} has increased by 2% and $e^2qQ/2$ has increased by 6% between Runs #1 and #2. Recall from Section 9.1 (see Fig. 9-1.2) that crystal #57-2 is a 6.7 μm thick crystal consisting primarily of 2 layers of YIG films having different lattice spacings. However, the data indicates that this crystal nonuniformity is not the reason for the difference in hyperfine fields between the two runs. The [0 0 2] reflection has a primary extinction length of 1.1 μm, thus these reflections probe only the

first micron of the crystal film. The χ^2 fits to the higher order reflections in both runs found that these reflections were probing a crystal film sublayer roughly 2.6 μm thick (see Section 11.4). Crystal #57-2 is then composed of two films 2.6 and 4.1 μm thick. Since the first micron of the crystal is uniform, the difference in B_{int} between Runs #1 and #2 for the [0 0 2] reflections is not due to thickness nonuniformity.

There is also reason to believe that a nonuniformity in the local hyperfine field environments across the surface area of the crystal is not responsible for the differences. As a result of the focusing properties of the upstream cylindrical mirror and the small Bragg angle, the incident beam lit up a stripe across the crystal 3 mm wide by 3 cm long for the [0 0 2] reflection. For the higher order reflections the area of this stripe substantially decreases--the [0 0 14] reflection lights up a stripe 3 mm wide by 1 mm long (the incident beam area was roughly 3×0.5 mm). However, the higher order reflections scanning ever smaller sections of the crystal area gave the same hyperfine parameters as the [0 0 2] reflection (as shown in Run #2). Nonuniformity of hyperfine fields across the crystal surface area is not evident in the data.

What may have occurred between the runs (which occurred $1\frac{1}{2}$ years apart) is that the crystal deteriorated to some degree. Some of the iron may have oxidized to become Fe_2O_3. The change in B_{int} is in the right direction (B_{int} for pure Fe_2O_3 is -515 kGauss) but the change in $e^2qQ/2$ is in the wrong direction ($e^2qQ/2$ for pure Fe_2O_3 is -0.12 mm/sec). The reason for the change remains unclear, but what is impressive is that 2% changes in the hyperfine field parameters is easily detectable through examining the quantum beat patterns.

Unlike crystal 57-2, crystal 57-6 is composed of a single layer of YIG (see Fig. 9-1.2). The χ^2 fit to the data yielded a thickness of 4.3±0.4 μm which is reasonably close to the expected value of 4.7 μm. The difference in hyperfine parameters between crystal 57-2 and 57-6 should be mainly due to the difference in lead concentrations in the two crystals. As a result of the odd behavior displayed by the other crystal, the effect of the lead upon the local electric quadrupole field is not readily determinable. $e^2qQ/2$ is 4% greater than Winkler's value for YIG, but there are large variations in this value stated throughout the literature (measured values varied from 0.78 to 1.03 mm/sec).[11-14]

Time-resolved spectroscopy is just as sensitive as Mössbauer velocity spectroscopy towards measuring hyperfine field parameters. They both can measure the hyperfine field values to within 1-2%. As a result, time-resolved spectroscopy was able to reveal subtle differences in the hyperfine properties of YIG between various thin film samples, and that these properties may slightly change over time for each thin film. Time-resolved spectroscopy using synchrotron x-rays may become more useful than Mössbauer spectroscopy when trying to measure the hyperfine fields of extremely small or very thin

Reflection	$\mathbf{B}_{int}$ direction	B_{int} (kGauss)	$e^2qQ/2$ (mm/sec)	# of time spectra
PEP Beamline Run #1				
[0 0 2]	∥	-369±2	-0.88±0.02	27
[0 0 2]	⊥	-369±1	-0.88±0.02	9
[0 0 6]	∥	-373±3	-0.87±0.02	1
[0 0 10]	∥	-373±2	-0.88±0.02	1
[0 0 10]	⊥	-370±2	-0.87±0.02	1
All reflections		-369±2	-0.88±0.02	39
PEP Beamline Run #2				
[0 0 2]	∥	-377±4	-0.93±0.04	1
[0 0 2]	⊥	-377±2	-0.94±0.01	7
[0 0 6]	∥	-374±3	-0.93±0.03	1
[0 0 6]	⊥	-376±2	-0.91±0.03	1
[0 0 10]	∥	-377±2	-0.92±0.01	2
[0 0 10]	⊥	-376±1	-0.93±0.02	1
[0 0 14]	∥	-376±2	-0.92±0.02	1
[0 0 14]	⊥	-376±1	-0.94±0.02	1
All reflections		-376±1	-0.93±0.01	15

Table 10-2.1. Hyperfine field parameters for crystal # 57-2. The uncertainties for each set of data represent the square root of the variance in the data using a weighted average for the mean. For each individual time spectrum the uncertainty in the parameters represents what it takes to produce a 10% change in the χ^2 minima. $\mathbf{B}_{int}$ is either parallel or perpendicular to the scattering plane.

Reflection	$\mathbf{B}_{int}$ direction	B_{int} (kGauss)	$e^2qQ/2$ (mm/sec)	# of time spectra
[0 0 2]	∥	-384±2	-0.95±0.01	2
[0 0 2]	⊥	-384±4	-0.96±0.04	1
[0 0 10]	⊥	-383±1	-0.96±0.01	2
All reflections		-383±1	-0.95±0.01	5

Table 10-2.2. Hyperfine field parameters for crystal # 57-6. The data was taken at the CESR F2 wiggler beamline.

materials consisting of just a few nuclei or a few layers of nuclei. Such materials would produce signals that are too weak to be measurable by Mössbauer spectroscopy techniques. However, time-resolved spectroscopy performed at future third generation synchrotrons having high powered undulator or wiggler insertion devices will provide way of probing such exotic materials.

10.3 Low Temperature Measurements

A low temperature experiment was performed to examine the scattering and hyperfine properties of YIG.[15] The crystal was mounted in a cryostat centered on a four circle diffractometer as explained in Section 9.2. Measurements were made at room temperature and at 150°K. A temperature controller was used to stabilize the temperature during the course of the measurements. The results are shown in Fig. 10-3.1.

One unexpected result can be quickly noticed in the two measurements shown in Fig. 10-3.1. Both measurements were taken for the same length of time, but the low temperature measurement has a much lower count rate than the room temperature measurement (17 counts/sec versus 110 counts/sec, or a factor of $6\frac{1}{2}$ times less). What was expected was an increase in counting rate as the temperature decreases because the Lamb-Mössbauer factor, or recoilless fraction of resonant nuclei, increases to the limit of unity as the number of phonon modes goes to zero. A cause for this discrepancy may be because the YIG crystal is a thin film epitaxially grown on a GGG substrate. There is naturally some strain in the film since YIG and GGG have different lattice constants. Going to low temperatures may have magnified these strains and caused the film to distort, or warp, resulting in the much lower counting rates. The measurement was done with crystal #57-2 before having any accurate knowledge of its structure. During or after the fabrication process, the crystal bifurcated due to lattice mismatching problems. What these results suggest is that YIG films thinner than 2.5 μm grown on GGG are not good samples to do low temperature perfect crystal diffraction experiments.

Though the crystal diffracts poorly at low temperature, the hyperfine parameters could still be measured and were found to be very different than the room temperature values. The internal magnetic field strength increased by 15% to 429 ± 4 kGauss when the temperature was lowered to 150°K. The value of B_{int} at low temperatures does not significantly depart from measurements made by others--Mössbauer transmission measurements at 85°K yielded values of B_{int} ranging from 460 to 467 kGauss, and a nuclear magnetic resonance measurement at 77°K yielded 468 kGauss (these were all done

on pure YIG polycrystalline samples).[16-18] Extrapolating to 150°K using the careful NMR measurements of Ogawa gives a value of 452 kGauss.[18] This is about 5% greater than the thin film measurement, and, since the room temperature measurements are about 7% greater than the thin film measurements, this difference is not unreasonable.

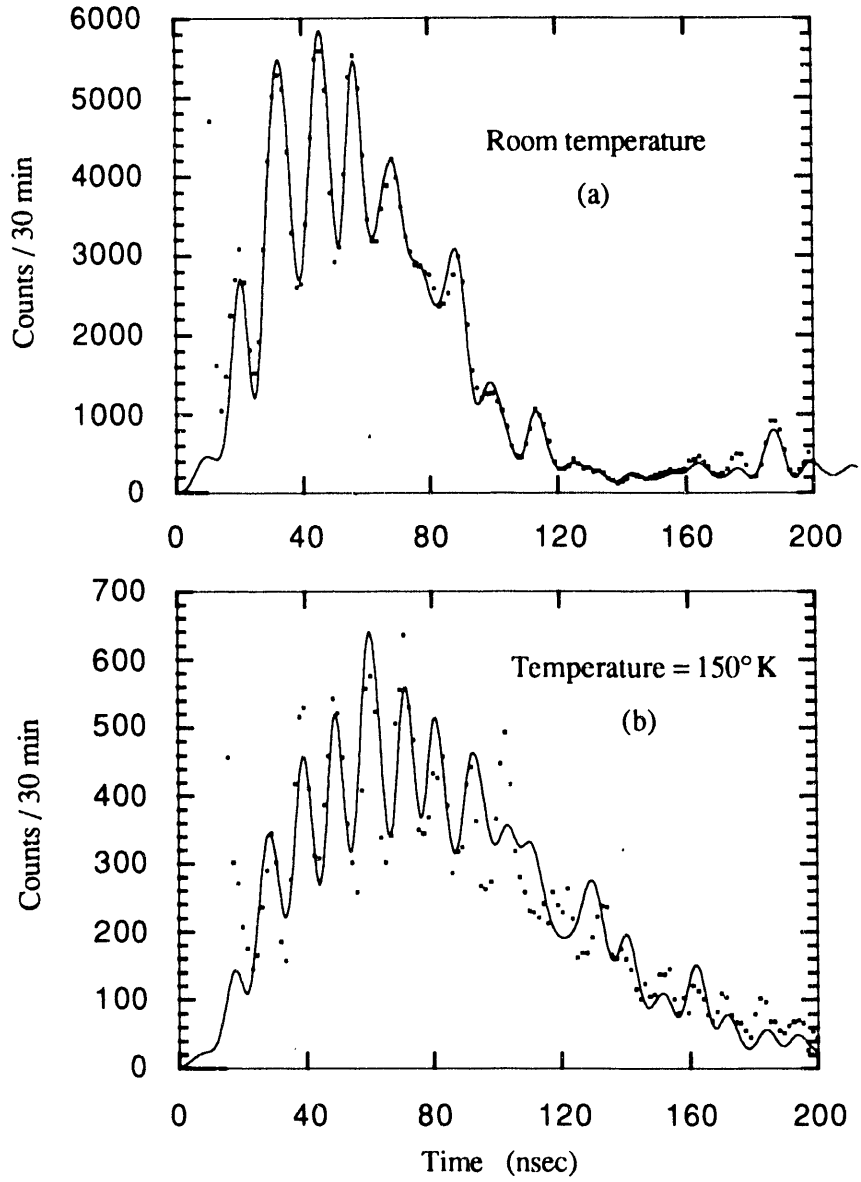

Fig. 10-3.1. Time spectra for [0 0 10] reflection at (a) room temperature and at (b) 150°K. $\mathbf{B}_{int}$ is parallel to the scattering plane and the crystal surface. At room temperature $B_{int} = -373 \pm 2$ kGauss and $e^2qQ/2 = -0.88 \pm 0.02$ mm / sec. At 150°K $|B_{int}|$ increased 15% to 429 ± 4 kGauss and $|e^2qQ/2|$ decreased 61% to 0.54 ± 0.04 mm / sec.

The electric quadrupole splitting factor decreased almost by half (61%) to 0.54 ± 0.04 mm/sec when the temperature was lowered to 150°K. The temperature dependence of $e^2qQ/2$ has apparently not been explored in detail experimentally since there is little information about it in the literature. Most early temperature dependence experiments have been done with polycrystals since they were easier to obtain, and these experiments examined the behavior of only the internal magnetic field. Since the direction between the electric field gradient and the magnetic field is completely random for a polycrystal, the electric quadrupole splitting should average to zero, thus no reliable value of $e^2qQ/2$ can be measured. This problem can be overcome by applying a sufficiently strong external magnetic field to remagnetize the polycrystal--in this case the angle between $\mathbf{B}_{int}$ and the electric field gradients is random and can be averaged over to obtain fits to the data. This was done to YIG polycrystals at room temperature (the external magnetic field strength was 20 kGauss), and quite accurate values of $e^2qQ/2$ were extractable from the data.[13] However, there is no account in the literature of using this procedure to find the temperature dependence of $e^2qQ/2$.

10.4 Angular Interferometry: Observation of the Phase Shift of a Rotated Quantum State

Scattering angle dependent quantum beat interference has been used to examine the phase shift of a quantum state that has undergone a rotation. A physical interpretation of this effect using the scattering theory formalism developed in Chapter 4 is given in Section 5.5. From a different perspective, the angular phase shift can be understood from basic rotational and mirror symmetry properties of free space[19] (see Appendix A.1).

The YIG $[0\,0\,10]$ reflection was chosen to get the maximum effect. In the experiment at the CESR beamline, the internal magnetic field was oriented, by using an external guide field, in the two antiparallel directions perpendicular to the scattering plane, and the net phase difference between the time beat patterns for the two orientations of the magnetic field was measured. Changing the direction of the magnetic field was equivalent to performing a $[0\,0\,+10]$ and a $[0\,0\,-10]$ reflection. This was observed during experiments at the PEP beamline where upward and downward reflecting experiments (without changing the direction of the magnetic field) gave phase shifts equivalent to orienting an internal magnetic field in the two antiparallel directions perpendicular to the scattering plane (without changing the orientation of the crystal).

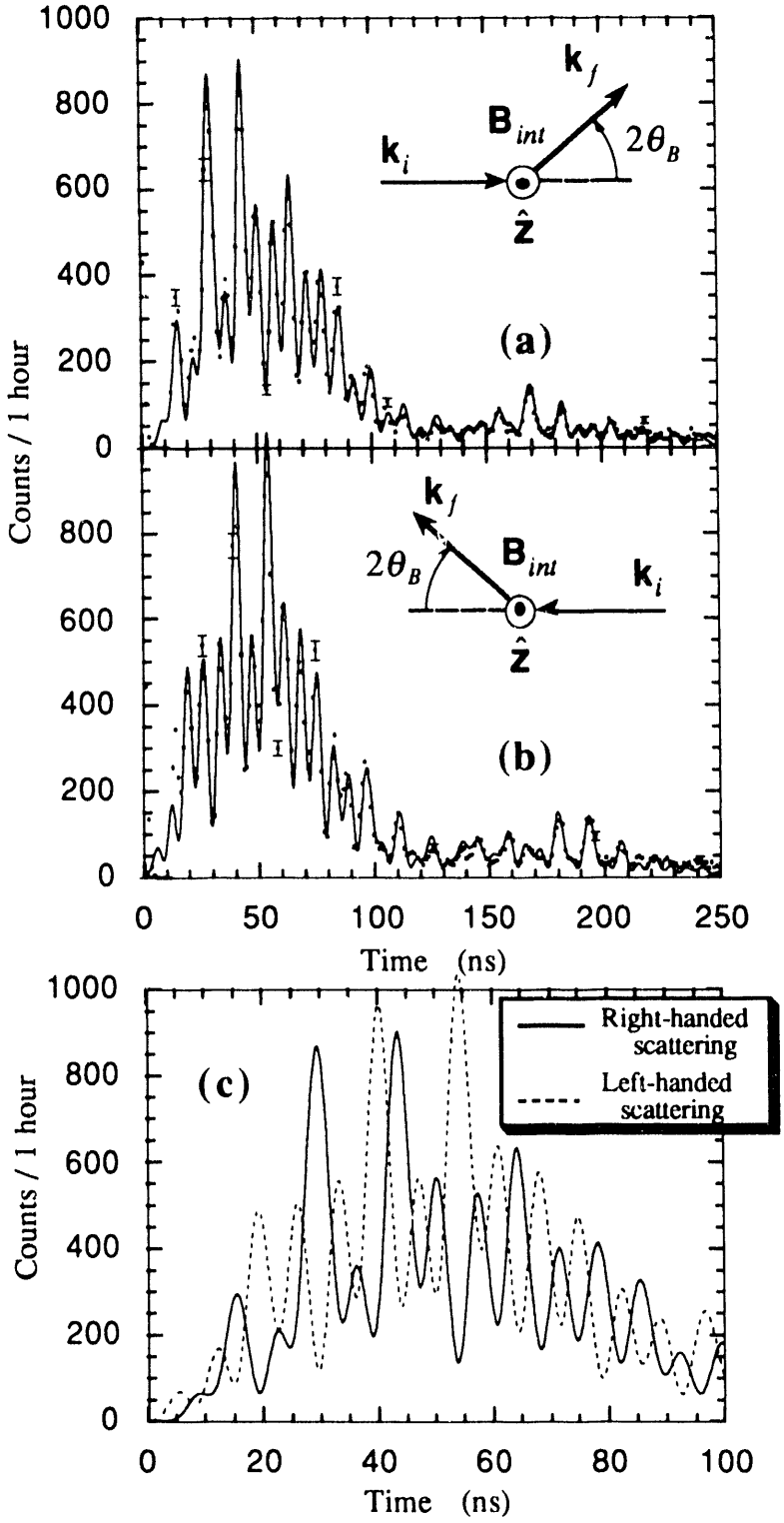

Fig. 10-4.1. Quantum beat patterns of YIG [0 0 10] reflections for (a) right-handed scattering and (b) left-handed scattering. (b) Calculated fits to the data are shown superimposed and expanded. The nearly 180° phase shift is clearly evident.

The results of the CESR beamline experiment is shown in Fig. 10-4.1. Note that in the diagram in Fig. 10-4.1 (a) the incident photon is rotated in a right-handed sense in going from $\mathbf{k}_i$ to $\mathbf{k}_f$--this will be called right-handed scattering. Left-handed scattering is illustrated in the diagram in Fig. (b) where the incident photon is rotated in a left-handed sense in going from $\mathbf{k}_i$ to $\mathbf{k}_f$. The Bragg angle for the YIG [0 0 10] reflection is about 20°. Diffraction from this reflection results in a net phase difference, $\Delta\varphi = 8\theta_B$, of 160° between the quantum beat patterns of left and right-handed scattering. As can be seen in Fig. 10-4.1 (c), the peaks of one beat pattern lie almost in the valleys of the other beat pattern. This dramatically illustrates the angular phase a photon acquires upon undergoing an angular momentum conserving rotation.[19]

As can be seen in Fig. 10-4.1, more is going on than the phase shifts discussed above, for the overall shapes of the beat patterns for left and right-handed scattering are not the same. The reason for this can be understood by examining Table 10-1.2. The quantum beats with the largest amplitudes comes from the interference between lines 1 and 6 having a beat period of 7 nsec (averaging over the two iron d-sites in the crystal). Since these lines have a total angular momentum component of $M = \pm 1$, they contribute to the $4\theta_B$ phase shift of the right or left-handed scattered photons that is observed in the experiment. However, there are 24 other beats affecting the net quantum beat pattern. Of these, 12 occur from pairs of lines having the same value of M. There is no phase shift for pairs of lines having identical M values, thus the phase shifted, dominant 7 nsec beat pattern is modulated by unshifted, though less dominant, beat patterns (having an average beat period of 130 nsec and 11 nsec). This additional unshifted amplitude modulation causes the difference in the shape of the beat patterns for right and left-handed scattering. For the [0 0 2] reflection where the net phase shift is negligible ($8\theta_B = 32°$ corresponds to a shift in time of $\frac{1}{2}$ nsec which is unobservable for detectors having a resolution of 2.5 nsec), these amplitude variations are the only predominant differences between left and right-handed scattering (see Fig. 10-4.2).

In addition to the perturbations upon the 7 nsec beat pattern, there are dynamical effects, such as resonance frequency shifts and decay rate speedups, that modify the beat pattern. Thus, to get good fits to the data, the full nuclear dynamical diffraction theory was applied. However, as can be noticed in Section 5.5, the angular phase shifts can be calculated using kinematical, or single particle, scattering theory.

Note that the scattering diagram in Fig. 10-4.1 (a) shows a scattering interaction that appears to be time reversed from that shown in the scattering diagram in Fig. 10-4.1 (b). A physical process and its time reversed process should give identical experimental results unless time reversal symmetry is broken. Since the time beat patterns

for the two scattering processes are different, time reversal symmetry appears to be violated. This perplexing problem is resolved by noting that the magnetic field behaves as a pseudovector that is odd under time reversal. Thus, the actual time reversed process of the diagram in Fig. (a) is the diagram in Fig. (b) with the magnetic field changed in sign to point in the opposite direction (into the page instead of out of it)--this gives back the scattering diagram in Fig. (a), and time reversal invariance is upheld.

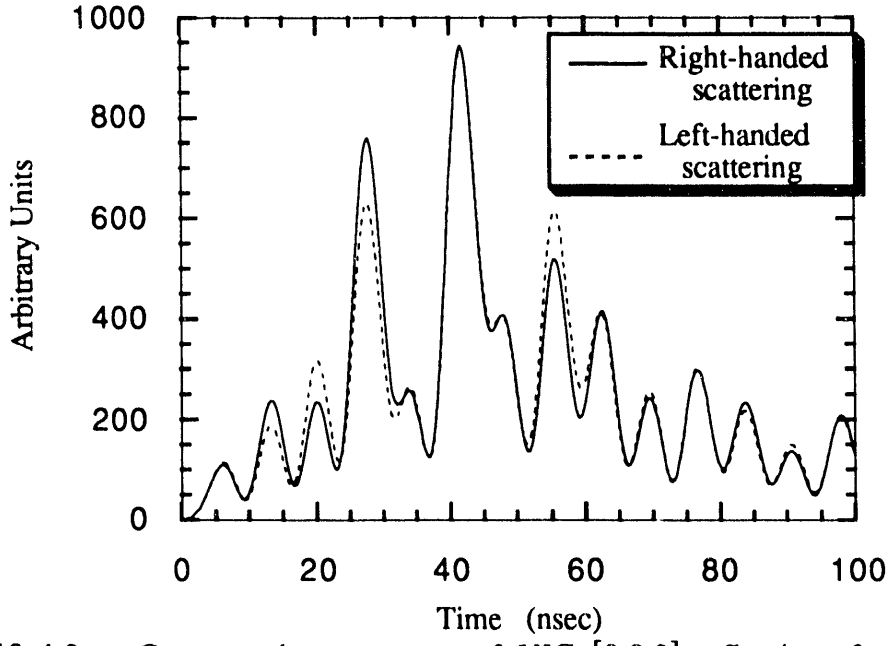

Fig. 10-4.2. Quantum beat patterns of YIG [0 0 2] reflections for right-handed scattering and left-handed scattering. The phase shift is imperceptible, but the amplitude variations between the patterns are noticeable.

This characteristic of magnetic fields makes them a common source of problems when trying to investigate the breaking of time reversal symmetry in physical interactions.

One interesting result from these angular interferometry experiments is that the sign of the internal magnetic field can be uniquely determined. Right-handed rotations of the photon quantum state about the quantization axis (which is the internal magnetic field direction) gives rise to quantum interference patterns that are phase retarded by $4\theta_B$. Left-handed rotations lead to quantum interference patterns that are phase advanced by $4\theta_B$. Finding which pattern is advanced or retarded in phase immediately gives the sign of the internal magnetic field. Upon careful examination of the [0 0 10] data in Fig. 10-4.1, the internal magnetic field at the iron d-sites was verified to be oriented antiparallel to the

externally applied magnetic field (this would have been more easily seen by going to a reflection that did not give nearly 180° net phase shifts).

REFERENCES

[1] E. B. Alexandrov, *Opt. Spectrosc.* **17**, 957 (1964).

[2] J. N. Dodd, R. D. Kaul, and D. M. Warrington, *Proc. Phys. Soc. (London)* **84**, 176 (1964).

[3] W. Gornik, D. Kaiser, W. Lange, J. Luther, and H. H. Schulz, *Opt. Comm.* **6**, 327 (1972).

[4] S. Haroche, J. A. Paisner, and A. L. Schawlow, *Phys. Rev. Lett.* **33**, 948 (1974).

[5] S. Haroche, *High-Resolution Laser Spectroscopy* , edited by K. Shimoda, (Springer Verlag, Berlin, 1976), p. 253.

[6] S. Haroche, M. Gross, and M. Silverman, *Phys. Rev. Lett.* **33**, 1063 (1974).

[7] C. Fabre, M. Gross, and S. Haroche, *Opt. Comm.* **13**, 393 (1975).

[8] A. Hese, A. Renn, and H. S. Schweda, *Opt. Comm.* **20**, 385 (1977).

[9] E. Gerdau and R. Rüffer, *Hyp. Int.* **27**, 59 (1986).

[10] H. Winkler, R. Eisberg, E. Alp, R. Rüffer, E. Gerdau, S. Lauer, A. X. Trautwein, M. Grodzicki, and A. Vera, *Z. Phys. B* **49**, 331 (1983).

[11] C. Alf and G. K. Wertheim, *Phys. Rev.* **122**, 1414 (1961).

[12] I. I. Nikolaev, L. S. Pavlyukov, and V. P. Mar'in, *Sov. Phys. Solid State* **17**, 1016 (1975).

[13] G. N. Belozerskii, Y. P. Khimich, and V. N. Gitsovich, *Phys. Stat. Sol. (b)* **79**, K125 (1977).

[14] V. N. Belogurov, V. A. Bylinkin, and V. I. Mosel, *Izv. Akad. Nauk. Latv. SSR* **3**, 3 (1979).

[15] J. Arthur, D. E. Brown, S. L. Ruby, G. S. Brown, and G. K. Shenoy, *J. Appl. Phys.* **67**, 5704 (1990).

[16] R. Bauminger, S. G. Cohen, A. Marinov, and S. Ofer, *Phys. Rev.* **122**, 743 (1961).

[17] S. S. Bashkirov, N. G. Ivoilov, and V. A. Chistyakov, *Sov. Phys. Solid State* **13**, 570 (1971).

[18] S. Ogawa and S. Morimoto, *J. Phys. Soc. Jpn.* **17**, 654 (1962).

[19] D. E. Brown, J. Arthur, A. Q. R. Baron, G. S. Brown, and S. Shastri, *Phys. Rev. Lett.* **69**, 699 (1992).

11. DYNAMICAL EFFECTS

11.1 Radiative Speedup

The nuclear hyperfine quantum beats are one of the most striking kinematical effects seen in the nuclear resonance time spectra. Similarly, one of the most dramatic dynamical effects seen in the nuclear resonance time spectra is the nuclear decay rate speedup. Rather than decaying with the lifetime of an isolated excited-state ^{57}Fe nucleus (which is 141 nsec), a group of ^{57}Fe nuclei, for a single photon interaction, behaves as an excited collective state that decays much faster than an isolated nucleus. This single photon quantum effect has been discussed in Sections 7.6 and 7.7.

As shown in Figs. 7-6.6 to 7-6.8, the collective total nuclear decay rate varies as a function of time. This is due to the non-Lorentzian nature of the collective nuclear resonance frequency response. Actually, there are two decay rate speedup factors: Γ_s resulting from forward scattering in the crystal and is important at early times, Ω_{sa} resulting from Bragg diffraction and is important at intermediate times, and both speedup factors are important at later times. Also, the definition of short, intermediate, and long times varies as a function of the deviation from the Bragg diffraction peak. An additional complication arises from hyperfine split nuclei. As shown in Fig. 7-7.1, the speedup factors are different for lines possessing different Clebsch-Gordan coefficients (see Eqs. 7-7.1 and 7-7.2). Thus, in the frequency domain, different lines can be homogeneously broadened in a non-Lorentzian fashion by different amounts at different deviation angles from Bragg.

The YIG crystal increases the complexity one notch further. Even for the simplest scattering geometries described in Section 10.1, there are up to 8 different resonance lines. Unambiguously clear dynamical speedup effects are therefore unobtainable from the YIG quantum beat spectra (to date, no single line crystals have been fabricated--such crystals would enormously simplify the task of observing clear dynamical effects).

Rather than trying to extract dynamical speedup factors such as Ω_{sa} or Γ_s from the data, an effective average speedup rate is determined. To do this, the time spectra for YIG [0 0 2] reflections at different deviation angles were fitted with a simple function

$$I(t) = I_0 e^{-(s+\Gamma)t/\hbar} \sin^2\left(\Delta\omega_{EQ} t/2\right) \qquad (11\text{-}1.1)$$

where $s/\hbar$ is the effective average speedup rate, and $\Delta\omega_{EQ}$ is the average electric quadrupole beat frequency due to the electric quadrupole splitting between the $d1$ and $d2$-sites (scattering geometries, described in Section 10.1, were chosen to make these the only sites contributing to a diffracted field). In this simple approximation to the time spectra, the magnetic hyperfine quantum beats are averaged away.

Typical fits for deviation angles below, at, and above the Bragg diffraction peak are shown in Fig. 11-1.1 where the internal magnetic field was oriented perpendicular to the scattering plane. The full nuclear dynamical diffraction theory was used to get the best fit to the data, and the fit is shown by the solid curve that closely follows the fast magnetic beats in the data. The modulation envelope that is characterized by a slow electric quadrupole beat is the fit of Eq. 11-1.1 to the data. The third curve presented in each figure characterizes what would happen if there were no magnetic dipole or electric quadrupole beats and no speedup. This curve is essentially the resonance exponential decay curve for an isolated nucleus:

$$I(t) = I_0 e^{-\Gamma t/\hbar}. \qquad (11\text{-}1.2)$$

When there is no speedup, the single nucleus decay curve is tangent to the peaks of the electric quadrupole beat curve, Eq. 11-1.1. This can be almost seen in Fig. 11-1.1 (a) where the speedup is only about a third of the single nucleus total decay rate.

All of the curves have been normalized to the data closest to the Bragg peak (Fig. 11-1.1 (b) where $\delta\theta = +2\mu$rad). At the Bragg peak, the diffracted intensity and the speedup maximizes. This is where the spatial phases of the electric fields scattered from the lattice of nuclei are all the same, and thus the collective, cooperative effect becomes prominent. As the crystal is rotated off the Bragg peak, spatial dephasing among the scattered fields occurs, and this results in diminishing the collective, cooperative effect among the nuclei--the speedup is therefore reduced.

The variation of speedup with angle is shown in Fig. 11-1.2 for the scattering geometries where the internal magnetic field is parallel and perpendicular to the scattering plane. The decay rate speedup tends to be greater when $\mathbf{B}_{int}$ is parallel to the scattering plane rather than perpendicular to the scattering plane. This occurs because the polarization matrices for the two orientations are different and give a larger nuclear structure factor when $\mathbf{B}_{int}$ is parallel to the scattering plane (see Eqs. 7-2.1, 5-1.22, and 5-1.28).

Since, in theory, the dynamical speedup factor follows a Lorentzian distribution as a function of deviation angle from Bragg, the data was fitted with a Lorentzian function. For the perpendicular (parallel) case the fit yielded a Bragg peak at $68 \pm 8\mu$rad ($67 \pm 3\mu$rad) which, within the uncertainty, agrees with the predicted value of 68μrad--

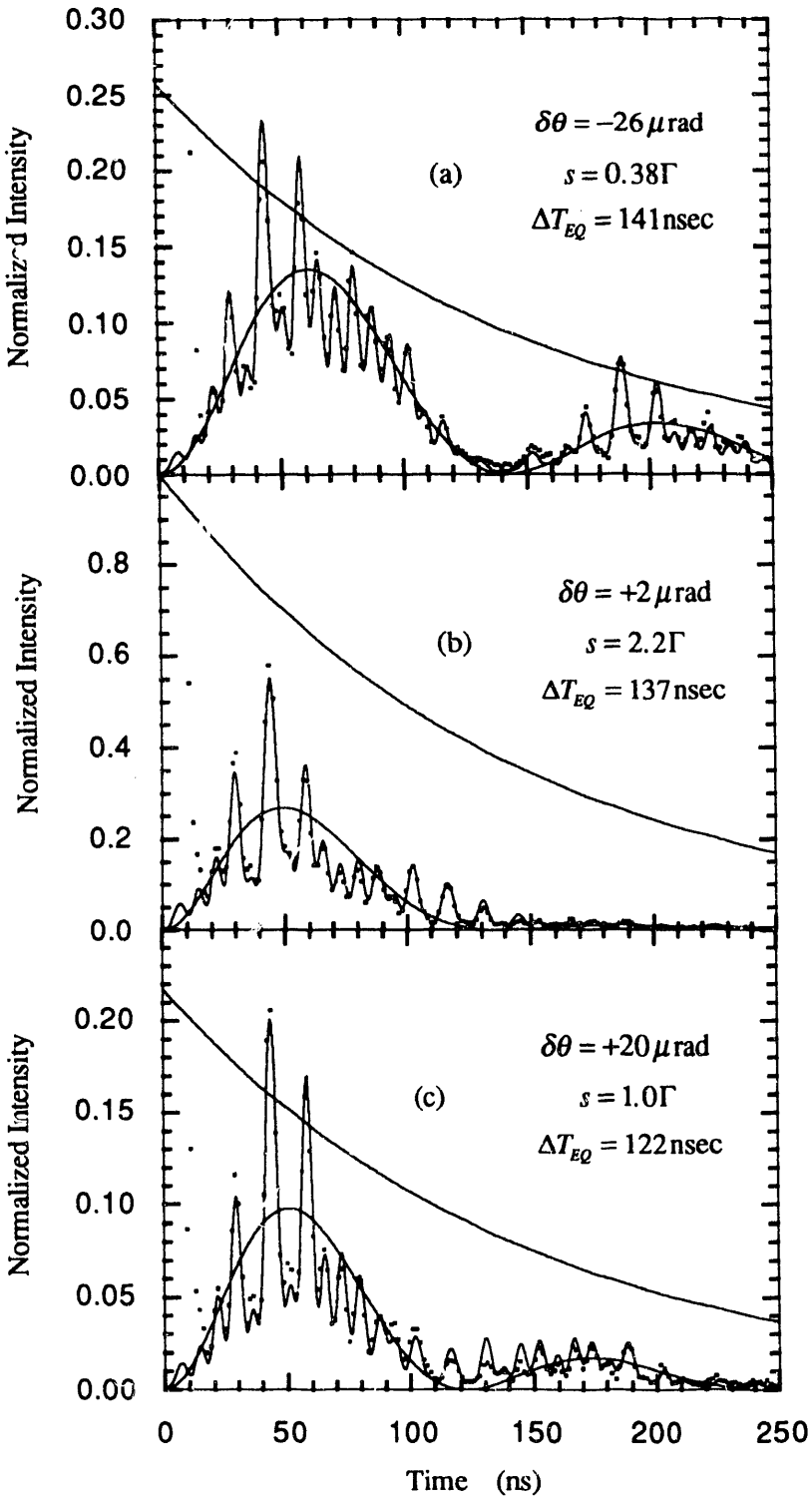

Fig. 11-1.1. YIG [0 0 2] quantum beat patterns for various angles near the Bragg peak: (a) -26μrad (b) $+2\mu$rad, and (c) $+20\mu$rad from the angle corresponding to the Bragg peak. The exponential decay curve is Eq. 11-1.2, the curve with slow beats is Eq. 11-1.1, and the data is fit using the full nuclear dynamical diffraction theory. The average electric quadrupole quantum beat period is ΔT_{EQ}, and s is the average decay rate speedup.

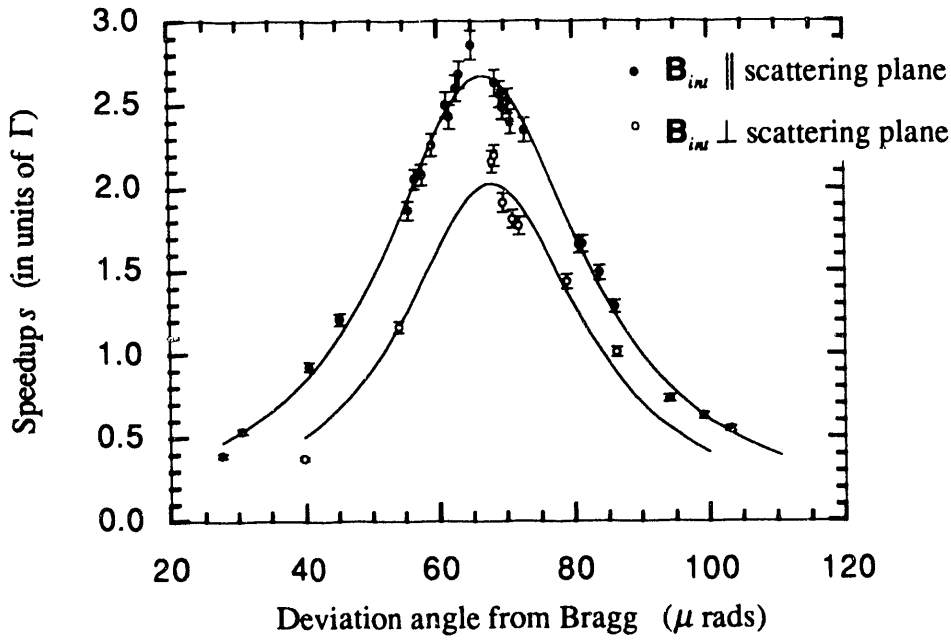

Fig. 11-1.2. A plot of the average speedup, s, versus the deviation angle from Bragg. At the Bragg peak, when $\mathbf{B}_{int}$ is parallel to the scattering plane, the average total decay rate is roughly 4 times as fast, and it becomes 3 times as fast when $\mathbf{B}_{int}$ is perpendicular to the scattering plane. All data was fitted with a Lorentzian function.

this is the position of the nonresonant Bragg peak. The angular linewidth was measured to be $32 \pm 20 \mu$rad ($36 \pm 11 \mu$rad). The large uncertainties for the perpendicular case result from collecting too few data points on the low angle side of the peak. On the basis of the fits, one can assume that s follows a Lorentzian angular distribution centered at the Bragg peak.

The average speedup, s, is not to be confused with the dynamical speedup factors. Even when factoring in the 20μrad angular resolution in the data, the dynamical speedup factors are much greater than the average speedup. This can be seen by examining Fig. 7-1.7 (c) (one can neglect lines 3 and 4 since they have small scattering amplitudes compared to lines 1 and 6). Thus, near the Bragg peak, the dynamical speedup factors Ω_{sa} and Γ_s do not describe the effective speedup of the quantum beat spectra (one could have inferred this from examining the collapse in the resonance width near the Bragg peak as shown in Fig. 7-6.4). At the Bragg peak the effective speedup is considerably smaller than the dynamical speedup factors. Also, the effective speedup may only increase marginally if the angular divergence of the incident beam is decreased significantly from the 20μrad that existed for these measurements.

11.2 Resonance Frequency Shifts

The other remarkable feature that stands out in the nuclear hyperfine quantum beat patterns are resonance frequency shifts. As discussed in Section 3.7, a single nucleus interacting with its own self-fields gives rise to frequency shifts. In a similar manner, the collective state of a distribution of nuclei interacts with its own self-fields which, in this case, are the multiply scattered fields in the medium. This cooperative interaction among the nuclei gives rise to a collective resonance frequency shift. This effect has been observed in the frequency domain through careful Mössbauer experiments by van Bürck.[1] In the time domain, this effect is much more dramatic and significantly modifies the time spectra.

The same problems encountered in trying to examine the dynamical speedup factors $\Omega_{s\alpha}$ and Γ_s discussed in Section 11.1 are present when trying to extract the characteristics of the dynamical frequency shift factor, ω_s, from the quantum beat data (except, fortunately, that the collective resonance frequency shift does not vary with time)--the non-Lorentzian resonance behavior, the variation of ω_s with the deviation angle from Bragg and for lines with different scattering amplitudes, and the plethora of hyperfine lines from YIG.

Determining the precise behavior of the collective resonance frequency shift becomes even more intractable because there are a myriad of other effects that can cause the resonance lines to shift about. For instance, the theory that gave rise to ω_s in Section 7-6 and 7-7 had some approximations made: that the crystal was infinitely thick and had a single resonance line. Neither of these cases hold for the YIG crystals used in the experiments. The effects of crystal thickness are discussed in Section 11-4. When there are two or more resonances, coupling can occur between them and produce phase shifts in the time spectrum [2, 3](see Appendix B.2), and, when the resonances are close together, the resonant lines can interfere with each other enough to shift the peak intensities of each resonance line.

The spectator iron atoms occupying the a and $d3$-sites also modify the frequency and time spectra. The a-sites have little effect upon the time spectra since, because their internal magnetic field strengths are much larger that those for the d-sites, their resonance lines interact little with the d-site resonance lines. However, the resonance lines of the $d3$-site lie at the same energies as the lines of the $d2$-site because they have the same quadrupole energy shifts. Because the geometrical structure factor for the $d3$-site is zero, this site does not reflect any fields and only transmission can occur. This transmission channel opens up another avenue for an incident photon to escape through rather than

traveling in the reflection channel of the $d2$-site. The interaction between the $d2$ and $d3$-sites in the frequency domain is shown in Fig. 11-2.1. In the figure the reflected fields from the $d1$ and $d2$-sites are shown--their hyperfine resonance lines are shifted from each other because they have different electric quadrupole energy shifts. However, the amplitude of each pair of lines should be identical. Yet the figure shows that for each pair of closely spaced lines the $d2$-line typically has a smaller amplitude. The reduction in amplitude of the $d2$-line is the result of photons being diverted into the transmission channel opened up by the $d3$-site. This interaction between the $d2$ and $d3$-sites significantly alters the shape and slightly shifts the position of the $d2$-resonance lines.

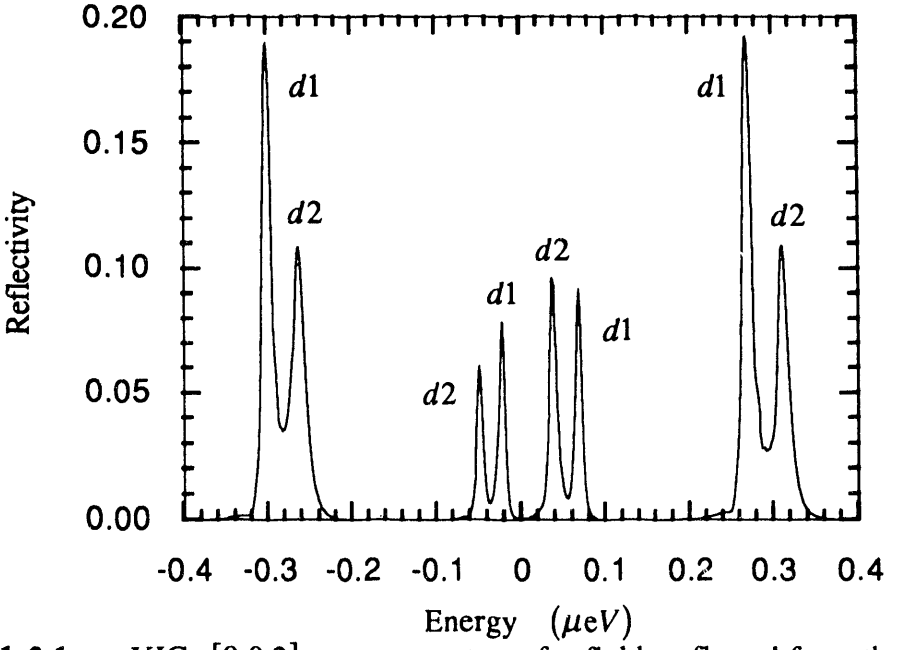

Fig. 11-2.1. YIG [0 0 2] energy spectrum for fields reflected from the $d1$ and $d2$-sites. The incident angle is $+20\mu rad$ from the Bragg peak. The incident field is $\hat{\boldsymbol{\sigma}}$ polarized and the internal magnetic field is parallel to the scattering plane and crystal surface (that is, nearly in the photon direction). The $d2$-lines suffer a diminution in amplitude because of additional absorption from the nonreflecting $d3$-site that has resonance lines coincident with the $d2$-lines.

The $d2$-$d3$ interaction is not the only effect that can cause frequency shifts. Nuclear level mixing resulting from two competing quantization axes (the magnetic field and electric field gradient directions) changes the scattering amplitudes of each hyperfine line. Since the resonance frequency shifts are proportional to the scattering amplitude, they will vary depending upon the amount of nuclear level mixing. When the electric field gradient axis is parallel to the internal magnetic field direction, there is no nuclear level

mixing since there is only one clearly defined quantization axis. When the two axes are perpendicular, the amount of nuclear level mixing maximizes. However, since the electric quadrupole interaction is small compared to the magnetic dipole interaction, this effect is small. Fig. 11-2.2 shows that shifts of up to 1.5 neV (or 0.3Γ) can occur when nuclear level mixing is included (for the case in which the internal magnetic field is parallel to the $d1$-electric field gradient and perpendicular to the $d2$-electric field gradient).

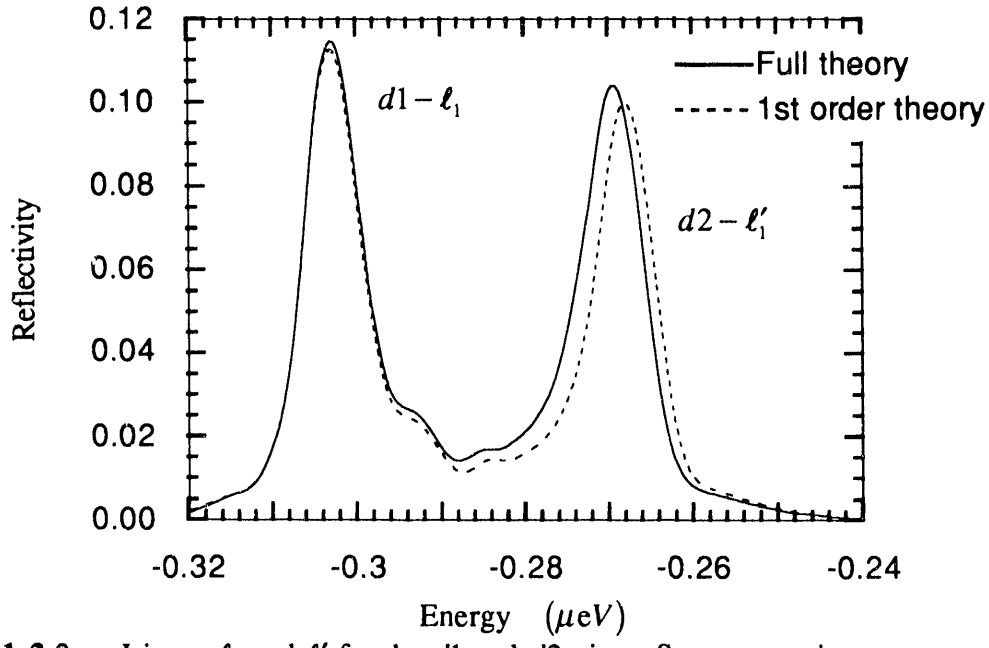

Fig. 11-2.2. Lines ℓ_1 and ℓ_1' for the $d1$ and $d2$-sites. Same scattering geometry as that used in Fig. 11-2.1 except that the incident angle is $+40\mu rad$ from the Bragg peak. The solid curve is calculated using the full dynamical diffraction theory including nuclear level mixing while the dotted curve excludes nuclear level mixing. Nuclear level mixing causes a shift in the $d2$-line of 1.5 neV (or 0.3Γ).

All the additional effects that cause apparent shifts in the resonant frequency increases the difficulty of conclusively stating anything about the dynamical resonance frequency shifts discussed in Chapter 7. And the multiplicity of hyperfine lines for complicated systems such as YIG can make life even harder. For instance, one would be hard pressed to say anything about dynamical resonance frequency shifts for the quantum beat data exhibited in Fig. 11-1.1 (the magnetic field, in this case, is perpendicular to the scattering plane). The asymmetry in the beat patterns for reflections on both sides of the Bragg peak is due to resonance frequency shifts and a host of other dynamical factors in a way that is not clearly apparent. This is because all of the hyperfine lines beat with each

other with the beating between the strongest lines, lines 1 and 6, dominating the pattern. Since lines 1 and 6 have the same scattering amplitude, these lines are frequency shifted by the same amount. Thus, to first order, the beat pattern will look the same between two angular positions symmetric about the Bragg diffraction peak even though the resonance frequency shift is antisymmetric about the Bragg diffraction peak (see Fig. 7-2.7). The differences in the beat patterns comes about because of the beating between lines 1 and 6 with the weaker lines 3 and 4, and due to the dynamical effects described earlier in this section.

Going to the scattering geometry where the magnetic field is parallel to the scattering plane simplifies matters. For this geometry the pair of line 1&4 and 3&6 beat with each other (see Fig. 8-1.4), and, most importantly, each pair of lines beats with the same amplitude. If lines 1 and 6 are frequency shifted by δ and lines 3 and 4 are frequency shifted by Δ, then the two possible beat frequencies are shifted by the difference between these individual frequency shifts:

$$(\omega_4 + \Delta) - (\omega_1 + \delta) = (\omega_4 - \omega_1) - (\delta - \Delta) = \Delta\omega_{14} - f$$

$$(\omega_6 + \delta) - (\omega_3 + \Delta) = (\omega_6 - \omega_3) + (\delta - \Delta) = \Delta\omega_{36} + f$$

where $\Delta\omega$ is the beat frequency shifted by $f = (\delta - \Delta)$. Going from one side of the Bragg peak to the other side causes f to change sign, and each beat frequency shifts in the opposite direction. For large enough f this results in clearly visible effects that can dominate other effects caused by all other possible sources of frequency shifts.

An illustration of how resonance frequency shifts modify quantum beat patterns is given in Figs. 11-2.3 and 11-2.4. They were calculated at symmetric positions about the Bragg peak for a horizontally polarized field incident at 40μrad from the Bragg peak. Since the incident and scattered field directions are nearly parallel to the magnetic field, the scattered fields can be approximated as both left $(\hat{\mathbf{e}}_+)$ and right $(\hat{\mathbf{e}}_-)$ circularly polarized for the pair of lines 1&4 and 3&6 respectively. The $\hat{\mathbf{e}}_+$ fields interfere producing the shifted beat frequency $\Delta\omega_{14} - f$, and the $\hat{\mathbf{e}}_-$ fields interfere producing the shifted beat frequency $\Delta\omega_{36} + f$. The quantum beat patterns of each polarized field is shown in (a) of Figs. 11-2.3 and 11-2.4. The sum of these beat patterns is shown in (b) of each figure. Because f changes sign on opposite sides of the Bragg peak, the total field intensity differs on symmetrical sides of the Bragg peak. These patterns were calculated only for reflections from the $d1$ and $d2$ sites. The effect of adding absorption from the $d3$ is shown in (c) of each figure--small additional frequency shifts results.

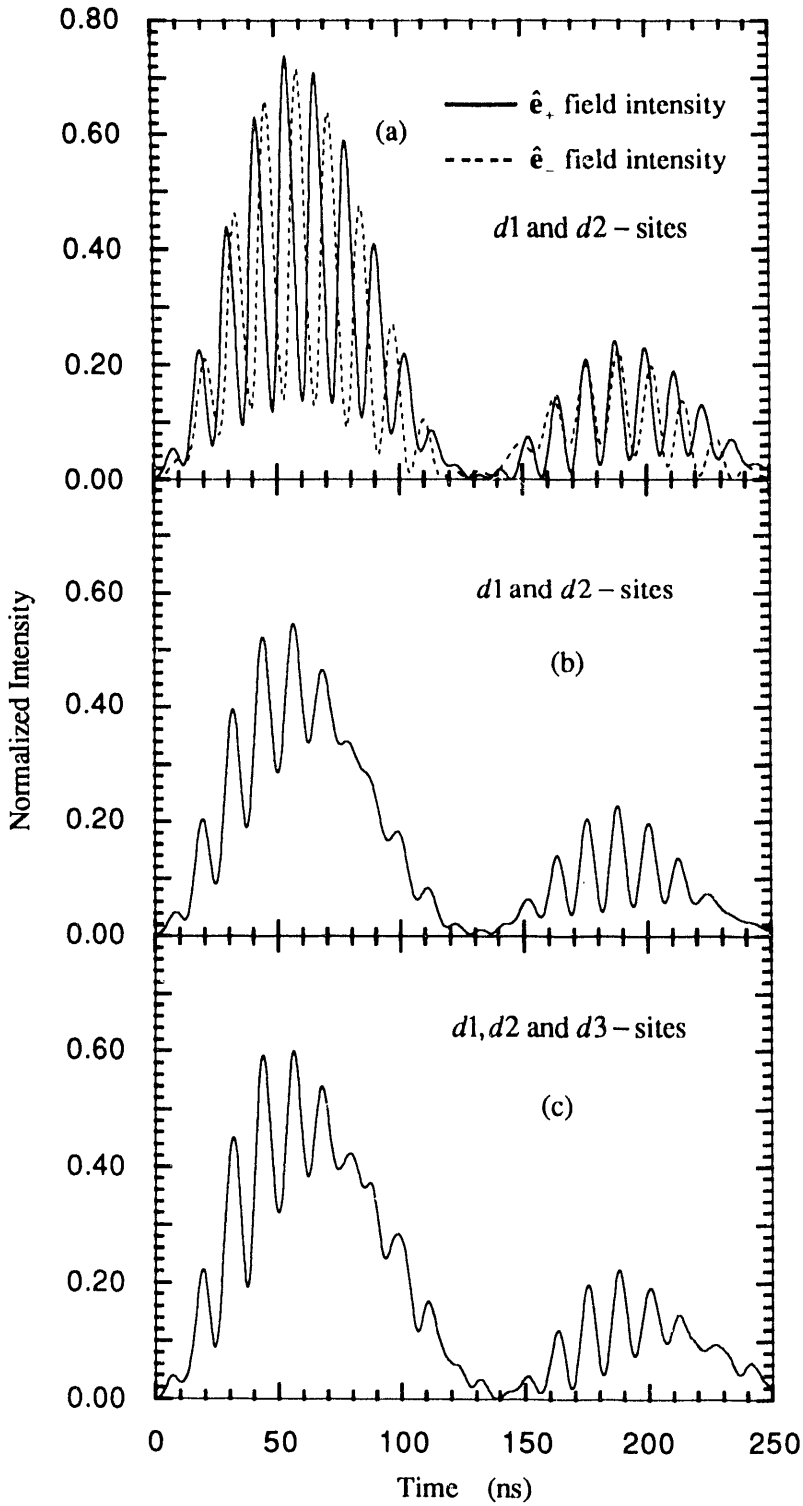

Fig. 11-2.3. YIG [0 0 2] beat patterns for a $\hat{\sigma}$ field incident $-40\mu rad$ from the Bragg peak. $\mathbf{B}_{int}$ is parallel to scattering plane and crystal surface (nominally in the incident and scattered photon directions). The $\hat{e}_+$ and $\hat{e}_-$ field intensities in (a) are summed to produce the net field intensity in (b) when only scattering from the $d1$ and $d2$-sites. The effect of including the $d3$-site is shown in (c).

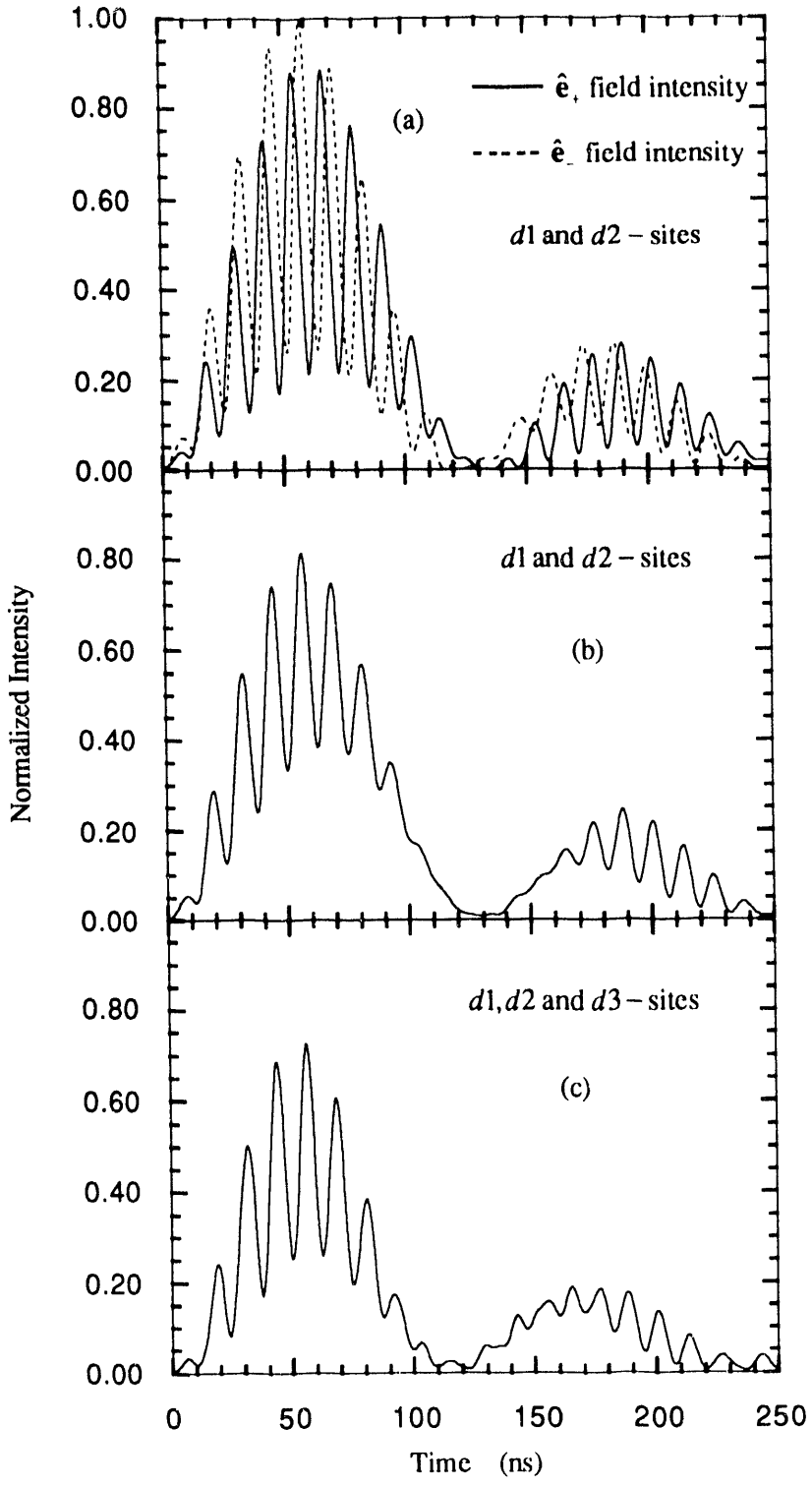

Fig. 11-2.4. Same as Fig. 11-2.3 except that the $\hat{\sigma}$ polarized field is incident $+40\mu rad$ from the Bragg peak.

To get a handle on understanding the resonant frequency shifts, a simple semi-kinematical theory based on average beat frequencies and frequency shifts can be applied. This is justified because the 4 magnetic beat periods are all nearly equivalent (the same goes for the 2 electric quadrupole beats) as illustrated in Table 10-1.2. The net intensity of the diffracted fields can be approximated as

$$I(t) = I_0 e^{-(s+\Gamma)t/\hbar}\left\{\sin^2\left[\frac{(\Delta\omega_{14} - f)t}{2}\right] + \sin^2\left[\frac{(\Delta\omega_{36} + f)t}{2}\right]\right\}\sin^2\left(\frac{\Delta\omega_{EQ}t}{2}\right) \quad (11\text{-}2.1)$$

where $\Delta\omega_{14}$, $\Delta\omega_{36}$, and $\Delta\omega_{EQ}$ are average magnetic and electric quadrupole beat frequencies, s is the average speedup discussed in Section 11.1, and f is an average beat frequency shift.

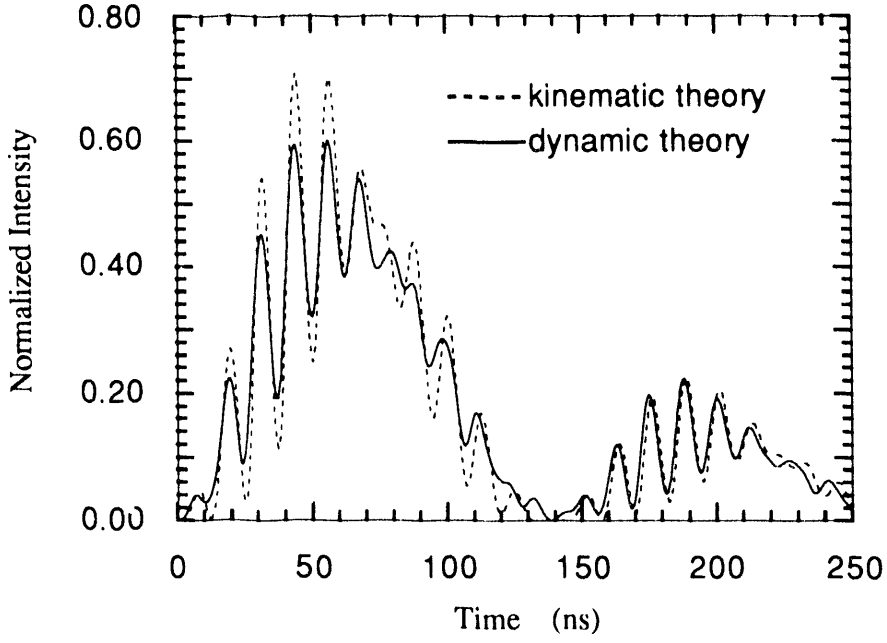

Fig. 11-2.5. As a demonstration, the semi-kinematical formula, Eq. 11-2.3, was fit to the dynamical diffraction calculation (shown in Fig. 11-2.3 (c)). The best kinematic fit gave an average beat frequency shift of $f = 3.4 \pm .5$ neV, or $0.7 \pm 0.1\Gamma$.

This formula was fitted to the quantum beat pattern shown in Fig. 11-2.3 (c). The average magnetic beat periods used were $\Delta T_{14} = 12.2$ nsec and $\Delta T_{36} = 13.0$ nsec. The values s, $\Delta\omega_{EQ}$, and f were allowed to vary to get the best χ^2 fit. The results of the fit, shown in Fig. 11-2.5, gave $s = 0.3 \pm 0.1\Gamma$, $\Delta T_{EQ} = 138 \pm 2$ nsec, and $f = 3.4 \pm .5$ neV, or $0.7 \pm 0.1\Gamma$ where Γ is the natural linewidth $\left(\Gamma = 4.67 \times 10^{-9}\ \text{eV}\right)$. What this fit

demonstrates is how closely semi-kinematical diffraction theory parallels dynamical diffraction theory when a few dynamical quantities are inserted into kinematical expressions. When using Eqs. 7-6.30 and 7-7.1, the collective dynamical frequency shift 40μrad below the Bragg peak (taking the difference in ω_s between lines 1&4 or 3&6) is 1.1neV (0.23Γ) which is the same order of magnitude as the average beat frequency shift. The discrepancy between the two values shows that there are other frequency shifts that must be taken into account.

For $f = 3.4$neV (at $\delta\theta = -40\mu$rad), the beat period between lines 1 and 4 decreases by 0.1 nsec and the beat period between lines 3 and 6 increases by 0.1 nsec--the beat periods then diverge by an extra 0.2 nsec forcing the beat pattern of the $\hat{\mathbf{e}}_+$ fields to be more out of phase with the pattern of the $\hat{\mathbf{e}}_-$ fields. This causes the beat pattern to become washed out as shown by the diminished peak to valley contrast in Fig. 11-2.3 (b). Symmetrically on the other side of the Bragg peak (at $\delta\theta = +40\mu$rad), the beat period between the two circularly polarized fields should converge by 0.2 nsec making the beat patterns more in phase and increasing the peak to valley contrast as shown in Fig. 11-2.4 (b). The effect of the $d3$-site causes additional frequency shifts that are not symmetrical on both sides of the Bragg peak--they appear to cause more drastic effects on the positive side of the Bragg peak (as shown in (c) in Figs. 11-2.3 and 11-2.4).

The striking changes in the quantum beat patterns as a function of the deviation angle from the Bragg peak are presented in Fig. 11-2.6. Full nuclear dynamical diffraction theory was used to obtain the fits (Eq. 11-2.1 was not used). As can be clearly noticed, in going from the low angle side of the Bragg peak to the high angle side, the $\hat{\mathbf{e}}_+$ and $\hat{\mathbf{e}}_-$ time beat patterns progress from nearly out of phase to nearly in phase. In other words, the contrast improves as the deviation from Bragg increases over the angular range given in the figure.

The data in Fig. 11-2.6 was also fit using the simple semi-kinematical formula described by Eq. 11-2.1. The average beat frequency shift as a function of angle is shown in Fig. 11-2.7. On the low side of the Bragg peak, the parameters $\Delta\omega_{14}$ and $\Delta\omega_{36}$ were fixed (their periods were set at $\Delta T_{14} = 12.2$nsec and $\Delta T_{36} = 13.0$nsec). However, on the high angle side of the Bragg peak, because of the drastic effects by the $d3$-site which played havoc with the fits, these parameters were varied. An attempt was made to fit the data with a Lorentzian dispersion curve noting that, since the angular divergence in the data was 20μrad, semi-kinematic fits near the Bragg peak become difficult to interpret since both positive and negative frequency shifts can exist simultaneously. The fit shows that, like the dynamical resonance frequency shift, the average beat frequency shift follows a

dispersive relationship. The data also reveals that it is possible to easily measure average frequency shifts smaller than a linewidth.

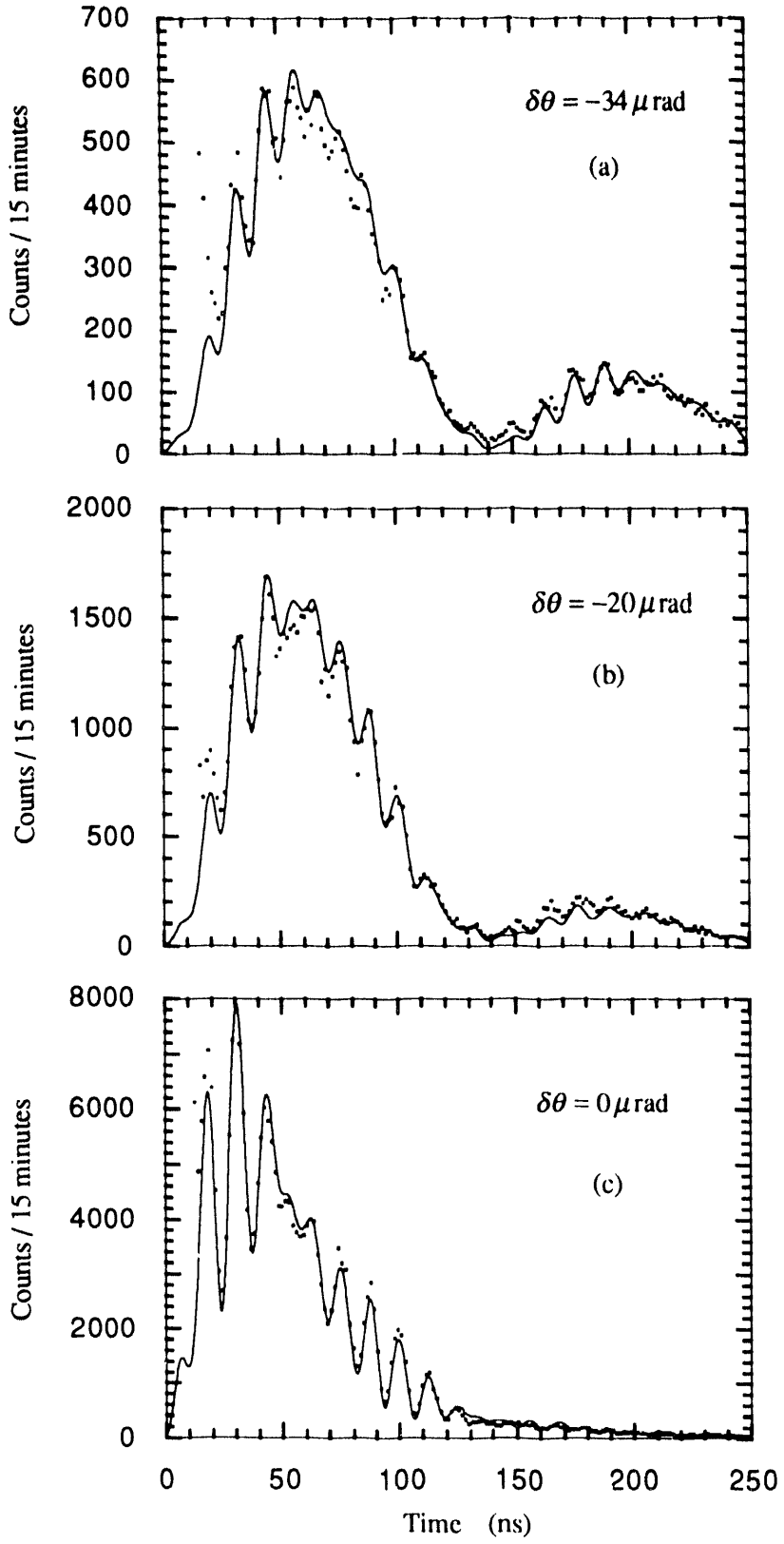

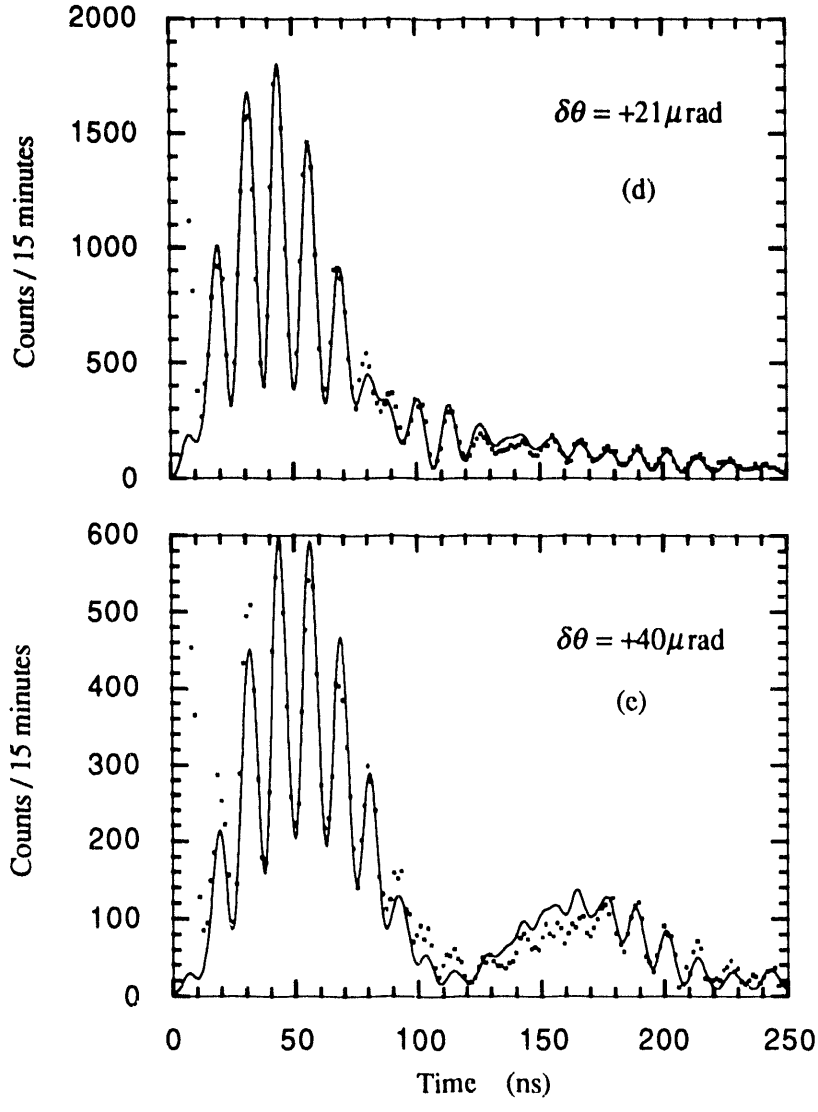

Fig. 11-2.6. Nuclear hyperfine quantum beat patterns as a function of the deviation from the Bragg peak. Measurements for (a), (b), and (c) were taken on the low angle side of the Bragg peak at -34, -20, and 0 μrad respectively. Measurements for (d) and (e) were taken on the high angle side of the Bragg peak at 21 and 40 μrad. Note that the contrast improves when going from the low angle side to the high angle side of the Bragg peak.

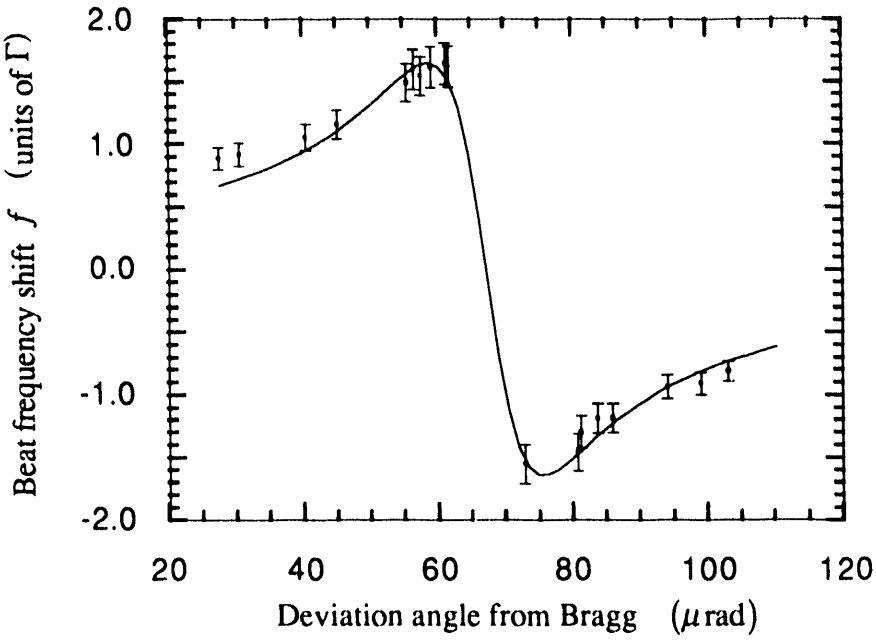

Fig. 11-2.7. The average beat frequency shift versus the deviation angle from Bragg appears to follow a Lorentzian dispersive curve. Average beat frequency shifts of up to $1\frac{1}{2}$ linewidths occurred near the Bragg peak. The dispersion curve is centered at $67 \pm 5\,\mu$rad and has a $17 \pm 7\,\mu$rad linewidth.

11.3 The Lamb-Mössbauer Factor

The change in the quantum beat patterns as a function of the deviation angle from Bragg provides a unique opportunity to measure the Lamb-Mössbauer factor. This opportunity comes about because the angular independent part of the structure factor, Eq. 7-2.10, is directly proportional to the Lamb-Mössbauer factor, $L_M(\mathbf{k}_i)L_M(\mathbf{k}_f)$, and three well known experimentally measured quantities: $\Gamma(L,\lambda)$ is the radiative decay rate $\Gamma_{rad} = \Gamma/(1+\alpha)$ where $\hbar/\Gamma = 140.95$ nsec and $\alpha = 8.23$ for ^{57}Fe, and C is the isotopic concentration which has been accurately measured to be 0.8097 for the YIG crystal samples. Since changes in the quantum beat patterns are directly correlated with the strength of the scattering amplitude, information can be extracted from these changes to determine the Lamb-Mössbauer factor.

Fitting the data in Fig. 11-2.6 by allowing the Lamb-Mössbauer factor to vary produces new fits that are precisely the same as the old fits except that the value of $\delta\theta$ giving the best fit is different. This results because increases in the Lamb-Mössbauer factor only serves to increase the nuclear Darwin width (see Fig. 11-3.1). If the Lamb-Mössbauer factor is increased to a new value, the new beat pattern can be made identical to the old pattern by simply going to a point further from the Bragg peak (a horizontal line drawn in Fig. 11-3.1 intercepts the curves having a larger Lamb-Mössbauer factor further out from the peak). Thus, by precisely measuring the difference in angle between two reflections, the Lamb-Mössbauer factor that most closely results in describing these differences can be found.

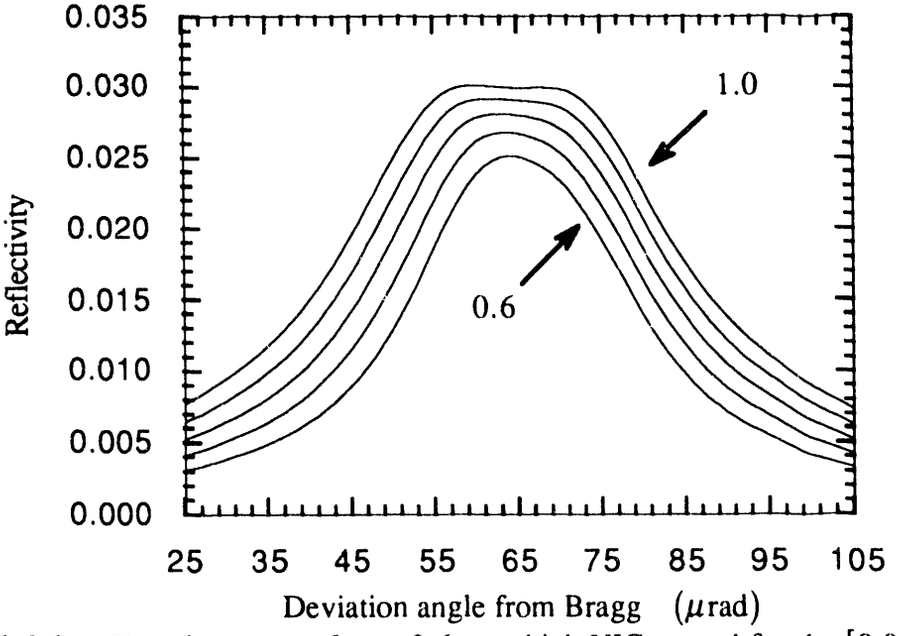

Fig. 11-3.1. Darwin curves for a 2.6μm thick YIG crystal for the [0 0 2] reflection and for a magnetic field parallel to the scattering plane. The Lamb-Mössbauer factor for the top curve was set at unity, and the lower curves illustrate what happens when this factor is decreased to 0.6 in steps of 0.1--the peak intensity decreases and the Darwin width narrows. The Bragg peak is centered at 65μrad, and the Darwin width is 41μrad for a Lamb-Mössbauer factor of 0.82 (this is the value used in all the previous fits in this and the preceding chapter).

Two experimental runs were made in which the YIG crystal was rotated in steps of 1 millidegree (17.4μrad). The crystal was centered on a Huber 4-circle diffractometer having a θ-circle consisting of a Huber 430 goniometer connected with a 20:1 gear reducer. As a result, the θ-circle was able to make step sizes of $\frac{1}{4}$ millidegrees.

Unfortunately, because these measurements were made without the intention of measuring the Lamb-Mössbauer factor (the possibility of doing this was discovered only after the measurements), the experiment was not carefully tailored for this application. Any backlash problems in the θ-circle would show up as large 4.4μrad discrepancies because of the large stepping size. For each run 4 measurements were taken at one and two millidegrees above and below the Bragg peak, and one measurement was taken at the Bragg peak. Before each off-Bragg measurement was made, a rocking curve measurement was performed to re-determine the position of the Bragg peak. This additional check was done because the synchrotron beam direction stability and the backlash problems of the Huber goniometers caused real or apparent shifts in the position of the Bragg peak.

The results are shown in Fig. 11-3.2. Plotted is the standard deviation, σ_N, between the actual and measured angle (obtained by the best fit to the data) versus the Lamb-Mössbauer factor

$$\sigma_N = \sqrt{\left(\Delta\theta_{act} - \Delta\theta_{meas}\right)^2 / N}\,. \qquad (11\text{-}3.1)$$

The quantity $\Delta\theta_{act}$ is either ± 1 or ± 2 millidegrees, and $\Delta\theta_{meas}$ is the difference in angle between the angle measured at the Bragg peak and the angle measured off-Bragg. The minimum standard deviation for two sets of runs lie at different Lamb-Mössbauer factors--a parabolic fit to the data yielded Lamb-Mössbauer factors of 0.78 and 0.86 at the minima. Thus, the Lamb-Mössbauer factor could be determined to only with 5%:

$$L_M(\mathbf{k}_i)L_M(\mathbf{k}_f) = 0.82 \pm 0.04.$$

On the agenda were improvements to the experimental apparatus in order to perform more sensitive measurements about the YIG Bragg peak. A Si [10 6 4] channel cut monochromator having a Darwin width of 2μrad was built and attached to an Ishikawa sine-bar rotation stage capable of making 0.05μrad steps. This system would have greatly improved the angle measurements, but, unfortunately due to lack of time, this system was never used (the Si [10 6 4] reflection reduces the nuclear counting rate by a factor of 10 forcing one to count 10 times longer to get the same statistics as before).

Also, of major interest would be to perform these measurements at other reflections than the YIG [0 0 2] reflection. Little is known about how the Lamb-Mössbauer factor varies with the order of reflection (or the scattering angle).

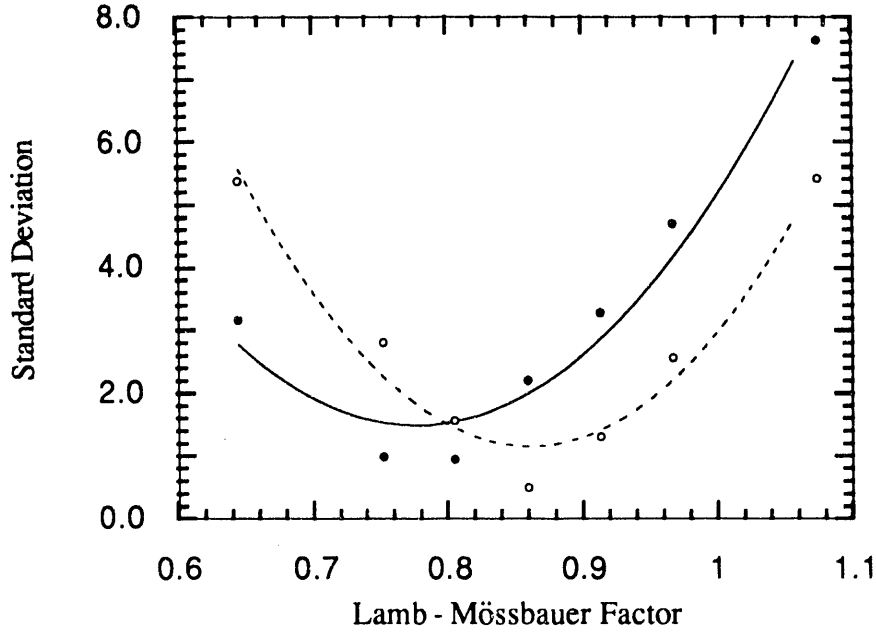

Fig. 11-3.2. Two trial runs to determine the Lamb-Mössbauer factor for the YIG [0 0 2] reflection. The minimum standard deviation gives an average Lamb-Mössbauer factor between the two trial runs of 0.82 ± 0.04.

11.4 Crystal Thickness Effects

The time evolution of radiation scattered by a collection of resonant particles can be significantly influenced by the total number of resonant scatterers. This property provides the opportunity to infer the thickness of a medium of scatterers directly from the time distribution of the scattered radiation.

The fields reflected from a thin crystal have characteristics that are similar to the fields transmitted through a thin isotropic slab (that is, a thin absorber) except that there are small resonance frequency shifts and small increases in the decay rate (see Section 7-6). For a thick crystal, because many more scatterers contribute to the scattered fields, there can be substantial frequency shifts and increases in the decay rate (as seen in Sections 11-1 and 11-2). Simply due to speedup effects, as the thickness of a crystal increases, the time distribution of the scattered radiation is squeezed into earlier times.

Care must be taken when trying to determine the thickness of crystals when Bragg scattering is used. This is because primary extinction can severely limit the depth that fields

can penetrate into the crystal. If the crystal is thicker that the extinction length for a particular order of reflection, then information about the crystal thickness cannot be extracted because changes in the time distribution saturate at the extinction length.

A YIG thickness greater than 1μm cannot be measured using the [0 0 2] reflection because the penetration depth for 14.413 keV radiation is about 1.1μm. However, the penetration depth for the [0 0 10] reflection is roughly six times greater giving the possibility of measuring crystal thicknesses up to 6.4μm.

Calculations of YIG [0 0 10] quantum beat patterns for various crystal thickness are shown in Fig. 11-4.1. The area of each curve is normalized to the area of the data presented in (a) in Figs. 10-3.1 and 10-4.1 for the case in which the internal magnetic field is parallel and perpendicular to the scattering plane (the intensity variation with thickness was normalized away because this information is absent in the data). From the figures, one can see that the second peak (past 150 nsec) of the electric quadrupole beat is much more prominent for thin crystals than for thick crystals. For the thicker crystals, the beat pattern is squeezed towards earlier time giving prominent peaks below 50 nsec.

Using the result that the quantum beat patterns were sensitive to thickness variations produced surprising results. One of the crystals grown by Gualtieri, crystal #57-2, was stated to have a thickness of 6.7 μm.[4] The YIG [0 0 2] quantum beat patterns were not sensitive to crystals this thick since the penetration depth is only 1.1 μm, thus the calculations showed no discrepancy. However, a significant discrepancy existed for the YIG [0 0 10] quantum beat patterns. The YIG [0 0 10] data (together with lower order YIG [0 0 6] and higher order [0 0 14] data) yielded a thickness for crystal #57-2 of $2.6 \pm 0.2\mu$m rather than the expected 6.7 μm. This unexpected result precipitated a second set of rocking curve measurements to understand more about the structure of this particular crystal. These precision rocking curve measurements are discussed in Section 9.1, and the results are shown in Fig. 9-1.2. The rocking curve for crystal #57-2 showed that the YIG film had bifurcated into two separate layers having slightly different lattice spacings. The YIG reflections were probing only one of these layers--the one 2.6μm thick.

No attempt was made in further experiments to investigate the second 4.1 μm thick layer of crystal #57-2. Instead, the crystal having the best crystal perfection, crystal #57-6, was used in further experiments. This determination was made using the data in Fig. 9-1.2. The YIG [0 0 10] quantum beat data for crystal #57-6 was consistent for a

crystal having a thickness of $4.3 \pm 0.4 \mu$m. Within the uncertainty, this value agrees with Gaultieri's measured value of 4.7μm.

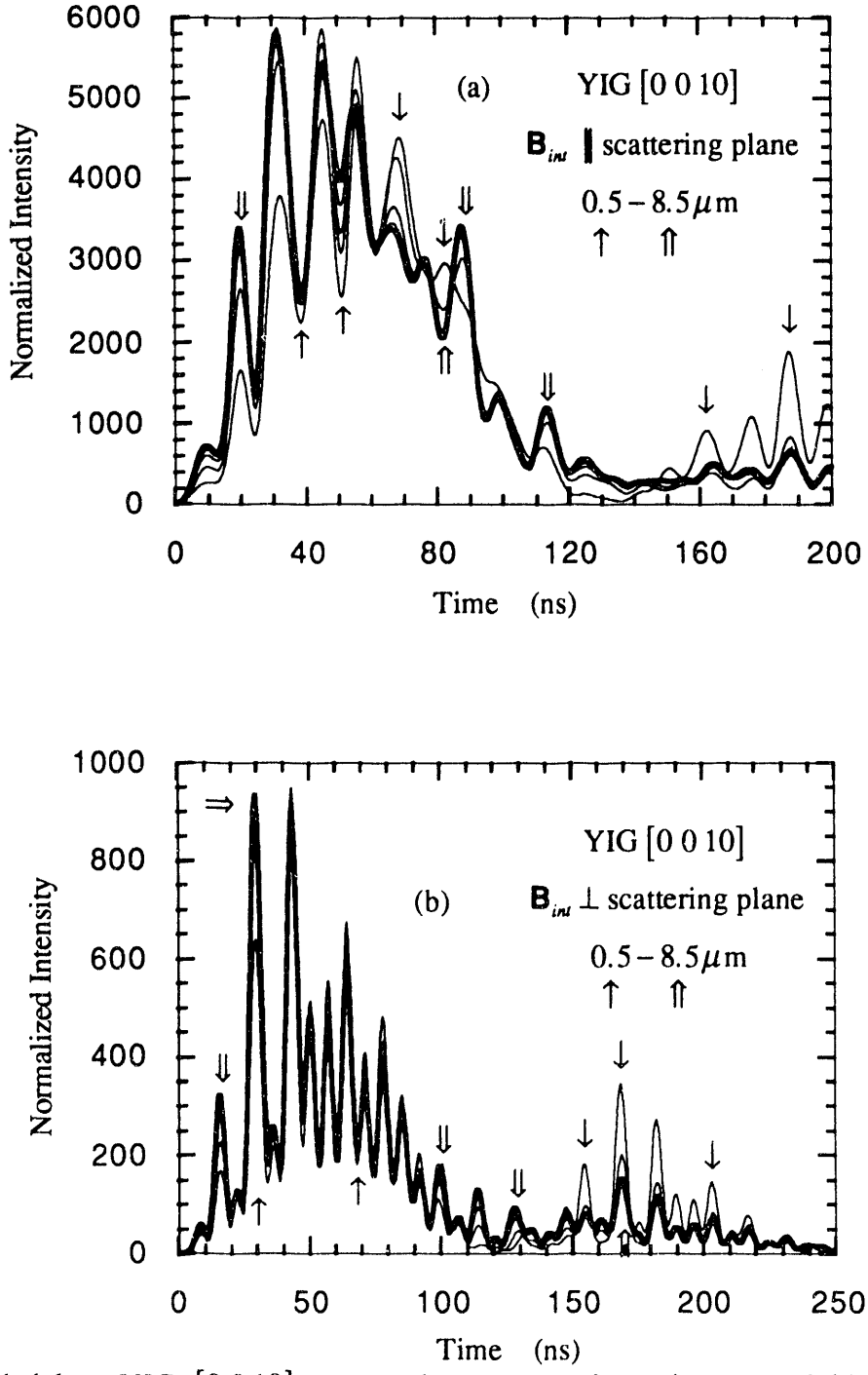

Fig. 11-4.1. YIG [0 0 10] quantum beat patterns for various crystal thicknesses (from 0.5 to 8.5 μm in steps of 2.0 μm). The bold-faced curve represents the 8.5 μm thick crystal and is pointed to by the ⇑ arrow.

11.5 Mössbauer Filter Experiment

Quantum beat patterns can be drastically modified by inserting x-ray optical elements in the beam path. For instance, consider the case when the magnetic field applied across a YIG crystal is parallel to the scattering plane. The net reflected field will then have a four line spectrum (see Fig. 8-1.4) composed of right and left circularly polarized fields. The lines having the same polarization interfere with each other to produce the typical quantum beat pattern having a 12 to 13 nsec beat period. However, this magnetic beating can be completely eliminated by inserting in the beam path a "black" Mössbauer absorber that completely absorbs all resonant photons of the inner lines (lines 3 and 4). With the inner two lines blocked out, the only beating that can occur is the electric quadrupole beating between the two *d*-site lines.

An experiment was performed to eliminate the magnetic hyperfine beats present in a quantum beat pattern. The experimental setup is described in Section 9.4. The "black" Mössbauer absorbers used in the push-pull arrangement shown in Fig. 9-4.4 were 91.2% enriched ammonium lithium ferrofluoride absorbers having a single line resonance energy spectrum. The push-pull arrangement ensures that both inner lines of YIG are filtered out simultaneously.

Figure 11-5.1 shows the YIG [0 0 2] quantum beat pattern without the "black" absorbers in the beam path. This figure requires some explaining. This experiment was the first time-resolved Mössbauer measurement made by the Stanford nuclear resonance group (in collaboration with Ercan Alp and Gopal Shenoy from Argonne National Labs). In this first successful search for the nuclear resonance signal, many problems were encountered that were unanticipated.

One problem is clearly shown in Fig. 11-5.1 (a) and (b). The nuclear resonance signal sat on top of a large undulating background that was later found out to be due to afterpulses in the phototubes of the detector. They had a large 1 in 10 afterpulse rate with the afterpulses occurring 460 and 540 nsec after a prompt pulse. The experiment was done on the 10-2 beamline at SSRL. This storage ring operated in a timing mode where electron pulses were separated by 195 nsec (unlike CESR and PEP where pulses were separated by 400 nsec and 2 μsec respectively). Thus, the oscillations seen in the background time data were due to afterpulses initiated by prompt pulses occurring well before the prompt pulse giving rise to the nuclear resonance signal. Fortunately, by using background runs, the background could be adequately subtracted from the nuclear resonance time data. The results of such a background subtraction is shown in Fig. 11-5.1 (c).

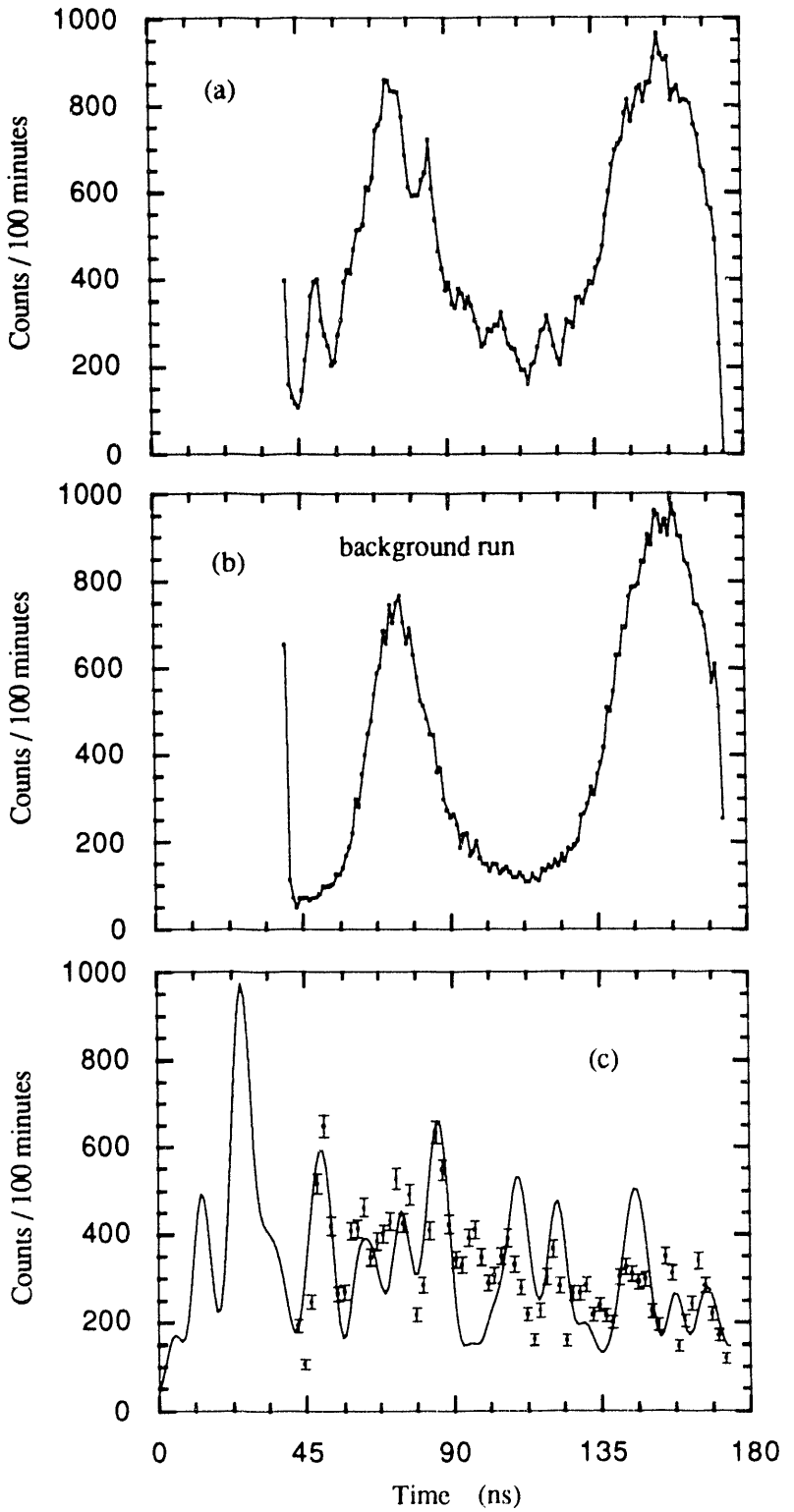

Fig. 11-5.1. Nuclear resonance signal for a scattering geometry that produces significant nuclear level mixing. Total signal plus background is in (a), background due to phototube afterpulses is in (b), and (c) is the result after background subtraction. Nuclear scattering counting rate was about 3.6 counts/sec. (Lines are drawn though data in (a) and (b)).

The other problem resulted from a confusion about the crystallographic directions in the YIG crystal samples. The YIG crystal #57-2 was aligned so that its flat was perpendicular to the incident beam. The flat turned out to be the YIG [1 1 0] direction. For this orientation of the YIG crystal, the internal magnetic field (which was nominally parallel to the incident beam direction) bisects the electric field gradient [1 0 0] and [0 1 0] directions. When the angle between the magnetic field and both electric field gradients is 45°, the electric quadrupole splitting between the $d1$ and $d2$-sites is identical. The lines from each site then lie at the same energy, and, because of the crystallographic 180° phase difference between the two sites, the reflection becomes forbidden for nuclear diffraction. In the experiment, the crystal was set at an azimuthal angle of 44° thus making the reflection nearly forbidden. At this orientation, the nuclear signal is reduced by a factor of 15 over the optimum orientation (that is, for an azimuthal angle of 0°). An extremely painstaking and time consuming effort was undertaken to find the nuclear resonance signal under such low counting rates (≈3.6 counts/sec).

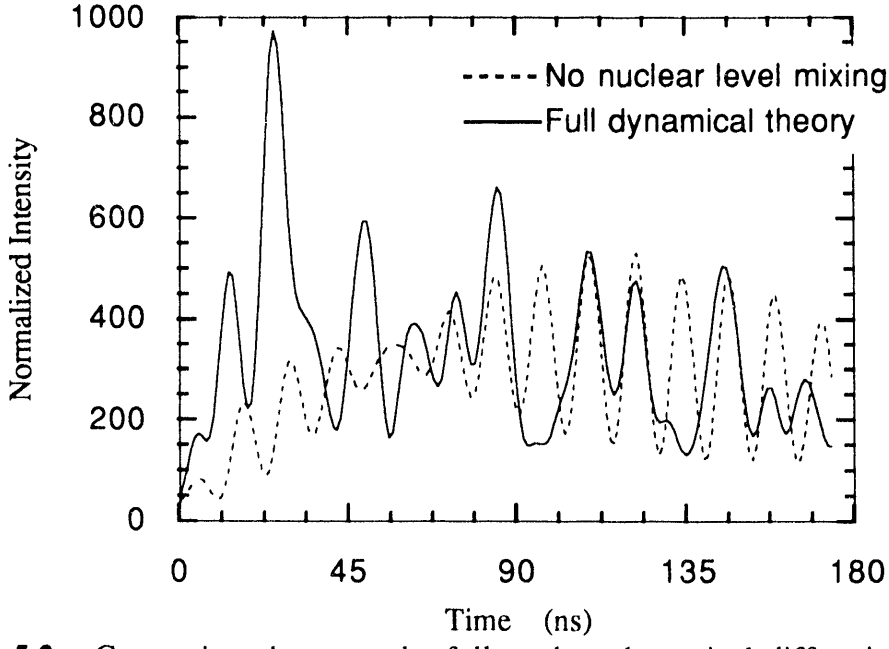

Fig. 11-5.2. Comparison between the full nuclear dynamical diffraction theory and when the theory neglects nuclear level mixing.

Sometimes accidents, as in this situation, can lead to some interesting physics. When the angle between the internal magnetic field and the $d1$ and $d2$-site electric field gradients is at 45°, the nuclear reflection is forbidden only to first order, and second order

effects come into prominence. Nuclear level mixing, which is almost negligible for other angles between the magnetic field and electric field gradients, becomes quite significant at the 45° angle. As described in Section 5.3, the mixing of nuclear states becomes so strong that linear polarization reversal occurs--incident $\hat{\sigma}$ polarized fields are scattered into outgoing π polarized fields. Including nuclear polarization mixing in the nuclear dynamical diffraction theory was necessary to fit the data. Fig. 11-5.2 shows the effect of nuclear level mixing for the fit in Fig. 11-5.1. This phenomena of strongly mixed nuclear states where each resonant line amplitude results from superpositions of all possible nuclear quantum states was later investigated more carefully by the Hamburg nuclear resonance scattering group.[5, 6]

The result of inserting the "black" Mössbauer absorbers in push-pull mode is shown in Fig. 11-5.3. Magnetic hyperfine beats are no longer visible--the "black" absorbers were successful in significantly filtering out the inner resonant lines. What is left is the slow electric quadrupole beat between the two d-sites. The data was fitted with the simple kinematic formula given by Eq. 11-1.1 to illustrate that the time distribution follows an expected slow beat pattern on top of an exponential decay curve. The data exhibited a speedup of $s = 2.9 \pm 0.3$ which is consistent for fields reflected at an angle near the Bragg

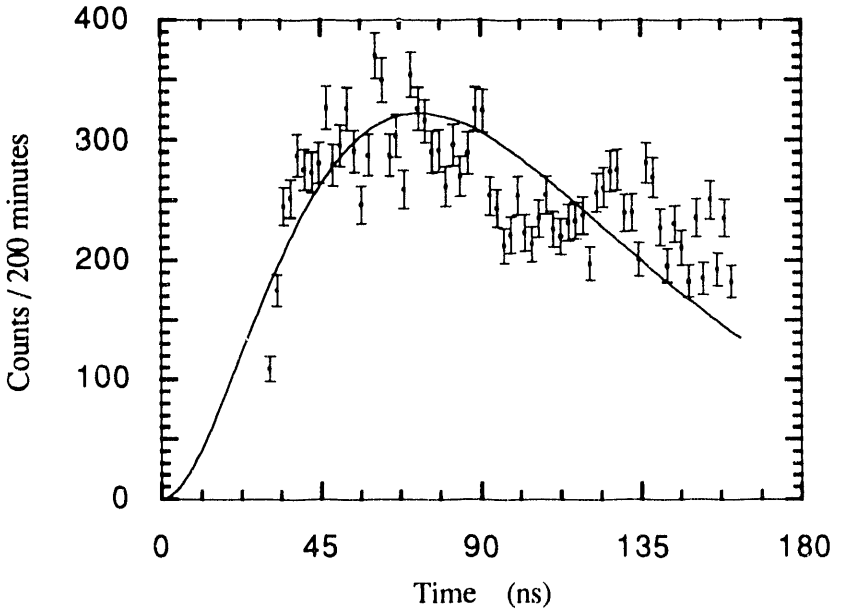

Fig. 11-5.3. Time distribution for an experiment where "black" Mössbauer absorbers filter out hyperfine lines to eliminate magnetic beats. Only the electric quadrupole beat is evident. The counting rate was about 1.3 counts/sec.

peak (the data in Fig. 11-5.1 indicates the reflection was about -5μrad from the Bragg peak). The precise quadrupole beat period was indeterminable due to the lack of good statistics in the data, so the theoretical value of 3.7 μsec was used in the fit.

11.6 General Dynamical Scattering

Nuclear dynamical diffraction theory has been quite successful in explaining all the data obtained by scattering resonant x-rays off ^{57}Fe enriched YIG crystals. The fits have not been perfect, but this problem may be due to crystal imperfection, nonuniformities in the hyperfine fields throughout the crystal, or the inability to accurately characterize the polarization of the field incident upon the crystal. Even certain physical interactions that one would neglect upon first thought because their effects are small can produce noticeable perturbations in the quantum beat patterns. For instance, even though the a-sites have much larger internal magnetic fields that the d-sites, and the a-sites do not reflect any fields for the scattering orders considered in the experiments, these sites can produce small, noticeable effects for incident angles near the Bragg peak. This is shown in Fig. 11-6.1 for

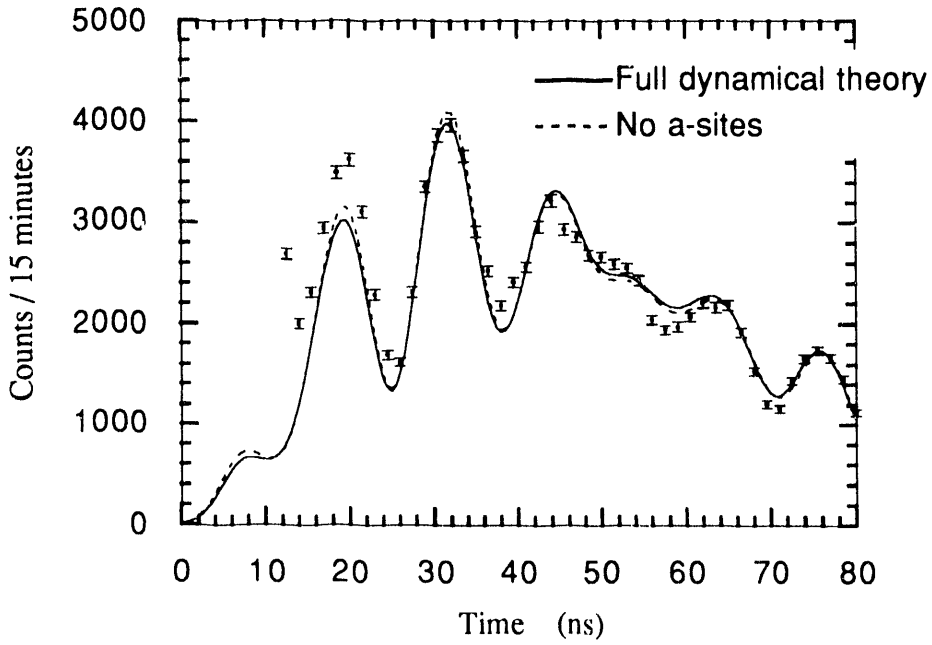

Fig. 11-6.1. Small perturbations upon the time beat patterns due to the presence of ^{57}Fe occupying the a-sites in YIG. The dotted curve shows the effect of eliminating the a-sites. The incident angle is -1μrad from the Bragg peak.

a case in which the internal magnetic field is parallel to the scattering plane. The major effect of the a-sites shows up in the null region where the $\hat{e}_+$ and $\hat{e}_-$ polarized field intensities are out of phase. Yet, theses effects are too small to yield any meaningful information about the a-sites in the data collected.

One interesting problem that was analyzed was whether there was any additional dephasing in the scattering process that would cause the quantum beats to wash out earlier than expected. To see this effect required a long count rate experiment that covered a range of several lifetimes. Two TACs were used to perform this experiment--one measured time spectra from 0 to 250 nsec, and the other measured spectra from 200 to 450 nsec. The TACs could be put in synch by using the overlapping measurement (the TACs were actually found to be in synch making time corrections between TACs unnecessary). The results are shown in Fig. 11-6.2. Clear, unmistakable beats can be seen up to $2\frac{1}{2}$ lifetimes (340 nsec), and beyond that time both data and theory start to become washed out--natural dephasing due to the decay of the nuclear excited state makes it necessary to perform

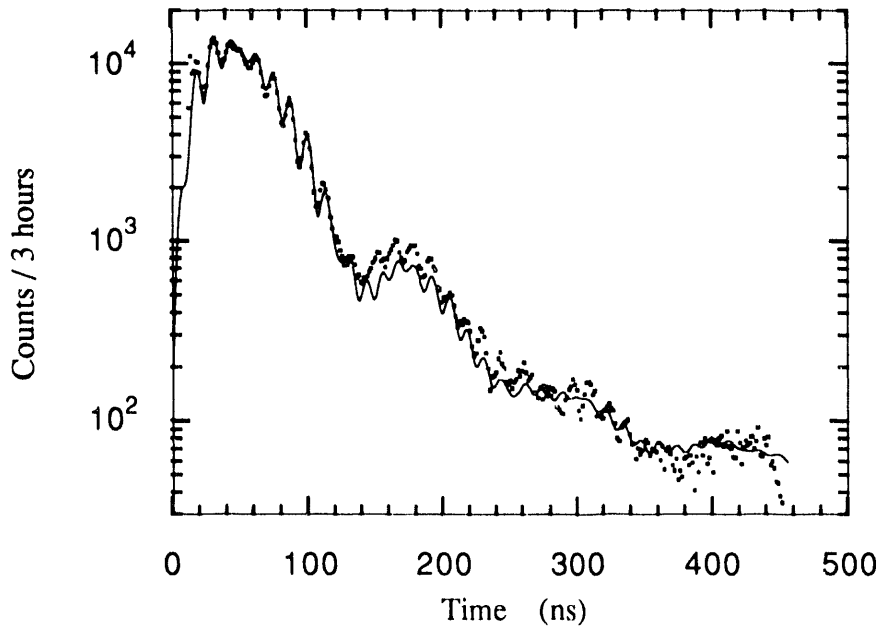

Fig. 11-6.2. Three hour measurement of YIG [0 0 2] time spectrum covering over 3 natural lifetimes. The incident angle is $-9\,\mu$rad from the Bragg peak, the internal magnetic field is parallel to the scattering plane, and a background of 1.5 counts/sec was used in the fit. Data collected over a long time is typically more difficult to fit than data collected over a short time. This is probably because there is more time for settings to change during the experiment (such as the incident beam direction). Ringing can be seen up to $2\frac{1}{2}$ lifetimes revealing that the crystal operates similar to a set of oscillators having a high Q.

measurements lasting longer than 3 hours to find out what is happening beyond $2\frac{1}{2}$ lifetimes.

The only difference between the scattering amplitudes for the YIG [0 0 2n] (where n is odd) reflections is that the angular factors in the polarization matrices change and that the real part of the photoelectric scattering amplitude decreases as the Bragg angle increases (that is, $f_0 \rightarrow 0$ in Eq. 7-2.2 as the scattering angle approaches 90°). The decrease in the real part of the photoelectric scattering amplitude only serves to decrease the index of refraction shift and the Darwin width of the Bragg peak. This makes the peak speedup and frequency shifts occur at a smaller deviation angle from Bragg, and it causes the reflected intensity to decrease. What significantly changes the shape of the beat patterns between the

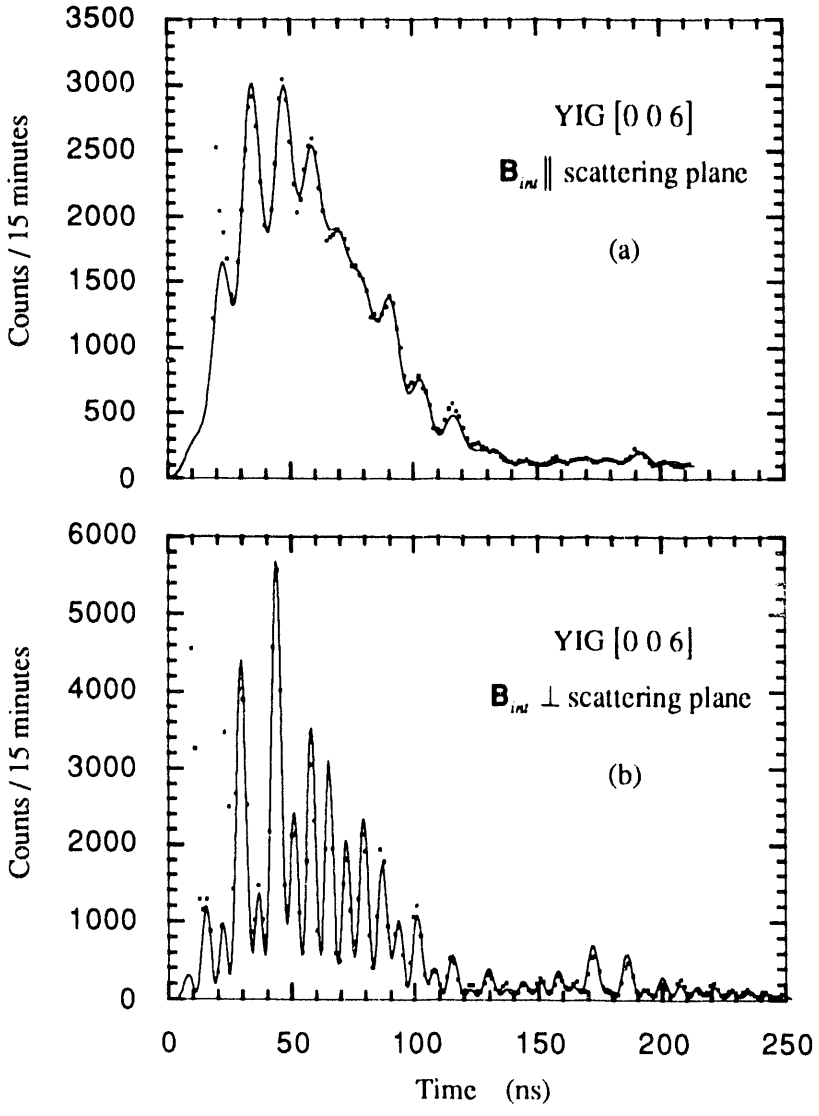

Fig. 11-6.3. YIG [0 0 6] quantum beat patterns for the cases in which the internal magnetic field is (a) parallel and (b) perpendicular to the scattering plane. A horizontally polarized field is incident at an angle (a) -2μrad (b) -1μrad from the Bragg peak.

various YIG reflections are the differences in the polarization matrices (Eqs. 5-1.22 and 5-1.28 for the common scattering geometries used in the experiments).

Time spectra for the YIG [0 0 2] and [0 0 10] reflections have already been shown in Figs. 10-1.3, 10-1.4, 10-3.1, and 10-4.1 for the two cases in which the magnetic field is parallel and perpendicular to the scattering plane (the incoming field was incident at an angle from the Bragg peak of -3μrad for Fig. 10-3.1 (a) and -4μrad for Fig. 10-4.1 (a)). To complete the set, YIG [0 0 6] and [0 0 14] are shown in Figs. 11-6.3 and 11-6.4.

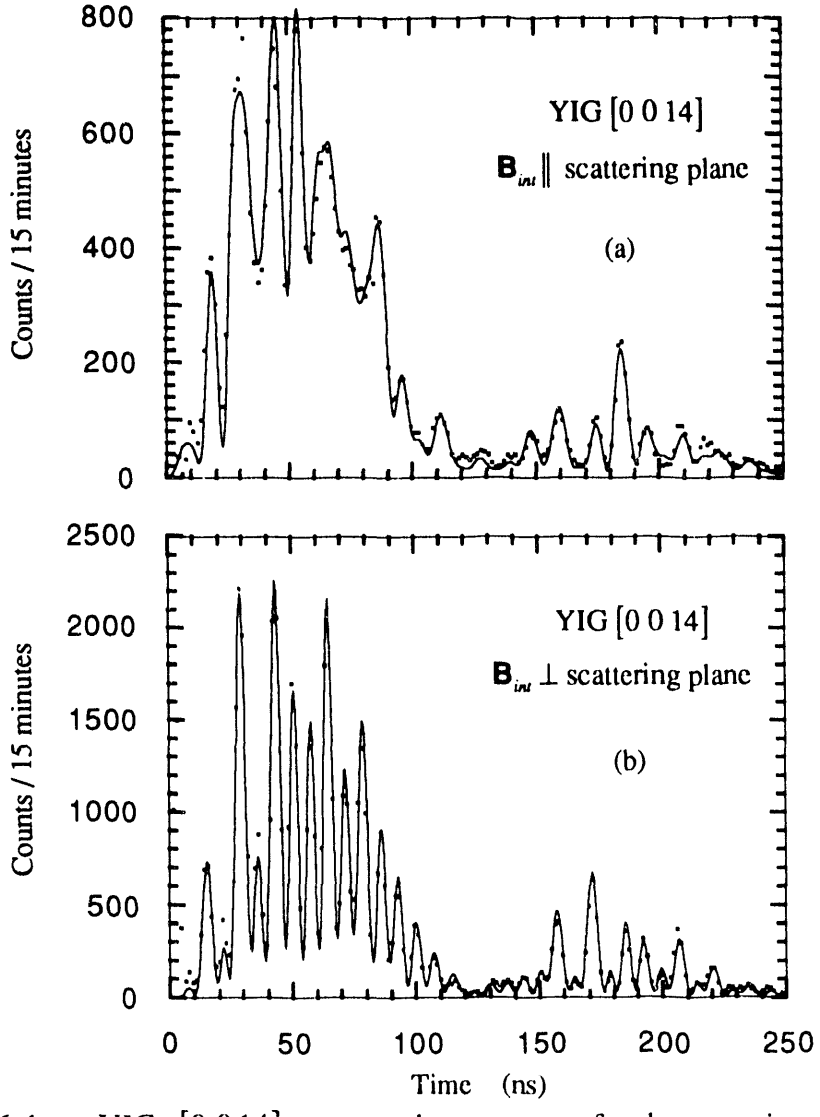

Fig. 11-6.4. YIG [0 0 14] quantum beat patterns for the cases in which the internal magnetic field is (a) parallel and (b) perpendicular to the scattering plane. A horizontally polarized field is incident at an angle (a) -6μrad (b) $+2\mu$rad from the Bragg peak.

Nuclear dynamical diffraction theory should hold equally well for multiple crystal reflections. The only change comes in the boundary conditions in which the incident field on the proceeding crystal is the reflected field from the preceding crystal. Double crystal diffraction experiments were performed by the nuclear resonance scattering group at Hamburg,[7] but only for the case in which both YIG crystals were operated identically. In contrast, double crystal diffraction experiments were performed for various orientations of the internal magnetic field across the two crystals and for various combinations of reflections. Fig. 11-6.5 shows the results of a double reflection from two YIG crystals oriented for the [0 0 2] reflection. In Fig. (a) and (b) both crystals have their internal magnetic fields parallel and perpendicular, respectively, to the scattering plane. In Fig. (c) the first crystal has its internal magnetic field oriented parallel to the scattering plane, while the second crystal has its field oriented perpendicular to the scattering plane. The very noticeable difference between the single and double reflection measurements is an overall shift in the quantum beat patterns. This shift results because the double crystal reflection performs a convolution of two single crystal beat patterns.

Another experiment was performed in which the first crystal was oriented for the [0 0 2] reflection and the second crystal was oriented for the [0 0 4] reflection (the internal magnetic field for both crystals was oriented parallel to the scattering plane). The results are shown in Fig. 11-6.6. The [0 0 4] reflection allows both photoelectric and nuclear diffraction. The double crystal beat pattern should then, to first order, show a YIG [0 0 2] beat pattern since the YIG [0 0 2] diffracted field should reflect promptly from the electrons in the second crystal. To second order, a convolution of single crystal YIG [0 0 2] and YIG [0 0 4] beat patterns should be present.

Double crystal experiments allows one to probe the hyperfine structure of crystals for allowed photoelectric reflections. For instance, observing the quantum beat signal from a YIG [0 0 4] reflection is not possible with the present detector because of the intensity of the allowed photoelectric reflection (unless one uses a narrow bandpass crystal monochromator, but these monochromators also drastically reduce the nuclear signal intensity). The YIG [0 0 2]-[0 0 4] double crystal reflection allows one to get around this problem and to extract information about the photoelectrically allowed [0 0 4] reflection.

Using the first crystal as a monochromator produces extremely monochromatic x-rays to be used in further experiments involving not only crystals but other types of samples. Unfortunately, YIG is a hyperfine split crystal, and its complicated time response must be deconvolved from any experimental results--its time response must, therefore, be

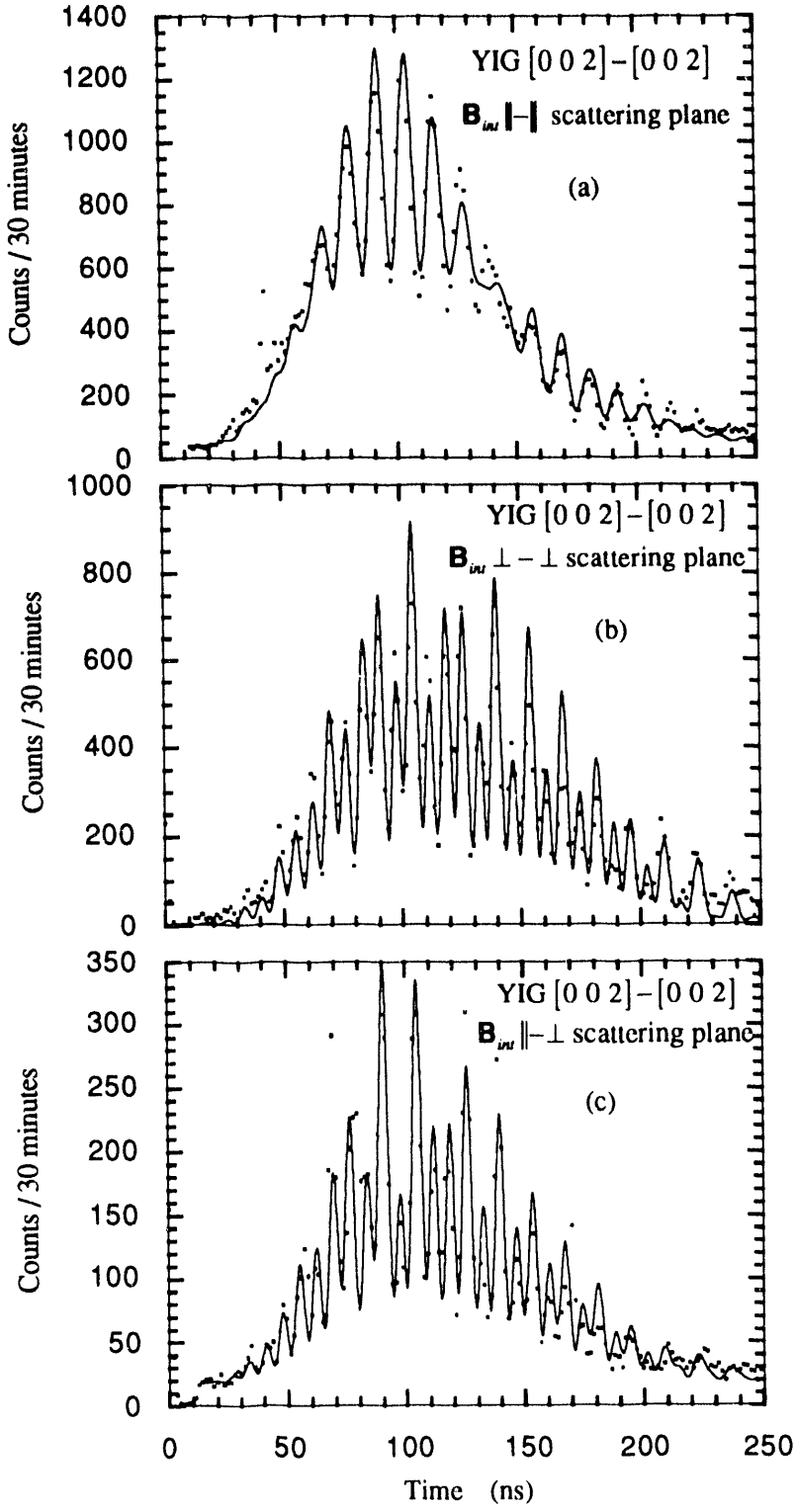

Fig. 11-6.5. Double crystal YIG quantum beat patterns. Both crystals are oriented in the [0 0 2] direction. The internal magnetic field is oriented parallel or perpendicular to the scattering for each crystal separately. In (c), the magnetic field is parallel to the first crystal and perpendicular to the second crystal.

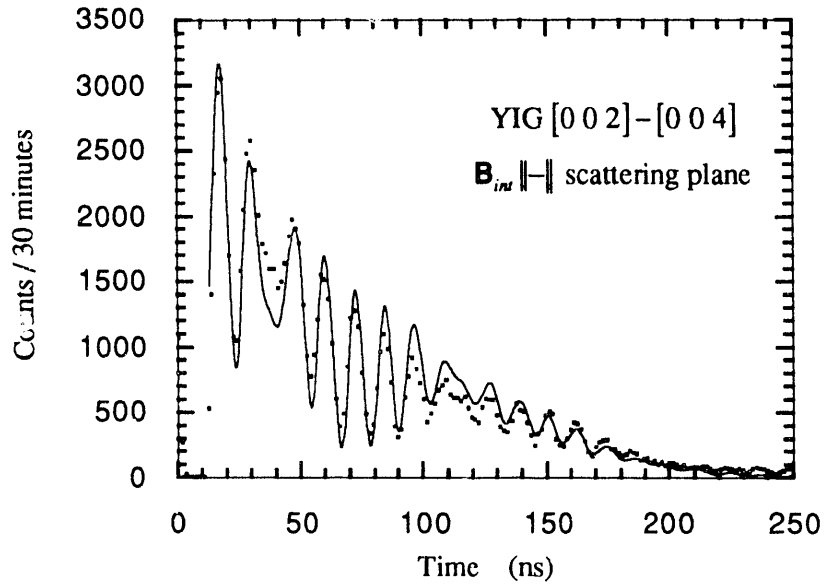

Fig. 11-6.6. Double crystal YIG quantum beat pattern. Both crystals have their internal magnetic fields oriented parallel to the scattering plane, but the first crystal is oriented in the [0 0 2] direction and the second crystal is oriented in the [0 0 4] direction.

well known. However, there is a possibility of constructing single line YIG crystals by impregnating them with certain elements. Even so, the linewidth would not be broad enough to eliminate the necessity of performing deconvolutions to erase the effects of the monochromator when it is used for experiments involving ^{57}Fe enriched samples (even using the properties of the decay rate speedup does not help because speedups, or, in frequency space, an increase in the linewidth, of only as great as 3 have been observed for YIG).

REFERENCES

[1] U. van Bürck, G. V. Smirnov, R. L. Mössbauer, H. J. Maurus, and N. A. Semioschkina, *J. Phys. C: Solid St. Phys.* **13**, 4511 (1980).

[2] A. I. Chumakov, G. V. Smirnov, M. V. Zelepukhin, U. van Bürck, E. Gerdau, R. Rüffer, and H. D. Rüter, *Europhys. Lett.* **17**, 269 (1991).

[3] U. van Bürck, D. P. Siddons, J. B. Hastings, U. Bergmann, and R. Hollatz, *Phys. Rev. B* , (To be published).

[4] D. M. Gualtieri, W. Lavender, and S. L. Ruby, *J. Appl. Phys.* **63**, 3795 (1988).

[5] R. Hollatz, W. Sturhahn, H. D. Rüter, and E. Gerdau, *Influence of Relative Phase Factors between Inequivalent Sites of Single Crystals on Mossbauer*

Experiments, International Conference on the Applications of the Mössbauer Effect (Budapest, Hungary, 1989), vol. 2, p. 14.11.

[6] H. D. Rüter, R. Rüffer, R. Hollatz, W. Sturhahn, and E. Gerdau, *Hyp. Int.* **58**, 2477 (1990).

[7] E. Gerdau, R. Rüffer, R. Hollatz, *Phys. Rev. Lett.* **57**, 1141 (1986).

12. CONCLUSION

The theory of the scattering of x-rays by resonant nuclei is, in principle, much simpler that the theory describing the scattering of x-rays from electrons. This is because electronic dynamical diffraction theory requires relativistic Hartree-Fock calculations to determine the resonant or nonresonant photoelectric scattering amplitude for many electron atoms. Because nuclei can be approximated as point particles, such calculations for nuclear systems are unnecessary. A simple nonrelativistic perturbation theory, treating the nuclei as point particles, can be used to understand the nature of electromagnetic fields scattered from nuclei.

Once the spherical multipole scattering amplitude, whether for nuclear or electronic interactions, has been formulated, the differences between nuclear and electronic scattering theory disappear. The electromagnetic fields scattered from particles can then be expressed in terms of spherical multipole fields. In this thesis, a dynamical scattering theory has been developed where spherical multipole fields interact with a system of particles and undergo multiple scattering. When elastic scattering is assumed, there is no way to determine which photon scattered off which particle since the state of the particle before and after the scattering process is the same. Thus, to describe the scattering interaction, one must coherently sum up all the probability amplitudes of scattering from all of the particles in the system. This sum forms a collective state of many particles--the system of particles acts collectively as an entirely different particle.

Dynamical scattering theory reveals that a collective state has properties similar to a single particle. A single particle interacting with a photon undergoes frequency shifts and has a resonance linewidth due to its interaction with the generated self-fields. Similarly, when the collective state interacts with a photon, it interacts with its generated self-fields which, in this case, are the multiply scattered fields in the medium. These interactions are shown to also lead to resonance frequency shifts and linewidth broadening (or radiative speedup).

The connection between quantum mechanics and classical mechanics was bridged by performing a sum over all of the multiply scattered fields in a medium. What was found was interesting but not surprising. The net electric field multiply scattered from a phased collection of particles was found to be identical to the solution of the Maxwell equations for a medium when the quantum mechanical form of the scattering amplitude is

used in the inhomogeneous wave equation. This semi-classical result confirms that dynamical diffraction theory rests on solid ground.

Nuclear dynamical diffraction effects were strongly evident in the time-resolved Mössbauer spectra measured in synchrotron x-ray diffraction experiments involving ^{57}Fe enriched YIG films. In the time domain, resonant frequency shifts and decay rate speedups were observed, and they were seen to vary as a function of the deviation from the Bragg angle of a YIG crystal. The average decay rate speedup varied in a Lorentzian fashion with the deviation angle, and the peak was centered at the nonresonant Bragg peak. The average resonant frequency shift was seen to vary in a Lorentzian dispersive fashion. Both effects were predicted by nuclear dynamical diffraction theory. A peak speedup of 3Γ and a peak frequency shift of 1.5Γ (where $\Gamma = 4.67\,\text{neV}$ is the natural linewidth) was measured for YIG. The incident beam from a monochromator had an angular divergence of about $20\mu\text{rad}$, and should this divergence be reduced in future experiments, larger peak speedups and frequency shifts should be obtainable.

By measuring the variations in the quantum beat patterns as a function of the deviation angle from the Bragg peak, the Lamb-Mössbauer factor was deduced. A Lamb-Mössbauer factor of 0.82 with a 5% uncertainty was measured for the YIG [0 0 2] reflection. Of interest would be to repeat these measurements for other orders of reflection. How this factor depends with scattering angle or upon the order of reflection is not well known.

Another nuclear dynamical effect observed was the variation in the quantum beat patterns due to the thickness of the crystal film. In one measurement using the YIG [0 0 10] reflection, the nuclear dynamical theory gave a thickness ($2.6\mu\text{m}$) that was inconsistent with a measurement made during the fabrication of the crystal film ($6.7\mu\text{m}$). With more careful diffraction experiments to measure the rocking curve of the crystal, the dynamical theory was vindicated--the rocking curve measurements showed that the crystal had bifurcated into two layers having different lattice constants. Thus, dynamical effects were shown to be sensitive to thickness variations in a crystal.

Nuclear dynamical diffraction theory was also tested in a double crystal reflection experiment. In this case, the idea of a collective state must be extended to two crystals separated in space. However, since diffraction is essentially a phased scattering phenomena, the separation of two crystals poses no problem as long as all of the diffracting particles have the same spatial phases (modulo 2π). The two crystal YIG $[0\,0\,2]-[0\,0\,2]$ reflection data was well explained by dynamical diffraction theory for different orientations of the internal magnetic field across each crystal. A double crystal

YIG [0 0 2]–[0 0 4] reflection experiment was also done. This experiment showed that, using the first [0 0 2] crystal as a monochromator source, an electronically allowed [0 0 4] reflection could be probed. Without the YIG [0 0 2] crystal, the photoelectric prompt reflection would have overwhelmed the detector (a scintillator coincidence photodetector where the scintillator is a plastic material possessing a short fluorescent lifetime).

Nuclear dynamical scattering theory is necessary to describe the results of time-resolved Mössbauer spectroscopy principally because multiple scattering is no longer insignificant. However, there remains a whole host of physical phenomena that have nothing to do with multiple scattering (such as nuclear hyperfine structure quantum beats, the orientation and strength of the various hyperfine fields, nuclear level mixing, polarization and angular scattering characteristics, and angular interferometry) which were also investigated in this thesis.

One such kinematic effect investigated involved a dual time and frequency experiment that utilized information from both frequency and time space. A "black" Mössbauer absorber was used to completely filter out the inner two lines of a hyperfine split YIG spectrum. The inner magnetic field was oriented nominally parallel to the incident and outgoing photon directions. For such a case, filtering out the inner two lines prevents any magnetic beating. The time-resolved experiment showed no fast magnetic hyperfine beats--only a slow electric quadrupole beat remained (due to the beating between lines from iron nuclei lying in different crystallographic sites).

Another kinematic scattering phenomena investigated involved a situation in which time domain measurements have advantages over frequency domain measurements. This advantage lies in the ability to easily detect relative phase differences between resonant amplitudes. Since resonant lines are usually spaced far apart, very little phase information can be extracted from the interference between the lines. However, since the interference between resonant lines shows up as a beat pattern in the time domain, phase shifts in the amplitudes show up as clearly observable shifts in the beat patterns.

An angular interferometry experiment took full advantage of the ability to observe purely geometrical phase changes in the time domain. In this experiment, the phase shift of the quantum state of a photon that has undergone a rotation was measured--these phase shifts are purely geometrical effects independent of dynamical, or multiple, scattering or the number of scatterers. By using nuclear transitions, photons could be prepared having a definite component of angular momentum along a quantization axis (the internal

magnetic field direction). These photons underwent phase shifts depending upon the amount of azimuthal (angular momentum-conserving) rotation about the quantization axis. These phase shifts were observed to be different between right-handed rotations and left-handed rotations about the quantization axis. For scattering angles near 45°, the phase difference was large enough to shift the quantum beat patterns for right and left-handed rotations almost 180° out of phase. Such striking phase effects would be extremely difficult, if not impossible, to observe through traditional Mössbauer velocity experiments.

One interesting question that may be posed by Mössbauer experimentalists is whether measurements made in the time domain reveal any information that cannot be obtained by traditional measurements in the frequency domain. For the samples used in this thesis, both time-resolved and conventional Mössbauer spectroscopy would most likely yield the same results when analyzing the internal hyperfine fields. The hyperfine field values for the internal magnetic field and the electric quadrupole splitting could be measured to within 1-2% through the analysis of quantum beat patterns. This is about as well as traditional Mössbauer velocity measurements. Where time-resolved measurements using synchrotron x-ray sources become more useful is in hyperfine field measurements of samples that are not amenable to conventional Mössbauer spectroscopy. For example, when using radioactive sources, the scattering intensity from extremely small samples is generally too small to extract information about the hyperfine fields. Such samples may include materials in highly pressurized diamond anvil cells where magnetic phase transitions can be explored, or nanostructures and micro-crystals where one, two, or three dimensional magnetism can be explored. For instance, one dimensional magnetism can be investigated in small magnetic fibers, and two dimensional magnetism can be explored in the surface layer of materials or in thin magnetic crystal or multilayer films composed of only a few monolayers of resonant nuclei. When the third generation synchrotron sources are constructed, undulator beamlines should be able to provide the necessary high brilliance to make such measurements not only possible but straightforward.

APPENDIX A

A.1 Angular Interferometry (Physical Review Letter)

The discussion in Chapter 5 explored the properties of angular phase shifts from the perspective of the S and T-matrix scattering formalism presented in the previous chapters. To complement the discussion, the angular phase shifts are understood in this appendix by using the fundamental rotational and mirror symmetry properties of free space which leads to the realization that bosons, such as photons, essentially behave as three dimensional irreducible representations of the group $O^+(3)$. (In a similar fashion, these symmetry properties reveal that fermions, such as electrons or neutrons, can be realized as two dimensional irreducible representations of the group $SU(2)$.) The following is a recently published journal article: D. E. Brown, J. Arthur, A. Q. R. Baron, G. S. Brown, and S. Shastri, *Phys. Rev. Lett.* **69**, 699 (1992).

Phase Shift of a Rotated Quantum State Observed in an X-ray Scattering Experiment

D. E. Brown, J. Arthur, A. Q. R. Baron
Stanford Synchrotron Radiation Laboratory, P. O. Box 4349, Bin 69, Stanford, California 94309

G. S. Brown
Dept. of Physics, University of California at Santa Cruz, Santa Cruz, California 95064

S. Shastri
Cornell High Energy Synchrotron Source and the School of Applied and Engineering Physics, Cornell Univ., Ithaca NY 14853

Abstract

The rotation of the reference frame of a particle is known to lead to a phase change of its wavefunction proportional to its angular momentum. This can manifest itself as an angle-dependent phase shift of a photon scattered by a fixed target, when the photon state is an eigenstate of the component of total angular momentum perpendicular to the scattering plane. This phase shift has been observed in the quantum beat pattern resulting from the transient excitation of ^{57}Fe nuclei by synchrotron radiation.

PACS number: 03.65.-w,78.70.Ck,42.10.Jd,76.80.+y

Quantum wavefunctions and classical wave fields reflect the symmetries of space and time that result in conservation laws and phase factors involving the conserved quantities. For example, the homogeneity of time leads to the conservation of energy and the uniformity of space leads to the conservation of total linear momentum for an isolated system. Such systems are invariant under translations in time or space, and the translated wavefunctions acquire phase shifts depending on the conserved values.[1,2] For simple eigenstates of energy and linear momentum

$$\psi(t+\Delta t)=e^{-iE\Delta t/\hbar}\psi(t) \tag{1}$$

$$\psi(\mathbf{r}-\Delta\mathbf{r})=e^{-i\Delta\mathbf{r}\cdot\mathbf{p}/\hbar}\psi(\mathbf{r}). \tag{2}$$

Of particular interest in this Letter are the effects of rotations on the properties of a system. Rotational symmetry results in the conservation of total angular momentum, $\mathbf{J}$, and a rotated eigenstate acquires an angular phase shift:

$$\psi(\phi-\Delta\phi)=e^{-i\Delta\phi\cdot\mathbf{J}/\hbar}\psi(\phi). \tag{3}$$

A vivid consequence of this angular phase is the 4π rotational symmetry of fermions that has been demonstrated in neutron interferometer experiments.[3-5] The angular phases for photons are dramatically illustrated in this Letter in an elastic scattering experiment involving resonant scattering of x-rays from nuclei.

Considering only basic symmetry properties of free space (such as rotational and mirror symmetry) angular momentum wavefunctions of a general particle can be constructed. The rotational symmetry properties lead to the formation of irreducible representations, $D^{(j)}\left(\hat{\mathbf{k}}\rightarrow\hat{\mathbf{z}}\right)$, describing rotations of a system with quantization axis $\hat{\mathbf{k}}$ into a system with quantization axis $\hat{\mathbf{z}}$, and having rotation-angle-dependent matrix elements that depend only upon the geometry of space and not upon the dynamics, or interactions, in the system. When j (the total angular momentum quantum number) is integral, these irreducible representations are naturally present in classical electrodynamics in the multipole field solutions of the Maxwell equations.

Consider a process that changes the direction of propagation of a photon without changing its total angular momentum. According to Eq.(3), a phase shift should arise depending on the projection of the total angular momentum along the axis of rotation. The angular momentum of a photon perpendicular to its direction of propagation is often not well-defined, but a photon state of well-defined propagation direction can be expanded in terms of basis states (spherical helicity states) having well-defined angular momenta about an axis that is not necessarily the propagation direction. Superpositions of these basis states form the multipole vector spherical harmonics.[6] In this case the total angular momentum

includes orbital angular momentum, and need not be limited to the photon spin value of 1. The rotated photon state has a phase factor $e^{-iM\Delta\phi}$, and the transition amplitude for forming such a rotated state has the conjugate phase factor $e^{+iM\Delta\phi}$. The quantity $\Delta\phi$ is the change in the photon's direction expressed as an azimuthal angle in a spherical coordinate system aligned along the axis of rotation, and M is the projection of the photon's total angular momentum along that axis. (If expressed in a spherical coordinate system that is not aligned along the rotation axis, the rotated wavefunction will in general also depend on the values of the polar angles of the photon propagation vectors.) The phase factor $e^{iM\Delta\phi}$ is independent of the polarization of the incident or rotated photon, and it is also independent of the dynamical details of the interaction that causes the photon direction to change.

To measure the angular phase change of a photon, it is sufficient to prepare a photon state with definite angular momentum about an axis perpendicular to its propagation direction, cause the state to rotate about this axis through a known angle without changing its total angular momentum, and observe the interference between the rotated state and another coherent reference photon state. We realized such an experiment using elastic scattering of synchrotron x-rays by nuclear resonances. The photon-nuclear interaction served to select photon states with definite values of M. Bragg scattering served to define the rotation angle, and the coherent, pulsed nature of the synchrotron excitation provided reference photons for the interference measurement.

For the experiment a yttrium iron garnet (YIG) crystal enriched with ^{57}Fe was used in Bragg geometry to diffract an incident beam of 14.4 keV photons through a scattering angle, $2\theta_B$, equal to twice the Bragg angle. The YIG magnetic crystal structure allowed us to observe pure nuclear resonant scattering from a ferromagnetically aligned subset of ^{57}Fe nuclei.[7] A small external magnetic field was used to orient the internal ferromagnetic field perpendicular to the scattering plane, so that the rotation angle of the scattered photons around the nuclear quantization axis was equal to $2\theta_B$.

In a magnetic field, the 14.4 keV ^{57}Fe nuclear resonance is generally split into a hyperfine six line spectrum (see Fig. 1). In our experiment the incident photons, due to the nature of the synchrotron source, were linearly polarized parallel to the nuclear quantization axis. Under these conditions the transitions labeled 2 and 5 in Fig. 1 are not allowed by polarization selection rules. The remaining four transitions are allowed, and the scattering process does not change the polarization state of the light. The two strongest transitions are those labeled 1 and 6 in Fig. 1. They are separated by about 6×10^{-7} eV, and the energy width of each resonance is approximately 5×10^{-9} eV. When excited coherently by an abrupt pulse of synchrotron light, the resonant states decay with a lifetime of about 141 ns. Because states with different frequencies are excited coherently, the decay curve exhibits

interference beats, principally the 7 ns beat period due to the interference of transitions 1 and 6.

Transitions 1 and 6 select photon states having total angular momentum projections along the nuclear quantization axis of $M = -1$ and $M = +1$. Thus, for the line with $M = +1$ the angular phase shift in the scattering amplitude is $2\theta_B$ while for the line with $M = -1$ it is $-2\theta_B$. The time beat pattern resulting from the interference of the two lines is phase retarded by $4\theta_B$:

$$I(t) \sim \left(1 + \cos[\Delta\omega t - 4\theta_B]\right) \tag{4}$$

where $\Delta\omega$ is the beat frequency. If the direction of scattering is reversed (see Fig. 2), the angular phase shifts change sign, resulting in a phase advanced time beat pattern

$$I(t) \sim \left(1 + \cos[\Delta\omega t + 4\theta_B]\right). \tag{5}$$

The time beat pattern contains a phase factor that is twice the scattering angle; the phase factor is negative for right handed rotations around the quantization axis and positive for left handed rotations. The net phase difference between time beat patterns with opposite rotation angles is four times the scattering angle: $8\theta_B$. This is a very noticeable effect for scattering angles near $45°$.

The YIG time beat pattern involves more than two resonant lines (the four lines mentioned above are further split by an electric quadrupole interaction giving a total of 8 lines), so the patterns are more complicated than those described by Eqs.(4) and (5). Yet, since all the lines have $M = \pm 1$, the $8\theta_B$ phase difference is the dominant effect.

The experiment was performed at the 24 pole wiggler beamline F2 at the Cornell High Energy Synchrotron Source (CHESS). A double crystal Si [1 1 1] monochromator provided a source beam having a 2 eV bandwidth at the nuclear resonance energy of 14.413 keV. A gold-coated flat mirror was used in grazing incidence geometry to filter out the higher order harmonics coming through the silicon monochromator. The diffracted light from the YIG crystal was detected by a fast plastic scintillator coincidence detector, and the photon arrival time was recorded by fast timing electronics. Similar experimental techniques have been used in a number of previous resonant nuclear scattering experiments.[8] The angular phase shift was not explicitly noted in these earlier experiments since they either involved small Bragg angles, or they involved antiferromagnetic samples from which all reflections involve both right and left handed scattering rotations. However, it should be pointed out that the angular phase factor is implicitly present in the polarization matrices for nuclear scattering described by various authors.[9-13] We found it experimentally convenient to change the sense of the scattering angle by reversing the

magnetic field direction, but it is conceptually simpler to think of the scattering angle being reversed, as shown in Fig. 2.

YIG $[0\,0\pm10]$ reflections have Bragg angles of ±20°, giving a net phase difference of 160° between their line 1—line 6 time beat patterns. The peaks of the $[0\,0\,10]$ pattern lie nearly in the valleys of the $[0\,0-10]$ pattern. This is shown in Fig. 3 where, despite complications due to the multiplicity of hyperfine levels, the advance or retardation of the 7 ns beat period is clearly visible. To get good fits to the data, we used the full Ewald-Laue dynamical diffraction theory for resonant scatterers,[11,14,15] including small contributions from the electronic and nuclear index of refraction. However, the angular phase shift which advances or retards the observed beat pattern is a purely kinematical, geometrical effect.

Recently, two resonant nuclear scattering experiments have demonstrated shifts in the time beat patterns due to passage of the radiation through the scattering material.[16,17] These shifts are caused by dynamical, index of refraction effects in the material, and they are not related to the angular phase shifts.

The fundamental symmetry properties of wave mechanics predict that an angular momentum-conserving rotation of a wavefunction is accompanied by an angular phase shift. A dramatic way to demonstrate this phase effect involves elastic resonant nuclear scattering of photons. The nuclear scatterer serves as a filter, allowing only photon states with well-defined angular momentum components to pass. Coherent generation of more than one angular momentum state using synchrotron light permits the angular phase shifts to be clearly observed in an interference measurement. A measurement of this type may have practical applications: for a given scattering angle, the time beat pattern can be used to uniquely determine the sign of the magnetic field at the scattering nuclei. In our experiment, the time beat patterns indicate that for the selected ^{57}Fe nuclei (the nuclei occupying the sites in YIG with local tetrahedral symmetry[7]), the internal magnetic field direction is opposite to the external guide field.

Support for this research was provided by the U. S. Department of Energy, Office of Basic Energy Science, Division of Materials Sciences. CHESS is supported by the National Science Foundation under Award No. 90-21700.

REFERENCES

[1] R. L. Liboff, *Introductory Quantum Mechanics* (Holden-Day, San Francisco, 1980).

[2] A. S. Davydov, *Quantum Mechanics* (Pergamon Press, Oxford, 1985).

[3] Y. Aharonov and L. Susskind, *Phys. Rev.* **158**, 1237 (1967).

[4] H. Rauch, A. Zeilinger, G. Badurek, and A. Wilfing, *Phys. Lett.* **54A**, 425 (1975).

[5] S. A. Werner, R. Colella, A. W. Overhauser, and C. F. Eagen, *Phys. Rev. Lett.* **35**,1053 (1975).

[6] V. B. Berestetskii, E. M. Lifshitz, and L. P. Pitaevskii, *Quantum Electrodynamics* (Pergamon Press, Oxford, 1982), vol. 4.

[7] H. Winkler, R. Eisberg, E. Alp, R. Rüffer, E. Gerdau, S. Lauer, A. X. Trautwein, M. Grodzicki, and A. Vera, *Z. Phys. B* **49**, 331 (1983).

[8] E. Gerdau, R. Rüffer, H. Winkler, W. Tolksdorf, C. P. Klages, and J. P. Hannon, *Phys. Rev. Lett.* **54**, 835 (1985); E. Gerdau, R. Rüffer, R. Hollatz, and J. P. Hannon, *Phys. Rev. Lett.* **57**, 1141 (1986); R. Rüffer, E. Gerdau, and R. Hollatz, *Phys. Rev. Lett.* **58**, 2359 (1987); U. van Bürck, R. L. Mössbauer, E. Gerdau, R. Rüffer, R. Hollatz, G. V. Smirnov, and J. P. Hannon, *Phys. Rev. Lett.* **59**, 355 (1987); G. Faigel, D. P. Siddons, J. B. Hastings, P. E. Haustein, J. R. Grover, and L. E. Berman, *Phys. Rev. Lett.* **61**, 2794 (1988); J. Arthur, G. S. Brown, D. E. Brown, and S. L. Ruby, *Phys. Rev. Lett.* **63**, 1629 (1989); S. Kikuta, Y. Yoda, Y. Kudo, K. Izumi, T. Ishikawa, C. K. Suzuki, H. Ohno, H. Takei, K. Nakayama, X. W. Zhang, T. Matsushita, S. Kishimoto, and M. Ando, *Jap. J. App. Phys.* **30**, L 1686 (1991).

[9] H. Frauenfelder, D. E. Nagle, R. D. Taylor, D. R. F. Cochran, and W. M. Visscher, *Phys. Rev.* **126**, 1065 (1962).

[10] M. Blume and O. C. Kistner, *Phys. Rev.* **171**, 417 (1968).

[11] J. P. Hannon and G. T. Trammell, *Phys. Rev.* **186**, 306 (1969).

[12] U. van Bürck, G. V. Smirnov, R. L. Mössbauer, F. Parak, and N. A. Semioschkina, *J. Phys. C* **11**, 2305 (1978).

[13] D. P. Siddons, J. B. Hastings, G. Faigel, L. E. Berman, P. E. Haustein, and J. R. Grover, *Phys. Rev. Lett.* **62**, 1384 (1989).

[14] B. W. Batterman and H. Cole, *Rev. Mod. Phys.* **36**, 681 (1964).

[15] A. M. Afanas'ev and Y. Kagan, *Zh. Eksp. Teor. Fiz.* **48**, 327 (1965) [*JETP* **21**, 215 (1965)]; Y. Kagan, A. M. Afanas'ev, and I. P. Perstnev, *Zh. Eksp. Teor. Fiz.* **54**, 1530 (1968) [*JETP* **27**, 819 (1968)]; Y. Kagan, A. M. Afanas'ev, and V. G. Kohn, *J. Phys. C* **12**, 615 (1979).

[16] A. I. Chumakov, G. V. Smirnov, M. V. Zelepukhin, U. van Bürck, E. Gerdau, R. Rüffer, and H. D. Rüter, *Europhys. Lett.* **17**, 269 (1991).

[17] U. van Bürck, D. P. Siddons, J. B. Hastings, U. Bergmann, and R. Hollatz, (To be published).

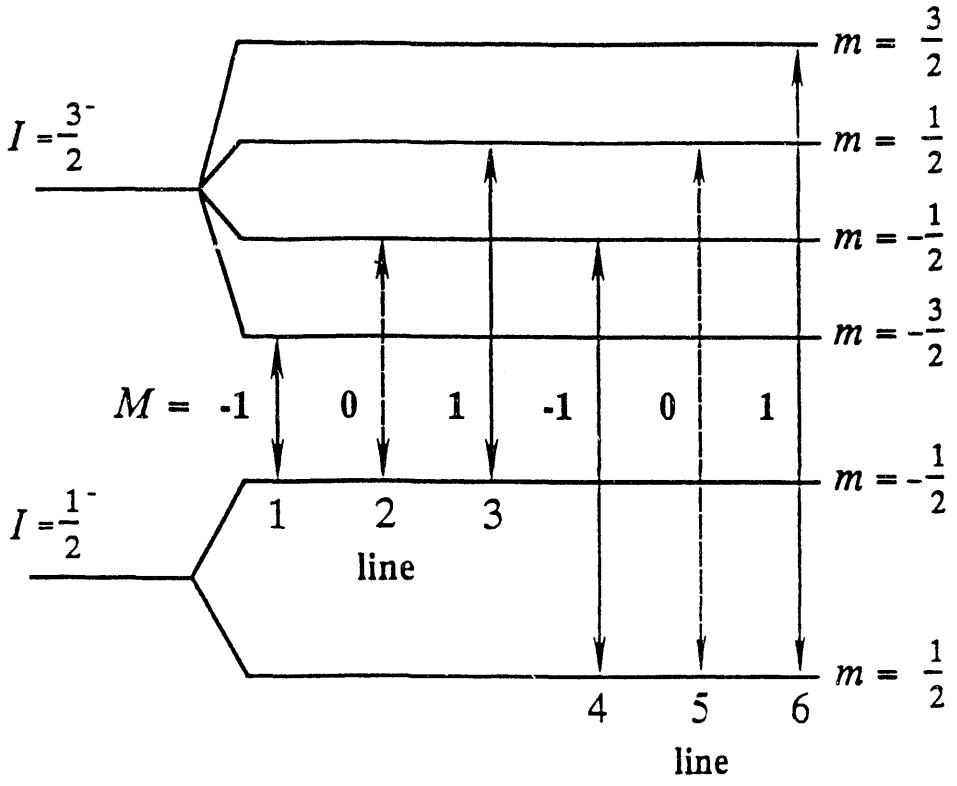

Fig. 1. Hyperfine nuclear resonance of ^{57}Fe. The magnetic quantum numbers are given with respect to a quantum axis oriented parallel to the internal magnetic field. When the magnetic field is perpendicular to the scattering plane, lines 2 and 5 are excitable by and radiate linearly polarized light perpendicular to the magnetic field. The other four lines are excitable by and radiate linearly polarized light parallel to the magnetic field. Radiated photons from lines 1,3,4,6 have the same polarization but different phases depending upon their scattering angles and angular momentum components, M.

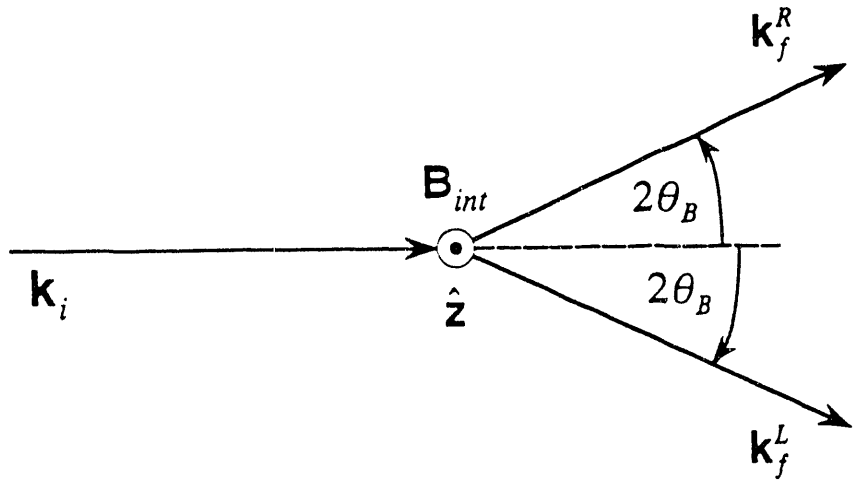

Fig. 2. Complementary scattering geometries. Incident photons $\mathbf{k}_i$ can be scattered by equivalent Bragg reflections in either a right-handed sense $\mathbf{k}_f^R$ or a left-handed sense $\mathbf{k}_f^L$ about the nuclear quantization axis, $\hat{\mathbf{z}}$, parallel to the internal magnetic field $\mathbf{B}_{int}$.

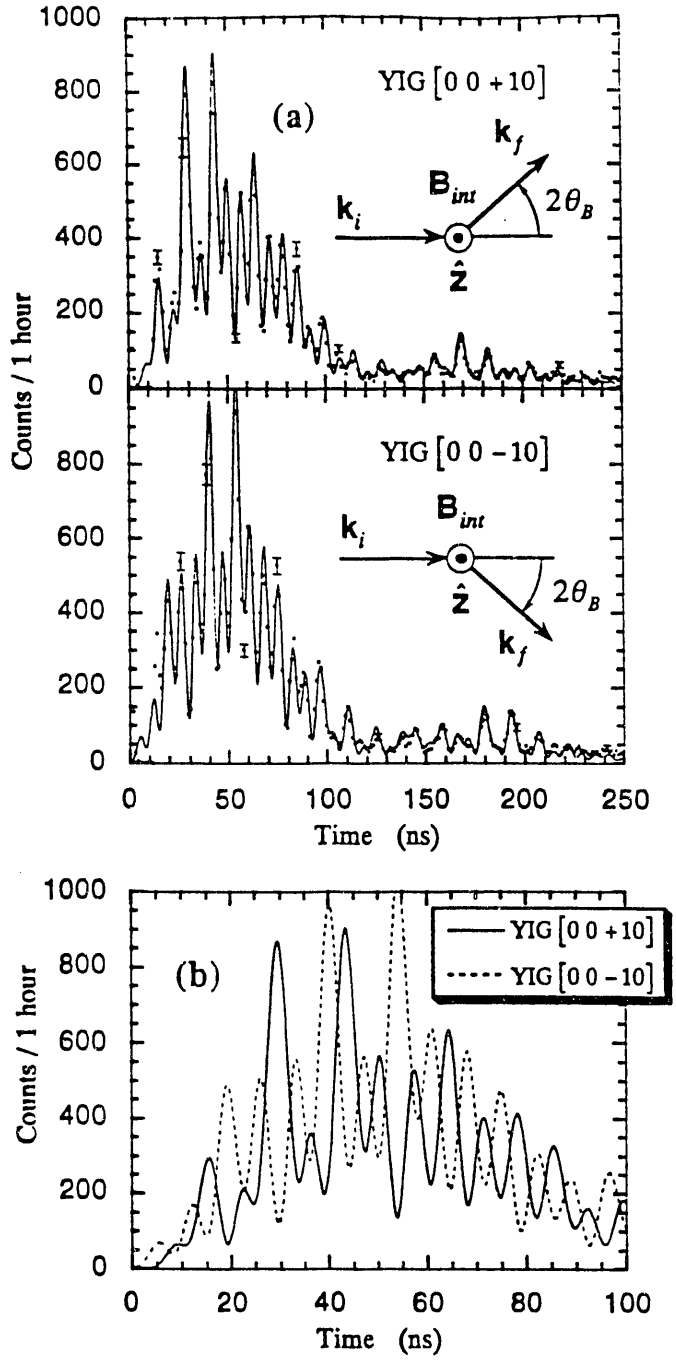

Fig. 3. (a) Time beat patterns for left and right handed scattering. Solid curves are dynamical diffraction theory calculations, including the angular phase. Because some of the interfering transitions share identical M values, the shifted beat patterns are modulated with an unshifted beat pattern of longer period, giving different heights to corresponding intensity peaks in the [0 0 10] and [0 0 −10] patterns. (b) Expanded, superimposed view of the fits to the data. The nearly 180° phase difference is clearly evident.

APPENDIX B

B.1 Time Domain Calculation for a Plane Parallel Slab of Resonant Scatterers Excited by a ^{57}Co Source

In this example, a plane parallel slab of single line resonant scatterers is excited by a ^{57}Co source. The field emanating from this source will be approximated as a decaying exponential wave Doppler shifted by $\Delta\omega$ to take into account the relative motion between the source and the scatterers:

$$a_0(t,z,z_0) = E_0 e^{ikz_0} e^{-i(\omega_0+\Delta\omega)t-\Gamma t/2\hbar}. \tag{B.1-1}$$

Let the scatterers have the same natural frequency, ω_0, and linewidth, Γ, as the source. The impulse response of the scatterers is then

$$H(t,z',z) = -(\Gamma_s/4\hbar L)e^{-i\omega_0 t-\Gamma t/2\hbar}\theta(t) \tag{B.1-2}$$

where Γ_s is given by Eq. 6-5.16

Using the multiple scattering equations, Eqs. 6-5.11 and 6-5.12, first order scattering gives

$$a_1(t,z,z_0)dz = \int_0^t \left[E_0 e^{ikz_0} e^{-i(\omega_0+\Delta\omega)t'-\Gamma t/2\hbar}\right]\left[-(\Gamma_s/4\hbar L)e^{-i\omega_0(t-t')-\Gamma(t-t')/2\hbar}\right]dt'\,dz$$

$$= A(t)\left(\frac{1}{-i\Delta\omega}\right)\left(e^{-i\Delta\omega t}-1\right)dz \tag{B.1-3}$$

where $$A(t) = -(\Gamma_s/4\hbar L)E_0 e^{ikz_0} e^{-i\omega_0 t-\Gamma t/2\hbar}. \tag{B.1-4}$$

Second order scattering gives

$$a_2(t,z,z_0)dz = \int_0^t\int_0^z dz'A(t')\left(\frac{1}{-i\Delta\omega}\right)\left(e^{-i\Delta\omega t'}-1\right)\left[-(\Gamma_s/4\hbar L)e^{-i\omega_0(t-t')-\Gamma(t-t')/2\hbar}\right]dt'\,dz$$

$$= A(t)\left(\frac{1}{-i\Delta\omega}\right)\left[\left(\frac{1}{-i\Delta\omega}\right)\left(e^{-i\Delta\omega t}-1\right)-t\right]\left[-\left(\frac{\Gamma_s z}{4\hbar L}\right)\right]dz. \tag{B.1-5}$$

Similarly, third and fourth order scattering gives

$$a_3(t,z,z_0)dz = A(t)\left(\frac{1}{-i\Delta\omega}\right)\left[\left(\frac{1}{-i\Delta\omega}\right)\left[\left(\frac{1}{-i\Delta\omega}\right)\left(e^{-i\Delta\omega t}-1\right)-t\right]-\frac{t^2}{2!}\right]\left[\left(\frac{\Gamma_s z}{4\hbar L}\right)^2\frac{1}{2!}\right]dz \tag{B.1-6}$$

$$a_3(t,z,z_0)dz = A(t)\left(\frac{1}{-i\Delta\omega}\right)\left[\left(\frac{1}{-i\Delta\omega}\right)\left[\left(\frac{1}{-i\Delta\omega}\right)\left[\left(\frac{1}{-i\Delta\omega}\right)\left(e^{-i\Delta\omega t}-1\right)-t\right]-\frac{t^2}{2!}\right]-\frac{t^3}{3!}\right]$$

$$\times\left[-\left(\frac{\Gamma_s z}{4\hbar L}\right)^3\frac{1}{3!}\right]dz. \qquad \text{(B.1-7)}$$

Adding up all the scattering terms, and ordering them in powers of $-1/i\Delta\omega$ results in a comprehensible series expansion:

$(a_1 + a_2 + a_3 + a_4 + \cdots)dz =$

$$= A(t)\left\{\left(\frac{e^{-i\Delta\omega t}}{-i\Delta\omega}\right)\left[1-\frac{\Gamma_s z}{4\hbar L(-i\Delta\omega)}+\left(\frac{\Gamma_s z}{4\hbar L(-i\Delta\omega)}\right)^2\frac{1}{2!}-\left(\frac{\Gamma_s z}{4\hbar L(-i\Delta\omega)}\right)^3\frac{1}{3!}+\cdots\right]\right.$$

$$-\left(\frac{1}{-i\Delta\omega}\right)\left[1-\frac{\Gamma_s zt}{4\hbar L}+\left(\frac{\Gamma_s zt}{4\hbar L}\right)^2\frac{1}{(2!)^2}-\left(\frac{\Gamma_s zt}{4\hbar L}\right)^3\frac{1}{(3!)^2}+\cdots\right]$$

$$-\left(\frac{1}{-i\Delta\omega}\right)^2\left[-\frac{\Gamma_s z}{4\hbar L}+\left(\frac{\Gamma_s z}{4\hbar L}\right)^2\frac{1}{2!}t-\left(\frac{\Gamma_s z}{4\hbar L}\right)^3\frac{1}{3!}\frac{t^2}{2!}+\cdots\right]$$

$$-\left(\frac{1}{-i\Delta\omega}\right)^3\left[\left(\frac{\Gamma_s z}{4\hbar L}\right)^2\frac{1}{2!}-\left(\frac{\Gamma_s z}{4\hbar L}\right)^3\frac{1}{3!}t+\cdots\right]$$

$$\left.-\left(\frac{1}{-i\Delta\omega}\right)^4\left[-\left(\frac{\Gamma_s z}{4\hbar L}\right)^3\frac{1}{3!}+\cdots\right]-\cdots\right.$$

$$= A(t)\left\{\left(\frac{e^{-i\Delta\omega t}}{-i\Delta\omega}\right)e^{-[\Gamma_s z/4\hbar L(-i\Delta\omega)]}-\left(\frac{i}{\Delta\omega}\right)J_0\left(\sqrt{\Gamma_s zt/\hbar L}\right)-\left(\frac{i}{\Delta\omega}\right)^2\frac{\partial}{\partial t}J_0\left(\sqrt{\Gamma_s zt/\hbar L}\right)\right.$$

$$\left.-\left(\frac{i}{\Delta\omega}\right)^3\frac{\partial^2}{\partial t^2}J_0\left(\sqrt{\Gamma_s zt/\hbar L}\right)-\cdots-\left(\frac{i}{\Delta\omega}\right)^{n+1}\frac{\partial^n}{\partial t^n}J_0\left(\sqrt{\Gamma_s zt/\hbar L}\right)\right\}. \qquad \text{(B.1-8)}$$

Using the expression for the scattering channel field, Eq. 6-5.13, and using the relations

$$\int_0^L J_0\left(\sqrt{\Gamma_s zt/\hbar L}\right)dz = 2L\frac{J_1\left(\sqrt{\Gamma_s t/\hbar}\right)}{\sqrt{\Gamma_s t/\hbar}} \qquad \text{(B.1-9)}$$

and
$$\frac{\partial^n}{\partial t^n}\frac{J_1\left(\sqrt{\Gamma_s t/\hbar}\right)}{\sqrt{\Gamma_s t/\hbar}} = \left(\frac{-\Gamma_s}{2\hbar}\right)^n \frac{J_{n+1}\left(\sqrt{\Gamma_s t/\hbar}\right)}{\left(\sqrt{\Gamma_s t/\hbar}\right)^{n+1}} \tag{B.1-10}$$

gives

$$E_{scf}(t,L,z_0) = E_0 e^{ikz_0} e^{-i\omega_0 t-\Gamma t/2\hbar}\left\{e^{-i\left[\frac{\Gamma_s}{4\hbar\Delta\omega}+\Delta\omega t\right]} - \sum_{n=1}^{\infty}\left(\frac{-i\Gamma_s}{2\hbar\Delta\omega}\right)^n \frac{J_n\left(\sqrt{\Gamma_s t/\hbar}\right)}{\left(\sqrt{\Gamma_s t/\hbar}\right)^n}\right\}. \tag{B.1-11}$$

This expression can be simplified by using the generating function for Bessel functions:

$$e^{\frac{1}{2}x\left(u-\frac{1}{u}\right)} = \sum_{m=-\infty}^{\infty} u^m J_m(x). \tag{B.1-12}$$

Then

$$\sum_{n=1}^{\infty}\left(\frac{-i\Gamma_s}{2\hbar\Delta\omega}\right)^n \frac{J_n\left(\sqrt{\Gamma_s t/\hbar}\right)}{\left(\sqrt{\Gamma_s t/\hbar}\right)^n} = \sum_{n=-\infty}^{\infty}\left(\frac{-i\Gamma_s}{2\hbar\Delta\omega}\right)^n \frac{J_n\left(\sqrt{\Gamma_s t/\hbar}\right)}{\left(\sqrt{\Gamma_s t/\hbar}\right)^n} - \sum_{n=-\infty}^{0}\left(\frac{-i\Gamma_s}{2\hbar\Delta\omega}\right)^n \frac{J_n\left(\sqrt{\Gamma_s t/\hbar}\right)}{\left(\sqrt{\Gamma_s t/\hbar}\right)^n}$$

where
$$\sum_{n=-\infty}^{\infty}\left(\frac{-i\Gamma_s}{2\hbar\Delta\omega}\right)^n \frac{J_n\left(\sqrt{\Gamma_s t/\hbar}\right)}{\left(\sqrt{\Gamma_s t/\hbar}\right)^n} = e^{-i\left[\frac{\Gamma_s}{4\hbar\Delta\omega}+\Delta\omega t\right]}$$

and
$$\sum_{n=-\infty}^{0}\left(\frac{-i\Gamma_s}{2\hbar\Delta\omega}\right)^n \frac{J_n\left(\sqrt{\Gamma_s t/\hbar}\right)}{\left(\sqrt{\Gamma_s t/\hbar}\right)^n} = \sum_{n=0}^{\infty}\left(\frac{-i2\hbar\Delta\omega}{\Gamma_s}\right)^n \left(\sqrt{\Gamma_s t/\hbar}\right)^n J_n\left(\sqrt{\Gamma_s t/\hbar}\right).$$

Finally, after collecting all terms, the scattering channel field can be expressed as

$$E_{scf}(t,L,z_0) = E_0 e^{ikz_0} e^{-i\omega_0 t-\Gamma t/2\hbar}\sum_{n=0}^{\infty}\left(\frac{-i2\hbar\Delta\omega}{\Gamma_s}\right)^n \left(\sqrt{\Gamma_s t/\hbar}\right)^n J_n\left(\sqrt{\Gamma_s t/\hbar}\right). \tag{B.1-13}$$

This result agrees precisely with Lynch, Holland, and Hamermesh's Fourier transform solution using contour integral methods.[1] The obvious drawback to this time domain multipole scattering approach is that one must have a deft faculty towards massaging complicated infinite series expansions into familiar analytical functions. The beauty of this time domain formalism is that one may completely work out problems entirely in the time domain and observe how the physics evolves at each step of the calculation--performing Fourier transforms can obscure the actual physics behind the scattering process (for instance, the entire issue of multiple scattering appears to be completely absent in the Fourier transform method).

REFERENCES

[1] F. J. Lynch, R. E. Holland, and M. Hamermesh, *Phys. Rev.* **120**, 513 (1960).

B.2 Investigation of the Dynamical Phase between Two Resonant Lines Excited by a Synchrotron Source

In this example the dynamical phase between two widely spaced resonant lines is calculated using the time domain multiple scattering formalism. For a plane parallel slab of scatterers, this phase is shown to be proportional to the thickness of the slab and inversely proportional to the frequency separation between the resonant lines. The source field incident upon the slab is a synchrotron pulse

$$a_0(t,z,z_0) = E_0 e^{ikz_0}\delta(t), \tag{B.2-1}$$

and the impulse response of the system of scatterers is the sum of two resonant amplitudes

$$H(t,z',z) = -(\Gamma_s/4\hbar L)\left\{e^{-i\omega_1 t} + e^{-i\omega_2 t}\right\}e^{-\Gamma t/2\hbar}\theta(t) \tag{B.2-2}$$

where Γ_s is given by Eq. 6-5.16, and ω_1 and ω_2 are the two resonant frequencies.

Using the multiple scattering equations, Eqs. 6-5.11 and 6-5.12, the first order scattered field amplitude is

$$\begin{aligned} a_1(t,z,z_0)dz &= \int_0^t\left[E_0 e^{ikz_0}\delta(t')\right]\left[-(\Gamma_s/4\hbar L)\left\{e^{-i\omega_1(t-t')} + e^{-i\omega_2(t-t')}\right\}e^{-\Gamma(t-t')/2\hbar}\right]dt'\,dz \\ &= A(t)\left\{1 + e^{-i\Delta\omega t}\right\}dz \end{aligned} \tag{B.2-3}$$

where $$A(t) = -(\Gamma_s/4\hbar L)E_0 e^{ikz_0}e^{-i\omega_1 t - \Gamma t/2\hbar}, \tag{B.2-4}$$

and $$\Delta\omega = \omega_2 - \omega_1. \tag{B.2-5}$$

The second order scattered field amplitude is

$$\begin{aligned} a_2(t,z,z_0)dz &= \int_0^t\int_0^z dz' A(t')\left\{1 + e^{-i\Delta\omega t'}\right\}\left[\left(A(t-t')e^{-ikz_0}/E_0\right)\left\{1 + e^{-i\Delta\omega(t-t')}\right\}\right]dt'\,dz \\ &= A(t)\left[-\left(\frac{\Gamma_s z}{4\hbar L}\right)\right]\left\{t\left(1 + e^{-i\Delta\omega t}\right) + \frac{2}{i\Delta\omega}\left(1 - e^{-i\Delta\omega t}\right)\right\}dz. \end{aligned} \tag{B.2-6}$$

Crunching out the convolution integrals for the third and fourth order scattered field amplitudes give

$$a_3(t,z,z_0)dz = A(t)\left[\left(\frac{\Gamma_s z}{4\hbar L}\right)^2\frac{1}{2!}\right]\left\{\frac{t^2}{2!}\left(1 + e^{-i\Delta\omega t}\right) + \frac{3t}{i\Delta\omega}\left(1 - e^{-i\Delta\omega t}\right)\right\}dz \tag{B.2-7}$$

and $$a_4(t,z,z_0)dz = A(t)\left[-\left(\frac{\Gamma_s z}{4\hbar L}\right)^3\frac{1}{3!}\right]\left\{\frac{t^3}{3!}\left(1+e^{-i\Delta\omega t}\right)+\frac{4t^2}{(i\Delta\omega)2!}\left(1-e^{-i\Delta\omega t}\right)\right.$$

$$\left.+\frac{2t}{(i\Delta\omega)^2}\left(1+e^{-i\Delta\omega t}\right)-\frac{4}{(i\Delta\omega)^3}\left(1-e^{-i\Delta\omega t}\right)\right\}dz. \quad \text{(B.2-8)}$$

The sum of the scattering terms up to fourth order can be expressed in a series expansion in $1/i\Delta\omega$:

$a_1 + a_2 + a_3 + a_4 + \cdots =$

$$= A(t)\left(1+e^{-i\Delta\omega t}\right)\left\{1-\left(\frac{\Gamma_s zt}{4\hbar L}\right)+\left(\frac{\Gamma_s zt}{4\hbar L}\right)^2\frac{1}{(2!)^2}-\left(\frac{\Gamma_s zt}{4\hbar L}\right)^3\frac{1}{(3!)^2}+\cdots\right\} \quad (1)$$

$$+A(t)\frac{\left(1-e^{-i\Delta\omega t}\right)}{(i\Delta\omega)}\left\{-2\left(\frac{\Gamma_s z}{4\hbar L}\right)+3t\left(\frac{\Gamma_s z}{4\hbar L}\right)^2\frac{1}{2!}-\frac{4t^2}{2!}\left(\frac{\Gamma_s z}{4\hbar L}\right)^3\frac{1}{3!}+\cdots\right\} \quad (2)$$

$$+A(t)\frac{\left(1+e^{-i\Delta\omega t}\right)}{(i\Delta\omega)^2}\left\{-2t\left(\frac{\Gamma_s z}{4\hbar L}\right)^3\frac{1}{3!}+\cdots\right\} \quad (3)$$

$$+A(t)\frac{\left(1-e^{-i\Delta\omega t}\right)}{(i\Delta\omega)^3}\left\{4\left(\frac{\Gamma_s z}{4\hbar L}\right)^3\frac{1}{3!}+\cdots\right\}+\cdots. \quad \text{(B-2.9)}$$

Whether this series expansion can be expressed in a compact analytical form is unknown, but, for widely separated lines, summing all the scattering terms is unnecessary. To first order in $1/i\Delta\omega$ only the first two separate series expansions labeled (1) and (2) in the expression above need be evaluated.

Using the Bessel function identity in Eq. 6-5.20, the series expansion (1) reduces to

$$(1) \longrightarrow A(t)\left(1+e^{-i\Delta\omega t}\right)J_0\left(\sqrt{\Gamma_s zt/\hbar L}\right),$$

and (2) reduces to the simpler form

$$(2) \longrightarrow A(t)\frac{\left(1-e^{-i\Delta\omega t}\right)}{(i\Delta\omega)}\frac{\partial^2}{\partial H_0\partial t}\left[H_0 J_0\left(2\sqrt{H_0 zt}\right)\right]$$

where $$H_0 = \Gamma_s/4\hbar L. \quad \text{(B-2.10)}$$

Using the relations expressed in Eqs. B.1-9 and B.1-10 and the following Bessel function relationships

$$\frac{\partial}{\partial t}\frac{J_1\left(\sqrt{4H_0Lt}\right)}{\sqrt{4H_0Lt}} = -\frac{1}{2t}J_2\left(\sqrt{4H_0Lt}\right) \tag{B-2.11}$$

$$\frac{d}{dx}J_n(x) = \frac{1}{2}\left[J_{n-1}(x) - J_{n+1}(x)\right] \tag{B-2.12}$$

$$J_{n-1}(x) = \frac{2n}{x}J_n(x) - J_{n+1}(x), \tag{B-2.13}$$

and after a little algebra, the scattering channel field (Eq. 6-5.13) reduces, to first order in $1/i\Delta\omega$, to

$$E_{scf}(t) = E_0 e^{ikz_0}\left\{\delta(t) - e^{-i\omega_1 t - \Gamma t/2\hbar}\frac{\Gamma_s}{2\hbar}\frac{J_1\left(\sqrt{\Gamma_s t/\hbar}\right)}{\sqrt{\Gamma_s t/\hbar}}\left[\left(1+e^{-i\Delta\omega t}\right) + i\frac{\Gamma_s}{4\hbar\Delta\omega}\left(1-e^{-i\Delta\omega t}\right)\right]\right\} \tag{B-2.14}$$

Ignoring the prompt delta function pulse, the resonant intensity is then

$$I_{res}(t) = \left|E_{scf}(t) - E_0 e^{ikz_0}\delta(t)\right|^2$$

$$= 2E_0^2\left(\frac{\Gamma_s}{2\hbar}\right)^2\left[1+\left(\frac{\Gamma_s}{4\hbar\Delta\omega}\right)^2\right]\left(\frac{J_1\left(\sqrt{\Gamma_s t/\hbar}\right)}{\sqrt{\Gamma_s t/\hbar}}\right)^2\left\{1+\cos(\Delta\omega t+\phi)\right\}e^{-\Gamma t/\hbar} \tag{B-2.15}$$

$$= 4E_0^2\left(\frac{\Gamma_s}{2\hbar}\right)^2\left[1+\left(\frac{\Gamma_s}{4\hbar\Delta\omega}\right)^2\right]\left(\frac{J_1\left(\sqrt{\Gamma_s t/\hbar}\right)}{\sqrt{\Gamma_s t/\hbar}}\right)^2\cos^2\left(\frac{\Delta\omega t}{2}+\frac{\phi}{2}\right)e^{-\Gamma t/\hbar} \tag{B-2.16}$$

where $\phi = \tan^{-1}\left\{\dfrac{2\left(\Gamma_s/4\hbar\Delta\omega\right)}{1-\left(\Gamma_s/4\hbar\Delta\omega\right)^2}\right\}$. (B-2.17)

The expression above is similar to the field intensity from a plane parallel slab (described in Section 6-5) multiplied by a sinusoidal beating term due to the beating between lines having different resonant frequencies. The interesting phenomenon is the dynamical phase shift, ϕ, of the quantum beat pattern. This dynamical phase shift is related to the thickness-rate, $\Gamma_s = n\sigma_0 L\Gamma$, and the splitting between the two resonance lines, $\Delta\omega$. Thus, when the splitting is large compared to the thickness-rate, $\Delta\omega >> \Gamma_s/4\hbar$, ϕ is directly proportional to the thickness of the slab and inversely proportional to the frequency separation of the resonance lines:

$$\phi \approx \Gamma_s/2\hbar\Delta\omega = \Gamma n\sigma_0 L/2\hbar\Delta\omega \tag{B-2.18}$$

This dynamical phase shift has been seen by van Bürck *et. al.*,[1] and, in the comparison of their data with Eq. B.2-15, the time domain multiple scattering formalism accurately describes the phase shift phenomenon for all thicknesses of the sample. The calculations van Bürck *et. al.* performed to fit their data relied upon the frequency domain Fourier transform method. Unfortunately, analytically performing the Fourier transform is difficult, so the fits were done by numerically Fourier transforming the frequency response, and this prevented any insight into the physics behind the dynamical phase shift. (One can integrate the Fourier transform using the method of contour integration, but the result is a complicated series expansion requiring a laborious amount of algebra to extricate the results expressed by Eq. B.2-15). The beauty of the multiple scattering formalism is that the physics behind the scattering process can be investigated at each order of scattering.

REFERENCES

[1] U. van Bürck, D. P. Siddons, J. B. Hastings, U. Bergmann, and R. Hollatz, *Phys. Rev. B* , (To be published).

BIBLIOGRAPHY

A. Abragam and R. V. Pound, *Phys. Rev.* **92**, 943 (1953).

M. Abramowitz and I. A. Stegun, *Handbook of Mathematical Functions* (National Bureau of Standards, Washington D.C., 1972).

A. M. Afanas'ev and Y. Kagan, *Sov. Phys. JETP* **21**, 215 (1965).

Y. Aharonov and L. Susskind, *Phys. Rev.* **158**, 1237 (1967).

A. I. Akhiezer, *Quantum Electrodynamics* (Interscience Publishers, New York, 1965).

K. Alder, A. Bohr, T. Huus, B. Mottelson, and A. Winther, *Revs. Mod. Phys.* **28**, 432 (1956).

E. B. Alexandrov, *Opt. Spectrosc.* **17**, 957 (1964).

C. Alf and G. K. Wertheim, *Phys. Rev.* **122**, 1414 (1961).

A. N. Artem'ev, I. P. Perstnev, V. V. Sklyarevskii, G. V. Smirnov, and E. P. Stepanov, *Sov. Phys.-JETP* **37**, 261 (1973).

J. Arthur, G.S. Brown, D.E. Brown, and S. L. Ruby, *Phys. Rev. Lett.* **63**, 1629 (1989).

J. Arthur, D. E. Brown, S. L. Ruby, G. S. Brown, and G. K. Shenoy, *J. Appl. Phys.* **67**, 5704 (1990).

K. Bane, K. Halbach, K.-J. Kim, J. Kirz, P. Morton, H.-D. Nuhn, C. Pellegrini, J. Rosenzweig, J. Seeman, R. Tatchyn, and H. Winick, *The 2 to 4 nm High Power Linear Coherent Light Source*, Workshop on Applications of X-ray FELs (Stanford University, Stanford, Ca., 1992),

S. S. Bashkirov, N. G. Ivoilov, and V. A. Chistyakov, *Sov. Phys.-Solid State* **13**, 570 (1971).

B. W. Batterman and H. Cole, *Rev. Mod. Phys.* **36**, 681 (1964).

R. Bauminger, S. G. Cohen, A. Marinov, and S. Ofer, *Phys. Rev.* **122**, 743 (1961).

V. N. Belogurov, V. A. Bylinkin, and V. I. Mosel, *Izv. Akad. Nauk. Latv. SSR* **3**, 3 (1979 Fizika Atomnogo Yadra I Spectroskopiya Atomov I Molekul).

G. N. Belozerskii, Y. P. Khimich, and V. N. Gitsovich, *Phys. Stat. Sol. (b)*, **79**, K125 (1977).

V. A. Belyakov, *Sov. Phys. -Usp.* **18**, 267 (1975).

V. B. Berestetskii, E. M. Lifshitz, and L. P. Pitaevskii, *Quantum Electrodynamics* (Pergamon Press, Oxford, 1982), vol. 4.

I. Bernal, C. W. Struck, and J. G. White, *Acta Cryst.* **16**, 849 (1963).

P. J. Black and P. B. Moon, *Nature (London)* **188**, 481 (1960).

P. J. Black and I. P. Duerdoth, *Proc. Phys. Soc.* **84**, 169 (1964).

M. Blume and O. C. Kistner, *Phys. Rev.* **171**, 417 (1968).

A. I. Borisenko and I. E. Tarapov, *Vector and Tensor Analysis with Applications* (Dover, New York, 1968).

E. O. Brigham, *The Fast Fourier Transform* (Prentice Hall, Englewood Cliffs, 1974).

D. M. Brink and G. R. Satchler, *Angular Momentum* (Clarendon Press, Oxford, 1968).

D. E. Brown, J. Arthur, A. Q. R. Baron, G. S. Brown, and S. Shastri, *Phys. Rev. Lett.* **69**, 699 (1992).

M. Brunel and F. D. Bergevin, *Acta Cryst.* **A37**, 324 (1981).

U. van Bürck, G. V. Smirnov, R. L. Mössbauer, F. Parak, and N. A. Semioschkina, *J. Phys. C: Solid State Phys.* **11**, 2305 (1978).

U. van Bürck, G. V. Smirnov, R. L. Mössbauer, H. J. Maurus, and N. A. Semioschkina, *J. Phys. C: Solid St. Phys.* **13**, 4511 (1980).

U. van Bürck, R. L. Mössbauer, E. Gerdau, R. Rüffer, R. Hollatz, G. V. Smirnov, and J. P. Hannon, *Phys. Rev. Lett.* **59**, 355 (1987).

U. van Bürck, D. P. Siddons, J. B. Hastings, U. Bergmann, and R. Hollatz, *Phys. Rev. B*, (To be published).

W. R. Busing and H. A. Levy, *Angle Calculations for 3- and 4-Circle X-Ray and Neutron Diffractometers*, ORNL Report 4056 (Oak Ridge National Laboratory, Oak Ridge, Tenn., 1967).

A. I. Chechin, N. V. Andronova, M. V. Zelepukhin, A. N. Artem'ev, and E. P. Stepanov, *JETP Lett.* **37**, 633 (1983).

A. I. Chumakov, G. V. Smirnov, M. V. Zelepukhin, U. van Bürck, E. Gerdau, R. Rüffer, and H. D. Rüter, *Europhys. Lett.* **17**, 269 (1991).

A. I. Chumakov, G. V. Smirnov, M. V. Zelepukhin, U. van Bürck, E. Gerdau, R. Rüffer, and H. D. Rüter, *Hyp. Int.* **71**, 1341 (1992).

R. L. Cohen, G. L. Miller, and K. W. West, *Phys. Rev. Lett.* **41**, 381 (1978).

C. Cohen-Tannoudji, B. Diu, and F. Laloë, *Quantum Mechanics* (Wiley, New York, 1977).

R. Colella, *Acta Cryst.* **A30**, 413 (1974).

D. T. Cromer and D. Liberman, *J. Chem. Phys.* **53**, 1891 (1970).

A. S. Davydov, *Quantum Mechanics* (Pergamon Press, Oxford, 1985).

R. H. Dicke, *Phys. Rev.* **93**, 99 (1954).

R. Diehl, *Solid St. Commun.* **17**, 743 (1975).

P. A. M. Dirac, *The Principles of Quantum Mechanics* (Clarendon Press, Oxford, 1958).

J. N. Dodd, R. D. Kaul, and D. M. Warrington, *Proc. Phys. Soc. (London)* **84**, 176 (1964).

I. Dzyaloshinsky, *Phys. Chem. Solids* **4**, 241-255 (1958).

A. Y. Dzyublik, *Phys. Stat. Sol. (b)* **123**, 53 (1984).

A. R. Edmonds, *Angular Momentum in Quantum Mechanics* (Princeton University Press, Princeton, N. J., 1960).

M. Eibschutz and M. E. Lines, *Phys. Rev. B* **7**, 4907 (1973).

C. Fabre, M. Gross, and S. Haroche, *Opt. Comm.* **13**, 393 (1975).

G. Faigel, D. P. Siddons, J. B. Hastings, P. E. Haustein, and J. R. Grover, *Phys. Rev. Lett.* **58**, 2699 (1987).

G. Faigel, D. P. Siddons, J. B. Hastings, P. E. Haustein, J. R. Grover, and L. E. Berman, *Phys. Rev. Lett.* **61**, 2794 (1988).

H. Frauenfelder, D. E. Nagle, R. D. Taylor, D. R. F. Cochran, and W. M. Visscher, *Phys. Rev.* **126**, 1065 (1962).

H. Frauenfelder, *The Mössbauer Effect* (W. A. Benjamin, New York, 1962).

H. Frauenfelder, *Subatomic Physics* (Prentice-Hall, Englewood Cliffs, N.J., 1974).

A. J. Freeman and R. B. Frankel, *Hyperfine Interactions* (Academic Press, New York, 1967).

B. S. Garbow, (Applied Mathematics Division of Argonne National Laboratory, Netlib%ANL-MCS.ARPA, 1983)

E. Gerdau, R. Rüffer, H. Winkler, W. Tolksdorf, C. P. Klages, and J. P. Hannon, *Phys. Rev. Lett.* **54**, 835 (1985).

E. Gerdau, R. Rüffer, R. Hollatz, and J. P. Hannon, *Phys. Rev. Lett.* **57**, 1141 (1986).

E. Gerdau and R. Rüffer, *Hyp. Int.* **27**, 59 (1986).

V. I. Goldanskii and R. H. Herber, *Chemical Applications of Mössbauer Spectroscopy* (Academic Press, New York, 1968).

M. L. Goldberger and K. M. Watson, *Collision Theory* (Wiley, New York, 1964).

W. Gornik, D. Kaiser, W. Lange, J. Luther, and H. H. Schulz, *Opt. Comm.* **6**, 327 (1972).

D. M. Gualtieri, W. Lavender, and S. L. Ruby, *J. Appl. Phys.* **63**, 3795 (1988).

F. Halzen and A. D. Martin, *Quarks and Leptons* (Wiley, New York, 1984).

W. C. Hamilton, *International Tables for X-Ray Crystallography* , edited by J. A. Ibers and W. C. Hamilton (Kynoch Press, Birmingham, England, 1974), vol. 4, pp. 275.

J. P. Hannon and G. T. Trammell, *Phys. Rev. Lett.* **21**, 726 (1968).

J. P. Hannon and G. T. Trammell, *Phys. Rev.* **169**, 169 (1968).

J. P. Hannon and G. T. Trammell, *Phys. Rev.* **186**, 306 (1969).

J. P. Hannon, N. J. Carron, and G. T. Trammell, *Phys. Rev. B* **9**, 2791 (1974).

J. P. Hannon, N. J. Carron, and G. T. Trammell, *Phys. Rev. B* **9**, 2810 (1974).

S. Haroche, J. A. Paisner, and A. L. Schawlow, *Phys. Rev. Lett.* **33**, 948 (1974).

S. Haroche, M. Gross, and M. Silverman, *Phys. Rev. Lett.* **33**, 1063 (1974).

S. Haroche, *High-Resolution Laser Spectroscopy* , edited by K. Shimoda, (Springer Verlag, Berlin, 1976) p. 253.

W. Heitler, *The Quantum Theory of Radiation* (Clarendon Press, Oxford, 1954).

A. Hese, A. Renn, and H. S. Schweda, *Opt. Comm.* **20**, 385 (1977).

R. Hollatz, W. Sturhahn, H. D. Rüter, and E. Gerdau, *Influence of Relative Phase Factors between Inequivalent Sites of Single Crystals on Mössbauer Experiments*, International Conference on the Applications of the Mössbauer Effect (Budapest, Hungary, 1989), vol. 2, p. 14.11.

R. M. Housley, R. W. Grant, and U. Gonser, *Phys. Rev.* **178**, 514 (1969).

T. Ishikawa, Y. Yoda, K. Izumi, C. K. Suziki, X. W. Zhang, M. Ando, and S. Kikuta, *Rev. Sci. Instrum.* **63**, 1015 (1992).

J. D. Jackson, *Classical Electrodynamics* (Wiley, New York, 1975).

R. W. James, *The Optical Principles of the Diffraction of X-Rays* (Ox Bow Press, Woodbridge, Conn., 1982).

Y. Kagan, A. M. Afanas'ev, and I. P. Perstnev, *Sov. Phys. JETP* **27**, 819 (1968).

Y. Kagan, A. M. Afanas'ev, and V. G. Kohn, *J. Phys. C* **12**, 615 (1979).

S. Kikuta, Y. Yoda, Y. Kudo, K. Izumi, T. Ishikawa, C. K. Suzuki, H. Ohno, H. Takei, K. Nakayama, X. W. Zhang, T. Matsushita, S. Kishimoto, and M. Ando, *Jpn. J. App. Phys.* **30**, L 1686 (1991).

P. P. Kovalenko, V. G. Labushkin, V. V. Rudenko, V. A. Sarkisyan, and V. N. Seleznev, *JETP Lett.* **26**, 85 (1977).

P. P. Kovalenko, V. G. Labushkin, A. K. Ovsepyan, E. R. Sarkisov, E. V. Smirnov, A. R. Prokopov, and V. N. Seleznev, *Sov. Phys. Solid State* **26**, 1849 (1984).

W. Kuhn, *Phil. Mag.* **8**, 625 (1929).

M. Lax, *Rev. Mod. Phys.* **23**, 287 (1951).

C. M. Lederer and V. S. Shirley, *Table of Isotopes* (Wiley, New York, 1978).

R. L. Liboff, *Introductory Quantum Mechanics* (Holden-Day, San Francisco, 1980).

B. A. Lippmann and J. Schwinger, *Phys. Rev.* **79**, 469 (1950).

S. P. Lloyd, *Phys. Rev.* **81**, 161 (1951).

P. R. Locher and S. Geschwind, *Phys. Rev.* **139**, A991 (1965).

F. J. Lynch, R. E. Holland, and M. Hamermesh, *Phys. Rev.* **120**, 513 (1960).

I. S. Lyubutin, E. F. Makarov, and V. A. Povitskii, *Sov. Phys. JETP* **26**, 44 (1967).

C. H. MacGillavry and G. D. Rieck, *International Tables for X-Ray Crystallography* (Kynoch Press, Birmingham, England, 1968), vol. 3.

S. Margulies and J. R. Ehrman, *Nucl. Instr. and Meth.* **12**, 131 (1961).

J. Mathews, *Tensor Spherical Harmonics* (California Institute of Technology, 1981).

E. Matthias, W. Schneider, and R. M. Steffen, *Phys. Rev.* **125**, 261 (1962).

E. Matthias, W. Schneider, and R. M. Steffen, *Arkiv Fur Fysik* **24**, 97 (1963).

H. J. Maurus, U. van Bürck, G. V. Smirnov, and R. L. Mössbauer, *J. Phys. C: Solid State Phys.* **17**, 1991 (1984).

W. H. McMaster, N. K. D. Grande, J. H. Mallett, J. H. Hubbell, and National Bureau of Standards, *Compilation of X-Ray Cross Sections*, UCRL Report 50174, Sec. III, Rev. 1 (Lawrence Radiation Laboratory, University of California, Livermore, Ca., 1969).

A. Messiah, *Quantum Mechanics* (Wiley, New York, 1962), vol. 2.

R. M. Mirzababaev, G. V. Smirnov, V. V. Sklyarevskii, A. N. Artemev, A. N. Izrailenko, and A. V. Babkov, *Phys. Lett.* **37A**, 441 (1971).

C. Moler and J. Dongarra, (Applied Mathematics Division of Argonne National Laboratory, Netlib%ANL-MCS.ARPA, 1978)

R. L. Mössbauer, *Z. Physik* **151**, 124 (1958).

R. Nathans, S. J. Pickart, H. A. Alperin, and P. J. Brown, *Phys. Rev.* **136**, A 1641 (1964).

I. I. Nikolaev, L. S. Pavlyukov, and V. P. Mar'in, *Sov. Phys. Solid State* **17**, 1016 (1975).

S. Ogawa and S. Morimoto, *J. Phys. Soc. Jpn.* **17**, 654 (1962).

A. Papoulis, *The Fourier Integral and its Applications* (McGraw-Hill, New York, 1962).

J. M. Paterson, *PEP as a Synchrotron Radiation Source: Status and Review*, SSRL ACD-NOTE **68**, (1989) [SLAC-PUB-4899, March 1989].

M. P. Petrov, G. A. Smolensky, A. P. Paugurt, and S. A. Kizhaev, *Nuclear Magnetic Resonance and Magnetic Properties of* $FeBO_3$*-Type Crystals*, edited by J. C. D. Graham, J. J.Rhynes, Proceedings of the Seventeenth Conference on Magnetism and Magnetic Materials (AIP, New York, 1971), p. 379.

R. V. Pound, *Phys. Rev.* **79**, 685 (1950).

R. S. Preston, S. S. Hanna, and J. Heberle, *Phys. Rev.* **128**, 2207 (1962).

H. Rauch, A. Zeilinger, G. Badurek, and A. Wilfing, *Phys. Lett.* **54A**, 425 (1975).

J. S. Rollett, *Computing Methods in Crystallography* (Pergamon Press, Oxford, 1965).

M. E. Rose, *Elementary Theory of Angular Momentum* (Wiley, New York, 1957).

S. L. Ruby, *J. Phys. (Paris) Colloq.* **6**, 209 (1974).

R. Rüffer, E. Gerdau, and R. Hollatz, *Phys. Rev. Lett.* **58**, 2359 (1987).

H. D. Rüter, R. Hollatz, W. Sturhahn, and E. Gerdau, *Dependence of Nuclear Diffraction on the Azimuthal Angle:* [0 0 2]- *and* [0 0 10]- *Reflections of* YIG, International Conference on the Applications of the Mössbauer Effect (Budapest, Hungary, 1989), vol. 2, p. 14.19.

H. D. Rüter, R. Rüffer, R. Hollatz, W. Sturhahn, and E. Gerdau, *Hyp. Int.* **58**, 2477 (1990).

J. J. Sakurai, *Advanced Quantum Mechanics* (Addison-Wesley, Reading, Mass., 1967).

L. I. Schiff, *Phys. Rev.* **70**, 761 (1946).

L. I. Schiff, *Quantum Mechanics* (McGraw-Hill, New York, 1968).

E. J. Seppi and F. Boehm, *Phys. Rev.* **128**, 2334 (1962).

Q. Shen, *Acta Cryst.* **A42**, 525 (1986).

C. G. Shull, W. A. Strauser, and E. O. Wollan, *Phys. Rev.* **83**, 333 (1951).

D. P. Siddons, J. B. Hastings, G. Faigel, L. E. Berman, P. E. Haustein, and J. R. Grover, *Phys. Rev. Lett.* **62**, 1384 (1989).

G. V. Smirnov, V. V. Sklyarevskii, R. A. Voskanyan, and A. N. Artem'ev, *JETP Lett.* **9**, 123 (1969).

G. V. Smirnov, V. V. Sklyarevskii, A. N. Artem'ev, and R. A. Voscanyan, *Phys. Lett.* **32A**, 532 (1970).

G. V. Smirnov, V. V. Mostovoi, Y. V. Shvyd'ko, V. N. Seleznev, and V. V. Rudenko, *Sov. Phys. JETP* **51**, 603 (1980).

G. V. Smirnov, Y. V. Shyvd'ko, and E. Realo, *JETP Lett.* **39**, 41 (1984).

P. B. Smith and P. M. Endt, *Phys. Rev.* **110**, 397 (1958).

R. M. Steffen and H. Frauenfelder, *Perturbed Angular Correlations*, edited by E. Karisson, E. Matthias, K. Siegbahn (North-Holland, Amsterdam, 1964).

H. Sugawara, *The Tristan Super Light Facility*, KEK Progress Report 92-1 (National Laboratory for High Energy Physics, Tsukuba, Japan, 1992).

C. P. Swann and F. R. Metzger, *Phys. Rev.* **108**, 982 (1957).

G. T. Trammell, *Phys. Rev.* **126**, 1045 (1962).

V. K. Voitovetskii, I. L. Korsunskii, A. I. Novikov, and Y. F. Pazhin, *Sov. Phys. JETP* **27**, 729 (1968).

V. K. Voitovetskii, I. L. Korsunskii, Y. F. Pazhin, and R. S. Silakov, *JETP Lett.* **12**, 212 (1970).

B. E. Warren, *X-Ray Diffraction* (Dover, New York, 1990).

M. Weissbluth, *Atoms and Molecules* (Academic Press, New York, 1978).

S. A. Werner, R. Colella, A. W. Overhauser, and C. F. Eagen, *Phys. Rev. Lett.* **35**,1053 (1975).

H. Wiedemann, *Storage Ring Optimization,* Handbook on Synchrotron Radiation, vol. 3, edited by G. S. Brown and D. E. Moncton (North-Holland, Amsterdam, 1991).

H. Winick, *Synchrotron Radiation*, Physics of Particle Accelerators (AIP Conference Proceedings No. **184**), vol. 2, edited by M. Month and M. Dienes (American Institute of Physics, New York, 1989)

H. Winkler, R. Eisberg, E. Alp, R. Rüffer, E. Gerdau, S. Lauer, A. X. Trautwein, M. Grodzicki, and A. Vera, *Z. Phys. B* **49**, 331 (1983).

R. W. G. Wyckoff, *Crystal Structures* , vol. 2. & 3 (Robert E. Krieger, Malabar, Florida, 1982).

W. H. Zachariasen, *Theory of X-Ray Diffraction in Crystals* (Dover, New York, 1945).

V. S. Zasimov, R. N. Kuz'min, and A. Yu. Aleksandrov, *Sov. Phys. Solid State* **17**, 2044 (1976).

X. W. Zhang, T. Mochizuki, H. Sugiyama, S. Yamamoto, H. Kitamura, T. Sioya, M. Ando, Y. Yoda, T. Ishikawa, S. Kikuta, and C. K. Suzuki, *Rev. Sci. Instrum.* **63**, 404 (1992).

END

DATE FILMED

8/12/93